

ADVANCES IN HEAT TRANSFER

Volume 43

Advances in **HEAT TRANSFER**

Volume Editors/Serial Editors

Young I. Cho

*Department of Mechanical Engineering and Mechanics
Drexel University
Philadelphia, Pennsylvania*

and

George A. Greene

*Energy Sciences and Technology
Brookhaven National Laboratory
Upton, New York*

Volume 43

Founding Editors

Thomas F. Irvine, Jr. *State University of New York at Stony Brook, Stony Brook, NY*

James P. Hartnett *University of Illinois at Chicago, Chicago, IL*



ELSEVIER

AMSTERDAM • BOSTON • HEIDELBERG • LONDON
NEW YORK • OXFORD • PARIS • SAN DIEGO
SAN FRANCISCO • SINGAPORE • SYDNEY • TOKYO
Academic Press is an imprint of Elsevier



Academic Press is an imprint of Elsevier
525 B Street, Suite 1900, San Diego, CA 92101-4495, USA
225 Wyman Street, Waltham, MA 02451, USA
32 Jamestown Road, London NW1 7BY, UK
Radarweg 29, PO Box 211, 1000 AE Amsterdam, The Netherlands

First edition 2011

Copyright © 2011 Elsevier Inc. All rights reserved

No part of this publication may be reproduced, stored in a retrieval system or transmitted in any form or by any means electronic, mechanical, photocopying, recording or otherwise without the prior written permission of the publisher

Permissions may be sought directly from Elsevier's Science & Technology Rights Department in Oxford, UK: phone (+44) (0) 1865 843830; fax (+44) (0) 1865 853333; email: permissions@elsevier.com. Alternatively you can submit your request online by visiting the Elsevier web site at <http://www.elsevier.com/locate/permissions>, and selecting *Obtaining permission to use Elsevier material*

Notice

No responsibility is assumed by the publisher for any injury and/or damage to persons or property as a matter of products liability, negligence or otherwise, or from any use or operation of any methods, products, instructions or ideas contained in the material herein. Because of rapid advances in the medical sciences, in particular, independent verification of diagnoses and drug dosages should be made

British Library Cataloguing in Publication Data

A catalogue record for this book is available from the British Library

Library of Congress Cataloging-in-Publication Data

A catalog record for this book is available from the Library of Congress

ISBN: 978-0-12-381529-3

ISSN: 0065-2717

For information on all Academic Press publications
visit our website at elsevierdirect.com

Printed and bound in USA

11 12 10 9 8 7 6 5 4 3 2 1

Working together to grow
libraries in developing countries

www.elsevier.com | www.bookaid.org | www.sabre.org

ELSEVIER

BOOK AID
International

Sabre Foundation

CONTENTS

Contributors	ix
Preface	xi

Pool Boiling Critical Heat Flux in Dielectric Liquids and Nanofluids

MEHMET ARIK, ALI KOŞAR, HUSEYİN BOSTANCI, AND AVRAM BAR-COHEN

I. Introduction	1
II. Parametric Effects on CHF	5
A. Subcooling Effects.....	6
B. Pressure Effects.....	13
C. Heater Thermal Properties.....	15
D. Heater Characteristic Length.....	22
E. Heater Surface Effect.....	24
F. Effect of Surface Orientation.....	44
G. Dielectric Liquid Mixtures	46
H. Dissolved Gas Effects.....	48
I. Effects of Nanofluids.....	49
III. Conclusions	67
References.....	70

Thermofluid Dynamics of Boiling in Microchannels

PART I

SUJOY KUMAR SAHA AND GIAN PIERO CELATA

I.1. Introduction.....	77
I.2. Flow Pattern and Bubble Growth	82
I.2.1 Bubble Behavior in a Narrow Channel.....	84
I.2.2 Flow Regime Transition	85
I.2.3 Bubble Behavior	93
I.3. Heat Transfer with Models	99
I.3.1 Saturated Boiling Correlation.....	105
I.3.2 Size Effect Mechanism.....	112
I.3.3 Boiling Curves and Heat Transfer Coefficients.....	113

I.3.4 Electric Double Layer	122
I.3.5 Boiling Curve and Local Heat Transfer Coefficient	123
I.3.6 Heat Transfer Coefficient Along the Tube Perimeter	125
I.3.7 Parametric Analyses of the Experimental Results	127
I.4. Pressure Drop	134
I.4.1 Flow Compressibility Effect	135
I.4.2 Effect of Surface Roughness	136
I.4.3 Variation of Predominant Forces	137
I.4.4 Variation of Other Predominant Factors	137
I.5. Instability	150
Nomenclature	156
Greek Symbols	158
Subscript	159

PART II

SATISH G. KANDLIKAR

II.1. Onset of Nucleate Boiling	159
II.1.1 Introduction	159
II.1.2 Pressure–Temperature Relationship in a Vapor Bubble	159
II.1.3 Bubble Nucleation on a Heated Surface	160
II.1.4 Nucleation in Microchannels	164
II.2. Void Fraction	172
II.2.1 Introduction	172
II.2.2 Influence of Flow Pattern on Void Fraction	174
II.2.3 Void Fraction Studies in Microchannels	176
II.2.4 Concluding Remarks	183
II.3. Liquid Film Thickness	184
II.3.1 Introduction	184
II.3.2 Challenges in Liquid Film Thickness Measurement	184
II.3.3 Liquid Film Measurement and Results	185
II.3.4 Concluding Remarks	190
II.4. Critical Heat Flux	190
II.4.1 Introduction	190
II.4.2 CHF Mechanisms During Flow Boiling in Microchannels	191
II.4.3 CHF Correlations	200
II.4.4 Concluding Remarks	200
II.5. Conclusions and Research Directions	200
II.5.1 Conclusions	200
II.5.2 Research Directions	203
Nomenclature	206
Greek Symbols	207
Subscripts	208
References	208

Direct Contact Condensation of Steam Jet in a Pool

CHUL-HWA SONG AND YEON-SIK KIM

I. Introduction	227
II. Steam Condensation Regime Map	229
III. Steam Jet	232
A. Shape of Steam Cavity	232
B. Expansion Ratio of Steam Cavity	237
C. Length of Steam Cavity	237
D. Thermal—Hydraulic Condition of Steam Cavity	240
E. Steam Jet Condensation Load	244
IV. Interfacial Transport Phenomena	249
A. Interfacial Heat Transfer Coefficient (HTC)	249
B. Interfacial Transport Model	250
V. Steam Jet-induced Turbulent Jet Flow	252
A. Measurement of Turbulent Jet Flow	252
B. Analysis of Steam Jet	262
VI. Pool Mixing Analysis	269
A. Review of Recent Works	269
B. Pool Mixing Issues and Future Works	279
VII. Conclusion	281
Acknowledgments	282
Nomenclature	282
Greek	284
Subscripts	285
References	285

Fluid Flow and Heat Transfer from Circular and Noncircular Cylinders Submerged in Non-Newtonian Liquids

R.P. CHHABRA

I. Introduction	289
II. Scope and Organization	292
III. Governing Equations, Boundary Conditions, and Dimensionless Parameters	292
A. Forced Convection Regime ($Ri = 0$)	296
B. Mixed Convection Regime	298
C. Free Convection Regime ($Ri \rightarrow \infty$)	298
IV. Flow Regimes	302
A. Circular Cylinder	306

B. Elliptic Cylinders 319

C. Semicircular Cylinder..... 321

D. Equilateral Triangular Cylinders 323

E. Square Cylinder..... 326

V. Fluid Mechanical Aspects..... 332

 A. Circular Cylinder 332

 B. Elliptical Cylinders 351

 C. Semicircular Cylinder..... 358

 D. Equilateral Triangular Cylinder..... 362

 E. Square Cylinder..... 363

VI. Heat Transfer 369

 A. Circular Cylinder 370

 B. Elliptical Cylinders 390

 C. Semicircular Cylinder..... 392

 D. Equilateral Triangular Cylinder..... 393

 E. Square Cylinder..... 395

VII. Concluding Remarks..... 398

Acknowledgments 400

Nomenclature..... 400

Greek Letters 402

Subscripts..... 402

Abbreviations..... 402

References..... 402

Author Index 419

Subject Index 435

CONTRIBUTORS

*Numbers in parentheses indicate the pages on which
the author's contributions begin.*

- AVRAM BAR-COHEN [1], Department of Mechanical Engineering, University of Maryland, College Park, MD
- HUSEYIN BOSTANCI [1], RINI Technologies, Inc., Oviedo, FL
- R.P. CHHABRA [291], Department of Chemical Engineering, Indian Institute of Technology, Kanpur, India
- SATISH G. KANDLIKAR [79], Mechanical Engineering Department, Rochester Institute of Technology, Rochester, New York, NY
- YEON-SIK KIM [229], Korea Atomic Energy Research Institute (KAERI), Daejeon, Republic of Korea
- ALI KOŞAR [1], Mechatronics Engineering Program, Sabanci University, Tuzla, Istanbul, Turkey
- MEHMET ARIK [1], Department of Mechanical Engineering, Ozyegin University, Istanbul, Turkey
- GIAN PIERO CELATA [79], ENEA Casaccia Research Centre, Division for Advanced Technologies for Energy and Industry, S. M. Galeria, Rome, Italy
- SUJOY KUMAR SAHA [79], Mechanical Engineering Department, Bengal Engineering and Science University, Shibpur, Howrah, India
- CHUL-HWA SONG [229], Korea Atomic Energy Research Institute (KAERI), Daejeon, Republic of Korea

PREFACE

For more than 40 years, *Advances in Heat Transfer* has filled the information gap between regularly published journals and university-level textbooks. The series presents review articles on topics of current interest, starting from widely understood principles and bringing the reader to the forefront of the topic being addressed. The favorable response by the international scientific and engineering community to the 42 volumes published to date is an indication of the success of our authors in fulfilling this purpose.

In recent years, the editors have published topical volumes dedicated to specific fields of endeavor. Examples of such volumes are Volume 22 (*Bioengineering Heat Transfer*), Volume 28 (*Transport Phenomena in Materials Processing*), Volume 29 (*Heat Transfer in Nuclear Reactor Safety*), and Volume 40 (*Transport Phenomena in Plasma*). The editors intend to continue publishing topical volumes as well as the traditional general volumes in the future. Volume 32, a cumulative author and subject index for the first 32 volumes, has become a valuable tool to search the series for contributions relevant to their current research interests.

The editorial board expresses its appreciation to the contributing authors of Volume 43, who have maintained the high standards associated with *Advances in Heat Transfer*. Finally, the editors would like to acknowledge the efforts of the staff at Academic Press and Elsevier, who have maintained the attractive presentation of the volumes over the years.

Pool Boiling Critical Heat Flux in Dielectric Liquids and Nanofluids

MEHMET ARIK¹, ALI KOŞAR², HUSEYİN BOSTANCI³,
and AVRAM BAR-COHEN⁴

¹*Department of Mechanical Engineering, Ozyegin University, Istanbul, Turkey*

²*Mechatronics Engineering Program, Sabanci University, Tuzla, Istanbul, Turkey*

³*RINI Technologies, Inc., Oviedo, Florida*

⁴*Department of Mechanical Engineering, University of Maryland, College Park, MD*

I. Introduction

Boiling on a surface that is immersed in a pool of stagnant liquid is called “pool boiling” heat transfer. Boiling takes place when evaporation occurs in cavities (nucleation sites) at a liquid–solid interface and produces a succession of vapor bubbles. This mode of heat transfer occurs in a variety of applications, such as heat exchangers, immersion cooled electronic systems, metallurgical quenching processes, and water heaters for domestic use. The rate of boiling heat transfer from the heated surface to the pool varies strongly with the liquid temperature, pressure, thermophysical properties of the liquid, heater geometry, heater surface, and heater orientation. In nucleate pool boiling, the heat flux increases steeply with the surface superheat, but when the generated vapor bubbles blanket the surface, a large temperature increase on the heater surface results, leading to the critical heat flux (CHF) condition and the termination of nucleate pool boiling. This condition is also known as the burn out point and the peak or maximum heat flux, and is associated with a temperature rise of approximately several hundred degree Celsius for water and 100°C for FC-72.

In spite of the last 70 years of research and numerous published papers, CHF still defies an accurate prediction. One of the earliest CHF models was proposed by Rohsenow and Griffith [1]. It was based on a bubble packing model. According to this model, CHF is initiated by the coalescence of discrete bubbles or columns into a large vapor mushroom leading to dry out of the liquid film on the heated surface. The empirical data

showed a linear relationship on log–log coordinates, leading to a CHF correlation given as:

$$\text{CHF}_{\text{R-G}} = 143(f_l/h) \left[\frac{(\rho_l - \rho_v)}{\rho_v g} \right]^{0.6} \rho_v h_{fg} \left(\frac{a}{g} \right)^{0.25} \quad (1)$$

The indicated gravitational term was subsequently introduced by Rohsenow [2] on the basis of observed bubble departure frequency and diameter. This correlation has been widely used by many researchers to predict CHF in saturated liquids, but does not account for heater geometry or properties, nor does it deal with fluid mixtures.

Later, pioneering studies served to provide a theoretical underpinning for the prediction of the CHF in nucleate boiling. Two major schools of thought have emerged on the controlling mechanism of CHF, classified as hydrodynamic instability models and surface-controlled CHF models, respectively. The first theoretical model of CHF is today known as the Kutateladze–Zuber model [3]. In this model, CHF is dictated by instability in the vapor–liquid interface of the vapor jets emanating from the heater surface in the high flux region of the nucleate boiling curve. It is postulated that the vertical coalescence of vapor bubbles in fully developed nucleate boiling results in the formation of cylindrical vapor columns or jets. Within these columns, there is an upward flow of vapor, and the jets are separated by counterflowing columns of liquid, as seen in Fig. 1.

In this model, jet breakdown leads to vapor blanketing of the surface and results in CHF. In a power-controlled system, this mechanism causes a drastic surface temperature increase, while in a temperature-controlled system, it dictates a reduction in the heat removal rate. Kutateladze obtained a relationship for CHF by solving the momentum and energy equations for

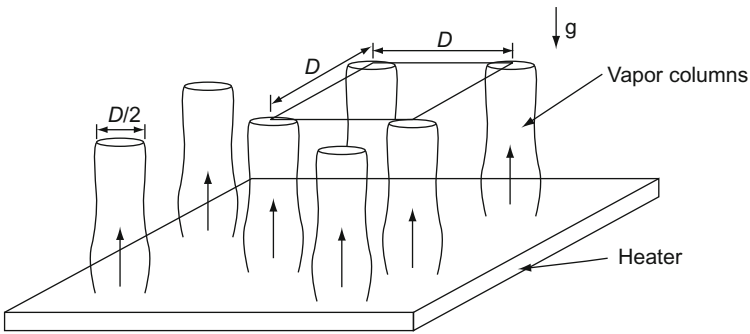


Fig. 1. Idealized liquid–vapor configuration in the Kutateladze–Zuber model.

two-phase flow near the heater. Later, Zuber assumed that CHF was controlled by hydrodynamic instability and derived an expression for CHF. This model assumes a horizontal heater surface of infinite extent, so there is no characteristic length. Accordingly, CHF can be expressed as:

$$\text{CHF}_{(K-Z)} = \frac{\pi}{24} h_{fv} \sqrt{\rho_v} \left[\frac{\sigma_f g (\rho_f - \rho_v)}{\rho_v^2} \right]^{1/4} \quad (2)$$

In this early, but very much accepted model, CHF is assumed to be only a function of the hydrodynamic instability and the heater surface properties and temperature do not enter into consideration. In that era, boiling research was driven largely by nuclear reactor cooling, using heat-flux-controlled heaters, and placed the emphasis on preventing catastrophic failure. Controlling surface temperature and determining the post-CHF changes in heat flux were of less interest than controlling heat flux and measuring the resulting surface temperatures.

Some of the early studies [4,5] interestingly described the existence of a thin liquid film under the large vapor columns/mushrooms which were observed on the heater surface and suggested that this thin liquid film, or macrolayer, might affect the CHF phenomena. The second CHF model was proposed by Haramura and Katto [6] and is known as the macrolayer model. This model focuses on the existence of a vapor mushroom hovering above the heater surface, caused by the coalescence of vapor bubbles, and postulates the existence of a thin layer of liquid trapped under the vapor mushroom and separating the “vapor stems” emanating from active nucleation sites and feeding vapor to the mushroom. The time period between the start of growth of the vapor mushroom and its departure from the surface is called the hovering period. The macrolayer thickness was determined to be 25% of the Helmholtz wavelength. CHF is thought to occur when the macrolayer is completely evaporated in one hovering period (i.e., τ_d). When evaporation, resulting from heat addition, depletes the liquid layer, the surface dries out as illustrated in Fig. 2 and CHF occurs. Based on this model, Haramura and Katto [6] proposed the following relationship for CHF:

$$\frac{\text{CHF}_{(H-K)}}{h_{fv} \sqrt{\rho_v} [\sigma_f (\rho_f - \rho_v) g]^{1/4}} = 0.7206 \left[\frac{1 + (\rho_f / \rho_v)}{1 + (11/16)(\rho_f / \rho_v)} \right] \left(\frac{A_v}{A_h} \right)^{5/8} \left(1 - \frac{A_v}{A_h} \right)^{5/16} \quad (3)$$

Their model still retained the basic elements (i.e., hydrodynamic instability) of the Zuber model. However, the controlling instabilities in this model did not occur on the walls of the large vapor columns but on the walls of the tiny

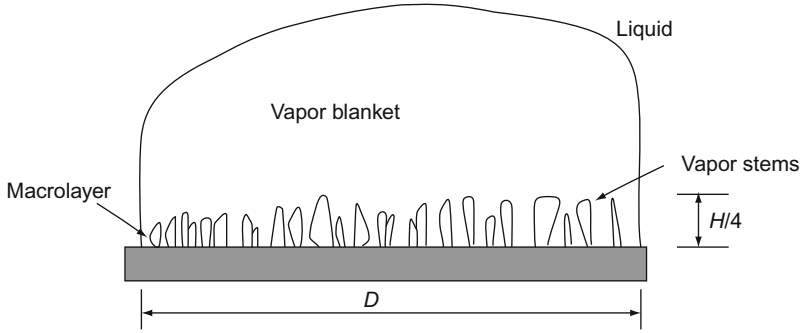


FIG. 2. Proposed macrolayer model by Haramura–Katto [6].

vapor stems around active nucleation sites that are interspersed in the liquid macrolayer on the heated surface.

As a consequence of using a semiempirical coefficient tailored to database previously used by Zuber [3], the results obtained from Eq. (3) are identical to the Kutateladze–Zuber prediction of CHF. As with any proposed predictive model for CHF, this model has some drawbacks as well. For example, the Helmholtz wavelength is too large to obtain complete dry out in one hovering period. Further, the role of the heater in causing the instability is not clear. However, this model refocused the attention of the scientific community on the region near the heater wall.

The study performed by Nishio et al. [117] focused on boiling structures near CHF. Bubble generation on the surface near the CHF point was found to be different from the physical image given by macrolayer model where vapor stems of small diameters are attached on the surface [7] and to reveal a bubble sublayer in the thin liquid film attached to the heated surface.

Although the effects of fluid properties, pressure, and subcooling, as well as heater geometry, on the pool boiling CHF are relatively well established, explanations for the surface property effects remain controversial. A composite correlation, accounting for the conduction and hydrodynamic limits, as well as the effects of pressure, subcooling, and length, was proposed by Arik and Bar-Cohen [8]. Their effort was devoted to extending the existing Thermal Management of Electronics (TME) pool boiling CHF correlation for horizontal square heaters and to embody an assumed dependence of CHF on the product of the heater thermal effusivity and thickness. The effusivity-based correlation, Eq. (4), was found to predict a broad range of pool boiling CHF data for dielectric liquids, for thermal effusivity values between 0.2 and 120, pressure from 100 to 450 kPa, and subcoolings from 0 to 75 K, with a standard deviation of 12.5% and a 95% confidence interval.

$$\text{CHF}_{\text{TME}} = \frac{\pi}{24} h_{\text{fv}} \sqrt{\rho_v} [\sigma_f g (\rho_f - \rho_v)]^{1/4} \left(\frac{\delta \sqrt{\rho_h C_h k_h}}{\delta \sqrt{\rho_h C_h k_h} + 0.1} \right) \times [1 + < 0.3014 - 0.01507 L'(P) >] \left\{ 1 + 0.030 \left[\left(\frac{\rho_f}{\rho_v} \right)^{0.75} \frac{C_f}{h_{\text{fv}}} \right] \Delta T_{\text{sub}} \right\} \quad (4)$$

This analytical expression was able to predict CHF within $\pm 20\%$. Based on the large number of published papers, on both the original and modified Kutateladze–Zuber and Haramura–Katto models and their applications, it is clear that there is a lack of agreement on the mechanism of CHF. Recognizing that no available model provides the desired level of accuracy in CHF prediction, the hydrodynamic stability theory is experiencing a strong challenge from the macrolayer dry out formulations. Heavy reliance on embedded sensors along with the use of advanced visualization techniques, with high-speed cameras, proper light sources, and innovative optical trains, can be expected to shed new light on the physical phenomena and lead to greater understanding of boiling heat transfer fundamentals. Such understanding will be critical to the application of ebullient cooling to the emerging high-heat-flux electronic chips, in high-performance computers, game systems, high-speed memory applications, solid-state lasers, and wideband gap power electronics technologies.

II. Parametric Effects on CHF

The parametric effects on CHF can be grouped into two primary categories, those associated with the heater and those associated with the working liquid. The effects due to these two main categories can be further divided into the primary subeffects that have been extensively studied. Heater properties, heater geometry, and surface characteristics are the heater parameters of greatest interest, while pressure, bulk temperature, liquid thermophysical properties, and component concentration in mixtures are the key parameters imposed by the working liquid. The following sections will review and summarize the published results on these effects.

An extensive study of commercially available perfluorinated liquids (FC-72, FC-87, etc.), L-1402, R113, and water with platinum wire heaters was presented by Danielsen et al. [9]. With this rich selection of liquids, the authors obtained the CHF values of 22.9 W/cm² (L-1402) and 13.5 W/cm² (FC-43). CHF for saturated FC-72 at 1 atm was 18.59 W/cm² with a standard deviation of 2.4 W/cm². Saturated pool boiling curves for inert liquids differing widely in boiling points were almost identical with one another on the same heater.

Heater properties, pressure, and subcooling are some of the known features affecting the CHF [10]. Increasing the boiling point has been another novel goal to increase CHF that was proposed by Lee et al. [11]. They used a fluorocarbon coolant and reported that maximum heat flux could be increased up to 45 W/cm².

A. SUBCOOLING EFFECTS

The beneficial effect of subcooled liquid (i.e., the bulk temperature is less than the saturation temperature) on the pool boiling CHF has been well documented. The rapid condensation of vapor contained within the bubbles is thought to raise the heat flux at which vapor blanketing of the heated surface occurs. Neither the Haramura–Katto model nor the Kutateladze–Zuber relationship takes the subcooling effect into account when CHF is predicted. A large number of studies have focused on predicting the subcooling effect and combining this effect with the widely known saturated boiling CHF models. A pioneering study completed in 1951 by Kutateladze [12] suggested that the CHF in subcooled liquid should increase relative to the saturated pool boiling CHF value and depends on the Jakob number. To confirm this understanding, Kutateladze and Schneiderman [13] performed subcooling experiments with rod heaters in various liquids (i.e., water, isooctane, and ethanol). Their reported results showed that CHF increased linearly with increasing subcooling. One of the most widely quoted studies was performed by Ivey and Morris [14]. Their experimental studies were performed in water with wire heaters, and a correlation was proposed linking CHF to the Jakob number. The equation was presented as:

$$\text{CHF}_{\text{sub}} = \text{CHF}_{\text{sat}} \left[1 + 0.1 \left(\frac{\rho_v}{\rho_l} \right)^{0.25} Ja \right] \quad (5)$$

Experimental results agreed with the predictions within 25%. It is unlikely that this kind of prediction will be able to attain a lower error, since it does not account for heater length and thermal properties. Later, Elkassabgi and Lienhard [15] studied the subcooling effect extensively with four different wire heaters ($0.8 < D < 1.54$ mm) in methanol, acetone, isopropanol, and R-113. They classified subcooling into three regimes: low, moderate, and high. Different correlation coefficients were proposed for each regime. Their correlations predicted CHF within 8% for low and moderate levels of subcooling. When high subcooling occurred, CHF had the highest value and they related the upper limit of CHF to the maximum rate at which the liquid molecules would leave a two-phase interface.

CHF in dielectric liquids, for possible use in the thermal management of electronic components, has been of interest for the last two decades. Hwang and Moran [16], in one of the early studies, presented experimental results for FC-86 boiling on 4.57 mm square heaters. A subcooling range of 0–80 K was

studied on the vertically oriented heaters. An increase in CHF with increasing subcooling was observed. However, it was not as strong as proposed in Eq. (5). Later, Mudawar and Anderson [17] performed a series of experimental studies in FC-72 with square heaters. This study focused on both subcooling and vertical orientation, and determined that setting the coefficient in Eq. (5) equal to 0.064, or just 65% of the previous value, as a result of density adjustment, yielded excellent agreement with the data, and provided a standard deviation of 1.4%. You [18] investigated the subcooling effect with square heaters in gassy FC-72. He observed a linear increase in CHF with increasing subcooling and suggested a value of 0.03 for the coefficient in Eq. (5).

The effect of bulk temperature was also studied by Carvalho and Bergles [19] for boiling in a dielectric liquid, FC-72, from thin nichrome foil heaters. To simulate electronic chips, the authors also performed experiments with silicon chips (4.57 mm² with 0.38 mm thickness). They found that CHF increased by ~3% per degree of subcooling for a range of 0–31 K, and the coefficient in Eq. (5) was presented as 0.030. They also reported that subcooling was not an effective means to decrease the wall superheat at high heat fluxes. At high heat fluxes, different enhancement techniques produced approximately the same wall superheat. Bergles [20] continued to investigate subcooling effects on CHF for FC-72 boiling on a vertically oriented thin nichrome foil heater. The most notable observation was that the rate of CHF increase with subcooling diminished as the pressure increased, due to the effect of pressure on the density ratio, captured in the last term of Eq. (4). Higher pressures increased the vapor density while decreasing the liquid density.

Some of the pool boiling experiments performed by Lee et al. [11] included results of subcooled pool boiling of FC-84 and FC-104 for both pure liquids and binary mixtures with flat heaters. Subcooling was as high as 50 K, and a similar behavior to the previous studies was reported. McNeil [21] performed experiments with silicon and platinum thin film sputtered on Pyrex heaters. He reported that CHF increased linearly with subcooling. A 66% enhancement with a 20 K subcooling was observed. Watwe and Bar-Cohen [22] presented experimental results of FC-72 with plastic pin grid array (PPGA) chip package for a wide range of subcooling, spanning the range of the 0–70 K. Higher subcooling was achieved by elevating the pressure. The effect was correlated and the coefficient was given as 0.0346. The TME composite CHF correlation (precursor to Eq. (4)) was able to predict CHF within $\pm 18\%$. At higher pressures, changes in the fluid properties diminished the effect of subcooling, so that the increase in pressure from atmospheric condition to 3 bar reduced the subcooling enhancement by 40% [23].

An experimental study of boiling at high heat fluxes and very low flow velocities (4 cm/s) in subcooled liquid was completed by Brusstar et al. [24]. The authors demonstrated the effects of subcooling and the heater orientation on CHF. Since the flow velocity was low, pool boiling conditions were

assumed. Fully degassed and purified (through a special filtering and distillation procedure) refrigerant, R-113, was used. The heater surface was 19.1 mm long and 38.1 mm wide and was horizontal to maintain a constant orientation between the buoyancy force and the heater surface. Experiments were performed for a wide range of vertical orientations, and the lowest subcooling result was obtained for 45° angle. Brusstar and Merte [25] studied effects of heater surface orientation and subcooling on the CHF. They presented a model for low velocity flow and pool boiling. They modeled the effect of subcooling such that the volume of vapor produced at CHF was independent of subcooling for a given orientation. The effects of subcooling correlated well with predictions for pool boiling given by Ivey and Morris [14]. Kandlikar [26] performed a study for CHF in subcooled flow boiling. In addition to his own experimental results, more data were collected to evaluate subcooling effects in both flow and pool boiling. His results displayed a similar trend (linear increase with decreasing bulk temperature) to that reported in the literature.

The results of subcooling studies may help us conclude that the data for both vertical and horizontal rectilinear heaters appear to follow a similar slope, displaying substantially weaker dependence on subcooling than for wires.

In the experimental study of Arik [27], a linear increase of heat flux with elevated subcooling at atmospheric pressure was observed using FC-72 as the working fluid (Fig. 3). The slope of the linear trend was found to be ~ 0.29 that is very close to the coefficient given in TME correlation. The author repeated the experiments at elevated pressure (202.6 kPa) and found that the subcooling enhancements were interestingly very similar to the atmospheric pressure conditions (Fig. 4). The increased pressure did not diminish the subcooling effect. The coefficient for this case was found to be 0.29. The subcooling effect at 303.9 kPa was observed as stronger than the previous cases (Fig. 5). The coefficient of 0.316 obtained from linear curve fitting in this case was 6% higher than those under 101.3 and 202.6 kPa conditions. While these results would appear to contradict the earlier observation on the weakening benefit of subcooling at higher pressures, it should be realized that the Arik [27] results pertain to the absolute value of CHF rather than its enhancement relative to the saturated value. Since the saturated CHF increases with pressure for FC-72 in the studied range, the competing effects result—in this pressure range—in a net increase in CHF for highly subcooled liquid.

The subcooling enhancement observed for the horizontal DIP (dual inline package) was higher than that observed by Watwe [28], but similar to the findings by McNeil [21]. Watwe [28] reported that his experiments revealed a weaker subcooling effect than that of McNeil [21]. The reason for the more dominant subcooling effect can be related to the rapid condensation of rising bubbles or columns. The heater size might also be an important effect. Another factor might be the effect of the alumina substrate. DIPs have a larger

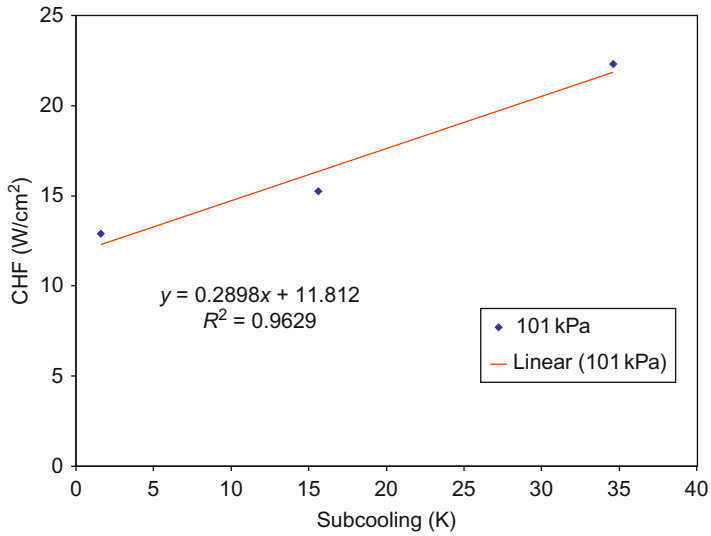


FIG. 3. Subcooling effect at $P = 101.3$ kPa [27]. For color version of this figure, the reader is referred to the web version of this book.

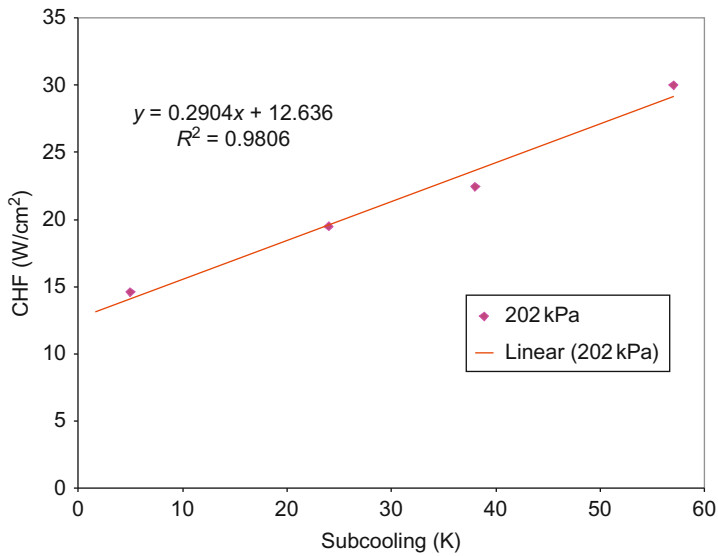


FIG. 4. Subcooling effect at $P = 202.6$ kPa [27]. For color version of this figure, the reader is referred to the web version of this book.

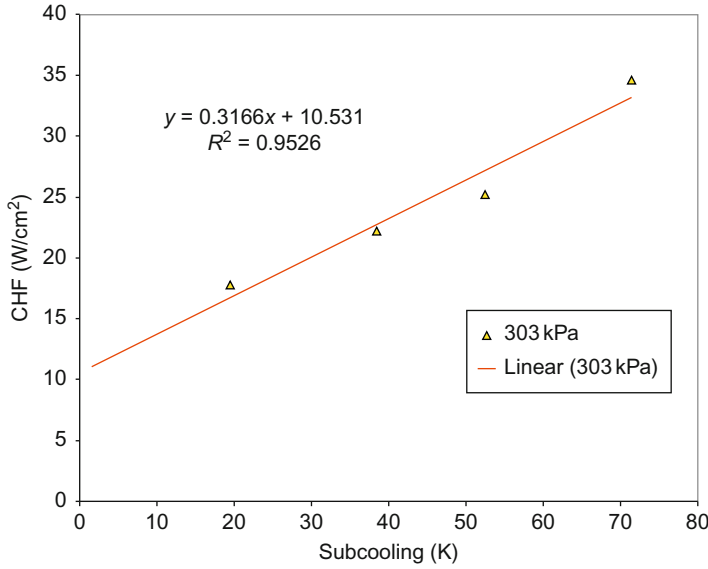


FIG. 5. Subcooling effect at $P = 303.9$ kPa [27]. For color version of this figure, the reader is referred to the web version of this book.

substrate surface area than PPGA packages. The extended surface area of the substrate might result in a much more effective flow pattern to the surface as a result of the buoyancy-induced convection.

Rainey and You [29] and Rainey et al. [30] investigated the effect of subcooling on CHF from 1 cm^2 flat and microporous-enhanced surfaces in FC-72 (Fig. 6). They operated over a broad liquid subcooling range (0–50 K). The subcooling delayed the formation of the dry out condition and thus increased CHF. They also recorded an increase in CHF with microporous surfaces. Moreover, they found that the enhancement of CHF due to the increase in subcooling was greater for microporous surfaces, consisting of aluminum particles (1–20 μm in diameter) and a binder with thickness of $\sim 50 \mu\text{m}$, than for plain surfaces (Fig. 7). Although they did not specify the total heat transfer area of the microporous surfaces, they reported that the heat transfer area enhancement with microporous surfaces was not significant. They correlated their data using a different relation for each category of working condition and surface, as listed below:

1. *Saturated conditions:*

$$\begin{aligned} \text{CHF}_{\text{sat}} &= 1.03 \times \text{CHF}_Z \text{ for plain surfaces} \\ \text{CHF}_{\text{sat}} &= 1.78 \times \text{CHF}_Z \text{ for microporous surfaces} \end{aligned} \quad (6)$$

where CHF_Z is given by Eq. (2).

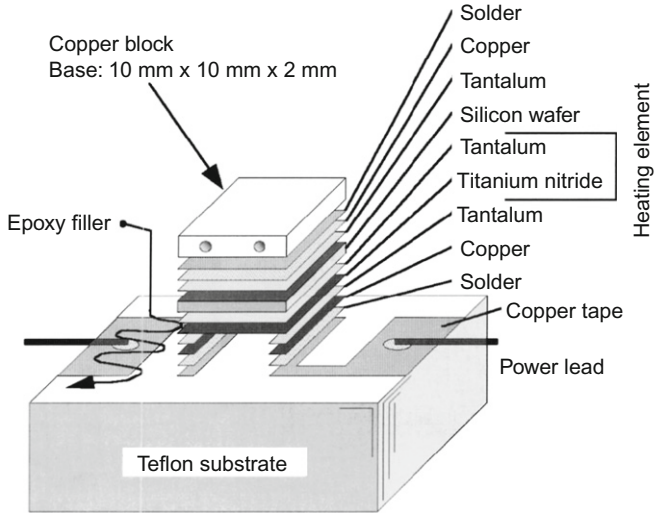


FIG. 6. Test heater design of Rainey et al. [30].

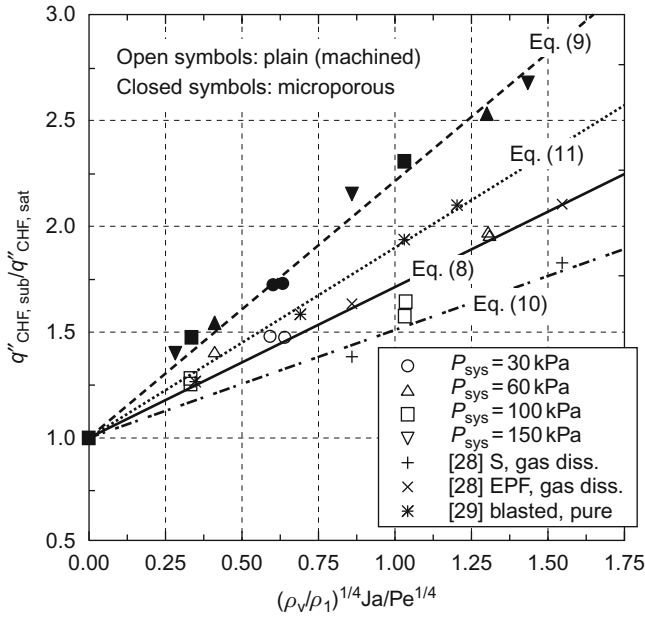


FIG. 7. Effect of subcooling on saturated CHF [30].

2. Subcooled conditions:

$$\begin{aligned} \text{CHF}_{\text{sub}} &= \text{CHF}_{\text{sat}} [1 + 0.70(\rho_v/\rho_L)^{1/4} Ja/Pe^{1/4}] \text{ for plain surfaces} \\ \text{CHF}_{\text{sub}} &= \text{CHF}_{\text{sat}} [1 + 1.20(\rho_v/\rho_L)^{1/4} Ja/Pe^{1/4}] \text{ for microporous surfaces} \end{aligned} \quad (7)$$

El-Genk and Parker [31] investigated pool boiling of saturated and subcooled HFE-7100 from both plain copper and porous graphite surfaces measuring $10 \text{ mm} \times 10 \text{ mm}$. They detected an increase in CHF with subcooling for both types of test surfaces. The CHF for the porous graphite was 31.8, 45.1, 55.9, and 66.4 W/cm^2 for saturated, 10, 20, and 30 K subcooling conditions, respectively, while the CHF for smooth copper was much lower at 21.5, 28.1, 33.7, and 37.3 W/cm^2 at corresponding conditions (Fig. 8). It could be noted that the effect of subcooling on the microporous surface was more pronounced compared to the plain copper surface. In addition, they developed the following correlations for both saturated and subcooled CHF to represent their experimental data:

$$\text{CHF}_{\text{sat}} = C_{f,w,\text{sat}} \{ \rho_v^{1/2} h_{\text{FG}} [g\sigma(\rho_L - \rho_v)]^{1/4} \} \quad (8)$$

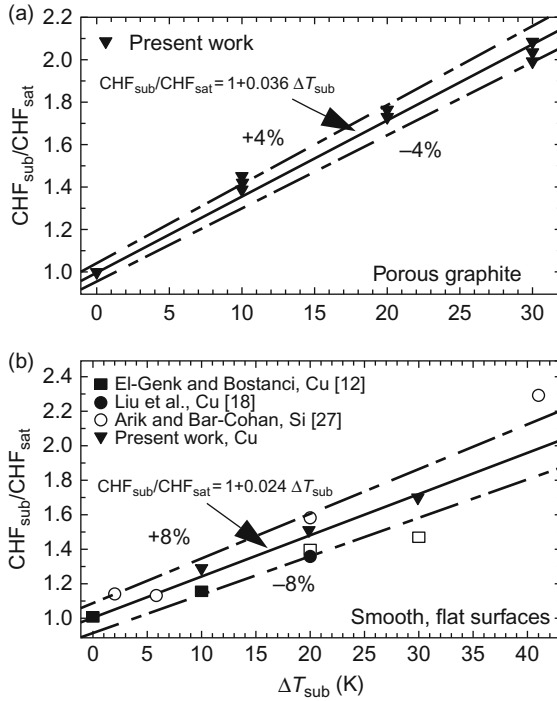


FIG. 8. Effect of liquid subcooling on CHF of HFE-7100 on smooth, flat, and porous graphite surfaces [31].

where $C_{f,w,sat} = 0.2$ and 0.296 for plain copper and porous graphite surfaces, respectively.

$$CHF_{sub} = CHF_{sat}(1 + C_{CHF,sub}\Delta T_{sub}) \quad (9)$$

where $C_{CHF,sub}$ is given as 0.024 and 0.0296 for plain copper and porous graphite surfaces, respectively.

The above correlations could predict their saturated and subcooled experimental CHF data as well as the data in the literature [8,32,33] within reasonable limits.

B. PRESSURE EFFECTS

Analytical predictions of CHF strongly depend on pressure since the correlations are defined as functions of latent heat, surface tension, and vapor and liquid densities. Both the latent heat and the surface tension decrease with increasing pressure and reach zero at the critical pressure. The liquid density has a decreasing trend with pressure, whereas vapor density increases with pressure. Figure 9 presents CHF dependence on the fluid pressure. As shown in this figure, CHF for Perfluorocarbon (PFCs) (FC-72) and Novec fluids (HFE-7100, HFE-7200) exhibit a similar dependence on pressure.

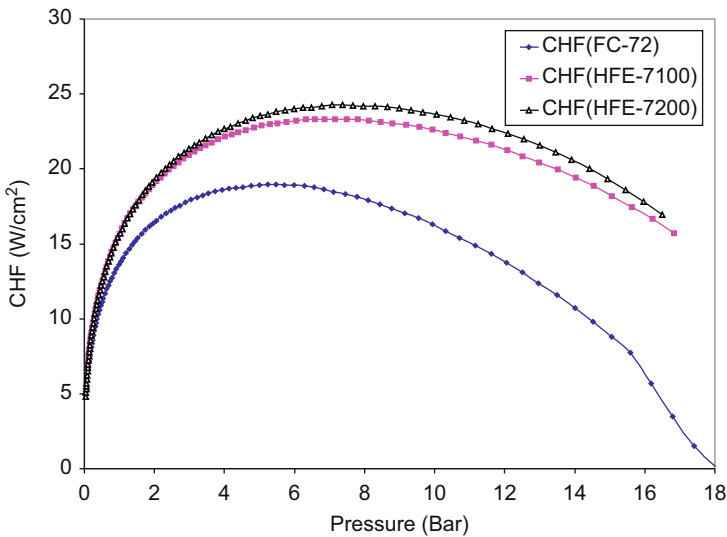


FIG. 9. Pressure effect on CHF in saturated liquids [27]. For color version of this figure, the reader is referred to the web version of this book.

Morozov [34] measured CHF on thin nichrome wire heaters in methyl isopropyl alcohol for pressures ranging from atmospheric to 0.90 of the critical pressure of the liquid. He found that CHF initially increased with increasing pressure and attained a maximum value at ~ 0.35 of the critical pressure before decreasing at higher pressures. Lienhard and Schrock [35] performed studies on pressure effects for wire heaters in water, acetone, benzene, methyl alcohol, and isopropyl alcohol environments and observed an increase in CHF values with elevated pressures similar to the previous studies [36]. They reported that the Kutateladze–Zuber correlation was able to account for the pressure effects and successfully predict CHF.

The effect of pressure on CHF for FC-72 boiling on square, vertically oriented, copper heaters has been studied by Mudawar and Anderson [17] for a pressure range of 101.3–303.9 kPa. A 23% increase in the CHF was observed with an increased pressure from atmospheric conditions to 202.7 kPa, but only an additional 3.7% increase was observed as the pressure was further raised to 303.9 kPa. Watwe [28] performed a series of experiments using a plastic pin grid array silicon heater (i.e., PPGA) immersed in FC-72 and observed similar effects of pressure on the pool boiling CHF.

Figure 9 presents the predicted variation of CHF for a pressure range of 0–20 bar based on the Kutateladze–Zuber correlation for an infinite heater and saturation condition. It may be seen that CHF for FC-72 reaches a maximum at 5.23 bar, with a CHF value of 18.9 W/cm^2 . Beyond this point, CHF decreases rapidly with increasing pressure. A similar behavior is observed for both HFE-7100 and -7200 with peak CHF values nearly 35 W/cm^2 , or approximately twice the value at 1 bar. Since surface tension is given only at the atmospheric condition for both liquids, this prediction assumes a constant value of $(13.6 \times 10^{-2} \text{ N/m})$. Further research to be performed by manufacturers is necessary to better define the properties of these liquids. However, with the known values (latent heat, liquid and vapor densities) at certain pressure and corresponding saturation temperature, the pressure effect on CHF for HFEs can be clearly described.

Rainey and You [29] and Rainey et al. [30] investigated the effect of pressure on CHF from 1 cm^2 flat and microporous-enhanced surfaces in FC-72 for a pressure range from 30 to 150 kPa, in agreement with the prevailing trend for lower operating pressure conditions reported in the literature. Figure 10 shows the CHF to increase with pressure over this range for both surfaces but with a somewhat larger slope for the microporous-enhanced surface.

Although CHF was expected to increase parabolically before reversing slope at $\sim 500 \text{ kPa}$, Arik [27] presented experimental findings revealing a substantial increase in CHF over a much larger range of elevated pressure, when combined with variable subcooling. Figure 11 illustrates the observed linear increase in CHF with pressure for several liquid temperatures. The

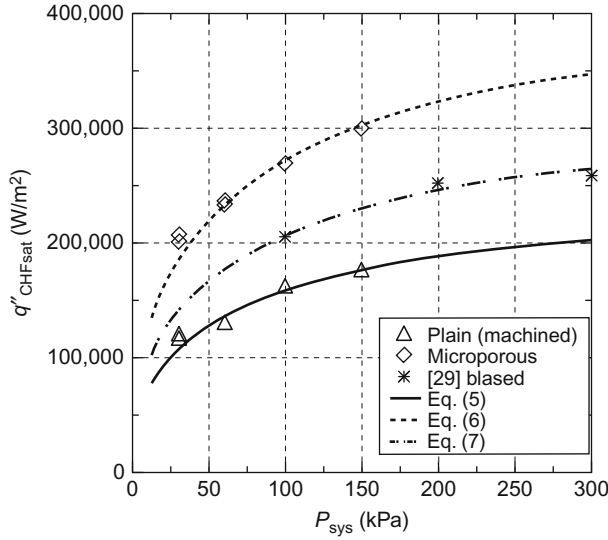


FIG. 10. Effect of pressure on saturated CHF [30].

graph also includes the curve fitting results for these three bulk temperatures. The lowest liquid temperature created the steepest slope with a coefficient of 0.0609 for 22°C, decreasing to 0.0493 for 41°C, and decreasing further to 0.0460 for 55°C. CHF was expected to have an asymptotic increasing behavior until 500 kPa. Therefore, the subcooling effect is seen to be very strong at atmospheric pressure and to decrease in impact with an elevation in pressures. It might be expected that for a fixed liquid temperature, the increased subcooling accompanying a rise in pressure would lead to higher CHF, while the decrease in latent heat, density ratio, and surface tension encountered at higher pressure would weaken CHF. It appears that the next result—in the range tested for FC-72—creates a substantial pressure-related enhancement.

C. HEATER THERMAL PROPERTIES

It has been widely known that the thermal properties of the heater, such as thickness, thermal conductivity, and specific heat, can affect pool boiling CHF. The second term on the right-hand side of Eq. (4) represents the heater effects on CHF. As seen from the TME correlation, CHF increases asymptotically with the product of the heater thickness and the square root of the thermal effusivity, reflecting the beneficial role of thermal conduction in smoothing the

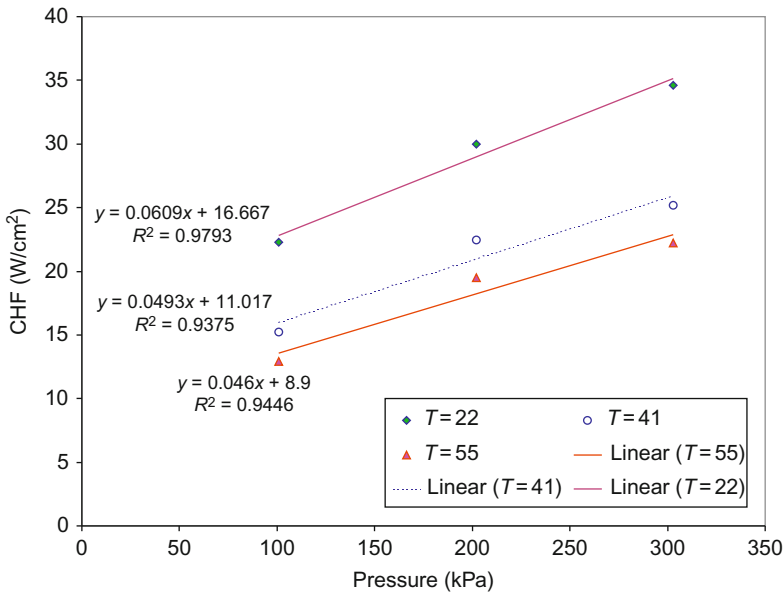


FIG. 11. Pressure effect on CHF in FC-72 for various liquid temperatures [27]. For color version of this figure, the reader is referred to the web version of this book.

surface temperature variations resulting from a nonuniform nucleation site density. Bernath [37] was the first researcher to investigate the effects of thermal properties and thickness of the heater on the CHF by observing that thicker heaters produced higher CHF than thinner structures. Later, his research on vertically oriented cylindrical heaters in water was extended to both solid and hollow cylinders. Experimental results revealed that the solid cylinders had about 43% higher CHF than hollow structures. A study employing zirconium ribbon heaters immersed in toluene was performed by Cole and Shulman [38]. Experimental results were similar to previously published studies, with 42% higher CHF for the thickest heater.

These early studies kept the attention of many researchers during the following years. Carne and Charlesworth [39] completed a detailed set of experiments with a wider heater thickness selection with ribbon heaters in a saturated *n*-propanol. Then, it was proposed that the effect of the heater could be best correlated with the product of thickness and thermal conductivity. The explanation for this correlating parameter was related to the assertion that some regions of the heater had more nucleation sites resulting in higher local heat flux values. Tachibana et al. [40] performed a series of experiments with a variety of materials and thicknesses in water. A theory on the transient effect

of the heater was proposed based on vapor shrouding of the surface, preventing fresh liquid from wetting the surface and leading to CHF. This effect could be correlated with the product of the volumetric heat capacity and the thickness. An experimental investigation was conducted under saturated pool boiling of water at the atmospheric pressure on thin, horizontally oriented, cylindrical walls of different metals and thicknesses [41]. The heated walls, ranging in thickness from 5 to 250 μm , were obtained by plating copper, silver, zinc, nickel, and tin on nonmetallic rods. They observed that the smaller the thermal conductivity of the metal layer, the higher the influence of the thickness. Guglielmini and Nannei [42] performed an experimental study with different cylindrical heaters formed with an electroplating technique. Lower CHF values on thin heaters were observed. The heater thermal parameter depended on a constant value, C . The thickness required to achieve 90% of the CHF thermal activity of the metal was given as:

$$\delta_{90} = C(\sqrt{\rho_h c_h k_h})^{-3.26} \quad (10)$$

Grigoriev et al. [43] conducted an experimental study with circular copper heaters in helium. CHF was reported to increase asymptotically until the thickness of 350 μm .

Based on a comprehensive review on the heater property effects on CHF, Saylor [44] proposed the following correlating parameter:

$$S = \delta_h \sqrt{\rho_h c_h k_h} \quad (11)$$

Carvalho and Bergles [45] performed an extensive study on the thermal property effect and agreed that S is the best correlating parameter. Their experimental studies showed that the Zuber [3] relationship underpredicted CHF by as much as 50% for thick copper blocks. An experimental study was carried out by Bar-Cohen and McNeil [21] with sputtered platinum and silicon heaters in dielectric liquids. They found silicon heaters had CHF about 80% higher than thin film heaters. The thin heater reduction in CHF was found to be captured by a factor:

$$\frac{S}{S + 0.8} \quad (12)$$

where S is the thermal activity parameter defined in Eq. (11). This relationship gives 90% of the hydrodynamically controlled CHF when $S = 8$, while the asymptotic value is approached for $S > 25$. However, there were no experimental results cited to confirm this asymptote.

A later comprehensive literature review was performed by Watwe and Bar-Cohen [23] to better understand the combined effects of the pressure, sub-cooling, and heater properties on the CHF. It was complemented by solving the energy equation numerically for both transient and steady-state cases. They

proposed an improvement to Bar-Cohen and McNeil [21] equation that was underpredicting CHF for very thin heaters (i.e., $S < 1$).

$$\frac{S}{S + 0.1} \quad (13)$$

Equation (13) reaches 90% of CHF value when $S = 1$ while the asymptotic value is seen to be approached at $S = 10$. By adding the effect of the thermal activity parameter to the CHF correlation, a composite expression was obtained for a limited data set [28].

The studies leading to the development of the TME correlation revealed that increasing heater thickness causes an asymptotic approach to a maximum CHF. Beyond this thickness, CHF appears to be independent of heater thermal properties. The maximum CHF obtained—for saturated conditions on large, horizontal heaters—was always approximately equal to the Kutateladze–Zuber prediction of Eq. (2). Although these points have been commonly accepted, there has been no agreement on the causative mechanism(s), and several different ways of correlating the data have been presented. Most studies correlated the heater effect with thickness; however, the choice of material properties introduces a change in the thermal conductivity, volumetric heat capacity, thermal effusivity, and finally in the thermal activity parameter.

Previous CHF studies at TME [10,23,44] had suggested that the pool boiling CHF increased strongly with values of S close to and less than unity and approached the asymptotic limit for S values in the range of 10–20. Moreover, these researchers linked the dependence of CHF on S to the role played by thermal diffusion/absorption in allowing the heater to coast through a temporary, local dry out and preventing this local event from escalating to a global dry out. In detailed numerical simulations by Watwe [28], the temperature rise at a point in the center of a region blanketed by vapor was found to be controlled by radial diffusion and governed by a relation with the following parameters:

$$T_{\text{sur}} - T_{\text{ini}} = f\left(\frac{qR_d}{\delta\sqrt{\rho_h c_h k_k}}, \frac{r}{R}, \sqrt{t}\right) \quad (14)$$

This finding served to justify the use of the thermal effusivity, along with the heater thickness, in the correlation of CHF. Previously published studies, for which S is < 30 , given in Bar-Cohen and McNeil [21] are shown with open markers, and recent studies are presented as closed markers. Published experimental CHF data were normalized by dividing by the maximum CHF value presented in each study. Normalization of the more recent results was completed by dividing the experimental results by the predicted asymptotic value.

Chang and You [46–49] performed experiments with heaters of various thicknesses, boiling in saturated FC-72 under atmospheric pressure with a

nondimensional heater characteristic length, L' , of 13.8. The thinnest heaters were created by sputtering thin platinum films on a glass substrate. Thick heater experiments were performed with copper heaters at various thicknesses. Following closely on the proposals of Ramilson and Lienhard [50] and Unal and Pasamehmetoglu [51], the Watwe—Bar-Cohen [23] model is predicted on the assumption of an ever-present nonuniform nucleation site density on the heater surface, which results in the formation of local vapor mushrooms, via lateral coalescence of individual vapor bubbles or the collapse of vapor columns. The depletion of the liquid under these vapor mushrooms then leads to the creation of local dry spots, whose temperature rises steeply under the influence of the imposed heat flux. This temperature rise rate is moderated by the ability of the underlying structure to locally absorb and/or conduct heat to parts of the heater still experiencing nucleate boiling.

If the temperature of the dry patch, at the end of the residence (or “hovering”) time of the vapor mushroom, exceeds the Leidenfrost temperature, the returning liquid is unable to quench the overheated surface, local dry out proceeds to global dry out, and CHF is said to occur. If the heater is very thin and has poor thermal properties, the dry patch temperature may exceed the Leidenfrost critical temperature soon after the formation of the first dry spot anywhere on the heater surface. CHF on such heaters will then be highly sensitive to the nonuniformities in the nucleation site density and dependent on the S value of the surface, yielding a diffusion-driven lower limit on CHF. At the other end of the spectrum, the heater thickness and thermal properties may be so large as to successfully absorb and conduct the heat away from the local dry patch for an extended period, thus keeping the dry patch temperature from exceeding the critical rewet temperature. For such a high S situation, the heater may be able to sustain the sequential formation and extinction of many dry spots, relying on the subsequent rewetting of the surface to locally cool the surface back to the nucleate boiling regime. CHF on such heaters would, then, occur primarily due to a hydrodynamic instability leading to an extensive interruption of liquid flow to the heater. The hydrodynamic instability models could, therefore, be expected to provide the upper or asymptotic limit for CHF.

The TME laboratory correlation for pool boiling CHF, which was derived for horizontal square heaters, was shown in the form of:

$$q''_{\text{CHF,TME}} = \frac{\pi}{24} h_{\text{fv}} \sqrt{\rho_v} [\sigma_f g (\rho_f - \rho_v)]^{1/4} \left(\frac{S}{S+0.1} \right) \times [1 + <0.3014 - 0.01507 L'(P)>] \left\{ 1 + 0.030 \left[\left(\frac{\rho_f}{\rho_v} \right)^{0.75} \frac{c_{\text{pf}}}{h_{\text{fv}}} \right] \Delta T_{\text{sub}} \right\} \quad (15)$$

where $L'(P) = L \sqrt{g(\rho_f - \rho_v)/\sigma}$

The first term on the right side represents the classical Kutateladze–Zuber prediction, considered the upper limit, saturation value of CHF on very large horizontal heaters. The second term is the effect of heater thickness and thermal properties. The third term accounts for the influence of the length scale on the CHF and is equal to unity or higher, while the last term represents the influence of subcooling on CHF.

Examination of Eq. (15) reveals that the approach of CHF to the asymptotic limit takes the form:

$$\frac{q_{\text{CHF}}}{q_{\text{CHF,asy}}} \propto \frac{S}{S + 0.1} \quad (16)$$

The CHF values calculated using Eq. (16) reach 90% of the asymptotic CHF value when $S = 1$, while their 1% deviation from the asymptotic value occurs at $S = 10$. However, it should be noted that the S range in their data was relatively modest, spanning values from 0.5 to 4.7.

Golobic and Bergles [52] offered an alternative correlation of the heater surface effects on CHF, based on their experimental study of saturated pool boiling CHF in FC-72. The authors also correlated the influence of the heater material on CHF in terms of the S parameter defined in Eq. (3). Their recommended correlation took the following form:

$$\frac{q_{\text{CHF}}}{q_{\text{CHF,asy}}} = 1 - e^{-[S/2.44]^{0.8498} - [S/2.44]^{0.0581}} \quad (17)$$

As presented above, the three most recent correlations taking the heater surface effects on CHF into account [10,22,52], all embody the dependence of CHF on the product of the heater thermal effusivity and thickness. It could be emphasized that all three expressions yield nearly identical CHF values for $S > 50$, and all reach 90% of the asymptotic CHF value when $S > 8$ (Fig. 12). However, significant differences do exist at intermediate values of S . Examining Fig. 12, it may be seen that the locus of Eq. (15) lies between the loci of Eqs. (14) and (16), while the Golobic and Bergles relation (Eq. (17)) yields higher fractions of the asymptotic CHF than the other correlations at very low S values, e.g., when $S = 0.001$, Eq. (17) results in $q_{\text{CHF}}/q_{\text{asy}}$ of 0.521 versus 0.0123 obtained from Eq. (14).

Arik and Bar-Cohen [8] performed a detailed study on the effect of effusivity and the underlining physics to understand the CHF behavior. In addition to their own experimental data, they established a database for CHF for a wide range of heaters used by different researchers. Figure 12 presents the experimental findings and analytical approximations for $S < 20$. Later, the authors extended the study to cover a large range of S values. Figure 13 provides the overall database, where S values are extended up to 120. Finally, Eq. (15) known as the TME CHF correlation is compared with the experimental

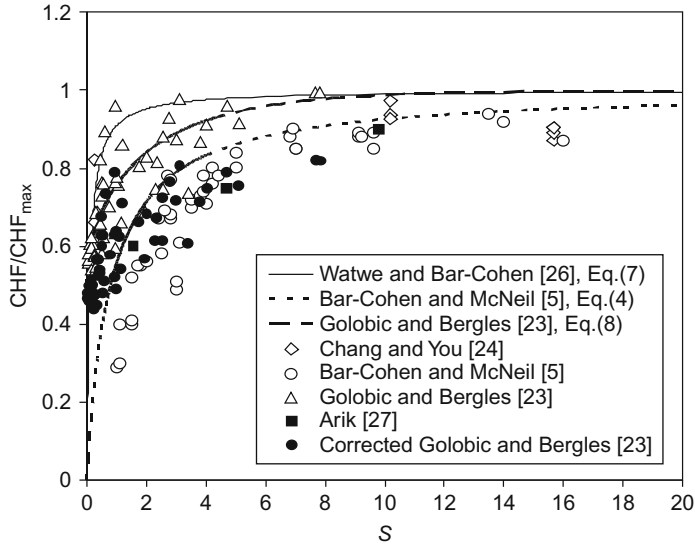


FIG. 12. Variation of the nondimensional experimental pool boiling CHF values with thermal activity parameter, $0 < S < 20$ [8].

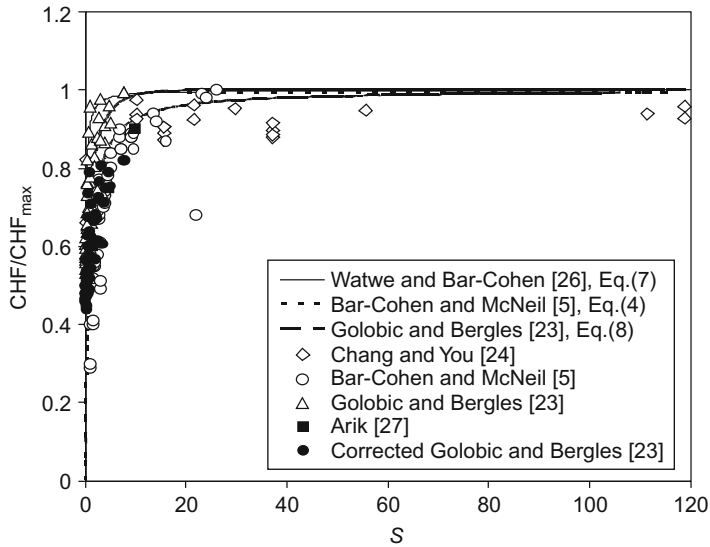


FIG. 13. Variation of the nondimensional experimental pool boiling CHF values with thermal activity parameter, $0 < S < 120$ [8].

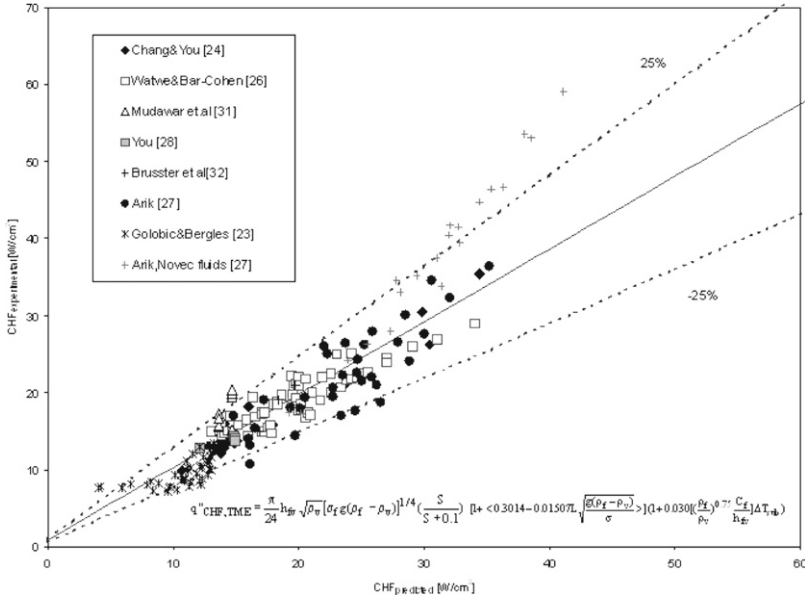


FIG. 14. Experimental and predicted pool boiling CHF values for a broad range of data [8].

findings using the modified effusivity factor. It is found that 98% of the data falls within $\pm 25\%$ of the TME correlation (Fig. 14).

D. HEATER CHARACTERISTIC LENGTH

The size of the heater influences CHF [53], and it has been widely observed that longer heaters experienced CHF condition at lower heat fluxes than shorter heaters. The variation of CHF with heater size has typically been expressed in terms of the nondimensional length, L' , defined as in Eq. (18):

$$L' = L \sqrt{\frac{g(\rho_f - \rho_v)}{\sigma_f}} \quad (18)$$

Lienhard and Watanabe [36] concluded that CHF depended inversely on the characteristic heater length, after performing experiments with wire heaters in organic liquids. A continuation of this research was reported by Lienhard and Dhir [54] in various liquids (i.e., acetone, benzene, isopropanol, and methanol) with a wide range of cylindrical, spherical, and rectangular heaters. CHF was found to decrease monotonically with increasing heater length, until reaching a unique asymptotic length for each heater geometry. Thus, the asymptotic

length was found to equal 2 for cylinders (based on the diameter), 6 for rectangular heaters (based on width), and 8 for spheres (based on diameters).

Circular horizontal copper heaters immersed in saturated nitrogen were studied by Grigoriev et al. [43]. Heater diameters were specified between 8 and 38 mm. Based on these diameters, corresponding dimensionless heater lengths L' were calculated as 7 and 34, respectively. CHF was reported as decreasing with increasing heater length. However, for L' values higher than 15, the authors did not observe any change in CHF values. Park and Bergles [55] performed a comprehensive study with 25.4- μm -thick nichrome heaters of three different sizes. They reported that CHF decreased with increasing characteristic heater length until L' was equal to 15.

Saylor [44] studied the heater size effect by performing experiments with dielectric liquids. His experiments were conducted with thin film platinum heaters on Pyrex substrates ($\sim 1400 \text{ A}^\circ + 10\%$). He reported that CHF increased with decreasing heater size for small heater sizes, while for larger heaters, the CHF converged to a constant value. Reflecting the impact of heater properties, the asymptotic value obtained from the large heater region was about 10.9 W/cm^2 , corresponding to a dimensionless CHF ratio ($\text{CHF}/\text{CHF}_{K-Z}$) equal to 0.79. The following correlation was proposed to account for the length scale effect:

$$\text{CHF} = 15.35 - 0.3639L' \quad (19)$$

Beyond a value of L' equal to 12.3, the author did not observe any changes in the CHF and concluded that $L' = 12.3$ was the corresponding asymptotic condition. Figure 15 clearly presents the heater length effect on CHF. Using horizontal square heaters, Saylor [44] further investigated the existence of oscillations in the dependence of CHF on L' s. The oscillations were first observed by Lienhard and Watanabe [36] in acetone for horizontal wire

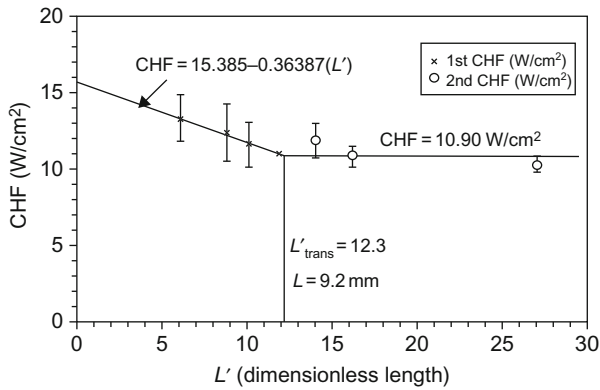


FIG. 15. Length scale, L' , effect on CHF [44].

heaters. The authors associated these oscillations with the interactions of a variety of instability wavelengths that manifest themselves on the wire surfaces. The Kutateladze–Zuber method assumes that it is the Taylor instability that predicts the location of vapor jets on long heaters and that it is the Helmholtz instability that predicts when the vapor jets will break down, leading to the CHF. Saylor [44] reported that the well-organized vapor columns that would be found on an infinite heater did not exist on his heaters. However, the Taylor wavelengths should still influence the vapor removal configuration leading to the variation in CHF with L' . He observed that CHF had a higher value at $L' = 14$ than at $L' = 9$ and speculated that an oscillation between two vapor removal patterns was occurring at this point and preventing the formation of a stable vapor film, thus delaying the onset of CHF.

Mudawar [56] reported a monotonic decrease in CHF values with increasing heater length. The reported CHF values in water are 158 and 81.8 for $L' = 12.7$ and $L' = 127$, respectively, corresponding to a 50% decrease for long heaters.

To better assess the heater length effect on the CHF, McNeil [21] expanded the asymptotic value of L' to 20. Watwe and Bar-Cohen [23] corrected the heater length effect in the composite equation that can predict for both L' less than and higher than 20. Finally, they proposed the following expression to represent the effect of heater length:

$$\text{CHF}_{L'} = 1 + \langle 0.3014 - 0.01507L' \rangle \text{CHF}_{K-Z} \quad (20)$$

Equation (20) clearly reflects the two key features of the heater length effect on CHF—an inverse linear dependence for low values of L' and an asymptotic limit. The “ $\langle \rangle$ ” bracket around the relevant term signifies that this term can be either positive or zero. This effect, then, is included as a correction factor in the Kutateladze–Zuber CHF correlation.

Mudawar et al. [57] developed an analytical model for nearly saturated pool boiling CHF on vertical surfaces. They used water and FC-72 as working fluids, and their analytical model was supported by the experimental results. Different sized heaters were employed in their experiments. FC-72 experimental results were obtained with $12.7 \text{ mm} \times 12.7 \text{ mm}$ copper heaters, while a rectangular heater (i.e., $12 \times 62 \text{ mm}^2$) was selected for water experiments. These copper blocks had a uniform thickness of 0.8 mm. The proposed CHF constant (i.e., $\pi/24$ in Eq. (2)) showed better agreement with long heaters than with short ones, especially when L' was higher than 18. The authors observed higher CHF values when $L' < 13$.

E. HEATER SURFACE EFFECT

In addition to the salutary effect of heater thickness and high thermal effusivity on CHF, surface modifications can also be used to further raise the pool

boiling CHF. The chemical composition and the physical character of the heat transfer surface are important to this effect. Surface enhancement methods, from the fabrication point of view, would fall into two main categories: (1) modifying an originally plain surface by removing material (e.g., roughening, blasting) or adding material (e.g., porous coatings, deposition with templates) and (2) manufacturing the surface with specially designed features (e.g., finned surfaces). Due to the differences in the techniques used to create these surface modifications, the resulting surface enhancement features are found to span the full range from macro- to nanosize scales.

In early efforts, Berensen [58] extensively investigated the effect of surface finish on nucleate boiling performance. In subsequent years, a variety of special surface arrangements have been developed to provide a high density of stable, artificially formed nucleation sites, leading to CHF enhancement that does not deteriorate with time. In 1972, a surface enhancement method to upgrade the nucleate boiling performance of silicon chips in dielectric liquids was devised by Oktay and Schmeckenbecher [59]. They mounted a dendritic heat sink on a plain silicon chip immersed in saturated FC-86 and achieved a significant reduction of the junction temperature at boiling incipience from 95°C to 60°C. Chu and Moran [60] obtained similar results using laser-drilled holes with diameters ranging from 50 to 100 μm . Marto and Lepere [61] studied heat transfer enhancement of three commercially available surfaces (Union Carbide High Flux, Hitachi Thermoexcel-E, Wieland GEWA-T) on a cylindrical tube geometry immersed in highly wetting liquids such as saturated FC-72 and R113. They presented a 60% decrease in nucleate boiling superheats and a negligible increase in CHF. Park and Bergles [62] investigated microholed and microfinned heat sinks formed by machining copper plates. They observed boiling heat transfer enhancement in saturated FC-72 primarily due to the increase in heat transfer surface area. Anderson and Mudawar [63] evaluated mechanically manufactured heat sinks (drilled holes, microfins, and inclined microfins) by attaching them to flat, vertically oriented chips in FC-72. They found that surface cavities of sizes about 300 μm in diameter were ineffective in lowering incipience superheats or in enhancing CHF. Carvalho and Bergles [19] studied the benefits of surface enhancement created by mounting small heat sinks on flat, vertically oriented surfaces immersed in both FC-72 and FC-87. The heat sinks studied included smooth copper blocks, Union Carbide High Flux (porous copper matrix of 0.77 mm thick with particle sizes of around 30 μm), Wieland GEWA-T19 (740 fins/m with 1.1 mm fin height and 0.25 mm gap), and Hitachi Thermoexcel-E (0.1 mm pores with 0.56 mm tunnel height). They reported reductions in incipient and nucleate boiling superheats at saturated and subcooled conditions for all heat sinks and indicated that the enhanced surfaces increased the CHF at all bulk liquid temperatures. CHF values up to 100 W/cm^2 were reached with a bulk temperature of 25°C.

Enhanced surfaces for boiling heat transfer are extensively covered in Thome [64], where a review of a large data set for boiling from porous coatings failed to identify consistent trends, observing instead that often the optimum coating geometry in one study only vaguely corresponded to those found in other studies. It was noted that the performance benefit of the coatings could be associated with the much enlarged vapor–liquid contact surface area within the pores formed between the stacked particles, leading to a *de facto* surface area enhancement within the thick porous layer. Additional thermal transport could be facilitated by internal and external convection mechanisms, generated by vapor bubble agitation and dynamic vapor/liquid exchange.

Mudawar [56] presented a comprehensive summary of his group's efforts on surface enhancement of FC-72 pool boiling. They applied various techniques such as creating microstructures on the surface with sandpaper, silica blast surface finish, and micro pin fin attachments. All of the surface attachments/treatments yielded some improvements in the CHF values. The microstructure-enhanced surface generated CHF values as high as 105.4 W/cm^2 , while microgroove-enhanced surfaces reached CHF values as high as 92.8 W/cm^2 . Webb and Pais [65] provided another excellent review on improvements in heat transfer resulting from the use of special enhanced surface geometries and provided a brief discussion about some of the aspects of boiling on enhanced surfaces reported in the literature.

Following the outlined initial studies, largely based on attaching enhancement structure to the active semiconductor chips, efforts on surface enhancement of ebullient heat transfer in the past 20 years have involved more sophisticated fabrication methods, reflecting the emergence of interdisciplinary approaches. To make this review easier to follow, these surface enhancements can be grouped into three categories: protrusions, cavities, and porous structures. Nanoscale surface modifications will also be examined.

1. Protrusions

Honda et al. [66] studied protrusion structures and utilized square micropin fins ($50 \times 50 \times 60 \mu\text{m}^3$ with $100 \mu\text{m}$ fin pitch) and submicron-scale roughness (Root mean square (RMS) roughness of $25\text{--}32 \text{ nm}$) to augment CHF in electronic components under both degassed and gassy conditions (Fig. 16). They conducted their experiments with FC-72 at liquid subcoolings of 0, 3, 25, and 45 K, and revealed a linear increase in CHF with subcooling, which agreed with the literature (Fig. 17). The CHF values for both degassed and gassy conditions appeared to be close to each other. The authors also discussed the effectiveness of the various heat transfer enhancement methods. They found that the use of micro pin fins were more effective in increasing the CHF than submicron-scale roughness method (Fig. 18). When they used both methods together, they obtained the maximum enhancement in CHF (1.8–2.3 times as large as that for

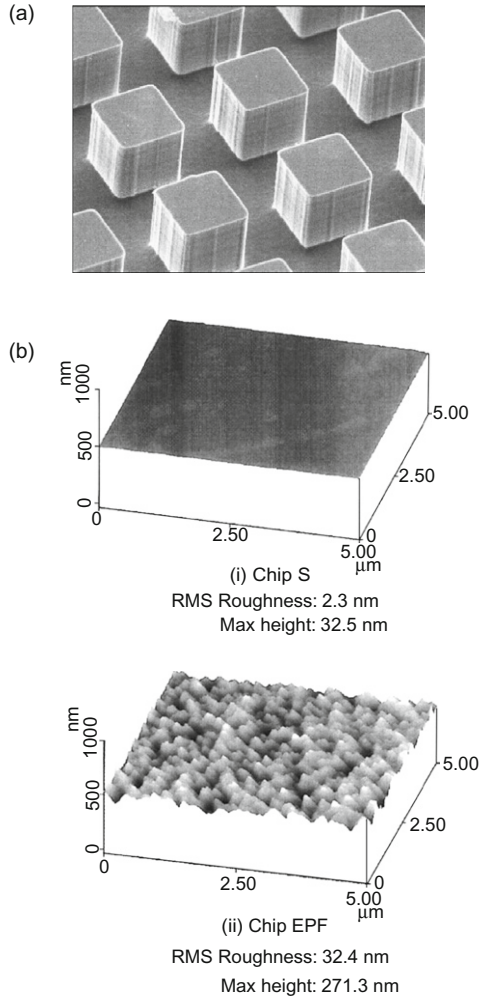
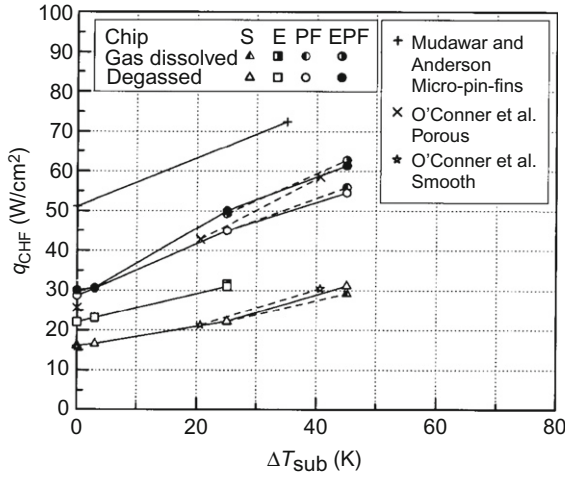
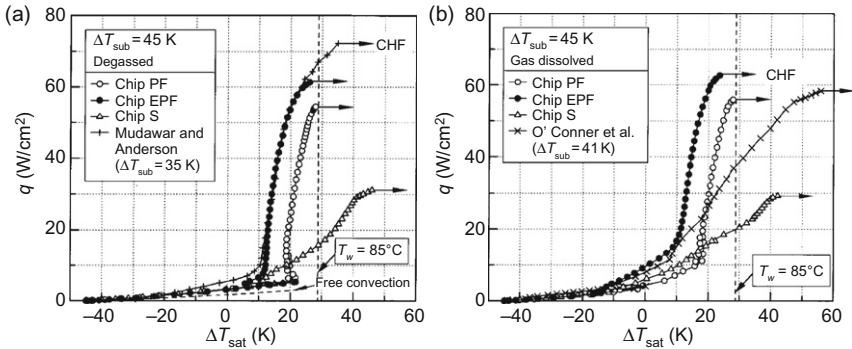


FIG. 16. (a) SEM image of chip PF (pin fin) [66], (b) AFM images of chips (i) S and (ii) EPF [66].

a smooth chip), which was comparable to the total area enhancement of 2.2. Honda and Wei [67] further studied the effect of the square micro-pin-fin thickness and tested fin thicknesses of 10, 20, 30, and 50 μm where fin pitch was twice the fin thickness. They found the 30 μm fin thickness to be optimum. Finally, Wei et al. [68] used a fixed fin thickness of 30 μm and increased the fin height up to 200 μm . Results indicated slightly increased CHF values with an increase in fin height.

FIG. 17. Variation of q_{CHF} with ΔT_{sub} [66].FIG. 18. Comparison of boiling curves: (a) $\Delta T_{sub} = 45$ K, $y_g = 2.1 \times 10^{-4} - 3.4 \times 10^{-4}$; (b) $\Delta T_{sub} = 45$ K, $y_g = 2.6 \times 10^{-3} - 3.3 \times 10^{-3}$ [66].

Yu and Lu [118] performed a recent study on the enhancement of pool boiling heat transfer on horizontal rectangular fin array in saturated FC-72 at atmospheric pressure. They investigated the effect of fin spacing and fin height on CHF. Their test surfaces had a base area of 10 mm \times 10 mm with different fin spacings (0.5, 1, and 2 mm) and fin lengths (0.5, 1, 2, and 4 mm) (Fig. 19). They complimented their thermal measurements with a visualization study to examine the CHF enhancement mechanism. Although they reported high uncertainty values for CHF ($>10\%$), a trend with fin spacing and fin length

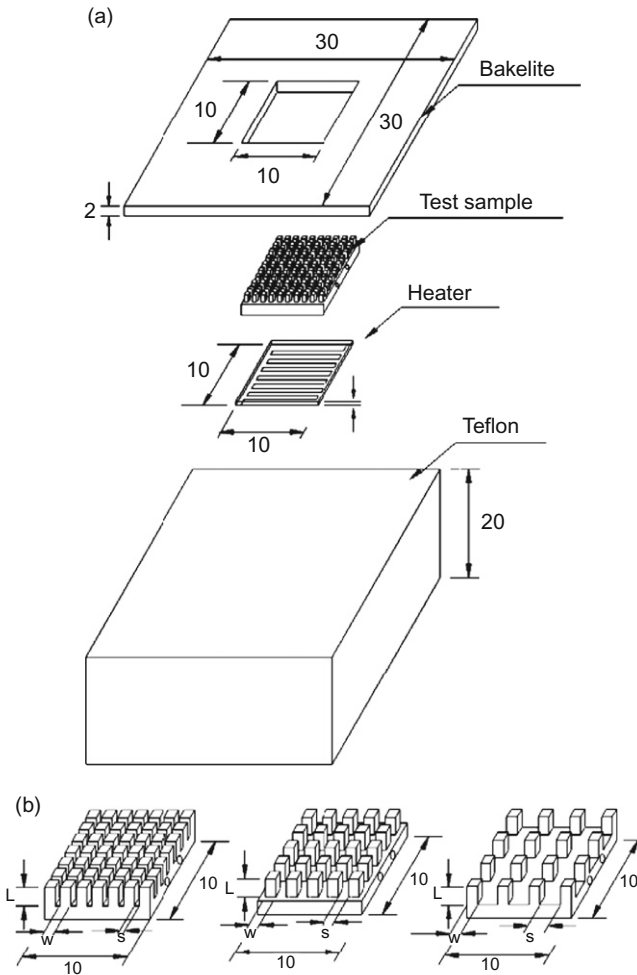


FIG. 19. Schematic of heating module and finned surfaces [118].

was apparent. As expected, CHF of the finned surfaces was higher than CHF on plain surfaces, since additional rewetting passages were available with finned structures, so that liquid replenishment improves and leads to higher CHF values (Fig. 20). At fluxes approaching CHF, vapor clouds were seen to form inside the fin spacings and then gave rise to a dry out condition. Closer fin spacings and longer fins produced highest heat dissipation; however, CHF enhancement was only possible for fins of aspect ratio less than unity. The authors noted that the observed bubble size in the visualization studies was

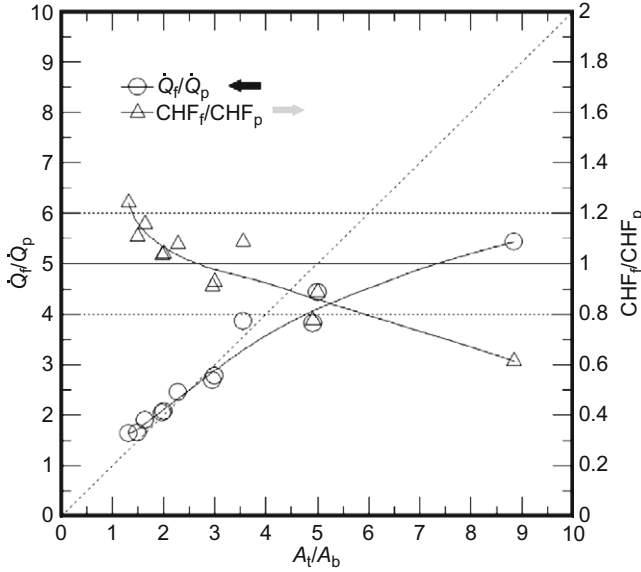


FIG. 20. Enhancement of CHF versus enhancement of area [118].

close to the dense fin spacings, so that the bubbles were likely to coalesce and occupy the gap between the densely spaced fins and make it difficult for the liquid to remove them and rewet the surface. Long fins, thus, introduced higher resistance to the departing bubbles and as a result introduced surface temperature increases that could lead to CHF. In this study, it was also shown that the enhancement of CHF, based on total surface area, was only marginally higher than that encountered on plain surfaces (<1.3 times).

Ujereh et al. [69] experimentally assessed the effect of carbon nanotube (CNT) arrays on FC-72 pool boiling (Fig. 21). The CNT arrays were grown on silicon and copper substrates, with individual tubes having a diameter of ~ 50 nm and a height ranging from 20 to 30 μm . Upon testing various surfaces, including fully CNT-covered (with light and dense meshes) and CNT-patterned (with grid and island layouts) samples, the authors concluded that fully CNT-covered surface was highly effective in improving the boiling incipience, nucleate boiling, and CHF performance, and provided up to 45% higher CHF over the smooth silicon surface as shown in Fig. 22.

Later, Ahn et al. [70] studied the effect of vertically aligned CNT arrays that were grown on the silicon wafer using chemical vapor deposition method. The CNT arrays featured uniform tubes with dimensions of 8–15 nm diameter and two different heights of 9 and 25 μm . For nucleate boiling of PF-5060, a 25 μm high CNT array yielded a 29% and 40% higher CHF under saturated

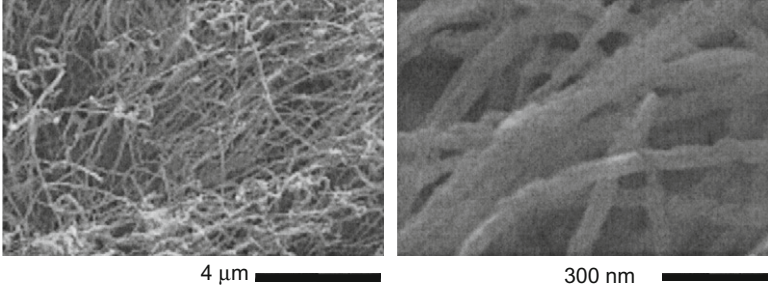


FIG. 21. SEM images of silicon surface coated with CNT arrays [69].

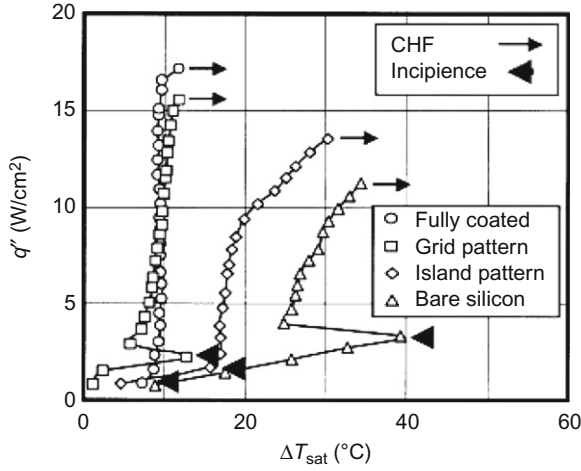


FIG. 22. Boiling curves for bare and CNT-coated silicon surfaces [69].

and 10°C subcooled conditions, respectively, compared to a bare silicon surface. However, the CHF values were still quite low ($<10 \text{ W/cm}^2$), which was attributed to the large heater size. The authors in Ref. [71] tested a smaller, $5.9 \times 3.2 \text{ cm}^2$, heater with the same setup and obtained a CHF of 18.4 W/cm^2 for saturated condition with the $25 \mu\text{m}$ high CNT array representing a 58% improvement over that of the bare silicon surface.

2. Cavities

In the other type of enhanced surfaces, featuring cavity structures, Nimkar et al. [72] developed a silicon heat sink having micropyramidal surface

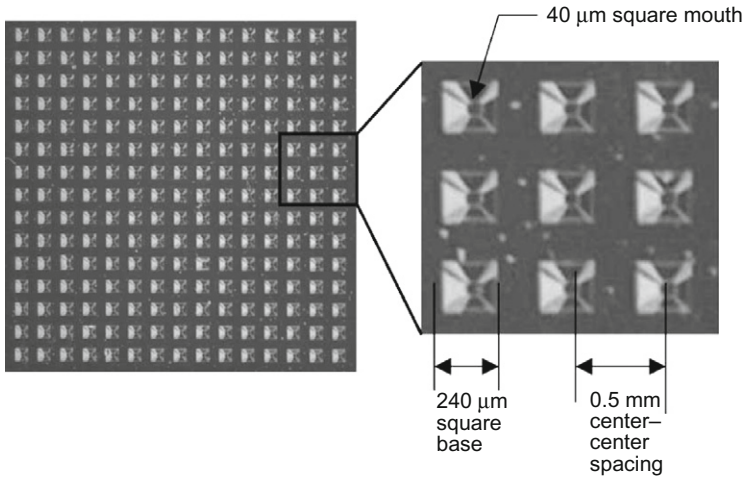


FIG. 23. Enhanced surface with 15×15 cavity array [72].

structures of $149 \mu\text{m}$ height and a $40 \mu\text{m}$ square mouth opening arranged in a square array (15×15 array and with 0.5 mm cavity spacing) and placed it on a glass substrate (Fig. 23). They performed a preliminary pool boiling study on this heat sink and detected CHF condition at a heat flux of 12.8 W/cm^2 , which was lower than the Zuber correlation [3] (Fig. 24). They associated this discrepancy with the working fluid FC-72, which was a more wetting fluid than water. Moreover, the CHF value was much lower than (less than one third) that in their previous design with a silicon substrate [73]. They claimed that the heat losses from their previous heat sink were very high compared to their new heat sink configuration. However, no information was presented for the predicted heat losses in this study. In a later study by Nimkar et al. [74], they focused on pool boiling heat transfer and CHF in more detail, using the same heat sink configuration. According to their CHF results, the Zuber correlation [3] overpredicted their experimental data (Fig. 25). Different working fluid characteristics (of FC-72) from water were held responsible for this overprediction. They emphasized the necessity of a CHF prediction tool for highly wetting fluids. There was no apparent effect of micropyramidal surface cavities on CHF in this study.

3. Porous Coatings

Ebullient heat transfer enhancement, through the use of porous structures, has been the focus of many researchers and great success has been achieved

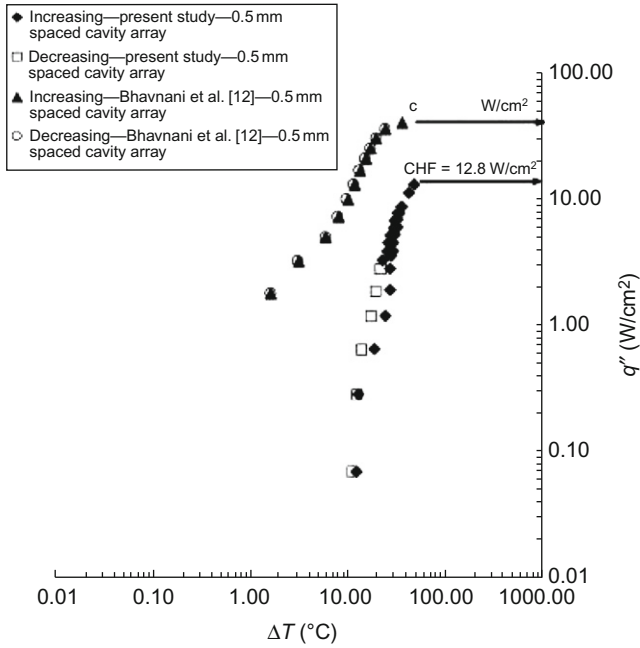


FIG. 24. Pool boiling curve for the enhanced surface [72].

through the use of thin microporous surface coatings. It is generally thought that such an enhancement results from a substantial increase in the nucleation site density and its uniformity across the heated surface. Alternatively, porous and microporous coatings can facilitate two-phase flow and boiling within the surface layer and produce substantial CHF augmentation. Figure 26 presents a schematic of a microporous coating by O'Connor and You [75].

Based on their comprehensive experimental study, Chang and You [76] brought forth additional explanations for the boiling heat transfer and porosity relationship. They found that the reduction in porosity might lead to lower internal vaporization rates (thin film and capillary vaporization) as a result of the existence of less liquid within the structure to vaporize. As summarized by Chang and You [46–49], a series of microporous enhancement coatings were developed by You et al. [77], O'Connor and You [75], O'Connor et al. [78], and Chang and You [76]. While many of the known enhanced surfaces have demonstrated the ability to reduce wall superheat and increase CHF, their feature sizes were apparently too large to effectively trap a large number of embryonic bubbles when immersed in dielectric liquids. By manufacturing optimum cavity sizes on a heated surface, both the boiling site density and the nucleate boiling heat transfer can be efficiently increased.

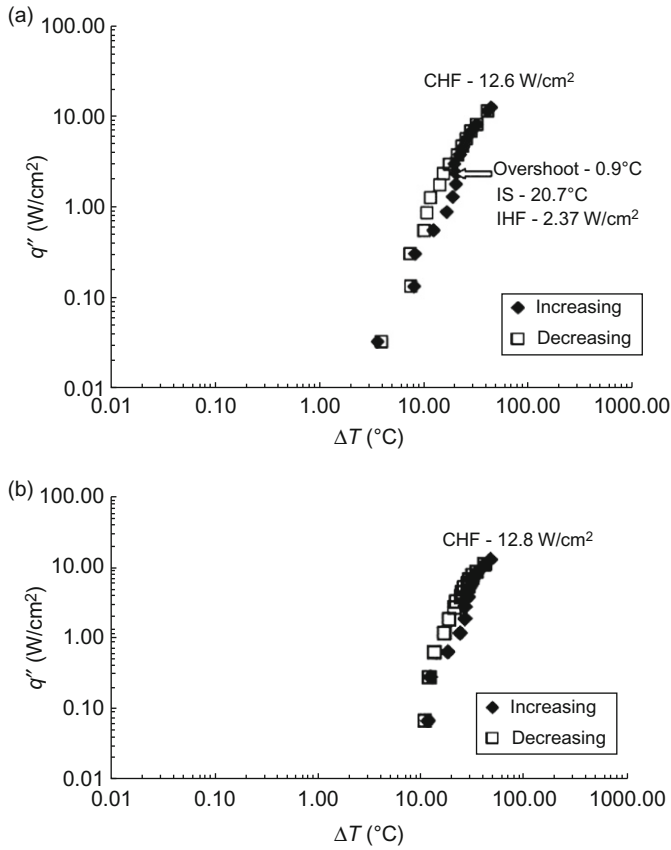


FIG. 25. Pool boiling curve for the plain surface (a) and the enhanced surface (b) [71].

O'Connor et al. [78] utilized two types of microporous structures, fabricated by “spraying” and “painting” techniques. With these techniques, they either sprayed alumina particles onto a flat surface or prepared a mixture of diamond particles, binder (glue), and carrier (alcohol) and applied (“painted”) it onto the heater surface. The treated surfaces immersed in FC-72 reached nearly 80 W/cm² for a 160% larger CHF under saturated conditions and nearly 160 W/cm² or 120% higher CHF for 45 K subcooling than the untreated surface (Figs. 27 and 28).

Gulliksen et al. [79] investigated enhanced boiling heat transfer with porous coatings for a possible application to electronic cooling. A porous coating was made by gluing 50 μ m thick porous silver membranes on silicon heaters with thin layers of silver epoxy. A decrease in boiling incipience and an increase in

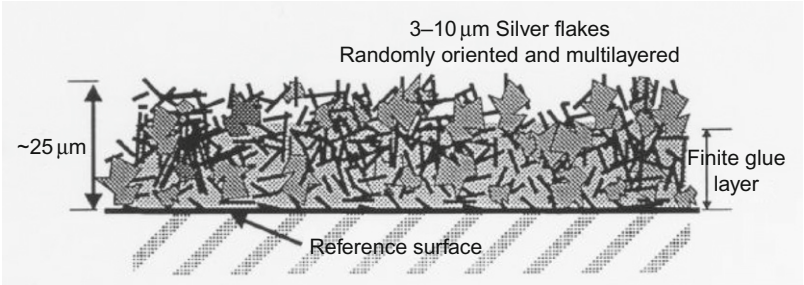


FIG. 26. Surface coating with silver flakes [75].

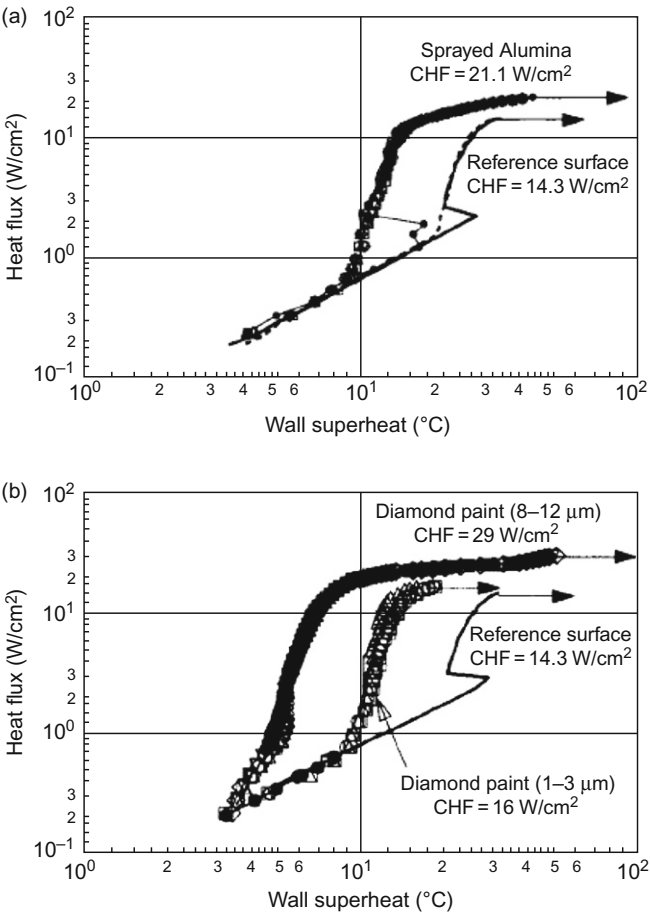


FIG. 27. Sprayed alumina (a) and painted diamond (b) enhancements [78].

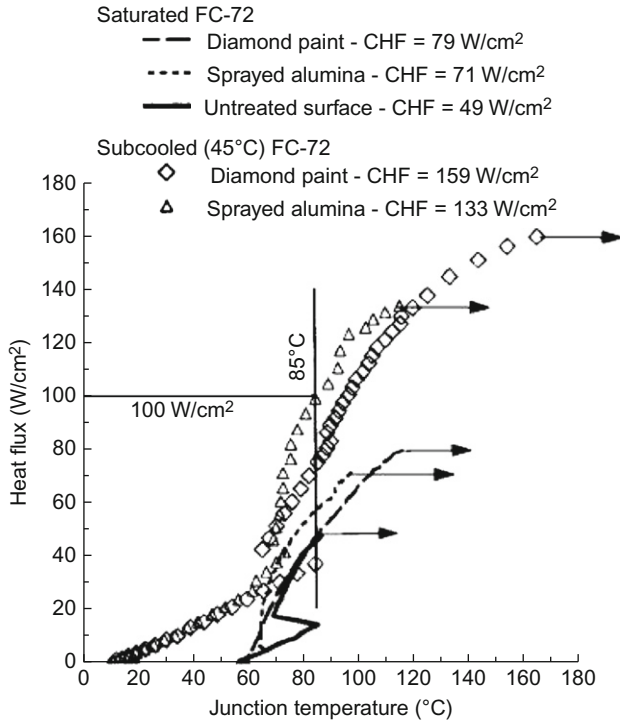


FIG. 28. Silicon test chip data [78].

heat transfer were observed over plain surfaces. Moreover, the plain surface performed better than polished silicon surfaces. The authors concluded that the heat transfer coefficient (HTC) scaled linearly with the permeability of the porous media, showing excellent agreement with their experimental studies.

An experimental study of pool boiling of FC-72 in highly porous metal foam was reported by Arbalaez et al. [80]. A heat generating electronic chip was simulated by placing an array of electrical resistors on an aluminum block. Experiments were conducted with samples of various porosities and pore sizes. The results indicated that the temperature excursion usually observed for fluorocarbon fluids at the onset of nucleate boiling was not present and an increase in the overall heat transfer performance and the CHF values were observed compared to a flat plate.

Vemuri and Kim [81] tested an aluminum oxide porous surface in their FC-72 pool boiling experiments. Their 70 μm thick porous layer featured nanosized pores with diameters ranging between 50 and 250 nm. Data with porous surface showed about 30% decrease in the incipience superheat compared to that of a

plain surface and suggested an improved vapor entrapment and nucleation site density. However, the authors did not report CHF data in this work.

El-Genk and Parker's study [31] provides more information about the geometry of microporous coatings in the scanning electron microscope (SEM) images of their graphite surface (Fig. 29). The surface pores and reentrant cavities in the porous graphite ranged from a few to hundreds of microns in size. The volume

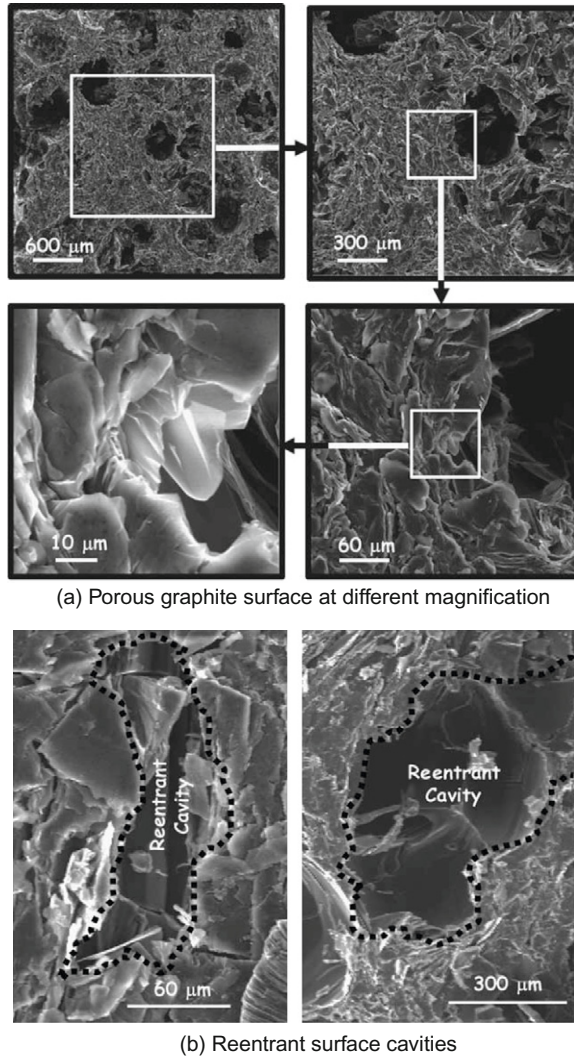


FIG. 29. SEM images of the porous graphite surface [31].

porosity was 60% of which about 95% were open and interconnected pores and reentrant cavities. They also recommended $C_{f,w,sat}$ values (0.263 for porous graphite surfaces and 0.166 for plain surfaces) for the existing FC-72 CHF data in the literature and correlated their results in the form of the Kutateladze–Zuber correlation for CHF under saturated conditions, thus extending the applicability of this venerable CHF_{sat} correlation. El-Genk and Parker were able to achieve predictions within $\pm 6\%$ for the enhanced surfaces and $\pm 13\%$ for the plain surfaces, for their own and other data in the literature, but required distinct coefficients for each surface and fluid combination (Fig. 30).

Microporous enhancement coatings were also studied by Arik et al. [82]. They focused on the experimental investigation of the effects of pressure and subcooling on the pool boiling CHF from a square silicon chip-like heater with a surface area of $\sim 41 \text{ mm}^2$. The dual inline silicon packages were immersed in FC-72, and the experiments were performed in the horizontal orientation. While subcooling was varied between 0 and 72 K, the pressure was kept between 101.3 kPa and 303.9 kPa. The maximum CHF values were determined to be 34.5 and 45 W/cm² for plain and microporous-coated heaters, respectively, based on the base area. It was found that an average increase of $\sim 50\%$ over the untreated plain silicon surface can be achieved by creating a porous synthetic diamond structure.

Table I [27] shows the summary of the experimental results with the microporous-coated heaters. The primary goal of their study was to map the enhancement in the CHF values over the plain chip packages. The experimental conditions are presented in the first and the second columns, while the corresponding subcooling condition is given in the next column. Columns four and five show the experimental findings for both coated and plain ATC2.6 chip packages, respectively. The last column displays the percentage of the CHF enhancement defined as:

$$\text{Enhancement } [\%] = \frac{(CHF_{\text{microporous}} - CHF_{\text{plain}})}{CHF_{\text{plain}}} \quad (21)$$

4. Nanoscale Surface Modifications

In addition to the three main surface enhancement structures mentioned so far, very thin, nanoscale surface modifications have become a research interest in recent years. Traditionally, surface enhancements that could provide sub-micron structures were assumed to be ineffective in pool boiling, since the small scale cavities would require a very high surface superheat to become active nucleation sites. However, recent studies on nanoscale structures indicated an opposite trend. The imperfections encountered during the processes resulted in micron-size cavities, along with the intended nanosize structures, which were

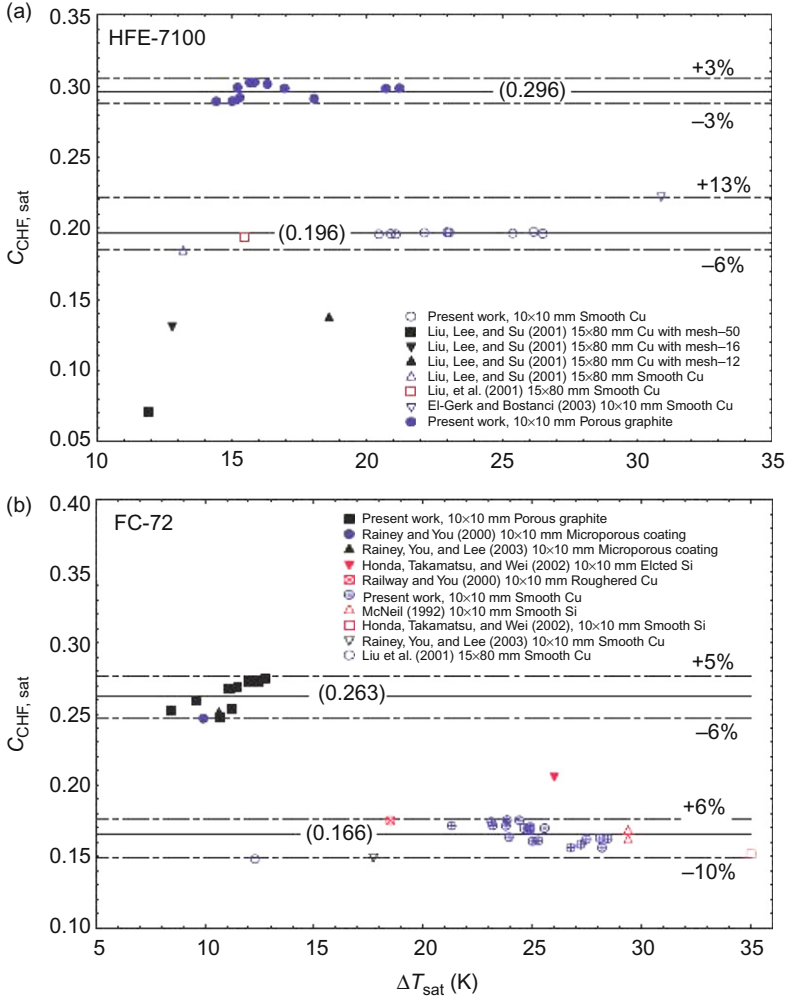


FIG. 30. Comparisons of saturated boiling CHF coefficients for HFE-7100 and FC-72 [31]. For color version of this figure, the reader is referred to the web version of this book.

able to help initiate boiling at favorably low superheats and where the nano-scale structures could still improve the wettability leading to higher CHF.

Im et al. [83] recently investigated a boiling surface, targeting an effective enhancement with micron-high, nanometer diameter wires. They fabricated copper nanowire arrays on silicon substrates by electrochemical deposition and utilized an anodic aluminum oxide template to achieve vertically aligned structures

TABLE I
COMPARISON OF CHF VALUES WITH COATED AND UNCOATED CHIPS [27]

P (kPa)	T ($^{\circ}\text{C}$)	ΔT_{sub} (K)	CHF_{exp} (W/cm^2)	$\text{CHF}_{\text{plain}}$ (W/cm^2)	Enhancement (%)
101.3	22	34.6	45.9	22.3	106
101.3	41	15.6	27.8	18.1	54
101.3	55	1.6	19.4	13.2	47
202.6	22	57	46.7	30.1	55
202.6	41	38	37.1	26.2	42
202.6	55	24	33.7	19.5	73
202.6	74	5	29.7	14.6	103
303.9	22	71.5	47.0	34.6	36
303.9	41	52.5	35.9	26.5	36
303.9	55	38.5	35.5	22.1	61
303.9	74	19.5	37.2	17.8	109

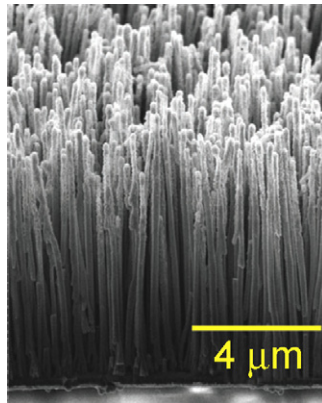


FIG. 31. SEM image of $8\text{ }\mu\text{m}$ tall vertically aligned copper nanowires attached to a silicon substrate [83].

having various heights (1 , 2 , 4 , and $8\text{ }\mu\text{m}$) with a fixed pitch ($\sim 300\text{ nm}$) and diameter ($\sim 200\text{ nm}$), as shown in Fig. 31. During saturated PF-5060 pool boiling tests, all of their nanowire array surfaces provided enhancement in both nucleate boiling and CHF over that of the plain surface. While taller nanowires increased the HTC, the highest CHF, of $20\text{ W}/\text{cm}^2$, was attained by the $2\text{ }\mu\text{m}$ high structures, as depicted in Fig. 32. The authors also presented a comparison based on CHF levels normalized for structure height and emphasized the importance of obtaining comparable CHFs with very thin surface structures that could be integrated with future semiconductor cooling schemes.

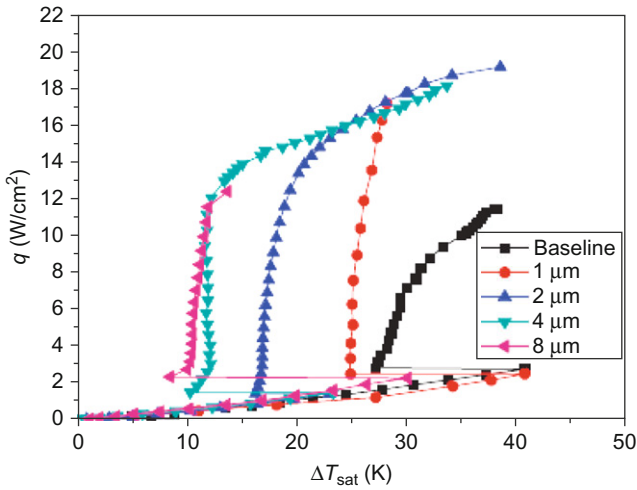


FIG. 32. Effect of nanowire length [83]. For color version of this figure, the reader is referred to the web version of this book.

It is known that reducing the solid–liquid contact angle helps in the improvement of boiling heat transfer. Several experimental studies showed that thin hydrophilic surface coatings, especially of the titanium oxide (TiO_2), were very effective in enhancing water boiling, mainly attributed to the high affinity of TiO_2 for water. Wu et al. [84] recently evaluated the effect of TiO_2 coating on the nucleate boiling and the CHF of water and FC-72. Their coating was composed of 10 nm size particles that were bonded to a substrate forming an $\sim 1 \mu\text{m}$ thick layer. The TiO_2 -coated surface increased CHF of FC-72 by 38.2% over a smooth copper surface, as shown in Fig. 33, and indicated that TiO_2 can also enhance the boiling performance of a highly wetting fluid. The authors concluded that hydrophilic TiO_2 surface possibly allowed more effective liquid–solid interaction, reduced the dry patches caused by growing bubbles, and eventually enhanced both nucleate boiling and CHF. A silicon oxide (SiO_2)-coated sample having surface roughness similar to that of the TiO_2 -coated surface was also tested to isolate the contribution of roughness to the overall enhancement. The acquired data confirmed that the hydrophilicity of the TiO_2 coating provided an additional mechanism for boiling enhancement beyond increasing the active nucleation site density.

In an effort to compare the reviewed studies featuring microscale protrusion, cavity, and porous type structures, along with the recent thin, nanoscale structures, representative CHF data for saturated FC-72 (or PF-5060) boiling, and all the specified surface conditions, are plotted in Fig. 34. As can be noticed,

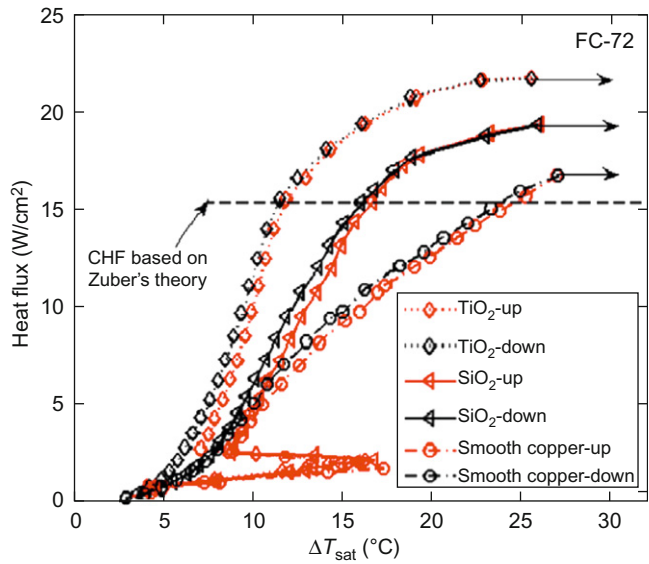


FIG. 33. Boiling curves for smooth copper and $\text{SiO}_2/\text{TiO}_2$ -coated surfaces in FC-72 [84]. For color version of this figure, the reader is referred to the web version of this book.

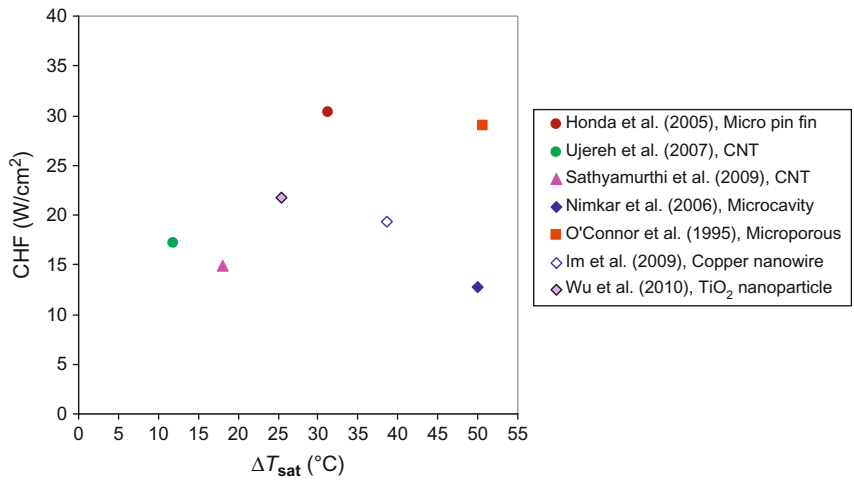


FIG. 34. Performance comparison of various surface enhancements with saturated FC-72 and PF-5060. For color version of this figure, the reader is referred to the web version of this book.

surfaces that offer higher CHF values tend to demand higher superheats. It should also be emphasized that in these studies, CHF values of the “plain” surfaces vary significantly, between 9.5 and 16.8 W/cm² with superheats of 16.3–45.6°C, due to the other effects such as heater size, material, thickness, and surface finish.

5. Correlations

Several studies attempted to correlate CHF data from enhanced surfaces. TME CHF correlation presented by Arik and Bar-Cohen [82] has been shown to be able to predict CHF for plain heaters in dielectric fluids as given in Figs. 14 and 35. It was also noted that TME correlation did not have the capability to analytically determine CHF from coated heaters since it did not have any term to incorporate the effect of surface microstructures into the correlation. Rainey et al. [30] proposed an empirical constant directly related to the active nucleation site density just before CHF. Their correlation was given as follows:

$$\text{CHF}_{\text{microporous}} = 1.78\text{CHF}_{\text{Kutateladze-Zuber}} \quad (22)$$

When it was compared to the current experimental findings, the correlation provided 24.4 and 29.3 W/cm² for 101.3 and 202.6 kPa saturated FC-72, respectively. From a close examination of the data for the corresponding

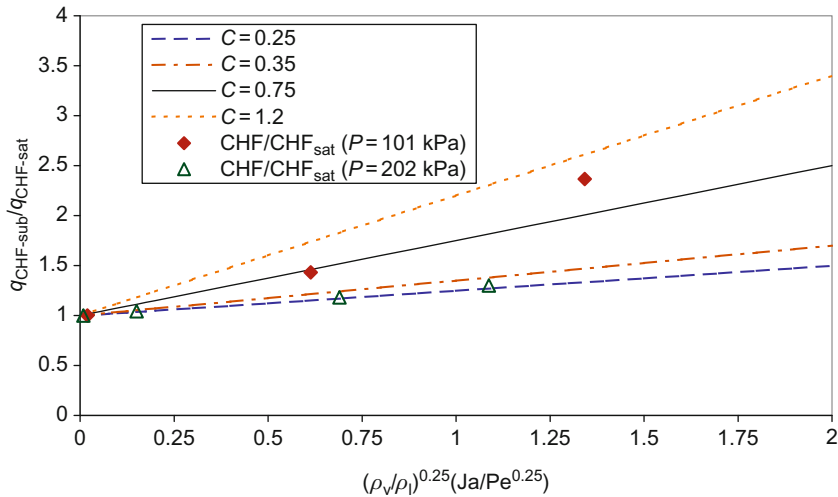


FIG. 35. Effect of subcooling on CHF with microporous-coated chips [82]. For color version of this figure, the reader is referred to the web version of this book.

conditions, the experimental findings could be read as 19.4 and 29.7 W/cm², respectively. The errors in these predictions (in percentages) are 25% and 2%, respectively. At pressures above atmospheric condition, the correlation was able to predict the CHF with a higher accuracy. The constant in Eq. (22) was also given as 1.35 by Mudawar and Anderson [17]. In that case, CHF was found to be 18.53 and 22.26 W/cm², respectively. The corresponding errors in percentages are 4.5% at low pressure and 25% at the elevated pressure. Rainey et al. [30] gave the modified Ivey and Morris [14] correlation for coated heaters as follows:

$$\text{CHF}_{\text{microporous}} = \text{CHF}_{\text{sat}} \left(1 + 1.20 \left(\frac{\rho_v}{\rho_l} \right)^{0.25} \frac{Ja}{Pe^{0.25}} \right) \quad (23)$$

The constant in the above correlation was modified to be 1.2 since the previously modified correlation coefficients underpredicted experimental CHF values [82]. Figure 27 presents the predicted and experimental CHF values from microporous-coated silicon heater surfaces immersed in saturated FC-72. At lower pressure condition ($P = 1$ bar), the relative enhancement was found to be higher than at the higher pressure conditions ($P \geq 2$ bar). At lower pressure condition, the coefficient in Eq. (23) was able to give better predictions for the value of 0.75, while for higher pressures, the value of this coefficient became 0.35. In order to better correlate the subcooling effect in the microporous structures, further experimental studies are necessary.

F. EFFECT OF SURFACE ORIENTATION

Priarone [119] investigated the effect of surface orientation on saturated CHF of both FC-72 and HFE-7100 over a 7.07 cm² copper flat plate. The trend of CHF with the orientation angle was similar to that generated by previous correlations [3] and [12] and previous findings for both FC-72 and HFE-7100 yielding maximum CHF values on upward-facing surfaces. CHF decreased slowly with the orientation angle from 0° to 90°, whereas it decreased rapidly for downward-facing surfaces (Fig. 36). The authors developed the following correlation for both their FC-72 and HFE-7100 data, to represent the effect of surface orientation:

$$\text{CHF} = C_{f,w,\text{sat}} f(\theta) \{ \rho_v^{1/2} h_{\text{FG}} [g\sigma(\rho_L - \rho_v)]^{1/4} \} \quad (24)$$

where

$$f(\theta) = 1 - 0.001117\theta + 7.79401 \times 10^{-6} \times \theta^2 - 1.37678 \times 10^{-7} \theta^3 \quad (25)$$

As noted in previous studies [8,33,46–49], due to the superior thermophysical properties of HFE-7100, the CHF values for HFE-7100 were higher than

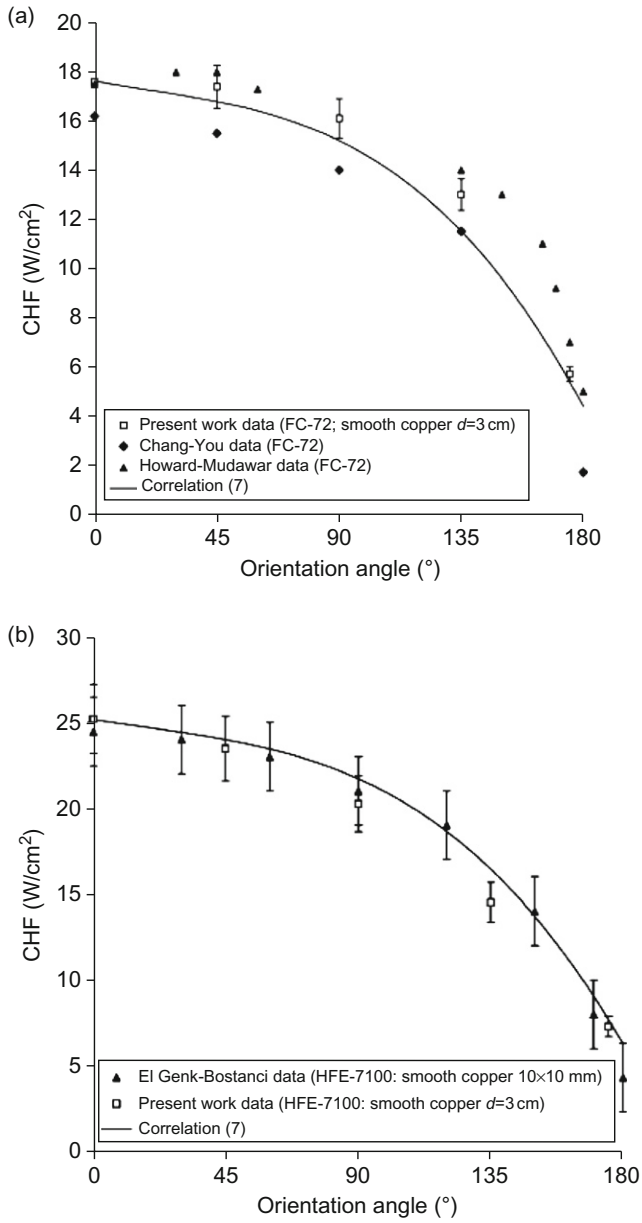


FIG. 36. CHF versus orientation angle for FC-72 (a) and HFE-7100 (b) [119].

for FC-72. However, the 25% increase in CHF was higher than could be ascribed to the thermophysical property component $(\rho_v^{1/2} h_{FG} [g\sigma(\rho_L - \rho_v)]^{1/4})$ in the conventional CHF correlations, which yields a predicted increase of about 12%. The high average uncertainty value ($\pm 8\%$) could have contributed to this discrepancy.

G. DIELECTRIC LIQUID MIXTURES

Understanding the behavior of boiling heat transfer and CHF in mixtures has been of interest for the last five decades. Dunskus and Westwater [85] reported results of an early study. They chose isopropanol as the main liquid and two additives to study the boiling process with a wide range of molecular weight (286–1600). The higher molecular weight additive produced higher saturation temperatures and CHF. In addition, a shift in the boiling curve to the right resulting in higher wall superheat could also be observed. The additive with higher viscosity also produced higher boiling HTC.

The need to raise the pool boiling CHF in electronic cooling applications has turned attention to the use of binary mixtures of dielectric liquids. Normington et al. [86] conducted several experiments with the binary liquid mixtures of the perfluoropolyether liquids, D80 and HT110, and perfluorocarbons, FC-84 and FC-104, with saturation temperatures of 81°C, 110°C, 80°C, and 101°C, respectively. The most noticeable change was a dramatic decrease in the temperature overshoot at the incipience when using mixtures compared to single pure liquids. The boiling curve shifted toward the right with increasing amounts of the higher boiling point liquid. CHF was observed to increase as much as 60% with increasing subcooling (50 K). Later, Lee and Normington [87] investigated the application of dielectric binary mixtures in electronic cooling with PPGA packages. Several mixtures of two perfluoropolyether liquids (D80 and HT1100)—varying by volumetric concentration—were tested. The observed deterioration in the HTC was similar to the hydrocarbon mixtures. They did not observe a shift in the boiling curve although two components had saturation temperatures of 81°C and 110°C, respectively. Enhanced CHF values were evident when the concentration of the higher boiling point liquid was increased.

An experimental study of CHF of binary miscible liquid mixtures on an effectively infinite surface was reported by Avedisian and Purdy [88]. Binary mixtures of *n*-pentane as the volatile component with *n*-propanol, *n*-heptane, and *n*-decane were studied for a pressure range of 136–205 kPa on smooth copper surfaces and high flux surfaces (Union Carbide). Higher CHF values with an increase in the concentration of the more volatile liquid were obtained. They also observed higher CHF for high flux surfaces than for smooth heater surfaces in a pentane/propanol mixture.

Two extremes were reported by Fujita and Tsutsui [89] in an experimental study with methanol, ethanol, *n*-butanol, benzene, and water. The boiling curves were not presented for the cylindrical heater, but the main goal was to obtain a correlation to predict the mixture CHF and nucleate boiling HTC. A correlation proposed by the authors could predict the HTC within $\pm 20\%$. For the same mixture (pentane/heptane) concentration, an increase from 136 to 205 kPa of pressure showed a CHF enhancement of 30%.

The influence of ultrasound on pool boiling heat transfer in mixtures of the refrigerants R23 and R134A was studied by Bonekamp and Bier [90]. The authors observed that boiling incipience was reduced to a great extent by exposure to ultrasound. The improvement of heat transfer with mixtures was caused by a decrease of local saturation temperature near the heated wall as a result of better mixing in the liquid boundary layer. The maximum influence of ultrasound on the HTC was observed at a medium saturation pressure ($P/P_c = 0.2$).

McGillis and Carey [91] experimentally examined the pool boiling of mixtures (water/methanol, 2-propanol/water, etc.) at low pressure on a 13-mm square heater with a concentration of 2-propanol in water of $< 20\%$ and found that mixture CHF may be enhanced above the CHF values of the pure liquids. Later, Ahmed and Carey [92] performed an experimental study of pool boiling in binary mixtures. A comprehensive study, including the published correlations in the literature of binary mixtures, was presented. They also discussed the water/2-propanol experimental results and related the difference to the lower surface tension of the more volatile liquid.

Watwe and Bar-Cohen [23] demonstrated significant enhancement of CHF by using low concentrations of FC-40 in FC-72. The addition of a liquid with higher saturation temperature, higher molecular weight, higher viscosity, and higher surface tension led to a significant enhancement in CHF and also an increase in wall temperature. Most of the temperature increase and the enhancement in CHF, associated with the presence of the additive, can be explained by the localized depletion of the lower boiling point liquid in the near-heater region. Liu et al. [32] investigated the role of the mass diffusion effect in pool boiling of binary mixtures. An experimental study was carried out with pure water, pure *n*-propanol, and their mixtures. Significant variation in the boiling characteristics with composition revealed that the mass diffusion effect of the binary mixtures might play an important role in the heat transfer process. A decreasing trend of CHF was observed with increasing *n*-propanol concentration as theoretically expected.

A more recent study by Arik and Bar-Cohen [93] focused on extending the available data on mixture CHF enhancement, as well as pool boiling, on polished silicon surfaces to FC-72/FC-40 mixture ratios of 10%, 15%, and 20% of FC-40 by weight, a pressure range of between 1 and 3 atm, and fluid temperature from 22°C to 45°C, leading to high subcooling conditions. It is

found that peak heat flux can be increased to as high as 56.8 W/cm^2 compared to 25.2 W/cm^2 for pure FC-72 at 3 atm and 22°C . They concluded that the increase in the mixture latent heat of evaporation and surface tension, accompanying the depletion of the lower boiling point fluid in the wall region, plays the major role in enhancing the CHF for binary mixtures.

H. DISSOLVED GAS EFFECTS

Dissolved gases in the boiling liquids can have an effect on the boiling characteristics (i.e., boiling curve, wall superheat, HTC, CHF, etc.). The effect of dissolved air on forced convection subcooled nucleate boiling of water was studied by McAdams et al. [94]. A strong enhancement of the boiling curve at the initial part of nucleate boiling with the inclusion of dissolved air was reported, although it had a weaker effect on the fully nucleate boiling and CHF. In an early study, Behar et al. [95] found that the first bubble formation is due to the degassing of the liquid and further bubble generation was controlled by gas diffusion in the gassy liquid. As a result of the gas saturation, boiling incipience occurred earlier than in a degassed liquid, resulting in a lower wall superheat on the boiling curve. However, they noted that in fully developed nucleate boiling, data obtained over a broad range of gas concentrations merged into a well-defined boiling curve. They performed their experiments in water, nitrogen, and *meta*-terphenyl for both pool and flow boiling.

Torakai et al. [96] performed experiments with platinum wire heaters in water to measure the effect of the dissolved air on the boiling incipience at low pressures. They observed an increase in the wall superheat with increasing air content. Later, Murphy and Bergles [97] performed several experiments with fully saturated R113 and the results showed lower wall superheat as a result of gas presence. Fisenko et al. [98] performed an experimental study with air saturated water and observed about 15–20% enhancement over the degassed water cases for vertically oriented heaters, although the horizontal orientation created 15–20% lower CHF values. A shift toward the left side of the boiling curve was also observed for gassy water conditions.

You [18] conducted detailed research on gas concentration effect in pool boiling to determine its effects on the incipience and wall superheat. They found that for a constant total pressure of 1 bar, CHF increased linearly with increasing dissolved gas content. The dissolved air effect on the incipience was very small for a dissolved gas content of 0.0025 moles/mole, although a significant reduction in the wall superheat was seen when the gas content was doubled. A similar behavior was also presented by Hong et al. [99], who performed an experimental investigation in FC-72 with wire heaters. A lower wall superheat at the same heat flux values led to higher HTCs for gassy liquid studies.

Watwe and Bar-Cohen [22] performed experiments in FC-72 with PPGA packages for both fully air saturated and degassed dielectric liquids. They concluded that the presence of dissolved gas resulted in lower wall superheat values for partially developed nucleate boiling. However, the presence of dissolved air had no effect on the fully developed nucleate boiling heat transfer and the near-heater liquid appeared to be degassed. Consequently, the presence of dissolved air had no additional effect on CHF. A simple gas diffusion model indicated that the degassing of the near-heater superheated liquid at high heat fluxes, by the formation and departure of bubbles, was indeed possible. Rainey and You [29] and Rainey et al. [30] investigated the effect of dissolved gas on FC-72 CHF from plain and microporous enhanced surfaces. They claimed that due to the depletion of dissolved gas near the heater surface, the effect of dissolved gas concentration on pool boiling diminished at higher heat fluxes. As a result, the effect of dissolved gas on CHF became insignificant.

I. EFFECTS OF NANOFLUIDS

Nanofluid enhancement of nucleate pool boiling, from incipience to CHF, has received considerable attention in recent years. Such fluids contain nanoparticles, typically below 100 nm in diameter, dispersed in a bulk liquid to augment thermal conductivity and/or the specific heat and to possibly alter other fluid properties in a favorable way. Due to their small size, it had been expected that these nanoparticles could avoid sedimentation, clogging, and abrasion—problems associated with the use of microsized particles. However, strong evidence exists that the pool boiling of nanofluids produces thin coatings on the heated surfaces, altering the nucleation site density and wetting characteristics of the surface. Nanofluids have been considered as promising candidates for pool boiling and CHF enhancement, but more recent data suggests that the augmentation is highly variable and, in many cases, following a steep initial improvement, deteriorates over time.

You et al. [100] initiated pool boiling CHF studies with nanofluids (water– Al_2O_3 nanofluids). They conducted their experiments on $1 \times 1 \text{ cm}^2$ polished copper surfaces, boiling under subatmospheric pressure conditions ($P = 19.94 \text{ kPa}$) and with nanoparticle concentrations between 0 and 0.05 g/l. They obtained an increasing trend in CHF with concentration of up to 0.005 g/l, where the CHF was three times higher than that for pure water, but beyond this point, there was no significant change in CHF with nanoparticle concentration (Fig. 37).

Vassallo et al. [101] studied pool boiling CHF enhancement with silica–water nanofluids on a 0.4 mm Ni–Cr wire. They used 15 and 90 nm silica nanoparticles at a volume concentration of 0.5%, as well as 3 μm silica particles with a volume concentration of 0.5%. The nanoparticles of bigger size

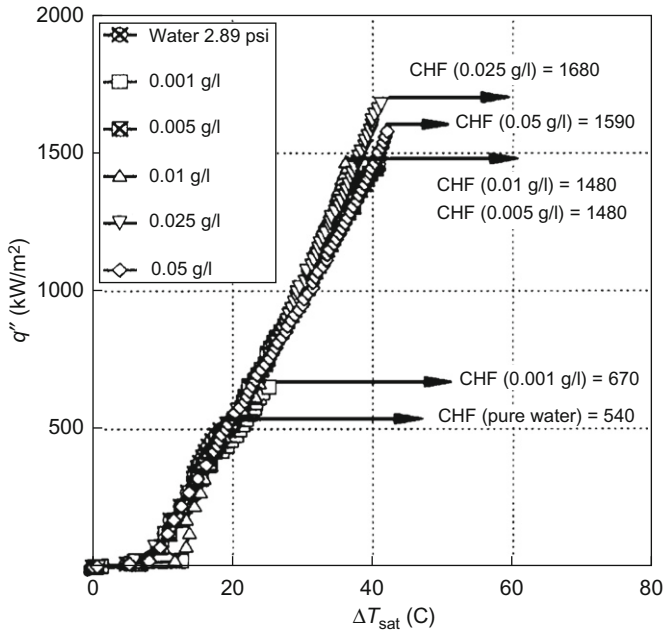


FIG. 37. Boiling curves for various conditions [100].

produced the highest CHF enhancement, reaching three times that of pure water, while 3 μm silica particles provided CHF enhancement only twice that of pure water (Fig. 38), both attained substantial increases in wall superheat. Interestingly, they observed the existence of a nanoparticle coating, formed on the heater surface and changing the surface roughness, but did not provide a mechanistic model to explain the large observed increase in CHF.

Milanova and Kumar [102] studied the effect of nanoparticle size and liquid pH on CHF in pool boiling of water-based silica nanofluids, using a 0.32 mm diameter Ni—Cr wire at atmospheric pressure as the boiling surface. They concluded that in a buffered solution, increased nanoparticle size could augment CHF up to 300% of the CHF of pure water (Fig. 39). They also observed significant deposition of silica particles on the Ni—Cr wire surface and, thus, an increase in the porosity on the surface, which could have played the major role in the enhancement of CHF (Fig. 40).

Bang and Chang [103] investigated pool boiling heat transfer characteristics of Al_2O_3 —water nanofluids, with volumetric concentrations ranging from 0.5% to 4%, for a $4 \times 100 \text{ mm}^2$ rectangular plain surface heater with a depth of 1.9 mm. They obtained modest CHF enhancements of up to 32% and 13% for horizontal and vertical flat surfaces, respectively (Table II), which were much

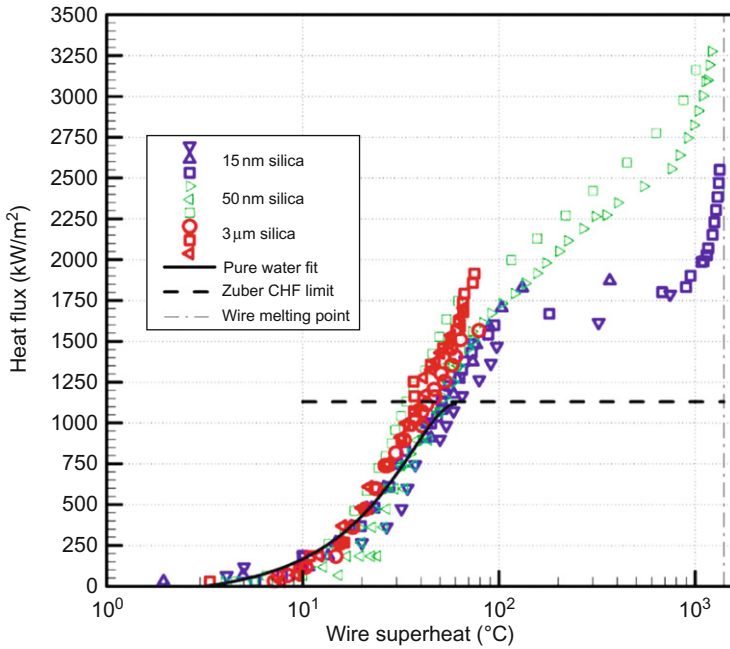


FIG. 38. Boiling curves of Ni-Cr wire ($D = 0.4$ mm) in silica-water solutions [101]. For color version of this figure, the reader is referred to the web version of this book.

smaller than the enhancements recorded in the past studies [100–102]. It was suggested that the flat ribbon heater used in this study, as opposed to the past studies of thin wire heaters, could have influenced the formation of the nanoparticle coating and the surface characteristics resulting from boiling of the nanofluids, leading to lower CHF enhancements.

Kim et al. [104] studied CHF enhancement in pool boiling of water with dilute dispersions ($<0.1\%$ by volume) of alumina (with particle size ranging from 110 to 210 nm), zirconia (110–250 nm), and silica (20–40 nm). In their initial CHF experiments with stainless steel wires of 0.381 mm diameter and 12 cm length, they observed an enhancement in CHF for all the nanofluids, reaching up to 52% with alumina, up to 75% with zirconia, and up to 80% for the silica nanofluids (Fig. 41). The observed enhancement of CHF was ascribed to the porous layer formed on the wire surface by nanoparticle precipitation during nucleate boiling. To examine this precipitate layer in more detail, they performed a second set of experiments with a stainless steel, flat ribbon heater, 5 mm wide, 45 mm long, and 0.05 mm thick. They determined that the roughness and total area of the surface boiled in the nanofluid were increased by a factor of 20 and 5, respectively, over those of a surface boiled

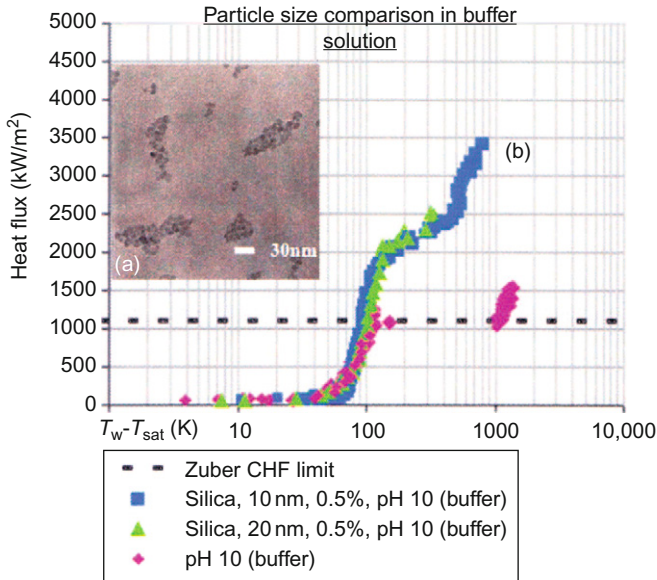


FIG. 39. (a) Agglomeration characteristics as seen in TEM of silica in buffer pH 10. (b) Pool boiling CHF for 10 and 20 nm particles in pH 10 solution [102]. For color version of this figure, the reader is referred to the web version of this book.

in pure water (Fig. 42). They could also detect a decrease in the contact angle on the flat heater and deduced that the improved wettability of the porous surface led to CHF enhancement. However, they could not provide any quantification for the change in the contact angle.

Kim et al. [105] conducted pool boiling experiments on 0.2 mm diameter Ni–Cr wire under atmospheric pressure, using TiO_2 and Al_2O_3 nanoparticles with volumetric concentrations from $10^{-5}\%$ to $10^{-1}\%$. They observed an increase in CHF of Al_2O_3 up to 170% of the value of pure water, as the particle concentration was increased to $10^{-3}\%$. Above this value, the authors reported only a slight increase in CHF (Fig. 43), as they had also reported in the previous CHF studies on Al_2O_3 [100]. A similar trend in the CHF of TiO_2 –water nanofluids was apparent, while with TiO_2 nanoparticles, the CHF enhancement increased to 180% at $10^{-2}\%$, it did continue to increase gently beyond this value. The authors detected nanoparticle coatings on their heater surface and postulated that the increase in surface roughness and the decrease in contact angle (thus the increase in wettability) contributed to enhancement of the CHF (Figs. 44 and 45). Lending support to the critical role played by the precipitate of nanoparticles coating the surface, these authors were able to reproduce the enhanced CHF values, while boiling pure water

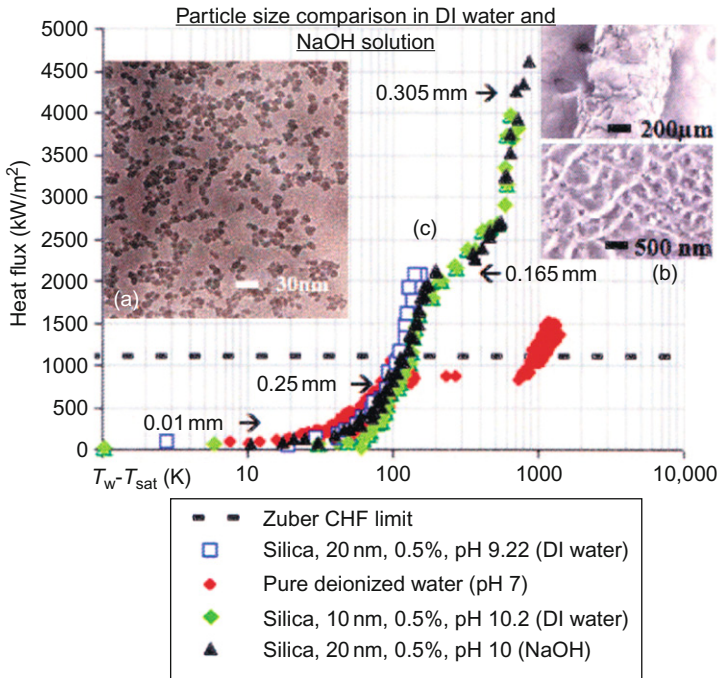


FIG. 40. (a) Colloidal behavior of silica in deionized water as seen in TEM; (b) TEM and SEM pictures of the nichrome wire after deposition of silica; (c) pool boiling CHF for 10 and 20 nm particles in deionized water with no additives and NaOH. Different levels of deposition on the wire are shown in millimeters at different stages of boiling [102]. For color version of this figure, the reader is referred to the web version of this book.

on nanoparticle-coated surfaces (Fig. 46). In contrast to boiling with the nanofluids, they did not observe any asymptote in CHF enhancement for pure water on TiO_2 nanoparticle-coated heaters, while for Al_2O_3 -coated surfaces the profile of pure water was similar to nanofluid profile over the entire particle concentration range. They interpreted this different behavior as resulting from the capillary wicking capability of the coating, observing that for pure water on a TiO_2 coating, the capillary wicking height increased significantly with the concentration and was much larger than for Al_2O_3 . The authors could not separate the effects of wettability, surface roughness, and capillary wicking caused by nanoparticle coating from each other, so that no quantification of the contribution from each parameter could be given.

Liu and Liao [106] performed pool boiling heat transfer experiments and used water- and alcohol-based nanofluids with CuO and SiO_2 nanoparticles having 50 and 35 nm average diameters, respectively. They focused on the

TABLE II
CHF ENHANCEMENT [103]

	Prediction of water	Pure water	0.5% NF	1% NF	2% NF	4% NF
Horizontal test	1.22	1.74	2.30	2.64	2.57	2.4
Section ($\theta = 90$)	MW/m ²	MW/m ²	MW/m ²	MW/m ²	MW/m ²	MW/m ²
Vertical test	0.88	1.2	1.36	1.36	1.36	1.36
Section ($\theta = 0$)	MW/m ²	MW/m ²	MW/m ²	MW/m ²	MW/m ²	MW/m ²

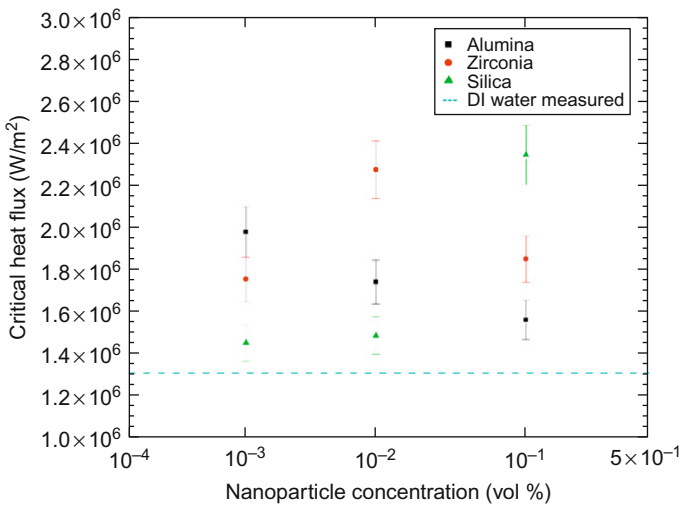


FIG. 41. CHF data for pure water and alumina, zirconia, and silica nanofluids [104]. For color version of this figure, the reader is referred to the web version of this book.

sorption and agglutination phenomenon of nanoparticle suspensions and their effects on pool boiling heat transfer. The authors observed a thin sorption layer of nanoparticles on the surface (Fig. 47), which remained as a residual very thin and smooth coating of nanoparticles even after cleaning (Fig. 48). They obtained enhancements in CHF of 27% and 18% with CuO and SiO₂ nanoparticle suspensions in water-based solutions, respectively, while a deterioration in heat transfer was apparent. Similar results were also acquired for the alcohol-based solutions, i.e., an enhancement of 31% and 20% in CHF for CuO and SiO₂ nanoparticle suspensions, respectively. These distinct CHF enhancement values revealed the effect of the nanoparticle material and prompted the authors to link the change in CHF and boiling heat transfer to the sorption layer formed on the heating surface during boiling. It was argued that this soprtion layer reduced the contact angle and the number of active

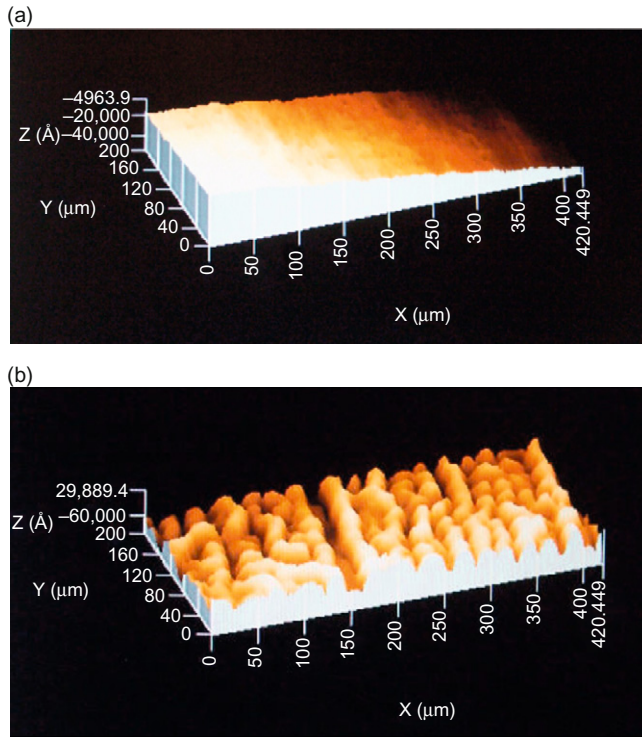


FIG. 42. Profilometer images of the flat heater surface after boiling (a) pure water and (b) 0.01 vol% alumina nanofluid. The RMS roughness values are 0.1 and 2 μm , respectively. Similar results were obtained with the other nanofluids [104]. For color version of this figure, the reader is referred to the web version of this book.

nucleation sites leading to less bubble formation and less probability of vapor blankets in the vicinity of the heater and resulted in an enhancement in CHF.

In a recent study, Wen [107] claimed that the nanoparticle coating modification of the heating surface alone could not account for the CHF enhancement reported in the previous studies. To support this claim, he utilized the concept of “structural disjoining pressure” proposed by Sefiane [108], which was hypothesized to arise in a microlayer in the presence of nanoparticles and was originated from the confinement of particles in a thin film. The arrangement of particles inside the resulting layer was held responsible for generating an excess pressure called as “structural disjoining pressure.” As a result of this pressure, improved wetting capabilities could be obtained. In order to quantify the effect of the structural disjoining pressure, the author developed a simple model based on the interfacial shape of a dry patch (Fig. 49). He found that

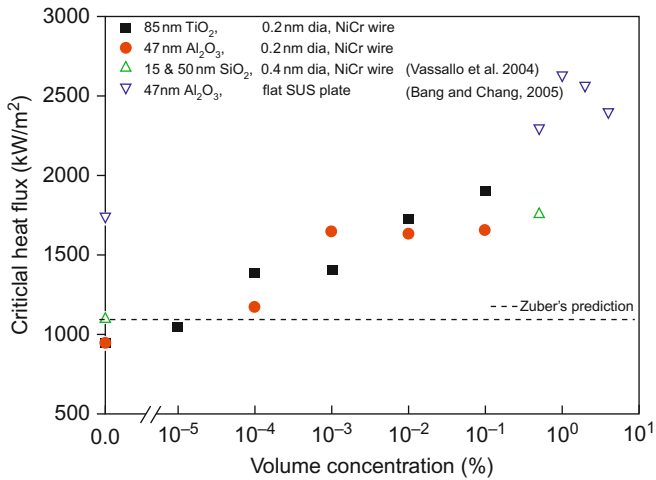


FIG. 43. Comparison of pool boiling CHF values with data from previous research [105]. For color version of this figure, the reader is referred to the web version of this book.

the influence of this resulting force could extend to a thickness of few nanoparticle diameters, a longer range than the more familiar van der Waals and electrostatic forces, and act to increase wettability and inhibit dry patch formation, leading to a delay in the CHF condition (Figs. 50 and 51).

Kathiravan et al. [109] conducted CHF experiments on stainless steel tube heaters of an outer diameter of 9 mm and an average surface roughness of 1.09 μm using copper nanoparticles of 0.125–1% concentrations (by weight) dispersed in water and water with 9 wt% of sodium dodecyl sulfate (SDS). Similar to the findings in the previous studies, they observed an asymptotic behavior of boiling heat transfer with an increase in nanoparticle concentration, which they associated with the filling up of tube surface cavities via nanoparticle deposition and consequent reduction of nucleation sites. CHF enhancement up to 50% was also evident in this study and was explained by a developed nanoporous layer on the heating surface, which reduced the contact angle and trapped liquid in this layer and thus prevented vapor blanket formation. The thickness of this sorption layer did not change beyond a certain nanoparticle concentration so that CHF became insensitive to the particle concentration (Fig. 52). This nanoporous layer also affected the surface roughness and had a reducing effect on this parameter (Table III). With the introduction of surfactant, boiling heat transfer was augmented by 30%, which was related to the reduction in the surface tension. The decreased surface tension might have led to a smaller CHF compared to water; however, CHF did benefit from the presence of the nanoparticles, increasing asymptotically with nanoparticle concentration.

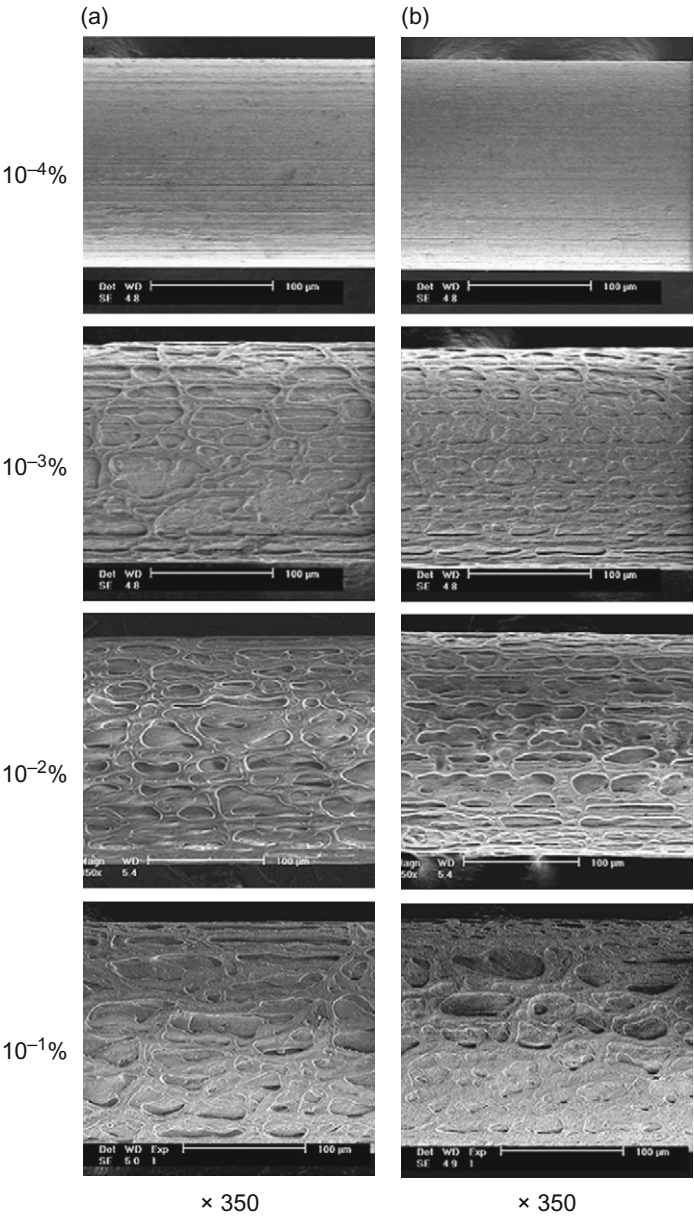


FIG. 44. SEM images of heater surfaces after pool boiling of (a) Al_2O_3 –water nanofluids on a bare heater and (b) pure water on Al_2O_3 nanoparticle-coated heaters [105].

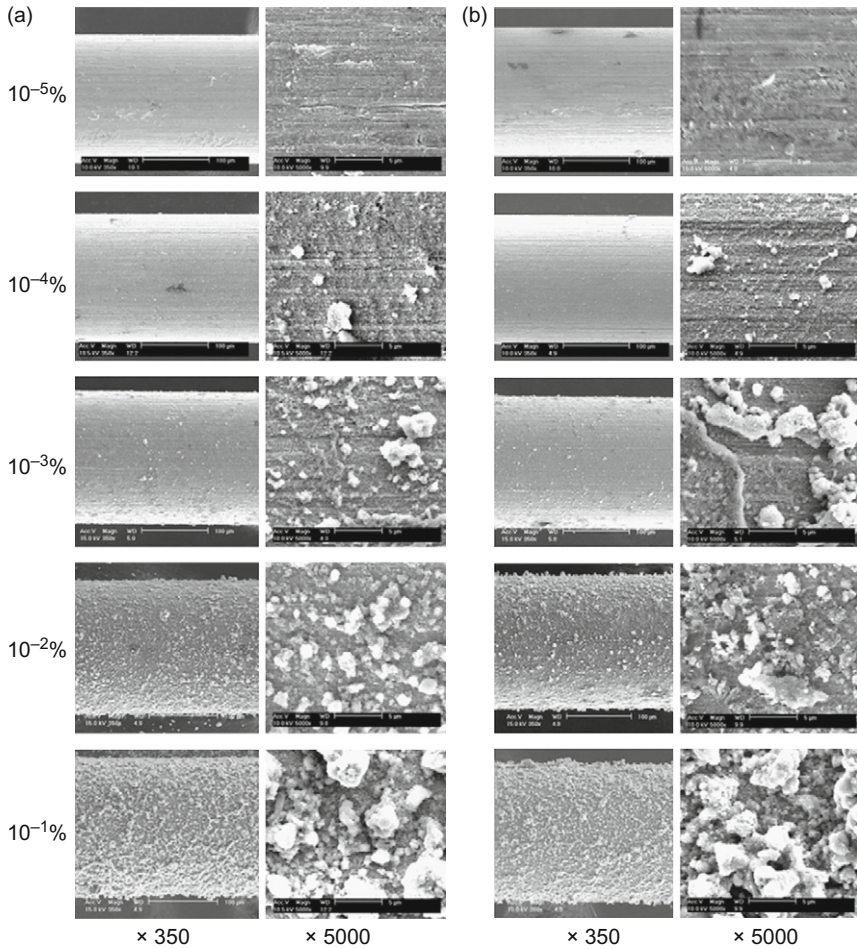


FIG. 45. SEM images of heater surfaces after pool boiling of (a) TiO_2 –water nanofluids on a bare heater and (b) pure water on TiO_2 nanoparticle-coated heaters [105].

Kim et al. [110] also studied the mechanism of pool boiling CHF enhancement in nanofluids. In their study they used water-based nanofluids, with alumina and titania particles occupying 0.01% (by volume) and investigated CHF on a disk heater under saturated conditions at atmospheric pressure. They reported enhancements in CHF of 30–40% and could observe nanoparticle deposition during pool boiling (Fig. 53). They repeated their experiments with pure water boiling on the nanoparticle-deposited surface to filter out the effect of nanoparticle deposition during pool boiling on CHF. The enhancement in

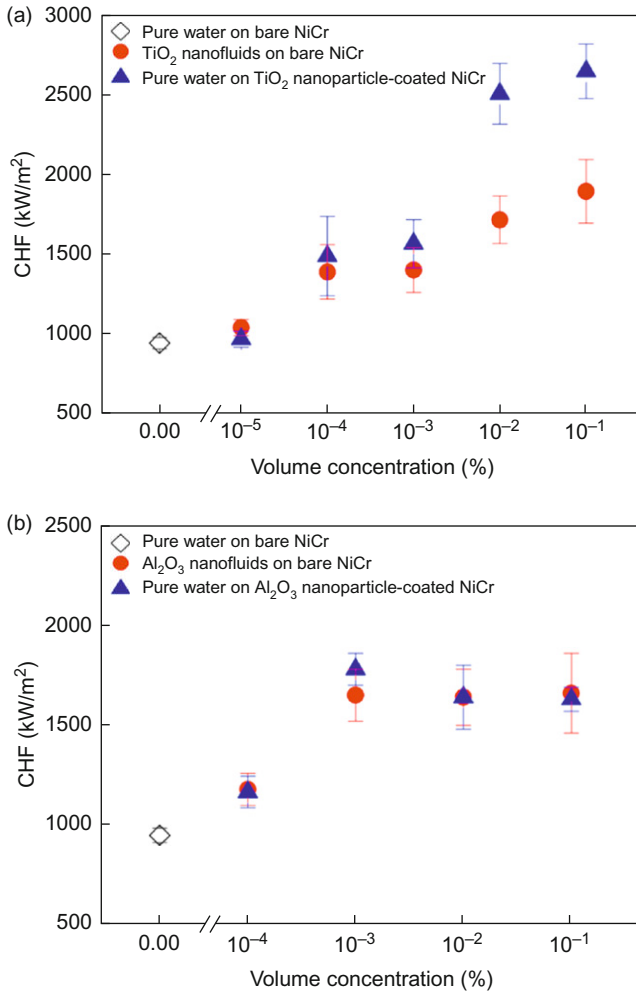


FIG. 46. Comparison of CHF enhancements of nanofluids on a bare heater and pure water on nanoparticle-coated heaters: (a) TiO₂; (b) Al₂O₃ [105]. For color version of this figure, the reader is referred to the web version of this book.

CHF with pure water was close to the nanofluid results, suggesting that the main contribution to CHF during pool boiling was the nanoparticle deposition on the heater (Table IV). Similar to the previous studies, the authors related the CHF enhancement on the deposited nanoparticle layer after pool boiling, which improved the wettability and also the stability of the evaporating meniscus on the heated surface, so that CHF condition was delayed and occurred at

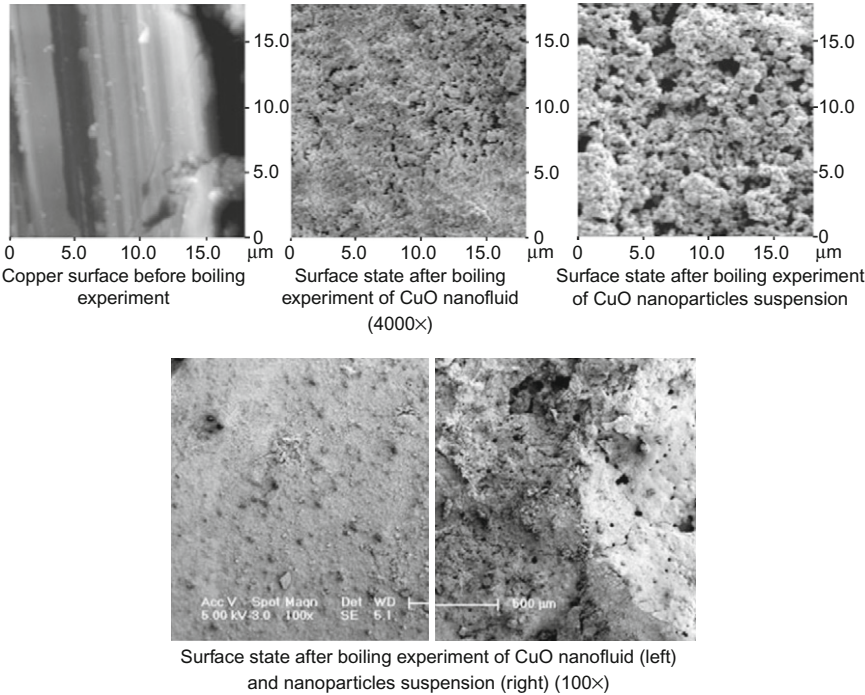


FIG. 47. Photographs of the heating surface after the water, CuO suspensions, and CuO fluids tests [106].

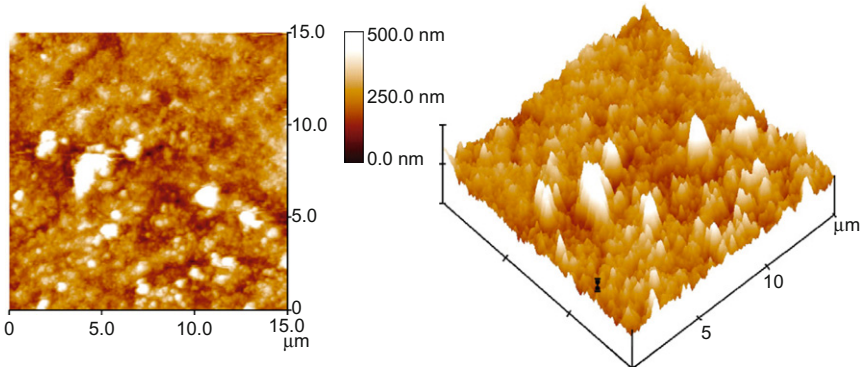


FIG. 48. 2D and 3D microphotographs of the surface status after CuO suspension test and cleaning process [106]. For color version of this figure, the reader is referred to the web version of this book.

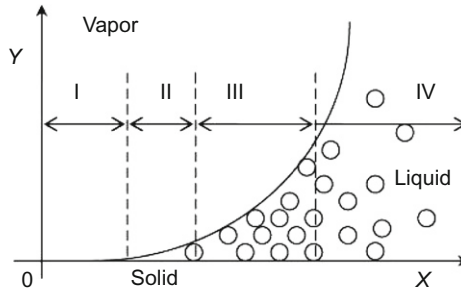


FIG. 49. Four-zoned microlayer model of thermal nanofluids [107].

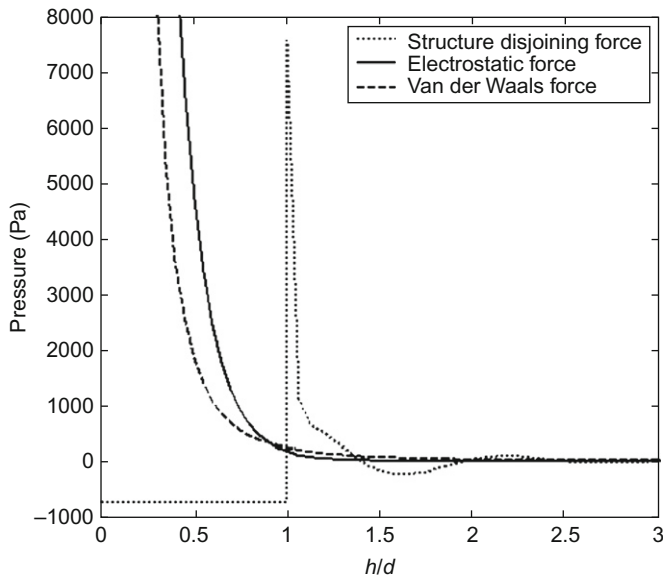


FIG. 50. Comparison of structural disjoining pressure with DLVO forces [107].

higher heat fluxes. They supported their claim with images of evaporating water droplets on clean and nanoparticle-deposited surfaces and combined consideration of a hot spot and the microhydrodynamics of a thin liquid meniscus to provide a physical mechanism for the CHF enhancement with nanofluids.

Truong et al. [111] investigated pool boiling CHF of nanofluids on sand-blasted heaters using water-based nanofluids, with diamond (0.01 vol%), zinc oxide (0.1 vol%), and alumina (0.1 vol%) nanoparticle concentrations; the authors observed nanoparticle deposition on the sandblasted plate heaters,

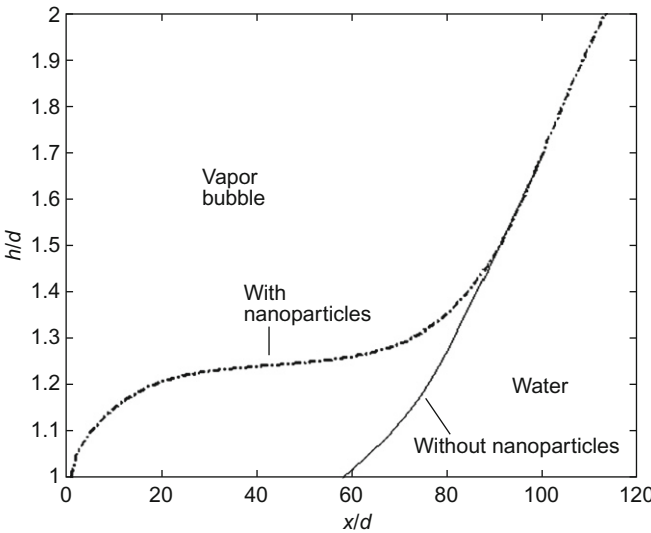


FIG. 51. Interfacial shapes with and without nanoparticles [107].

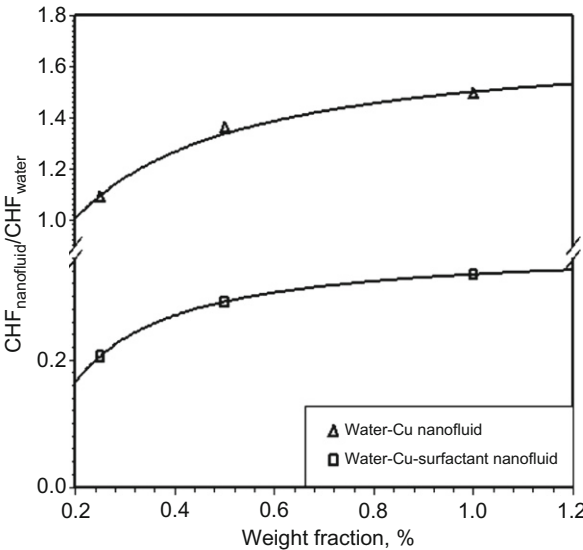


FIG. 52. Increase in critical heat flux with concentration of nanoparticles.

TABLE III
ROUGHNESS OF HEATER BEFORE AND AFTER BOILING [109]

No.	Before experiment (μm)		After experiment (mm)	
	R_a	R_q	R_a	R_q
1	0.877	1.35	513.5	659.54
2	1.31	1.79	660.57	990.87
3	1.22	1.58	774.38	1,220
4	0.975	1.38	338.2	518.99

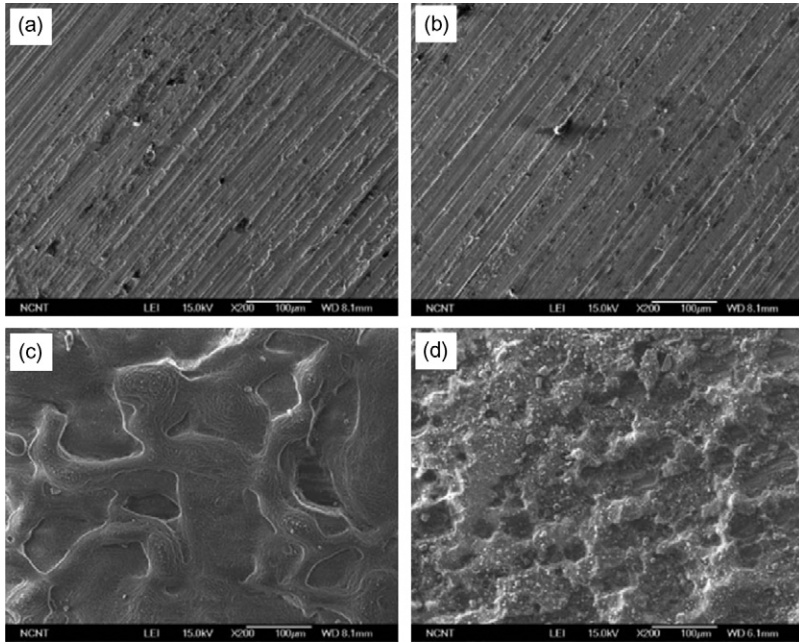


FIG. 53. SEM photographs of various copper heater surfaces: (a) fresh, (b) water boiled, (c) alumina nanofluid boiled, and (d) titania nanofluid boiled [110].

leading to an increase of $\sim 35\%$ in CHF for zinc oxide and alumina coatings, while the enhancement was 11% for diamond coatings (Fig. 54). This study revealed the potential of the use of nanofluids for enhancing CHF on engineered surfaces, in addition to the effect of nanoparticle material on CHF enhancement. As in previous studies, the increase in the wettability with nanoparticles and the consequent decrease in contact angle were considered as the reason behind CHF enhancement (Table V).

TABLE IV
HEAT FLUX AND WALL SUPERHEAT AT THE CHF POINTS DURING NANOFUID BOILING ON A CLEAN SURFACE AND PURE WATER BOILING ON A NANOPARTICLE-FOULED SURFACE [110]

Substrate	Nanoparticle	Nanofluids on a clean surface		Pure water on a fouled surface	
		q''_{CHF} (kW/m ²)	ΔT_{wall} (K)	q''_{CHF} (kW/m ²)	ΔT_{wall} (K)
Copper	Alumina	2,400 (1.40)	67	2,640 (1.51)	45
		2,280 (1.33)	60	2,170 (1.27)	46
		2,260 (1.32)	76	2,240 (1.31)	31
	Titania	2,410 (1.41)	76	2,240 (1.31)	57
Nickel	Alumina	2,185 (1.29)	72	N/A	N/A
	Titania	2,260 (1.34)	77	2,300 (1.36)	57

The average CHF values of pure water were 1710 kW/m² for copper and 1690 kW/m² for nickel, respectively. The values in parenthesis indicate the enhancement above the CHF values of pure water on the same substrate material.

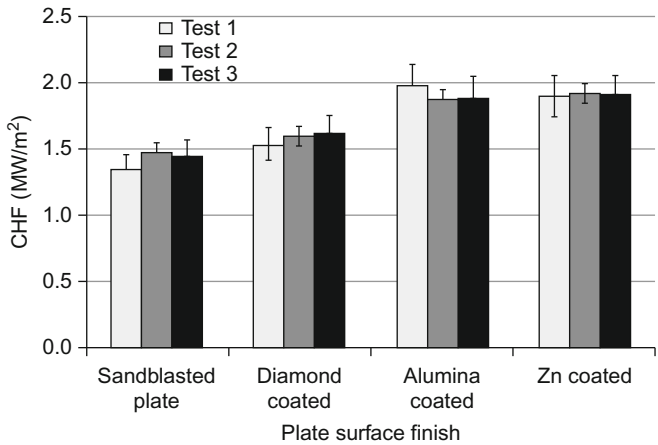


FIG. 54. CHF of water with different plate surface finish [111].

Kwark et al. [112] experimentally studied pool boiling of low concentration nanofluids (<1 g/l) containing Al₂O₃, CuO, and diamond nanoparticles over a flat heater under atmospheric conditions. They reported an increase in CHF with nanoparticle concentration up to a critical value (~0.025 g/l), beyond which CHF displayed a nearly constant profile (Fig. 55). They associated this increase with nanocoating occurring during boiling, whose thickness increased with time and which significantly influenced both CHF and boiling heat

TABLE V
CONTACT ANGLES OF WATER ON DIFFERENT HEATER SURFACES ($\pm 5^\circ$) [111]

Surface	At time $t = 0$ min	At time $t = 1.5$ min
Sandblasted bare	94	67
Diamond coated	74	48
Alumina coated	43	18
Zinc oxide coated	44	13

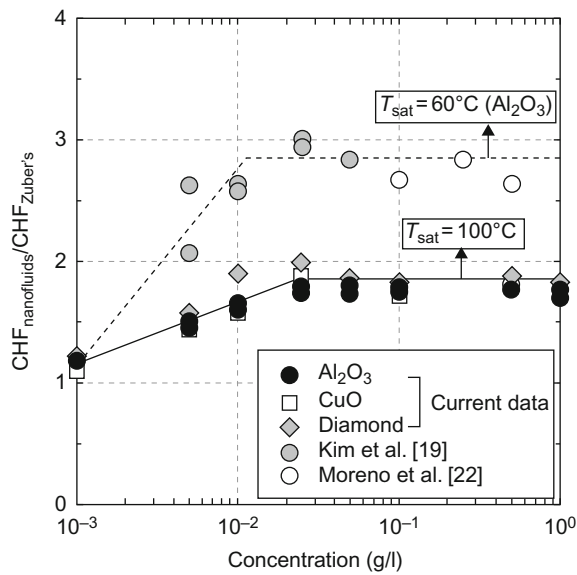


FIG. 55. CHF enhancement, defined as the ratio of nanofluid CHF over water CHF as predicted by Zuber's correlation, for the various nanofluids [112].

transfer. Increasing the nanoporous layer thickness beyond a certain value generated no further increase in CHF, whereas boiling heat transfer was degraded for thicker layers. With the assistance of a visualization study, microlayer evaporation was observed to be responsible for nanoparticle coating resulting from nucleate boiling (Fig. 56). As the microlayer evaporated, nanoparticles in this layer bonded to the heater surface. In their later study, Kwark et al. [113] repeated their experiments with Al_2O_3 –ethanol nanofluids. They obtained similar findings and observed that the nanoparticle coating forming during boiling experiments was more uniform compared to water-based nanofluids, which

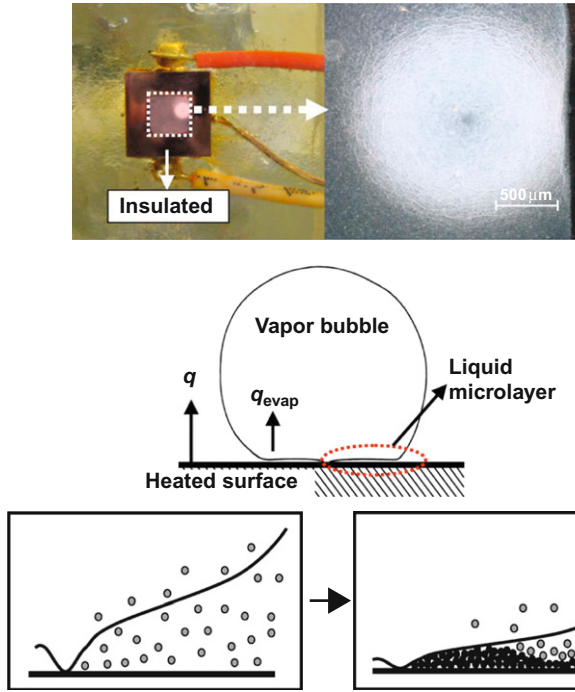


FIG. 56. Images of nanoparticle coating generated on the heater surface, from a single bubble (top) and mechanism of the particle deposition during the boiling process (microlayer evaporation) [112]. For color version of this figure, the reader is referred to the web version of this book.

was explained with smaller bubble diameters and the lower surface tension of ethanol. Using the contact angle data they acquired, they developed an expression relating CHF to contact angle based on linear regression (Fig. 57), which implied a strong dependence of CHF on surface wettability affected by nanoparticle coating. Haramura [114] investigated the effect of contact angle on CHF and could provide the following curve fit for the CHF data of Liaw and Dhir [115] and Maracy and Winterton [116] as a function of contact angle to account for the effect of contact angle on CHF:

$$\frac{\text{CHF}}{h_{\text{fv}}\sqrt{\rho_v}[\sigma_f g(\rho_f - \rho_v)]^{1/4}} = (0.1 \exp(-\theta/45^\circ) + 0.055) \quad (26)$$

According to the above curve fit equation, a decrease of 74% in CHF will occur when the contact angle varies from 20° to 90°. As can be observed from Fig. 57, a decrease of 67%, which is about the same decrease as predicted by Eq. (26), in CHF is apparent when the contact angle is changed from

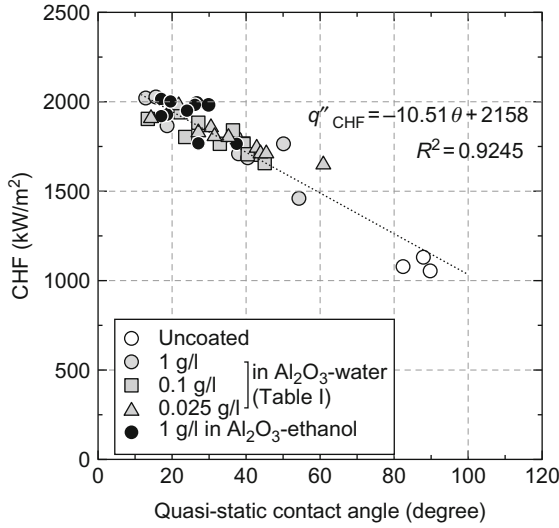


FIG. 57. Overall relationship between quasi-static contact angle (values at 60 s) and CHF for coatings developed in nanofluids (water- and ethanol-based) throughout current study (various heat fluxes, concentrations, and durations) [113].

20° (corresponding to uncoated surface) to 90° (corresponding to nanoparticle-coated surface). This implies that the change in CHF with nanofluids is due to the change in the contact angle with nanoparticle deposition.

III. Conclusions

The growing demand for aggressive thermal management of consumer and power electronics has directed considerable attention to characterizing, harnessing, and augmenting boiling and evaporative thermal transport from electronic materials to inert, dielectric liquids. Passive pool boiling of the dielectric perfluorocarbon liquids is a most effective technique for thermal management of electronic components but is limited by the CHF, representing the upper limit of the nucleate pool boiling regime. The present study provides a comprehensive review and summary of the extensive body of work on dielectric liquid, pool boiling CHF, as reported in more than 100 archival papers by research groups from around the globe, and seeks to clearly define the state of the art in this specific domain of ebullient thermal transport. This review of the parametric effects of fluid properties, pressure, subcooling, binary mixtures,

micro/nanoporous-coated surfaces, heater thermophysical properties, and nanofluids on the pool boiling heat transfer characteristics suggests the following general and specific conclusions.

The effects of subcooling and pressure on pool boiling CHF of the dielectric liquids are substantial and appear to follow the accepted behavior for pool boiling heat transfer. The use of liquid mixtures, with low-to-moderate concentrations of the higher molecular weight liquid, has been found to provide significant enhancement of CHF, with an associated increase in the wall superheat and temperature. Modification of an initially plain surface by removing material (e.g., roughening, blasting), adding material (e.g., porous coatings, deposition with templates), and/or manufacturing the surface with specially designed features (e.g., finned surfaces) is one of the very effective ways to enhance CHF.

More recently, under the influence of interdisciplinary micro-/nanoscale fabrication techniques, attention has turned to more sophisticated surface enhancements mainly targeted at electronics cooling applications and including protrusions, cavities, and porous structures. The results for these surfaces, as well as for pool boiling of nanofluids and nanostructured surfaces, have shown highly variable results, with some highly significant enhancement in CHF compared to unseeded liquids.

- Pool boiling experiments of FC-72 revealed that wall superheat values shift toward left of the boiling curve with the increasing pressure. The effect of elevated pressure on CHF is beneficial and higher CHF values were obtained with increasing pressure.
- CHF increased linearly with decreasing bulk temperature at a specified pressure. Greater effects on CHF were observed in silicone flat surfaces than thin wire heater results published in the literature.
- The addition of a moderate concentration of FC-40, a liquid with higher saturation temperature, higher molecular weight, higher viscosity, and higher surface tension than FC-72, was found to lead to a significant enhancement in CHF, relative to that attained in pure FC-72. Most of this binary mixture increase in the wall superheat and the enhancement in CHF can be explained by the localized depletion of the lower boiling point liquid in the near-heater region. In addition, the surface tension gradient, created on the surface of the bubbles by the concentration gradient in the binary mixture, may act to enhance liquid motion near the surface. An increase of the CHF by as much as 60%, accompanied by a shift of the boiling curve to as much as 40 K higher wall superheats, was observed. Only marginal CHF improvement was found for FC-40 concentrations $> 15\%$. This enhancement of CHF has not been well understood and further research has to be performed to understand the localized distribution of fluids. In addition, there is not any sophisticated model available for predicting CHF and local fluid distribution in the liquid pool.

- The typical CHF performance benefit of a microporous coating of diamond particles was found to be in the range of 50% above the bare surface, though exceptional improvements by more than 200% were also observed. Coated heaters showed that increasing pressure decreased the subcooling effect on CHF.
- Despite comparable saturation temperatures, CHF values 50–90% higher than FC-72 were obtained for both HFE-7100 and HFE-7200 with silicon chip packages. CHF increased linearly with increasing subcooling at a constant pressure. The highest subcooling effect was observed at the atmospheric condition.
- In addition to the effects of fluid properties, liquid pressure, and liquid subcooling, prior work had revealed that CHF varied with the product of the heater thickness and the square root of thermal effusivity $(\rho ck)_h$ reflecting the beneficial role of transient thermal conduction in smoothing the surface temperature variations. The thinnest chip was found to yield the lowest CHF value, and the measured values of CHF increased asymptotically with the product of the heater thickness and the square root of thermal effusivity.
- In a pool boiling process, enhanced surfaces are generally capable of lowering boiling incipience, increasing nucleate boiling HTC, and extending CHF limit beyond what a plain surface can normally achieve. Depending on the specific structure type, these can be attributed to several mechanisms including larger surface area, higher active nucleation site density, increased hydrodynamic stability, and improved wetting characteristics.
- In addition to the three types of microscale surface enhancement structures, very thin, nanoscale surface modifications have become a research interest in recent years. Studies indicated that the imperfections encountered during the processes resulted in micron-size cavities, along with the intended nanosize structures. Micron-size cavities were able to help initiate boiling at favorably low superheats, while the nanoscale structures could still improve the wettability leading to higher CHF.
- Therefore, nanoscale surface enhancements seem to achieve reasonable CHF increase with much thinner structures. This extends the applicability of enhanced surfaces into new areas previously restricted by size, such as microchannels.
- Based on the reviewed studies with saturated FC-72, micro- and nanoscale surface enhancement structures could provide CHF improvement of up to 100% and 70%, respectively.
- Due to the many variations of surface structures, and their effects on other parameters, there is no general correlation that can accurately predict the CHF of enhanced surfaces. Available correlations are usually applicable for certain fluid and surface types. Nevertheless, existing and ever-expanding literature would still provide useful design guidelines.

- Nanoparticle coating on their heater surface, which modified the surface characteristics, was apparent during pool boiling of nanofluids. This leads to the increase in surface roughness and the decrease in contact angle (thus the increase in wettability), both of which contribute to enhance CHF.
- After the nanoparticle coating on heated surfaces with pool boiling, pool boiling experiments with unseeded fluids produced CHF values close to the ones with nanofluids suggesting that the reason behind the CHF enhancement is the modifications in surface characteristics.
- There exists a critical value of nanoparticle concentration in nanofluids, beyond which CHF is insensitive to the nanoparticle concentration. More research efforts are necessary to determine this critical concentration.
- The concept of “structural disjoining pressure” proposed as the alternative reason to surface modification due to nanoparticle coating during pool boiling for the CHF enhancement mechanism should be further developed to better assess CHF phenomenon in nanofluid pool boiling.
- Even though there are several attempts to improve the CHF prediction capability, regrettably an accurate correlation does not exist that will capture all of the parameters that impact CHF. An attempt to expand CHF database was given by compiling a total of 336 CHF values for a wide range of pressure, subcooling, and heater size, as well as heater material and thickness. The modified TME correlation proposed by Arik and Bar-Cohen [8] was found to predict CHF to within 24.8% with a 95% confidence level but still misses mixture, coating, and nanofluid effects over the pool boiling CHF.

References

- [1] W.M. Rohsenow, P. Griffith, Correlation of maximum heat flux data for boiling of saturated liquids, *Chem. Eng. Prog. Symp. Ser.* 52 (1956) 47–49.
- [2] W.M. Rohsenow, Heat transfer with boiling, *Modern Developments in Heat Transfer*, The MIT Press, Cambridge, MA, 1964, pp. 169–260.
- [3] N. Zuber, Atomic energy commission technical information service, Atomic Energy Commission Report AECU-4439, 1959.
- [4] D.B. Kirby, J.W. Westwater, Bubble and vapor behavior on a heated horizontal plate during pool boiling near burnout, *Chem. Eng. Prog. Symp. Ser.* 57 (1965) 238–248.
- [5] C.L. Yu, R.B. Mesler, Study of nucleate boiling near the peak heat flux through measurements of transient surface temperature, *Int. J. Heat Mass Transfer* 20 (1988) 827–840.
- [6] Y. Haramura, Y. Katto, A new hydrodynamic model of critical heat flux applicable widely to both pool and forced convective boiling on submerged bodies in saturated liquids, *Int. J. Heat Mass Transfer* 26 (1983) 389–399.
- [7] J.E. Galloway, I. Mudawar, CHF mechanism in flow boiling from a short heated wall—Part I: Examination of near wall conditions with the aid of photomicrography and high speed video imaging, *Int. J. Heat Mass Transfer* 36 (1993) 2511–2526.

- [8] M. Arik, A. Bar-Cohen, Effusivity-based correlation of surface property effects in pool boiling CHF of dielectric liquids, *Int. J. Heat Mass Transfer* 46 (2003) 3755–3765.
- [9] R.D. Danielsen, L. Tousignat, A. Bar-Cohen, Saturated pool boiling characteristics of commercially available perfluorinated inert liquids, *Proceedings of 1987 ASME/JSME Thermal Engineering Joint Conference*, Honolulu, Hawaii, vol. 3, 1987, pp. 419–430.
- [10] A. Bar-Cohen, A. McNeil, Parametric effects on pool boiling critical heat flux in highly wetting liquids, *Proceedings of Engineering Foundation Conference on Pool and External Flow Boiling*, Santa Barbara, CA, 1992, pp. 171–175.
- [11] T.Y.T. Lee, M. Mahalingam, P.J.C. Normington, Subcooled pool boiling critical heat flux in dielectric liquid mixtures, 28th National Heat Transfer Conference, ASME HTD vol. 206, 1992, pp. 55–62.
- [12] S.S. Kutateladze, A hydrodynamic theory of changes in the boiling process under free convection conditions, *Izv. Akad. Nauk SSSR, Otdel. Tekhn. Nauk* 4, Translated in AEC-TR-1441, 1951, p. 529.
- [13] S.S. Kutateladze, L.L. Schneiderman, Experimental study of influence of temperature of liquid on change in the rate of boiling, USAEC Report—AEC Transactions 3405, 1953, pp. 95–100.
- [14] H.J. Ivey, D.J. Morris, CHF of saturation and subcooled pool boiling in water at atmospheric pressure, *Proceedings of 3rd International Heat Transfer Conference*, 1966, p. 129.
- [15] Y. Elkassabgi, J.H. Lienhard, Influences of subcooling on burnout of horizontal cylindrical heaters, *J. Heat Transfer* 110 (1988) 479.
- [16] U.P. Hwang, K.P. Moran, Boiling heat transfer of silicon integrated circuits chip mounted on a substrate, *Heat Transfer in Electronic Equipment*, ASME HTD vol. 20, 1981, pp. 53–59.
- [17] I. Mudawar, T.M. Anderson, High flux electronic cooling by means of pool boiling—Part I: Parametric investigation of the effects of coolant variation pressurization, subcooling and surface augmentation, *Heat Transfer in Electronics*, 26th National Heat Transfer Conference, ASME HTD vol. 111, 1984, pp. 25–34.
- [18] S.M. You, Pool Boiling Heat Transfer with Highly-Wetting Dielectric Fluids, Ph.D. Thesis, Mechanical Engineering, University of Minnesota, Minneapolis, 1990.
- [19] R.D.M. Carvalho, A.E. Bergles, The influence of subcooling on the pool nucleate boiling and critical heat flux of simulated electronic chips, 1990 IHTC, 1990, pp. 289–294.
- [20] A.E. Bergles, What is real mechanism of CHF in pool boiling? *Pool and External Flow Boiling ASME* 1992, 1992, pp. 165–170.
- [21] A.C. McNeil, Pool Boiling Critical Heat Flux in a Highly Wetting Liquid, Master's Thesis, University of Minnesota, Minneapolis, 1992.
- [22] A.A. Watwe, A. Bar-Cohen, Nucleate pool boiling and critical heat flux in gas-saturated dielectric coolants, 2nd European Thermal Sciences Conference and 14th UIT National Heat Transfer Conference, 1996, pp. 1631–1638.
- [23] A.A. Watwe, A. Bar-Cohen, Enhancement of pool boiling critical heat flux using dielectric liquid mixtures, *Proceedings of IRSEE, Germany*, 1997.
- [24] M.J. Brusstar, H. Merte, R.B. Keller, B. Kirby, Effects of heater surface orientation on the critical heat Flux—I. An experimental evaluation of models for subcooled pool boiling, *Int. J. Heat Mass Transfer* 40(17) (1997) 4007–4019.
- [25] M.J. Brusstar, H. Merte, Effects of heater surface orientation on the critical heat Flux—II. A model for pool and forced convection subcooled boiling, *Int. J. Heat Mass Transfer* 40(17) (1997) 4021–4031.
- [26] S.G. Kandlikar, Critical heat flux in subcooled flow boiling—an assessment of current understanding and future directions for research, *Boiling 2000—Engineering Science Foundation Conference*, Alaska, 2000.

- [27] M. Arik, Enhancement of Pool Boiling Critical Heat Flux in Dielectric Liquids, Ph.D. Dissertation, Department of Mechanical Engineering, University of Minnesota, Minneapolis, 2001.
- [28] A.A. Watwe, Measurement and Prediction of the Pool Boiling Critical Heat Flux in Highly Wetting Liquids, Ph.D. Thesis, University of Minnesota, Minneapolis, 1996.
- [29] K.N. Rainey, S.M. You, Pool boiling heat transfer from plain and microporous, square pin finned surfaces in saturated FC-72, *J. Heat Transfer* 122(3) (2000) 509–516.
- [30] K.N. Rainey, S.M. You, S. Lee, Effect of pressure, subcooling, and dissolved gas on pool boiling heat transfer from microporous surfaces in FC-72, *J. Heat Transfer* 125(1) (2003) 75–83.
- [31] M.S. El-Genk, J.S. Parker, Enhanced boiling of HFE-7100 dielectric liquid on porous graphite, *Energy Convers. Manage.* 46 (2005) 2455–2481.
- [32] M.N. Liu, Y.M. Yang, J.R. Maa, The role of the mass diffusion effect in pool boiling of binary mixtures, in: M. Lehner, F. Mayinger (Eds.), Taylor and Francis, Philadelphia, PA, 1999, pp. 71–77.
- [33] M.S. El-Genk, H. Bostanci, Combined effects of subcooling and surface orientation on pool boiling of HFE-7100 from a simulated electronic chip, *J. Exp. Heat Transfer* 16 (2003) 281–301.
- [34] V.G. Morozov, An experimental study of critical heat flux loads at boiling of organic liquids on a submerged heating surfaces, *Int. J. Heat Mass Transfer* 2 (1960) 252–258.
- [35] J.H. Lienhard, V.E. Schrock, The effect of pressure, geometry, and the equation of state upon the peak and minimum boiling heat flux, *J. Heat Transfer* 85 (1963) 261–272.
- [36] J.H. Lienhard, K. Watanabe, On correlating the peak and minimum boiling heat fluxes with pressure and heater configuration, *J. Heat Transfer* 88 (1966) 94–100.
- [37] L. Bernath, A theory of local boiling burnout and its application to existing data, *Chem. Eng. Prog. Symp. Ser.* 56 (1960) 95.
- [38] R. Cole, H.L. Shulman, Critical heat flux at sub-atmospheric pressures, *Chem. Eng. Sci.* 21 (1966) 723–724.
- [39] M. Carne, D.H. Charlesworth, Thermal conduction effects on the CHF in pool boiling, *Chem. Eng. Prog. Symp. Ser.* 62 (1966) 24.
- [40] F. Tachibana, M. Akiyama, H. Kawamura, Non hydrodynamic aspects of pool boiling burnout, *J. Nucl. Sci. Technol.* 4 (1967) 121.
- [41] U. Magrini, E. Nannei, On the influence of the thickness and thermal properties of heating walls on the heat transfer coefficients in nucleate pool boiling, *J. Heat Transfer* (1975) 173–178.
- [42] G. Guglielmini, E. Nannei, On the effect of heating wall thickness on pool boiling burnout, *Int. J. Heat Mass Transfer* 19 (1976) 1073.
- [43] V.A. Grigoriev, V.V. Klimenko, Y.M. Pavlov, Y.V. Amitestov, The influence of some heating surface properties on the CHF in cryogenics liquids boiling, *Proceedings of 6th International Heat Transfer Conference*, vol. 1, 1978, p. 215.
- [44] J.R. Saylor, An Experimental Study of the Size Effect in Pool Boiling CHF on Square Surfaces, Master's Thesis, University of Minnesota, Minneapolis, 1989.
- [45] R.D.M. Carvalho, A.E. Bergles, The effects of the heater thermal conductivity/capacitance on the pool boiling critical heat flux, *Proceedings of Engineering Foundation Conference on Pool and External Flow Boiling*, Santa Barbara, CA, 1992, pp. 203–212.
- [46] J.Y. Chang, S.M. You, Pool boiling heat transfer from inclined, micro-porous surfaces simulating microelectronics devices, *INTERpack '97*, Hawaii. E. Suhir, et al., ASME EEP vol. 192, 1997, pp. 2055–2063.
- [47] J.Y. Chang, S.M. You, Boiling heat transfer phenomena from micro-porous and porous surfaces in saturated FC-72, *Int. J. Heat and Mass Transfer* 40(18) (1997) 4437–4447.

- [48] J.Y. Chang, S.M. You, Enhanced boiling heat transfer from micro-porous surfaces: effects of coating composition and method, *Int. J. Heat and Mass Transfer* 40(18) (1997) 4449–4460.
- [49] J.Y. Chang, S.M. You, Enhanced boiling heat transfer from micro-porous cylindrical surfaces in saturated FC-87 and R123, *J. Heat Transfer* 119 (1997) 319–325.
- [50] J.M. Ramilson, J.H. Lienhard, Transition boiling heat transfer and film transition regime, *J. Heat Transfer* 109 (1987) 746–752.
- [51] C. Unal, K.O. Pasamehmetoglu, Numerical modeling of the effect of surface topology on the saturated pool nucleate boiling curve, 1993 ASME Winter Annual Meeting, November 28–December 3, New Orleans, 1993.
- [52] I. Golobic, A.E. Bergles, Effects of heater side factors on the saturated pool boiling critical heat flux, *Exp. Thermal Fluid Sci.* 5 (1997) 43–51.
- [53] K.H. Sun, J.H. Lienhard, The peak pool boiling heat flux on horizontal cylinders, *Int. J. Heat and Mass Transfer* 13 (1970) 1425–1439.
- [54] J.H. Lienhard, V.K. Dhir, Hydrodynamic prediction of peak pool boiling heat fluxes from finite bodies, *J. Heat Transfer* 95 (1973) 152–158.
- [55] K.A. Park, A.E. Bergles, Effects of size and simulated microelectronics chips on boiling and critical heat flux, *J. Heat Transfer* 110 (1988) 728–734.
- [56] I. Mudawar, Direct-immersion cooling of high-flux electronic chips, I-Term, 1992.
- [57] I. Mudawar, A.H. Howard, C. Gersey, An analytical model for near saturated pool boiling critical heat flux on vertical surfaces, *Int. J. Heat and Mass Transfer* 40(10) (1997) 2327–2339.
- [58] P.J. Berensen, Experiments on pool boiling heat transfer, *Int. J. Heat Mass Transfer* 5 (1962) 985–999.
- [59] S. Oktay and A.F. Schmeckenbecher, Method for forming heat sinks on semiconductor device chips, U.S. Pat. No. 3,706,127, December 1972.
- [60] R.C. Chu, K.P. Moran, Method for customizing nucleate boiling heat transfer from electronic units immersed in dielectric coolant, U.S. Pat. No. 4,050,507, September 1977.
- [61] P.J. Marto, V.J. Lepere, Pool boiling heat transfer from enhanced surfaces to dielectric fluids, *Trans. ASME* 104 (1982) 292–299.
- [62] K.A. Park, A.E. Bergles, Boiling heat transfer characteristics of simulated microelectronic chips with detachable heat sinks, *Heat Transfer* 1986, Proceedings of the 8th International Heat Transfer Conference 4, Hemisphere, Washington, DC, 1986, pp. 2099–2104.
- [63] T.M. Anderson, I. Mudawar, Microelectronic cooling by enhanced pool boiling of a dielectric fluorocarbon liquid, *Trans. ASME* 11 (1989) 752–759.
- [64] J.R. Thome, *Enhanced Boiling Heat Transfer*, Hemisphere Publishing, New York, 1990.
- [65] R.L. Webb, C. Pais, Nucleate pool boiling data for five refrigerants on plain, integral-fin and enhanced tube geometries, *Int. J. Heat and Mass Transfer* 35 (1992) 1893–1904.
- [66] H. Honda, H. Takamastu, J.J. Wei, Enhanced boiling of FC-72 on silicon chips with micro-pin-fins and submicron-scale roughness, *J. Heat Transfer* 124 (2002) 383–390.
- [67] H. Honda, J.J. Wei, Enhanced boiling heat transfer from electronic components by use of surface microstructures, *Exp. Thermal and Fluid Sci.* 28 (2004) 159–169.
- [68] J.J. Wei, L.J. Guo, H. Honda, Experimental study of boiling phenomena and heat transfer performances of FC-72 over micro-pin-finned silicon chips, *Heat and Mass Transfer* 41 (2005) 744–755.
- [69] S. Ujereh, T. Fisher, I. Mudawar, Effects of carbon nanotube arrays on nucleate pool boiling, *Int. J. Heat Mass Transfer* 50 (2007) 4023–4038.
- [70] H.S. Ahn, V. Sathyamurthi, D. Banerjee, Pool boiling experiments on a nano-structured surface, *IEEE Trans. Compon. Packag. Technol.* 32(1) (2009) 156–165.
- [71] V. Sathyamurthi, H.-S. Ahn, D. Banerjee, S.C. Lau, Subcooled pool boiling experiments on horizontal heaters coated with carbon nanotubes, *J. Heat Transfer* 131(7) (2009) 071501.

- [72] N.D. Nimkar, S.H. Bhavnani, R.C. Jaeger, Nucleation characteristics of a structured surface in a dielectric coolant in the absence of spreading effects, *Proceedings of ITherm 2004—Ninth Intersociety Conference on Thermal and Thermomechanical Phenomena in Electronic*, vol. 2, 2004, pp. 82–89.
- [73] S.H. Bhavnani, S.E. Balch, R.C. Jaeger, Control of incipience hysteresis effects in liquid cooled electronics heat sinks, *J. Electron. Manuf.* 9 (1999) 179–190.
- [74] N.D. Nimkar, S.H. Bhavnani, R.C. Jaeger, Benchmark heat transfer data for microstructured surfaces for immersion-cooled microelectronics, *IEEE Trans. Compon. Packag. Technol.* 29 (2006) 89–97.
- [75] J.P. O'Connor, S.M. You, A painting technique to enhance pool boiling heat transfer in saturated FC-72, *ASME J. Heat Transfer* 117 (1995) 387–393.
- [76] J.Y. Chang, S.M. You, Heater orientation effects on pool boiling of microporous enhanced surfaces in saturated Fc-72, *Proceedings of 1995 ASME IMECE*, ASME 95-WA/HT-19, 1995.
- [77] S.M. You, T.W. Simon, A. Bar-Cohen, A technique for enhancing boiling heat transfer with application to cooling of electronic equipment, *1992 Intersociety Conference on Thermal Phenomena*, 1992, pp. 66–73.
- [78] J.P. O'Connor, S.M. You, D.C. Price, Thermal management of high power microelectronics via immersion cooling, *IEEE Trans. CMPT* 18(3) (1995) 656–663.
- [79] M. Gulliksen, H. Haugerud, H. Kristiansen, Enhanced boiling heat transfer with porous silver coatings for electronics cooling, *ASME/JSME Thermal Engineering Conference*, 1999.
- [80] F. Arbalaez, S. Sett, R.L. Mahajan, An experimental study on pool boiling of saturated FC-72 in highly porous aluminum metal foams, *34th National Heat Transfer Conference NTH2000-12192*, 2000.
- [81] S. Vemuri, K.J. Kim, Pool boiling of saturated FC-72 on nano-porous surface, *Int. Commun. Heat Mass Transfer* 32 (2005) 27–31.
- [82] M. Arik, A. Bar-Cohen, S.M. You, Enhancement of pool boiling dielectric liquid critical heat flux by microporous coatings, *Int. J. Heat Mass Transfer* 50 (2007) 997–1009.
- [83] Y. Im, Y. Joshi, C. Dietz, S.S. Lee, Enhanced boiling of a dielectric liquid on copper nano-wire surfaces, *Int. J. Micro-Nano Scale Transp.* 1(1) (2010) 79–95.
- [84] W. Wu, H. Bostanci, L.C. Chow, Y. Hong, M. Su, J.P. Kizito, Nucleate boiling heat transfer enhancement for water and FC-72 on titanium oxide and silicon oxide surfaces, *Int. J. Heat Mass Transfer* 53 (2010) 1773–1777.
- [85] T. Dunskus, J.W. Westwater, The effect of trace additives on the heat transfer to boiling isopropanol, *Chem. Eng. Prog. Symp. Ser.* 57 (1961) 173–181.
- [86] P.J. Normington, M. Mahalingam, T.Y. Lee, Thermal management control without overshoot using combinations of boiling liquids, *IEEE Intersociety Conference on Thermal Phenomena*, 1992, pp. 49–58.
- [87] T.Y.T. Lee, P.J.C. Normington, Application of dielectric binary mixtures in electronic cooling-nucleate pool boiling regime, *Adv. Electron. Packag. ASME* 1993 (1993) 927–935.
- [88] C.T. Avedisian, D.J. Purdy, Experimental study of pool boiling critical heat flux of binary fluid mixtures on an infinite horizontal surface, *Adv. Electron. Packag. EEP-4(2)* (1993) 909–915.
- [89] Y. Fujita, M. Tsutsui, Heat transfer in nucleate boiling of binary mixtures: development of a heat transfer correlation, *JSME Int. J. Ser. B* 40(1) (1997).
- [90] S. Bonekamp, K. Bier, Influence of ultrasound on pool boiling heat transfer to mixtures of the refrigerants R23 and R134A, *Int. J. Refrig.* 20(8) (1998) 606–615.
- [91] W.R. McGillis, V.P. Carey, On the role of Marangoni effects on the critical heat flux for pool boiling of binary mixtures, *J. Heat Transfer* 11 (1996) 103109.
- [92] S. Ahmed, V.P. Carey, Effects of gravity on the boiling of binary fluid mixtures, *Int. J. Heat Mass Transfer* 41(16) (1998) 2469–2483.

- [93] M. Arik, A. Bar-Cohen, Pool boiling of perfluorocarbon mixtures on silicon surfaces, *Int. J. Heat Mass Transfer* (2010).
- [94] W.H. McAdams, W.E. Kennel, C.S. Minden, P.M. Rudolf Carl, P.M. Picornell, E. Dew, Heat transfer at high rates to water with surface boiling, *Ind. Eng. Chem.* 41(9) (1949) 1945–1953.
- [95] M. Behar, M. Courtaud, R. Ricque, R. Semeria, Fundamental aspects of subcooled boiling with and without dissolved gases, 3rd International Heat Transfer Conference, vol. 4, 1962, pp. 985–999.
- [96] K. Torakai, H. Shimamune, T. Fujishior, The effects of dissolved gas content upon incipient boiling superheats, 4th International Heat Transfer Conference, vol. V, B2.11, 1970.
- [97] R.W. Murphy, A.E. Bergles, Subcooled flow boiling of fluorocarbons: hysteresis and dissolved gas effects on heat transfer, *Proceedings of Heat Transfer and Fluid Mechanics Institute*, Stanford University Press, 1972, pp. 400–416.
- [98] V.V. Fisenko, V.I. Baranenko, L.A. Belov, V.A. Korenevskiy, Effect of dissolved gas on nucleate boiling and critical heat flux, *Heat Transfer Soviet Res.* 20 (1988) 294–299.
- [99] Y.S. Hong, C.N. Ammerman, S.M. You, Boiling characteristics of cylindrical heaters in saturated gas-saturated and pure subcooled FC-72, 29th National Heat Transfer Conference, ASME HTD, vol. 2, 1995.
- [100] S.M. You, J.H. Kim, K.H. Kim, Effect of nanoparticles on critical heat flux of water in pool boiling heat transfer, *Appl. Phys. Lett.* 83 (2003) 3374–3376.
- [101] P. Vassallo, R. Kumar, S. D'Amico, Pool boiling heat transfer experiments in silica–water nano-fluids, *Int. J. Heat Mass Transfer* 47(2) (2004) 407–411.
- [102] D. Milanova, R. Kumar, Role of ions in pool boiling heat transfer of pure and silica nano-fluids, *Appl. Phys. Lett.* 87 (2005) 233107.
- [103] I.C. Bang, S.H. Chang, Boiling heat transfer performance and phenomena of Al_2O_3 –water nano-fluids from a plain surface in a pool, *Int. J. Heat Mass Transfer* 48(12) (2005) 2407–2419.
- [104] S.J. Kim, I.C. Bang, J. Buongiorno, L.W. Hu, Surface wettability change during pool boiling of nanofluids and its effect on critical heat flux, *Int. J. Heat Mass Transfer* 50 (2007) 4105–4116.
- [105] H. Kim, J. Kim, M. Kim, Experimental study on CHF characteristics of water– TiO_2 nano-fluids, *Nucl. Eng. Technol.* 38(1) (2006) 61–68.
- [106] Z. Liu, L. Liao, Sorption and agglutination phenomenon of nanofluids on a plain heating surface during pool boiling, *Int. J. Heat Mass Transfer* 51 (2008) 2593–2602.
- [107] D. Wen, Mechanisms of thermal nanofluids on enhanced critical heat flux (CHF), *Int. J. Heat Mass Transfer* 51 (2008) 4958–4965.
- [108] K. Sefiane, On the role of structural disjoining pressure and contact line pinning in critical heat transfer enhancement during boiling in nanofluids, *Appl. Phys. Lett.* 89 (2006) 044106.
- [109] R. Kathiravan, R. Kumar, A. Gupta, R. Chandra, Characterization and pool boiling heat transfer studies of nanofluids, *J. Heat Transfer* 131 (2009) 081902.
- [110] H. Kim, H.S. Ahn, M.H. Kim, On the mechanism of pool boiling critical heat flux enhancement in nanofluids, *J. Heat Transfer* 132 (2010) 061501.
- [111] B. Truong, L. Hu, J. Buongiorno, T. McKrell, Modification of sandblasted plate heaters using nanofluids to enhance pool boiling critical heat flux, *Int. J. Heat Mass Transfer* 53 (2010) 4105–4116.
- [112] S.M. Kwark, R. Kumar, G. Moreno, J. Yoo, S.M. You, Pool boiling characteristics of low concentration nanofluids, *Int. J. Heat Mass Transfer* 53 (2010) 972–981.
- [113] S.M. Kwark, G. Moreno, R. Kumar, H. Moon, S.M. You, Nanocoating characterization in pool boiling heat transfer of pure water, *Int. J. Heat Mass Transfer* 53 (2010) 4579–4587.
- [114] Y. Haramura, Critical heat flux in pool boiling, *Handbook of Phase Change: Boiling and Condensation*, Taylor and Francis, Philadelphia, 1999, Chapter 6, pp. 145–163

- [115] S.P. Liaw, V.K. Dhir, Effect of surface wettability on transition boiling heat transfer from a vertical surface, 8th International Heat Transfer Conference, vol. 4, 1986, pp. 2031–2036.
- [116] M. Maracy, R.H.S. Winterton, Hysteresis and contact angle effects in transition boiling of water, *Int. J. Heat Mass Transfer* 31 (1988) 1443–1449.
- [117] S. Nishio, T. Gotoha, N. Nagaib, Observation of boiling structures in high heat-flux boiling, *Int. J. Heat and Mass Transfer* 41 (1988) 3191–3201.
- [118] C.K. Yu, D.C. Lu, Pool Boiling Heat Transfer on Horizontal Rectangular Fin Array in Saturated FC-72, *Int. J. Heat and Mass Transfer* 50 (2007) 3624–3637.
- [119] A. Priarone, Effect of surface orientation on nucleate boiling and critical heat flux of dielectric fluids, *Int. J. Thermal Sci.* 44 (2005) 822–831.

Thermofluid Dynamics of Boiling in Microchannels

Abstract

State of the art of the thermofluid dynamics of boiling in microchannels has been presented. Part I gives introduction with the scale differentiation of thermofluid mechanics in flow regime. This is followed by detailed discussion of flow pattern and bubble growth, heat transfer with models, pressure drop, and instability. Part II deals with onset of nucleate boiling, void fraction, liquid film thickness, critical heat flux, and this part also makes conclusion and gives direction for future research.

PART I

SUJOY KUMAR SAHA¹ and GIAN PIERO CELATA²

¹*Professor of Mechanical Engineering, Bengal Engineering and Science University Shibpur, Howrah, India*

²*ENEA Casaccia Research Centre, Division for Advanced Technologies for Energy and Industry, S. M. Galeria, Rome, Italy*

PART II

SATISH G. KANDLIKAR³

³*Gleason Professor of Mechanical Engineering, Rochester Institute of Technology, Rochester, NY, USA*

I.1. Introduction

Microscale two-phase flow and heat transfer are of great interest in many industrial applications, such as thermosiphons for cooling of microelectronic components, micro heat pipe systems, micro heat exchangers, materials processing, oil industry, biological cell reactors, and biotechnology. Microchannels are used for cooling high power density devices such as microprocessors and laser diode arrays. Liquids such as water and fluorochemicals are used as coolant in microchannel heat sinks.

Examples of studies on single-phase microchannel heat sinks are Tuckerman and Pease [1], Phillips [2], Rahman and Gui [3], Kawano et al. [4], Harms et al. [5], and Qu and Mudawar [6]. Microchannel cooling systems have very large heat transfer coefficients, small size and volume per unit heat load, and

small coolant inventory requirements. Better temperature uniformity is achieved with a two-phase microchannel heat sink. Unprecedented power densities can be dissipated by two-phase microchannel heat sinks [7,8].

There is a scale effect which becomes evident when the hydraulic diameter is less than the capillary length $(\sigma/g(\rho_l - \rho_v))^{0.5}$. In microchannels, the hydraulic diameter of the channels is smaller than the capillary length. Identifying the threshold, or the transition band, beyond which a two-phase flow may be considered “micro” is, however, very difficult. The channel classification has been given by Kandlikar and Grande [9]. This classification is, however, not a rigid demarcation based on specific criteria. It is worth referring to Kawaji and Chung [10] for this purpose. Confinement number (Co) as the distinguishing parameter gives only a rough idea:

$$Co = \frac{1}{D} \sqrt{\frac{\sigma}{(\rho_l - \rho_v)g}} \quad (I.1)$$

Suo and Griffith [11] set $Co_{th} = 3.3$, Kew and Cornwell [12] suggest $Co_{th} = 0.5$, whereas that suggested by Brauner and Moalem-Maroon [13] is 0.16.

Two classifications based on the hydraulic diameter were given by Mehendale et al. [14] and Kandlikar et al. [15]. According to Mehendale et al. [14], microchannel 1–100 μm , mesochannel 100 μm –1 mm, compact passages 1–6 mm, and conventional channels >6 mm. According to Kandlikar et al. [15], molecular nanochannel <0.1 μm , transitional nanochannel 0.1–1 μm , transitional microchannel 1–10 μm , microchannel 10–200 μm , minichannels 200 μm –3 mm, and conventional channels >3 mm.

A more general definition would have to address situations where classical theory is no longer fully applicable, that is, it does no longer correctly predict the mechanical and thermal process in terms of friction and heat transfer. The definition also depends on the fluid and the working conditions.

Feng and Serizawa [16] defines a microchannel as being one in which the Laplace constant is larger than the diameter of the channel.

Another criterion is when the bubble departure diameter is larger than the channel diameter, bubble growth is confined by the size of the channel cross-section (there are many bubbles in a macrochannel). Hence, the threshold to confined bubble flow could be taken as the microscale threshold. The bubble departure diameter in nucleate pool boiling $d_{bub,F}$ is given by [17]:

$$d_{bub,F} = 0.0208\beta \left[\frac{\sigma}{g(\rho_L - \rho_G)} \right]^{1/2} \quad (I.2)$$

where the contact angle β is in degrees and the effect of crossflow on bubble departure is ignored. For application to a wider range of pressures,

$$d_{bub} = 0.0012 \left(\frac{\rho_L - \rho_G}{\rho_G} \right)^{0.9} d_{bub,F} \quad (I.3)$$

The confinement number is the square root of the inverse of Eotvos number or the inverse of Bond number.

Another way to define the microchannel threshold, from the nucleation superheat equation, is

$$r_{\text{nuc}} = \frac{2\sigma}{\Delta T_{\text{sat}} \left(\frac{dp}{dT} \right)_{\text{sat}}} \quad (\text{I.4})$$

r_{nuc} gives a criterion to see as to whether or not it is possible to nucleate in channels smaller than $2r_{\text{nuc}}$.

Another possible microscale transition for horizontal tubes is the tube diameter at which stratified flow becomes impossible and the capillary force prevails over the stratifying effect of the gravity. The criterion, of course, also depends on the mass flux.

Li and Wu [18] recommend that the Bond number and liquid Reynolds number should be considered a new transitional criterion and they have given a new generalized correlation. According to them, it is reasonable and useful to set $Bo \times Re_L^{0.5} = 200$ as the conventional-to-micro/minichannel criterion. When $Bo \times Re_L^{0.5} \leq 200$, the micro/minichannel phenomenon dominates; for $Bo \times Re_L^{0.5} > 200$, conventional macrochannel theory can explain the experimental data.

Harirchian and Garimella [19] defined a heat flux-independent parameter named the convective confinement number as:

$$Bo^{0.5} \times Re = \frac{1}{\mu_f} \left[\frac{g(\rho_f - \rho_g)}{\sigma} \right]^{0.5} GD^2 \quad (\text{I.5})$$

This flow boiling transition criterion recommends that for $Bo^{0.5} \times Re \leq 160$, vapor bubbles are confined and the channel is microchannel. For $Bo^{0.5} \times Re > 160$, it is a macrochannel.

The criterion for transition between confined and unconfined flow is compared in Fig. 1.1 [19] with available data. Details of the fluid geometry, mass flux, and heat flux of the data points used in this comparison are listed in Table 1.1 [19].

Microchannels invariably involve cooling channels in blocks, as opposed to mini and larger diameter normal size channels that have individual confining walls and are usually thermally well controlled. Commonly accepted dimensions of microchannels are 10 mm long with 10–200 μm hydraulic diameter. The channels are usually cut in a block. For silicon, microelectronic fabrication techniques are used. For copper or other metals, an end mill or a lamination and bonding process is used. Typically, there will be 100 or so parallel channels. Heat is usually supplied to one side of the block. If the channels are cut from one side, a cover plate is provided on that side and inlet and outlet headers couple the microchannel heat exchanger to the flow system.

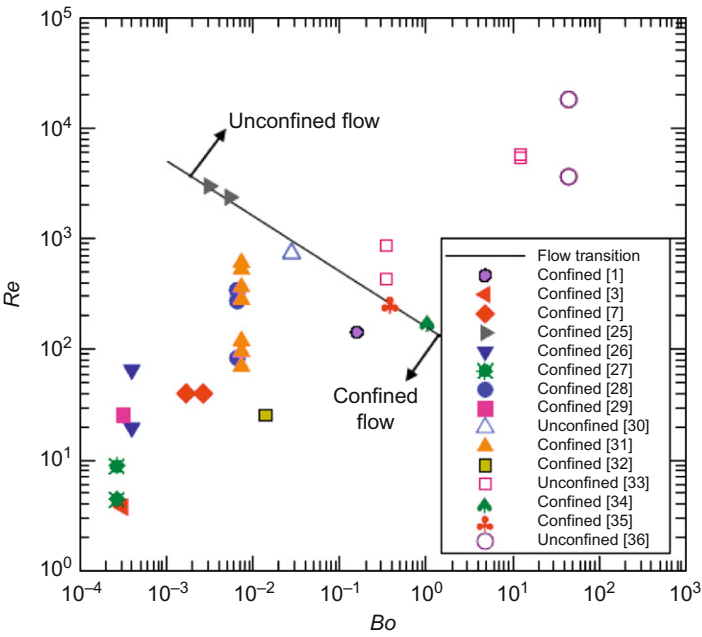


FIG. I.1. Comparison of the confinement criterion with experimental data from a variety of sources in the literature. For color version of this figure, the reader is referred to the web version of this book. Source: From Harirchian and Garimella [19].

Boiling is desirable in microchannel heat sinks for more probable uniform wall temperature since then wall temperature is constrained to the fluid saturation temperature. The flow rate in microchannels is low to contain the pressure drop. Therefore, large enthalpy rise of the fluid for high heat flux is inevitable.

Small microchannel flow boiling systems are sensitive to oscillatory instabilities. The oscillations may be

1. parallel channel instabilities in the case of parallel channel evaporators with common inlet headers, or
2. the compressible volume instabilities which may develop even in single-channel systems.

Parallel channel instabilities are primarily due to the interaction of the two-phase flow among adjacent channels. Compressible volume instabilities may propagate in the presence of a degree of compressibility (i.e., a body of vapor, flexible hosing, etc.) upstream or within the heated length.

Thermally induced two-phase flow instability must be avoided by all means to prevent any disastrous effect in the thermal systems. Two-phase flow instabilities

TABLE I.I

SUMMARY OF EXPERIMENTAL DATA USED IN THE COMPARISON OF CONFINEMENT TRANSITION CRITERION AND FLOW REGIME MAP

Reference	Fluid	Geometry	Mass flux ($\text{kg/m}^2 \text{ s}$)	Wall heat flux (kW/m^2)
Peles et al. [25]	Water	Parallel microchannels, $D_h = 157, 207 \mu\text{m}$	3500, 6000	—
Jiang et al. [26]	DI water	Parallel grooves, $w = 50 \mu\text{m}$	110–365	—
Kandlikar [1]	DI water	Parallel microchannels, $w = 1 \text{ mm}$, $d = 1 \text{ mm}$	40	—
Serizawa et al. [3]	DI water	Circular tube, $D = 50 \mu\text{m}$	24	—
Lee et al. [27]	DI water	Parallel microchannels, $w = 120 \mu\text{m}$, $d = 14 \mu\text{m}$	30–60	—
Hetsroni et al. [7]	Water	Parallel triangular microchannels, $D_h = 103, 129 \mu\text{m}$	87–108	80–220
Steinke and Kandlikar [28]	DI water	Parallel microchannels, $w = 214 \mu\text{m}$, $d = 200 \mu\text{m}$	115–467	55–839
Zhang et al. [29]	DI water	Single microchannel, $w = 50 \mu\text{m}$, $d = 40 \mu\text{m}$	160	—
Garimella et al. [30]	DI water	Parallel microchannels, $w = 275 \mu\text{m}$, $d = 636 \mu\text{m}$	651	160
Wang et al. [31]	DI water	Parallel trapezoidal microchannels, $w = 208, 427 \mu\text{m}$, $d = 146 \mu\text{m}$	91–787	365, 486
Hetsroni et al. [32]	Vertrel XF	Parallel triangular microchannels, $D_h = 130 \mu\text{m}$	148	36
Mukherjee and Mudawar [33]	FC-72	Parallel mini- and microchannels in a gap, $w = 200 \mu\text{m}$, $d = 660 \mu\text{m}$, $w = 1.57 \text{ mm}$, $d = 3.05 \text{ mm}$	500–1100	—
Zhang et al. [34]	FC-72	Parallel microchannels, $w = 200 \mu\text{m}$, $d = 2000 \mu\text{m}$	120	42
Chen and Garimella [35]	FC-77	Parallel microchannels, $w = 389 \mu\text{m}$, $d = 389 \mu\text{m}$	345	9–56
Coleman and Garimella [36]	R134a	Glass tube, $w = 4.9 \text{ mm}$	150, 750	—

From Harirchian and Garimella [19].

in minichannels and microchannels are more intense than that in conventional channels due to the low flow velocities and confined space available for bubble growth. These instabilities result in a lower critical heat flux (CHF) than would be obtained with stable flow in the microchannels-based heat sink [20].

Boiling in mini- and microchannels seems to occur as a combination of both nucleate and convective boiling mechanisms. Some overviews of the progress made in the field of boiling in macro and small channels can be found in Refs. [21–42].

The use of minichannel heat exchangers (hydraulic diameter about 1 mm) in compact heat exchangers improves heat transfer coefficients and thermal efficiency while requiring a lower fluid mass. They are widely used in condensers for automobile air conditioning and are now being used in evaporators and other applications like domestic air-conditioning systems.

In this chapter, the thermofluid dynamics of boiling in microchannels has been discussed in detail.

I.2. Flow Pattern and Bubble Growth

Bubble dynamics in microchannel is quite different from that in an ordinary sized channel. Bubble growth in a microchannel is restrained by the channel wall and in the transverse direction. The two-phase flow pattern observed simultaneously in the channels may be different, depending on heat and mass fluxes.

In microchannels, it is found that the pressure drop and average heat transfer coefficient are significantly dependent on the boiling flow pattern, which is similar to that for boiling in conventional large channels. However, the behavior of boiling flow regime transition in narrow channels is much different from that in large channels. Yang et al. [43] have followed the previous works of Qian et al. [44], Nourgaliev et al. [45], and Yang et al. [46–48] and used the Lattice-Boltzmann method (LBM)-based FlowLab code to simulate the movement of single Taylor bubbles and for regime transition of two-phase flow in narrow channel. They have employed the interaction potential model of Shan and Chen [49] to simulate the hydrodynamic interaction between the two phases and the Martys and Chen [50] model to describe the interaction between a fluid and a wall. Also, the White and Beardmore [51] graphical correlation for the terminal velocity of slugs to analyze the Taylor bubble movement was used.

A new type of two-phase flow pattern map developed by Revellin and Thome [52] was applied by Kaew-On et al. [53] to identify the flow regime (Fig. I.2). The coalescing bubble (CB) regime occurs when bubble generation rate is smaller than the bubble coalescence rate and the semiannular flow pattern appears. The heat transfer coefficient is a function of heat transfer but is independent of vapor quality or mass flux.

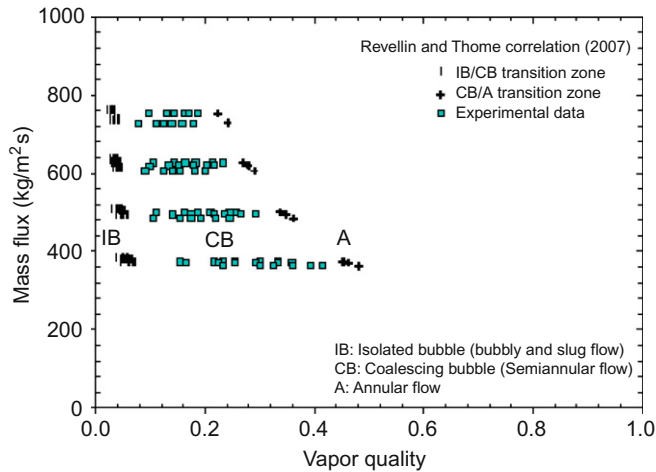


FIG. I.2. Flow pattern maps with the experimental transition zone of Revellin and Thome [52] correlation. For color version of this figure, the reader is referred to the web version of this book. Source: From Kaew-On et al. [53].

Saisorn et al. [54] carried out flow visualization and heat transfer experiments with R-134a. They have observed slug flow, throat-annular flow, and churn flow regimes under conditions of low heat flux and studied three-zone flow boiling model for various flow patterns with R-134a in a 1.75 mm channel.

Flow patterns observed by Saisorn et al. [54] and Saisorn and Wongwises [55,56] can be summarized as follows:

- Slug flow in which small bubbles coalesce with each other and elongated bubbles are larger in length than the channel diameter in low vapor quality region.
- Throat-annular flow in which two consecutive elongated bubbles or vapor slugs coalesce to form the ripple leading to a throat region having gas core, and it is located near the transition from coalescing bubble flow to annular flow. Such location is far from slug flow pattern.
- Distortion of elongated bubbles forms a disruptive region and churn flow occurs. This unstable condition is not included in the model and model prediction is not good. However, the deviation decreases with decreasing heat flux.
- Annular flow in which tube wall gets liquid film flows and the tube core is occupied by continuous vapor flow.
- Alternate annular-rivulet flow in which there is rivulet-like liquid stream on the tube surface in addition to the annular flow.

Usually the flow pattern data is classified by visual observation and the data is plotted as a flow pattern map in terms of system parameters such as heat flux, mass flux, vapor quality, and saturation pressure. The flow regime map comprises different zones according to bubble coalesce phenomena.

The isolated bubble (IB) regime is characterized by higher bubble generation rate compared to bubble coalescence rate. Either or both bubbly flow and slug flow appear.

Isolated bubble (IB) to coalescing bubble (CB) transition vapor quality, taking care of heat flux, viscosity, and surface tension, is given by:

$$x_{IB/CB} = 0.763 \left(\frac{Re_{LO} Bo}{We_{GO}} \right)^{0.41} \quad (I.6)$$

Similarly, the transition from coalescing bubble to annular flow is given by:

$$x_{CB/A} = 0.00014 Re_{LO}^{1.47} We_{LO}^{-1.23} \quad (I.7)$$

I.2.1. BUBBLE BEHAVIOR IN A NARROW CHANNEL

Figure I.3 shows the typical movement behavior of a single Taylor bubble in a vertical narrow channel calculated by the FlowLab code.

The deformation of the bubble occurs only at the initial time period, after that the shape and movement of the bubble is stable, and a constant rising velocity is established.

Figure I.4 shows the interface shape of the single Taylor bubble in a vertical channel for different capillary numbers.

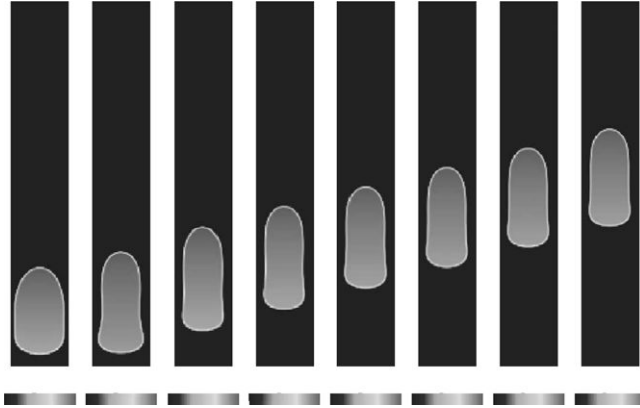


FIG. I.3. The movement of a single Taylor bubble in a vertical narrow channel. Source: From Yang et al. [43].

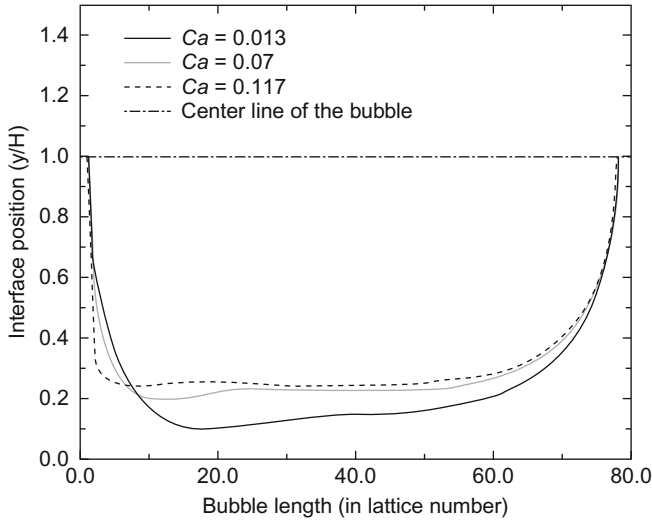


FIG. I.4. The interface shapes of single Taylor bubble in a vertical narrow channel for different capillary numbers Ca . Source: From Yang et al. [43].

As the capillary number increases, the stagnant flow region thickens and the wiggles vanish. The results of Yang et al. [43] compare well with the curvature of the meniscus of the bubble obtained by Giavedoni and Saita [57] by Galerkin finite element discretization of the governing equations.

I.2.2. FLOW REGIME TRANSITION

The phase-change mechanism causes the increase of the bubble size, bubble shape, and flow regime. Also coalescence of the bubbles changes the flow regime rapidly. Yang et al. [43] have investigated the effect of body force, surface tension, and bubble size on the flow regime transition behavior. From Figs. I.5 and I.6, it can be seen that the coalescence between the small bubbles with the slug ahead is earlier in smaller body force condition than that in larger body force condition since the velocity difference between the small bubble and the slug is larger in smaller body force condition than that in larger body force condition. The transition from bubbly slug flow regime to pure slug regime occurs earlier in smaller body force condition than that in larger body force condition.

The surface tension has little effect on the movement of the bubbles and the flow regime transition. However, the coalescence of small bubble with the slug ahead of it occurs a little later with larger surface tension due to different acceleration in the initial period leading to different deformation of the bubble at the

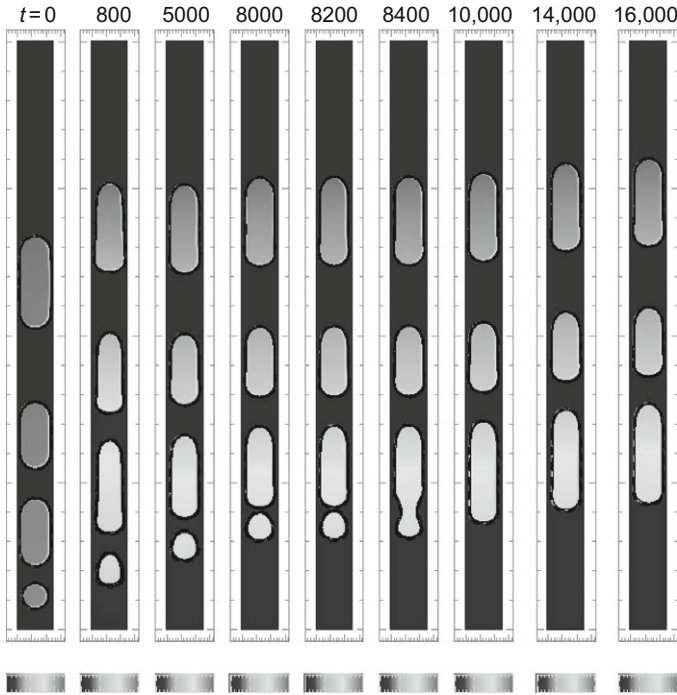


FIG. I.5. The bubble movement in a narrow channel: surface tension 0.038, body force 0.0008. Source: From Yang et al. [43].

beginning and different moving dynamics. After a certain time, the movement of the bubbles in different surface tension cases does not differ greatly.

The bubbles with smaller size move faster than those with larger size. Without any perturbations on the moving bubbles, the bubbly flow does not change to slug flow. The larger slugs will never merge with each other if no phase change occurs at two-phase interface.

Molecular dynamics (MD) simulation study on surface tension of bubbles and their related characteristics was made by Park et al. [58]. A stable bubble regime with respect to simulation domain sizes was defined for the Lennard-Jones molecules. They calculated local densities, normal and tangential pressure components, and bubble surface tension. Also, a simple binary molecule system was investigated to understand the effects of foreign molecules on the surface tension of a bubble. Further information on surface tension of micro-bubbles and the interfacial phenomena may be obtained from Thompson et al. [59], Rowlinson and Widom [60], Israelachvili [61], Weng et al. [62], Allen and Tildesley [63], Haile [64], Maruyama [65], Yang and Tsutsui [66], Parker

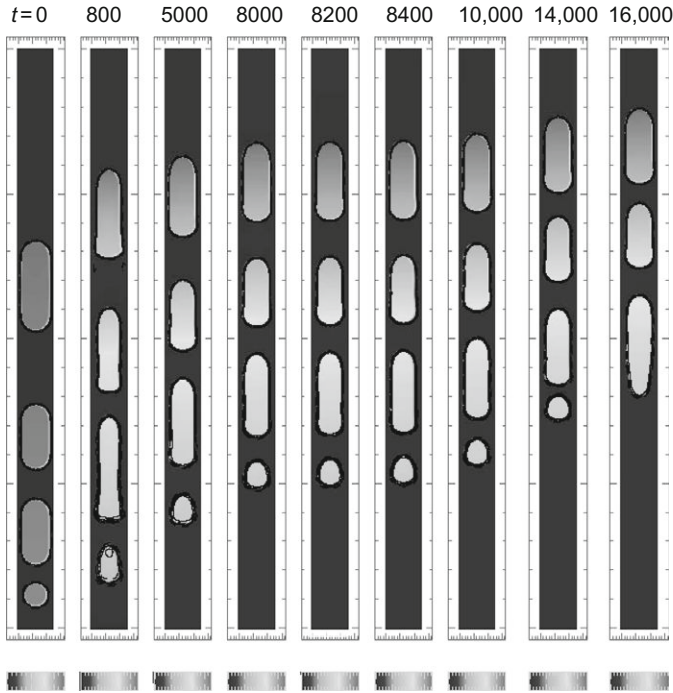


FIG. I.6. The bubble movement in a narrow channel: surface tension 0.038, body force 0.0012. Source: From Yang et al. [43].

and Heyes [67], Kinjo and Matsumoto [68], Kinjo et al. [69], Park et al. [70], and Tolman [71].

Figure I.7 [58] shows the cross-sectional snapshot of the molecular distribution of a bubble.

It may be noted from Fig. I.7 [58] that the central region is a vapor phase and the outer region of higher density is a liquid phase. The liquid-vapor interface in this microscopic system cannot be defined sharply. The average density should be smaller than a critical value to maintain a stable bubble. Figure I.8 [58] shows the regime map for stable bubbles and corresponding liquid-phase densities.

Figure I.9 [58] shows the surface tension (γ) and Tolman's length (δ) for bubbles and droplets.

Nucleate boiling, once initiated, quickly becomes fully developed [72,73]. Increasing heat flux causes an abrupt change in flow pattern to unstable slug flow followed by stable annular flow [74]. Nucleation and small bubble growth were observed inside the microchannels [75].

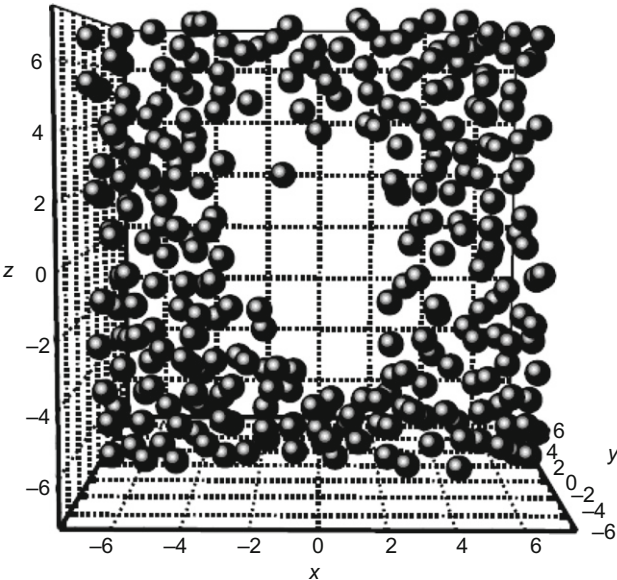


FIG. I.7. A cross-sectional snapshot of the molecular distribution of a bubble. Source: From Park et al. [58].

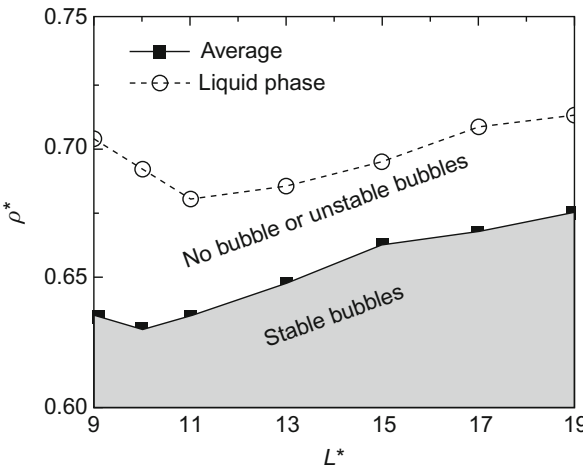


FIG. I.8. Regime map for stable bubbles and liquid-phase densities. Source: From Park et al. [58].

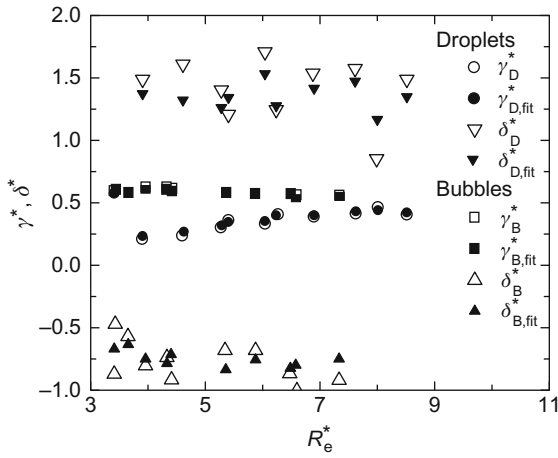


FIG. I.9. Surface tension (γ) and Tolman's length (δ) for bubbles and droplets. Source: From Park et al. [58].

The onset of nucleate boiling (ONB) criterion predicts the boiling incipience in conventional large channels with the assumption that a bubble grows beyond the mouth of a cavity when the surrounding liquid has sufficient superheat to maintain mechanical equilibrium at the bubble interface. Even wall-attached small bubbles nucleate, grow, and collapse as a thin bubble layer forms along the channel wall [76–78].

Bubble behavior at incipient boiling in microchannels is much different from that in large channels. At incipient boiling, bubble form at bottom and side walls at some nucleation sites; then bubbles grow to detachment size comparable to channel cross-section or lower depending on the velocity, before departing into the liquid flow. Mechanistic models for bubble detachment are due to Levy [79], Staub [80], Al-Hayes and Winterton [81], Winterton [82], and Rogers et al. [83]. Microchannel exit hydrodynamic and thermal conditions are responsible for local boiling incipience phenomenon. A two-dimensional unit cell containing a single microchannel and surrounding solid was examined by Qu and Mudawar [84]. Figure I.10 shows that the bubble size increases with decreasing mean liquid exit velocity. Figure I.11 shows that the model predictions of Qu and Mudawar [84] compare well with the incipient boiling heat flux data.

Peng et al. [73] theoretically analyzed the liquid phase change transition in microchannels using thermodynamic phase stability theory. They obtained a bubble formation/nucleation criterion analytically. The channel size and geometry have a significant impact for sufficiently small hydraulic diameters,

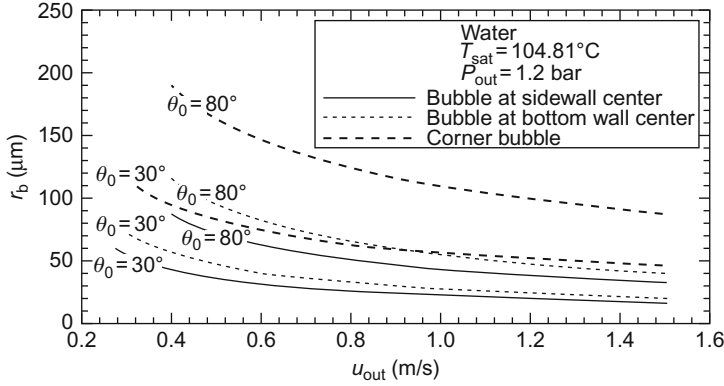


FIG. I.10. Variation of bubble departure radius with mean liquid exit velocity. Source: From Qu and Mudawar [84].

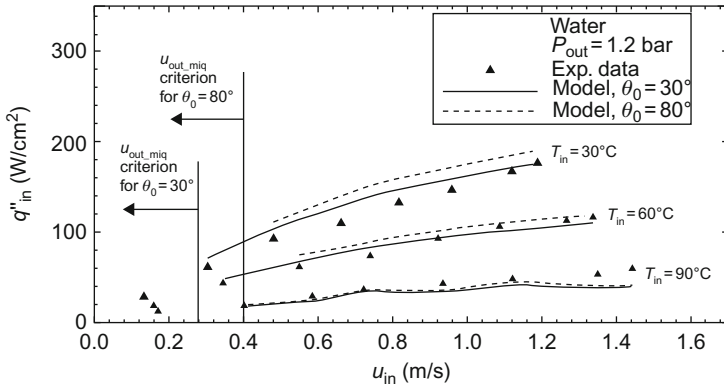


FIG. I.11. Comparison of incipient boiling heat flux data and model predictions. Source: From Qu and Mudawar [84].

resulting in dramatically higher heat fluxes for nucleation [72,85–94]. The liquid thermophysical properties also have an important influence on the nucleation. The evaporating space quantification illustrates fictitious boiling [94]. A nondimensional relationship, $N_{mb} \leq 1$, where

$$N_{mb} = \frac{h_{lv} a_v}{c\pi(v'' - v')q''D_h} \quad (\text{I.8})$$

h_{lv} = latent heat

a_v = vapor phase thermal diffusivity

- c = experimentally determined empirical constant
- v'' = vapor specific volume at saturation
- v' = liquid specific volume at saturation
- q'' = heat flux
- D_h = hydraulic diameter

describes the conditions for phase-change transition or nucleation in microchannels.

Hsu [95] investigated pool boiling characteristics of liquids and theoretically predicted a range of active cavity sizes on heated surfaces and the corresponding equilibrium bubble embryo radii.

Bowers and Mudawar [87] noted that the heat transfer and flow friction or pressure drop behavior in microchannels is different from that observed in macrochannels. Lin et al. [88] have observed bubble growth and boiling characteristics on microwire and microchip heaters in microchannels, and they found that it is extremely difficult to generate bubbles in the constrained liquid in the microchannels.

Peng and Wang [91] have defined two hypothetical concepts, “evaporating space” and “fictitious boiling,” to describe the physical processes and fundamental phenomena in boiling in microchannels. The “evaporating space” is the space necessary for evaporation. “Fictitious boiling” refers to the attainment of conventional nucleate boiling conditions but before the start of internal evaporation and bubble growth. The microbubbles cannot be visualized by ordinary means. Liquids with greater liquid/vapor density differences, higher latent heats, and larger thermal diffusion coefficients need larger heat fluxes to initiate nucleation. The liquid is in a highly nonequilibrium state with an exceptional capability to absorb, transfer, and transport thermal energy. Figure I.12 [73] shows the minimum heat flux required for nucleation.

Experimental data of Ding et al. [96] testifies the prediction given by Peng et al. [73]. If the microchannel size is smaller than the “evaporating space,” then “fictitious boiling” occurs before nucleation is initiated. Otherwise, normal nucleate boiling occurs. Figure I.13 [73] shows the wall superheats required for nucleation in microchannels.

By measurements with infrared radiometer and thermography, Hetsroni et al. [97] have shown that the bubble behavior and the heat transfer mechanism for the cationic surfactant (the surfactant additive can also be anionic or nonionic) solution with water are quite different from those of pure water. They studied saturated pool boiling on a heated surface and on a heated tube. They examined the effect of the surface tension and viscosity on the heat transfer coefficient. In contrast to the turbulent pipe flow with surfactants, where friction factor and heat transfer coefficient reduce, surfactant

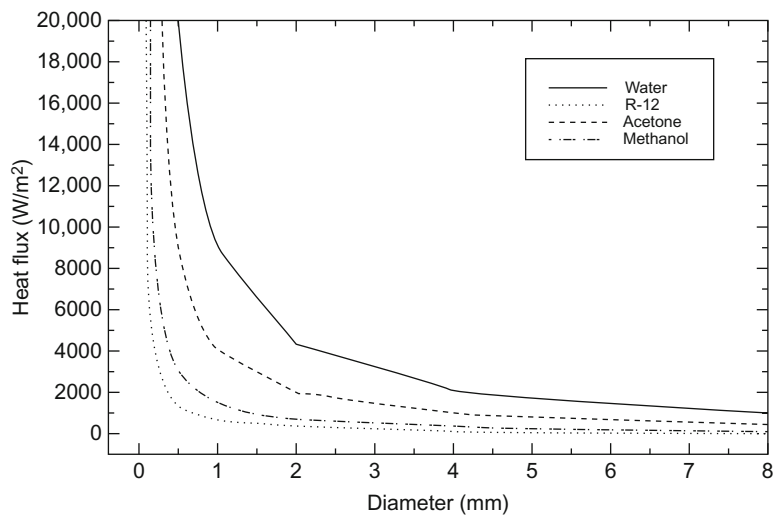


FIG. I.12. Minimum heat flux for nucleation. Source: From Peng et al. [73].

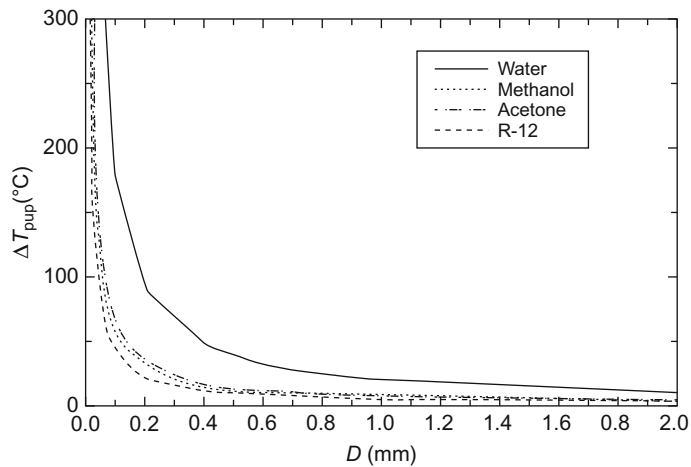


FIG. I.13. Wall superheat for nucleation. Source: From Peng et al. [73].

solutions in the pool boiling shows a significant enhancement of the boiling mechanism due to reduced surface tension and viscous drag and causing different bubble size and dynamics. There is an optimum additive concentration for highest heat flux.

I.2.3. BUBBLE BEHAVIOR

I.2.3.1. Bubble Visualization

Figure I.14 [97] shows the typical stages of bubble growth. After the onset of nucleate boiling, the regime of single bubbles occurs close to the heated wall and bubble coalescence takes place as the heat flux increases. The tendency of bubble coalescence reduces significantly in the surfactant solution. Figure I.15 [97] shows the bubble initiation, bubble growth, and bubble

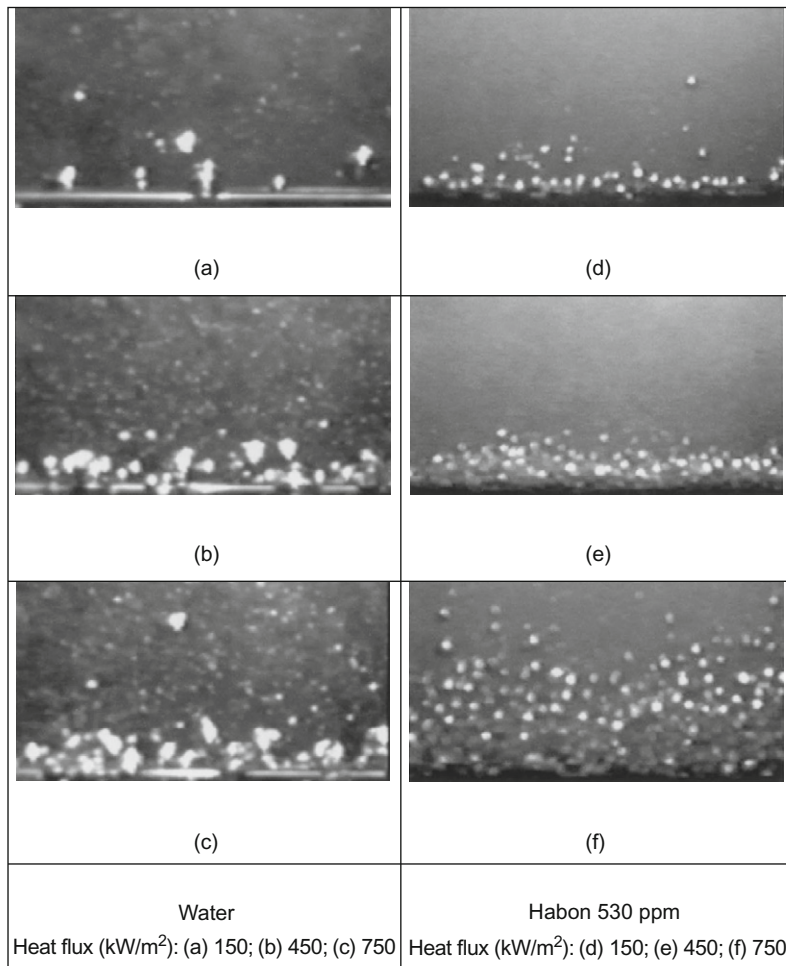


FIG. I.14. Boiling of water (a–c) and 530 ppm Habon G solution (d–f) on the pipe at various heat fluxes. Source: From Hetsroni et al. [97].

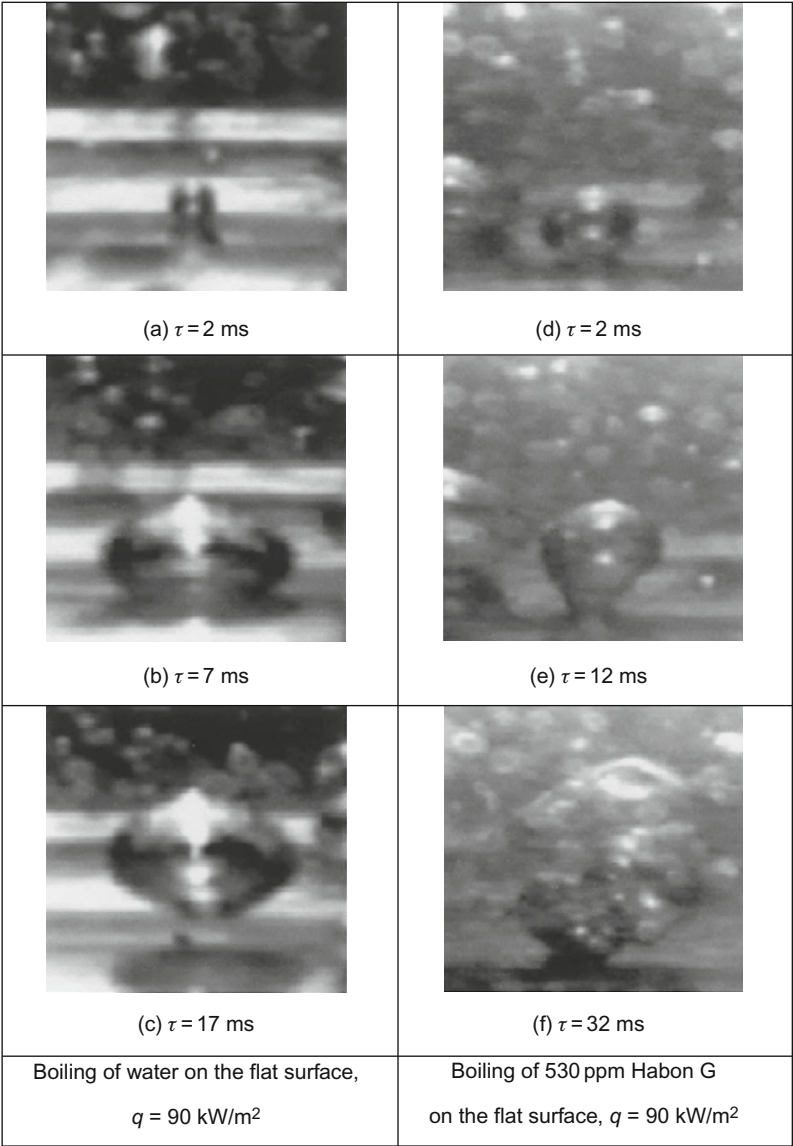


FIG. I.15. The dynamics of bubble growth on the heated flat plate in clear water and 530 ppm Habon G solution. Source: From Hetsroni et al. [97].

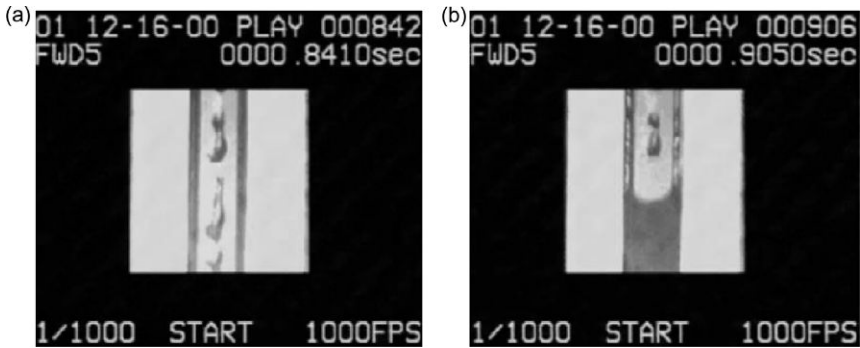


FIG. I.16. Flow pattern downstream of the ONB: (a) dryout, (b) single-phase water flow. Source: From Hetsroni et al. [101].

departure. The time from bubble initiation to bubble departure increases in the surfactant solution. Wu et al. [98] tried to correlate the nucleate boiling heat transfer coefficient with the equilibrium and dynamic surface tension of the aqueous surfactant solutions. In the surfactant solution, the nucleate boiling behavior depends on heat flux, thermal patterns on the heated surface, Marangoni effects, and critical micelle concentration (CMC) of the surfactant.

The heat transfer coefficient in the surfactant solution is higher and the assumption of uniformity of wall superheat cannot be realistic.

Yao and Chang [99] have shown that boiling in confined space depends on bubble deformation characterized by the ratio of gap size and nominal bubble departure diameter, that is, Bond number or Eotvos number.

Lee et al. [100] observed bubble nucleation and growth in parallel microchannels for some cases with wall temperature lower than the saturation temperature corresponding to the system pressure.

Figure I.16 [101] shows the regime downstream of ONB. Hot spots (dry out) were observed [101]. The temperature of the heated wall did not increase sharply, as in the CHF case, due to periodical nature of the process. After a certain time, the microchannel was again supplied with liquid.

Arcanjo et al. [102] performed quasi-diabatic two-phase bubbly, elongated bubbles, churn and annular flow pattern visualizations and measurements of elongated bubble velocity, frequency, and length based on high-speed videos (8000 fps). They also characterized dry out conditions. They compared their results with those of Barnea et al. [103] and Felcar et al. [104]. The bubble velocity increases with increasing mass velocity and vapor quality, and decreases with saturation temperature and is independent of bubble length since the vapor-/liquid-specific volume ratio decreases with increasing

saturation temperature and so, the fluid acceleration, inherent to the evaporation process, also decreases. They correlated bubble velocity as a linear function of two-phase superficial velocity. Instead of Kelvin–Helmholtz instability, assumed by Taitel and Dukler [105], Barnea et al. [103] proposed surface tension, inertial, capillary, and gravitational effects (modified Eotvos number and Weber number) as the leading transition mechanism from stratified to intermittent flows in microchannels.

Ullmann and Brauner [106] observed that the transition to annular flow in microchannels is a result of wetting and inertial effects since, for smaller channels, the meniscus radius of the wall–liquid interface may have the same order of magnitude of the tube diameter.

The relative elongated bubble velocity (vapor velocity minus the homogeneous flow velocity) increases with increasing bubble length until a plateau is reached, and also increases with increasing tube diameter and mass velocity and a semianalytical model for the vapor velocity as a function of the bubble length is [107–109] as follows:

$$U_G = \frac{D\gamma}{1 - 0.58/Co} \frac{1 - \exp((-2L_G f)/D)}{2f} + U_H \quad (I.9)$$

where γ is given by:

$$\gamma = \frac{4q}{Dh_{LG}\rho_G} \quad (I.10)$$

and f is the friction factor.

The model for predicting the collision of elongated bubbles in horizontal microchannel flows takes into account differences of velocities among elongated bubbles related to distinct bubble length and the vapor input into the bubble due to evaporation process [109].

Vaillancourt et al. [110] and Akbar et al. [111] presented models for flow pattern transition in microchannels.

Arcanjo et al. [102] characterized flow patterns (Fig. I.17) as follows:

- Dispersed flow that includes bubbly and mist flows, with the gas bubbles in the liquid having smaller diameter than the tube, and gas dispersed in a continuous liquid phase and all the liquid detached from the wall and flowing as small droplets within the gas core.
- Annular flow when the gas core is surrounded by a liquid film on the tube wall.
- Intermittent flow when the flow geometry has a periodic or time varying character.
- Stratified flow (smooth + wavy) when two-phases flow separately with the liquid in the lower region of the tube due to gravitational effects.

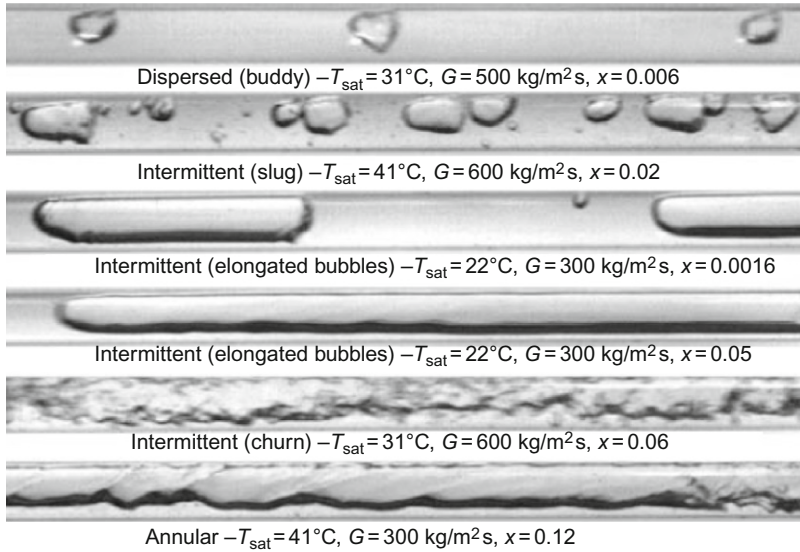


FIG. I.17. Flow pattern visualizations and their nomenclature. Source: From Arcanjo et al. [102].

Churn, slug, elongated bubbles, plug, and pseudo-slug flows are characterized as intermittent flows. Annular and slug-annular flows are considered as annular flows.

Unlike Agostini et al. [108], according to which the bubble velocity increases with its length, Arcanjo et al. [102] observed an almost negligible effect of bubble length on the bubble velocity (Fig. I.18). This is perhaps due to the fact that for $Co < 0.58$, the model of Agostini et al. [108] validated for $Co \geq 0.58$ provides unrealistic results characterized by a bubble velocity higher than the homogeneous velocity and for Arcanjo et al. [102], Co varied from 0.32 to 0.37.

Arcanjo et al.'s [102] two-phase superficial velocity data are well predicted by the drift-flux model of Zuber and Findlay [112], and the superficial void fraction may be obtained.

The elongated bubble frequency passes through a peak with increasing vapor quality from zero. The frequency peak value increases with increasing mass velocity due to increase of turbulence intensity with mass velocity and its effect on elongated bubble coalescing and growing processes. The bubble frequency peak moves to lower vapor quality with increasing mass velocity since larger number of elongated bubbles and the bubble coalescing process affect the bubble frequency at lower vapor quality. The elongated bubble frequency

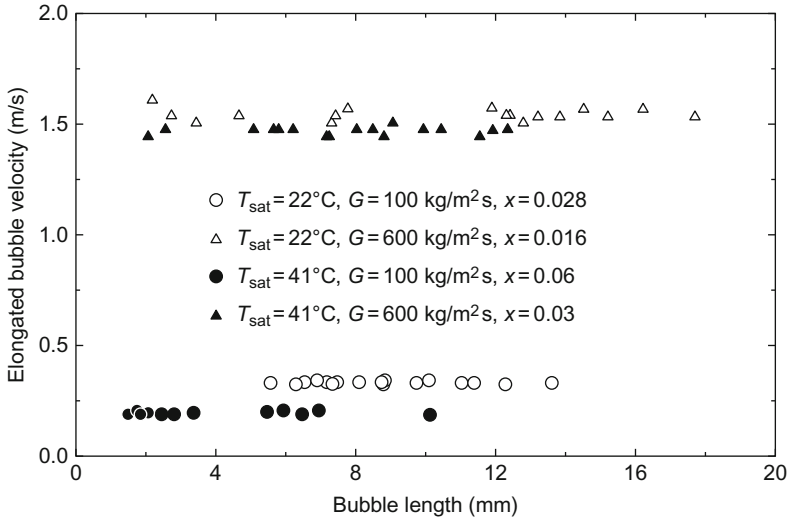


FIG. I.18. The variation of the bubble velocity with its length. Source: From Arcanjo et al. [102].

increases with increasing saturation temperature due to increase in the ratio between two-phase dynamic viscosity and density and Reynolds number. Also, surface tension decreases with increasing saturation temperature and the breaking of bubbles by turbulence is favored.

Figure I.19 shows the comprehensive flow regime map developed by Harirchian and Garimella [19] based on experimental results and flow visualizations performed with FC-77. There are four distinct regions: confined slug flow, churn/confined annular flow, bubbly flow, and churn/annular/wispy-annular flow. The vertical transition line given by $Bo^{0.5} \times Re = 160$ represents the transition to confined flow. The other transition line is a curve fit to the points of transition from bubbly or slug flow to alternating churn/annular or churn/wispy-annular flow and is given by:

$$Bl = 0.017(Bo^{0.4} \times Re^{-0.3}) \quad (I.11)$$

For $Bo^{0.5} \times Re \leq 160$, vapor confinement is observed in both slug and churn/annular flow regimes. For $Bo^{0.5} \times Re > 160$, the flow is not confined. For low heat fluxes with $Bl \leq 0.017(Bo^{0.4} \times Re^{-0.3})$, flow patterns of slug (if $Bo^{0.5} \times Re \leq 160$) or bubbly (if $Bo^{0.5} \times Re > 160$) flow exist in the microchannels. At higher heat fluxes with $Bl > 0.017(Bo^{0.4} \times Re^{-0.3})$, vapor bubbles coalesce resulting in a continuous vapor core in the alternating churn/annular or churn/wispy-annular flow regimes.

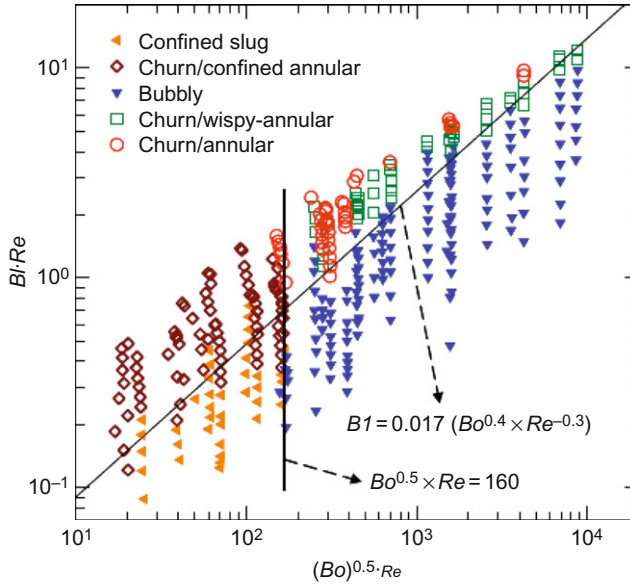


FIG. I.19. Comprehensive flow map regime. For color version of this figure, the reader is referred to the web version of this book. Source: From Harirchian and Garimella [19].

I.3. Heat Transfer with Models

In the mini- and microchannels, for sufficiently high temperature difference between heated wall and adjacent fluid, vapor bubbles generate at the wall nucleation sites and nucleate boiling occurs. The heat transfer is a strong function of the thermophysical properties of the fluid, surface structure, and material.

The data of Wang et al. [113] is well predicted by the correlation of Mishima and Hibiki [114] for macrochannel with, of course, some underprediction by the correlation for high vapor quality ($x_e > 0.1$). The reason for underprediction is that the flow behavior is different in microchannels. The coalesced bubbles in microchannels are confined, elongated, and finally they form the annular flow downstream, while in a macrochannel, many bubbles grow and flow along the channel without restriction. Also local dry out occurs in microchannels at high vapor quality causing vapor blocking in the channels. The heat transfer coefficient increases, as shown in Fig. I.20 [113], with the increase in vapor quality in the subcooled boiling region ($x_e < 0$) due to a transition from partial to fully developed nucleate boiling. For saturated boiling region ($x_e > 0$), h decreases with increasing x . This finding corroborates the experience of

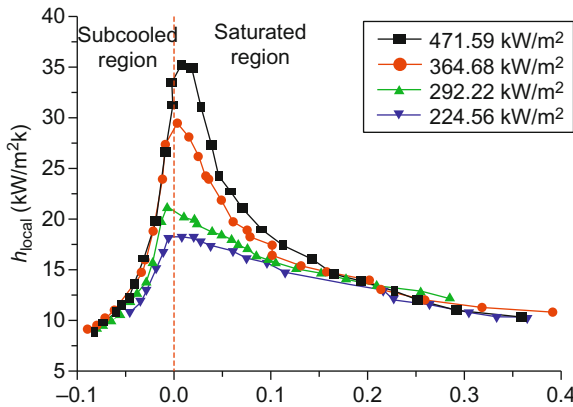


FIG. I.20. Heat transfer coefficient versus exit quality. For color version of this figure, the reader is referred to the web version of this book. Source: Wang et al. [113].

Hetsroni et al. [115] and Qu and Mudawar [116], but it is contradictory to the observations of Chen and Garimella [117]. Kandlikar [118] correlation overpredicts heat transfer coefficient data of Wang et al. [113] as shown in Fig. I.21.

Kandlikar [119] discussed comprehensively heat transfer mechanisms during flow boiling in microchannels. The forces due to surface tension and momentum change during evaporation, in conjunction with the forces due to viscous shear and inertia, govern the two-phase flow patterns and heat transfer characteristics during flow boiling in microchannels. In low Reynolds number flows occurring in microchannels, nucleate boiling systemically emerges as the dominant mode of heat transfer. Kandlikar [119] has observed nondimensional groups relevant to two-phase flow studies in microchannels. These are Martinelli parameter, Convection number, Boiling number, Bond number, Eotvos number, Capillary number, Ohnesorge number, Weber number, and Jakob number. While studying the effects of these numbers individually, Kandlikar [119] has found that following two nondimensional groups K_1 and K_2 [120] are capable of representing some of the key flow boiling characteristics including CHF in microchannels:

$$K_1 = \left(\frac{q}{G h_{fg}} \right)^2 \frac{\rho_L}{\rho_G} \quad (\text{I.12})$$

$$K_2 = \left(\frac{q}{h_{fg}} \right)^2 \frac{D}{\rho_G \sigma} \quad (\text{I.13})$$

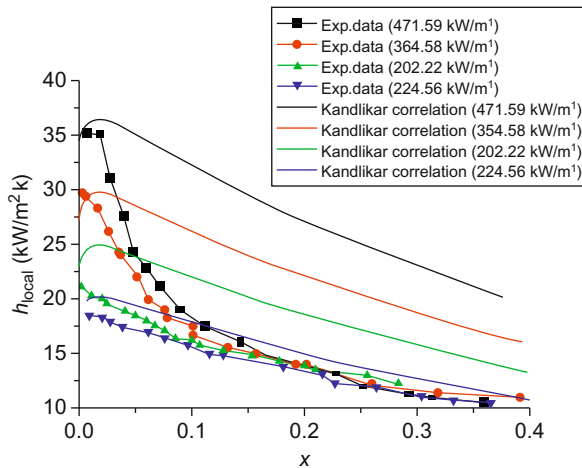


FIG. I.21. Comparison of boiling heat transfer coefficient with Kandlikar [118] correlation. For color version of this figure, the reader is referred to the web version of this book. Source: Wang et al. [113].

Kandlikar [119] has made an attempt to see the range of K_1 and K_2 in the data available [121–124] for minichannels and microchannels.

Hetsroni et al. [115] visualized the flow pattern and measured heat transfer coefficient during explosive boiling of water in parallel triangular microchannels. The behavior of long vapor bubbles at low Reynolds number was not similar to annular flow with interposed intermittent slugs of liquid between two long vapor trains. Figure I.22 shows the dependence of time interval between cycles on heat flux obtained from the histograms of statistical distribution as observed by Hetsroni et al. [115]; increasing the heat flux about two-fold leads to increasing the cycles of dry out about sevenfold.

Figure I.23 shows the typical nature of the dependence of the saturated flow boiling heat transfer coefficient on the thermodynamic equilibrium vapor quality at the outlet of the test section. As observed by Hetsroni et al. [115] and other investigators [116,119,125–127], h decreases appreciably with increasing x . However, Hetsroni et al. [115] observed that heat transfer coefficient does not depend on mass flux. This observation of Hetsroni et al. [115] contradicts the observations of Qu and Mudawar [116,125] who pointed to annular flow as the dominant two-phase flow pattern in microchannels at $Re = 60 - 300$ and concluded that the saturated flow boiling heat transfer coefficient is a strong function of the mass flux and only a weak function of the heat flux. Explosive boiling in microchannels could not be clearly attributed to any single nondimensional number like Reynolds number, Weber number, or Ohnesorge number.

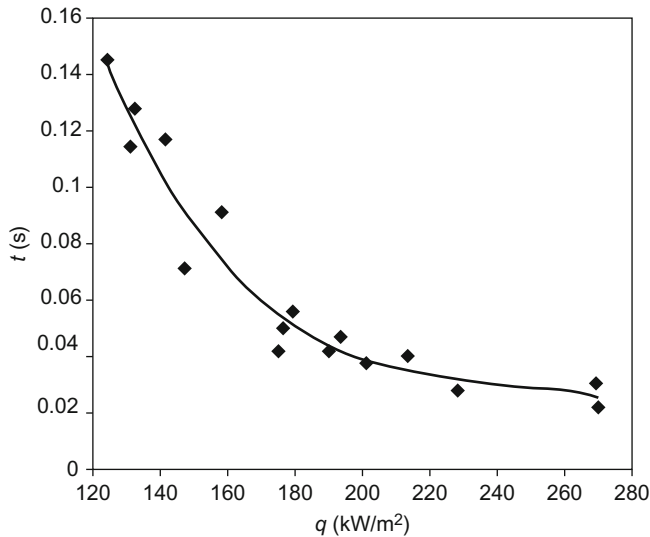


FIG. I.22. Dependence of time interval between cycles on heat flux. Source: Hetsroni et al. [115].

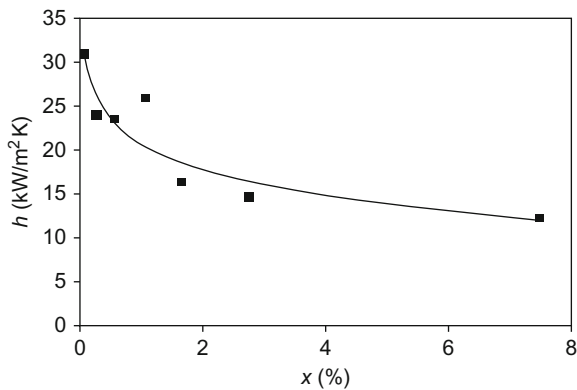


FIG. I.23. Dependence of the saturated flow boiling heat transfer coefficient on thermodynamic equilibrium quality at the outlet of the test section. Source: Hetsroni et al. [115].

Kandlikar et al. [128] have observed that actual nucleation wall superheat may decrease due to the presence of dissolved gases in the liquid. The periodic wetting, dryout, and rewetting phenomena in microchannels have been observed by Hetsroni et al. [129] for parallel microchannels of hydraulic diameter 103–129 μm .

Kandlikar and Steinke [130] observed with their water data that at low Reynolds number, the convective boiling does not become the dominant mechanism in the entire vapor quality range. Simple models given by Jacobi and Thome [131] and others contain empirical variables that are fitted to the data; they do not consider the effect of transient phenomena, rapid bubble growth, localized flow reversal, periodic dry out, and also flow distribution through parallel microchannels. Their use is not recommended beyond the specific operating and geometrical conditions employed by the authors.

Kandlikar and Balasubramanian [126,132] experimented with three gravitational orientations under the same operating conditions. Bubbly, thin film nucleation, slug flow, and churn flow have been observed in all three orientations. Time-dependent flow patterns have been found. They have observed decreasing trends in heat transfer coefficients with increasing quality. These trends are in consonance with observations where nucleating bubbles are at the wall during liquid flow and also in the liquid film near the wall in plug or annular flow.

Dupont and Thome [133] and Tiselj et al. [134] studied influence of the channel diameter and axial conduction on heat transfer during flow boiling in microchannels. Harirchian and Garimella [135] studied microchannel size effects on local flow boiling heat transfer to a dielectric fluid. Investigators [136–139] dealt with scale effects on flow boiling in microchannels, the applicability of the flow boiling correlation to low Reynolds number flows in microchannels, and effects of gravitational orientation and channel geometry on flow boiling in parallel minichannels. Wang and Cheng [140] and Xu et al. [141,142] studied microbubble emission, transient flow pattern, and heat transfer mechanism in microchannels.

Consolini [35] proposed a one-dimensional heat transfer model, based on the effect of interfacial shear on the temporal evolution of film thickness, for slug flow which is dominant flow mode at low and intermediate vapor qualities in microchannel evaporators.

Diaz and Schmidt [143] observed that the heat transfer coefficient decreases with increasing quality of vapor. This trend is consistent with the results of others and indicates that nucleate boiling dominates the low quality region.

Xu et al. [141] used acetone as the working fluid and they proposed the boiling number as the key for establishing the relative dominance of boiling mechanisms, since it gives information on the evaporation momentum force relative to the inertia force.

Lazarek and Black [144] showed that, beyond the start of saturation boiling, the heat transfer coefficient remains unaffected by vapor quality (Fig. I.24); but it is a function of heat flux, leading them to conclude that nucleate boiling is dominant heat transfer mechanism as in macroscale flow boiling. Similar results have been observed by Moriyama and Innoue [145] (Fig. I.25). This

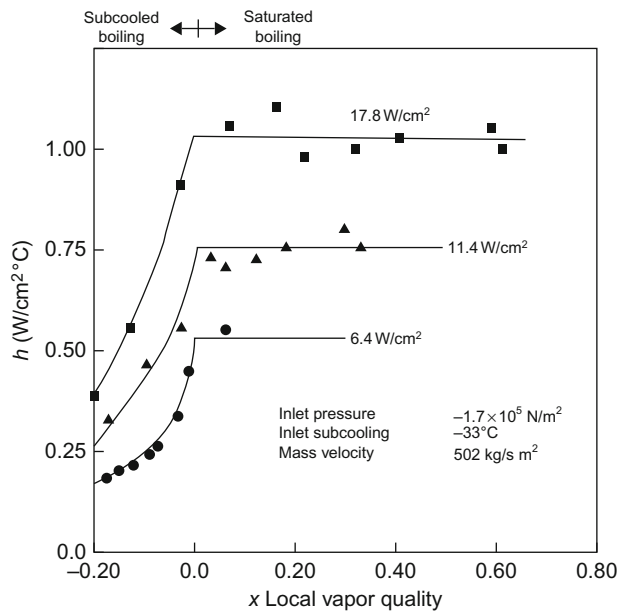


FIG. I.24. Local heat transfer coefficient as a function of local vapor quality. Source: From Lazarek and Black [144].

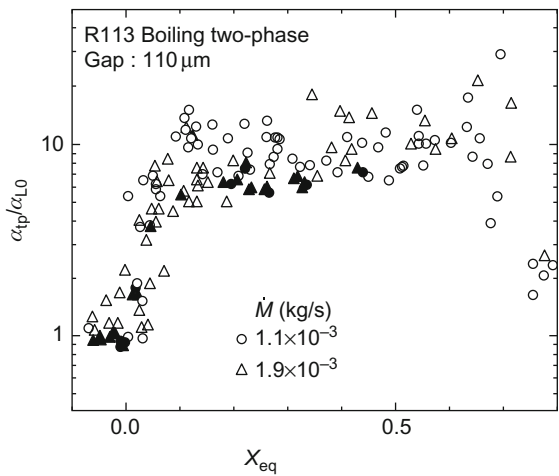


FIG. I.25. Heat transfer coefficient versus vapor quality. Source: From Moriyama and Innoue [145].

trend as well as contradictory findings has been discussed at length in Agostini and Thome [146]. The relative importance of nucleate boiling and convection in the individual flow patterns that are characteristic to a micro-channel flow is thus still unclear [20,119,131,147–152]. Vapor formation and flow development in microchannels have been discussed at length in Refs. [29,123,124,142,153–169]. Heat transfer prediction methods in microchannels are discussed in Refs. [92,120,123,132,140,170–181].

Li and Wu [182] formulated a generalized correlation for evaporative heat transfer in micro/minichannels. They considered both nucleate boiling and convection boiling in terms of Bond number, Reynolds number, and Boiling number.

Table I.II lists the experimental data of saturated two-phase heat transfer in micro/minichannels.

I.3.1. SATURATED BOILING CORRELATION

Saturated boiling correlation given by Lazarek and Black [144] is as follows:

$$Nu = 30Re^{0.857}Bo^{0.714} \quad (I.14)$$

where

$$Re = GD/\mu_l \quad (I.15)$$

$$Bo = \phi/Gh_{fg} \quad (I.16)$$

$$Nu = hD/k_l \quad (I.17)$$

Equation (I.14) is applicable for the following range of parameters:

$$\varphi: 1.4 \times 10^4 - 3.8 \times 10^5 \text{ W/m}^2$$

$$G: 125 - 750 \text{ kg/m}^2 \text{ s}$$

$$Re: 860 - 5500$$

$$Bo: 2.3 \times 10^{-4} - 76 \times 10^{-4}$$

$$\text{Static pressure: } 1.3 \times 10^5 - 4.1 \times 10^5 \text{ N/m}^2$$

Liu and Winterton [183] have developed a general correlation for saturated and subcooled flow boiling in tubes and annuli based on a nucleate pool boiling equation. They have used the basic postulate that both convective and nucleate boiling heat transfer mechanisms play a role in flow boiling. Liu and Winterton [183] have removed the original empirical boiling number correction concept from the correlation since the boiling number correction is not applicable to subcooled boiling although, for saturated boiling, this allows for the enhancement of the forced convective heat transfer mechanisms arising

TABLE I.II
SUMMARY OF STUDIES RELATED TO SATURATED FLOW BOILING HEAT TRANSFER IN MICRO/MINICHANNELS

Reference	Fluid/substrate/number of channels/geometry/ d_h (mm)	Parameter ranges, G (kg/m ² s), P (bar), q (kW/m ²), T (°C)	Remarks
Tran et al. [3]	R12/brass/1 Circular/rectangular $d_h = 2.46, 24$	$G = 44-832$ $q = 3.6-129, x = 0-1.0$ $P_{sat} = 8.25$	Nucleate boiling dominates the heat transfer Convection-dominant region occurred for $\Delta T_{sat} < 2.75^\circ\text{C}$ Little difference exists between h in a circular and rectangular channel
Rao et al. [4]	R11, R123/copper 1/circular $d_h = 1.95$	$G = 50-1800$ $q = 5-200, x = 0-0.9$ $P_{sat} = 2.94-5.09$	Nucleate boiling is dominant over a wide range of flow conditions Convective boiling is less important because of the relatively low Reynolds numbers and liquid conductivity
Lin et al. [5]	R141b 1/circular	$G = 300-2000$ $q = 10-1150, x = 0-1.0$	At low x , nucleate boiling dominates; at high x , convective boiling dominates For heat flux greater than 60, nucleate boiling is dominant throughout
Lin et al. [6]	$d_h = 1.1$ R141b/-/1 Circular, rectangular $d_h = 1.1, 1.8, 2.8, 2$	$P_{in} = 1.35-2.2$ $G = 50-3500$ $q = 1-300, x = 0-1.0$ $P_{in} = 1.0-3.0$	h is a strong function of q and x and a weaker function of G Both nucleate boiling and convective evaporation occurs The average h is independent of tube diameter
Warrier et al. [7]	FC84/aluminum 5/rectangular $d_h = 0.75$	$G = 557-1600$ $q = 0-45, x = 0-0.5$ $T_{in} = 26, 40, 60$	Flow pattern develops quickly into annular flow No significant misdistribution is found for 5-channel configuration
Qu and Mudawar [8]	Water/copper 21/rectangular $d_h = 0.349$	$G = 135-402$ $x = 0-0.2$ $T_{in} = 30, 60$	An abrupt transition to annular flow near zero x The dominant heat transfer mechanism is forced convective boiling h is shown to decrease with increasing quality
Sumith et al. [9]	Water/stainless steel 1/circular $d_h = 1.45$	$G = 23.4-152.7$ $q = 10-715, x = 0-0.8$ $T_{in} = 97.5, 98$	The dominant flow pattern is slug-annular or an annular flow liquid film evaporation is found to dominate the heat transfer
Yen et al. [10]	R123/stainless steel	$G = 50-300$	h is suppressed under higher q or G due to the limited evaporating space

	1/circular	$q = 5-30, x = 0-1.0$	h is monotonically decreased with increasing x , and becomes independent of G
Huo et al. [11]	$d_h = 0.19-0.51$ R134a/stainless steel 1/circular $d_h = 2.01$	$P_{out} = 1.01$ $G = 100-500$ $q = 13-150, x = 0-0.9$ $P = 8-12$	Nucleate boiling is dominant when x is less than about 20–30% Above these quality values, h decreases with vapor quality
Owhaib et al. [12]	R134a/stainless steel circular/3 $d_h = 1.7, 1.224, 0.876$	$G = 50-400$ $q = 3-34, x = 0.06$ $P = 6.4-8.6$	Diameter change affects the slug to churn and to annular boundaries h is a strong function of wall heat flux and system pressure
Pettersen [13]	CO ₂ /aluminum 25/circular	$G = 190-570$ $q = 5-20, x = 0-1.0$	Fairly independent upon mass flux and vapor quality Strongly related to nucleate boiling Nucleate boiling dominates prior to dry out
Saitoh et al. [14]	$d_h = 0.81$ R134a/– 1/circular	$T_{sat} = 0, 10, 20, 25$ $G = 150-450$ $q = 5-39, x = 0-1.0$	Two-phase observations show increasing entrainment at higher mass flux, and a dominance of annular flow As tube diameter decreases, the flow approaches homogeneous flow Forced convective heat transfer decreases with decreasing tube diameter
Yun et al. [15]	$d_h = 0.51, 1.12, 3.1$ CO ₂ /stainless steel 1/circular	$T_{sat} = 5, 10, 15$ $G = 500-3570$ $q = 7-48, x = 0-1.0$	The effect of mass flux on h decreases with decreasing tube diameter The effects of heat flux on h are very strong at all mass fluxes The effects of mass flux on h are only significant when $G < 500 \text{ kg/m}^2 \text{ s}$
Yun et al. [16]	$d_h = 0.98, 20$ CO ₂ /– 6–10/rectangular $d_h = 1.08-1.54$	$T_{sat} = 0, 5, 10$ $G = 200-400$ $q = 10-20, x = 0-0.9$ $T_{sat} = 0, 5, 10$	The effects of heat flux on h is very significant Increasing of the saturated pressure enhanced heat transfer The Copper model and Coreflo model yield relatively good predictions
Chen and Carimella [17]	FC-77/silicon 24/rectangular $d_h = 0.389$	$q = 40-800, x = 0-0.8$ $P_{out} = 1.01$	Convective boiling occurs at lower heat fluxes Nucleate boiling is dominant at higher heat fluxes
Yun et al. [18]	R410a/–	$G = 200-400$	

(Continued)

TABLE I.II

(CONTINUED)

Reference	Fluid/substrate/number of channels/geometry/ d_h (mm)	Parameter ranges, G (kg/m ² s), P (bar), q (kW/m ²), T (°C)	Remarks
			h of R410a in microchannels is much higher than those in large or small diameter single tubes at similar test conditions
Choi et al. [19]	7–8/rectangular $d_h = 1.36, 1.44$ CO ₂ /stainless steel	$q = 10–20, x = 0–1.0$ $T_{sat} = 0, 5, 10$ $G = 200–600$	Bo, We, Re, were introduced in the new correlation Nucleate boiling dominates particularly at low quality region
Choi et al. [20]	1/circular $d_h = 1.5, 3.0$ R22, R134a, CO ₂	$q = 20–40, x = 0–1.0$ $T_{sat} = -10, -5, 0, 10$ $G = 200–600$	Laminar flow appears for flow boiling in small channels Nucleate boiling dominates particularly at low quality region
Diaz and Schmidt [21]	Stainless steel/1 circular/ $d_h = 1.5, 3.0$ Water, ethanol	$q = 10–40, x = 0–1.0$ $T_{sat} = 10$ $G = 50–500$	The ratio of h , R22:R134a:CO ₂ was approximately 1.0:0.8:2.0 Laminar flow was observed in minichannels h decreases with increasing x for water, indicating that nucleate boiling dominates in the low quality region
Sobierska et al. [22]	Nickel alloy/1 Rectangular/ $d_h = 0.586$ Water copper	$q = 0–400, x = 0–0.3$ $P_{out} = 0.1$ MPa $G = 200–1500$	Fir ethanol, h increases with increasing x at low heat fluxes Three basic flow regimes: bubbly, slug, and annular flow
Bertsch et al. [23]	1/rectangular $d_h = 0.48$ R134a/copper	$q = 65–200, x = 0–0.3$ $T_{sat} = 100$ $G = 20.3–81$	Nucleate boiling dominates in the bubbly and slug regime at low x Convective boiling becomes considerable in annular flow regime h is relatively dependent on heat flux
Harirchian and Garimella [24–26]	17/rectangular $d_h = 1.09$ FC-77/silicon	$q = 0–200, x = 0–1.0$ $P_{sat} = 4–7.5$ $G = 240–1600$	h varied significantly with x and showed a peak at $x = 0.2$ The influence of saturation pressure is almost negligible Mainly governed by nucleate boiling
			Increasing the channel width beyond 0.4 mm does not affect h for fixed q

Consolini and Thorne [27]	2–60/rectangular $d_h = 0.16–0.20$ R134a, R236fa, R245fa Stainless steel/1	$q = 0–400$, $x = 0–0.8$ $P_{out} = 1.01$ $G = 300–2000$ $q = 12–200$, $x = 0–0.8$	h has a weak dependence on channel width for smaller microchannels h is strongly dependent on heat flux up to high x for R134a and R236fa For R245fa: at low x , h is heat flux dependent as in the case of R134a; at higher x , heat flux dependence disappears and h increases with x
	Circular/ $d_h = 0.51$, 0.79 R123, R134a	$T_{sat} = 31$ $G = 314–470$	
In and Jeong [28]	Stainless steel/1	$q = 10–20$, $x = 0.2–0.85$	Flow boiling heat transfer of R123 is dominated by the evaporation of thin liquid films around elongated bubbles Nucleate boiling is dominant for R134a until its suppression at high x
	Circular/ $d_h = 0.19$ R134a, R236fa, R245fa Stainless steel/1	$P_{sat} = 1.58–2.08$, 9–11 $G = 100–1500$ $q = 23–250$, $x = 0–1.0$	h displays heat flux and mass flux dependency but no subcooling effects Convective boiling seems to dominate at higher x in the annular regime
Ong and Thorne [29]	Circular/ $d_h = 1.03$ Propane/stainless steel	$T_{sat} = 31$ $G = 50–400$	
			Nucleate boiling was predominant, especially at low quality region
Pamitran et al. [30]	1/circular $d_h = 1.5$, 3.0	$q = 5–20$, $x = 0–1.0$ $T_{sat} = 0$, 5, 10	At moderate quality region, h increases with mass flux and vapor quality

From Li and Wu [182].

from the generation of vapor in the boundary layer next to the wall. The correlation for saturated boiling is

$$h_{\text{TP}}^2 = (Fh_L)^2 + (Sh_{\text{pool}})^2 \quad (\text{I.18})$$

where

$$h_L = 0.023(k_1/d)Re_L^{0.8}Pr_1^{0.4} \quad (\text{I.19})$$

$$h_{\text{pool}} = 55p_r^{0.12}q^{2/3}(-\log_{10}p_r)^{-0.55}M^{-0.5} \quad (\text{I.20})$$

$$F = \left[1 + xPr_1 \left(\frac{\rho_l}{\rho_v} - 1 \right) \right]^{0.35} \quad (\text{I.21})$$

$$S = (1 + 0.055F^{0.1}Re_L^{0.16})^{-1} \quad (\text{I.22})$$

If the tube is horizontal and the Froude number is less than 0.05, then Fh_L and Sh_{pool} should be multiplied by the following Froude number correction factors:

$$e_r = Fr^{(0.1 - 2Fr)} \quad (\text{I.23})$$

and

$$e_r = \sqrt{Fr} \quad (\text{I.24})$$

respectively.

If the heat flux is known, then the correlation can be used directly to calculate the heat transfer coefficient and hence the wall temperature. If the wall temperature rather than heat flux is known, then following set of equations can be used to calculate the h_{TP} :

$$q^2 = (Fh_L\Delta T_S)^2 + (A_pS\Delta T_S)^2q^{4/3} \quad (\text{I.25})$$

$$A_p = 55p_r^{0.12}(-\log_{10}p_r)^{-0.55}M^{-0.5} \quad (\text{I.26})$$

$$q_L = Fh_L\Delta T_S \quad (\text{I.27})$$

$$q_*^3 = \left[\frac{q}{Fh_L\Delta T_S} \right]^3 = \left[\frac{q}{q_L} \right]^3 \quad (\text{I.28})$$

$$C = (A_pS/Fh_L)^2q_L^{4/3} \quad (\text{I.29})$$

$$q_*^3 - Cq_*^2 - 1 = 0 \quad (\text{I.30})$$

$$h_{\text{TP}} = Fh_Lq_*^{3/2} \quad (\text{I.31})$$

For flow boiling in annuli, the heated equivalent hydraulic diameter should be used.

For subcooled flow boiling,

$$q = \sqrt{((Fh_L \Delta T_b)^2 + (Sh_{\text{pool}} \Delta T_S)^2)} \quad (\text{I.32})$$

where

$$\Delta T_b = T_w - T_b \quad (\text{I.33})$$

and

$$\Delta T_S = T_w - T_S \quad (\text{I.34})$$

If the temperature difference is known, then h_{TP} can be calculated from the foregoing equations with

$$q_L = Fh_L \Delta T_b \quad (\text{I.35})$$

and the term $A_p S / Fh_L$ replaced by $A_p S \Delta T_S / Fh_L \Delta T_b$.

If the temperature difference is unknown, then

$$\Delta T_b = \frac{T_S - T_b}{1 + A_{\text{bp}}^2} \left[1 + \sqrt{(1 + (1 + A_{\text{bp}}^2)(A_{\text{qp}}^2 - 1))} \right] \quad (\text{I.36})$$

where

$$A_{\text{bp}} = \frac{Fh_L}{Sh_{\text{pool}}} \quad (\text{I.37})$$

$$A_{\text{qp}} = \frac{q}{Sh_{\text{pool}}(T_S - T_b)} \quad (\text{I.38})$$

and the two-phase heat transfer coefficient h_{TP} is

$$h_{\text{TP}} = \frac{q}{\Delta T_b} \quad (\text{I.39})$$

Results for the flow and heat transfer characteristics such as the variation of friction factor, the heat transfer coefficient, and the early transition from laminar to turbulent flow in small/microchannels are profoundly different from those for conventional size channels. Due to the larger surface to volume ratio for microchannels and microdevices, factors related to surface effects such as flow compressibility have more impact to microscale flow and heat transfer. Flatter fluid velocity profiles cause higher friction factor and Nusselt number. Surface roughness causes early transition from laminar to turbulent flow. Viscous force modifies natural convection in microenclosure. Channel surface geometry, surface electrostatic charges, and axial heat conduction in the channel cause substantial variation in flow and heat transfer behavior from that at conventional scales.

I.3.2. SIZE EFFECT MECHANISM

The physics related to breakdown of the Navier–Stokes equations is important. The thermophysical properties of the fluid change markedly as the fluid flows along the channel so that Reynolds number at the channel exit could be twice that at the inlet causing the early transition from laminar to turbulent flow in microscale tubes. The temperature-dependent variations of the fluid transport properties along the microchannel may invalidate the often used assumption of constant properties. The rarefaction effect, represented by Knudsen number, Kn , for which the Navier–Stokes equations and the Fourier heat conduction equation break down, may cause the flow and heat transfer behavior change considerably.

A model for the radial heat transfer of a grooved heat pipe evaporator has been presented by Stephan and Busse [184]. They have shown that the assumption of an interface temperature equal to the saturation temperature of the fluid may erroneously give higher radial heat transfer coefficient. The analysis of Stephan and Busse [184] has taken care of the influence of the meniscus curvature and adhesion forces on the volatility of the liquid. The above assumption and the constant interface curvature are not valid in a very small microregion. Figure I.26 shows the meniscus shape, heat flux, and interface temperature in the microregion observed by Stephan and Busse [184].

Increase in capillary pressure due to transverse flow of the liquid causes rise in the interface temperature. In the beginning, the rise in the capillary pressure

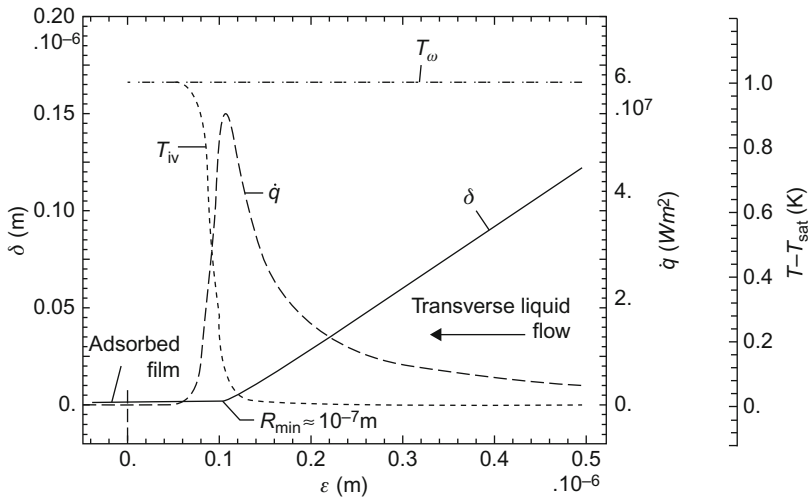


FIG. I.26. Meniscus shape, heat flux, and interface temperature in the microregion. Source: From Stephan and Busse [184].

is due to a strong increase of the curvature of the meniscus because the meniscus is still too far away from the wall for the adhesion forces to contribute to the rise in capillary pressure. At the end, the curvature goes to zero and the meniscus levels off into a flat nonevaporating film.

Ravigururajan [139] observed decrease in heat transfer coefficient with increase in wall superheat and exit vapor quality. Qu and Mudawar [185] focused on measuring and predicting, by a model, the incipient boiling heat flux in a microchannel heat sink.

I.3.3. BOILING CURVES AND HEAT TRANSFER COEFFICIENTS

Figure I.27 [97] shows boiling curves. Figure I.28 [97] shows boiling heat transfer coefficient. As the heat flux increases, the boiling curve shifts toward left with the increase of surfactant concentration.

The annular flow model of Qu and Mudawar [125] took care of laminar liquid and vapor flow, smooth interface, strong droplet entrainment, and deposition effects. The model predicted saturated flow boiling heat transfer coefficient.

Thome et al. [186,187] modeled heat transfer for evaporation of R-11, R-12, R-113, R-123, R-134a, R-141b, and CO₂ in the elongated bubble regime in

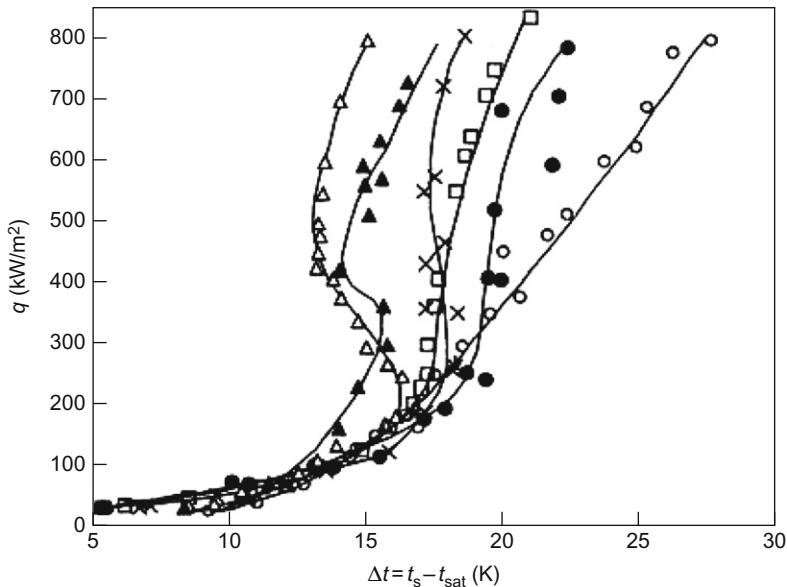


FIG. I.27. Boiling curves of water and aqueous surfactant solutions: O—water; Habon G: ●—65 ppm, □—130 ppm, ×—260 ppm, △—530 ppm, ▲—1060 ppm. Source: From Hetsroni et al. [97].

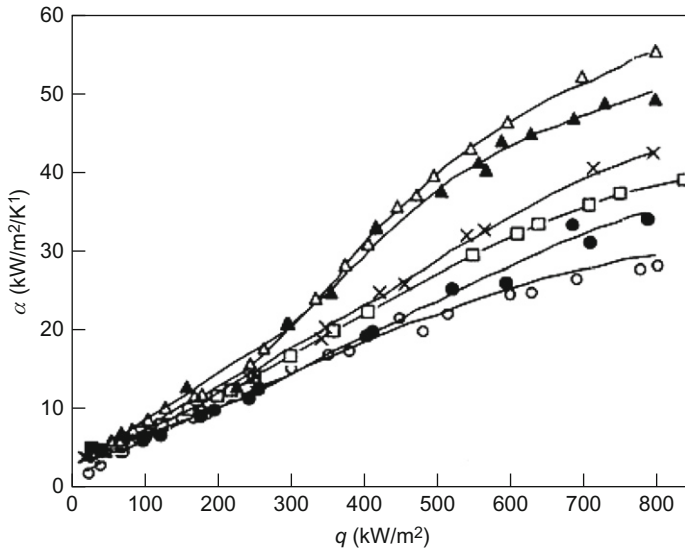


FIG. I.28. Boiling heat transfer coefficient of water and aqueous surfactant solutions: O—water; Habon G: ●—65 ppm, □—130 ppm, ×—260 ppm, △—530 ppm, ▲—1060 ppm. Source: From Hetsroni et al. [97].

microchannels. The sequential and cyclic passage of a liquid slug, an evaporating elongated bubble, and a vapor slug were taken care of in the model.

Hetsroni et al. [188] studied governing forces and their mutual interactions in a heated small size tube on the basis of fundamental theoretical considerations. Subsequently, Hetsroni et al. [189] determined the effect of physical properties, wall heat flux, mass flux, and channel size.

Figure I.29 shows the dependence of average heat transfer coefficient on boiling number, Hetsroni et al. [189].

Hetsroni et al. [189] found the following correlation (Fig. I.30):

$$Nu/Eo = 0.030Bo^{-1.5} \quad (I.40)$$

Sun and Mishima [190], Boye et al. [191], and Ribatski et al. [40] have found that Chen [192] method and Chen-type correlations are not suitable for minichannels. Sun and Mishima [190] have observed that the heat transfer coefficient weakly depends on the vapor quality and mostly depends on the ratio of the fluid's inertia force to its surface tension, that is, the Weber number and they proposed a correlation:

$$h_{tp} = \frac{6Re_{lo}^{1.05}Bo^{0.54}}{We_1^{0.191}(\rho_l/\rho_v)^{0.142}} \frac{k_l}{D} \quad (I.41)$$

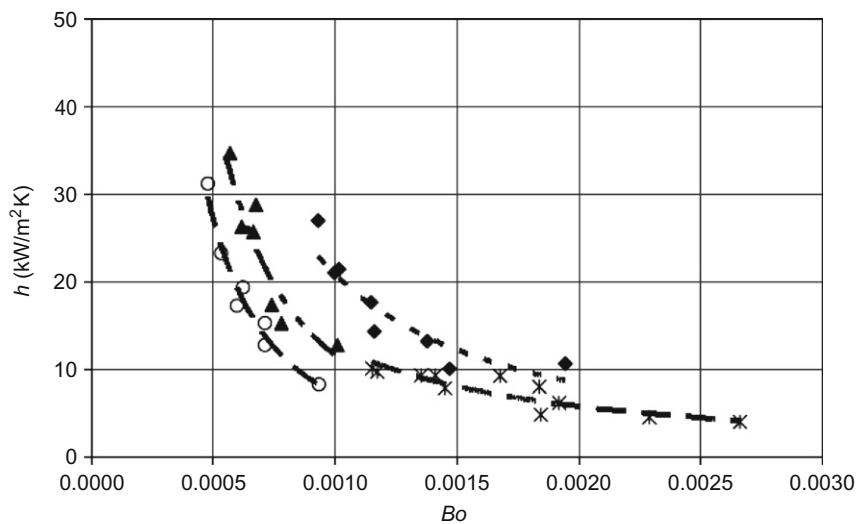


FIG. I.29. Dependence of average heat transfer coefficient on boiling number. Source: From Hetsroni et al. [189].

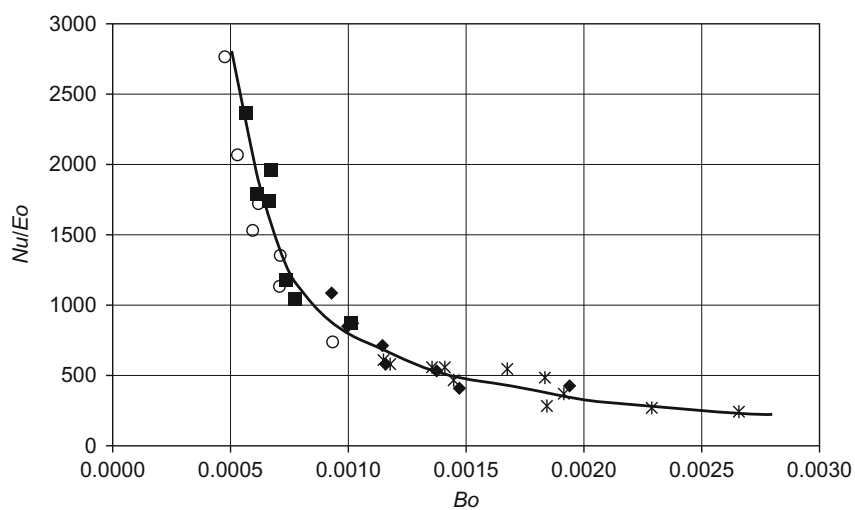


FIG. I.30. Dependence of Nu/Eo on Bo . Source: From Hetsroni et al. [189].

where Weber number, We_1 , is given by

$$We_1 = \frac{G^2 D}{\sigma \rho_1} \quad (I.42)$$

Chen [192] proposed a general correlation for flow boiling heat transfer:

$$h_{tp} = Eh_{sp} + Sh_{nb} \quad (I.43)$$

where

E = enhancement factor

S = suppression factor

$$h_{sp} = 0.023 Re_1^{0.8} Pr_1^{0.4} \left(\frac{k_1}{D} \right), \quad (I.44)$$

$$Re_1 = \frac{G(1-x)D}{\mu_1} \quad (I.45)$$

$$h_{nb} = 0.00122 \left(\frac{k_1^{0.79} C_{pl}^{0.45} \rho_1^{0.49}}{\sigma^{0.5} \mu_1^{0.29} h_{fg}^{0.24} \rho_v^{0.24}} \right) \Delta T_{sat}^{0.24} \Delta P_{sat}^{0.75} \quad (I.46)$$

Zhang et al. [171] observed that a liquid-laminar and gas-turbulent flow is a common feature in many applications of minichannels and modified the Chen [192] correlation as follows:

for $Re_1 \leq 2000$ and a vertical flow,

$$h_{sp} = \frac{k_1}{D} \max(Nu_{sp,l}, Nu_{Collier}) \quad (I.47)$$

for $Re_1 \leq 2300$ and a horizontal flow,

$$h_{sp} = \frac{k_1}{D} \max(Nu_{sp,l}, Nu_{sp,t}) \quad (I.48)$$

for $Re_1 > 2300$

$$h_{sp} = \frac{k_1}{D} Nu_{sp,t} \quad (I.49)$$

$$Nu_{Collier} = 0.17 Re_1^{0.33} Pr_1^{0.43} \left(\frac{Pr_1}{Pr_{1w}} \right)^{0.25} \left[\frac{g \beta \rho_1^2 D^3 (T_w - T)}{\mu_1^2} \right]^{0.1} \quad (I.50)$$

The correlation of Saitoh et al. [193] is the modification of Chen [192] correlation and it is given by:

$$h_{nb} = 207 \frac{k}{D_b} \left(\frac{q D_b}{k_1 T_1} \right)^{0.745} \left(\frac{\rho_v}{\rho_l} \right)^{0.581} Pr^{0.533} \quad (I.51)$$

$$E = 1 + \frac{X^{-1.05}}{1 + We_g^{-0.4}} \quad (I.52)$$

$$S = \frac{1}{1 + 0.4 (Re_{tp} \times 10^{-4})^{-1.4}} \quad (I.53)$$

Kew-Cornwell [12] correlation allows for the increase in the heat transfer coefficient with the vapor quality in larger tubes; this is

$$h_{tp} = 30Re_{lo}^{0.857}Bo^{0.714}(1-x)^{-0.143}(k_l/D) \quad (I.54)$$

Kandlikar [194] correlation is

$$h_{tp} = \max(E, S)h_{sp} \quad (I.55)$$

where

$$E = 0.6683Co^{-0.2}f(Fr_1) + 1058Bo^{0.7} \quad (I.56)$$

$$S = 1.136Co^{-0.9}f(Fr_1) + 667.2Bo^{0.7} \quad (I.57)$$

$$Co = \left(\frac{1-x}{x}\right)^{0.2} \left(\frac{\rho_v}{\rho_l}\right)^{0.5} \quad (I.58)$$

$$Fr_1 = \frac{G^2}{\rho_l^2 g D} \quad (I.59)$$

$$f(Fr_1) = 1 \quad \text{for } Fr_1 > 0.04 \quad (I.60)$$

$$f(Fr_1) = (25Fr_1)^{0.3} \quad \text{for } Fr_1 < 0.04 \quad (I.61)$$

Tran et al. [195] and Yu et al. [196] correlations are:

$$h_{tp} = 8.4 \times 10^5 Bo^{0.6} We_l^{0.3} \left(\frac{\rho_l}{\rho_v}\right)^{-0.4} \quad (I.62)$$

and

$$h_{tp} = 6.4 \times 10^6 Bo^{0.54} We_l^{0.27} \left(\frac{\rho_l}{\rho_v}\right)^{-0.2} \quad (I.63)$$

respectively.

Warrier et al. [197] proposed a correlation, which is

$$h_{tp} = (1 + 6Bo^{1/16} + f(Bo)x^{0.65})h_{sp} \quad (I.64)$$

$$f(Bo) = -5.3(1 - 855Bo) \quad (I.65)$$

Kenning and Cooper [198] observed that the saturated convective coefficient depends primarily on local parameters in the annular flow regime and they proposed a correlation by modifying the correlation of Chen [192]. It can be seen that saturated convective and nucleate boiling are not additive. Their correlation is

$$h_{tp} = (1 + 1.8X^{-0.87})h_{sp} \quad (I.66)$$

Pamitran et al. [199] proposed a correlation based on Chen [192] method with

$$S = 9.4626(\varphi_1^2)^{-0.2747}Bo^{0.1285} \quad (I.67)$$

$$E = 0.062\varphi_1^2 + 0.938 \quad (I.68)$$

where φ^2 is the two-phase friction multiplier.

The Lazarek and Black [144] correlation can well predict the database on the whole; however, because of its independence of the vapor quality, it cannot reproduce the variation trend of the heat transfer coefficient with the vapor quality. The Sun and Mishima [190] correlation as well as the Kew-Cornwell [12] correlation also cannot always correctly predict the variation trend of the heat transfer coefficient with the vapor quality.

Gungor and Winterton [200] correlation is

$$h_{tp} = Eh_{sp} \quad (I.69)$$

where

$$h_{sp} = 0.023Re_L^{0.8}Pr^{0.4}\left(\frac{\lambda_l}{d_h}\right) \quad (I.70)$$

$$E = 1 + 3000Bl^{0.86} + 1.12\left(\frac{x}{1-x}\right)^{0.75}\left(\frac{\rho_l}{\rho_g}\right)^{0.41} \quad (I.71)$$

Lee and Mudawar [167] correlation is

$$h_{tp} = 3.856X^{0.267}h_{sp}, \quad 0 < X < 0.05 \quad (I.72)$$

$$h_{tp} = 436.48Bl^{0.522}We_{Lo}^{0.351}X^{0.665}h_{sp}, \quad 0.05 < X < 0.55 \quad (I.73)$$

$$h_{tp} = \max[(108.6X^{1.665}h_{sp,g}), h_{sp,g}], \quad 0.55 \leq X < 1 \quad (I.74)$$

where

$$X^2 = \frac{(dp/dz)_f}{(dp/dz)_g} \quad (I.75)$$

Table I.III shows statistical comparison of prediction methods.

TABLE I.III
COMPARISON OF THE HEAT TRANSFER CORRELATIONS AGAINST THE DATABASE

Correlation	e_R^a (%)	σ_N^b (%)	Proportion of $\pm 30\%$ h_{exp}	Proportion of $\pm 50\%$ h_{exp}
Gungor–Winterton	101.0	352.3	36.84	58.69
Lazarek–Black	36.94	70.46	52.15	79.11
Tran et al.	45.62	102.6	20.69	44.95
Kandlikar	90.2	200.8	34.06	56.94
Yu et al.	1197	751.7	1.98	3.29
Warrier et al.	63.19	118.7	13.85	31.01
Lee–Mudawar	134.3	342.5	23.44	37.15
New correlation	26.13	45.71	65.50	85.75

$$^a e_i = \left[\frac{(h_c)_{\text{cal}} - (h_c)_{\text{exp}}}{(h_c)_{\text{exp}}} \right] \cdot 100\%, e_R = \frac{1}{N_p} \cdot \sum_{d=1}^{N_p} \left| \frac{(h_c)_{\text{cal}} - (h_c)_{\text{exp}}}{(h_c)_{\text{exp}}} \right| \cdot 100\%.$$

$$^b \sigma_N = \sqrt{\frac{\sum_{d=1}^{N_p} (e_i - e_R)^2}{N_p - 1}} \cdot 100\%.$$

From Li and Wu [182].

Li and Wu [182] correlation is

$$Nu_{\text{tp}} = 334Bl^{0.3}(BoRe_L^{0.36})^{0.4} \quad (I.76)$$

Li and Wu [182] correlation does a fair job for wide range of Bo for different working fluids flowing in various micro/minichannels under different operating conditions.

Figure I.31 verifies the correlation of Li and Wu [182] against the experimental data sets.

Li and Wu [182] obtained a better prediction method based on the transitional threshold:

$$Bo^* Re_L^{0.5} \leq 200, \quad Nu_{\text{tp}} = 22.9(Bo^* Re_L^{0.5})^{0.355} \quad (I.77)$$

$$Bo^* Re_L^{0.5} > 200, \quad Nu_{\text{tp}} = 30Re_{\text{Lo}}^{0.857} Bl^{0.714} \quad (I.78)$$

The work by Steinke and Kandlikar [201] focused on obtaining heat transfer data during flow boiling in microchannels.

The work by Steinke and Kandlikar [201] was followed by Kandlikar and Balasubramanian [126] and the latter presented a new correlation applicable to transition, laminar and very low Reynolds numbers deep laminar flow in microchannels:

For $Re_{\text{LO}} > 100$:

$$h_{\text{TP}} = \text{larger of } \begin{cases} h_{\text{TP,NBD}} \\ h_{\text{TP,CBD}} \end{cases} \quad (I.79)$$

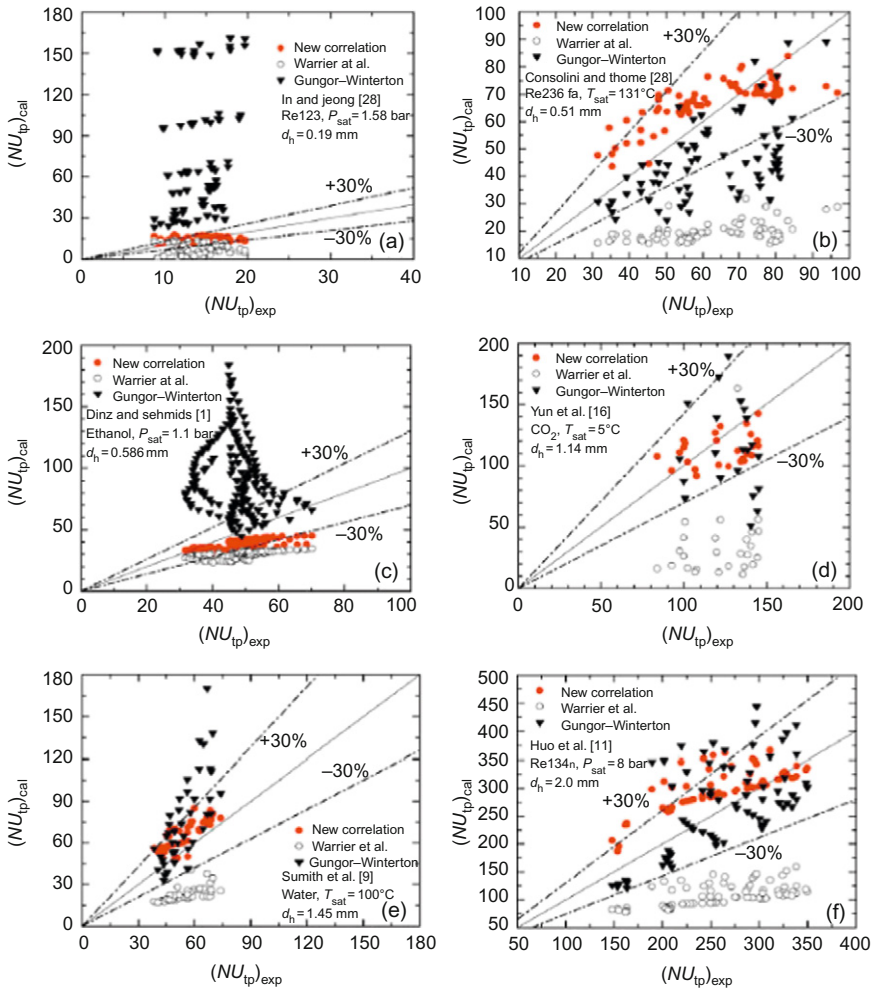


FIG. I.31. Verification of Li and Wu [182] correlation against experimental data sets. For color version of this figure, the reader is referred to the web version of this book. Source: From Li and Wu [182].

$$h_{TP,NBD} = 0.6683Co^{-0.2}(1-x)^{0.8}h_{LO} + 1058.0Bo^{0.7}(1-x)^{0.8}F_{FI}h_{LO} \quad (I.80)$$

$$h_{TP,CBD} = 1.136Co^{-0.9}(1-x)^{0.8}h_{LO} + 667.2Bo^{0.7}(1-x)^{0.8}F_{FI}h_{LO} \quad (I.81)$$

where

$$Co = [(1-x)/x]^{0.8}[\rho_V/\rho_L]^{0.5} \quad (I.82)$$

and

$$Bo = q''/(Gh_{LV}) \quad (I.83)$$

The single-phase all-liquid flow heat transfer coefficient h_{LO} is given by:
for $10^4 \leq Re_{LO} \leq 5 \times 10^6$

$$h_{LO} = \frac{Re_{LO} Pr_L (f/2) (k_L/D)}{1 + 12.7(Pr_L^{2/3} - 1)(f/2)^{0.5}} \quad (I.83)$$

for $3000 \leq Re_{LO} \leq 10^4$

$$h_{LO} = \frac{(Re_{LO} - 1000) Pr_L (f/2) (k_L/D)}{1 + 12.7(Pr_L^{2/3} - 1)(f/2)^{0.5}} \quad (I.84)$$

for $100 \leq Re_{LO} \leq 1600$

$$h_{LO} = \frac{Nuk}{D_h} \quad (I.85)$$

In the transition region between Reynolds numbers of 1600 and 3000, a linear interpolation is suggested for h_{LO} .

For Reynolds number below and equal to 100 ($Re \leq 100$), the nucleate boiling mechanism governs, and the following correlation is proposed:

for $Re_{LO} \leq 100$,

$$h_{TP} = h_{TP,NBD} = 0.6683 Co^{-0.2} (1-x)^{0.8} h_{LO} + 1058.0 Bo^{0.7} (1-x)^{0.8} F_{FI} h_{LO} \quad (I.86)$$

The single-phase, all-liquid flow heat transfer coefficient is h_{LO} . F_{FI} is the surface-dependent parameter representing nucleation characteristics of the liquid on the given heater surface.

The effect of the inside surface roughness of small tubes (620 and 1032 μm) on single-phase heat transfer and pressure drop was investigated by Kandlikar [29]. Only the smaller diameter tube had heat transfer enhancement with increased pressure drop due to surface roughness.

Peng et al. [92] observed distinct heat transfer enhancement with smaller channels caused by an immediate initiation of fully developed nucleate boiling after reaching a sufficient wall superheat (Fig. I.32). There was no partial nucleate boiling. There was no influence of the liquid velocity and subcooling on the nucleate boiling itself. However, there was an influence on ONB.

For single microchannel, nucleate boiling is dominant; whereas for multi-channels, convective boiling is also important. The heat transfer enhancement in small channels depends on the fluid, the flow channel, and the operating pressure. The conflicting experimental observations of partial nucleate boiling

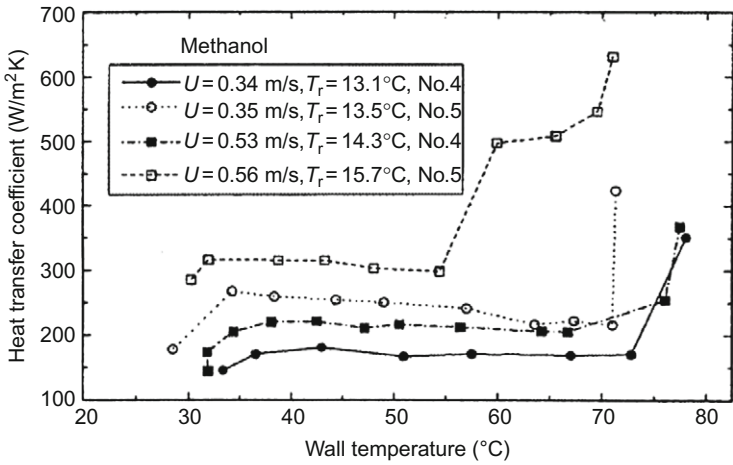


FIG. I.32. Heat transfer in parallel microchannels with working fluid methanol. Source: From Peng et al. [92].

and vapor bubbles in the nucleate boiling regime in microchannel flow boiling are due to limitations of measuring instrumentation.

I.3.4. ELECTRIC DOUBLE LAYER

The boiling thermohydraulics of the microchannels are largely affected by the interfacial electric double layer (EDL). This EDL effect can be ignored in macroscale fluid mechanics. But, in microchannels, the electric surface potential due to electrostatic charges causes the counterions to establish an electric field, as illustrated in Fig. I.33 [202].

The ionic concentration near the solid surface is higher than that in the bulk liquid. In compact layer, the immobile ions are found in the vicinity of the wall. However, the ions are mobile in the diffuse double layer. The thickness of the EDL ranges from a few nanometers up to several hundreds of nanometers. This depends on the electric potential, bulk ionic concentration, and other liquid properties.

Streaming current is developed since the ions in the mobile part of the EDL are carried toward one end in case of liquid flow through a microchannel. An opposing conduction current also develops due to the streaming potential in the electric field generated downstream. In steady state, these currents are equal. Thus the liquid flow and the associated heat transfer are affected by the EDL. The liquid flow is reduced and the EDL at the solid–liquid interface results in reduced velocity which directly affects the heat transfer in the

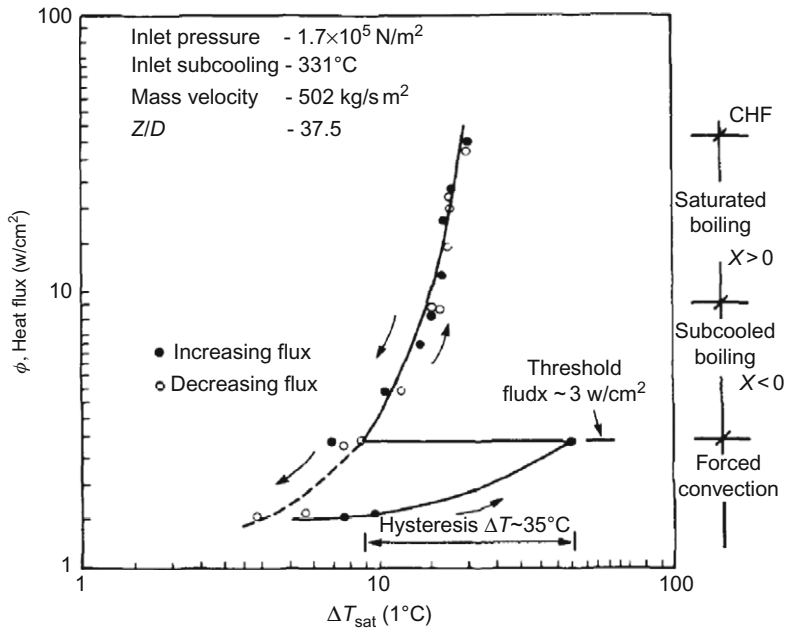


FIG. I.34. Boiling curve for R-113 in commercially smooth stainless steel tube. Source: From Lazarek and Black [144].

flux is due to the local size distribution of active cavity sites and surface wettability characteristics of R-113.

During the subcooled boiling, the local heat transfer coefficient increases rapidly from a low value at the test section inlet to a large value coincident with the start of saturated boiling. Beyond that point, the saturated boiling heat transfer coefficient is independent of quality suggesting that the mechanism of nucleate boiling is controlling the wall heat transfer process.

Saitoh et al. [193] incorporated the effect of tube diameter in a Chen-type correlation for flow boiling heat transfer of R-134a in horizontal microchannels. Weber number in gas phase characterizes the effect of tube diameter on flow boiling heat transfer coefficient. They have used the annular flow model to study the dryout point and the heat transfer characteristics after the dryout point. Their correlation can predict both the dryout quality and the post dryout heat transfer coefficient.

It is generally observed that (i) contribution of forced convective evaporation to boiling heat transfer decreases; (ii) onset of dryout occurs in a lower quality region; (iii) prediction of pressure drop by using a homogeneous model is better than that by using the Lockhart–Martinelli correlation; and (iv) local

heat transfer coefficient decreases at high vapor quality with the change of flow pattern from continuous annular flow to intermittent slug or plug flow. Therefore, prediction of both the onset of dryout and the post-dryout heat transfer coefficient is crucial in the design of compact heat exchangers.

In general, as the vapor quality increases, vapor velocity increases and the contribution of convective evaporation increases, while the contribution of nucleate boiling decreases because the superheat of the liquid film decreases due to film evaporation. As the tube diameter decreases, the surface tension rather than the buoyancy affects the two-phase flow. The predominance of surface tension over buoyancy leads to the insensitivity of channel orientation with respect to gravity, and reduces the slip velocity, that is, the difference in velocity between liquid and vapor phases [147]. This reduction in slip velocity suppresses the generation of shear stress at the vapor–liquid interface and also suppresses the occurrence of interfacial waves.

Figure I.35 [193] shows the experimental flow boiling heat transfer coefficient versus calculated heat transfer coefficient for R-134a in horizontal smooth tubes.

The three-zone model of Thome et al. [149], Fig. I.36, provides the time average heat transfer coefficient during the cyclic passage of a liquid slug, an evaporating elongated bubble, and a vapor slug when present. It has empirical constants directly related to the film thickness during the elongated bubble passage.

The heat transfer model of Qu and Mudawar [125] is based on the liquid film progressive evaporation during annular flow and it provides the local film thickness. The heat transfer coefficient is obtained by the ratio between the thermal conductivity and liquid film thickness. Effects on the liquid film thickness related to liquid droplets detachment and deposition are also observed.

The heat transfer model of Revelin et al. [109] predicts critical heat flux and local dryout under saturated stable condition in annular flow occurring when the film thickness becomes equal to the interfacial wave height during evaporation.

In flow boiling, different heat transfer mechanisms are dominant according to the vapor quality range, and heat flux and mass velocity levels. At low vapor quality, nucleate boiling effects prevail while at high vapor quality and prior to liquid dryout, the heat transfer coefficient is mainly controlled by convective effects. Ribatski et al. [170] made a study on the prediction of heat transfer in microscale flow boiling.

I.3.6. HEAT TRANSFER COEFFICIENT ALONG THE TUBE PERIMETER

Stratification effects are present and a thicker liquid film is observed in the tube bottom region, Fig. I.37 [205]. This behavior affects the heat transfer

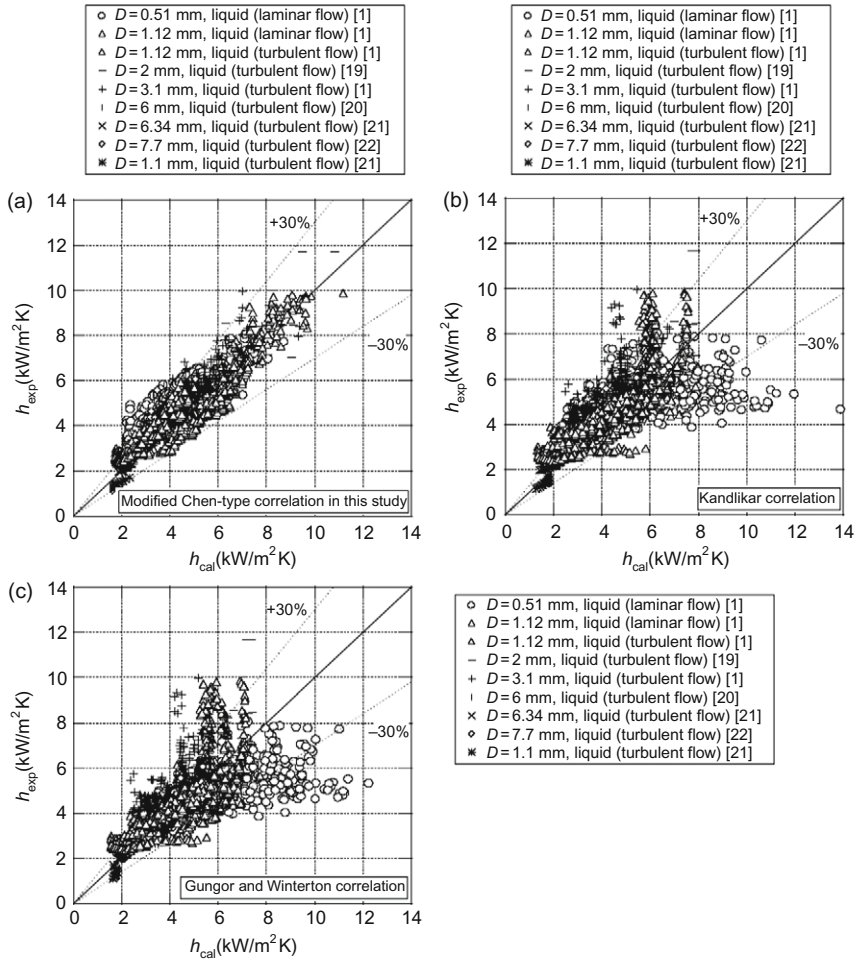


FIG. I.35. Experimental flow boiling heat transfer coefficient versus calculated heat transfer coefficient: (a) Saitoh et al. [193], (b) Kandlikar [118], and (c) Gungor and Winterton [200]. Source: From Saitoh et al. [193].

coefficient: (i) for $x \leq 0.85$, the heat transfer coefficient increases in the upward direction along the tube perimeter because of lower thermal resistance in the upper part of the tube and the upward decrease of the liquid film thickness, (ii) for $x > 0.85$, the heat transfer coefficient decreases in the upward direction. Progressive surface dryout occurs from the upper part of the tube with increasing vapor quality.

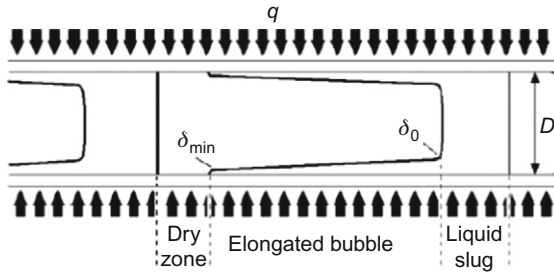


FIG. I.36. Diagram of a triplet of liquid slug, elongated bubble, and vapor slug in the three-zone heat transfer model. Source: From Thome et al. [149].

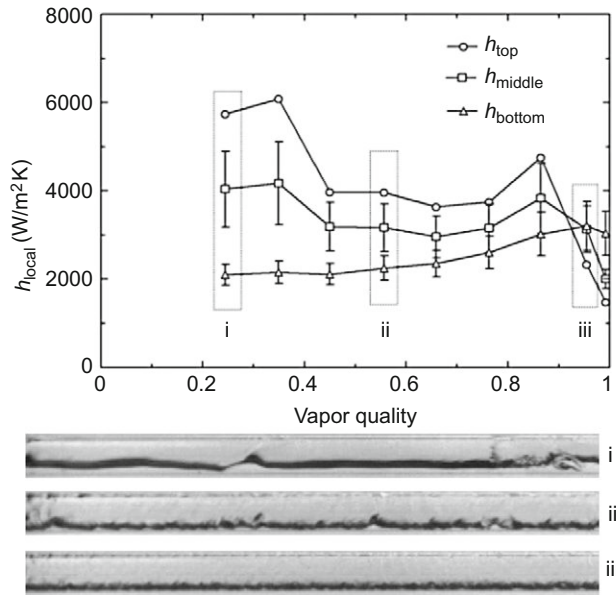


FIG. I.37. Heat transfer coefficient distribution along the tube perimeter and the corresponding two-phase flow images. Source: From Tibirica and Ribatski [205].

I.3.7. PARAMETRIC ANALYSES OF THE EXPERIMENTAL RESULTS

For a given heat flux, the heat transfer coefficient increases with increasing mass velocity up to a mass velocity threshold. This effect becomes more pronounced as the vapor quality increases. For mass velocity higher than the threshold, the heat transfer coefficient increases with vapor quality

for $x \leq 0.9$, while for mass velocity lower than the threshold, a premature and smooth decrease of heat transfer coefficient occur with increasing vapor quality.

Figure I.38 [205] shows that the heat transfer coefficient increases with increasing saturation temperature. This is more pronounced at low vapor quality and mass velocity and becomes almost negligible at high mass velocity and vapor quality.

Except for some of the results at $x > 0.9$, the heat transfer coefficient increases with heat flux irrespective of the range of mass velocity. This is different from the behavior found in macroscale channels for which the heat transfer coefficient increases with increasing heat flux only at low vapor quality and mass velocity. This is due to the persistent nucleate boiling heat transfer mechanism for elongated bubbly flow.

Multiport minichannels have applications in compact evaporators. Kaew-On et al. [53] studied flow boiling heat transfer of R-134a in multiport minichannel heat exchangers. They proposed predictive heat transfer coefficient correlation. Yan and Lin [123] studied evaporation heat transfer and pressure drop of refrigerant R-134a in a small pipe. They have developed correlations to predict the evaporation heat transfer coefficient and friction factors.

Owhaib et al. [206] presented experimental results on saturated flow boiling of R-134a in vertical circular tubes and observed that wall heat flux and system pressure have profound effects on heat transfer coefficients. However, mass flux and vapor quality do not significantly affect heat transfer coefficient. Also, heat transfer coefficient is dominated by nucleate boiling. Huai et al. [207] and Pettersen [163] observed, for multiport channels, that both larger mass flux and higher heat flux lead to higher heat transfer coefficients due to dominant nucleate boiling over low/moderate vapor quality region. Pettersen [163] observed that dryout effects become very important at higher mass flux and higher temperature resulting in substantially reduced heat transfer coefficient at high vapor qualities. Heat transfer coefficient of experimental data for low vapor quality region is compared with heat transfer correlations based on nucleate boiling mechanisms.

Yun et al. [208,209] observed that uniform flow distribution to each channel reduces the dependence of heat transfer coefficients on heat flux, mass flux, and saturation. They have observed that dryout phenomenon is promoted by an increase in mass flux and the effect of mass flux on heat transfer coefficient is less than that of heat flux. Also, the heat transfer coefficient increases with decrease in channel hydraulic diameter. Lie et al. [210] showed that the heat transfer coefficient increased substantially with increases in heat flux, mass flux, and saturation temperature. Heat transfer coefficient for R-407C is higher than that of R-134a. They proposed the correlations to predict heat transfer coefficient.

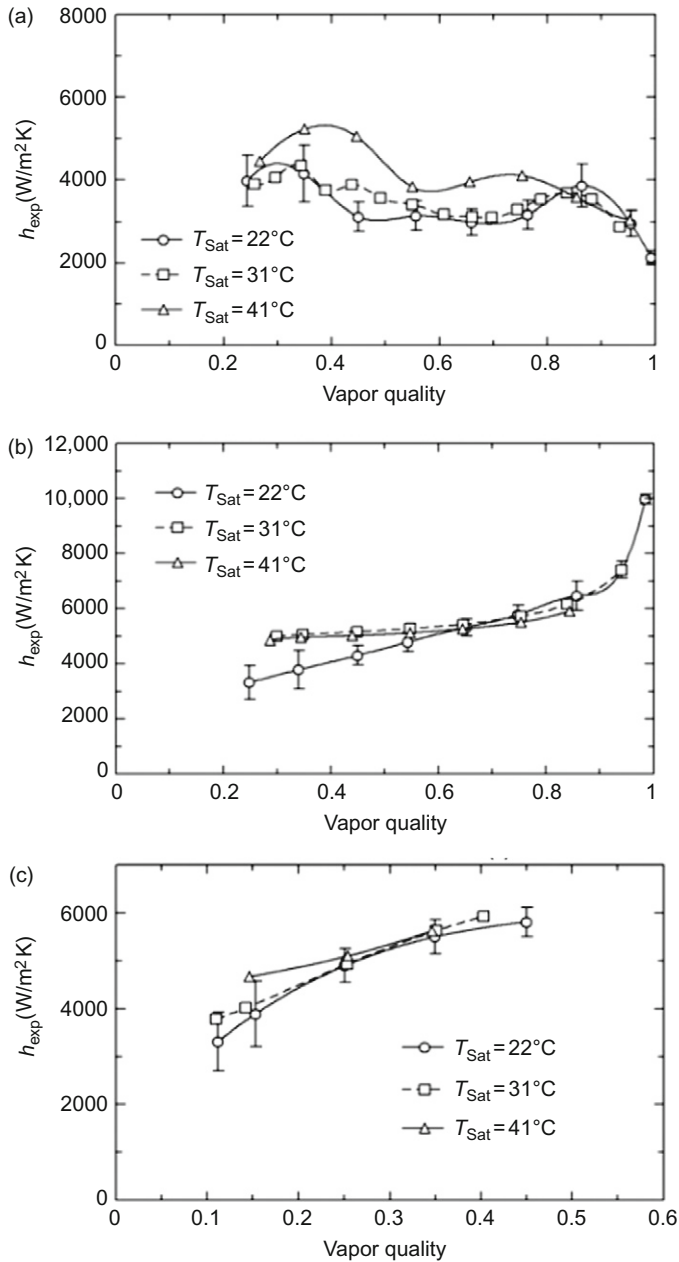


FIG. I.38. Effect of saturation temperature on the heat transfer coefficient: mass velocity increases from (a) to (c). Source: From Tiberica and Ribatski [205].

Results of Shiferaw et al. [211] showed that in the low vapor quality region, the local heat transfer coefficient is independent of vapor quality, while in the high vapor quality region, the heat transfer coefficient decreases with increasing vapor quality. In the low vapor quality region, the heat transfer coefficient is dominated by nucleate boiling and the partial dryout occurs at high vapor quality. The heat transfer coefficient increases with increasing heat flux and saturation pressure.

Fernando et al. [212–214] recommended that correlations emphasizing nucleate boiling are in better agreement with the experimental data than correlations emphasizing convective evaporation. Ong and Thome [215] modified an isolated bubble/coalescing bubble/annular flow map to investigate the influence of flow pattern on the heat transfer coefficient.

Kaew-On and Wongwises [216] worked with R-410A in multiport minichannel and observed that the average heat transfer coefficient tended to increase with increasing average quality, mass flux, and heat flux. Whereas the heat transfer coefficient tended to decrease with increasing saturation temperature. The pressure drop increased with increasing mass flux and decreased with increasing saturation temperature. The heat flux does not affect pressure drop much. They also proposed heat transfer coefficient and frictional pressure drop predictive correlations.

Figure I.39 shows the boiling curves for flow boiling through multiport minichannels as observed by Kaew-On et al. [53]. The boiling curves correspond to the nucleate boiling regime which gives bubbly, slug, or low velocity annular flow patterns. Mass flux does not affect boiling curve much. Excess temperature increases with increases in saturation pressure. The heat transfer coefficient increases with increases in heat flux, especially at high heat flux and low saturation temperature conditions. Increase in mass flux has no significant effect on the heat transfer coefficient irrespective of saturation pressure.

The average heat transfer coefficient is a strong function of heat flux but is independent of mass flux and vapor quality indicating that the effect of forced convection on overall flow boiling heat transfer is small and the nucleate boiling dominates. Increase in heat flux causes increase in the number of bubbles, entrainment of droplets, and degree of turbulence leading to increase in heat transfer coefficient. The heat transfer coefficient at lower saturation pressure is significantly higher than those at higher saturation pressure because of higher thermal conductivity of liquid film. Also, density of vapor increases with increasing pressure strongly affecting the velocity of generated vapor [216–218].

Kaew-On et al. [53] observed that increased heat transfer surface area gives better load distribution resulting in the increase of number of bubbles at the inner wall surface which causes increased heat transfer coefficient. In this case of nucleate boiling, bubbles formed at the interface are dissipated

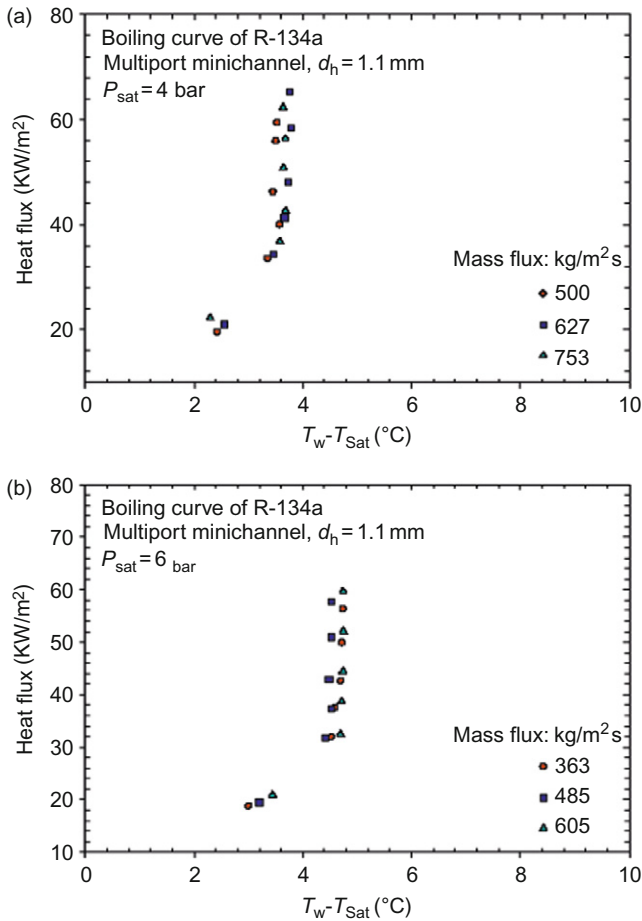


FIG. I.39. The boiling curve of R-134a in multiport minichannel: (a) at 4 bar (b) at 6 bar. For color version of this figure, the reader is referred to the web version of this book. Source: From Kaew-On et al. [205].

in the liquid shortly after they are separated from the surface. The space vacated by the rising bubbles gets occupied by the liquid in the vicinity of the heater surface, and the process is repeated. Liquid entrainment to the heat transfer surface causes stirring and agitation which in turn increases heat transfer coefficient.

Figure I.40 shows the comparison of experimental data of Kaew-On et al. [53] with available correlations. Different channel diameters and working fluids cause large deviations. Maldistribution of flow in multiport channels

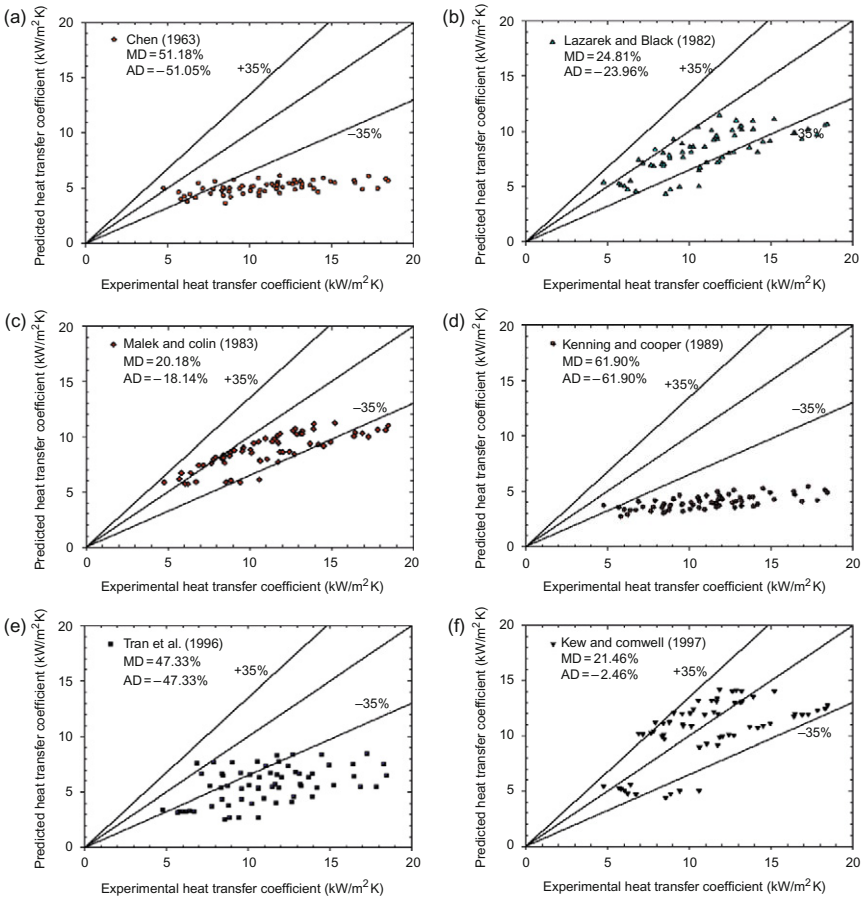


FIG. I.40. Comparison of experimental average heat transfer coefficient with existing correlations. For color version of this figure, the reader is referred to the web version of this book. Source: From Kaew-On et al. [53].

gives differences in heat transfer coefficient. Kaew-On et al. [53] have developed a new correlation.

Huo et al. [219] studied experimentally boiling heat transfer of R-134a. For low vapor quality, the heat transfer coefficient increased with increasing heat flux and saturation pressure, but the heat transfer coefficient is independent of vapor quality. This is due to the dominant nucleate boiling. Smaller diameter tube has larger heat transfer coefficient.

Choi et al. [217] observed nucleate boiling in the low vapor quality region, whereas convective evaporation is dominant in the high vapor quality region.

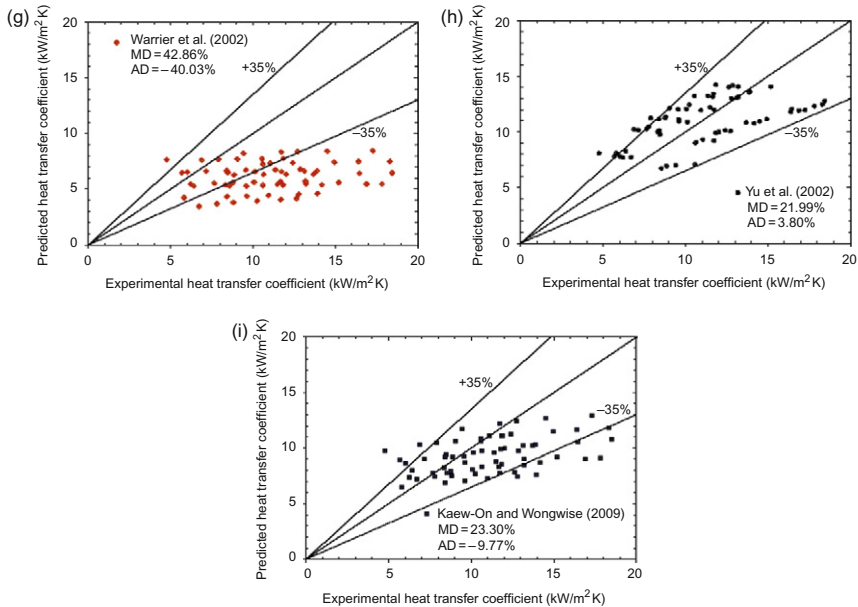


FIG. I.40 (CONTINUED).

Convective evaporation is less dominant as the channel diameter decreases. The effect of saturation temperature on heat transfer coefficient is more important for small diameter channel. They reported that the use of CO₂ causes higher heat transfer coefficient than that with R-134a and R-22.

Ong and Thome [215] observed that the heat transfer coefficient depends on heat flux at low vapor quality and on mass flux at high vapor quality. At low vapor quality, R-134a has the highest heat transfer coefficient followed by R-236fa and R-245fa, respectively.

Thome et al. [186,187] worked with a three-zone flow boiling model based on the elongated bubble flow regime and they observed that the heat transfer is controlled mainly by the conduction through the evaporation film trapped between the elongated bubble and the tube wall.

The heat transfer data of Saisorn et al. [54] compared well with the transition zones of Revellin and Thome [155]. The churn flow and throat-annular flow obtained by Saisorn et al. [54] agreed well with the coalescing bubble regime of Revellin and Thome [155], whereas annular-rivulet flow and slug flow of the Saisorn et al. [54] resemble annular region and transition zone between isolated bubble and coalescing bubble regions of Revellin and Thome [155].

The heat transfer coefficient of Saisorn et al. [54] increases with increasing heat flux and is less affected by vapor quality and mass flux. Similar results are observed by Saitoh et al. [193] and Shiferaw et al. [211].

The three-zone model of Saisorn et al. [54] and Thome et al. [186,187] is a mechanistic flow boiling heat transfer model comprising heat transfer zones including a pair of liquid slug and elongated bubble zones, followed by vapor slug in case of dryout. Each zone is modeled as a fixed location occurring sequentially and cyclically. The heat transfer is not dominated by nucleate boiling. It is dominated by transient conduction through the thin liquid film trapped between the elongated bubble and the tube wall.

The cyclic passage through each zone is expressed by a time-average local heat transfer coefficient as:

$$h(z) = \frac{t_L}{\tau} h_L(z) + \frac{t_{\text{film}}}{\tau} h_{\text{film}}(z) + \frac{t_{\text{dry}}}{\tau} h_G(z) \quad (\text{I.87})$$

where

τ = period of bubble generation

z = reciprocal of the frequency empirically determined by Dupont and Thome [133]

t_L = time for liquid slug to pass a fixed location z along the tube

t_{film} = time for film formation

t_{dry} = local wall dry out time

h_{film} = heat transfer coefficient in the stagnant film across which one-dimensional conduction takes place

h_L = heat transfer coefficient in the liquid

h_G = heat transfer coefficient in the vapor slug

The Saisorn et al. [54] and Choi et al. [217] heat transfer models do not do a good job since the liquid film under high saturation pressure tends to break up easily leading to unstable condition near the tube wall. The Saisorn et al. [54] heat transfer model does a fairly good job to slug flow, throat-annular flow, and churn flow regimes.

I.4. Pressure Drop

Lazarek and Black [144] generated pressure drop data. Pressure drop data for frictional, spatial acceleration, and 180° bend losses were correlated by employing slight modifications to commonly accept two-phase technique reported in the literature, for example, Lockhart–Martinelli [220], Martinelli–Nelson [221], and Chisholm–Sutherland [222].

Lazarek and Black [144] developed predictive correlations for frictional, spatial acceleration, and bend pressure drop components with the help of

Zuber and Findlay [112], Lockhart and Martinelli [220], Martinelli and Nelson [221], and Chisholm and Sutherland [222]. A model for the total pressure drop from the test section inlet to exit was constructed by summing the individual pressure drop components. However, the analytical model underpredicts the experimental pressure drop because of subcooled boiling which increases friction factors, and additional work is needed in this area to improve the agreement with the experimental data. Replacing the equilibrium vapor quality in the saturated boiling pressure drop correlations with estimates of the flowing quality obtained from an available subcooled void model may be the solution.

I.4.1. FLOW COMPRESSIBILITY EFFECT

Figure I.41 [223] shows the compressibility effect on the friction factor.

The correlation for the friction factor in terms of Mach number is given by Li et al. [224]:

$$f = \frac{64}{Re} + \frac{64}{Re} \frac{M^2}{1.5 - 0.66M - 1.14M^2} \quad (\text{I.88})$$

The viscous dissipation and the work due to expansion cannot be neglected. The Eckert number of the downstream flow may be rather large, even though the inlet Eckert number is small as shown in Fig. I.42 [225].

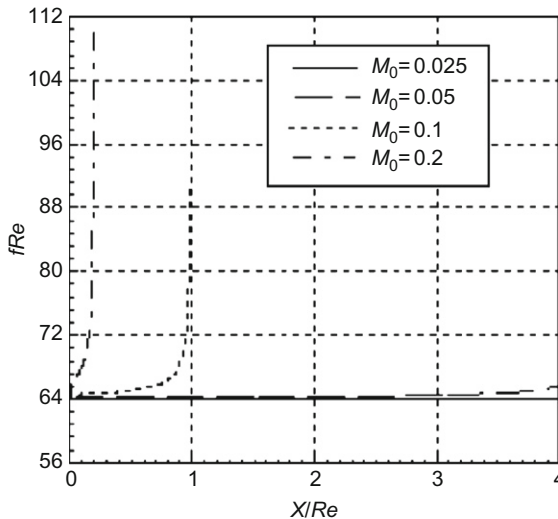


FIG. I.41. Dependence of fRe on location for various inlet Mach number. Source: From Guo and Li [223].

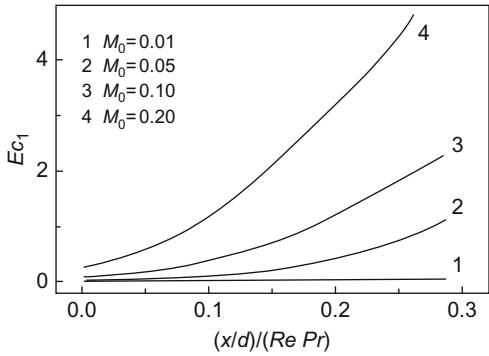


FIG. I.42. Variation of Eckert number along the tube. Source: From Du [225].

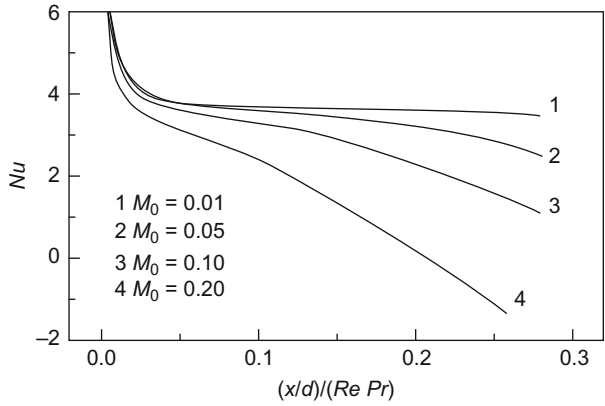


FIG. I.43. Variation of Nusselt number along the tube. Source: From Du [225].

The conventionally defined Nusselt number may even be negative as shown in Fig. I.43 if the Mach number and the resulting consequent temperature decrease in the channel interior are large enough [225].

I.4.2. EFFECT OF SURFACE ROUGHNESS

Celata et al. [226] and Li et al. [227] measured friction factor for flow in a microchannel. The form drag resulting from the more number of roughness elements per unit channel length leads to increased friction factor. Roughness generated flow disturbances also affect the flow in microchannels.

I.4.3. VARIATION OF PREDOMINANT FORCES

Dao et al. [228], Leung et al. [229], Milanovic et al. [230], and Luo et al. [231] studied the relative importance of inertial and viscous forces.

I.4.4. VARIATION OF OTHER PREDOMINANT FACTORS

Effects of surface geometry, surface electrostatic charges, axial heat conduction equation in the channel wall, and measurement accuracy have been studied in Mala et al. [232], Yang and Li [233], Ren et al. [234] Mori et al. [235], and Pfahler et al. [236].

Guo and Wu [237] numerically examined the compressibility effect on friction coefficient and Nusselt number of gas flows in smooth microtubes. The large friction induced pressure gradient and the flow acceleration for gas flows in microtubes may increase dimensionless velocity gradient at the wall surface resulting in increase in local friction coefficient. The hydrodynamically and thermally fully developed flow may not be attained due to continuous change of the radial variation of the axial velocity and hence the temperature profile caused by compressibility effect; therefore, the product of the friction coefficient and Reynolds number is not constant, but dependent on Reynolds number. Also the local Nusselt number increases along the length due to compressibility effect. Higher tube inlet Mach number causes larger friction coefficient and Nusselt number.

Wu and Little [238] measured the friction factor for laminar and turbulent flow of gases in very fine microchannels used for microminiature Joule–Thomson refrigerators. They observed higher friction factor and early transition from laminar to turbulent flow. Wu and Little [239] observed Nusselt number varying with Reynolds number for laminar flow. The Reynolds analogy was not valid for the turbulent flow in the rough channels tested. Pfahler et al. [236,240] observed that friction factor decreased with decreasing Reynolds number for laminar flow at small Reynolds number. Choi et al. [241] observed similar results.

Bowers and Mudawar [242–244] studied pressure drop characteristics for R-113 in mini- and microchannel heat sinks.

In Lee and Mudawar [245], the separated flow model is more appropriate than the homogeneous flow model. Zhang et al. [246] developed correlations of two-phase friction pressure drop and void fraction based on the separated flow and drift-flux models using artificial neural network (ANN) method.

A comprehensive understanding of pressure drop and void fraction during two-phase flow in mini- and microchannel is very important for the design and performance evaluation of the heat sinks.

Mishima et al. [247] successfully correlated the Chisholm's parameter C , Chisholm [248], by the hydraulic diameter of the channel and they observed that the separated flow model could well predict the pressure drop data.

High Reynolds number bubbly and slug flow two-phase frictional pressure drop data are well predicted by the homogeneous model, Triplett et al. [249]. However, for low Reynolds number flow and for annular flow, the homogeneous model and Friedel's correlation, Friedel [250] do a poor job. Kawahara et al. [251] showed that, for microchannel, the two-phase friction multiplier data are in good agreement with existing correlations for conventional channels.

Kariyasaki et al. [252], Moriyama et al. [253], Bao et al. [254], Hazuku et al. [255], Zhang et al. [171,256], and Zhang and Webb [257] studied void fraction and two-phase friction pressure drop.

Figure I.44 shows the pressure drop of single- and two-phase flow in tubes and channels observed by Tong et al. [258]. Similar results were observed by Bowers and Mudawar [242] and Zhao et al. [259]. Hwan and Kim [260] and Tong et al. [258] studied influence of mass flux, inlet temperature, exit pressure, tube diameter, and L/d on the pressure drop in small channels. The pressure drop is directly proportional to mass flux, L/d , and inversely proportional to tube diameter. Pressure drop is also a strong function of heat flux [261]. Hapke et al. [262] noticed a strong influence of Reynolds number on pressure drop. Figure I.45 shows the pressure drop during evaporation versus the boiling number, Bo , as observed by Hapke et al. [262].

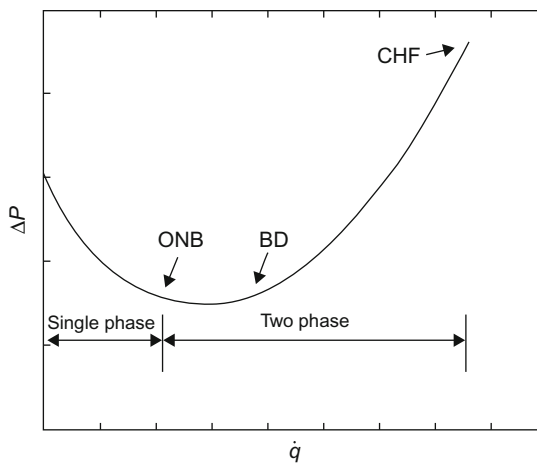


FIG. I.44. Pressure drop of single- and two-phase flow in tubes and channels. ONB, onset of nucleate boiling; BD, bubble departure; CHF, critical heat flux. Source: From Tong et al. [258].

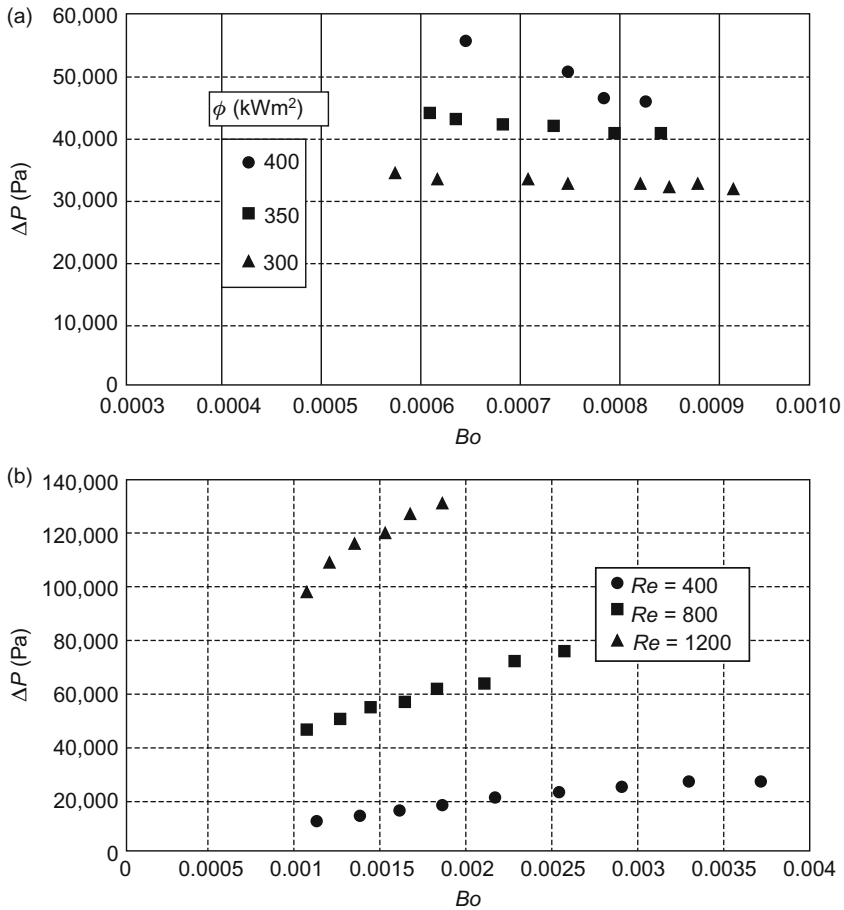


FIG. I.45. Pressure drop versus boiling number for *n*-heptane (a) and water (b). Source: From Hapke et al. [262].

Kandlikar et al. [15] observed that single-phase pressure drop and heat transfer in microchannels are higher with increasing surface roughness in the turbulent flow regime (Fig. I.46).

The flow patterns, for example, bubbly flow, slug flow, and annular flow, affect the local pressure drop in microchannels. The pressure drop in the microchannel two-phase region is expressed as the sum of the acceleration and friction components [173].

The added complexity of two-phase flow in a microchannel is caused by interaction between liquid inertia, liquid viscous force, and surface tension characterized by Reynolds number and Weber number.

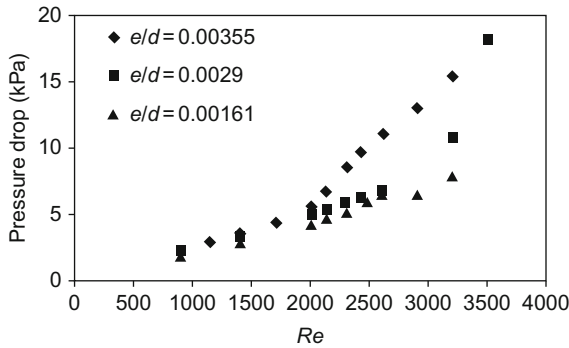


FIG. I.46. Pressure drop versus Reynolds number for a microchannel. Source: From Kandlikar et al. [15].

The two-phase frictional pressure drop multiplier

$$\varphi_L^2 = 1 + \frac{C}{X} + \frac{1}{X^2} \quad (\text{I.89})$$

is modified by Lee and Mudawar [166] with a new dimensionless parameter

$$C = C_1 Re_L^{C_2} We_L^{C_3} \quad (\text{I.90})$$

where $C_1 = 2.16$, $C_2 = 0.047$, and $C_3 = 0.60$, and X is the Martinelli parameter.

The Chisholm parameter given by Zhang et al. [246] for flow boiling pressure drop is

$$C = 21(1 - \exp(-0.358/Co)) \quad (\text{I.91})$$

Table I.IV gives available data sets for two-phase friction pressure drop in mini- and microchannels [246]. Table I.V [246] lists the comparison of correlations with the data for flow boiling. Figure I.47 compares the correlation of Dukler et al. [263] with the data obtained by Tran et al. [161,175]. Table I.VI [246] evaluates frictional pressure drop correlations based on separated flow model with the data for flow boiling. Table I.VII lists the average values of the confinement number Co with the Chisholm parameter C [246].

Quiben and Thome [264,265] showed that while the fluid, tube diameter, and mass velocity had a strong effect on pressure drop over the entire range of vapor quality, the heat flux influences the pressure drop only for a particular range of vapor qualities near and after the onset of dryout. The flow pattern effects are important at low flow rates (stratification effects) and high vapor qualities (dryout effects). The model is good for annular flow and it captures the pressure drop peak under condition of dryout at high vapor quality.

TABLE I.IV
DATABASES FOR TWO-PHASE FRICTIONAL PRESSURE DROP IN MINICHANNELS

Symbols	Reference	Adiabatic or diabatic	Geometry	Diameter or gap \times width (mm)	Working fluids	Flow direction	Channel material	Data number
○○	Moriyama et al. [9]	Adiabatic	Rectangular duct	(0.007, 0.025, 0.052, 0.098) \times 30	R113—N ₂	Horizontal	Nickel + Pyrex glass plates	104
△	Mishima et al. [1]		Rectangular duct	(1.07, 2.45, 5.00) \times 40	Water—air	Vertical upward	Acrylic resin	306
◇	Mishima and Hibiki [2]		Round tube	1.05, 2.05, 3.12, 4.08	Water—air	Vertical upward	Pyrex glass	299
▽	Triplett et al. [4]		Round tube duct	1.10, 1.45, 1.09, 1.49	Water—air	Horizontal	Pyrex, acrylic, polycarbonate	192
▷	Lee and Lee [23]		Rectangular duct	(0.4, 1.0, 2.0, 4.0) \times 20	Water—air	Horizontal	Acrylic	42
◇	Kawahara et al. [7]		Round duct	0.10	Water—N ₂	Horizontal	Fused silica	64
◁	Chung and Kawaji [24]	Adiabatic	Round duct	0.0495, 0.0996, 0.250, 0.526	Water—N ₂	Horizontal	Fused silica	0
▲	Liu et al. [35]		Round tubes, square ducts	0.91, 2, 3.02, 0.99 \times 0.99, 2.89 \times 2.89	(Water, ethanol, oil)—air.	Vertical	Pyrex glass	205
●	Ungar and Cornwell [31]		Round tube	1.46, 1.78, 2.58, 3.15	Ammonia—vapor	Horizontal	Unknown	133

(Continued)

TABLE I.IV
(CONTINUED)

Symbols	Reference	Adiabatic or diabatic	Geometry	Diameter or gap × width (mm)	Working fluids	Flow direction	Channel material	Data number
▲	Zhang and Webb [19]		Round tube Round multiport	2.13, 3.25, 6.20	(R134a, R22, R404a)—vapor	Horizontal	Aluminum, copper	51
◆	Cavallini et al. [32]		Rectangular	1.4	(R134a, R236ea, R410a)—vapor	Horizontal	Aluminum	38
●	Tran [6]	Diabatic	Round tube	2.46	(R134a, R12)—vapor	Horizontal	Brass, stainless steel	440
▶	Yu et al. [33]		Round tube	2.98	Water—vapor	Horizontal	Stainless steel	327
	Total (13 databases)	Adiabatic, diabatic	Round tube, rectangular duct	0.007–6.25	(Water, R12, R113, R22, R134a, R404a, ammonia)—(air, N ₂ , vapor)	Vertical, horizontal	Nickel, Pyrex, acrylic, polycarbonate, silica, aluminum, copper, brass, stainless steel	2201

From Zhang et al. [246].

TABLE I.V
EVALUATION OF CORRELATION OF FRICTIONAL PRESSURE DROP BASED ON HOMOGENEOUS MODEL WITH DATA FOR FLOW BOILING

Reference	Diameter (mm) or gap \times width	Working fluids	Geometry	Mean deviation ^a					
				McAdams [45]	Ackers [38]	Cicchitti [46]	Dukler [36]	Beattie– Whalery [37]	Lin et al. [47]
Tran et al. [6]	2.46	R12, R134a	Round tube	49.0	40.3	35.4	53.1	44.2	45.0
Yu et al. [33]	2.46	Water	Round tube	59.0	50.6	42.9	62.4	55.7	55.9
	2.98			76.8	64.1	162	40.8	45.5	91.6
Total				64.8	54.5	92.5	51.5	49.3	69.2

^aMean deviation defined as $(1/N)\Sigma|(\Delta p_{F,tp,exp} - \Delta p_{F,tp,cal})/\Delta p_{F,tp,cal}| \times 100\%$.
From Zhang et al. [246].

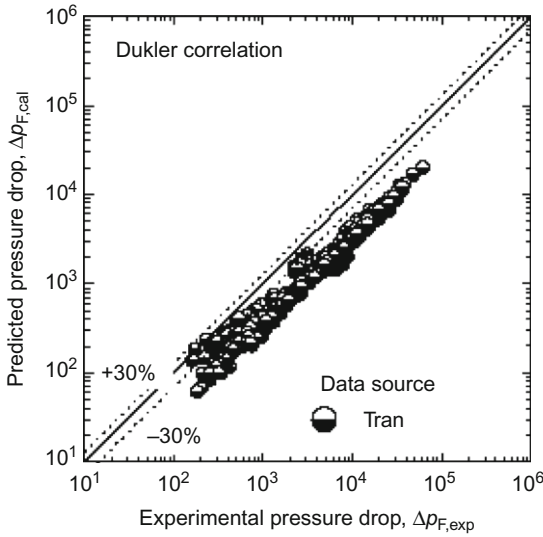


FIG. I.47. Evaluation of Dukler et al. [263] correlation with data for flow boiling. Source: From Zhang et al. [246].

Li and Wu [266] presented a general correlation for adiabatic two-phase pressure drop in micro/minichannels. The Chisholm parameter C is

$$C = 11.9Bo^{0.45}, \quad Bo \leq 1.5 \quad (\text{I.92})$$

in the surface tension dominant region.

$$C = 109.4(BoRe_L^{0.5})^{-0.56}, \quad 1.5 < Bo \leq 11 \quad (\text{I.93})$$

in the region where surface tension, inertia force, and viscous force are equally important.

Table I.VIII [266] gives collected database of adiabatic two-phase pressure drop in micro/minichannels. Table I.IX [266] shows homogeneous and separated predictive models. Figure I.48 [266] shows distribution of the database against different models. Table I.X [266] gives the assessment of Li and Wu [266] correlation according to the three Bo ranges. For parameter definitions, Li and Wu [266] may be referred.

Saisorn and Wongwises [55] observed that pressure drop increases with mass flow and vapor quality but decreases as temperature increases. The frictional pressure drop data have been compared with the existing correlations. Saisorn and Wongwises [56] experimentally studied two-phase air–water flow frictional pressure drop in a circular microchannel. The frictional multiplier has been calculated.

TABLE I.VI

EVALUATION OF CORRELATIONS OF FRICTIONAL PRESSURE DROP BASED ON SEPARATED FLOW MODEL WITH DATA FOR FLOW BOILING

Reference	Diameter or gap × width (mm)	Working fluids	Geometry	Mean deviation									
				Lockhart— Martinelli [18]	Friedel [5]	Mishima— Hibiki [2]	Tran [6]	Lee— Lee [23]	Yu et al. [33]	Zhang and Webb [19]	Qu and Mudawar [39]	Lee and Mudawar [40]	This study
Tran [6]	2.46	R12, R134a	Round tube	47.8	36.1	38.0	25.9	40.3	56.9	31.1	/	56.9	46.5
Yu et al. [33]	2.46	Water	Round tube	23.1	35.1	29.0	13.2	25.2	65.1	33.5	/	119	28.1
	2.98			39.0	181	48.3	×	84.6	28.8	×	/	51.9	31.4
Total				35.1	97.4	39.2	×	55.0	40.6	×	/	92.9	32.8

From Zhang et al. [246].

TABLE I.VII
AVERAGES OF PARAMETER C FOR EACH DATA SETS IN MINICHANNELS

Reference	Adiabatic or diabatic	Geometry	Diameter or gap \times width (mm)	Working fluids	Flow Direction	Lo^*	Parameter C
Moriyama et al. [9]	Adiabatic	Rectangular duct	0.007×30 0.025×30 0.052×30 0.098×30	R113–N ₂	Horizontal	— 21.50 — 5.50	— 0.22 — 0.69
Mishima et al. [1]	Adiabatic	Rectangular duct	1.07×40 2.45×40 5.00×40	Water–air	Vertical upward	1.30 0.58 0.30	6.66 11.28 22.69
Mishima and Hibiki [2]	Adiabatic	Round tube	1.05 2.05 3.12 4.08	Water–air	Vertical upward	2.61 1.34 0.88 0.67	7.57 12.38 15.07 13.16
Triplett et al. [4]	Adiabatic	Round tube duct	1.10 1.45 1.09 1.49	Water–air	Horizontal	2.49 1.89 2.51 —	4.95 6.79 2.87 —
Lee and Lee [23]	Adiabatic	Rectangular duct	0.4×20 1.0×20 2.0×20 4.0×20	Water–air	Horizontal	3.49 1.43 0.75 0.41	2.03 7.56 11.59 13.04
Kawahara et al. [7]	Adiabatic	Round duct	0.10	Water–N ₂	Horizontal	27.38	0.24
Chung and Kawaji [24]	Adiabatic	Round duct	0.0495 0.0996 0.250 0.526	Water–N ₂	Horizontal	54.89 27.28 10.87 5.17	0.15 0.22 1.74 3.18

Ungar and Cornwell [31]	Adiabatic	Round tube	1.46	Ammonia—vapor	Horizontal	1.42	2.85
			1.78			1.16	6.74
			2.58			0.80	3.49
			3.15			0.66	2.67
Zhang and Webb [19]	Adiabatic	Round tube, round multiport	2.13	R134a—vapor	Horizontal	0.28	6.89
			3.25			0.23	10.30
			6.20			0.12	8.71
			3.25			0.26	9.01
Cavallini et al. [32]	Adiabatic	Rectangular multiport	—	R404a—vapor	Horizontal	—	—
			1.4			0.54	8.92
				R236ea—vapor		0.62	10.45
				R410A—vapor		—	—

From Zhang et al. [\[246\]](#).

TABLE I.VIII
COLLECTED DATABASE OF ADIABATIC TWO-PHASE PRESSURE DROP IN MICRO/MINICHANNELS

Authors	Geometry	Working fluid and operating conditions	Relative surface roughness, material, and Bond number
Revellin and Thome [2]	Circular, single channel, $d_h = 0.509$, 0.790 mm	R134a/R245fa, $T_{sat} = 26, 30, 35^\circ\text{C}$, $G = 210\text{--}2000 \text{ kg/m}^2\text{s}$	Smooth (0.011%), sight glass, 0.258–0.948
Cavallini et al. [3]	Rectangular, 11 parallel channel, $d_h = 1.4$ mm	R134a/R236ea/R410a, $T_{sat} = 40^\circ\text{C}$, $G = 200\text{--}1400 \text{ kg/m}^2\text{s}$	0.14%, copper, 2.58–5.14
Field and Hrnjak [4]	rectangular, single channel, $d_h = 0.148$ mm	R134a/R410a/ammonia/propane, $T_{sat} = 22\text{--}25^\circ\text{C}$, $G = 290\text{--}450 \text{ kg/m}^2\text{s}$	0.14%, aluminum, 0.0051–0.040
Zhang and Webb [5]	Circular, 8 parallel channels/single channel, $d_h = 2.13/3.25$ mm	R134a/R22/R404a, $T_{sat} = 25\text{--}65^\circ\text{C}$, $G = 400\text{--}1000 \text{ kg/m}^2\text{s}$	Smooth ($< 0.094\%$), aluminum/copper, 7.90–13.01 (2.13 mm) 14.69–33.40 (3.25 mm)
Yang and Webb [6]	Rectangular, 4 parallel channels, $d_h = 2.64$ mm	R12, $T_{sat} = 65^\circ\text{C}$, $G = 400\text{--}1400 \text{ kg/m}^2\text{s}$	Smooth ($< 0.076\%$), aluminum, 18.25
Qi et al. [7]	Circular, single channel, $d_h = 0.531$, 0.834 mm	Liquid nitrogen, $P_{in} = 360\text{--}837$ kPa, $G = 400\text{--}2000 \text{ kg/m}^2\text{s}$	0.206%, 0.435%, stainless steel, 0.353–0.999
Hwang and Kim [8]	Circular, single channel, $d_h = 0.244$, 0.430, 0.792 mm	R134a, $T_{sat} = 20^\circ\text{C}$, $G = 140\text{--}1000 \text{ kg/m}^2\text{s}$	0.043–0.16%, stainless steel, 0.248–0.841
Rosato et al. [9]	Circular, single channel, $d_h = 3.0$ mm	R422d, $T_{sat} = 8.5\text{--}11.8^\circ\text{C}$, $G = 198\text{--}350 \text{ kg/m}^2\text{s}$	Smooth (0.067%), stainless steel, 10.78–14.24
Cavallini et al. [10]	Circular, single channel, $d_h = 0.96$ mm	R134a/R32, $T_{sat} = 40^\circ\text{C}$, $G = 200\text{--}1000 \text{ kg/m}^2\text{s}$	0.27%, copper, 1.62–1.66

From Li and Wu [266].

TABLE I.IX
EXISTING PREDICTING METHODS

Authors	Equations
Homogeneous model	$\left(\frac{dP}{dz}\right)_f = \frac{2f_p G^2}{d_t \rho_q}, Re_{tp} = \frac{G d_{ss}}{\mu_{tp}}$
McAdams et al. [11]	$\mu_{tp} = \left(\frac{x}{\mu_v} + \frac{1-x}{\mu_t}\right)^{-1}$
Cicchitti et al. [12]	$\mu_{tp} = x\mu_v + (1-x)\mu_t$
Dukler et al. [13]	$\mu_{tp} = \rho_{tp}[x(\mu_v/\rho_v) + (1-x)(\mu_t/\rho_t)]$
Beattie and Whalley [14]	$\mu_{tp} = \mu_t - 2.5\mu_t \left[\frac{x\rho_{ss}}{x\rho_{ss}+(1-x)\rho_v}\right]^2 + \left[\frac{x\rho_{ss}(1.5\mu_{ss}+\mu_v)}{x\rho_{ss}+(1-x)\rho_v}\right]$
Awad and Muzychka [15]	$\mu_{tp} = \mu_v \frac{2\mu_v+\mu_t-2(\mu_v-\mu_t)(1-x)}{2\mu_v+\mu_t+(\mu_v-\mu_t)(1-x)}$
Friedel [16]	$\left(\frac{dP}{dz}\right)_f = \left(\frac{dP}{dz}\right)_{LO} \Phi_{LO}^2, \left(\frac{dP}{dz}\right)_{LO} = f_{LO} \frac{2G^2}{d_{ss}\rho_t},$ $\Phi_{LO}^2 = (1-x)^2 + x^2 \frac{\rho_{ss}f_{vo}}{\rho_{ss}\rho_{ss}} + \frac{3.24x^{0.78}(1-x)^{0.55}(\rho_v/\rho_t)^{0.91}}{Fr_{tp}^{ss} We_{tp}^{ss}(\mu_v/\mu_t)^{-0.19}(1-\mu_v/\mu_t)^{-ss}}$
Muller-Steinhagen and Heck [17]	$\left(\frac{dP}{dz}\right)_f = \left\{ \left(\frac{dP}{dz}\right)_{LO} + 2 \left[\left(\frac{dP}{dz}\right)_{VO} - \left(\frac{dP}{dz}\right)_{LO} \right] x \right\} (1-x)^{1/3} + \left(\frac{dP}{dz}\right)_{VO} x^3, \left(\frac{dP}{dz}\right)_{VO} = f_{VO} \frac{2G^2}{d_{ss}\rho_v}, \left(\frac{dP}{dz}\right)_t = f_t \frac{2G^2(1-x)^2}{d_{ss}\rho_t}, \left(\frac{dP}{dz}\right)_v = f_v \frac{2G^2 x^2}{d_{ss}\rho_v}$
Zhang and Webb [5]	$\Phi_{LO}^2 = (1-x)^2 + 2.87x^2(P/P_{crit})^{-1} + 1.68x^{0.8}(1-x)^{0.25}(P/P_{crit})^{-1.64}$
Tran et al. [18]	$\Phi_{LO}^2 = 1 + \left[4.3 \left(\frac{dP}{dz}\right)_{VO} / \left(\frac{dP}{dz}\right)_{LO} - 1 \right] [Bo^{-0.5} x^{0.875} (1-x)^{0.875} + x^{1.75}]$
Hwang and Kim [8]	$\left(\frac{dP}{dz}\right)_f = \left(\frac{dP}{dz}\right)_t \Phi_t^2, \Phi_t^2 = 1 + \frac{C}{x} + \frac{1}{x^2}, X^2 = \left(\frac{dP}{dz}\right)_t / \left(\frac{dP}{dz}\right)_v, C = 0.227 Re_{LO}^{0.452} X^{-0.32} Bo^{0.41}$
Lee et al. [19]	$C = 121.1(1 - e^{-23.8Bo})x^{1.8}$

From Li and Wu [266].

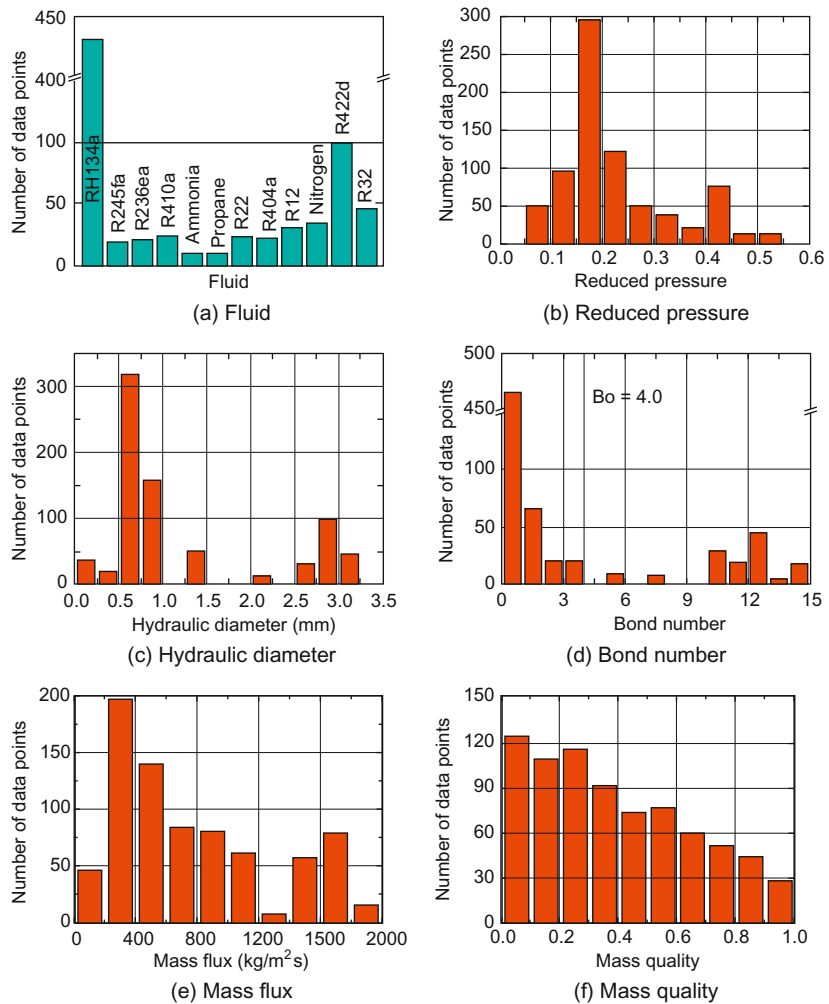


FIG. I.48. Distribution of the database against different parameters. For color version of this figure, the reader is referred to the web version of this book. Source: From Li and Wu [266].

I.5. Instability

Two-phase flow instabilities in a microchannel can be dynamic and static instabilities. The dynamic instability generally reflects the feedback control process of a number of parameters such as pressure, mass flux, and temperature. The unsteady behaviors caused by three types of commonly recognized

TABLE I.X
ASSESSMENT OF LI AND WU [266] CORRELATIONS ACCORDING TO THE THREE Bo RANGES

Equations	e_A	σ_N	λ	θ
$Bo \leq 1.5$, 454 data points Eq. (1.5)	20.8	30.3	80.6	95.2
$1.5 < Bo \leq 11$, 157 data points Eq. (1.6)	24.2	33.7	72.6	89.7
$11 < Bo$, 158 data points McAdams et al. [11]	32.9	39.9	50.6	83.1
Cicchitti et al. [12]	44.1	61.9	58.7	67.7
Beattie and Whalley [14]	31.2	42.0	60.0	88.9
Friedel [16]	59.9	71.7	56.3	68.6
Muller–Steinhagen and Heck [17]	52.5	61.3	59.2	73.2
Zhang and Webb [5]	64.0	86.2	59.3	66.4
Hwang and Kim [8]	658	410	0.0	0.0

From Li and Wu [266].

oscillations: pressure drop, density wave, and thermal oscillations can trigger a boiling crisis that causes mechanical damages.

A flow is stable if any perturbations in the systems eventually die down and the system asymptotically returns to the original operating conditions. If the system, when perturbed, returns to a new equilibrium condition different from the original equilibrium condition, then the system is subject to static instability. A system having delayed feedback and sufficient interaction between the inertia of flow and compressibility is said to be subject to a dynamic instability. Dynamic instability may also result from multiple feedbacks between flow rate, pressure drop, and the change in density.

Many mechanisms can trigger boiling instabilities in macro- and microsystems. Depending on the mechanism, various types of static and dynamic instabilities, for example, nucleation instabilities, flow pattern instabilities, Ledinegg instabilities, thermal oscillations, density-wave type oscillations, and pressure drop type oscillations, may arise. Early works on boiling in micro- and minichannels focused on stable boiling. Studies of flow boiling instability in microchannels are relatively more recent.

Dynamic instabilities can be characterized as

- a. Density-wave type oscillations
- b. Pressure-drop type oscillations
- c. Acoustic oscillations
- d. Thermal oscillations.

Pressure drop type oscillations occur in boiling two-phase flow systems where the amount of upstream compressible volume is significant. The period of this type of oscillation is usually long. The oscillations of pressure and mass flux are out of phase.

Density wave type oscillations are related to kinematic wave-propagation phenomena and, therefore, the alternative name for this oscillation is flow-void feedback instability. Its period is on the order of the time required for a density wave to travel through the system. Alternate fluid waves of higher and lower density travel in the system. The oscillation amplitudes and periods of pressure, mass flux, and wall temperature are generally small.

Thermal oscillations are compound dynamic instabilities related to the instability of the liquid film next to the tube walls. Temperature fluctuations occur. The amplitudes and periods of pressure and mass flux oscillations are very small. The occurrence of different oscillations is function of G , q , and T_{inlet} .

Kennedy et al. [75] studied incipient boiling and onset of flow instability (OFI) for subcooled water flow in uniformly heated microchannels.

Hetsroni et al. [101] evaluated explosive boiling oscillations (EBO) and heat transfer phenomenon under condition of periodic flow boiling of water and ethanol in parallel triangular microchannels. The period between successive periodic events depended on the boiling number and decreased with an increase in the boiling number. The initial film thickness decreased with increasing heat flux and reached minimum at CHF. Unlike conventional channels, parallel channel instability amplified prior to CHF. Nusselt number was presented as a function of Eotvos number and boiling number. The trigger mechanism of the explosive boiling is venting of elongated bubble due to very rapid expansion.

Boiling instability, second density wave oscillation, density wave oscillation (DWO), and pressure drop type instability in conventional channels were studied by Kakac and Veziroglu [267] and Kakac et al. [268].

Wang et al. [269] investigated DWO in a single tube. The DWO are related to kinematic wave-propagation phenomenon. Pressure and temperature oscillations are associated with boiling in microchannels because the flow velocities are low and bubble formation can cause a significant disruption of low-quality flow.

Bergles and Kandlikar [20] showed that CHF in microchannels under conditions of low mass flux and low quality may be due to instabilities rather than conventional dryout mechanism.

Figure 1.49 shows the unsteady flow, upstream of ONB in one of the parallel microchannels [101]. Clusters of water appeared as a jet and penetrated the bulk of water. The vapor jet moved in the upstream direction, and the space that it occupied increased.

Figures 1.50–1.52 show that the time period (frequency) is the same for pressure drop, fluid temperature at outlet manifold, and mean and maximum heat temperature fluctuations [101]. The fluctuations are in phase.

Compressible volume instabilities, also known as “explosive boiling,” are a common phenomenon in microscale flow boiling. These instabilities can promote severe pressure and temperature oscillations in the flow [35].

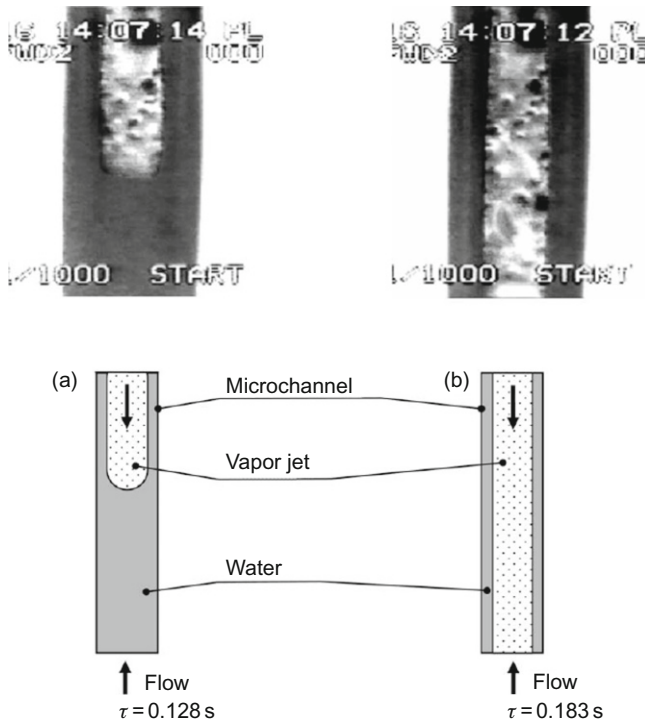


FIG. I.49. Flow pattern upstream the ONB: (a) single-phase water flow, (b) jet that penetrate the bulk of the water. Source: From Hetsroni et al. [101].

The flow boiling in small systems like microchannels is sensitive to oscillatory instabilities. The oscillations refer to either parallel channel instabilities or compressible volume instabilities occurring in both parallel channels and single-channel system. Parallel channel instabilities are due to the interaction of the two-phase flow among adjacent channels. Compressible volume instabilities may be due to a body of vapor, flexible hosing, etc. upstream or within the heated length.

The cyclic boiling behavior caused by oscillation is manifested periodically in the form of (1) single-phase liquid filling in the channel, (2) bubble nucleation, (3) growth and coalescence of bubbles to form a vapor pouch, (4) rapid expansion of the vapor, and (5) evaporation of the quasistatic liquid film. The stage (4) is important since the bubble expansion may cause blockage of the flow and/or backflow of liquid in the upstream section of the channel or adjacent channels. These instabilities result in oscillations in pressure drop, flow, wall temperatures, and periodic development of substantial dry zones. For

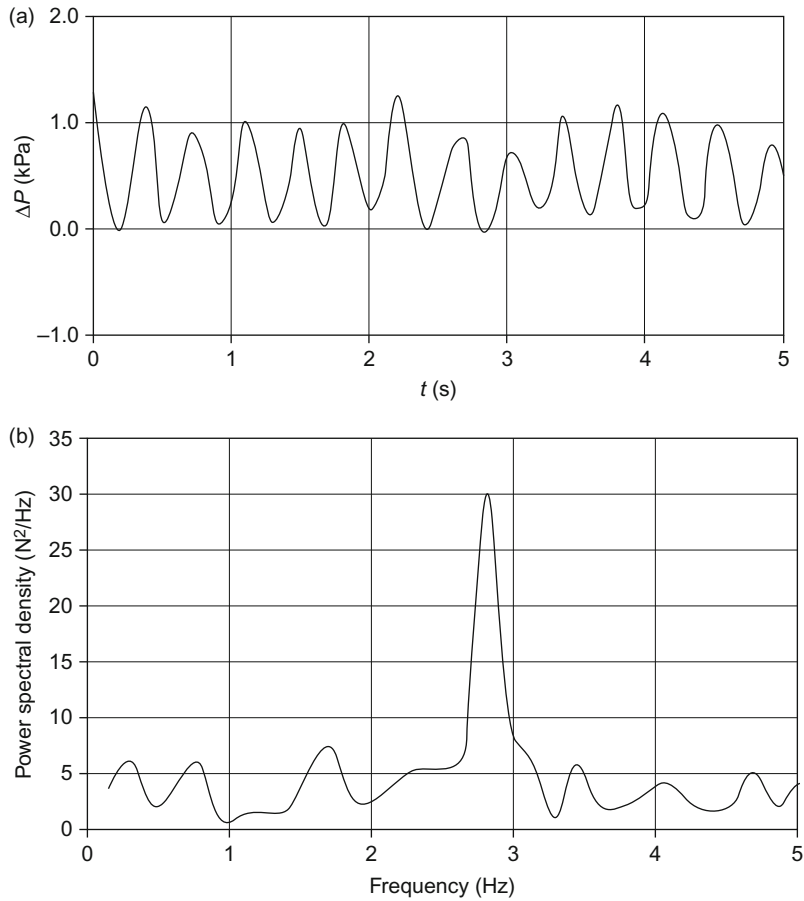


FIG. 1.50. Time variation of pressure drop: (a) pressure drop fluctuation, (b) pressure drop amplitude spectrum (FFT). Source: From Hetsroni et al. [101].

higher heat fluxes and lower mass velocities, even nucleate boiling may occur resulting in severe bubble excursions. Very high values of heat transfer coefficients at low vapor qualities that decrease rapidly with the increase in vapor quality is the consequence of this instability. There may or may not be characteristic frequency of oscillation due to the instability.

The influence of pressure fluctuations on the flow phenomena and heat transfer in small single channels as well as in multichannels is important. Pressure pulses are generated by the growth of confined bubbles near the channel inlet. There are two kinds of confined bubble growth, depending upon the

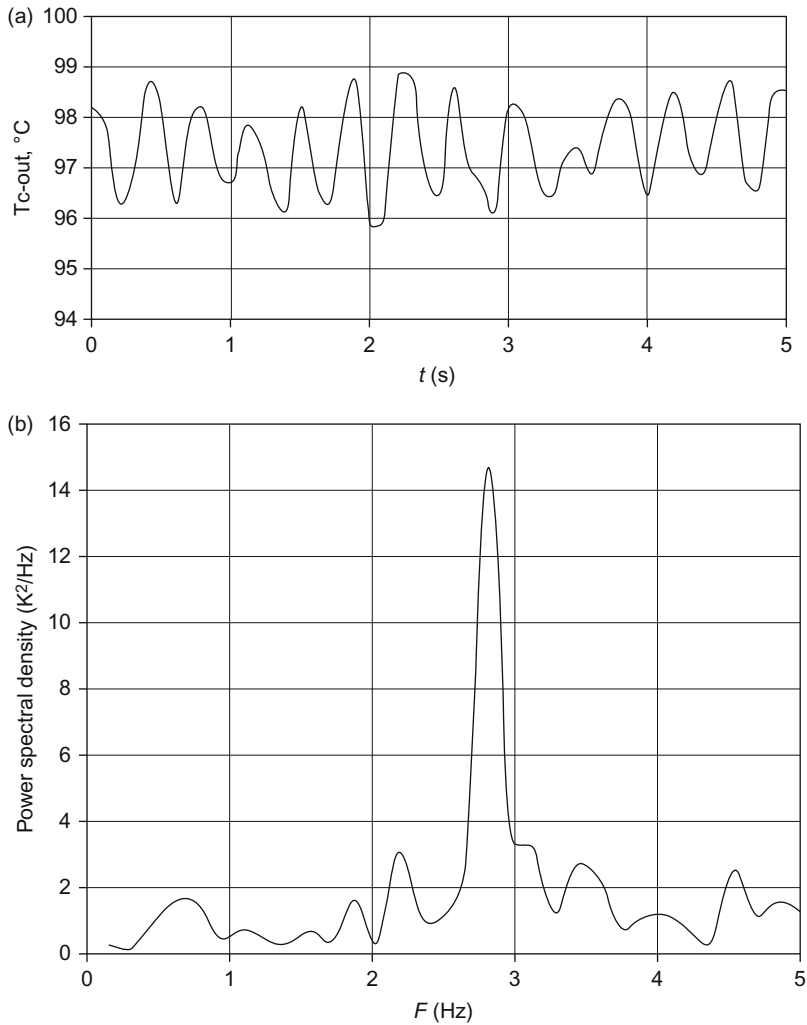


FIG. I.51. Time variation of fluid temperature at the outlet manifold: (a) temperature fluctuations, (b) temperature amplitude spectrum (FFT). Source: From Hetsroni et al. [101].

system compressibility upstream in the channels. A high compressibility results in an upward and downward growth of the confined bubble until the inlet is reached. For low compressibility, however, only an upward growth is observed and so additional bubbles are generated sequentially. Taking into account the observed temperature fluctuations, the pressure fluctuations have a thermal origin.

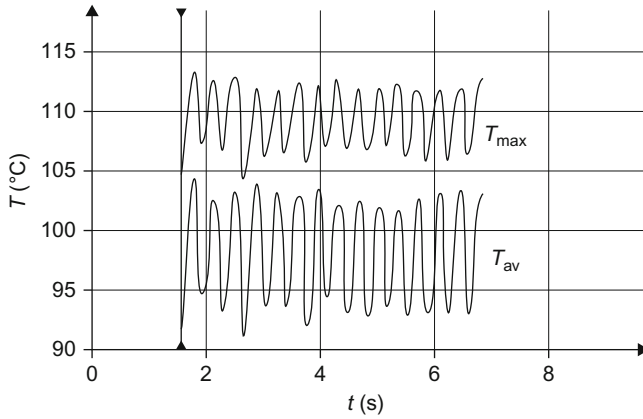


FIG. 1.52. Time variation of average and maximum heater temperature. Source: From Hetsroni et al. [101].

For low heat fluxes, a stable bubbly flow is observed. There are no pressure or temperature fluctuations. However, at high heat fluxes, oscillation starts resulting in inlet and outlet pressure fluctuations with characteristic frequencies. With still higher heat fluxes, the oscillation disappears and again a stable flow boiling regime is observed.

Large pressure fluctuations result from violent vapor generation, especially in the slug flow regime and annular/slug flow regime. Starting with the slug flow regime, a reverse flow occurs with the slugs growing counter to the bulk flow so that vapor and liquid flow back into the inlet. Figures 1.53 and 1.54 show the stable and unstable flow boiling regimes in parallel microchannels and in a single microchannel, respectively [270]. More detailed information about instability in flow boiling in microchannels may be obtained from the recent work of Saha et al. [271] and Saha and Celata [272].

Nomenclature

Bl, Bo	Boiling number, dimensionless
Bo	Bond number
Ca	Capillary number, dimensionless
Co	Convective number, dimensionless
C_p	Specific heat, J/kg K
D	Tube inner (or hydraulic) diameter, m
D_b	Departure diameter of bubble, m

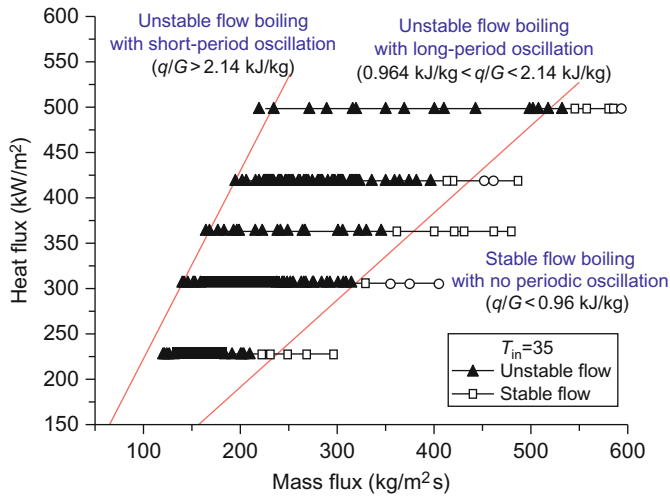


FIG. I.53. Stable and unstable flow boiling regimes in parallel microchannels. For color version of this figure, the reader is referred to the web version of this book. Source: From Wang et al. [270].

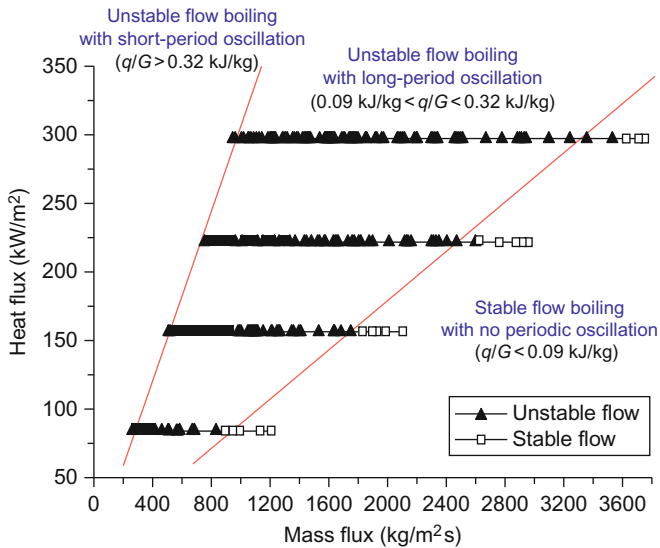


FIG. I.54. Stable and unstable flow boiling regimes in a single microchannel. For color version of this figure, the reader is referred to the web version of this book. Source: From Wang et al. [270].

Ec	Eckert number, dimensionless
Eo	Eotvos number, dimensionless
F	Forced convection heat transfer enhancement factor, dimensionless
Fr	Froude number
G	Mass velocity, $\text{kg/m}^2/\text{s}$
g	Gravity acceleration, m/s^2
h	Heat transfer coefficient, $\text{W/m}^2/\text{K}$
h_{fg}	Latent heat of vaporization, J/kg
Kn	Knudsen number, dimensionless
k	Thermal conductivity, W/m/K
L	Test section length, m
M	Morton number, Mach number, dimensionless; molecular weight
Ma	Marangoni number, dimensionless
Nu	Nusselt number, dimensionless
P	Pressure, N/m^2
ΔP	Pressure drop, N/m^2
ΔP_{sat}	Vapor pressure change according to the ΔT_{sat} , N/m^2
Pr	Prandtl number, dimensionless
p_r	Reduced pressure (absolute pressure/critical pressure), dimensionless
q	Heat flux W/m^2
Re	Reynolds number, dimensionless
S	Suppression factor, dimensionless
T	Temperature, K
ΔT_{sat}	Channel wall superheat, K
t	Time, s
We	Weber number, dimensionless
X	Martinelli parameter
x	Local vapor quality, dimensionless
Z	Axial distance, m

Greek Symbols

α	Void fraction, dimensionless
β	Expansion coefficient, K^{-1}
δ	Liquid film thickness, μm
Δ	Difference
μ	Dynamic viscosity, kg/m/s
ρ	Density, kg/m^3
σ	Surface tension, N/m
φ	Heat flux, W/m^2

Subscript

b	Bulk fluid
c, CBD	Critical, convective boiling dominated
e	Exit
fg	From liquid to vapor
i, in	Inlet
l	Liquid
lo	Liquid only
L	All the mass flow rate taken as liquid
Nb, NBD	Nucleate boiling, nucleate boiling dominated
pool	Pool boiling
sat	Saturation
sp	Single phase
tp, TP	Two phase
v	Vapor
w	Wall

PART II

II.1. Onset of Nucleate Boiling

II.1.1. INTRODUCTION

Bubble nucleation on a heater surface occurs at preferential locations where preexisting cavities provide a cluster of gas or vapor embryo. In the absence of such cavities, very high wall superheats are reached without nucleation on a smooth surface. Cavities are found to occur naturally on the boiling surface due to the manufacturing process employed. The onset of boiling is closely linked to the local temperature field and the size of the cavity mouth opening. These fundamental relationships are discussed in this chapter and the current status of our understanding of the onset of nucleate boiling in microchannels is reviewed.

II.1.2. PRESSURE–TEMPERATURE RELATIONSHIP IN A VAPOR BUBBLE

At saturation condition across a planar liquid–vapor interface under thermal equilibrium, the temperature and pressure are the same in the liquid and vapor phases. A curved liquid–vapor interface introduces an excess pressure on the concave side of the interface and thus alters the thermodynamic and static equilibrium condition between the two phases. This is illustrated by

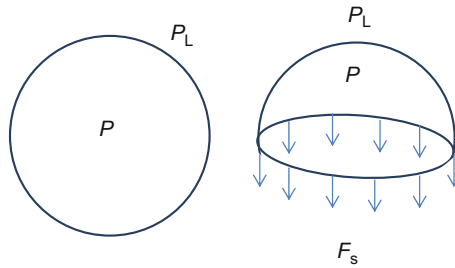


FIG. II.1. Forces on a spherical bubble in a stagnant pool of liquid.

considering a spherical vapor bubble in equilibrium with its surrounding liquid as shown in Fig. II.1

The excess pressure inside the bubble, $P_V - P_L$, is balanced by the surface tension force acting along the liquid–vapor interface. Taking a section through the diametric plane, the surface tension force F_s acts along the perimeter of the interface and is balanced by the force due to the pressure difference acting normal to the diametric plane over the projected area of the hemisphere:

$$(P_V - P_L) \frac{\pi}{4} D^2 = \pi D \sigma \quad (\text{II.1})$$

The excess pressure is given by the following expression after rearrangement:

$$(P_V - P_L) = \frac{4 \sigma}{D} \quad (\text{II.2})$$

It can be seen that as the diameter of the bubble becomes smaller, the excess pressure inside the bubble increases in an inverse proportion to the diameter. Using properties of water at a temperature of 100°C, the surface tension is 0.0589 N/m, and the excess pressure varies from 118 Pa for a 1 mm diameter bubble to 11,780 Pa for 10 μm and 117,800 Pa for 1 μm diameter bubbles.

Since the thermal requirements dictate that the temperature in both phases be equal at the equilibrium condition, the liquid will be in a superheated state corresponding to a planar liquid–vapor interface. Using the excess pressures for different diameter bubbles, the corresponding liquid superheat in water at atmospheric pressure is estimated to be 0.2°C, 3.1°C, and 23.2°C for 1 mm, 10 and 1 μm bubbles, respectively. For smaller bubble sizes, the liquid superheat required to sustain a vapor bubble in stable equilibrium increases dramatically.

II.1.3. BUBBLE NUCLEATION ON A HEATED SURFACE

Bubble nucleation occurs preferentially over a cavity present on the heated surface submerged in liquid. The surface tension force pins the bubble on the

edges of the cavity as the bubble emerges from the cavity interior into the liquid. The contact angle of the bubble interface on the heater surface determines the maximum size of the bubble that can stay pinned on the cavity opening.

For nucleation to occur, a simple static thermodynamic condition dictates that the entire liquid–vapor interface be at a temperature above the minimum liquid superheat requirement discussed in the previous section. Since the temperature in the liquid reduces farther away from the heater surface, the lowest temperature in the liquid is experienced at the tip of the growing bubble. A simple condition is thus derived when the liquid temperature at the tip exceeds the minimum required temperature to sustain the vapor bubble.

Figure II.2 shows a schematic of a heater surface on which boiling occurs. The cavity shown is a reentrant cavity that traps gas and vapor that act as an embryo for nucleation as the first bubbles are produced during start-up.

Different stages of bubble growth, 1–4, are shown in Fig. II.2. The bubble emerges from the interior of the cavity and establishes a shape dictated by the receding contact angle θ_r on the walls of the cavity shown by interface 1. As the bubble grows, it gets pinned on the cavity mouth (interface 2). As the bubble continues to grow, it takes shapes 3 and 4, until the contact angle is reestablished on the heater surface.

Hsu [273] proposed a nucleation criterion that considered the growth corresponding to interface 4 as the limiting case, with the contact angle set as 53.1° . Later, in analyzing the onset of nucleate boiling (ONB) during flow boiling,

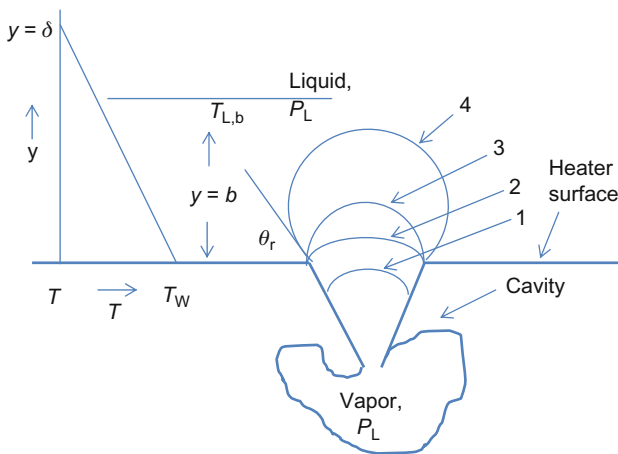


FIG. II.2. Nucleation of a vapor bubble over a reentrant cavity on a heated surface.

Davis and Anderson [274] considered when the contact angle is reestablished as the limiting stage, as depicted by interface 4. Sato and Matsumura [275] and Bergles and Rohsenow [276] considered a hemispherical bubble (interface 3) as the limiting case. Here the radius of curvature is the smallest during the bubble growth. The bubble growth condition in different models check whether the temperature at the tip of the bubble interface is at a temperature greater than the saturation liquid temperature corresponding to the vapor pressure inside the bubble. For example, considering case 4, the temperature $T_{L,b}$ is greater than T_{sat} corresponding to pressure of the vapor inside the bubble 4.

II.1.3.1. Active Cavity Radii for Bubble Nucleation

The cavity mouth diameter determines the shape and size of the bubble. Applying various criteria, the following conditions are derived for the range of nucleation cavity radii that will nucleate under a given wall superheat and liquid subcooling conditions. Detailed derivations may be found in the original papers or in other publications, such as Kandlikar et al. [277,278].

Davis and Anderson [274] criterion, for a given contact angle θ_r :

$$\{r_{c,min}, r_{c,max}\} = \frac{\delta_t \sin \theta_r}{2(1 + \cos \theta_r)} \left(\frac{\Delta T_{Sat}}{\Delta T_{Sat} + \Delta T_{Sub}} \right) \left[1 \mp \sqrt{1 - \frac{8\sigma T_{Sat}(\Delta T_{Sat} + \Delta T_{Sub})(1 + \cos \theta_r)}{\rho_V h_{LV} \delta_t \Delta T_{Sat}^2}} \right] \quad (II.3)$$

where $r_{c,min}$ and $r_{c,max}$ are the minimum and maximum cavity radii that will nucleate under these conditions, δ_t is the thermal boundary layer thickness, T_{Sat} is the saturation temperature corresponding to a planar interface corresponding to the liquid pressure, ρ_V is the vapor density, and h_{LV} is the latent heat of vaporization.

The thermal boundary layer thickness is given by:

$$\delta_\tau = \frac{k_L}{h} \quad (II.4)$$

where k_L is the liquid thermal conductivity and h is the heat transfer coefficient for the single-phase liquid flow prior to nucleation.

Hsu [273] criterion, with a contact angle $\theta_r = 53.1^\circ$:

$$\{r_{c,min}, r_{c,max}\} = \frac{\delta_t}{4} \left(\frac{\Delta T_{Sat}}{\Delta T_{Sat} + \Delta T_{Sub}} \right) \left[1 \mp \sqrt{1 - \frac{12.8\sigma T_{Sat}(\Delta T_{Sat} + \Delta T_{Sub})}{\rho_V h_{LV} \delta_t \Delta T_{Sat}^2}} \right] \quad (II.5)$$

Bergles and Rohsenow [276] and Sato and Matsumura [275]:

$$\{r_{c,\min}, r_{c,\max}\} = \frac{\delta_t}{2} \left(\frac{\Delta T_{\text{Sat}}}{\Delta T_{\text{Sat}} + \Delta T_{\text{Sub}}} \right) \left[1 \mp \sqrt{1 - \frac{8\sigma T_{\text{Sat}}(\Delta T_{\text{Sat}} + \Delta T_{\text{Sub}})}{\rho_V h_{\text{LV}} \delta_t \Delta T_{\text{Sat}}^2}} \right] \quad (\text{II.6})$$

Finally, another criterion proposed by Kandlikar was based on the liquid streamlines sweeping over the top of the bubbles. The stagnation point was noted on a bubble at a height of 1.1 times the bubble radius r_b for a range of receding contact angles between 20° and 60° as shown in Fig. II.3. The resulting nucleating cavity radii are given by the following equation.

Kandlikar et al. [279]:

$$\{r_{c,\min}, r_{c,\max}\} = \frac{\delta_t \sin \theta_r}{2.2} \left(\frac{\Delta T_{\text{Sat}}}{\Delta T_{\text{Sat}} + \Delta T_{\text{Sub}}} \right) \left[1 \mp \sqrt{1 - \frac{8.8\sigma T_{\text{Sat}}(\Delta T_{\text{Sat}} + \Delta T_{\text{Sub}})}{\rho_V h_{\text{LV}} \delta_t \Delta T_{\text{Sat}}^2}} \right] \quad (\text{II.7})$$

II.1.3.2. Critical Cavity Radius and Wall Superheat at ONB

Onset of nucleate boiling (ONB) is defined as the condition when nucleate boiling is first initiated. In flow boiling, this condition represents the first appearance of departing bubbles on the heater surface along the flow direction. The critical cavity radius $r_{c,\text{crit}}$ is defined as the radius of the cavity on which nucleation occurs first as the wall temperature gradually increases in the flow direction. It is given by setting the radical term, in Eqs. (II.3) and (II.5)–(II.7), to zero, respectively, under each criterion. The critical radius and wall superheat at ONB, $\Delta T_{\text{Sat,ONB}}$, corresponding to this cavity radius under these nucleation criteria are given below. For detailed derivations, readers are referred to Kandlikar et al. [277].

Davis and Anderson [274]:

$$r_{c,\text{crit}} = C_1 \left(\frac{\Delta T_{\text{Sat}}}{\Delta T_{\text{Sat}} + \Delta T_{\text{Sub}}} \right) \quad (\text{II.8})$$

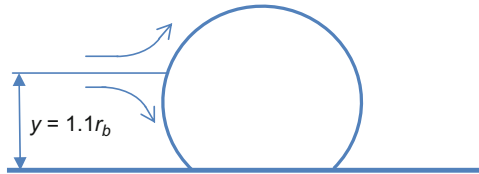


FIG. II.3. Liquid flow streamlines around a growing bubble [279].

and

$$\Delta T_{\text{Sat,ONB}} = \sqrt{C_2 \sigma T_{\text{Sat}} q'' / (\rho_V h_{LV} k_L)} \quad (\text{II.9})$$

where the constants C_1 and C_2 under different conditions are as follows:

Davis and Anderson [274]:

$$C_1 = \frac{\delta_\tau \sin \theta_r}{2(1 + \cos \theta_r)} \quad \text{and} \quad C_2 = 8 \quad (\text{II.10})$$

Hsu [273]:

$$C_1 = \frac{\delta_\tau}{4} \quad \text{and} \quad C_2 = 12.8 \quad (\text{II.11})$$

Bergles and Rohsenow [276] and Sato and Matsumura [275]:

$$C_1 = \frac{\delta_\tau}{2} \quad \text{and} \quad C_2 = 8 \quad (\text{II.12})$$

Kandlikar et al. [279]:

$$C_1 = \frac{\delta_\tau \sin \theta_r}{2.2} \quad \text{and} \quad C_2 = 8.8 \quad (\text{II.13})$$

Alternatively, the heat flux at ONB under a given local liquid subcooling may be written as:

$$q_{\downarrow \text{ONB}}^{\uparrow u} = (\rho_{\downarrow} V h_{\downarrow LV} k_{\downarrow L}) / (C_{\downarrow 2} \sigma T_{\downarrow \text{Sat}}) (\Delta T_{\downarrow}(\text{Sat}, \text{ONB}))^{\uparrow 2} \quad (\text{II.14})$$

The values for C_2 are given by Eqs. (II.10)–(II.13) for different criteria. The heat flux and wall superheat at ONB are also related through the single-phase heat transfer equation:

$$q_{\downarrow \text{ONB}}^{\uparrow u} = h(\Delta T_{\downarrow}(\text{Sat}, \text{ONB}) + \Delta T_{\downarrow}(\text{Sub}, \text{ONB})) \quad (\text{II.15})$$

If the cavity size given by Eq. (II.8) is not available, then among the available cavity sizes, the cavity size that requires the lowest wall superheat will nucleate first. For a cavity size of r_c , applying the criteria given by Kandlikar et al. [279], Eq. (II.13), the corresponding wall superheat at ONB is given by:

$$\begin{aligned} \Delta T_{\downarrow}(\text{Sat}, \text{ONB}) = & (1.1 r_{\downarrow c} q^{\uparrow u}) / (k_{\downarrow L} \sin[(\theta_{\downarrow} r)]) \\ & + (2\sigma \sin[(\theta_{\downarrow} r)]) / r_{\downarrow c} T_{\downarrow}(\text{Sat}, \text{ONB}) / (\rho_{\downarrow} V h_{\downarrow LV}) \end{aligned} \quad (\text{II.16})$$

II.1.4. NUCLEATION IN MICROCHANNELS

Flow boiling in microchannels is sometimes implemented with subcooled liquid entry. As the liquid gets heated, at some point the nucleation requirement is met over some existing cavities and bubble nucleation takes place.

Since the heat transfer coefficients in microchannels are quite high due to small hydraulic diameters, smaller sized cavities are preferentially nucleated. The high wall superheat at the ONB causes the vapor bubble to grow very rapidly. This rapid growth has been recognized as the cause of instability, leading to backflow in the microchannels. The flow conditions, including flow rate, heat flux, and upstream compressibility, are believed to affect the instability.

II.1.4.1. Nucleation Criterion

Zhang et al. [280] noted the validity of Hsu's model for flow boiling in microchannels of dimensions 100×130 , 50×40 , 120×50 , and 50×44 μm single rectangular channels. They found that the wall superheat requirements were in agreement with Hsu's model. Another interesting factor noted in their work was that the effect of surface tension was negligible on the nucleation phenomenon. Since surface tension does not enter in any of the nucleation models, the role of surface tension on nucleation has been confirmed to be insignificant. Lee et al. [281] studied nucleation in channels as a function of channel height. The height varied from 5 to 10 μm . It was found that a minimum height was needed to obtain nucleation. Bubble growth and departure were also studied. The results were obtained at very low heat fluxes, with bubble frequency on the order of 1 Hz. Their results are unique in terms of the small channel sizes employed in their experiments.

II.1.4.2. Effect of Roughness

Roughness influences the boiling processes through the changes in the local temperature profile in the liquid and changes in the cavity sizes present on the channel walls. For small values of uniform wall roughness, the variation in local transport phenomena are small [282]. Kandlikar and Spiesman [283] studied the effect of different roughness treatments on the cavity size distributions. Table II.I shows the details of five different surfaces tested. Surface A-188 was finished using 0.03 μm particles in a slurry suspension on a polishing wheel. Sandpapers of three different grit sizes were employed in preparing surfaces B-363, C-716, and D-3064. Surface E-UOP was a high flux surface with a sintered porous material.

The respective cavity size distributions obtained from high-magnification microscope images are shown in Fig. II.4(a)–(c). These figures show that there is a slight variation in the cavity size distributions, but cavities of all ranges are nonetheless present on all surfaces in relative abundance. The boiling tests confirmed that there was little change in the ONB characteristics of these surfaces. The sintered surface showed significant reduction in wall superheat at ONB. The study concluded that simple techniques such as sandpaper polishing

TABLE II.I
SURFACE PREPARATION TECHNIQUE AND AVERAGE ROUGHNESS OF SURFACES STUDIED IN FLOW BOILING,
KANDLIKAR AND SPIESMAN [283]

Surface	Preparation technique	Average roughness, Ra
A-188	0.03 μm solution	0.188 μm
B-363	600 grit sandpaper	0.363 μm
C-716	400 grit sandpaper	0.716 μm
D-3064	120 grit sandpaper	3.064 μm
E-UOP	UOP high flux surface	Sintered layer thickness 225–300 μm , porosity 40–60%

do not provide any meaningful improvement in the nucleation characteristics of a surface.

Similar observations were made by Jones and Garimella [284], who found surface roughness, induced by a sawtooth cutting process, had no effect on ONB or the heat transfer coefficient. Roughness induced by an electrical discharge machining (EDM) process enhanced both ONB and the heat transfer performance. Although cavity size distributions were not measured, the EDM process is believed to induce different cavity sizes, similar to the sintered surface tested by Kandlikar and Spiesman [283].

II.1.4.3. Location of Nucleation Sites

Nucleation is closely related to the local heat transfer coefficient in a channel. Considering uniform heat flux around the channel wall, a numerical simulation was conducted by Dharaia and Kandlikar [285] to study the variation of wall temperature around the channel. The channel studied was 150 μm high and 300 μm wide. Figure II.5 shows the variation of the heat transfer coefficient along the width and the height of the channel. It can be seen that there is a wide variation, with the heat transfer coefficient being lowest in the corner region. The local wall temperature profile in a microchannel is obtained by conducting a conduction analysis in the fin and substrate of a silicon microchannel. The side walls were made of fins.

The temperature profile depends on the fin thickness and the aspect ratio of the channel. Nucleation further depends on the availability of appropriate sized cavities at a given location. The results of Kuo and Peles [286] show an increased nucleation activity with tall reentrant shaped tunnels in the side walls. Since the tunnels and the opening mouth sizes are quite large as compared to the nucleating cavity dimensions of only a few micrometers, it is not immediately apparent whether the actual nucleation cavities are located on the walls inside the tunnels, or the tunnel openings themselves are acting as

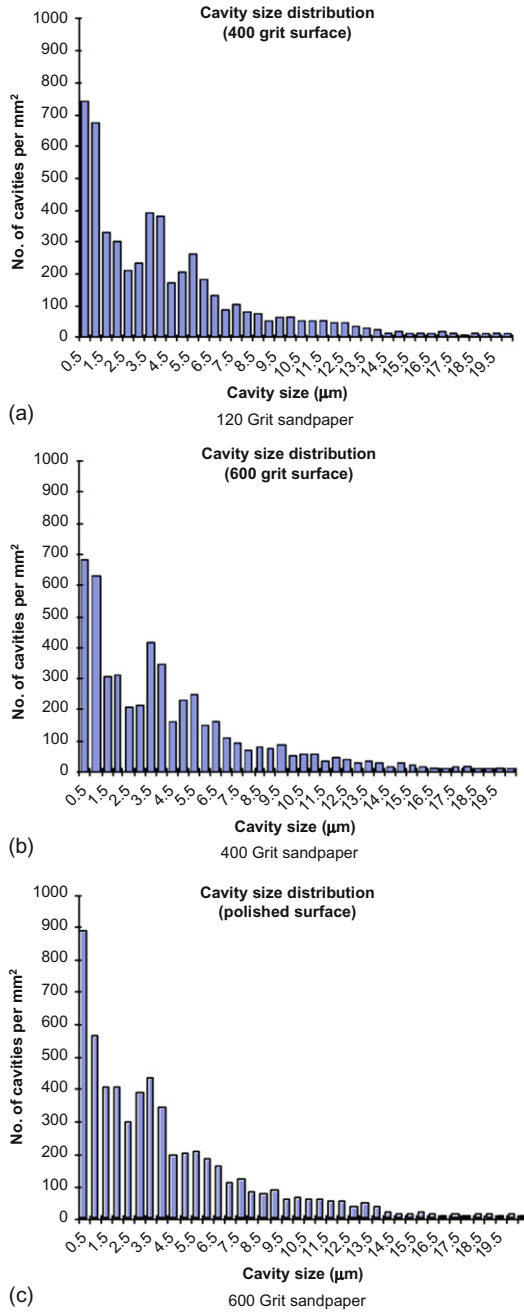


FIG. II.4. Cavity size density ($\#/mm^2$) as a function of cavity size in μm for different sandpaper roughened surfaces [283].

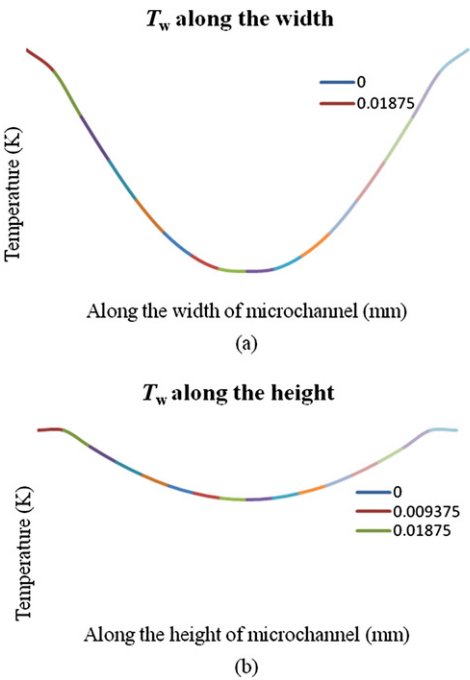


FIG. II.5. Variation of heat transfer coefficient variation along the width (300 μm) and height (150 μm) of a microchannel [285].

nucleation sites. Visualization studies by Kandlikar et al. [277] and Liu et al. [287] observed bubble nucleation on the bottom surface of the channel, in the central region or somewhat away from the corners. Zhang et al. [280] indicates that nucleation occurs on the bottom wall although they have similar reentrant cavities as Kuo and Peles [286] on the side walls. Kandlikar et al. [277] conducted experiments with large cavities of around 20–100 μm punched in the center of the bottom wall of copper minichannels. Nucleation was seen to occur arbitrarily on the bottom surface, and sometimes bubbles were seen to nucleate over the smaller cavities present on the sloping edges of the punch marks. Sometimes the cavities present in the corners were also seen to nucleate. Li and Cheng [288] suggested that the microchannel corners themselves may act as nucleation cavities. Such nucleation was not reported by other investigators who conducted high-speed visualization of bubble nucleation. It is therefore difficult to make a general comment on the location of nucleating cavities—the phenomenon depends on the local thermal field in the fluid and the wall, and the availability of appropriate sized cavities.

II.1.4.4. Effect of Nanostructures on Nucleation and Flow Boiling in Microchannels

Carbon nanotubes were employed by Khanikar et al. [289] in an effort to enhance flow boiling heat transfer in microchannels. The study reported significant increase in the generation of small bubbles at low mass fluxes. At higher mass fluxes, no benefits of placing carbon nanotubes were observed.

Liu et al. [290] report the nucleation characteristics of a silicon microchannel embedded with nanostructures at the bottom of the channel. The surface became very hydrophilic, but the bundling effect of nanowires provided a large number of nucleation sites. The study reports morphological changes seen in the two-phase structures due to the presence of nanowires. Current research indicates that nanostructures do not provide any significant enhancement in heat transfer or CHF during flow boiling in microchannels. However, there are very few studies reported and further research in this field is warranted.

II.1.4.5. Nucleation and Instability

In the absence of appropriate sizes of nucleating cavities on smooth microchannel surfaces, nucleation is delayed and the liquid becomes superheated [291]. When the bulk liquid also becomes superheated, a nucleating bubble encounters an explosive growth. This leads to expansion of the bubble in both upstream and downstream directions. Placing nucleation cavities upstream reduces the bulk liquid superheating and stabilizes the flow. This technique was successfully employed by several investigators, for example, Kandlikar et al. [277] and Kuo and Peles [286].

Lee and Pan [292] studied nucleation in smooth silicon microchannels using a high-speed camera. They observed that large superheats were needed to nucleate over the small cavity sizes, and the nucleation was followed by eruptive bubble growth, leading to formation of large slugs as observed by previous investigators. Introducing nucleation cavities on the surface is therefore seen as a good way to reduce the instabilities.

II.1.4.6. Emission Boiling

Transition boiling occurs past the critical heat flux location as the wall superheat is further increased, resulting in an unstable region beyond the CHF location. However, with highly subcooled liquid, a new type of boiling phenomenon was observed by Inada et al. [293] in which a large number of tiny bubbles emerge from the surface. This leads to very high heat fluxes, significantly beyond CHF. Subsequently, Shoji and Yoshihara [294] were able to dissipate heat fluxes in excess of 10 MW/m^2 with water on a thin heated platinum

wire. Wang et al. [295] used a high-speed camera and a microscope to observe pool boiling phenomenon on a heated platinum wire with high subcooling. They observed jets emerging from nucleation sites, some of which broke down into fine bubbles similar to emission boiling.

Suzuki et al. [296] extended the study of microbubble emission to flow boiling in channels and reported the microbubble emission phenomenon. Subsequently, Suzuki et al. [297] proposed microbubble emission boiling for cooling of high heat flux devices. Tange et al. [298] conducted experiments with pool boiling and flow boiling conditions and obtained high-speed images of the microbubble emission boiling phenomenon. Figure II.6(a) and (b) show the respective images using a frame rate of up to 3000 fps. Using a channel height of 200 μm , they were able to dissipate a heat flux of 8 MW/m^2 with a

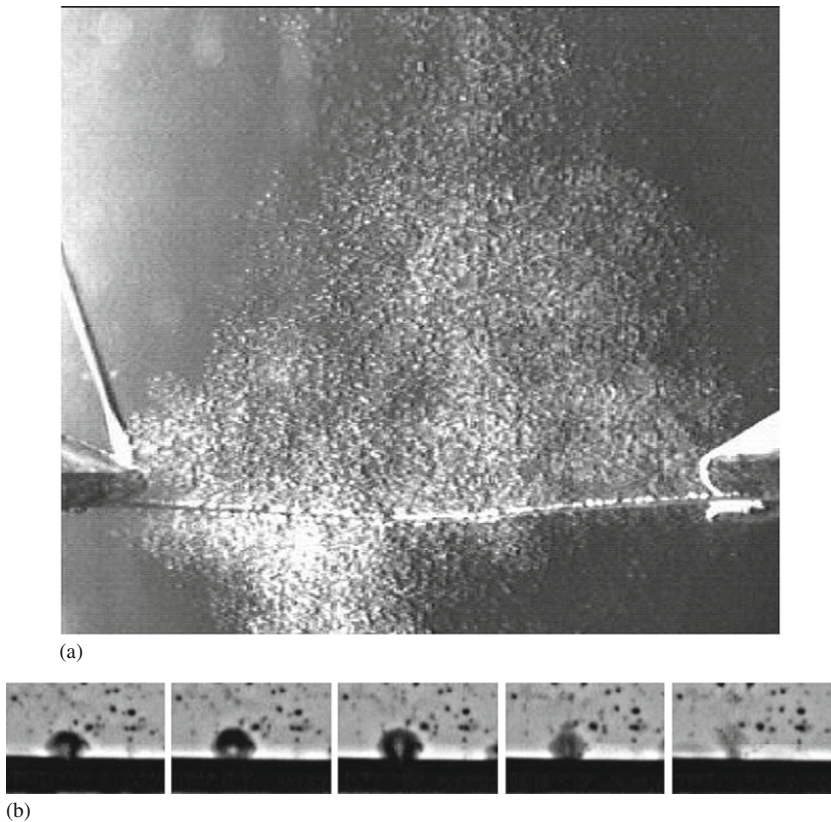


FIG. II.6. Microbubble Emission Boiling (MEB) in (a) pool boiling of water on a heated platinum wire and (b) flow boiling of subcooled water in a microchannel [298].

wall superheat of 50 K. Similar results were reported by Suzuki et al. [299] for water and different water–alcohol mixtures. The maximum heat flux reported for water–alcohol mixtures were 2–3 MW/m² higher than those for pure water.

Wang and Cheng [300] studied MEB in 155 μm glass channels with platinum micro heaters embedded on the bottom channel wall. The glass surface was smooth and single-phase flow of water could be sustained and nucleation occurred at very high wall superheats. As the bubbles contacted subcooled liquid, they broke into microbubbles. With a mass flux of 883.8 kg/m²s, a heat fluxes of 14.41 MW/m² was reached. In the presence of nucleation sites, boiling started as the usual flow boiling in microchannels, with the bubbles causing the backflow. However, at high heat fluxes, emission boiling was established and the boiling curve merged with that for the smooth surface. This indicates that the MEB can be achieved in microchannels made by the microfabrication processes. The MEB is shown to have great promise in electronics cooling application. Although the heat transfer mechanism for microbubble emission boiling is quite different, the heat transfer coefficient could be well predicted by the conventional macroscale flow boiling correlation.

The mechanism of bubble formation in MEB is not clearly understood. There are two possible explanations that have been proposed in literature. Based on these explanations, two models are proposed here for the microbubble emission.

The schematics showing the two mechanisms are depicted in Fig. II.7(a) and (b). The first bubble collapse model shown in Fig. II.7(a) is based on the cavitation phenomenon that occurs as a bubble grows on a heater surface and its interface comes in contact with a highly subcooled liquid. The bubble experiences rapid condensation at the interface which results in the collapse of the bubble. The impact of the retracting high-velocity interface on the heater

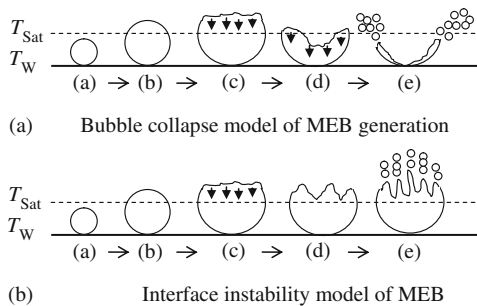


FIG. II.7. (a) Bubble collapse model and (b) interface instability model describing MEB generation mechanisms during subcooled pool and flow boiling.

surface creates a large number of secondary bubbles that are released into the bulk fluid. This theory is supported by the observation of surface erosion caused by the collapsing bubbles reported by Wang and Cheng [300]. The image sequence depicted in Fig. II.6(b) by Tange et al. [298] shows the vapor bubble collapsing after frame 4 and resulting in the production of fine bubbles. The authors report a series of bubbles being emitted from the heater surface.

The interface instability model is supported by observations of Makuta et al. [301] and Kuzma-Kitcha et al. [302] as discussed by Tange et al. [298]. Makuta et al. [301] observed fragmentation of gas bubbles as they emerged from a needle into a liquid under an ultrasonic field. Kuzma-Kitcha et al. observed interface oscillations of a vapor bubble in a subcooled liquid. These oscillations provide a mechanism for the fission of the larger bubble into smaller MEB bubbles.

Although there is no conclusive evidence, it seems that both mechanisms are at play in the MEB generation. The condensation at the interface in the subcooled liquid causes interface instability and oscillation for some time, and is followed by bubble collapse on the heater surface. Both these mechanisms lead to MEB. In addition, strong jets of liquid emerging from a heater wire in subcooled nucleate boiling were reported by Wang et al. [303]. These jets also lead to emission of small bubbles. Further visualization studies are warranted by using controlled heating elements and time-lag imaging as employed in the study of bubble nucleation and growth in ink-jet print heads.

Suzuki et al. [304] studied flow boiling in eleven 155 μm hydraulic diameter parallel multichannels on a 5.25 mm \times 5.25 mm copper block. As the heat flux increased, the CHF condition was reached with saturated liquid flow. Introducing liquid subcooling did not yield MEB phenomenon that was observed by Wang and Cheng [300]. The main reason is thought to be the short heated length of only 200 μm employed by Wang and Cheng. Long heated microchannels were unable to generate MEB bubbles. This can be further explained by noting that it is difficult to sustain a high degree of liquid subcooling in the long heated channels. Short heated sections with multiple inlet and outlet headers may provide favorable conditions. Further research in this area is warranted.

II.2. Void Fraction

II.2.1. INTRODUCTION

Void fraction is defined as the ratio of the volume of the gaseous phase occupied in a channel to the total volume of the channel. Significant spatial and temporal variations are present due to the chaotic nature of the two-phase

flow. The local void fraction at any given section varies as a function of time, and it is therefore necessary to consider time averaged values of void fraction.

The homogeneous void fraction is based on the assumption that the two phases are flowing at the same velocity in the channel. It is an important parameter that is often used in correlating actual void fraction with other parameters. The difference in the velocities of the two phases causes the void fraction in a channel to be different than the homogeneous void fraction.

The volume flow fraction β is defined as the ratio of the volume flow rates of the two phases:

$$\beta = \frac{Q_G}{Q_L + Q_G} \quad (\text{II.17})$$

where Q is the volumetric flow rate. Subscript L is used to indicate liquid phase, while G indicates gaseous phase, which represents the vapor phase under flow boiling conditions.

The volume flow fraction is related to the quality x (defined as the ratio of the mass flow rate of vapor to the total mass flow rate) by the following equation:

$$\beta = \frac{1}{1 + ((1 - x)/x)(\rho_G/\rho_L)} \quad (\text{II.18})$$

Since the velocities of the two phases are equal under the homogeneous flow model, the homogeneous void fraction is the same as the volumetric flow fraction. Thus

$$\alpha_{\text{Hom}} = \beta \quad (\text{II.19})$$

The assumption of equal flow velocities under the homogeneous flow model is reasonably accurate for bubbly flow and mist flow regimes. For annular and separated flow regimes, the liquid velocity is lower than the gas velocity and the void fraction is lower than the corresponding homogeneous void fraction.

For large diameter tubes, $D > 3$ mm, the separated flow model equation by Premoli et al. [305] is recommended.

$$\alpha = \frac{1}{1 + S((1 - x)/x)(\rho_G/\rho_L)} \quad (\text{II.20})$$

where S is the slip ratio given by the following equation:

$$S = 1 + E_1 \left(\frac{y}{1 + yE_2} - yE_2 \right)^{1/2} \quad (\text{II.21})$$

$$y = \frac{\beta}{1 - \beta} \quad (\text{II.22})$$

$$E_1 = 1.578 Re^{-0.19} \left(\frac{\rho_L}{\rho_G} \right)^{0.22} \quad (\text{II.23})$$

$$E_2 = 0.0273 WeRe^{-0.51} \left(\frac{\rho_L}{\rho_G} \right)^{-0.08} \quad (\text{II.24})$$

The Reynolds number and Weber number are defined with total mass flow rate and liquid viscosity and density as follows:

$$Re = \frac{\dot{m}D}{\mu_L A} \quad (\text{II.25})$$

$$We = \frac{\dot{m}^2 D}{\sigma \rho_L A} \quad (\text{II.26})$$

where \dot{m} is the total flow rate, μ_L is the liquid phase viscosity, and σ is the surface tension. The use of Weber number confirms the effect of surface tension forces on the interface and the two-phase flow structure even in the large diameter tubes.

The effect of surface tension is expected to be more significant in micro-channel flows. Recent interest in microchannels has led to a number of experimental studies on void fraction measurement in microchannels, especially under adiabatic flow conditions. These and some other void fraction studies under flow boiling conditions are discussed in the next section.

II.2.2. INFLUENCE OF FLOW PATTERN ON VOID FRACTION

Void fraction is closely related to the flow pattern existing in a channel. Void fraction departs from the homogeneous flow value when the two phases flow at different velocities in a channel. The phase flowing near the wall will experience an increased drag due to wall shear stress and flow at a lower velocity in the channel. A closer look is presented at the void fraction in different flow regimes.

Bubbly flow: In bubbly flow, gas bubbles flow freely with the liquid. Ideally, if the bubbles are distributed evenly around the cross section, the void fraction is close to α_{Hom} . If the gas phase is distributed as small bubbles flowing in the center of the channel where the flow velocity is higher than the mean flow velocity, the void fraction will be lower than α_{Hom} . In the subcooled flow boiling, bubbles are attached to the channel walls and are essentially stagnant. This will lead to a void fraction greater than α_{Hom} .

Slug flow: During slug flow, liquid and gas slugs flow alternately, completely filling the channel. When a liquid slug passes, there is no vapor

present in the cross section and the local void fraction is zero. When a gas bubble passes, completely filling the channel, the void fraction is unity. Void fraction in this case can be estimated through visual observation in a transparent test section by measuring the time duration of each phase at a given section, or by measuring the individual phase slugs over a sufficiently long time period to average out the local flow fluctuations. Since the two phases are flowing in tandem, the flow velocity of both phases is equal and the void fraction is the same as α_{Hom} .

However, a liquid film is generally present on the wall around an elongated gas bubble and the void fraction at the section where the vapor slug is present is lower than unity. Special care and instrumentation is needed to measure the liquid film thickness and relating it to the time averaged void fraction. The presence of a liquid film will cause the local void fraction during the gas bubble passage to be less than unity, and will result in a time averaged void fraction to be lower than α_{Hom} .

Another case arises for short channels. As a liquid slug exits, the gas is released at a high velocity before another liquid slug enters the channel. This will lead to a lower void fraction. This condition is dependent on the type of the mixing chamber used at the inlet section. However, for long channels that accommodate several liquid slugs, the void fraction will be closer to α_{Hom} further depending on the liquid film thickness on the wall during flow of elongated gas bubbles.

Annular flow: During annular flow, the gas phase flows in the core, while the liquid phase flows in an annular ring which is in contact with the channel walls. The liquid phase is subjected to the wall shear stress and therefore flows at a lower velocity than the gas phase. The void fraction is therefore lower than α_{Hom} .

Mist flow: Mist flow comprises small liquid droplets flowing in a continuous vapor phase. When the droplets are uniformly distributed in the channel, the void fraction is equal to α_{Hom} . However, if the droplets flow preferentially in the center region where the flow velocity is higher, the void fraction will be lower than α_{Hom} .

Void fraction in adiabatic two-phase flow is thus seen to be equal to α_{Hom} for bubbly flow, slug flow without a liquid film on the wall during gas bubble passage, and mist flow with uniform droplet distribution. The void fraction is lower than α_{Hom} for other cases where the liquid velocity is reduced due to the wall effects. The only case where the void fraction could be higher than α_{Hom} in adiabatic two-phase flow is during mist flow with a larger concentration of liquid droplets in the center. Mist flow generally occurs at low liquid superficial velocities where the void fraction is expected to be close to unity. In the case of inverted annular flow, which is not a commonly encountered flow pattern, the void fraction is also lower than α_{Hom} . This flow pattern may occur in microchannels following the inlet mixing section where liquid is introduced in a central nozzle surrounded by an annular gas flow inlet.

Void fraction during flow boiling and condensation will follow the same trends as in the adiabatic two-phase flow, except for the case where the vapor bubbles remain attached to the wall in the vicinity of the location where net vapor generation begins.

II.2.3. VOID FRACTION STUDIES IN MICROCHANNELS

A number of experimental studies on void fraction in channels smaller than $200\text{ }\mu\text{m}$ diameter have been reported in the last decade. One of the early research was reported by Serizawa et al. [306]. They conducted experiments with air–water flow in 20, 25, and $100\text{ }\mu\text{m}$ circular tubes. The test sections were made of transparent silica and quartz capillary tubes of circular cross-section positioned horizontally. Air and water were supplied at the inlet in a mixing section. Two different mixing sections were employed as shown in Fig. II.8(a) and (b). In both designs, air was introduced in the center and water

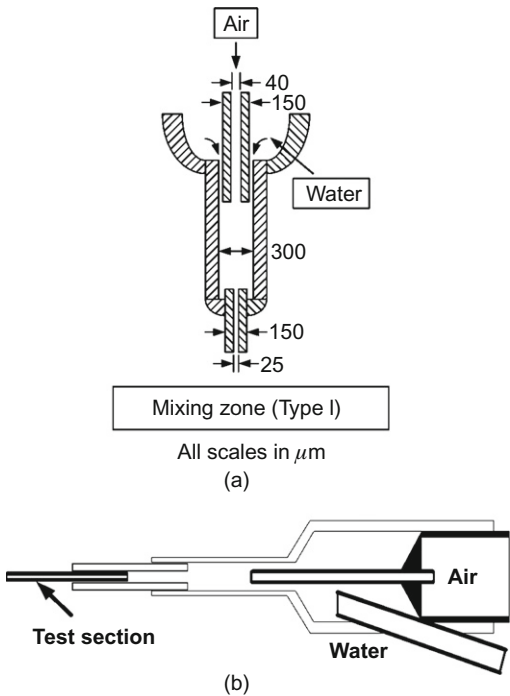


FIG. II.8. Entrance mixing zone types: (a) mixer with concentric annulus, (b) mixer with annulus fed by an angular water inlet into the manifold around the air supply tube. Redrawn from Serizawa et al. [306].

was introduced peripherally either through an annular ring, Fig. II.8(a), or through a tube supplying water in the annular space around the air tube. However, both designs result in a similar water entry in the collar around the air tube.

Serizawa et al. [306] used a high-speed camera with a shutter speed of $1/10,000$ s and a frame rate of 600 fps. The superficial velocities were j_L from 0.0032 to 17.5 m/s and j_G from 0.0022 to 295.3 m/s. They reported the flow to be highly unstable. They observed dispersed bubbly flow, slug flow, liquid ring flow, and liquid lump flow. The liquid ring flow is the result of a progression from slug flow when the vapor penetrates the slug to give the ring-like structure. The liquid lump flow results when the ring in the slug becomes asymmetric. The experiments with steam-water resulted in an additional flow pattern termed as liquid droplet flow, where droplets of liquid were carried in the vapor flow.

The void fraction was calculated from the high-speed image frames for only the bubbly and slug flow patterns. The flow structure was assumed to be symmetrical around the centerline.

Figure II.9 shows their results for void fraction as a function of volumetric flow fraction. The spread in the data is rather large, but in general, the authors suggest that their data follows the Armand's [307] correlation given by the following equation:

$$\alpha = 0.833\beta \quad (\text{II.27})$$

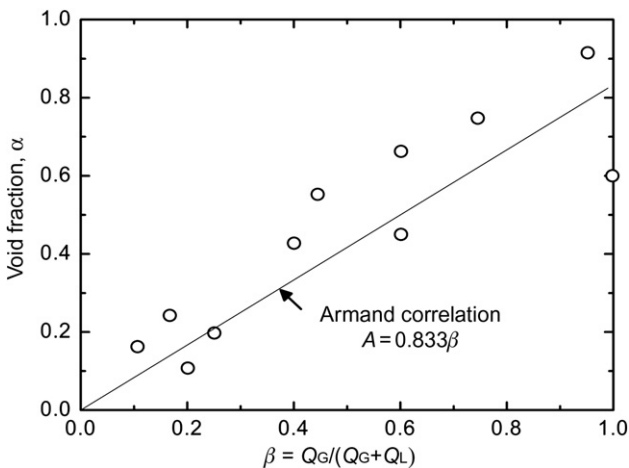


FIG. II.9. Cross-sectional average void fraction in air–water two-phase flow in a $20\text{ }\mu\text{m}$ i.d. silica tube (Type I). Replotted from Serizawa et al. [306].

It is interesting to note that Serizawa's data shows a void fraction for many data points to be greater than the homogeneous flow model. This indicates that the liquid phase is moving faster than the gas phase in the channels. It seems somewhat counterintuitive, as the bubbles in the bubbly flow pattern would tend to flow in the center where the flow velocity is higher than near the periphery which is largely occupied by the liquid. In the slug flow region, the void fraction is expected to be the same as the homogeneous flow void fraction as the two phases travel at the same velocities neglecting the film thickness around the gas slugs. With a finite liquid film thickness around the gas bubbles, the void fraction will be lower than the homogeneous flow model. In both cases, void fraction is expected to be lower, not higher, than the homogeneous void fraction value.

The discrepancy may be further explained as follows. In the bubbly flow, distortion is caused by refraction while viewing through the curved tube in determining the size of the bubbles. Bubbles would seem to be larger than their actual size. In the slug flow, errors in determining the liquid film thickness at the wall could be quite dramatic. For example, in a 25 μm diameter tube, a liquid film thickness of 1 μm indicates an equivalent void fraction of 7.8%. Such a small thickness measurement is difficult due to the curvature of the glass and the chaotic nature of the two-phase flow. Another reason may be due to the uncertainty associated with the tube diameter measurement.

The still images presented by Serizawa et al. [306] indicate that the contact angle of the liquid–vapor interface of liquid slugs is close to 90° . The quartz surface seems to be hydrophobic as seen from these images. This may in fact cause the liquid film to not adhere to the wall, and the results shown by them may be reasonable for such hydrophobic surfaces. The spread and higher values of void fraction above the homogeneous void fraction may be due to uncertainties in measurements.

Another exhaustive study reported by Kawahara et al. [308] focused on a 100 μm diameter transparent capillary tube made of fused silica. The inlet section employed in their study is shown in Fig. II.10. The liquid enters in the central tube, while air is introduced in the annular region. These air and water supply locations are opposite to that employed by Serizawa et al. [306] shown in Fig. II.8(a) and (b).

Kawahara et al. [308] conducted experiments with air–water two-phase flow under the following flow rate ranges— j_G from 0.1 to 60 m/s and j_L from 0.02 to 4 m/s. These ranges are considerably smaller than the ranges employed by Serizawa et al. [306]. The two-phase flow images were captured by a video camera with a shutter speed of 1/16,000 s and a frame rate of 30 fps. The frame rate employed by Kawahara et al. [308] is significantly lower than that employed by Serizawa et al. [306], who employed a frame rate of 600 fps.

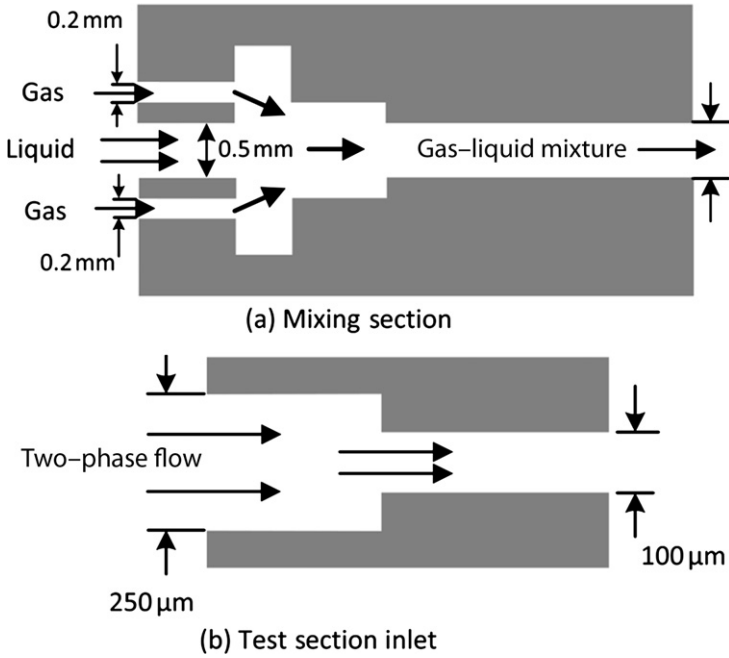


FIG. II.10. Inlet mixing section employed by Kawahara et al [308].

The video image frames were analyzed by Kawahara et al. [308] after considering the refraction effects and the liquid film thickness estimation. The resulting variation in void fraction is shown in Fig. II.11. Note that ε is the same as α , indicating void fraction. The data was correlated by the following correlation.

$$\alpha = \frac{A\beta^{0.5}}{1 - B\beta^{0.5}} \quad (\text{II.28})$$

The void fraction remains low over the range $0 < \beta < 0.8$ but increases rapidly between 0.8 and 1. The reason for the low void fraction was attributed by the authors to the high slip between the two phases as the liquid experienced severe wall shear stress, while the gas flow in the core was less influenced.

This trend is quite different from the trend displayed by Serizawa et al.'s data shown in Fig. II.10. The main difference in Kawahara et al.'s experiments are (i) hydrophilic walls as seen from the video images, (ii) accounting for the liquid film thickness while calculating void fraction, and (iii) inlet mixing section with liquid entry in the center.

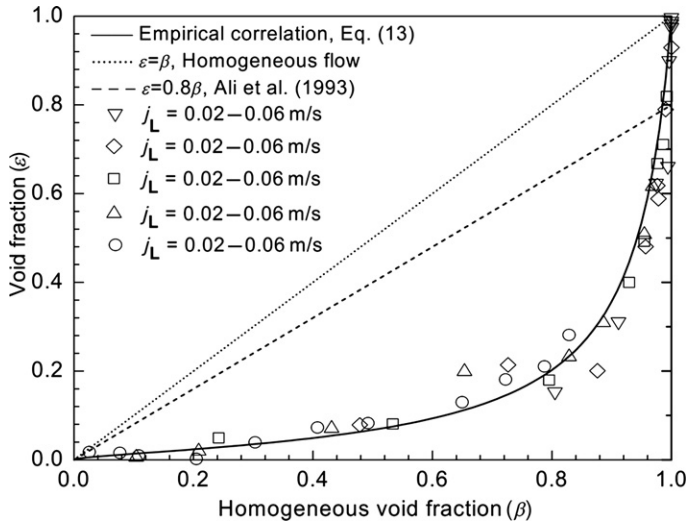


FIG. II.11. Void fraction variation with air–water data in a $100\text{ }\mu\text{m}$ diameter circular fused silica tube, $A = 0.03$ and $B = 0.97$ (ε is the same as α , the void fraction). Replotted from Kawahara et al. [308].

Chung et al. [309] extended the work of Kawahara et al. [308] to cover square channels. They studied nitrogen–water flow in a $96\text{ }\mu\text{m}$ square channel. The test sections were made of fused silica tubes of square cross-section. The cross-sectional dimensions were measured with a microscope. Figure II.12 shows their void fraction results. Equation (II.28), derived for circular microchannels, is also plotted on the same figure. It can be seen that the square microchannels followed the same trend as the circular microchannels, and agreed very well with Eq. (II.28).

Chung and Kawaji [310] conducted another study to investigate the effect of channel diameter on adiabatic two-phase flow characteristics. Four circular tubes of fused silica coated internally with a polyimide coating were used as test sections. The tube diameters and lengths were $49.5\text{ }\mu\text{m}/46.0\text{ mm}$, $99.6\text{ }\mu\text{m}/63.9\text{ mm}$ and 65.1 mm , $250\text{ }\mu\text{m}/156.7\text{ mm}$, and $526\text{ }\mu\text{m}/277\text{ mm}$, respectively. The experiments covered a range of superficial liquid and nitrogen gas velocities of $0.01 \leq j_L \leq 5.77$ and $0.02 \leq j_{G,\text{avg}} \leq 72.98\text{ m/s}$, respectively. The video image sequences were obtained near the outlet end of the test sections using two different cameras with maximum frame rates of 30 and 125 fps, respectively. Clear images were obtained using a short exposure time of $1/16,000\text{ s}$.

The experimental results from Chung and Kawaji [310] indicate that the larger tubes of 250 and $526\text{ }\mu\text{m}$ exhibited an almost linear relationship following the Armand correlation, while the smaller tubes of $49.5\text{ }\mu\text{m}$ and

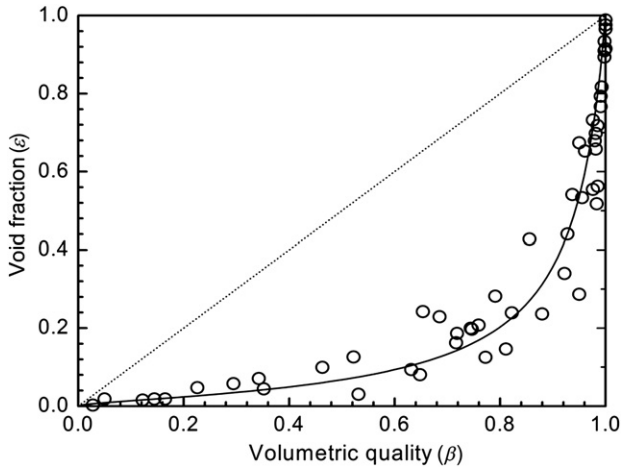


FIG. II.12. Void fraction results for nitrogen–water flow in a 96- μm square fused silica microchannels. Replotted from Chung et al. [309], Fig. 4(a).

99.6 (100) μm exhibited a nonlinear relationship similar to that shown in Fig. II.11. Equation (II.28) was able to correlate their data as well as with $A = 0.03$ and $B = 0.97$ for 100 μm tube, and $A = 0.02$ and $B = 0.98$ for 50 μm tube.

The results of Chung et al. [309] and Chung and Kawaji [310] clearly show the effect of small diameters on void fraction. These trends need to be further verified for a broader range of tube diameters and tube surface conditions. Another aspect that may need further attention is the camera speed employed in obtaining the video images for determining void fraction. With a frame rate of 30 fps, the time interval between two successive frames is 33.3 ms. At the highest superficial gas velocity of 72.98 m/s, the distance traveled by the fluid between two successive frames is 2.43 m with the 30 fps camera and 0.584 m with the 125 fps camera. It is recommended that a higher frame rate be employed so that individual slugs can be tracked and an image analysis algorithm be employed to guarantee that complete slug lengths are captured. To capture the entire slugs in a 1-mm window at a superficial flow velocity of 72.98 m/s, a frame rate of 73,000 fps would be needed. This would certainly pose challenges in providing proper lighting. Another improvement may be made by moving the visualization section to the center of the tube to avoid sudden expansion of the vapor bubbles following a liquid slug exiting the test section. Nevertheless, the results indicate a consistent departure from the linear behavior in their tests for microchannel tubes. As stated earlier, the presence of a liquid film on the wall has a more dramatic effect in reducing the void fraction for microchannel tubes as compared to large diameter tubes.

The effect of tube lengths on the void fraction relationship was studied recently by Ide et al. [311]. Microchannels of 100 μm inner diameters with two tube lengths of 146 and 1571 mm were studied over a superficial gas velocity range of 0.03–14 m/s, and superficial liquid velocity range of 0.04–0.7 m/s. It was found that the shorter tube length followed the earlier nonlinear void fraction behavior displayed in Figs. II.11 and II.12 by Kawahara et al. [308] and Chung et al. [309]. For the longer tube, the void fraction followed the linear trend from the Armand's correlation. In the shorter tube, slow and fast moving gas and liquid slugs were observed. As the liquid slug exited, fast moving gas escaped until another liquid slug entered the tube. Such behavior was not observed in the long tube. In microfluidics application, shorter tubes are more commonly employed and the nonlinear void fraction relationship is expected.

Recognizing the importance of the video capture speed, Ide et al. [312] developed a technique utilizing optical fibers and infrared sensors to measure the slug lengths and correlate them with the void fraction data. Their work confirmed the nonlinear trend in void fraction versus α_{Hom} obtained by Chung et al. [309] and Chung and Kawaji [310]. Equation (II.28) is therefore recommended for estimating void fraction in microchannels smaller than about 200 μm . A slight adjustment in the constants A and B is recommended by Chung and Kawaji [310] to improve the prediction for different diameter tubes. This correlation has been developed and is applicable to hydrophilic tubes made of fused silica.

Another set of experiments was conducted by Cullion et al. [313] on branching network of microchannels emerging from a central source. The channels were 150 μm deep and varied in widths from 100 to 400 μm , covering a total channel length of 17 mm. Their results indicate that the void fraction varies considerably with time even after averaging over long time intervals of up to 30 min.

Kawahara et al. [314] conducted experiments to study the effect of fluid properties on the two-phase flow characteristics. They used deionized (DI) water and aqueous solutions of ethanol (0%, 4.9%, 48%, and 100% mass concentration) as test fluids. The tubes were of 250 and 500 μm inner diameters and were made of fused silica. In their experiments, they used transparent fused silica tubes. To avoid the inlet and exit effects, the tubes were made 99 mm long and the camera was located at the center of the tube length. A high-speed camera at 8000 fps was used to capture slug lengths. They used a T-junction mixer with gas entry from the side. Their results indicated a very small effect of ethanol concentration on void fraction. The void fraction followed the trend between $\alpha = \alpha_{\text{Hom}}$ and Armand's correlation of $\alpha = 0.83\alpha_{\text{Hom}}$. The trend in void fraction versus homogenous void fraction was similar to those obtained by Chung et al. [309] for large diameter tubes ($>200 \mu\text{m}$).

Choi et al. [315] conducted visualization experiments to study the effect of channel aspect ratio on flow patterns and void fraction. The channels'

dimensions in μm and the aspect ratio were 510×470 (0.92), 608×410 (0.67), 501×237 (0.47), and 503×85 (0.16). Although the flow patterns were affected considerably with the change in the aspect ratio, the void fraction was found to follow Armand's linear relationship given by Eq. (II.27). The authors first introduced liquid flow in the tube followed by nitrogen gas supply through a T-junction inlet. However, information about the tube surface and the contact angles was not provided.

Void fraction measurement under flow boiling was studied by two investigators. Singh et al. [316] studied flow boiling of water in a $173 \mu\text{m} \times 119 \mu\text{m}$ rectangular microchannel ($140 \mu\text{m}$ hydraulic diameter). Heat fluxes ranged between 5 and 50 W/cm^2 , and the quality ranged between 0 and 0.3. Their results indicate a linear relationship between α and α_{Hom} over the ranges of parameters investigated.

Fogg et al. [317] developed a new technique to measure the liquid temperature and the local void fraction during flow boiling. The method uses the fluorescence technique in which a molecule becomes energized by absorbing a photon and in turn emits another photon of different wavelength. Then, the ratio of the emitted radiation to the absorbed radiation is taken as a function of temperature. As a result, the radiation intensity is indicative of liquid volume in which the dye is present and can thus be used for void fraction measurement. This technique provides a very rapid measurement that can be digitally processed to provide temperature and void fraction measurements averaged over any desired time period. This method also has a very low uncertainty in measurements: 3°C in temperature measurement and 2% full scale in void fraction measurement.

II.2.4. CONCLUDING REMARKS

The void fraction measurement in microchannels presents several challenges due to the small channel sizes. The inlet manifold used in generating the two-phase adiabatic flows has a considerable effect on the resulting void fraction. Therefore this area needs further attention. Optical measurement techniques require high-speed video imaging over sufficiently long periods to account for the flow transients. Discerning the liquid film thickness, obtaining accurate three-dimensional views of the bubbles and droplets, and avoiding distortion due to the tube wall are some of the additional challenges. The fluorescence-based void fraction measurement technique used by Fogg et al. [317] overcomes these difficulties and seems promising under both adiabatic and diabatic flow conditions.

The void fraction in tubes larger than about $200 \mu\text{m}$ is seen to follow Armand's correlation irrespective of the inlet manifold configuration. The microchannels ($<200 \mu\text{m}$ hydraulic diameter) have been reported to follow a

nonlinear trend. It is not entirely clear whether it is due to the inlet manifold configuration or the contact angles of the inner wall surface. Future research in these areas is warranted.

II.3. Liquid Film Thickness

II.3.1. INTRODUCTION

Liquid films are encountered in microchannel flows during various conditions. In adiabatic two-phase flow, liquid films are formed during annular flow. During slug flow, the vapor slug is often surrounded by a thin film of liquid. During flow boiling conditions, evaporating liquid films are present during the annular and slug flow pattern. Additionally, as bubbles nucleate during flow boiling, a thin liquid film is present underneath the bubble. Similarly, condensation in microchannels results in a liquid film that occurs in various flow patterns.

The liquid film experiences wall shear stress and causes the liquid holdup resulting in a reduction in void fraction. In boiling, as well as condensation applications, a thermal resistance is introduced in the heat transfer path that adversely affects the heat transfer rate.

Liquid film thickness is affected by various factors. Some of the important parameters are gas and liquid properties such as viscosity and density of the two phases and surface tension, liquid and gas flow rates, channel geometry, channel surface properties such as roughness and surface energy (resulting in hydrophobic and hydrophilic surfaces). This chapter will first focus on some measurement techniques for measuring the liquid film thickness during two-phase flows in microchannels. It will be followed by some predictive models and results.

II.3.2. CHALLENGES IN LIQUID FILM THICKNESS MEASUREMENT

Liquid film thickness measurement during two-phase flow in microchannels poses a number of challenges:

- a. The measurement accuracy of the film thickness needs to be higher. For example, in a 25 μm diameter channel, a film thickness of 1 μm at the wall represents a cross-sectional area coverage of 7.8%. This will directly affect void fraction estimation based on the film thickness measurement.
- b. Difficulty in obtaining local values representative of the circumferential and axial variation in the channel requires statistical analysis during data reduction.
- c. Wall refraction effects introduce challenges that need to be resolved at micro or even submicron level in optical measurement techniques. Image

distortion due to curvature of the channel wall and nonuniformity in optical properties of the channel introduce errors that require special attention in the design of the imaging equipment and further image analysis.

- d. Fast response at microscopic level is needed to capture the rapidly changing nature of two-phase flow structure.
- e. In the case of boiling and condensation systems, interference may be caused by the film thickness measurement system and cause a local change in the underlying heat transfer process.

Several techniques have been employed by researchers to address these concerns. A brief review of the techniques employed by researchers in the area of two-phase flow in microchannels is presented.

II.3.3. LIQUID FILM MEASUREMENT AND RESULTS

Visible light is used to detect the interface using microscopic lenses in conjunction with a high-speed camera. The test section is made of transparent material, such as quartz or fused silica, to provide the optical clarity necessary in using the images for further image analysis. The image quality is determined by the resolution of the camera and the lens. A simple image analysis may consist of counting the number of pixels occupied by the liquid film and translating this into a film thickness through the known resolution of the optical system employed.

Image distortions are introduced as the light travels from the liquid–gas interface through the liquid and then through the transparent channel wall material. Differences in refractive indices of these media cause the images to be distorted as different pathways are followed by light coming from different regions of the interface and the channel walls. Nonhomogeneity of the transparent medium, especially the channel wall, may introduce distortions which reduce the image quality for further image analysis.

Refraction at the curved interfaces is another source of concern. In the case of circular channels, both the inner and outer channel walls cause image distortions. Measuring the thickness of thin liquid films in microchannels causes the light to interact with the internal channel walls at a very small angle. The wavy nature of the film will cause the interface “thickness” to be magnified due to the changing curvature of the interface in this region. Additional distortions will be introduced at the outer wall as well.

Although the flow rates are quite small in microchannels, the flow velocities could be quite large. In the case of fuel cell applications, it is not uncommon to have gas flow velocities higher than 100 m/s. These will result in wavy interfaces. In the case of slug flow, the slug passages may occur at a high speed and the liquid film thickness changes will be quite fast. To capture the

corresponding instantaneous values of the liquid film thickness, a high shutter speed and a high frame rate are needed. The shutter speed will determine the sharpness of the interface and will also have a direct influence on the lighting requirement.

The frame rate of the imaging system is determined by the nature of the transients present in the two-phase flow. Again, considering the slug flow pattern, the length of the slugs, the time it takes for a slug to pass, the waviness of the liquid–vapor interface, and the axial variation in film thickness are important considerations.

Another important consideration that is often overlooked is the duration of the image capture. The high-speed imaging, for example at a frame rate of 100,000 fps, will generate 100 frames in 1 ms duration. However, 1 ms may not be an adequate time window to capture the system transients. The two-phase dynamics associated with the supply lines, inlet manifolds, and neighboring channel interactions in a multichannel system may introduce significantly long transients which may be difficult to capture in an image sequence. Taking several image sequences may not provide the necessary averaging from a statistical viewpoint. These factors may result in film thickness measurements that contain the secondary influences of the system dynamics, and any interpretation from such data on the nature of the two-phase dynamics may be misleading. For example, if the film thickness information is used for measuring void fraction under a slug flow pattern, the time duration for image capture should include any variations in the slug lengths, as well as any change in flow pattern occurring at lower frequencies. The inlet manifold may be experiencing a time varying pressure fluctuation that causes only gas to flow for some time before resuming the slug flow pattern. Obtaining high-speed images at 100,000 fps over a period of 30 s would be a formidable task. However, without considering these effects, the data interpretation may be severely in error.

A number of investigators have used this technique. A good review on this topic is provided by Tibiriță et al. [318] for measurement of liquid film thickness in large, as well as small, tubes and open channels.

Serizawa et al. [306] used a microscope with a 150 \times lens which provided a good resolution, although the actual values of pixel sizes were not reported. The highest frame rate employed was 600 fps and an exposure of 1/10,000 s was employed. The images were not corrected for the refraction. The highest superficial gas velocity employed was 295.3 m/s. Although the exposure is small, it is still not enough to capture the fast dynamics of the flow. The frame rate of 600 fps is too low to capture two images within a slug at higher flow rates. These factors caused a large scatter in their data for void fraction which was obtained from the measured liquid film thickness. Nevertheless, their work is important as one of the first measurements of liquid film thickness in

microchannels providing useful information regarding void fraction trends in air–water two-phase flows.

Kawahara et al. [308] obtained the liquid film thickness information in microchannels by employing a regular CCD camera with 30 fps and an exposure of 1/16,000 s. The authors studied the refraction effects on the liquid film thickness due to the curvature of the tube. To quantify the film thickness changes as obtained in the images, they employed a refraction matched fluid in an outside container. The resulting images of the liquid film thickness were considerably reduced. They estimated that the refraction effects caused the thickness to be magnified by 50%. This factor was used in their assessment of the film thickness during image analysis. The magnification factor is, however, expected to be a function of the film thickness due to rapidly changing curvature near the bottom of the channel. The low frame rate of 30 fps would be unable to provide an adequate averaging effect. Nevertheless, the experimental data by Kawahara et al. [308] provided a new trend in void fraction versus a homogeneous void fraction plot that departed from the established linear behavior. The differences between their results and those by Serizawa et al. [306] are attributed to the differences in the inlet mixing region for introducing the two-phase mixture.

Hazuku et al. [319] presented a new technique of measuring the displacement of the interface with a laser focus displacement meter that is capable of detecting the interface thickness with a $0.2\text{ }\mu\text{m}$ resolution and at a frequency of 1 kHz. The technique was successfully applied to detect the film thickness in annular flow in tubes of $25\text{ }\mu\text{m}$ diameter. The specifics of the method are given in detail by the authors. They measured the passages of liquid film during annular flow.

The laser focus displacement meter was effectively used by Han and Shikazono [320] in measuring the liquid film thickness in square channels of 300, 500 μm , and 1 mm. They were able to measure the film thickness for ethanol with a millisecond time resolution.

Han et al. [321] also employed the laser focus displacement meter technique for liquid film thickness measurements in parallel channels with heights of 100, 300, and 500 μm . The liquid film thickness under a passing bubble was measured. They found that the flow velocity had a significant effect on the liquid film thickness. They also measured the liquid film thickness using the interferometer technique in which the light reflected from the interface and the channel walls was utilized to form interference fringes. When the value of the twice liquid film thickness becomes an even multiple of the half laser wavelength divided by the refracted index of the liquid, reflected light makes consecutive interference and white fringes appear, while black fringes appear with odd multiples. The results obtained from the two techniques agreed quite well with each other.

Steinbrenner et al. [322] developed an optical fluorescence imaging technique to measure the water film thickness during stratified flow in the flow field channels of a proton exchange membrane fuel cell. The technique

provides detailed information about the flow regime and water film thickness within the channel. The fluorescence imaging provides a better contrast between the two phases as compared to the visible light. The film thickness decreased rapidly with an increase in the flow velocity initially, and then tapered off to a monotonically decreasing value. The technique was helpful in providing insight into flow characteristics in the channels.

Fang et al. [323] measured the liquid film thickness during annular two-phase flow in condensation using optical interferometry in rectangular microchannels with hydrophilic walls, aspect ratios between 1 and 5, and hydraulic diameters between 100 and 500 μm . A fluorescent lamp was used with a 520 nm filter to obtain interference patterns resulting in the light being reflected from the inner channel wall and the liquid–vapor interface. They noted that the film thickness decreases from the centerline toward the corner, until it reaches a minimum and then abruptly increases as the film merges on the side walls. The film thickness increased along the flow length and reached a fairly constant value. Their work provides useful information on the flow transition between annular and bubbly flow patterns.

Huh et al. [324] utilized video and confocal microscopy to study the two-phase flow patterns in parallel microchannels. They noted that the surface wettability has a profound effect on the spatial distribution of air and water moving in the channel. It is therefore recommended that future studies in a two-phase flow in microchannels incorporate the surface wettability as a parameter.

Liquid film thickness under a vapor slug (Taylor bubble) was measured and correlated by Aussillous and Quere [325], and the following correlation was proposed for mini tubes:

$$\frac{\delta}{D} = \frac{0.67Ca^{2/3}}{1 + 3.35Ca^{2/3}} \quad (\text{II.29})$$

where δ is the film thickness and D is the channel diameter. The capillary number is given by:

$$Ca = \frac{\mu_L U_G}{\sigma} \quad (\text{II.30})$$

where μ_L is the liquid viscosity, U_G is the gas phase velocity, and σ is the surface tension. For circular microtubes, Han and Shikazono [326] correlated their data with a slightly modified form of Eq. (II.29) given below for the initial film thickness δ_0 :

$$\frac{\delta_0}{D} = \frac{0.67Ca^{2/3}}{1 + 3.13Ca^{2/3} + 0.504Ca^{0.672}Re^{0.589} - 0.352We^{0.629}} \quad \text{for } Re < Re_{\text{crit}} \quad (\text{II.31})$$

where Re_{crit} is the critical Reynolds number for turbulent transition, taken as 2000.

Han et al. [321] correlated their narrow parallel channel data and found that Eq. (II.31) is able to correlate their data when D is replaced by the channel height H . Thus:

$$\frac{\delta_0}{H} = \frac{0.67Ca^{2/3}}{1 + 3.13Ca^{2/3} + 0.504Ca^{0.672}Re^{0.589} - 0.352We^{0.629}} \quad \text{for } Re < Re_{crit} \quad (\text{II.32})$$

These correlations are developed for the initial liquid film thickness under slug flow conditions. It would be desirable to see if these correlations are applicable to annular flow conditions.

Fries et al. [327] used laser induced fluorescence (LIF) and laser confocal scanning microscopy (LSM) to characterize the gas–liquid flow in 2 m long rectangular microchannels of 200 μm hydraulic diameters. They noted that the slugs were very stable in length, within 5% for gas and 10% for liquid lengths. The capillary number ranged from 0.0002 to 0.01. They used different fluids such as ethanol and aqueous solutions of glycerol with nitrogen. Their results shed important light on the liquid distribution in the corner regions. The film thickness in the corners decreases with Ca . For low Ca , the film thickness on the wall stays nearly constant. Another important observation was made in that 70% of liquid was held up in the corner regions of a rectangular microchannel.

The effect of channel geometry on liquid film distribution is an important consideration in rectangular microchannels. Depending on the gas flow rate and fluid properties, the liquid may take different shapes as shown in Fig. II.13 [328]. The shape of the liquid–vapor interface was found to depend on the capillary number.

Kolb and Cerro [329] experimentally observed the transition of the asymmetric interface from (a) to (b) in Fig. II.13 in square channels of 2 mm sides

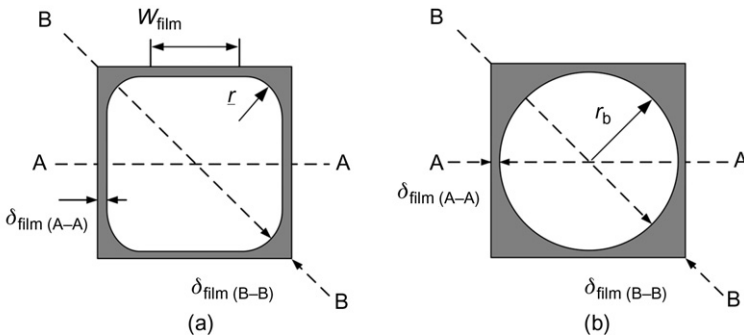


FIG. II.13. Liquid film distribution in a rectangular channel: (a) corners filling with flat interface near the center of the wall, (b) corners filling with curved interface at the center of the wall. Replotted from Yue et al. [328], Fig. 4(b) and (c).

to occur at $Ca = 0.1$. Later, Thuslasidas et al. [330] reported the transition to occur at $Ca = 0.04$ based on their more accurate observations. The effect of the size and aspect ratio of the rectangular microchannels on the transition Ca is not yet clearly identified. Further, the contact angles of the liquid–vapor interfaces on the individual walls are also expected to play a role.

A recent study by Rath and Kandlikar [331] explores the conditions for filling the corners as a function of the contact angles on the two walls and the included angle at the corner (2α). The corners will be filled if the corner angle satisfies the following condition:

$$2\alpha \geq (\theta_1 + \theta_2) - \pi \quad (\text{II.33})$$

where 2α is the corner angle, and θ_1 and θ_2 are the contact angles on the two adjoining surfaces. For the commonly used materials in microchannels, the surfaces are hydrophilic and the corners would always fill. These considerations are of great practical interest in studying the flow field channels of a proton exchange membrane fuel cells.

Finally, the liquid film thickness under a growing vapor bubble in microchannel flows is of interest in studying flow boiling heat transfer. Zhang et al. [332] measured the film thickness values for water, ethanol, and toluene, and presented extensive results. The film thickness is expected to be a function of surface wettability which needs to be included in these studies.

II.3.4. CONCLUDING REMARKS

Liquid film thickness in microchannels during adiabatic two-phase flow, condensation, and evaporation has been studied in the last decade. Optical techniques have been used extensively, but they need to be corrected for the refraction from the curved surfaces. Use of a microscope and a high-speed camera are becoming more prevalent. Some of the advanced techniques such as optical fluorescence, interferometry, and laser induced fluorescence have been developed and used where accurate quantitative data is desired.

II.4. Critical Heat Flux

II.4.1. INTRODUCTION

Boiling heat transfer provides an excellent mechanism for heat removal from a heated surface. High heat transfer rates are achieved through the phase change process that is aided by the localized motion of the liquid–vapor interface. This efficient boiling mechanism is a result of the liquid being able to convectively transport heat away from the heater surface, and utilize it in

generating vapor that removes large amounts of heat from the liquid and provides a driving force for the localized liquid motion.

However, at higher heat transfer rates, the liquid is unable to remain in contact with the surface, thereby reducing the ability to remove heat efficiently. This condition is called critical heat flux (CHF) and may be defined as the maximum heat flux that can be transferred from a heater surface at the termination of the nucleate boiling process.

CHF in flow boiling systems is influenced by additional factors resulting from the forces caused by the bulk fluid motion. These forces become dominant at higher flow rates, thereby reducing the influence of gravitational forces. This feature makes flow boiling an attractive option in microgravity application.

Flow boiling in microchannels faces additional challenges that have a direct bearing on CHF. The small channel diameter makes the viscous and surface tension forces more important compared to the inertia force. Localized nucleation sometimes causes a very rapid bubble growth causing the flow reversal at the trailing interface of a bubble. This leads to flow instability and the flow temporarily slows down, or even reverses its direction, and exposes the regions of the heater surface to be covered by vapor for a long duration depending on the severity of the instability. This further causes the thin liquid layer underneath an expanding bubble to evaporate and bring the vapor in contact with the heater surface over an extended period of time, again depending on the severity of the instability. These events cause a dramatic reduction in the CHF. Additionally, multiple parallel microchannels experience flow maldistribution as well as parallel channel instabilities, which cause further deterioration in the CHF. It is therefore important to understand the particular events and mechanisms leading to the CHF condition. The rest of this chapter deals with a detailed description of the CHF mechanism, followed by a listing of correlations that are available to the heat exchanger designers.

II.4.2. CHF MECHANISMS DURING FLOW BOILING IN MICROCHANNELS

Excellent reviews have been presented in the literature on the CHF mechanisms and correlations in conventional tubes (Katto [333], Hewitt [334], Bergles [335], Tong and Tang [336], and Celata and Mariani, [337]). Kandlikar [338] provides a comprehensive summary of these mechanisms as listed below:

- Flooding of the heater surface [339].
- Destruction of stability between the liquid–vapor interface [340,341].
- Coaxial two-phase instability [342].
- Liquid flow inhibition to the heater surface [343].
- Instability in vapor jets above nucleating bubbles [344].

- Critical Weber number based on a force balance [345].
- Small jet instability in the microlayer [346,347].
- Effect of size and geometry on vapor column instability [348].
- Contact angle effect [349].
- Temperature of the heater surface under dry patches [350].
- Incorporation of evaporation momentum force in a force balance at the base of a nucleating bubble [351].

CHF in microchannels has received considerable attention in the last decade. The heat transfer performance enhancements expected during flow boiling were not realized in the experiments conducted by researchers worldwide. The high-speed visualization techniques, employed by a number of researchers, identified the flow instability during nucleation and boiling in parallel channels as a major reason for the low heat transfer performance during flow boiling. They reported several methods to mitigate them—for example, Kandlikar et al. [352], Wang et al. [353], Kuo and Peles [354], and Kandlikar [355].

Kandlikar [356] and Kandlikar et al. [278] identified some of the critical factors influencing flow boiling in microchannels. Flow instability was listed as perhaps the most important factor that reduced the heat transfer coefficient as well as the CHF in microchannels. Bergles and Kandlikar [357] provide a comprehensive evaluation of factors responsible for flow boiling instabilities in microchannels. They identified upstream compressible volume instability and excursive instability in the parallel channels as being mainly responsible for the unstable operation. They further identified the presence of instabilities in a number of experimental CHF data sets reported in the literature. There is still a need to obtain accurate experimental CHF data under fully stabilized conditions over a broad range of operating conditions with different working fluids. A more detailed discussion is provided in a separate chapter of this book.

The predictive methods for CHF in microchannels have been largely based on empirical correlations derived from available experimental data. At high qualities, the film dryout mechanism seems to be appropriate, but the CHF attained in microchannels has been at relatively low qualities. The availability of the liquid phase in the two-phase flow at low qualities indicates that there must be a mechanism at play that prevents the liquid from rewetting the surface. This has been the basis for deriving a theoretical model that is presented next.

II.4.2.1. Theoretical Model for CHF in Microchannels

Kandlikar [351] proposed a theoretical model for pool boiling CHF based on the evaporation momentum force at an evaporating interface. This force is responsible for pushing liquid away and preventing the rewetting of the dry

heater surface. Kandlikar [338] extended this model to microchannels. A brief description of the underlying mechanisms and derivation is given below.

A schematic representation of the liquid–vapor interface near the heater surface is shown in Fig. II.14. The interface near the contact line is at a higher temperature and experiences intense evaporation resulting from the transient conduction and microconvection mechanisms. The higher specific volume of the vapor phase results in an unbalanced momentum force at the evaporating interface due to the phase change process. This evaporation momentum force causes the contact line and the interface close to the heater surface to move into the liquid phase.

The other forces acting on the interface near the contact line region are due to surface tension, inertia of the bulk flow, and shear force due to viscous effects. Kandlikar [338] derived these forces with a two-dimensional interface assumption, which has been successfully applied in the literature for pool boiling application. The resulting forces per unit length of the interface are given by the following equations:

$$F'_{S,1} = \sigma \cos \theta_R \quad (\text{II.34})$$

$$F'_{S,2} = \sigma \quad (\text{II.35})$$

$$F'_I = \frac{[G(1-x)((\pi/4)D^2)](G/\rho_m)}{\pi D} = \frac{4}{\pi} \frac{G^2(1-x)D}{\rho_m} \sim \frac{G^2(1-x)D_h}{\rho_m} \quad (\text{II.36})$$

where ρ_m is the specific volume averaged density given by:

$$\frac{1}{\rho_m} = \frac{x}{\rho_V} + \frac{1-x}{\rho_L} \quad (\text{II.37})$$

$$F'_\tau = \frac{\mu_L G(1-x)}{\rho_L} \quad (\text{II.38})$$

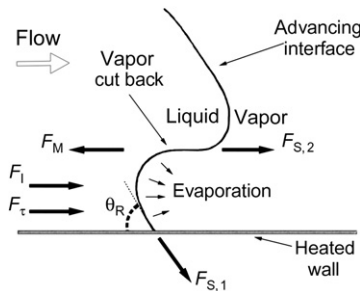


FIG. II.14. Schematic representation of the liquid-vapor interface near the heater surface at the CHF condition [338].

and

$$F'_M = \left(\frac{q}{h_{LV}} \right)^2 \frac{D_h}{\rho_V} \quad (\text{II.39})$$

The liquid–vapor interface facing the upstream is considered for determining the CHF condition. The evaporation momentum force causes the interface to push the liquid away backward against the flow, thereby increasing the dry surface of the heater, while the inertia, viscous, and surface tension forces act to restore the liquid on the dry patch (rewetting).

The CHF condition is reached when the evaporation momentum force exceeds the sum of the restoring surface tension, inertia, and shear forces. Introducing nondimensional parameters, the resulting equation takes the following form after further simplification.

$$K_{2,\text{CHF}} = a_1(1 + \cos \theta_R) + a_2 We(1 - x) + a_3 Ca(1 - x) \quad (\text{II.40})$$

where the nondimensional parameters are defined as follows:

K_2 is the ratio of the evaporation momentum and the surface tension forces introduced by Kandlikar [358].

$$K_{2,\text{CHF}} = \left(\frac{q_{\text{CHF}}}{h_{LV}} \right)^2 \left(\frac{D_h}{\rho_V \sigma} \right) \quad (\text{II.41})$$

We is the Weber number representing the ratio of the inertia to the surface tension forces:

$$We = \frac{G^2 D_h}{\rho_m \sigma} \quad (\text{II.42})$$

The capillary number Ca represents the ratio of the viscous force to the surface tension force:

$$Ca = \frac{\mu_L G}{\rho_L \sigma} \quad (\text{II.43})$$

Thirteen different experimental data sets with the working fluids water, R-12, R-113, R-123, R-22, R-236a, and R-245fa in flow channels of hydraulic diameters ranging from 127 μm to 3.36 mm were employed in evaluating the constants. The data were found to be divided in the following subregions.

- Low inertia region (LIR): $We < 900$.
 - High CHF subregion (LIR-HC)
 - Low CHF subregion (LIR-LC)
- High inertia region (HIR): $We \geq 900$.
 - High CHF subregion (HIR-HC)
 - Low CHF subregion (HIR-LC)

The final correlation takes the following form.

Low inertia region, LIR: $We < 900$:

High CHF subregion: LIR-HC – $L - D \leq 140$

$$K_{2,\text{CHF}} = a_1(1 + \cos \theta) + a_2We(1 - x) + a_3Ca(1 - x) \quad (\text{II.44})$$

Low CHF subregion: LIR-LC – $L - D \geq 230$

$$K_{2,\text{CHF}} = a_4[a_1(1 + \cos \theta) + a_2We(1 - x) + a_3Ca(1 - x)] \quad (\text{II.45})$$

High inertia region, HIR: $We \geq 900$:

High CHF subregion: HIR-HC – $L - D < 60$

$$K_{2,\text{CHF}} = a_1(1 + \cos \theta) + a_2We(1 - x) + a_3Ca(1 - x) \quad (\text{II.46})$$

Low CHF Subregion: HIR-LC – $L - D \geq 100$

$$K_{2,\text{CHF}} = a_4[a_1(1 + \cos \theta) + a_2We(1 - x) + a_3Ca(1 - x)] \quad (\text{II.47})$$

where the constants a_1 – a_4 are:

$$\begin{aligned} a_1 &= 1.03 \times 10^{-4}; \\ a_2 &= 5.78 \times 10^{-5}; \\ a_3 &= 0.783; \\ a_4 &= 0.125. \end{aligned} \quad (\text{II.48})$$

The above correlating scheme was able to correlate the data sets with an absolute mean error of 19.7%. A total of 76% of the data points fell within a 30% error band, while 93% of the data fell within a 50% error band. Figure II.15 shows a comparison of the data with 13 experimental data sets reported in the literature. Note that the references cited in Fig. II.15 correspond to those in the original publication by Kandlikar [338]. These are Qu and Mudawar [359], Inasaka and Nariai [360], Kosar et al. [361], Roach et al. [362], Kosar and Peles [363], Cheng et al. [364], Kosar et al. [365], Kuan and Kandlikar [366], Roday and Jensen [367], and Agostini et al. [368], respectively.

II.4.2.2. Effect of L/D Ratio on CHF

The effect of the length to diameter ratio, L/D , has been an important consideration in CHF modeling at macroscale in literature. It is well known that the CHF is affected by the inlet fluid condition as well as the length to diameter ratio. A simple energy balance shows that the L/D ratio is directly linked to these parameters:

$$G \frac{\pi}{4} D^2 (x_{\text{CHF}} - x_{\text{inlet}}) h_{\text{LV}} = \pi D L q_{\text{CHF}} \quad (\text{II.49})$$

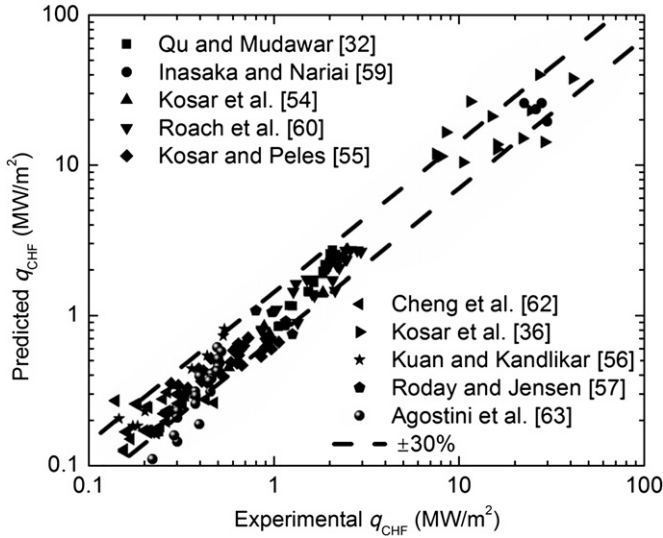


FIG. II.15. Comparison of the model with the experimental data. Note the citation numbers refer to those referred in the original publication.

Rearranging, the $L - D$ ratio at the CHF location is given by:

$$\left(\frac{L}{D}\right)_{\text{CHF}} = \frac{1}{4} \times (x_{\text{CHF}} - x_{\text{inlet}}) \left(\frac{q_{\text{CHF}}}{Gh_{\text{LV}}}\right)^{-1} \quad (\text{II.50})$$

It is thus seen that the L/D ratio effect is represented by the local quality and other parameters used in the model development. However, this ratio is seen to affect the ranges of the CHF in the low inertia region. Since the CHF is considered as the local phenomenon and no direct effect of inlet quality should therefore be expected, the effect of L/D seen in the experimental data may be indicative of the instability conditions present in the data sets as reported by Bergles and Kandlikar [357]. The effect of the L/D ratio on CHF is thus seen through its influence on the stability during the flow boiling process. The transition from the high CHF region to a low CHF region is seen to occur between 140 and 230 based on the available data. This boundary needs to be further studied to reveal the influence of any additional parameters affecting this transition.

II.4.2.3. Relative Influence of Surface Tension, and Viscous and Inertia Forces on CHF at Microscale

The relative importance of the surface tension, and viscous and inertia forces on the CHF mechanism changes as the channel diameter reduces from

conventional dimensions (>3 mm) to minichannels ($200\text{ }\mu\text{m}$ to 3 mm), and to microchannels (10 – $200\text{ }\mu\text{m}$). These effects can be studied using the model presented above.

Figures II.16–II.19 show the relative contributions from the three forces toward $K_{2,\text{CHF}}$ for water and R123 at two different mass fluxes. The relative contributions from the surface tension, and viscous and inertia forces toward the $K_{2,\text{CHF}}$ are shown in these figures as a function of the channel hydraulic diameter, respectively. The sum of these three contributions gives the value of $K_{2,\text{CHF}}$, from which the actual value of CHF can be calculated using Eq. (II.41).

For water, which has a high surface tension and a high value of latent heat of evaporation, Fig. II.16 shows that at a mass flux of $200\text{ kg/m}^2\text{s}$, the inertia force contribution is dominant above a diameter of about $100\text{ }\mu\text{m}$. Above a diameter of about 1 mm, the contributions from the viscous and the surface tension forces are negligible. However, between 10 and $100\text{ }\mu\text{m}$, the viscous force contribution dominates and the inertia and surface tension force contributions become of secondary importance. Below about $10\text{ }\mu\text{m}$ diameter, the viscous force contribution becomes dominant, and the inertia force contribution becomes quite negligible.

For the refrigerants, the latent heat is low, and the CHF for a given value of K_2 is correspondingly lower as compared to water. The inertia and surface

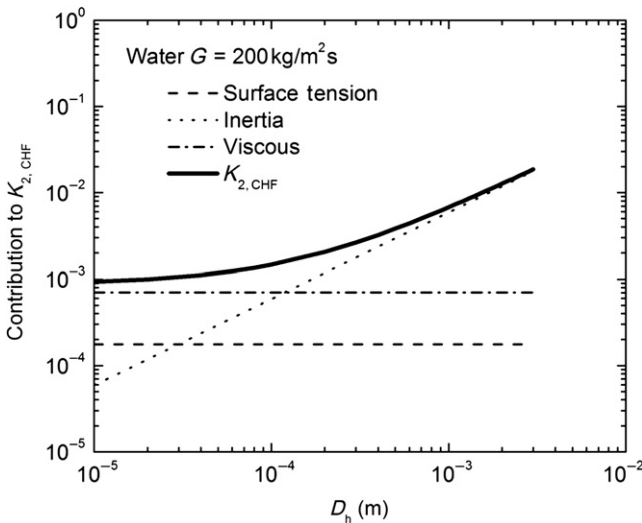


FIG. II.16. Contribution from surface tension, viscous and inertia forces toward the CHF condition as a function of channel hydraulic diameter for water at $G = 200\text{ kg/m}^2\text{s}$ [338].

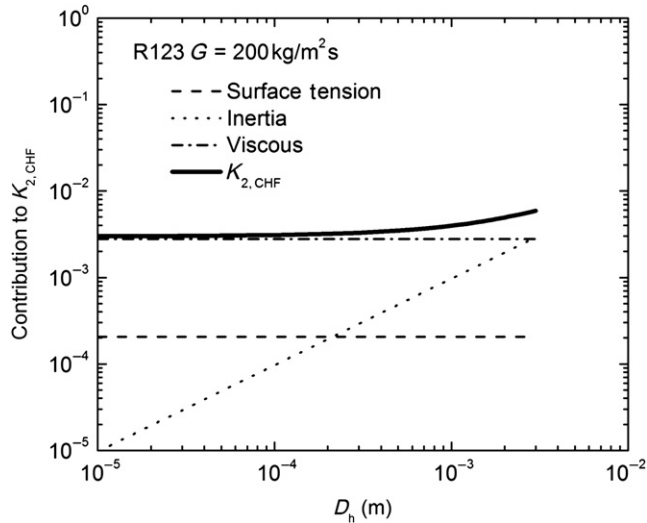


FIG. II.17. Contribution from surface tension, viscous and inertia forces toward the CHF condition as a function of channel hydraulic diameter for R123 at $G = 200 \text{ kg/m}^2 \text{ s}$ [338].

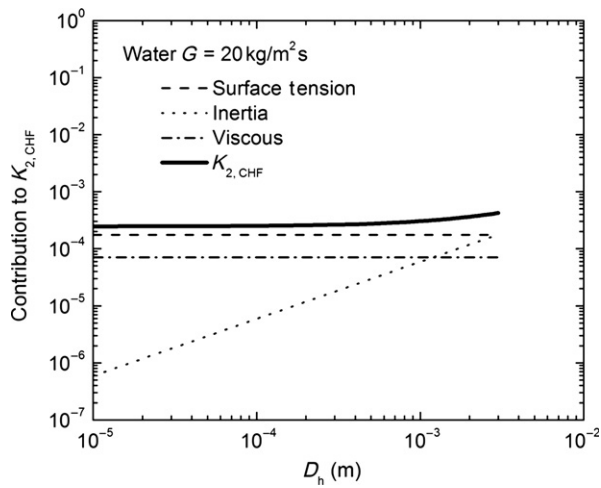


FIG. II.18. Contribution from surface tension, viscous and inertia forces toward the CHF condition as a function of channel hydraulic diameter for water at $G = 20 \text{ kg/m}^2 \text{ s}$ [338].

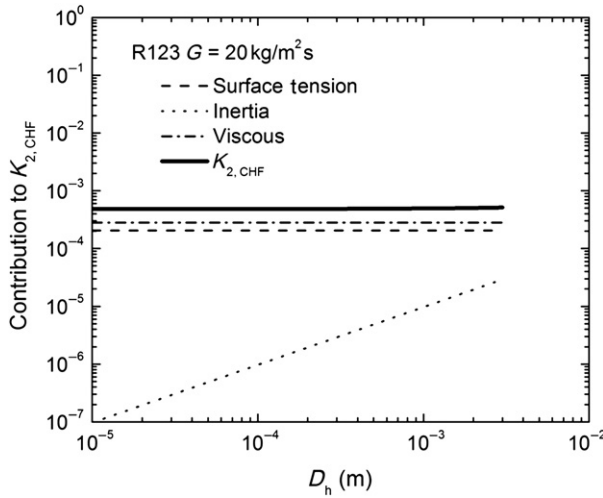


FIG. II.19. Contribution from surface tension, viscous and inertia forces toward the CHF condition as a function of channel hydraulic diameter for R123 at $G = 20 \text{ kg/m}^2 \text{ s}$ [338].

tension force contributions are lower compared to water. Figure II.17 shows the contribution of these forces to $K_{2,CHF}$. For R123, in channel diameters below about 1 mm, the viscous force is the dominating contributor at $200 \text{ kg/m}^2 \text{ s}$, while the contributions from the inertia and surface tension forces can be effectively neglected.

As the mass flux decreases, the inertia force reduces in an inverse square proportion, the viscous force decreases in an inverse proportion, while the surface tension contribution remains constant. Figure II.18 shows the contributions to $K_{2,CHF}$ at a lower mass flux of $10 \text{ kg/m}^2 \text{ s}$. It is seen that the inertia force contribution can be effectively neglected below a channel diameter of about 1 mm, while the viscous contribution becomes quite small as well. Thus for water at low flow rates, the surface tension force is the most dominating contributor.

In case of R123, as the mass flux reduces to $10 \text{ kg/m}^2 \text{ s}$, the contribution from the inertia force reduces even further making it quite insignificant even at diameters as high as 10 mm, while the viscous force contribution is still higher than the surface tension force contribution as shown in Fig. II.19.

It is seen from Figs. II.16–II.19 that as the scale of the system (diameter) changes, the relative importance of contributions from inertia, and viscous and surface tension forces change as well. The inertia force contribution decreases with the channel diameter, while the viscous and surface tension force contributions remain unaltered. However, the mass flux plays an important role as

well. As the mass flux reduces, the importance of the inertia force decreases dramatically, while the contribution from the viscous force decreases in an inverse proportion. Further, the properties of the working fluid, particularly surface tension, the density ratio of gas phase to liquid phase, and liquid viscosity play a significant role in determining the relative contributions from these forces. The actual CHF value further depends on the latent heat of evaporation, with fluids having a higher latent heat value yielding a higher CHF as expected.

II.4.3. CHF CORRELATIONS

There are a number of empirical correlations available in the literature. These correlations are derived from the available experimental data on CHF. The ranges of parameters and fluids used in the original correlation development, along with the correlations, are listed in [Table II.II](#). Although some of these correlations are based on a relatively large data set, the underlying instability present in some of the underlying experiments may have influenced the correlation. Nevertheless, these correlations provide important guidance in determining parametric trends and in estimating the CHF.

II.4.4. CONCLUDING REMARKS

CHF in microchannels is an important consideration in determining the safe operating limit of the flow boiling heat transfer process in a heat exchanger. Some of the applications foreseen for this type of heat exchanger are chip cooling and thermal control of biofluids, so reliable operation is extremely important.

The flow boiling process is influenced by flow maldistribution, instabilities, and specific system geometrical effects. Understanding CHF and predicting it accurately have been challenges that still remain unresolved even at macro-scale. Obtaining further experimental data and gaining a fundamental understanding of this phenomenon remain areas of immense research interest in the heat transfer community worldwide.

II.5. Conclusions and Research Directions

II.5.1. CONCLUSIONS

Fluid flow and heat transfer in microchannels encounter a number of additional issues due to the small flow passage sizes. To limit the excessive pressure drops, the heat exchangers employing microchannels are generally

TABLE II.II

SOME OF THE AVAILABLE CHF CORRELATIONS

Reference	Correlation	Comment
Katto [369]	$q_{\text{CHF}} = q_{\text{CHF0}} \left(1.0 + K \frac{\Delta h_{\text{sub,inlet}}}{h_{\text{LV}}} \right)$ $q_{\text{CHF01}} = 0.25 (G h_{\text{LV}}) \frac{1}{L/D_e}$ $q_{\text{CHF02}} = C (G h_{\text{LV}}) \text{We}^{-0.043 \frac{1}{L/D_e}}$ $q_{\text{CHF03}} = 0.15 (G h_{\text{LV}}) \left(\frac{\rho_V}{\rho_L} \right)^{0.133} \text{We}^{-1/3 \frac{1}{1+(0.0077L/D_e)}}$ $q_{\text{CHF04}} = 0.26 (G h_{\text{LV}}) \left(\frac{\rho_V}{\rho_L} \right)^{0.133} \text{We}^{-0.433 \frac{(L/D_e)^{0.171}}{1+(0.0077L/D_e)}}$ $C = 0.25 \text{ for } \frac{L}{D_e} < 50; C = 0.34 \text{ for } \frac{L}{D_e} > 50;$ $K_1 = 1; K_2 = \frac{0.261}{C \text{We}^{-0.043}}; K_3 = \frac{0.556(0.0308 + D_e)}{(\rho_V/\rho_L)^{0.133} \text{We}^{-1/3}}$ <p>When $q_{\text{CHF01}} < q_{\text{CHF02}}$, $q_{\text{CHF0}} = q_{\text{CHF01}}$, $K = K_1$ When $q_{\text{CHF01}} > q_{\text{CHF02}}$, if $q_{\text{CHF02}} < q_{\text{CHF03}}$, $q_{\text{CHF0}} = q_{\text{CHF02}}$, $K = K_2$ if $q_{\text{CHF02}} > q_{\text{CHF03}}$, if $q_{\text{CHF03}} < q_{\text{CHF04}}$, $q_{\text{CHF0}} = q_{\text{CHF03}}$, $K = K_3$ if $q_{\text{CHF03}} > q_{\text{CHF04}}$, $q_{\text{CHF0}} = q_{\text{CHF04}}$</p>	
Mishima and Ishii [370]	$q_{\text{CHF}} = \frac{A_{\text{ch}}}{A_{\text{h}}} h_{\text{LV}} \left[\frac{G \Delta h_{\text{sub,inlet}}}{h_{\text{LV}}} + \left(\frac{1}{C_0} - 0.11 \right) \sqrt{\rho_V g (\rho_L - \rho_V) D_e} \right]$ $C_0 = 1.35 - 0.35 \sqrt{\frac{\rho_V}{\rho_L}}$	
Sudo et al. [371]	$q_{\text{CHF}} = 0.005 h_{\text{LV}} G^{0.611} [\lambda \rho_V g (\rho_L - \rho_V)]^{0.195}$ $\lambda = \sqrt{\frac{\sigma}{(\rho_L - \rho_V) g}}$	
Shah [372]	$\frac{q_{\text{CHF}}}{G \cdot h_{\text{LV}}} = 0.124 \left(\frac{L}{D} \right)^{-0.89} \left(\frac{10^4}{Y_{\text{shah}}} \right)^n (1 - x_{\text{inlet}})$ $Y_{\text{shah}} = G^{18} \cdot D^{0.6} \left(\frac{c_p}{k_L \cdot \rho_L^{0.8} \cdot g^{0.4}} \right) \left(\frac{\mu_L}{\mu_V} \right)^{0.6}$ <p>When $Y_{\text{shah}} \leq 10^4$, $n = 0$ When $10^4 < Y_{\text{shah}} \leq 10^6$, $n = (D/L)^{0.54}$</p>	

(Continued)

TABLE II.II

(CONTINUED)

Reference	Correlation	Comment
Oh and Englert [373]	When $Y_{\text{shah}} > 10^6$, $n = \frac{0.12}{(1 - x_{\text{inlet}})^{0.5}}$ $q_{\text{CHF}} = \frac{A_{\text{sh}}}{A_{\text{h}}} h_{\text{LV}} \left[0.458 G \left(1.0 - \frac{\Delta h_{\text{Sub,inlet}}}{h_{\text{LV}}} \right) + 2.412 \sqrt{\lambda \rho_{\text{V}} g (\rho_{\text{L}} - \rho_{\text{V}})} \right]$	
Qu and Mudawar [359]	$\frac{q_{\text{CHF}}}{G h_{\text{LV}}} = 33.43 \left(\frac{\rho_{\text{V}}}{\rho_{\text{L}}} \right)^{1.11} \text{We}^{-0.21} \left(\frac{L}{D_{\text{c}}} \right)^{-0.36}$ $\text{We} = \frac{G^2 L}{\sigma \rho_{\text{L}}}$	
Wojtan et al. [374]	$\frac{q_{\text{CHF}}}{G h_{\text{LV}}} = 0.437 \left(\frac{\rho_{\text{V}}}{\rho_{\text{L}}} \right)^{0.073} \text{We}^{-0.24} \left(\frac{L}{D} \right)^{-0.72}$ $\text{We} = \frac{G^2 L}{\sigma \rho_{\text{L}}}$	
Zhang et al. [375]	$\frac{q_{\text{CHF}}}{G h_{\text{LV}}} = 0.0352 \left[\text{We} + 0.0119 \left(\frac{L}{D} \right)^{2.31} \left(\frac{\rho_{\text{V}}}{\rho_{\text{L}}} \right)^{0.361} \right]^{-0.295} \cdot \left(\frac{L}{D} \right)^{-0.311} \left[2.05 \left(\frac{\rho_{\text{V}}}{\rho_{\text{L}}} \right)^{0.170} - x_{\text{inlet}} \right]$ $\text{We} = \frac{G^2 D}{\sigma \rho_{\text{L}}}$	
Qi et al. [376]	$\frac{q_{\text{CHF}}}{G h_{\text{LV}}} = (0.214 + 0.140 \text{Co}) \left(\frac{\rho_{\text{V}}}{\rho_{\text{L}}} \right)^{0.133} \left(\frac{1}{\text{We}} \right)^{0.333} \frac{1}{1 + (0.03L/D)}$ $\text{We} = \frac{G^2 L}{\sigma \rho_{\text{L}}}$ $\text{Co} = \left[\frac{\sigma}{(\rho_{\text{L}} - \rho_{\text{V}}) g D^2} \right]^{0.5}$	
Kandlikar [338]	Eqs. (II.44)–(II.48) in this chapter	
Wu et al. [377]	$\frac{q_{\text{CHF}}}{G h_{\text{LV}}} = 0.60 \left(\frac{L}{D_{\text{c}}} \right)^{-1.19} x_{\text{exit}}^{0.817}$ $x_{\text{exit}} = \frac{q_{\text{CHF}}}{G h_{\text{LV}}} \frac{4L}{D_{\text{c}}} - \frac{\Delta h_{\text{Sub,inlet}}}{h_{\text{LV}}}$ $\frac{q_{\text{CHF}}}{G h_{\text{LV}}} = 0.25 \left(x_{\text{exit}} + \frac{\Delta h_{\text{Sub,inlet}}}{h_{\text{LV}}} \right) \left(\frac{L}{D_{\text{c}}} \right)^{-1}$	

operated in the laminar region. The single-phase heat transfer coefficient is quite high as compared to the macroscale heat exchangers essentially due to the small channel dimensions. The research in the microchannel heat transfer has been mainly driven by the chip cooling and micro heat exchanger applications in the last decade.

Single-phase heat transfer has been successfully applied to chip cooling using strip-fin enhancement structures. To limit the pressure drop, multiple parallel fluid flow paths are employed and flow lengths are kept to within a few millimeters. Heat fluxes up to 790 W/cm^2 have been successfully removed using water as the heat transfer fluid. Further efforts on developing more efficient heat transfer surfaces with low pressure drop penalty are expected to continue as the microchannels find their usage in more diverse applications.

Our current understanding of the single-phase liquid heat transfer is quite comprehensive. However, a detailed understanding of the flow boiling phenomenon is lacking. The flow boiling systems are still facing a number of operational issues and their performance has not met the expectations. The specific research areas are elaborated in the following sections.

II.5.2. RESEARCH DIRECTIONS

II.5.2.1. Void Fraction and Liquid Film Thickness

Void fraction information is useful in the design and modeling of microscale processes in various applications. In developing models for adiabatic two-phase flows, such information is helpful in designing drug delivery and diagnostic devices. The change in the void fraction behavior as a function of channel dimensions from macroscale to microscale is an important discovery that needs to be further evaluated. Additionally, there is a need to evaluate the effects of the following parameters on void fraction:

- a. Effect of channel aspect ratio for rectangular channels.
- b. Void fraction in other channel geometries, such as triangular and trapezoidal cross-sections.
- c. Effect of test section length (length to diameter ratio may be a better correlating parameter).
- d. Effect of entrance condition.
- e. New techniques are needed to measure local void fraction and liquid film thickness accurately.

Void fraction measurement using optical techniques has been used extensively in the literature. These techniques are limited to transparent test sections. They are also affected by the refraction at the curved interfaces. During annular flow, accurate liquid film thickness measurement is needed for

determining the void fraction. Since the films are only a few micrometers in thickness on the microchannel walls, any errors in their measurement will be significantly magnified in the void fraction estimation. The optical techniques are also limited to transparent sections.

New techniques to measure liquid film thickness in opaque channels are needed. Some of the available techniques such as fluorescence and capacitance based methods are expensive and can be applied only in high-end laboratory settings. They are not easily adaptable to practical systems. It is recommended that further research in this area be conducted in developing inexpensive techniques to measure liquid film thickness and local void fraction in a microchannel.

II.5.2.2. Flow Patterns and Bubble Growth

Flow patterns in adiabatic and boiling two-phase flows in microchannels have been at the forefront of research efforts during the last decade. The main drive for these efforts is to unravel the underlying mechanism in both adiabatic and flow boiling systems. Some of the ideas where future research efforts are needed are:

Adiabatic two-phase flows:

- f. Effect of surface conditions on the flow patterns (hydrophobic and hydrophilic surfaces), including nanostructures on flow patterns.
- g. Effect of microscale structures and roughness elements on flow patterns.
- h. Modeling of flow parameters to predict flow patterns.

Flow boiling:

- i. Effect of multiscale surface elements on nucleation, bubble growth, and flow patterns.
- j. New techniques to identify flow patterns in nontransparent channels under high heat flux conditions.
- k. Durability of surface coatings for hydrophobic and hydrophilic surfaces.
- l. Modeling of flow and geometrical parameters to predict flow patterns.

II.5.2.3. Heat Transfer

Development of appropriate flow boiling heat transfer enhancement techniques is perhaps the most urgent topic of current interest. The improvements seen during flow boiling in macroscale channels have not been realized in microchannels. At this time, it is not clear what specific techniques hold promise in providing such enhancement in microchannels. A thorough investigation of the effects of different enhancement strategies on improving

boiling performance is recommended. Some of the techniques that are identified include:

- m. Efficient techniques employed in fluid mixing application.
- n. Turbulence generators.
- o. Effective microstructures of different shapes, sizes, and orientations.

A different research strategy may be employed by considering the flow boiling process at the system level. Currently the research is focused on systems with subcooled liquid entry. Effect of different quality inlet on the system performance may be studied. Another way is to remove vapor from the channels to provide a higher heat transfer coefficient and CHF.

At the fundamental level, efforts need to be intensified in developing experiments to shed light on the flow boiling and CHF mechanisms. These efforts will provide new directions for heat transfer enhancement. The overall goal is to exceed the performance seen in single-phase flow with the implementation of offset strip fins. Such aggressive elements may not be needed during flow boiling, as the flow resistance offered by the fins to vapor may result in extremely high pressure drops. New concepts need to be identified that are suitable for enhancing flow boiling.

II.5.2.4. Flow Instability and CHF

Flow instability is an inherent concern facing all flow boiling systems. A clear understanding of the underlying phenomena has been established for macroscale systems that are employed in nuclear and other power and process industries. A clear identification of parametric ranges that lead to unstable operation needs to be developed. As the next step, active and passive techniques are needed to effectively mitigate the negative effects arising from the unstable operation, such as deterioration in heat transfer and CHF.

Our understanding of CHF is currently being hampered by the presence of instabilities. CHF values under stable operating conditions need to be established after ascertaining the flow stability. These two research efforts should be combined as the main penalty from the unstable operation is seen through a drastic reduction in the CHF.

Similar to heat transfer enhancement techniques, specific techniques for enhancing CHF are needed. Some of the possibilities include:

- p. Nanostructures.
- q. Hydrophilic coatings.
- r. Microscale structures.
- s. Hybrid microscale and nanoscale structures.
- t. Enhancement techniques found useful in micromixer applications.

II.5.2.5. New Applications

Finally, research on new applications of flow boiling is long overdue. One area is to use microscale flow boiling in large-scale systems. Heat exchangers, reboilers, distillation columns, high efficiency heat exchangers in air separation and chemical process industries are expected to provide significant performance enhancements. Overall, the application of micro heat exchangers in energy sector is expected to yield large returns as new sources and techniques for harvesting energy are being studied worldwide. Pharmaceutical industry is also expected to benefit significantly by implementing microchannels in the process equipment.

Nomenclature

A	Constant in Eq. (II.28)
A_{ch}	Channel cross-sectional area, m^2
A_{h}	Heated inside area, m^2
a_1-a_4	Constants in Eqs. (II.40), (II.44)–(II.47), values given in Eq. (II.48)
B	Constant in Eq. (II.28)
C	Constants in empirical correlations [369], Table II.II
C_0	Parameter in empirical correlations [370], Table II.II
C_1-C_2	Constants in Eqs. (II.8)–(II.14)
Ca	Capillary number, defined by Eq. (II.30) or (II.43)
Co	Confinement number [376], Table II.II
c_p	Specific heat capacity at constant pressure (J/kg K) [372], Table II.II
D	Bubble diameter, channel diameter, or tube diameter, m
D_e	Equivalent diameter, same as hydraulic diameter, m
D_h	Hydraulic diameter, m
E_1	Parameter defined by Eq. (II.23)
E_2	Parameter defined by Eq. (II.24)
F	Force, N
F'	Force per unit length, N/m
F_S	Surface tension force
G	Mass flux, $\text{kg/m}^2 \text{s}$
g	Gravitational acceleration, m/s^2
h	Heat transfer coefficient, $\text{W/m}^2 \text{K}$
h_{LV}	Latent heat of vaporization, J/kg
Δh_{Sub}	Subcooling enthalpy, J/kg
j	Superficial velocity, m/s
k	Thermal conductivity, W/m K
K	Inlet subcooling parameter in empirical correlations [369], Table II.II

K_1-K_3	Parameters in empirical correlations [369], Table II.II
K_2	Nondimensional group introduced by Kandlikar [358], Eq. (II.41)
L	Length, m
\dot{m}	Mass flow rate, kg/s
n	Parameter in empirical correlation [372], Table II.II
P_V	Vapor pressure, Pa
P_L	Liquid pressure, Pa
Q	Volumetric flow rate, m ³ /s
q	Heat flux, W/m ²
q_{CHF}	Heat flux at CHF, W/m ²
q_{CHF0}	CHF based on channel heated inside area for zero inlet subcooling
q_{CHF01}	Parameters in empirical correlations [369], Table II.II
to	
q_{CHF04}	
q''	Heat flux, W/m ²
r	Radii, m
Re	Reynolds number
Re_{crit}	Critical Reynolds number
S	Slip ratio
T	Temperature, °C
ΔT	Temperature difference, °C
U	Velocity, m/s
We	Weber number, defined by Eq. (II.26) or (II.42)
x	Quality (defined as the ratio of the mass flow rate of vapor to the total mass flow rate)
y	Parameter defined by Eq. (II.22)
Y_{shah}	Shah's correlation parameter [372], Table II.II

Greek symbols

α	Void fraction, or half angle at the corner included by two channel walls, Eq. (II.33)
α_{Hom}	Homogeneous void fraction
β	Volume flow fraction
δ	Film thickness
δ_0	Initial film thickness
δ_t	Thermal boundary layer thickness, m
ε	Void fraction, same as α
θ	Contact angle, °
θ_1	Contact angle on one channel surface, °
θ_2	Contact angle on the adjoining surface, °

θ_R	Receding contact angle, $^\circ$
λ	Parameter in empirical correlations, Sudo et al. [371] and Oh and Englert [373], Table II.II
μ	Dynamic viscosity, kg/m s
ρ	Density, kg/m ³
ρ_m	Average density, given by Eqn. (II.37)
σ	Surface tension, N/m

Subscripts

c	Cavity
CHF	At critical heat flux condition
crit	Critical
eq	Equivalent
exit	At the exit section
G	Gaseous phase
I	Inertia
inlet	At the inlet section
L	Liquid phase
M	Evaporation momentum
min	Minimum
max	Maximum
ONB	onset of nucleate boiling
r	Receding
S	Surface Tension
Sat	Saturation
Sub	Subcooling
τ	Shear (viscous)
V	Vapor
wall	Channel Wall

References

- [1] D.B. Tuckerman, R.F. Pease, High performance heat sinking for VLSI, IEEE Electron. Device Lett. EDL-2 (1981) 126–129.
- [2] R.J. Phillips, Microchannel heat sinks, in: A. Bar-Cohen, A.D. Kraus (Eds.), Advances in Thermal Modeling of Electronic Components and Systems, Hemisphere, New York, NY, 1990 (Chapter 3).
- [3] M.M. Rahman, F. Gui, Experimental measurements of fluid flow and heat transfer in micro-channel cooling passages in a chip substrate, Proceedings of ASME International Electronics Packaging Conference, 29 September–02 October, vol. 4-2, ASME publications, Binghamton, NY, 1993, pp. 685–692.

- [4] K. Kawano, K. Minakami, H. Iwasaki, M. Ishizuka, Microchannel heat exchanger for cooling electrical equipment, *ASME HTD* 361(3) (1998) 173–180.
- [5] T.M. Harms, M.J. Kazmierczak, F.M. Gerner, Developing convective heat transfer in deep rectangular microchannels, *Int. J. Heat Fluid Flow* 20 (1999) 149–157.
- [6] W. Qu, I. Mudawar, Experimental and numerical study of pressure drop and heat transfer in a single-phase microchannel heat sink, *Int. J. Heat Mass Transfer* 45(12) (2002) 2549–2565.
- [7] I. Mudawar, M.B. Bowers, Ultra high critical heat flux (CHF) for subcooled water flow boiling, Part I: CHF data and parametric effects for small diameter tubes, *Int. J. Heat Mass Transfer* 42 (1999) 1405–1428.
- [8] D.D. Hall, I. Mudawar, Critical heat flux (CHF) for water flow in tubes, Part II: subcooled CHF correlations, *Int. J. Heat Mass Transfer* 43 (2000) 2605–2640.
- [9] S.G. Kandlikar, W.J. Grande, Evolution of microchannel flow passages—thermohydraulic performance and fabrication technology, *Heat Transfer Eng.* 24(1) (2003) 3–17.
- [10] M. Kawaji, P.M. Chung, Unique characteristics of adiabatic gas liquid flows in microchannels: diameter and shape effects on flow patterns, void fraction and pressure drop, ICMM2003-1013, Proceedings of 1st International Conference on Microchannels and Minichannels, ASME, New York, 2003, pp. 115–127.
- [11] M. Suo, P. Griffith, Two phase flow in capillary tubes, *ASME J. Basic Eng.* 86 (1964) 576–582.
- [12] P.A. Kew, K. Cornwell, Correlations for the prediction of boiling heat transfer in small diameter channels, *Appl. Thermal Eng.* 17 (1997) 705–715.
- [13] N. Brauner, D. Moalem-Maron, Identification of the range of small diameter conduits regarding two phase flow transition, *Int. Commun. Heat Mass Transfer* 19 (1992) 29–39.
- [14] S.S. Mehendale, A.M. Jacobi, R.K. Shah, Fluid flow and heat transfer at micro and meso scales with application to heat exchanger design, *Appl. Mech. Rev.* 53(7) (2000) 175–193.
- [15] S.G. Kandlikar, J. Shailesh, S. Tian, Effect of channel roughness on heat transfer and fluid flow characteristics at low Reynolds numbers in small diameter tubes, Proceedings of 35th National Heat Transfer Conference, ASME, Anaheim, CA, 2001, Paper 12134.
- [16] Z. Feng, A. Serizawa, Two-phase flow patterns in ultra-small channels, 2nd Japanese–European Two-Phase Flow Group Meeting, Tsukuba, Japan, 2000.
- [17] W. Fritz, Berechnung des Maximalvolumens von Dampfblasen, *Phys. Z.* 36 (1935) 379–388.
- [18] W. Li, Z. Wu, A general criterion for evaporative heat transfer in micro/mini-channels, *Int. J. Heat Mass Transfer* 53 (2010) 1967–1976.
- [19] T. Harirchian, S.V. Garimella, A comparative flow regime map for microchannel flow boiling with quantitative transition criteria, *Int. J. Heat mass Transfer* 53 (2010) 2694–2702.
- [20] A.E. Bergles, S.G. Kandlikar, On the nature of critical heat flux in microchannels, *ASME J. Heat Transfer* 127 (2005) 101–107.
- [21] M. Groll, R. Mertz, Minichannel heat transfer: an overview on activities in Europe, Proceedings of 1st International Conference on Microchannels and Minichannels, Rochester, NY, ASME, Paper no. ICMM2003-1002, 2003, pp 7–14.
- [22] P. Cheng, H.Y. Wu, Mesoscale and microscale phase change heat transfer, *Adv. Heat Transfer* 39 (2006) 461–573.
- [23] P. Cheng, H.Y. Wu, F.J. Hong, Phase change heat transfer in microsystems, *ASME J. Heat Transfer* 129 (2007) 101–108.
- [24] P. Cheng, G.D. Wang, X.J. Quan, Recent work on boiling and condensation in microchannels, *ASME J. Heat Transfer* 131 (2009) 043211-1–043211-15.
- [25] J.D. Lee, C. Pan, Dynamics of multiple parallel boiling channel systems with forced flows, *Nucl. Eng. Des.* 192 (1999) 31–44.
- [26] C. Vlasie, H. Machi, J. Guilpart, B. Agostini, Flow boiling in small diameter channels, *Int. J. Refrig.* 27 (2004) 191–201.

- [27] L. Zhang, E.N. Wang, K.E. Goodson, T.W. Kenny, Phase change phenomena in silicon microchannels, *Int. J. Heat Mass Transfer* 48 (2005) 1572–1582.
- [28] E. Ishibashi, K. Nishikawa, Saturated boiling heat transfer in narrow spaces, *Int. J. Heat Mass Transfer* 12 (1969) 863–894.
- [29] S.G. Kandlikar, Fundamental issues related to flow boiling in minichannels and microchannels, *ExHFT-5*, 1, Edizioni ETS, Pisa, Italy, 2001, pp. 129–146.
- [30] S.G. Kandlikar, Fundamental issues related to flow boiling in mini channels and micro channels, *Exp. Thermal Fluid Sci.* 26 (2002) 389–407.
- [31] S.G. Kandlikar, Two phase flow patterns, pressure drop and heat transfer during boiling in minichannel flow passages of compact evaporators, *Heat Transfer Eng.* 23(1) (2002) 5–23.
- [32] J.R. Thome, Boiling in microchannels: a review of experiment and theory, *Int. J. Heat Fluid Flow* 25 (2004) 128–139.
- [33] L.P. Yarin, A. Mosyak, G. Hetsroni, Boiling in microchannels, in: *Fluid Flow, Heat Transfer and Boiling in Microchannels*, Springer, Berlin, 2009.
- [34] S.S. Bertsch, E.A. Groll, S.V. Garimella, Review and comparative analysis of studies on saturated flow boiling in small channels, *Nanoscale Microscale Thermophys. Eng.* 12 (2008) 187–227.
- [35] L. Consolini, Convective Boiling Heat Transfer in a Single Microchannel, Ph.D. Thesis, EPFL, Lausanne, Switzerland, 2008.
- [36] D. Bogojevic, K. Sefiane, A.J. Walton, H. Lin, G. Cummins, Two phase flow instabilities in a silicon microchannels heat sink, *Int. J. Heat Fluid Flow* 30 (2009) 854–867.
- [37] J.A. Boure, A.E. Bergles, L.S. Tong, Review of two phase flow instability, *Nucl. Eng. Des.* 25 (1973) 165–192.
- [38] L. Tadrist, Review on two phase flow instabilities in narrow spaces, *Int. J. Heat Fluid Flow* 28(1) (2007) 54–62.
- [39] E. Lorenzini, A simplified method proposal for practical determination of a periodic two phase flow instability, *Int. J. Multiphase Flow* 7(6) (1981) 635–645.
- [40] G. Ribatski, L. Wojtan, J.R. Thome, An analysis of experimental data and prediction methods for two phase frictional pressure drop and flow boiling heat transfer in micro-scale channels, *Exp. Thermal Fluid Sci.* 31 (2006) 1–19.
- [41] S. Kakac, B. Bon, A review of two-phase flow dynamic instabilities in tube boiling systems, *Int. J. Heat Mass Transfer* 51 (2008) 399–433.
- [42] S.V. Garimella, C.B. Sobhan, Transport in microchannels—a critical review, *Ann. Rev. Heat Transfer* 13 (2003) 1–50.
- [43] Z.L. Yang, B. Palm, B.R. Sehgal, Numerical simulation of bubbly two-phase flow in a narrow channel, *Int. J. Heat Mass Transfer* 45 (2002) 631–639.
- [44] Y.H. Qian, D. D’Humières, P. Lallemand, Lattice BGK models for Navier–Stokes equation, *Europhys. Lett.* 17(6) (1992) 479–484.
- [45] R.R. Nourgaliev, T.N. Dinh, B.R. Sehgal, Numerical simulation of droplet deformation and break-up by a lattice-Boltzmann method, *Proceedings of 3rd International Conference on Multiphase Flow*, Lyon, France, 1998, pp. 8–12.
- [46] Z.L. Yang, T.N. Dinh, R.R. Nourgaliev, B.R. Sehgal, Parametric investigation of two-phase flow characteristics in a debris particle bed by a lattice-Boltzmann model, *Proceedings of 2nd International Symposium on Two-phase Flow Modeling and Experimentation*, Pisa, Italy, May 23–25, 1999.
- [47] Z.L. Yang, T.N. Dinh, R.R. Nourgaliev, B.R. Sehgal, Numerical investigation of bubble growth, detachment and coalescence characteristics by a lattice-Boltzmann model, *33rd National Heat Transfer Conference*, Albuquerque, NM, 1999, pp. 15–17.
- [48] Z.L. Yang, T.N. Dinh, R.R. Nourgaliev, B.R. Sehgal, Numerical investigation of boiling regime transition mechanism by a lattice-Boltzmann model, *NURETH-9*, San Francisco, CA, October 3–8, 1999.

- [49] X. Shan, H. Chen, Lattice Boltzmann model for simulating flows with multiple phases and components, *Phys. Rev. E* 47(3) (1993) 1815–1819.
- [50] N.S. Martys, H. Chen, Simulation of multicomponent fluids in complex three-dimensional geometries by the lattice Boltzmann method, *Phys. Rev. E* 53(1) (1996) 743–750.
- [51] E. White, R.H. Beardmore, The velocity of rise of single cylindrical bubbles through liquids contained in vertical tubes, *Chem. Eng. Sci.* 17(5) (1962) 351–361.
- [52] R. Revellin, J.R. Thome, A new type of adiabatic flow pattern map for boiling heat transfer in microchannels, *J. Micromech. Microeng.* 17 (2007) 788–796.
- [53] J. Kaew-On, K. Sakamatapan, S. Wongwises, Flow boiling heat transfer of R 134a in the multiport minichannel heat exchangers, *Exp. Thermal Fluid Sci.* 35 (2011) 364–374.
- [54] S. Saisorn, J. Kaew-On, S. Wongwises, Flow pattern and heat transfer characteristics of R-134a refrigerant during flow boiling in a horizontal circular mini-channel, *Int. J. Heat Mass Transfer* 53 (2010) 4023–4038.
- [55] S. Saisorn, S. Wongwises, The effects of channel diameter on flow pattern, void fraction and pressure drop of two-phase air-water flow in circular micro-channels, *Exp. Thermal Fluid Sci.* 34(4) (2010) 454–462.
- [56] S. Saisorn, S. Wongwises, Flow pattern, void fraction and pressure drop of two-phase air-water flow in a horizontal circular micro-channel, *Exp. Thermal Fluid Sci.* 32(3) (2008) 748–760.
- [57] A.D. Giavedoni, F.A. Saita, The rear meniscus of a long bubble steadily displacing a Newtonian liquid in a capillary tube, *Phys. Fluids* 11(4) (1999) 786–794.
- [58] S.H. Park, J.G. Weng, C.L. Tien, A molecular dynamics study on surface tension of micro-bubbles, *Int. J. Heat Mass Transfer* 44 (2001) 1849–1856.
- [59] S.M. Thompson, K.E. Gubbins, J.P.R.B. Walton, R.A.R. Chantry, J.S. Rowlinson, A molecular dynamics study of liquid drops, *J. Chem. Phys.* 81 (1984) 530–542.
- [60] J.S. Rowlinson, B. Widom, *Molecular Theory of Capillarity*, Oxford University Press, New York, NY, 1982.
- [61] J. Israelachvili, *Intermolecular and Surface Forces*, second ed., Academic Press, San Diego, 1992.
- [62] J.G. Weng, S.H. Park, C.L. Tien, Interfacial ambiguities in microdroplets and microbubbles, *Microscale Thermophys. Eng.* 4 (2000) 83–87.
- [63] M.P. Allen, D.J. Tildesley, *Computer Simulation of Liquids*, Oxford University Press, Oxford, UK, 1987.
- [64] J.M. Haile, *Molecular Dynamics Simulation*, Wiley, New York, NY, 1992.
- [65] S. Maruyama, Molecular dynamics method for microscale heat transfer, in: (W.J. Minkowycz, E.M. Sparrow (Eds.)), vol. 2, Taylor and Francis, New York, NY, 2000, pp. 189–226.
- [66] W.J. Yang, K.T. Tsutsui, Overview of boiling on microstructures—macro bubbles from micro heaters, *Microscale Thermophys. Eng.* 4 (2000) 7–24.
- [67] M.E. Parker, D.M. Heyes, Molecular dynamics simulation of stretched water: local structure and spectral signatures, *J. Chem. Phys.* 108 (1998) 9039–9049.
- [68] T. Kinjo, M. Matsumoto, Cavitation processes and negative pressure, *Fluid Phase Equilib.* 144 (1998) 343–350.
- [69] T. Kinjo, K. Ohguchi, K. Yasuoka, M. Matsumoto, Computer simulation of fluid phase change: vapor nucleation and bubble formulation dynamics, *Comput. Mater. Sci.* 14 (1999) 138–141.
- [70] S.H. Park, J.G. Weng, C.L. Tien, Cavitation and bubble nucleation using molecular dynamics simulation, *Microscale Thermophys. Eng.* 4 (2000) 161–175.
- [71] R.C. Tolman, The effect of droplet size on surface tension, *J. Chem. Phys.* 17 (1949) 333–337.
- [72] X.F. Peng, B.X. Wang, Forced convection and flow boiling heat transfer for liquid flowing through microchannels, *Int. J. Heat Mass Transfer* 36(14) (1993) 3421–3427.

- [73] X.F. Peng, H.Y. Hu, B.X. Wang, Boiling nucleation during liquid flow in microchannels, *Int. J. Heat Mass Transfer* 41(1) (1998) 101–106.
- [74] L. Jiang, M. Wong, Y. Zohar, Forced convection boiling in a microchannel heat sink, *J. Microelectromech. Syst.* 10 (2001) 80–87.
- [75] J.E. Kennedy, G.M. Roach Jr., M.F. Dowling, S.I. Abdel-Khalik, S.M. Ghiaasiaan, S.M. Jeter, et al., The onset of flow instability in uniformly heated horizontal microchannels, *ASME J. Heat Transfer* 122 (2000) 118–125.
- [76] T. Sato, H. Matsumura, On the conditions of incipient subcooled boiling and forced convection, *Bull. JSME* 7 (1963) 392–398.
- [77] E.J. Davis, G.H. Anderson, The incipience of nucleate boiling in forced convection flow, *AIChE J.* 12 (1966) 774–780.
- [78] J.H. Collier, J.R. Thome, *Convective Boiling and Condensation*, third ed., Oxford University Press, Oxford, UK, 1994.
- [79] S. Levy, Forced convection subcooled boiling—prediction of vapor volumetric fraction, *Int. J. Heat Mass Transfer* 10 (1967) 951–965.
- [80] F.W. Staub, The void fraction in subcooled boiling—prediction of the initial point of net vapor generation, *ASME J. Heat Transfer* 90 (1968) 151–157.
- [81] R.A.M. Al-Hayes, R.H.S. Winterton, Bubble diameter in detachment in flowing liquids, *Int. J. Heat Mass Transfer* 24 (1981) 223–230.
- [82] R.H.S. Winterton, Flow boiling: prediction of bubble departure, *Int. J. Heat Mass Transfer* 27 (1984) 1422–1424.
- [83] J.T. Rogers, M. Salcudean, Z. Abdullah, D. Mcleod, D. Poirier, The onset of significant void in up-flow boiling of water at low pressure and velocities, *Int. J. Heat Mass Transfer* 30 (1987) 2247–2260.
- [84] W. Qu, I. Mudawar, Prediction and measurement of incipient boiling heat flux in microchannel heat sinks, *Int. J. Heat Mass Transfer* 45 (2002) 3933–3945.
- [85] W.J. Yang, N.L. Zhang, Micro and nanoscale heat transfer phenomena research trends, in: (B.X. Wang (Ed.), *Higher Education Press*, Beijing, 1992, pp. 1–15.
- [86] C.L. Tien, T.Q. Qiu, P.M. Norris, Microscale thermal phenomena in contemporary technology, *Thermal Sci. Eng.* 2(1) (1994) 1–11.
- [87] M.B. Bowers, I. Mudawar, High flux boiling in low flow rate, low pressure drop minichannel and microchannel heat sinks, *Int. J. Heat Mass Transfer* 37(2) (1994) 321–332.
- [88] L. Lin, K.S. Udell, A.P. Pisano, Liquid–vapor phase transition and bubble formation in microstructures, *Thermal Sci. Eng.* 2(1) (1994) 52–59.
- [89] X.F. Peng, B.X. Wang, Cooling characteristics with microchanneled structures, *J. Enhanced Heat Transfer* 1(4) (1994) 315–326.
- [90] X.F. Peng, B.X. Wang, Liquid flow and heat transfer in microchannels with/without phase change, KN lecture, 10th International Heat Transfer Conference, Brighton, England, vol. 1, 1994, pp. 159–178.
- [91] X.F. Peng, B.X. Wang, Evaporating space and fictitious boiling for internal evaporation of liquid, *Sci. Found. China* 2(2) (1994) 55–59, English Version.
- [92] X.F. Peng, G.P. Peterson, B.X. Wang, Flow boiling of binary mixtures in microchanneled plates, *Int. J. Heat Mass Transfer* 39(6) (1996) 1257–1264.
- [93] X.F. Peng, B.X. Wang, G.P. Peterson, H.B. Ma, Experimental investigations of heat transfer in flat plates with rectangular microchannels, *Int. J. Heat Mass Transfer* 38(1) (1995) 127–137.
- [94] B.X. Wang, X.F. Peng, H.Y. Hu, Study of bubble formation conditions for liquid flow boiling in microchannels, *Proceedings of 6th National Conference in Engineering Thermophysics*, Wuhan, China, 1996.

- [95] Y.Y. Hsu, On the size range of active nucleating cavities on a heating surface, *ASME J. Heat Transfer* 84 (1962) 207–213.
- [96] L.S. Ding, M.J. Jiang, H. Sun, Measurement of heat transfer characteristics and friction factors for the flow boiling of CFC-12 through triangular microchannels used for the refrigerating evaporators, in: (B.X. Wang (Ed.), Higher Education Press, Beijing, China, 1996, pp. 360–365.
- [97] G. Hetsroni, J.L. Zakin, Z. Lin, A. Mosyak, E.A. Pancallo, R. Rozenblit, The effect of surfactants on bubble growth, wall thermal patterns and heat transfer in pool boiling, *Int. J. Heat Mass Transfer* 44 (2001) 485–497.
- [98] W.T. Wu, Y.M. Yang, J.R. Maa, Nucleate pool boiling enhancement by means of surfactant additives, *Exp. Thermal Fluid Sci.* 18 (1998) 195–209.
- [99] S.C. Yao, Y. Chang, Pool boiling heat transfer in a confined space, *Int. J. Heat Mass Transfer* 26 (1983) 841–848.
- [100] P.C. Lee, F.G. Tseng, C. Pan, Bubble dynamics in microchannels, Part II: two parallel microchannels, *Int. J. Multiphase Flow* 47 (2004) 5591–5601.
- [101] G. Hetsroni, A. Mosyak, E. Pogrebnyak, Z. Segal, Periodic boiling in parallel microchannels at low vapor quality, *Int. J. Multiphase Flow* 32 (2006) 1141–1159.
- [102] A.A. Arcanjo, J.O. Freitas, C.B. Tibirica, G. Ribatski, Two-phase flow characteristics during flow boiling of halocarbon refrigerants in micro-scale channels, ECI International Conference on Boiling Heat Transfer, Florianopolis-SC, Brazil, May 3–7, 2009.
- [103] D. Barnea, Y. Luninski, Y. Taitel, Flow pattern in horizontal and vertical two-phase flow in small diameter pipes, *Can. J. Chem. Eng.* 61 (1983) 617–620.
- [104] H.O.M. Felcar, G. Ribatski, J.M. Saiz-Jabardo, A gas–liquid flow pattern predictive method for macro- and mini-scale round channels, *Proceedings of 10th UK Heat Transfer Conference*, Edinburgh, Scotland, 2007.
- [105] Y. Taitel, A.E. Dukler, A model for predicting regime transitions in horizontal and near horizontal gas–liquid flow, *AIChE J.* 22 (1976) 47–55.
- [106] A. Ullmann, N. Brauner, The prediction of flow pattern maps in minichannels, *Multiphase Sci. Technol.* 19(1) (2007) 49–73.
- [107] R. Revellin, B. Agostini, T. Ursenbacher, J.R. Thome, Experimental investigation of velocity and length of elongated bubbles for flow of R134-a in a 0.5 mm microchannel, *Exp. Thermal Fluid Sci.* 32 (2008) 870–881.
- [108] B. Agostini, R. Revellin, J.R. Thome, Elongated bubbles in microchannels, Part I: experimental study and modeling of elongated bubble velocity, *Int. J. Multiphase Flow* 34 (2008) 590–601.
- [109] R. Revellin, B. Agostini, J.R. Thome, Elongated bubbles in microchannels, Part II: experimental study and modeling of bubble collisions, *Int. J. Multiphase Flow* 34 (2008) 602–613.
- [110] M. Vaillancourt I.G. Hassan, K.K. Pehlivan, Two-phase flow regime transitions in microchannels, *Proceedings of 5th International Conference on Multiphase Flow*, Yokohoma, Japan, 2004.
- [111] M.K. Akbar, D.A. Plummer, S.M. Ghiaasiaan, On gas–liquid two-phase flow regimes in microchannels, *Int. J. Multiphase Flow* 29 (2003) 855–865.
- [112] N. Zuber, J.A. Findlay, Average volumetric concentration in two phase flow systems, *ASME J. Heat Transfer* 87 (1965) 458–463.
- [113] G.D. Wang, P. Cheng, A.E. Bergles, Effects of inlet outlet configurations on flow boiling instability in parallel microchannels, *Int. J. Heat Mass Transfer* 51 (2008) 2267–2281.
- [114] K. Mishima, T. Hibiki, Some characteristics of air–water two-phase flow in small diameter vertical tubes, *Int. J. Multiphase Flow* 22 (1996) 703–712.

- [115] G. Hetsroni, A. Mosyak, E. Pogrebnyak, Z. Segal, Explosive boiling of water in parallel microchannels, *Int. J. Multiphase Flow* 31 (2005) 371–392.
- [116] W. Qu, I. Mudawar, Flow boiling heat transfer in two phase micro channel heat sink, Part I: experimental investigation and assessment of correlation methods, *Int. J. Heat Mass Transfer* 46 (2003) 2755–2771.
- [117] T. Chen, S. Garimella, Measurements and high speed visualizations of flow boiling of a dielectric fluid in a silicon microchannel heat sink, *Int. J. Multiphase Flow* 32 (2006) 957–971.
- [118] S.G. Kandlikar, A general correlation for saturated two phase boiling heat transfer inside horizontal and vertical tubes, *ASME J. Heat Transfer* 112 (1990) 219–228.
- [119] S.G. Kandlikar, Heat transfer mechanisms during flow boiling in microchannels, *ASME J. Heat Transfer* 126 (2004) 8–16.
- [120] M.E. Steinke, S.G. Kandlikar, Flow boiling and pressure drop in parallel flow microchannels, ICMM2003-1070, Proceedings of 1st International Conference on Microchannels and Minichannels, ASME, New York, 2003, pp. 567–579.
- [121] S. Lin, P.A. Kew, K. Cornwell, Flow boiling of refrigerant R141B in small tubes, *Chem. Eng. Res. Des.* 79 (2001) 417–424.
- [122] M.W. Wambsganss, D.M. France, J.A. Jendrzejczyk, T.N. Tran, Boiling heat transfer in a horizontal small diameter tube, *ASME J. Heat Transfer* 115 (1993) 963–972.
- [123] Y. Yan, T. Lin, Evaporation heat transfer and pressure drop of refrigerant R-134a in a small pipe, *Int. J. Heat Mass Transfer* 41 (1998) 4183–4194.
- [124] Z.Y. Bao, D.F. Fletcher, B.S. Haynes, Flow boiling heat transfer of Freon 11 and HCFC123 in narrow passages, *Int. J. Heat Mass Transfer* 43 (2000) 3347–3358.
- [125] W. Qu, I. Mudawar, Flow boiling heat transfer in two phase micro channel heat sink, Part II: annular two phase flow model, *Int. J. Heat Mass Transfer* 46 (2003) 2773–2784.
- [126] S.G. Kandlikar, P. Balasubramanian, An extension of the flow boiling correlation to transition, laminar and deep laminar flows in mini channels and microchannels, *Heat Transfer Eng.* 25 (2004) 86–93.
- [127] W. Yu, D.M. France, M.W. Wambsganss, J.R. Hull, Two phase pressure drop, boiling heat transfer, and critical heat flux to water in a small diameter horizontal tube, *Int. J. Multiphase Flow* 28 (2002) 927–941.
- [128] S.G. Kandlikar, M.E. Steinke, P. Balasubramanian, Single phase flow characteristics and effect of dissolved gases on heat transfer near saturation conditions in microchannels, IMECE2002-32382, International Mechanical Engineering Conference and Exposition, New Orleans, November 17–21, 2002.
- [129] G. Hetsroni, Z. Segal, A. Mosyak, Nonuniform temperature distribution in electronic devices cooled by flow in parallel microchannels, *Packaging of Electronic and Photonic Devices*, EEP, vol. 28, ASME, NY, 2000, pp. 1–9.
- [130] S.G. Kandlikar, M.E. Steinke, Predicting heat transfer during flow boiling in minichannels and microchannels, *ASHRAE Trans.* 109(1) (2003) 1–9.
- [131] A.M. Jacobi, J.R. Thome, Heat transfer model for evaporation of elongated bubble flows in microchannels, *ASME J. Heat Transfer* 124 (2002) 1131–1136.
- [132] S.G. Kandlikar, P. Balasubramanian, Effect of gravitational orientation on flow boiling of water in 1054×197 parallel minichannels, Proceedings of the 2nd International Conference on Microchannels and Minichannels, ASME, Rochester, NY, 2004, pp. 539–550.
- [133] V. Dupont, J.R. Thome, Evaporation in microchannels: influence of the channel diameter on heat transfer, *Microfluid. Nanofluid.* 1 (2005) 119–127.
- [134] I. Tiselj, G. Hetsroni, B. Mavko, A. Mosyak, E. Pogrebnyak, Z. Segal, Effect of axial conduction on the heat transfer in microchannels, *Int. J. Heat Mass Transfer* 47 (2004) 2251–2265.

- [135] T. Harirchian, S.V. Garimella, Microchannel size effects on local flow boiling heat transfer to a dielectric fluid, *Int. J. Heat Mass Transfer* 51 (2008) 3274–3735.
- [136] S.G. Kandlikar, Scale effects on flow boiling in microchannels: a fundamental perspective, ECI Conference on Boiling Heat Transfer, Florianopolis, Brazil, May 3–7, 2009.
- [137] S.G. Kandlikar, P. Balasubramanian, Extending the applicability of the flow boiling correlation to low Reynolds number flows in microchannels, ICMM2003-1075, Proceedings of 1st International Conference on Microchannels and Minichannels, ASME, Rochester, NY, 2003, pp. 603–608.
- [138] S.G. Kandlikar, P. Balasubramanian, An experimental study on the effect of gravitational orientation on flow boiling of water in $1054 \times 197 \mu\text{m}$ parallel minichannels, *ASME J. Heat Transfer* 127(8) (2005) 820–829.
- [139] T.S. Ravigururajan, Impact of channel geometry on two phase flow heat transfer characteristics of refrigerants in microchannel heat exchangers, *ASME J. Heat Transfer* 120 (1998) 485–491.
- [140] G.D. Wang, P. Cheng, Subcooled flow boiling and microbubble emission boiling phenomena in a partially heated microchannel, *Int. J. Heat Mass Transfer* 52 (2009) 79–91.
- [141] J.L. Xu, S. Shen, Y. Gan, Y. Li, W. Zhang, Q. Su, Transient flow pattern based microscale boiling heat transfer mechanisms, *J. Micromech. Microeng.* 15 (2005) 1344–1361.
- [142] J.L. Xu, Y.H. Gan, D.C. Zhang, X.H. Li, Microscale boiling heat transfer in a micro-time-scale at high heat fluxes, *J. Micromech. Microeng.* 15 (2005) 1362–1376.
- [143] A.C. Diaz, J. Schmidt, Experimental investigations of transient boiling heat transfer in microchannels, *Int. J. Heat Fluid Flow* 28 (2007) 95–102.
- [144] G.M. Lazarek, S.H. Black, Evaporative heat transfer, pressure drop and critical heat flux in a small vertical tube with R-113, *Int. J. Heat Mass Transfer* 25 (1982) 945–959.
- [145] K. Moriyama, A. Innoue, The thermohydraulic characteristics of two-phase flow in extremely narrow channels (The frictional pressure drop and heat transfer of boiling two-phase flow, analytical model), *Heat Transfer—Jpn. Res.* 21(8) (1992) 838–856.
- [146] B. Agostini, J.R. Thome, Comparison of an extended database for flow boiling heat transfer coefficients in multi microchannel elements with the three-zone model, ECI Conference on Heat Transfer and Fluid Flow in Microscale, Italy, September 25–30, 2005.
- [147] K. Triplett, S. Ghiaasiaan, S. Abdel Khalik, D.L. Sadowski, Gas liquid two phase flow in microchannels, Part I: two phase flow patterns, *Int. J. Multiphase Flow* 25 (1999) 377–394.
- [148] J.R. Thome, V. Dupont, A.M. Jacobi, Heat transfer model for evaporation in microchannels, Part I: presentation of the model, *Int. J. Heat Mass Transfer* 47(2004) (2004) 3375–3385.
- [149] J.R. Thome, V. Dupont, A.M. Jacobi, Heat transfer model for evaporation in microchannels, Part II: comparison with database, *Int. J. Heat Mass Transfer* 47 (2004) 3387–3401.
- [150] A. Serizawa, Z. Feng, Z. Kawara, Two phase flow in microchannels, *Exp. Thermal Fluid Sci.* 26 (2002) 703–714.
- [151] R. Revellin, V. Dupont, J.R. Thome, I. Zun, Characterization of diabatic two phase flows in microchannels: flow parameter results for R-134a in a 0.5 mm Channel, *Int. J. Multiphase Flow* 32 (2006) 755–774.
- [152] K. Cornwell, P.A. Kew, Boiling in small parallel channels, Proceedings of the International Conference on Energy Efficiency in Process Technology, Elsevier Applied Science, London, 1993, pp. 624–638.
- [153] S. Lin, P.A. Kew, K. Cornwell, Flow boiling of refrigerant R141B in small tubes, *Chem. Eng. Res. Des.* 79 (2001) 417–424.
- [154] J. Li, G.P. Peterson, Boiling nucleation and two phase flow patterns in forced liquid flow in microchannels, *Int. J. Heat Mass Transfer* 48 (2005) 4797–4810.

- [155] R. Revellin, J.R. Thome, New diabatic flow pattern map for evaporating flows in microchannels, 13th International Heat Transfer Conference, Sydney, August 14–18, 2006.
- [156] P.M.Y. Chung, M. Kawaji, The effect of channel diameter on adiabatic two phase flow characteristics in small tubes, *Int. J. Multiphase Flow* 30 (2004) 735–761.
- [157] T.S. Zhao, Q.C. Bi, Co-current air water two phase flow patterns in vertical triangular microchannels, *Int. J. Multiphase Flow* 27 (2001) 765–782.
- [158] T. Cubaud, H. Chih-Ming, Transport of bubbles in square microchannels, *Phys. Fluids* 16(12) (2004) 4575–4585.
- [159] S. Lin, P.A. Kew, K. Cornwell, Two phase heat transfer to a refrigerant in a 1 mm diameter tube, *Int. J. Refrig.* 24 (2001) 51–56.
- [160] W. Owhaib, B. Palm, C. Martin-Callizo, Flow boiling visualizations in a vertical circular minichannel at high vapor quality, *Exp. Thermal Fluid Sci.* 30 (2006) 755–763.
- [161] T.N. Tran, M.W. Wambsganss, D.M. France, Small circular and rectangular channel boiling with two refrigerants, *Int. J. Multiphase Flow* 22 (1996) 485–498.
- [162] J.L. Xu, J.J. Zhou, Y.H. Gan, Static and dynamic flow instability of a parallel microchannel heat sink at high heat flux, *Energy Convers. Manage.* 46 (2005) 313–334.
- [163] J. Pettersen, Flow visualization of CO₂ in microchannel tubes, *Exp. Thermal Fluid Sci.* 28 (2004) 111–121.
- [164] B. Agostini, A. Bontemps, Vertical flow boiling of refrigerant R134a in small channels, *Int. J. Heat Fluid Flow* 26 (2005) 296–306.
- [165] P.C. Lee, F.C. Tseng, C. Pan, Bubble dynamics in microchannels, Part I: single microchannel, *Int. J. Heat Mass Transfer* 47 (2004) 5575–5589.
- [166] H.J. Lee, I. Mudawar, Two-phase flow in high heat flux microchannel heat sink for refrigeration cooling applications, Part I: pressure drop characteristics, *Int. J. Heat Mass Transfer* 48 (2005) 928–940.
- [167] H.J. Lee, I. Mudawar, Two-phase flow in high heat flux microchannel heat sink for refrigeration cooling applications, Part II: heat transfer characteristics, *Int. J. Heat Mass Transfer* 48 (2005) 941–955.
- [168] W. Qu, I. Mudawar, Measurement and correlation of critical heat flux in two phase microchannel heat sinks, *Int. J. Heat Mass Transfer* 47 (2004) 2045–2059.
- [169] W. Qu, I. Mudawar, Transport phenomena in two phase microchannel heat sinks, *J. Electron. Packag.* 126 (2004) 213–224.
- [170] G. Ribatski, L. Wojtan, J.R. Thome, An analysis of experimental data and prediction methods for two phase frictional pressure drop and flow boiling heat transfer in micro-scale channels, *Exp. Thermal Fluid Sci.* 31 (2006) 1–19.
- [171] W. Zhang, T. Hibiki, K. Mishima, Correlation for boiling heat transfer in minichannels, *Int. J. Heat Mass Transfer* 47 (2004) 5749–5763.
- [172] G.P. Celata, Preface to the special issue dedicated to the ECI International Conference on Heat Transfer and Fluid Flow in Microscale, Italy, September 25–30. *Exp. Thermal Fluid Sci.* 30 (8) (2006) 711–712.
- [173] W. Qu, I. Mudawar, Measurement and prediction of pressure drop in two phase microchannel heat sinks, *Int. J. Heat Mass Transfer* 46 (2003) 2737–2753.
- [174] H.J. Lee, S.Y. Lee, Pressure drop correlations for two-phase flow within horizontal rectangular channels with small heights, *Int. J. Multiphase Flow* 27 (2001) 783–796.
- [175] T.N. Tran, M.C. Chiyu, M.W. Wambsganss, D.M. France, Two phase pressure drop of refrigerants during flow boiling in small channels: an experimental investigation and correlation development, *Int. J. Multiphase Flow* 26 (2000) 1739–1754.
- [176] R. Muller-Steinhagen, K. Heck, A simple friction pressure drop correlation for two-phase flow in pipes, *Chem. Eng. Process.* 20(6) (1986) 297–308.

- [177] B. Brutin, L. Tadrist, Pressure drop and heat transfer analysis of flow boiling in microchannel: influence of the inlet condition on two-phase flow stability, *Int. J. Heat Mass Transfer* 47 (2004) 2365–2377.
- [178] D.S. Wen, D.B.R. Kenning, Two phase pressure drop of water during flow boiling in a vertical narrow channel, *Exp. Thermal Fluid Sci.* 28 (2004) 131–138.
- [179] M. Zhang, R.L. Webb, Correlation of two phase friction for refrigerants in small diameter tubes, *Exp. Thermal Fluid Sci.* 25 (2001) 131–139.
- [180] B. Agostini, B. Watel, A. Bontemps, B. Thonon, Friction factor and heat transfer coefficient of R134a liquid flow in minichannels, *Appl. Thermal Eng.* 22(16) (2002) 1821–1834.
- [181] H. Cheol, H.K. Moo, Pressure drop, boiling heat transfer and flow patterns during flow boiling in a single microchannel, *Heat Transfer Eng.* 28(8-9) (2007) 730–737.
- [182] W. Li, Z. Wu, A general correlation for evaporative heat transfer in micro/mini channels, *Int. J. Heat Mass Transfer* 53 (2010) 1778–1787.
- [183] Z. Liu, R.H.S. Winterton, A general correlation for saturated and subcooled flow boiling in tubes and annuli, based on a nucleate pool boiling equation, *Int. J. Heat Mass Transfer* 34 (1991) 2759–2766.
- [184] P.C. Stephan, C.A. Busse, Analysis of the heat transfer coefficient of grooved heat pipe evaporator walls, *Int. J. Heat mass Transfer* 35(2) (1992) 383–391.
- [185] W. Qu, I. Mudawar, Prediction and measurement of incipient boiling heat flux in microchannel heat sinks, *Int. J. Heat Mass Transfer* 45 (2002) 3933–3945.
- [186] J.R. Thome, V. Dupont, A.M. Jacobi, Heat transfer model for evaporation in microchannels, Part I: presentation of the model, *Int. J. Heat Mass Transfer* 47 (2004) 3375–3385.
- [187] J.R. Thome, V. Dupont, A.M. Jacobi, Heat transfer model for evaporation in microchannels, Part II: comparison with database, *Int. J. Heat Mass Transfer* 47 (2004) 3387–3401.
- [188] G. Hetsroni, L.P. Yarin, E. Pogrebnyak, Onset of flow instability in a heated capillary tube, *Int. J. Multiphase Flow* 30 (2004) 1421–1449.
- [189] G. Hetsroni, A. Mosyak, E. Pogrebnyak, Z. Segal, Periodic boiling in parallel microchannels at low vapor quality, *Int. J. Multiphase Flow* 32 (2006) 1141–1159.
- [190] L. Sun, K. Mishima, An evaluation of prediction methods for saturated flow boiling heat transfer, *Int. J. Heat Mass Transfer* 52 (2009) 5323–5329.
- [191] H. Boye, Y. Staate, J. Schmidt, Experimental investigation and modeling of heat transfer during convective boiling in a minichannel, *Int. J. Heat Mass Transfer* 50 (2006) 208–215.
- [192] J.C. Chen, Correlation for boiling heat transfer to saturated fluids in convective flow, *Ind. Eng. Chem. Process. Des. Dev.* 5 (1966) 322–329.
- [193] S. Saitoh, H. Daiguji, E. Hihara, Correlation for boiling heat transfer of R-134a in horizontal tubes including effect of tube diameter, *Int. J. Heat Mass Transfer* 50 (2007) 5215–5225.
- [194] S.G. Kandlikar, A model for flow boiling heat transfer in augmented tubes and compact evaporators, *ASME J. Heat Transfer* 113 (1991) 966–972.
- [195] T.N. Tran, M.W. Wambsganss, D.M. France, Small circular and rectangular channel boiling with two refrigerants, *Int. J. Multiphase Flow* 22 (1996) 485–498.
- [196] W. Yu, D.M. France, M.W. Wambsganss, J.R. Hull, Two phase pressure drop, boiling heat transfer, and critical heat flux to water in a small diameter horizontal tube, *Int. J. Multiphase Flow* 28 (2002) 927–941.
- [197] G.R. Warrier, T. Pan, V.K. Dhir, Heat transfer and pressure drop in narrow rectangular channels, *Exp. Thermal Fluid Sci.* 26 (2002) 53–64.
- [198] D.B.R. Kenning, M.G. Cooper, Saturated flow boiling of water in vertical tubes, *Int. J. Heat Mass Transfer* 32 (1989) 445–458.
- [199] A.S. Pamitran, K. Choi, J.T. Oh, H.K. Oh, Forced convective boiling heat transfer of R-410A in horizontal minichannels, *Int. J. Refrig.* 30 (2007) 155–165.

- [200] K.E. Gungor, R.H.S. Winterton, A general correlation for flow boiling in tubes and annuli, *Int. J. Heat Mass Transfer* 29 (1986) 351–358.
- [201] M.E. Steinke, S.G. Kandlikar, An experimental investigation of flow boiling characteristics of water in microchannels, *ASME J. Heat Transfer* 126 (2004) 518–526.
- [202] G.M. Mala, D. Li, J.D. Dale, Heat transfer and fluid flow in microchannels, *Int. J. Heat Mass Transfer* 40(13) (1997) 3079–3088.
- [203] C.L. Rice, R. Whitehead, Electronic flow in narrow cylindrical capillaries, *J. Phys. Chem.* 69 (1965) 4017–4023.
- [204] S. Levine, J.R. Marriott, G. Neale, N. Epstein, Theory of electrokinetic flow in fine cylindrical capillaries at high zeta potential, *J. Colloid Sci.* 52 (1975) 136–149.
- [205] C.B. Tibirica, G. Ribatski, An experimental study on microscale flow boiling heat transfer, *ECI International Conference on Boiling Heat Transfer*, Florianapolis-SC, Brazil, May 3–7, 2009.
- [206] W. Owhaib, C. Martin-Callizo, B. Palm, Evaporative heat transfer in vertical circular microchannels, *Appl. Thermal Eng.* 24 (2004) 1241–1253.
- [207] X. Huai, S. Koyama, T.S. Zhao, E. Shinimura, K. Hidehiko, M. Masaki, An experimental study of flow boiling characteristics of carbon dioxide in multipoint minichannels, *Appl. Thermal Eng.* 24 (2004) 1443–1463.
- [208] R. Yun, Y. Kim, M.S. Kim, Convective boiling heat transfer characteristics of CO₂ in microchannels, *Int. J. Heat Mass Transfer* 48 (2005) 335–342.
- [209] R. Yun, J.H. Heo, Y. Kim, Evaporative heat transfer and pressure drop of R410A in microchannels, *Int. J. Refrig.* 29 (2006) 92–100.
- [210] Y.M. Lie, F.Q. Su, R.I. Lai, T.F. Lin, Experimental study of evaporation heat transfer characteristics of refrigerants R134a and R407C in horizontal small tubes, *Int. J. Heat Mass Transfer* 49 (2006) 207–218.
- [211] D. Shiferaw, X. Huo, T.G. Karayiannis, D.B.R. Kenning, Examination of heat transfer and a model for flow boiling of R134a in small diameter tubes, *Int. J. Heat Mass Transfer* 50 (2007) 5177–5193.
- [212] P. Fernando, B. Palm, T. Ameel, P. Lundquist, E. Granryd, A minichannel aluminum tube heat exchanger, Part I: evaluation of single-phase heat transfer coefficients by the Wilson plot method, *Int. J. Refrig.* 31 (2008) 669–680.
- [213] P. Fernando, B. Palm, T. Ameel, P. Lundquist, E. Granryd, A minichannel aluminum tube heat exchanger, Part II: evaporation performance with propane, *Int. J. Refrig.* 31 (2008) 681–695.
- [214] P. Fernando, B. Palm, T. Ameel, P. Lundquist, E. Granryd, A minichannel aluminum tube heat exchanger, Part III: condenser performance with propane, *Int. J. Refrig.* 31 (2008) 696–708.
- [215] C.I. Ong, J.R. Thome, Flow boiling heat transfer of R134a, R236fa and R245fa in a horizontal 1.030 mm circular channel, *Exp. Thermal Fluid Sci.* 33 (2009) 651–663.
- [216] J. Kaew-On, S. Wongwises, Experimental investigation of evaporation heat transfer coefficient and pressure of R410A in multipoint minichannel, *Int. J. Refrig.* 32 (2009) 124–137.
- [217] K.I. Choi, A.S. Pamitran, C.Y. Oh, J.T. Oh, Boiling heat transfer of R-22, R-134a and CO₂ in horizontal smooth minichannels, *Int. J. Refrig.* 30 (2007) 1336–1346.
- [218] S.S. Bertsch, E.A. Groll, S.V. Garimella, Refrigeration flow boiling in parallel minichannels as a function of local vapor quality, *Int. J. Heat Mass Transfer* 51 (2008) 4775–4787.
- [219] X. Huo, L. Chen, Y.S. Tian, T.G. Karayiannis, Flow boiling and flow regimes in small diameter tubes, *Appl. Thermal Eng.* 24 (2004) 1225–1239.
- [220] R.W. Lockhart, R.C. Martinelli, Proposed correlation of data for isothermal two phase two component flow in pipes, *Chem. Eng. Prog.* 45 (1949) 39–48.
- [221] R.C. Martinelli, D.B. Nelson, Prediction of pressure drop during forced circulation boiling of water, *ASME J. Heat Transfer* 70 (1948) 695–702.

- [222] D. Chisholm, L.A. Sutherland, Prediction of pressure gradients in pipeline systems during two-phase flow, Paper No. 4, Proceedings of Fluid Mechanics and Measurements in Two-Phase Flow Systems, Leeds, UK, 1969, pp. 26–34.
- [223] Z.Y. Guo, Z.X. Li, Size effect on microscale single-phase flow and heat transfer, *Int. J. Heat Mass Transfer* 46 (2003) 149–159.
- [224] Z.X. Li, Z.Z. Xia, D.X. Du, Analytical and experimental investigation on gas flow in a microtube, Kyoto University–Tsinghua University Joint Conference on Energy and Environment, Kyoto, Japan, 1999, pp. 1–6.
- [225] D.X. Du, Effect of Compressibility and Roughness on Flow and Heat Transfer in Microtubes, Ph.D. Thesis, Tsinghua University, Beijing, 2000.
- [226] G.P. Celata, M. Cumo, M. Gulielmi, G. Zummo, Experimental investigation of hydraulic and single phase heat transfer in 0.130 mm capillary tube, in: G.P. Celata (Eds.), Proceedings of International Conference on Heat Transfer and Transport Phenomena in Microscale, Banff, Canada, 2000, pp. 108–113.
- [227] Z.X. Li, D.X. Du, Z.Y. Guo, Experimental study on flow characteristics of liquid in circular microtubes, Proceedings of International Conference on Heat Transfer and Transport Phenomena in Microscale, Banff, Canada, 2000, pp. 162–167.
- [228] R. Dao, D.E. Morgan, H.H. Kries, D.M. Bachelder, Convective accelerometer and inclinometer, US Patent 5581034, 1996.
- [229] A.M. Leung, J. Jones, E. Czyzewska, J. Chen, M. Pascal, Micromachined accelerometer with no proof mass, Proceedings of Technical Digest of International Electron Device Meeting, 1997, pp. 899–902.
- [230] V. Milanovic, V. Bowen, M.E. Zaghoul, Micromachined convective accelerometers in standard integrated circuits technology, *Appl. Phys. Lett.* 76(4) (2000) 508–510.
- [231] X.B. Luo, Y.J. Yang, Z. Zhang, Z.X. Li, Z.Y. Guo, An optimized micromachined convective accelerometer with no proof mass, *J. Micromech. Microeng.* 11 (2001) 504–508.
- [232] G.M. Mala, D. Li, C. Werner, Flow characteristics of water through a microchannel between two parallel plates with electrokinetic effects, *Int. J. Heat Fluid Flow* 18(5) (1997) 491–496.
- [233] C. Yang, D. Li, Analysis of electrokinetic effects on the liquid flow in rectangular microchannels, *Colloid Surf. A* 143 (1998) 339–353.
- [234] L. Ren, W. Qu, D. Li, Interfacial electrokinetic effects on liquid flow in microchannels, *Int. J. Heat Mass Transfer* 44 (2001) 3125–3134.
- [235] S. Mori, M. Sakakibara, A. Tanimoto, Steady heat transfer to laminar flow in a circular tube with conduction in tube wall, *Heat Transfer—Jpn. Res.* 3(2) (1974) 37–46.
- [236] J. Pfahler, J. Harley, H. Bau, Liquid and gas transport in small channels, *ASME DSC* 19 (1990) 149–157.
- [237] Z.Y. Guo, X.B. Wu, Compressibility effect on the gas flow and heat transfer in a micro tube, *Int. J. Heat Mass Transfer* 40 (1997) 3251–3254.
- [238] P.Y. Wu, W.A. Little, Measurement of friction factors for the flow of gases in very fine channels used for microminiature Joule–Thomson refrigerators, *Cryogenics* 23 (1983) 273–277.
- [239] P.Y. Wu, W.A. Little, Measurement of the heat transfer characteristics of gas flow in fine channel heat exchangers used for microminiature refrigerators, *Cryogenics* 24 (1984) 415–420.
- [240] J. Pfahler, J. Harley, H. Bau, Gas and liquid flow in small channels, *ASME DSC* 32 (1991) 49–60.
- [241] S.B. Choi, R.F. Barron, R.Q. Warrington, Fluid flow and heat transfer in microtubes, *ASME DSC* 32 (1991) 123–133.
- [242] M.B. Bowers, I. Mudawar, High heat flux boiling in low flow rate, low pressure drop mini channel and micro channel heat sinks, *Int. J. Heat Mass Transfer* 37 (1994) 321–332.

- [243] M.B. Bowers, I. Mudawar, Two phase electronic cooling using minichannel and microchannel heat sinks, Part 1: design criteria and heat diffusion constraints, *J. Electron. Packag.* 116 (1994) 290–297.
- [244] M.B. Bowers, I. Mudawar, Two phase electronic cooling using minichannel and microchannel heat sinks, Part 2: flow rate and pressure drop constraints, *J. Electron. Packag.* 116 (1994) 298–305.
- [245] H.J. Lee, I. Mudawar, Two-phase flow in high heat flux microchannel heat sink for refrigeration cooling applications, Part I: pressure drop characteristics, *Int. J. Heat Mass Transfer* 48 (2005) 928–940.
- [246] W. Zhang, T. Hibiki, K. Mishima, Correlations of two-phase frictional pressure drop and void fraction in mini-channel, *Int. J. Heat Mass Transfer* 53 (2010) 453–465.
- [247] K. Mishima, T. Hibiki, H. Nishihara, Some characteristics of gas–liquid flow in narrow rectangular ducts, *Int. J. Multiphase Flow* 19 (1993) 115–124.
- [248] D. Chisholm, Pressure gradients due to friction during the flow of evaporation of two phase mixtures in smooth tubes and channels, *Int. J. Heat Mass Transfer* 16 (1973) 347–358.
- [249] K. Triplett, S. Ghiaasiaan, S. Abdel Khalik, A. LeMouel, B. McCord, Gas liquid two phase flow in microchannels, Part II: void fraction and pressure drop, *Int. J. Multiphase Flow* 25 (1999) 395–410.
- [250] L. Friedel, Improved friction pressure drop correlations for horizontal and vertical two-phase pipe flow, *Proceedings of the European Two-Phase Flow Group Meeting*, Ispra, Italy, 1979.
- [251] A. Kawahara, P.M.Y. Chung, M. Kawaji, Investigation of two-phase flow pattern, void fraction and pressure drop in microchannel, *Int. J. Multiphase Flow* 28 (2002) 1411–1435.
- [252] A. Kariyasaki, T. Fukano, A. Ousaka, M. Kagawa, Isothermal air–water two-phase up- and downward flows in a vertical capillary tube (first report, flow pattern and void fraction), *JSME Ser. B.* 58 (1992) 2684–2690.
- [253] K. Moriyama, A. Inoue, H. Ohira, The thermohydraulic characteristics of two-phase flow in extremely narrow channels (the frictional pressure drop and void fraction of adiabatic two-component two-phase flow), *JSME Ser. B.* 58 (1992) 401–407.
- [254] Z.Y. Bao, M.G. Bosnick, B.S. Haynes, Estimation of void fraction and pressure drop for two-phase flow in passages, *Trans. IChE* 72 (1994) 625–632.
- [255] T. Hazuku, N. Tamura, N. Fukamachi, T. Takamasa, T. Hibiki, M. Ishii, Axial development of vertical upward bubbly flow in a mini pipe, *Proceedings of Summer Heat Transfer Conference*, San Francisco, CA, 2005.
- [256] W. Zhang, T. Hibiki, K. Mishima, Y. Mi, Correlation of critical heat flux for flow boiling of water in minichannels, *Int. J. Heat Mass Transfer* 47 (2006) 1058–1072.
- [257] M. Zhang, R.L. Webb, Correlation of two phase friction for refrigerants in small diameter tubes, *Exp. Thermal Fluid Sci.* 25 (2001) 131–139.
- [258] W. Tong, A.E. Bergles, M.K. Jensen, Pressure drop with highly subcooled flow boiling in small diameter tubes, *Proceedings of 1st Symposium on Two Phase Flow Modeling and Experimentation*, Rome, Italy, 1995, pp. 617–628.
- [259] Y. Zhao, M. Molki, M.M. Ohadi, S.V. Dessiatoun, Flow boiling of CO₂ in microchannels, *ASHRAE Trans.* 106(Part 1) (2000) 437–445.
- [260] Y.W. Hwan, M.S. Kim, The pressure drop in micro tubes and correlation development, *Int. J. Heat Mass Transfer* 49 (2006) 1804–1812.
- [261] J. Shuai, R. Kulenovic, M. Droll, Heat transfer and pressure drop for flow boiling of water in narrow vertical rectangular channels, *Proceedings of 1st International Conference on Microchannels*, ICMN 2003, Rochester, NY, April 24–25, 2003, p. 1084.
- [262] I. Hapke, H. Boye, J. Schmidt, Flow boiling of water and *n*-heptane in microchannels, *Microscale Therm. Eng.* 6 (2002) 99–115.

- [263] A.E. Dukler, M. Wicks III, R.G. Cleveland, Pressure drop and hold-up in two-phase flow, *AIChE J.* 10 (1964) 38–51.
- [264] J.M. Quiben, J.R. Thome, Flow pattern based two phase pressure drop model for horizontal tubes, Part I: diabatic and adiabatic experimental study, *Int. J. Heat Fluid Flow* 28(5) (2007) 1049–1059.
- [265] J.M. Quiben, J.R. Thome, Flow pattern based two phase pressure drop model for horizontal tubes, Part II: new phenomenological model, *Int. J. Heat Fluid Flow* 28(5) (2007) 1060–1072.
- [266] W. Li, Z. Wu, A general correlation for adiabatic two-phase pressure drop in micro/mini-channels, *Int. J. Heat Mass Transfer* 53 (2010) 2732–2739.
- [267] S. Kakac, T.N. Veziroglu, A review of two-phase flow instabilities, in: S. Kakac, M. Ishii (Eds.), *Advances in Two-Phase Heat Transfer*, vol. 11, Martunus Nijhoff, Boston, 1983, pp. 577–668.
- [268] S. Kakac, T.N. Veziroglu, M.M. Padki, L.Q. Fu, X.J. Chen, Investigation of thermal instabilities in a forced convection upward boiling system, *Exp. Thermal Fluid Sci.* 3 (1990) 191–201.
- [269] Q. Wang, X.J. Chen, S. Kakac, Y. Ding, An experimental investigation of density wave-type oscillations in a convection boiling up-flow system, *Int. J. Heat Fluid Flow* 15 (1994) 241–246.
- [270] G. Wang, P. Cheng, H. Wu, Unstable and stable flow boiling in parallel microchannels and in a single microchannel, *Int. J. Heat Mass Transfer* 50 (2007) 4297–4310.
- [271] S.K. Saha, G. Zummo, G.P. Celata, Review on flow boiling in microchannels, *Int. J. Microscale Nanoscale Thermal Fluid Transp. Phenomena* 1(2) (2010) 1–67.
- [272] S.K. Saha, G.P. Celata, *Boiling and Evaporation*, Heat Exchanger Design Handbook Online, Section 2.13.4, Begell House, Connecticut, 2011.
- [273] Y.Y. Hsu, On the size range of active nucleation cavities on a heating surface, *J. Heat Transfer* 84 (1962) 207–216.
- [274] E.J. Davis, G.H. Anderson, The incipience of nucleate boiling in forced convection flow, *AIChE J.* 12(4) (1966) 774–780.
- [275] T. Sato, H. Matsumura, On the condition of incipient subcooled boiling with forced convection, *Bull. JSME* 7(26) (1964) 392–398.
- [276] A.E. Bergles, W.M. Rohsenow, The determination forced-convection surface boiling heat transfer, *J. Heat Transfer* 86 (1964) 365–372.
- [277] S.G. Kandlikar, D.A. Willistein, J. Borrelli, Experimental evaluation of pressure drop elements and fabricated nucleation sites for stabilizing flow boiling in microchannels, *ASME J. Heat Transfer* 128(4) (2005) 389–396.
- [278] S.G. Kandlikar, S. Garimella, D. Li, S. Colin, M. King, *Heat transfer and fluid flow in mini-channels and microchannels*, Elsevier, Kidlington, Oxford, UK, 2006.
- [279] S.G. Kandlikar, V.R. Mizo, M.D. Cartwright, E. Ikenze, Bubble nucleation and growth characteristics in subcooled flow boiling of water, *HTD-Vol. 342*, ASME Proceedings of the 32nd National Heat Transfer Conference, vol. 4, 1997, pp. 11–18.
- [280] L. Zhang, E. Wang, K.E. Goodson, T.W. Kenny, Phase change phenomena in silicon micro-channels, *Int. J. Heat Mass Transfer* 48 (2005) 1572–1582.
- [281] M. Lee, L.S.L. Cheung, Y.K. Lee, Y. Zohar, Height effect on nucleation-site activity and size-dependent bubble dynamics in microchannel convective boiling, *J. Micromech. Microeng.* 15 (2005) 2121–2129.
- [282] S.G. Kandlikar, D. Schmitt, A.L. Carrano, J.B. Taylor, Characterization of surface roughness effects on pressure drop in single-phase flow in minichannels, *Phys. Fluids* 17(10) (2005) 100606.
- [283] S.G. Kandlikar, P.H. Spiesman, Effect of surface finish on flow boiling heat transfer, *Proceedings of Engineering Foundation Conference on Convective and Pool Boiling*, Irsee, Germany, May 18–25, 1997.

- [284] B.J. Jones, S. Garimella, Surface roughness effects on flow boiling in microchannels, *Proceedings of ASME Interpack2009 Conference*, vol. 2, 2009, pp. 409–418.
- [285] V.V. Dharaiya, S.G. Kandlikar, Heat transfer in rectangular microchannels under H₂ boundary condition during developing and fully developed laminar flow, *Accepted for publication in ASME J. Heat Transfer*, 2012.
- [286] C.J. Kuo, Y. Peles, Local measurement of flow boiling in structured surface microchannels, *Int. J. Heat Mass Transfer* 50 (2007) 4513–4526.
- [287] D. Liu, P.-S. Lee, S.V. Garimella, Prediction of the onset of nucleate boiling in microchannel flow, *Int. J. Heat Mass Transfer* 48 (2005) 5134–5149.
- [288] J. Li, P. Cheng, Bubble cavitation in a microchannel, *Int. J. Heat Mass Transfer* 47 (2004) 2689–2698.
- [289] V. Khanikar, I. Mudawar, T.S. Fisher, Flow boiling in a micro-channel coated with carbon nanotubes, *IEEE Trans. Compon. Packag. Technol.* 32(3) (2009) 639–649.
- [290] T.Y. Liu, P.L. Li, C.W. Liu, C. Gau, Boiling flow characteristics in microchannels with very hydrophobic surface to super-hydrophilic surface, *Int. J. Heat Mass Transfer* 54 (2011) 126–134.
- [291] S.G. Kandlikar, Nucleation characteristics and stability considerations during flow boiling in microchannels, *Exp. Thermal Fluid Sci.* 30(5) (2006) 441–447.
- [292] P.C. Lee, C. Pan, On the eruptive boiling in silicon-based microchannels, *Int. J. Heat Mass Transfer* 51(2008) (2008) 4841–4849.
- [293] S. Inada, Y. Miyasaka, S. Sakamoto, G.R. Chandratilleke, Liquid-solid contact state in subcooled pool transition boiling system, *J. Heat Transfer* 108 (1986) 219–221.
- [294] M. Shoji, M. Yoshihara, Burnout heat flux of water on a thin wire, *Proceedings of the 28th National Heat Transfer Symposium of Japan*, 1991, pp. 121–123.
- [295] H. Wang, X.F. Peng, B.X. Wang, D.J. Lee, Jet flow phenomena during nucleate boiling, *Int. J. Heat Mass Transfer* 45 (2002) 1359–1363.
- [296] K. Suzuki, K. Torikai, H. Satoh, J. Ishimaru, Y. Tanaka, Boiling heat transfer of subcooled water in a horizontal rectangular channel (observation of MEB and MEB generation), *Trans. JSME* 65(637) (1999) 3097–3104.
- [297] K. Suzuki, H. Kawamura, M. Ishizuka, H. Iwasaki, K. Kawano, High heat flux cooling for electronic devices by subcooled flow boiling with microbubble emission, *Proceedings of the 6th ASME-JSME Thermal Engineering Conference*, CR-ROM TEDAJ03-106, 2003.
- [298] M. Tange, M. Yuasa, S. Takagi, M. Shoji, Microbubbles emission boiling in microchannels and minichannels, *Proceedings of the ASME Second International Conference on Nanochannels, Microchannels and Minichannels*, Paper No. ICNMM2004-2385, June 17-19, Rochester, NY, 2004.
- [299] K. Suzuki, T. Kokubu, M. Nakano, H. Kawamura, I. Ueno, H. Shida, Enhancement of heat transfer in subcooled flow boiling with microbubble emission, *Exp. Thermal Fluid Sci.* 29 (2005) 827–832.
- [300] G. Wang, P. Cheng, Subcooled flow boiling and microbubble emission boiling phenomena in a partially heated microchannel, *Int. J. Heat Mass Transfer* 52(1-2) (2009) 79–91.
- [301] T. Makuta, F. Takemura, E. Hihara, Y. Matsumoto, M. Shoji, Generation of micro gas bubbles of uniform diameter in an ultrasonic field, *J. Fluid Mech.* 548 (2006) 113–131.
- [302] Y. Kuzma-Kichta, Investigation of interface oscillations during boiling, *Sci. J. Riga Tech. Univ. Heat Power Thermal Phys.* 21 (2006) 70–76.
- [303] H. Wang, X.F. Peng, D.M. Christopher, B.X. Wang, Flow structures around micro-bubbles during subcooled nucleate boiling, *Chin. Phys. Lett.* 22(1) (2004) 154–157.
- [304] K. Suzuki, T. Nomura, C.P. Hong, K. Yuki, Subcooled flow boiling with microbubble emission in a microchannel, *Proceedings of ASME Micro/Nanoscale Heat and Mass Transfer International Conference*, Shanghai, Peoples Republic of China, DEC 18-21, MNHMT2009, vol. 2, 2009, pp. 83-89.

- [305] A. Premoli, D. Francesco, A. Prina, A dimensionless correlation for determining density of two-phase mixtures, *Termotecnica* 25 (1971) 17–26.
- [306] A. Serizawa, Z. Feng, Z. Kawara, Two-phase flow in micro-channels, *Exp. Thermal. Fluid Sci.* 26 (2002) 703–714.
- [307] A.A. Armand, The resistance during the movement of a two-phase system in horizontal pipes, *Izv. Vses. Teplotekh. Inst.* 1 (1946) 16–23 (AERE-Lib/Trans 828)
- [308] A. Kawahara, P.M.-Y. Chung, M. Kawaji, Investigation of two-phase flow pattern, void fraction and pressure drop in a microchannel, *Int. J. Heat Mass Transfer* 28 (2002) 1411–1435.
- [309] P.M.-Y. Chung, M. Kawaji, A. Kawahara, Y. Shibata, Two-phase flow through square and circular microchannels—effect of channel geometry, *ASME J. Fluids Eng.* 126 (2004) 546–552.
- [310] P.M.-Y. Chung, M. Kawaji, The effect of channel diameter on adiabatic two-phase flow characteristics in microchannels, *Int. J. Multiphase Flow* 30 (2004) 735–761.
- [311] H. Ide, R. Kimura, H. Hashiguchi, M. Kawaji, Effect of channel length on gas-liquid two-phase flow phenomena in a microchannel, *Heat Transfer Eng.* (2011). DOI: 10.1080/01457632.2011.562745
- [312] H. Ide, R. Kimura, M. Kawaji, Optical measurement of void fraction and bubble size distributions in a microchannel, *Heat Transfer Eng.* 28(8-9) (2007) 713–719.
- [313] R. Cullion, D. Pence, J. Liburdy, V. Narayan, Void fraction variations in a fractal-like branching microchannel network, *Heat Transfer Eng.* 28(10) (2007) 806–816.
- [314] A. Kawahara, M. Sadatomi, K. Nei, H. Matsuo, Experimental study on bubble velocity, void fraction and pressure drop for gas-liquid two-phase flow in a circular microchannel, *Int. J. Heat Mass Transfer* 30 (2009) 831–841.
- [315] C.W. Choi, D.I. Yu, M.H. Kim, Adiabatic two-phase flow in rectangular microchannels with different aspect ratios: Part I – flow pattern, pressure drop and void fraction, *Int. J. Heat Mass Transfer* 54 (2011) 616–624.
- [316] S.G. Singh, A. Jain, A. Sridharan, S.P. Duttagupta, A. Agrawal, Flow map and measurement of void fraction and heat transfer coefficient using an image analysis technique for flow boiling of water in a silicon microchannel, *J. Micromech. Microeng.* 19 (2009) 075004.
- [317] D. Fogg, M. David, K. Goodson, Non-invasive measurement of void fraction and liquid temperature in microchannel flow boiling, *Exp. Fluids* 46 (2009) 725–736.
- [318] C.B. Tibiriçá, F. Júlio do Nascimento, G. Ribatski, Film thickness measurement techniques applied to micro-scale two-phase flow systems, *Exp. Thermal Fluid Sci.* 34 (2010) 463–473.
- [319] T. Hazuku, N. Fukamachi, T. Takamasa, T. Hibiki, M. Ishii, Measurement of liquid film in microchannels using a laser focus displacement meter, *Exp. Fluids* 38 (2005) 780–788.
- [320] Y. Han, N. Shikazono, Measurement of the liquid film thickness in micro square channel, *Int. J. Multiphase Flow* 35 (2009) 896–903.
- [321] Y. Han, N. Shikazono, N. Kasagi, Measurement of liquid film thickness in a micro parallel channel with interferometer and laser focus displacement meter, *Int. J. Multiphase Flow* 37 (2011) 36–45.
- [322] J.E. Steinbrenner, C.H. Hidrovo, F.-M. Wang, S. Vigneron, E.S. Lee, T.A. Kramer, et al., Measurement and modeling of liquid film thickness evolution in stratified two-phase micro-channel flows, *Appl. Thermal Eng.* 27 (2007) 1722–1727.
- [323] C. Fang, M. David, F.-M. Wang, K.E. Goodson, Influence of film thickness and cross-sectional geometry on hydrophilic microchannel condensation, *Int. J. Multiphase Flow* 36 (2010) 608–619.

- [324] D. Huh, C.-H. Kuo, J.B. Grotberg, S. Takayama, Gas-liquid two-phase flow patterns in rectangular polymeric microchannel: effect of surface wetting properties, *New J. Phys.* 11 (2009) 075034.
- [325] P. Aussillous, D. Quere, Quick deposition of a fluid on the wall of a tube, *Phys. Fluids* 12 (2000) 2367–2371.
- [326] Y. Han, N. Shikazono, Measurement of the liquid film thickness in micro tube slug flow, *Int. J. Heat Fluid Flow* 30(5) (2009) 842–853.
- [327] D.M. Fries, F. Traschsel, P.R. von Rohr, Segmented gas-liquid flow characterization in rectangular microchannels, *Int. J. Multiphase Flow* 34 (2008) 1108–1118.
- [328] J. Yue, L. Luo, Y. Gonthier, G. Chen, Q. Yuan, An experimental study of air-water taylor flow and mass transfer inside square microchannels, *Chem. Eng. Sci.* 64 (2009) 3697–3708.
- [329] W.B. Kolb, R.L. Cerro, Coating the inside of a capillary of square section, *Chem. Eng. Sci.* 46 (1991) 2181–2195.
- [330] T.C. Thulasidas, M.A. Abraham, R.L. Cerro, Bubble-train flow in capillaries of circular and square cross section, *Chem. Eng. Sci.* 50 (1995) 183–199.
- [331] C.D. Rath, S.G. Kandlikar, Liquid filling in a corner with a fibrous wall – an application to two-phase flow in PEM fuel cell gas channels, *Colloids Surf. A* (2011). doi:10.1016/j.colsurfa.2011.05.039
- [332] Y. Zhang, Y. Utaka, Y. Kashiwabara, Formation mechanism and characteristics of a liquid microlayer in microchannel boiling system, *J. Heat Transfer* 32(122403) (2010). p.7.
- [333] Y. Katto, Critical heat flux, in: (J.P.Hartnett, T.F. Irvine (Eds.), 17, Academic Press, 1985.
- [334] G.F. Hewitt, Burnout, in: (ed G. Hetsroni (Ed.), Hemisphere Publishing Corp., New York, 1982.
- [335] A.E. Bergles, Burnout in boiling heat transfer, Part II: subcooled and low quality forced-convection systems, in: S. Kakac, T.N. Veziroglu (Eds.), vol. II, Two-Phase Flows and Heat Transfer, Hemisphere, Washington, DC, 1976.
- [336] L.S. Tong, Y.S. Tang, Flow boiling crisis: Boiling Heat Transfer and Two-Phase Flow, Taylor and Francis, Washington, DC, 1997 (Chapter 5)
- [337] G.P. Celata, A. Mariani, CHF and Post-CHF heat transfer, in: (S.G. Kandlikar, M. Shoji, V.K. Dhir (Eds.), Taylor and Francis, Philadelphia, PA, 1999 (Chapter 17)
- [338] S.G. Kandlikar, A scale analysis based theoretical force balance model for critical heat flux (CHF) during saturated flow boiling in microchannels and minichannels, *J. Heat Transfer* 131(081501) (2010). p.13.
- [339] C.F. Bonilla, C.W. Perry, Heat transmission to boiling binary liquid mixtures, *Trans. Am. Soc. Chem. Eng.* 37 (1941) 685–705.
- [340] S.S. Kutateladze, On the transition to film boiling under natural convection, *Kotloturbostroenie* 3 (1948) 10–12.
- [341] S.S. Kutateladze, A hydrodynamic theory of changes in a boiling process under free convection, *Izv. Akad. Nauk S.S.S.R. Otdelenie Tekhnicheskii Nauk* 4 (1951) 529–536.
- [342] V.M. Borishanskii, On the problem of generalizing experimental data on the cessation of bubble boiling in large volume of liquids, *Ts. K.I.T.*, 28, Moscow, 1955.
- [343] W.M. Rohsenow, P. Griffith, Correlation of maximum heat transfer data for boiling of saturated liquids, *Chem. Eng. Prog.* 52 (1956) 47–49.
- [344] N. Zuber, Hydrodynamic Aspects of Boiling Heat Transfer, Ph.D. Thesis, Research Laboratory, Los Angeles and Ramo-Wooldridge Corporation, University of California, Los Angeles, CA, 1959.
- [345] Y.P. Chang, An Analysis of the Critical Conditions and Burnout in Boiling Heat Transfer, USAEC Rep. TID-14004, Washington, DC, 1961.

- [346] Y. Katto, S. Yokoya, Principal mechanism of boiling crisis in pool boiling, *Int. J. Heat Mass Transfer* 11 (1968) 993–1002.
- [347] Y. Haramura, Y. Katto, New hydrodynamic model of critical heat flux applicable widely to both pool and forced convection boiling on submerged bodies in saturated liquids, *Int. J. Heat Mass Transfer* 26 (1983) 389–399.
- [348] J.H. Lienhard, V.K. Dhir, Extended hydrodynamic theory of the peak and minimum pool boiling heat fluxes, NASA CR-2270, Contract No. NGL, 1973, 18-001-035.
- [349] Y.A. Kirishenko, P.S. Cherniakov, Determination of the first critical thermal heat flux on flat heaters, *J. Eng. Phys.* 20 (1973) 699–702.
- [350] C. Unal, V. Daw, R.A. Nelson, Unifying the controlling mechanisms for the critical heat flux and quenching: the ability of liquid to contact the hot surface, *ASME J. Heat Transfer* 114 (1992) 972–982.
- [351] S.G. Kandlikar, A theoretical model to predict pool boiling CHF incorporating effects of contact angle and orientation, *J. Heat Transfer* 123 (2001) 1071–1079.
- [352] S.G. Kandlikar, W.K. Kuan, D.A. Willistein, J. Borrelli, Stabilization of flow boiling in microchannels using pressure drop elements and fabricated nucleation sites, *J. Heat Transfer* 128(4) (2006) 389–396.
- [353] G.D. Wang, P. Cheng, H.Y. Wu, Unstable and stable flow boiling in parallel microchannels and in a single microchannel, *Int. J. Heat Mass Transfer* 50 (2007) 4297–4310.
- [354] C.J. Kuo, Y. Peles, Flow boiling instabilities in microchannels and means for mitigation by reentrant cavities, *J. Heat Transfer* 130 (2008) Article No. 072402
- [355] S.G. Kandlikar, Methods for Stabilizing Flow in Channels and Systems Thereof, U.S. Patent No. 7,575,046, issued August 2009.
- [356] S.G. Kandlikar, Fundamental issues related to flow boiling in minichannels and microchannels, *Exp. Thermal Fluid Sci.* 26(2-4) (2002) 389–407.
- [357] A.E. Bergles, S.G. Kandlikar, On the nature of critical heat flux in microchannels, *J. Heat Transfer* 127(1) (2005) 101–107.
- [358] S.G. Kandlikar, Heat transfer mechanisms during flow boiling in microchannels, *J. Heat Transfer* 126 (2004) 8–16.
- [359] W. Qu, I. Mudawar, Measurement and correlation of critical heat flux in two-phase microchannel heat sinks, *Int. J. Heat Mass Transfer* 47 (2004) 2045–2059.
- [360] F. Inasaka, H. Nariiai, Critical heat flux of subcooled flow boiling in uniformly heated straight tubes, *Fusion Eng. Des.* 19 (1992) 329–337.
- [361] A. Kosar, C.-J. Kuo, Y. Peles, Boiling heat transfer in rectangular microchannels with reentrant cavities, *Int. J. Heat Mass Transfer* 48 (2005) 4867–4886.
- [362] G.M. Roach, S.I. Abdel-Khalik, S.M. Ghiaasiaan, M.F. Dowling, S.M. Jeter, Low-flow critical heat flux in heated microchannels, *Nucl. Sci. Eng.* 131 (1999) 411–425.
- [363] A. Kosar, Y. Peles, Critical heat flux of R-123 in silicon-based microchannels, *J. Heat Transfer* 129 (2007) 844–851.
- [364] X. Cheng, F.J. Erbacher, U. Muller, F.G. Pang, Critical heat flux in uniformly heated vertical tubes, *Int. J. Heat Mass Transfer* 40 (1997) 2929–2939.
- [365] A. Kosar, Y. Peles, A.E. Bergles, G.S. Cole., Experimental investigation of critical heat flux in microchannels for flow-field probes, Paper No. ICNMM2009-82214, ASME Seventh International Conference on Nanochannels, Microchannels, and Minichannels, Pohang, Korea, 2009.
- [366] W.K. Kuan, S.G. Kandlikar, Critical heat flux measurement and model for refrigerant-123 under stabilized flow conditions in microchannels, *J. Heat Transfer* 130(3) (2008) Article Number 034503, p.5.
- [367] A.P. Roday, M.K. Jensen, Study of the critical heat flux condition with water and r-123 during flow boiling in microtubes, Part I: experimental results and discussion of parametric trends, *Int. J. Heat Mass Transfer* 52 (2009) 3235–3249.

- [368] B. Agostini, R. Revellin, J.R. Thome, M. Fabbri, B. Michel, D. Calmi, et al., High heat flux flow boiling in silicon multi-microchannels, Part III: saturated critical heat flux of R236fa and two-phase pressure drops, *Int. J. Heat Mass Transfer* 51 (2008) 5426–5442.
- [369] Y. Katto, General features of CHF of forced convection boiling in uniformly heated rectangular channels, *Int. J. Heat Mass Transfer* 24 (1981) 1413–1419.
- [370] K. Mishima, M. Ishii, Critical Heat Flux Experiments Under Low Flow Conditions in a Vertical Annulus, ANL-82-6, NUREG/CR-2647, 1982.
- [371] Y. Sudo, K. Miyata, H. Ikawa, M. Kaminaga, M. Ohkawara, Experimental study of differences in DNB heat flux between upflow and downflow in vertical rectangular channel, *J. Nucl. Sci. Tech.* 22 (1985) 604–618.
- [372] M.M. Shah, Improved general correlation for critical heat flux during upflow in uniformly heated vertical tubes, *Int. J. Heat Fluid Flow* 8(4) (1987) 326–335.
- [373] C.H. Oh, S.B. Englert, Critical heat flux for low flow boiling in vertical uniformly heated thin rectangular channels, *Int. J. Heat Mass Transfer* 36 (1993) 325–335.
- [374] L. Wojtan, R. Revellin, J.R. Thome, Investigation of saturated critical heat flux in a single, uniformly heated microchannel, *Exp. Thermal Fluid Sci.* 30 (2006) 765–774.
- [375] W. Zhang, T. Hibiki, K. Mishima, Y. Mi, Correlation of critical heat flux for flow boiling of water in mini-channels, *Int. J. Heat Mass Transfer* 49 (2006) 1058–1072.
- [376] S. Qi, P. Zhang, R. Wang, L. Xu, Flow boiling of liquid nitrogen in micro-tubes, Part II: heat transfer characteristics and critical heat flux, *Int. J. Heat Mass Transfer* 50 (2007) 5017–5030.
- [377] Z. Wu, W. Li, S. Ye, Correlations for saturated critical heat flux in microchannels, *Int. J. Heat Mass Transfer* 54 (2011) 379–389.

Direct Contact Condensation of Steam Jet in a Pool

CHUL-HWA SONG and YEON-SIK KIM

Korea Atomic Energy Research Institute (KAERI), Daejeon, Republic of Korea.

E-mail address: chsong@kaeri.re.kr

I. Introduction

In the design of traditional boiling water reactor (BWR) plants, safety/relief valves (SRVs) for controlling the reactor pressure are connected to a pressure suppression pool (PSP) as a receiving tank of discharged steam. The design basis for such kind of a system was to cope with rapid transients, such as a turbine trips, and so on. For these transients, the SRVs mounted on the steam line are actuated to divert the steam in the reactor into the PSP. Once the SRV opens, the steam released from the reactor is discharged through SRV lines to the pool in a stable condition. If the steam is discharged for an extended period, the pool temperature becomes high due to condensed steam, and the condensation process might become unstable. This instability of steam condensation may cause severe damages in the form of vibratory loads on the wall and internal structures of the pool. Currently available regulatory practice in dealing with this safety issue is just to restrict the allowable operating temperature so that this kind of instability will not occur during the steam discharge process [1].

In the development of advanced nuclear power plants, a safety depressurization system based on the BWR's design has been adopted to cope with fast transients and beyond design bases accident, e.g., loss of condenser vacuum (LOCV) and total loss of feedwater (TOLFW), respectively. For example, the in-containment refuelling water storage tank (IRWST) and the sparger, as a steam discharging device, have been adopted in the nuclear reactor design of EPR, AP1000, APR1400, and APWR, whereas the PSP and the sparger in the design of ABWR and ESBWR. In the design developments of the IRSWT or PSP with steam spargers, a variety of research works has been conducted since early 1990.

In the system of condensing pool, such as PSP or IRWST, with spargers connected to the SRVs, there are typically three different phases on the

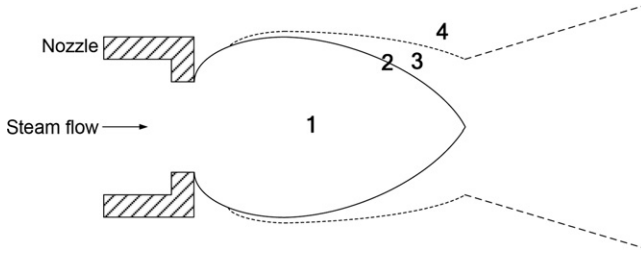


FIG. 1. Different regions in DCC of steam jet in water: (1) steam cavity, (2) steam–water interface, (3) hot water layer, and (4) pool water.

discharge processes. When the SRVs open, the air column within the discharging pipe line is compressed by the high-pressure steam from the reactor and, in turn, accelerates the water column in the partially submerged part of the piping and then clears out to a pool. This is called the *water clearing* phase. Then the compressed air in the discharge line is also accelerated into a pool to form high-pressure air bubbles. These oscillatory air bubbles experience a number of expansion and contraction, which can induce a hydrodynamic instability, while rising up to the free surface of the pool, and this is called the *air clearing* phase.

Following the air clearing phase, essentially pure steam is discharged into the pool and is condensed by the surrounding cold water through the mechanism of direct contact condensation (DCC). This is the *steam discharge* phase, where the steam injected into the water pool is completely condensed. There are few works performed for the water and air clearing phases, whereas various kinds of research works can be found for the steam discharge phase. Actually, the DCC is a common phenomenon that occurs when steam is introduced into subcooled water. It is a thermal–hydraulic phenomenon of great importance in nuclear, chemical, and marine engineering applications.

When steam is discharged into a subcooled water pool as a *forced jet* or *buoyant plume* through a sparger, the DCC occurs. In general, the DCC of steam jetting consists of four different regions as shown in Fig. 1. The first region to form in the process of condensation is the *steam cavity*. This region occurs at the tip of the steam sparger (or nozzle) exit through which the steam is introduced, as a jet or plume, into water pool. The outer surface of the steam cavity is the steam–water interface. The hot water layer is named the bulk water, which is usually a two-phase layer of conductively heated water toward the saturation temperature at the interface and is mixed with small steam bubbles. The temperature in this region directly influences the condensation efficiency. And the pool water is a single-phase region of water at certain

temperature. When steam is discharged into a water pool, the condensation modes of discharged steam due to the DCC can be classified into three main patterns: *chugging*, *jetting*, and *bubbling*. These modes can be depicted onto the so-called *condensation regime map*. From the viewpoint of engineering design, the analysis of condensation-induced thermal mixing in a pool is clearly related to the DCC process.

In this paper, the local and macroscopic characteristics of the DCC-related thermo-fluid dynamic features, such as the condensation regime map and four different regions of DCC, and the pool mixing analysis will be reviewed in detail. They include the fundamental characteristics of condensing steam jets and the resultant turbulent jet, which importantly affect the macroscopic circulation motion in a pool. The local behavior of condensing jets includes the shapes steam jet cavity, interfacial mass and heat transfer around the cavity, jet expansion and penetration length, and the condensation regime map. And a global motion analysis of thermal mixing in a pool is discussed in terms of local hot spot and the thermal stratification.

II. Steam Condensation Regime Map

A condensation regime map for DCC has been widely investigated since Chan and Lee [2]. They illustrated the condensation regime map as shown in Fig. 2, which is typically characterized by the steam mass flux and the pool

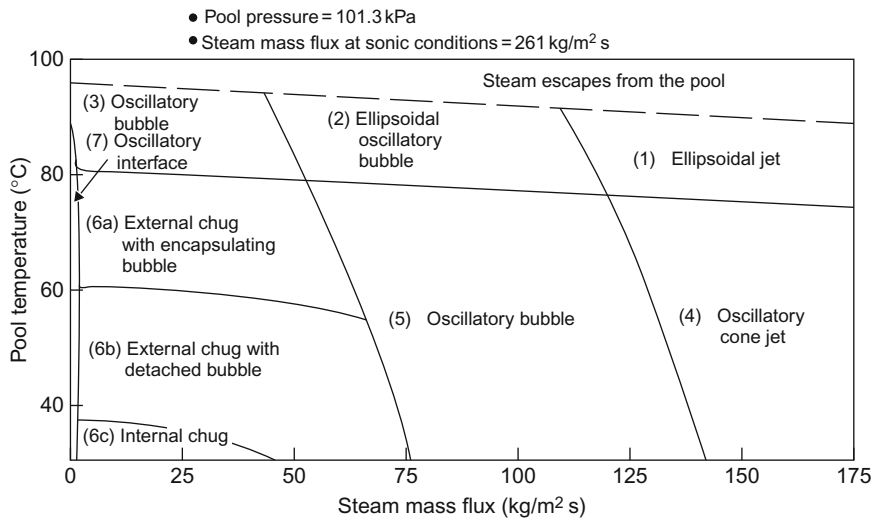


FIG. 2. Condensation regime map for low steam mass flux [2].

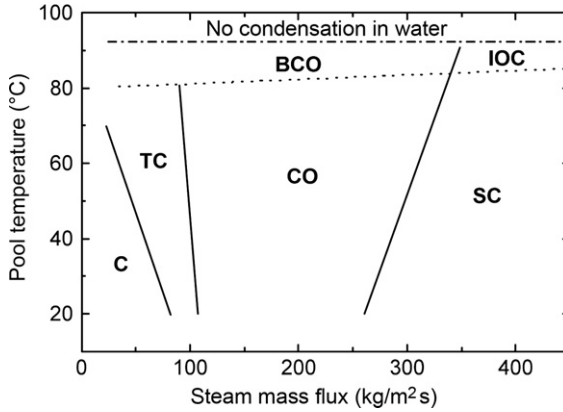


FIG. 3. Condensation regime map up to high steam mass flux [4].

temperature (or the degree of water subcooling). Although this regime map shows seven different kinds of steam cavity shapes, the condensation regime can be simply divided into typically three kinds of modes: *chugging*, *bubbling*, and *jetting*. While they tried to illustrate these steam cavity shapes, it has been actually observed that their shape changes abruptly and oscillates irregularly. They classified these three modes in more detail into internal chug, external chug (detached bubble or encapsulating bubble), ellipsoidal oscillatory bubble, oscillatory bubble, and oscillatory cone jet. The chugging region is usually characterized by the pressure spikes of low frequency and large amplitude. It has been observed that there is no stable cavity shapes for chugging, bubbling, and jetting modes in the case of a relatively small range of steam flux, e.g., up to around $175 \text{ kg/m}^2 \text{ s}$.

Chun et al. [3] investigated a condensation regime map for a higher range of steam mass flux up to $700 \text{ kg/m}^2 \text{ s}$. They suggested several condensation modes which include condensation oscillation (CO), transitional region from chugging to CO (TC), bubbling condensation oscillation (BCO), stable condensation (SC), and interfacial oscillation condensation (ICO) in addition to previously observed modes (e.g., chugging (C)). Cho et al. [4] suggested an improved condensation regime map based on their new experimental results, as shown in Fig. 3. It is noteworthy that the boundary between CO and SC in Fig. 3 seems to be corresponding to the steam mass flux at sonic conditions, i.e., $261 \text{ kg/m}^2 \text{ s}$. Table I shows a summary of some previous investigations on the condensation regime map.

Recently, De With et al. [12] developed a three-dimensional condensation regime map of steam jet in water, which includes the effect of injector diameter

TABLE I
SUMMARY OF PREVIOUS INVESTIGATIONS ON THE CONDENSATION REGIME MAP

Authors	Water temperature, T_{pool} (°C)	Hole size, D (mm)	Steam mass flux, G (kg/m ² s)	Number of classified condensation regimes
Young et al. [5]	37	6.4	341–746	Six regions
Cumo et al. [6]	20–80	1	300–2500	Stability map
Del Tin et al.[7]	20–70	2–6	200–800	Stability map
Fukuda [8]	25–90	8–27.6	50–400	Five types
Nariai and Aya [9]	20–80	18.29	0–200	Six regions
Aya and Nariai [10]	10–85	18.29	0–40	Four regions
Kim and Song [11]	18–90	10	0–500	Three regions (multi-hole)

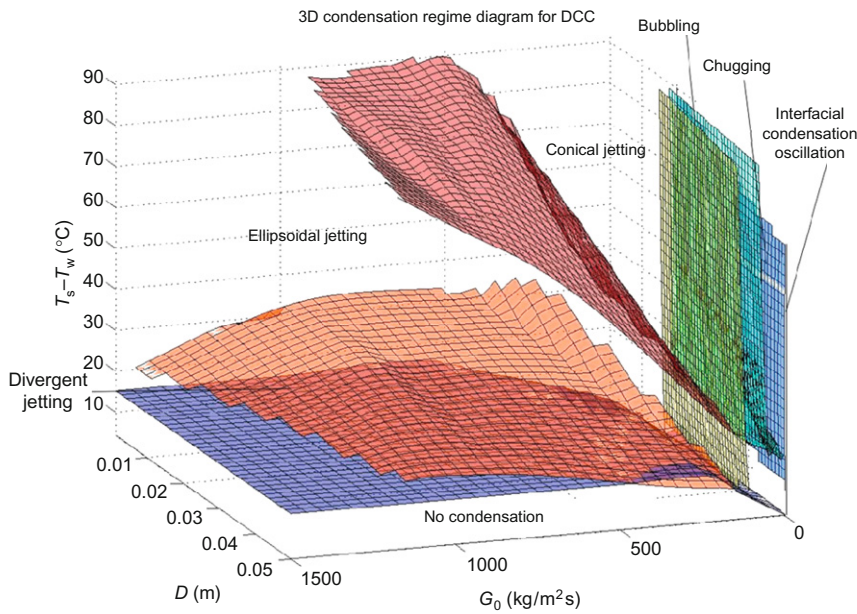


FIG. 4. Three-dimensional condensation regime map [12].

using available experimental data of previous researches, as shown in Fig. 4. And Wu et al. [13] suggested a three-dimensional condensation regime map of steam jet in water for supersonic and subsonic conditions, especially including the pressure ratio between nozzle inlet and outlet, as shown in Fig. 5.

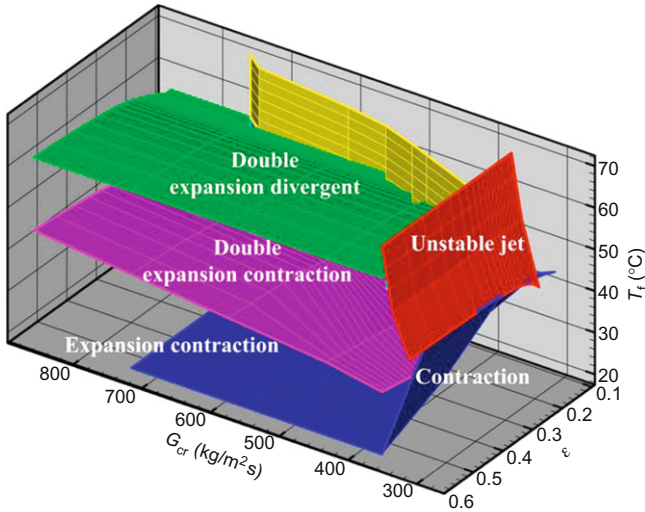


FIG. 5. Three-dimensional condensation regime map for supersonic and sonic conditions [13].

III. Steam Jet

A. SHAPE OF STEAM CAVITY

The shape of steam jet cavity is closely related to the characteristics of DCC phenomenon when steam is injected into subcooled water. Chan and Lee [2] found that the cavity shapes changed abruptly and oscillated irregularly and there was no stable cavity shape under a relatively small range of steam flux. But for a higher range of steam flux, relatively stable shapes for SC and IOC as defined in Fig. 3 were observed. Chun et al. [3] presented the distribution and shapes of steam cavity with the nozzle diameter in the range of 1.35–10.85 mm and under higher steam mass flux as shown in Fig. 6. For high steam mass flux, there have been found three different shapes of cavity such as *conical*, *ellipsoidal*, and *divergent* shapes. It is noteworthy that the conical shape appears at relatively low steam flux around $400 \text{ kg/m}^2\text{s}$ with high subcooling (or low pool temperature). And there is a transition point (TP) like a convergent point in the ellipsoidal shape.

In general, the jet can be divided into *under-expanded* and *over-expanded* jets. In the case of under-expanded jet, based on the theory of expansion and compression waves, the jet flow will expand at the nozzle exit due to expansion wave, and then the flow will contract due to compression wave. On the other hand, in the case of over-expanded jet, the flow will contract due to

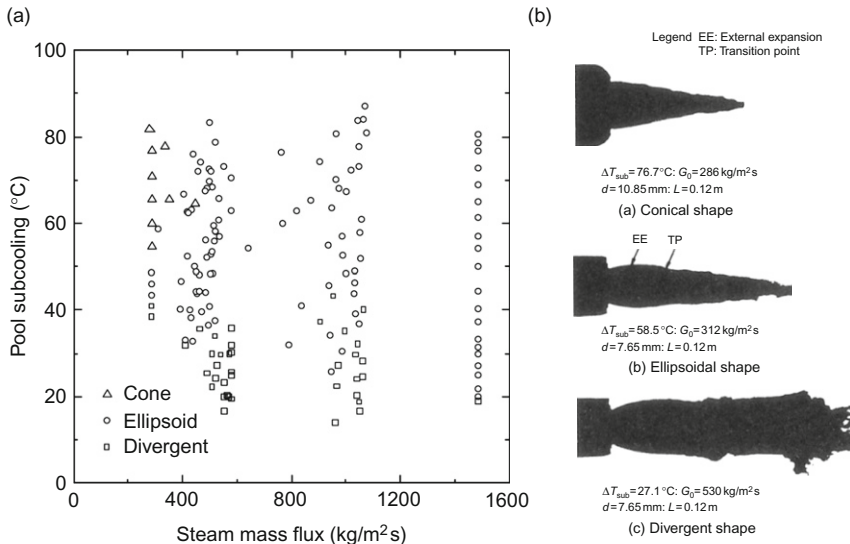


FIG. 6. Characteristics of the steam cavity for high steam mass flux: (a) Cavity shape distribution; (b) steam cavity shapes [3].

compression wave, and then the flow will expand due to expansion wave. For these two cases, the expansion and compression waves may occur periodically if there is no mass, momentum, and energy transfer. For the case of condensing steam jet in water, however, the periodicity of expansion and compression waves will disappear quickly due to condensation and viscosity. For example, Fig. 7 showed an analysis model of the steam cavity for under-expanded jet [13].

Kim et al. [14] initially suggested that the concept of wave propagation characterized by the method of characteristic (MOC) could be used for the estimation of the expansion ratio and length of a steam cavity. They showed a comparison between test data and the model predictions using the MOC in terms of the steam jet expansion and then concluded that the wave propagation characterized by the MOC could be helpful to understand the characteristics of steam cavity itself. Wu et al. [13,15–18] performed more works to investigate the characteristics of steam cavity at supersonic/sonic conditions using the theory of expansion and compression waves as proposed by Kim et al. [14].

In the case of under-expanded steam jet as shown in Fig. 8, the nozzle exit pressure is higher than the ambient pressure, so the expansion wave will occur at the exit, and then the steam flows outward. When water temperature is low, the expansion–contraction shape is observed due to a high condensation

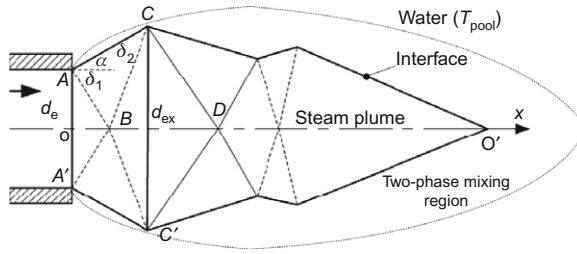


FIG. 7. Analysis model of the under-expanded steam jet discharged into water [13].

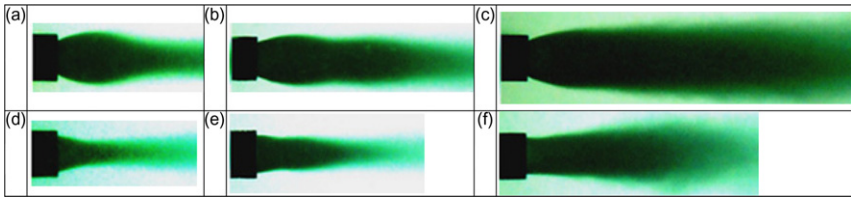


FIG. 8. Typical steam cavity shapes at various test conditions (sonic/supersonic): (a)–(c) Under-expanded steam jet; (d)–(f) over-expanded steam jet [13].

capacity as shown in Fig. 8(a). With the increase of water temperature, the condensation capacity of water decreases, and the inflexed jet will expand again due to the expansion wave, which leads to the flowing outward, then the flow is compressed by the ambient water, and the flow becomes inflexed again due to the compression wave. Finally, the steam is condensed by the surrounding water, which leads to the occurrence of the double expansion–contraction shape as shown in Fig. 8(b). When the water temperature becomes higher, the steam cavity tends to be divergent, and the double expansion–divergent shape is observed as shown in Fig. 8(c). Additionally, in the case of over-expanded supersonic steam jet, nozzle exit pressure is lower than the ambient pressure, so the oblique shock wave will occur at the exit, and the flow will be inflexed. When water temperature is low, the contraction shape is observed due to the high condensation capacity as shown in Fig. 8(d). With the increasing water temperature and decreasing condensation capability, the inflexed steam will expand due to the expansion wave, which leads to the flowing outward, and then the flow trend is similar to the expansion–contraction shape, which leads to occurrence of the contraction–expansion–contraction shape as shown in Fig. 8(e). Also, the steam cavity tends to be divergent, and the contraction–expansion–divergent shape occurs at higher water temperature as shown in Fig. 8(f).

TABLE II
TYPICAL SONIC STEAM CAVITY SHAPES VERSUS STEAM MASS FLUX AND POOL WATER TEMPERATURE

		Pool water temperature					
		Low	Fig. 8	Medium	Fig. 8	High	Fig. 8
Steam mass flux	Low	Cone [SC] ^a	—	Unstable [CO]	—	Unstable [CO]	—
	Medium	Ellipsoidal [SC]	(a)	Ellipsoidal/TP ^b [SC]	(b)	Divergent [IOC]	(c)
	High	Ellipsoidal/TP [SC]	(b)	Ellipsoidal/TP [SC]	(b)	Divergent [IOC]	(c)

^aDefined as in Fig. 3.

^bEllipsoidal shape with transition point.

Wu et al. [13] found that the shape of steam cavity for the supersonic steam jet (pressure ratio $\eta < 0.577$) is different from that of sonic steam jet (pressure ratio $\eta = 0.577$), and the pressure ratio also plays an important role in characterizing the condensing flow pattern in addition to both the steam mass flux at the nozzle throat and the water temperature as the influencing factors. It is noteworthy from the comparison between Chun et al. [3] and Wu et al. [13] that the shapes of the steam cavity between sonic and highly under-expanded supersonic conditions are very similar to each other. In Table II, the shapes of steam cavity for sonic condition were depicted with the condensation regime maps suggested in Refs. [3, 4, and 6].

The appropriateness of applying the theory of expansion and compression waves could be confirmed from another research [19], which observed a shock for an under-expanded moisturized air jet using the Schlieren method. The author took a typical picture of under-expanded jet as shown in Fig. 8 and showed the moist air jet boundary and barrel shock configuration with a variation of relative humidity ($\phi_0 = 30\%, 50\%, 70\%$) as shown in Fig. 9. The author also suggested a correlation for the prediction of the location of Mach disk as Eq. (1):

$$\frac{x}{d_e} = 0.5673 \sqrt{\frac{p_o}{p_b}} \left(5.3 < \frac{p_o}{p_b} < 12.3, \quad 30\% < \phi_0 < 70\% \right) \quad (1)$$

Although the experiment of Baek [19] did not consider the condensation effect, this work would give some insight of understanding the shape of condensing steam jet in water. From the comparison between Baek [19] and others [3,13–18], the shape of condensing steam cavity in water seems to follow the trend of jet boundary as shown in Fig. 10, which was expected by a theoretical approach [14]. And the external expansion (EE) of the ellipsoidal shape

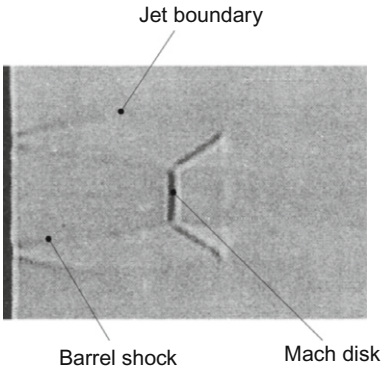


FIG. 9. Typical picture of under-expanded jet [19].

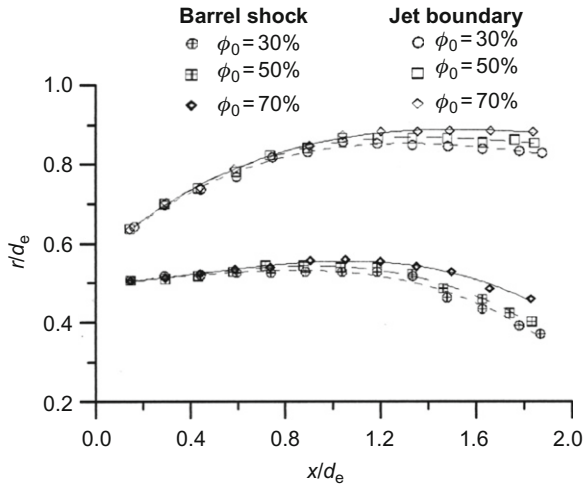


FIG. 10. Moist air jet boundary and the barrel shock configuration ($p_0/p_b = 12.3$) [19].

indicated by Chun et al. [3] would be related to the Mach disk from Figs. 9 and 10. Kim and Song [11] also investigated the effect of multiple discharge holes on the shape of a combinatory cavity and this observation provided a firm basis of developing the concept of the so-called steam condensation region model (SCRM), which will be discussed later.

TABLE III
EXPANSION RATIO AND LOCATION FOR ELLIPSOIDAL STEAM JET [14]

			d_{EE}/d_e	x_{EE}/d_e
$d_e = 15.5 \text{ mm};$ $G_e = 440 \text{ kg/m}^2 \text{ s}$	MOC	No condensation	1.24	0.95
	Test	$T_{\text{pool}} = 35^\circ\text{C}$	1.06	0.44
		$T_{\text{pool}} = 55^\circ\text{C}$	1.16	0.48
$d_e = 10.15 \text{ mm};$ $G_e = 825 \text{ kg/m}^2 \text{ s}$	MOC	No condensation	1.87	1.72
	Test	$T_{\text{pool}} = 35^\circ\text{C}$	1.33	0.96
		$T_{\text{pool}} = 75^\circ\text{C}$	1.49	1.08
$d_e = 7.1 \text{ mm};$ $G_e = 1045 \text{ kg/m}^2 \text{ s}$	MOC	No condensation	2.35	2.21
	Test	$T_{\text{pool}} = 35^\circ\text{C}$	1.59	1.10
		$T_{\text{pool}} = 75^\circ\text{C}$	1.87	1.60
$d_e = 5 \text{ mm};$ $G_e = 1188 \text{ kg/m}^2 \text{ s}$	MOC	No condensation	2.33	2.20
	Test	$T_{\text{pool}} = 40^\circ\text{C}$	1.73	1.40
		$T_{\text{pool}} = 70^\circ\text{C}$	2.09	1.70

B. EXPANSION RATIO OF STEAM CAVITY

The expansion of a steam cavity in water has been a common feature of interest for the steam jet of high steam flux. Kim et al. [14] compared the experimental data with a theoretical prediction using the MOC. They presented a summary of comparison between the MOC and the experimental result in terms of the EE of the ellipsoidal cavity as in Table III. From the table, it is shown that the condensation effect had some influence on the expansion ratio and location, e.g., smaller in expansion ratio and shorter in location rather than the case of no condensation. If the pool temperature becomes higher, i.e., with reduced condensation capacity, the expansion ratio becomes larger and the location farther.

Wu et al. [16] suggested a correlation to predict the expansion ratio for sonic steam jet, by deducing from their test data, represented by Eq. (2). The predicted expansion ratio was compared with the experimental data of their work and Kim et al. [14], and the discrepancy was within $\pm 15\%$ approximately:

$$\frac{d_{EE}}{d_e} = k \frac{\cos\alpha \sin(\alpha + \mu_2)}{\sin\mu_2} \quad (2)$$

where α is the patulous angle of steam flow, μ_2 is the expansion angle, and k is the correction coefficient, depending on water temperature T_{pool} , defined as $k = (T_{\text{pool}} + 273.15)/273.15$.

C. LENGTH OF STEAM CAVITY

As shown in Fig. 7, the penetration length of steam cavity, oo' , is defined as the axial distance of pure steam. For the stable sonic steam jet condensation,

TABLE IV
CORRELATIONS FOR THE STEAM JET PENETRATION LENGTH

Authors	Definition of B	Correlation for jet penetration length
Kerney et al. [20]	$C_p(T_{\text{sat}} - T_\infty)/h_{\text{fg}}$	$l/d = 0.2588B^{-1}(G/G_c)^{0.5}$
Weimer et al. [21]	$(h_f - h_\infty)/(h_s - h_f)$	$l/d = 17.75 (G/G_c)^{0.5}/((\rho_\infty/\rho_s)^{0.5}B)$
Chun et al. [3]	$C_p(T_s - T_\infty)/h_{\text{fg}}$	$l/d = 0.5923B^{-0.66}(G/G_c)^{0.3444}$
Kim et al. [14]	$C_p(T_s - T_\infty)/(h_s - h_\infty)$	$l/d = 0.503B^{-0.7013}(G/G_c)^{0.4769}$
Wu et al. [15]	$C_p(T_s - T_\infty)/h_{\text{fg}}$	$l/d = 0.868B^{-0.6}(p/p_\infty)^{0.2}(G/G_c)^{0.5}$

this length has been investigated by many researchers [3,14,15,20–24]. There are two experimental methods to measure the penetration length: (1) analyzing the pictures obtained by the high-speed video camera, and (2) measuring the temperature profiles along the nozzle axis. Since the accuracy of the first method is determined by the spatial resolution of taking pictures and image analysis, so it is difficult to estimate the penetration length when the water temperature is high and the shape of steam cavity becomes unstable.

Kerney et al. [20] derived an analytical relation using the conservations of mass and energy, and the heat transfer across the cavity interface. In this mode, it was assumed that the shape of steam cavity is arbitrary and the rate of mass, energy, and heat transfer is balanced for the selected control volume, and the cavity length correlation can be defined in a dimensionless form as follows:

$$\frac{l}{d} = \frac{(G_0/G_m)^{1/2}}{(BS_m)} \tag{3}$$

where $B = C_p(T_s - T_\infty)/h_{\text{fg}}$ and $S = h_i/C_pG$. The parameter B represents a dimensionless driving potential for the condensation process. The transport modulus, S , is analogous to the Stanton number of convective heat transfer, and S_m in Eq. (3) represents a mean value for cavity. This equation has been widely used for a basic form of the correlation to describe a steam jet penetration length, and a summary of those results is shown in Table IV.

Petrovic [24] performed a parametrical study of different steam cavity shapes using the laws of conservation, e.g., the change of the steam in a cavity volume must be equal to the mass of steam that condenses through a surface of the same volume as shown in Fig. 11. The mass conservation equation then can be described by Eq. (4):

$$\rho v(x)A_j(x) - \rho v(x + dx)A_j(x + dx) = \frac{h_i}{h_{\text{fg}}} \Delta TA_i(x) \tag{4}$$

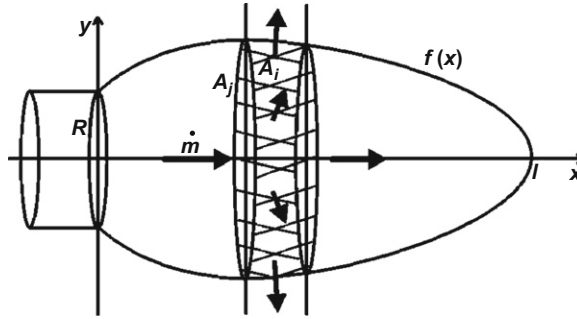


FIG. 11. Control volume for the laws of mass conservation [24].

Assuming an axi-symmetric shape of steam cavity as shown in Fig. 11, Eq. (3) can be transformed into an integral equation as follows:

$$\int_{\dot{m}_0}^0 d\dot{m} = -\frac{h_i}{h_{fg}} \Delta T \cdot 2\pi \int_0^l f(x) \sqrt{1 + f'^2(x)} dx \quad (5)$$

where the surface through which condensation occurs is calculated correctly using the declination of the function. The form of Eq. (4) is such that it can be easily used for different shapes of cavity, described by function, $f(x)$, defined as follows:

$$\text{Conical: } f(x) = -(R/l)x + R \quad (6)$$

$$\text{Parabolic: } f(x) = R\sqrt{1 - x/l} \quad (7)$$

$$\text{Ellipsoidal: } f(x) = R\sqrt{1 - x^2/l^2} \quad (8)$$

$$\text{Spherical: } f(x) = \sqrt{(l-a)^2 - (x-a)^2} \quad (9)$$

where $a = \pm (l^2 - R^2)/(2l)$.

In addition, the average heat transfer coefficient (HTC) of DCC should be reasonably assumed for correct prediction. From the comparison between the proposed model and existing experimental data, the ellipsoidal mode shows the best agreement with data and is believed to be the most appropriated shape for a wide range of experimental data.

De With [25] developed two-dimensional steam cavity length diagram for DCC. They found that a much more coherent plot of the experimental data can be found when the steam cavity length is described as a function of Reynolds number (Re) and condensation potential (B).

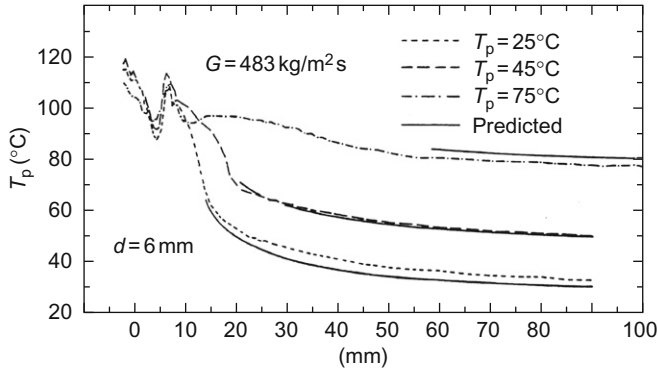


FIG. 12. Axial temperature profiles at center line [23].

D. THERMAL-HYDRAULIC CONDITION OF STEAM CAVITY

Del Tin et al. [7,23] measured the axial profiles of temperature and static pressure for various operating conditions. A micrometric device was used for the displacements of the thermocouples and pressure probe with a resolution of smaller than 0.05 mm. Among their test results, data referring to 6 mm nozzle diameter are shown for three different water temperatures in Fig. 12. It has been observed at the nozzle exit that the jet diameter tends to increase, the steam temperature rapidly falls, and then it increases again in a manner practically nondependent on the pool water temperature. Subsequently, the temperature decreases with a trend that is clearly dependent on the pool water temperature. The sharp decrease of the temperature inside the vapour jet might be caused by the subcooled liquid entrainment near the phasic interface. Song et al. [26] and Kim et al. [14] also observed similar results of the temperature profiles for different test conditions. Similar trends were found in the static pressure profiles, as in the case of the temperature profiles, as shown in Fig. 13, which shows both the total and static axial pressure profiles.

Wu et al. [17] also measured the temperature distributions along the steam jet axis and in the surrounding water. Figure 14 shows the axial temperature distributions for two different steam mass fluxes under the water temperature in the range of 293–343 K. For low mass flux, the axial temperature distributions decreased to the value of ambient water directly, which represents the trend of the contraction of steam cavity shape, like the shape (1) in Fig. 14. For high mass flux, the axial temperature variation is independent of the water temperature near the nozzle exit inside the steam cavity. When the water

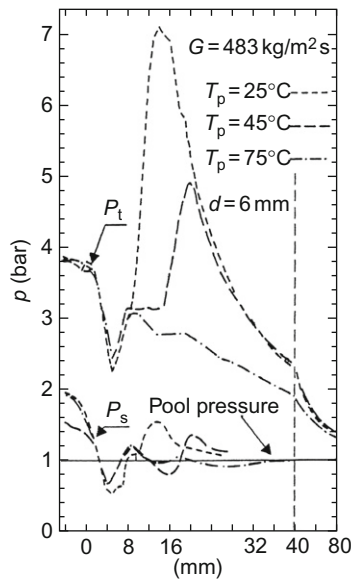


FIG. 13. Axial profiles of total and static pressures [23].

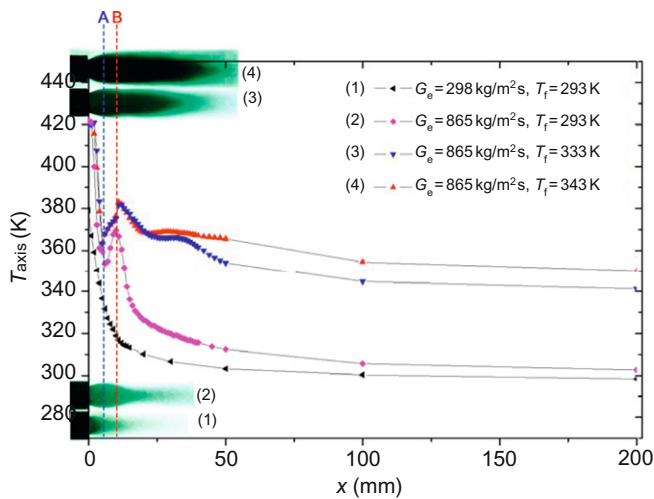


FIG. 14. Relations of axial temperature distributions and steam cavities [17].

temperature is low, the axial temperature decreases first, and then increases, and after a peak, the temperature decreases again to the ambient water temperature. Such a temperature distribution represents the expansion–contraction steam cavity shape, e.g., the shape (2) in Fig. 14. For high water temperature, the axial temperature tended to increase slightly again after the first peak, and then decreased to the ambient water temperature due to condensation, and this represents the double expansion–contraction steam cavity shape, e.g., the shape (3) in Fig. 14. When the water temperature is above 343 K, the second peak of axial temperature becomes smooth, which represents the double expansion–divergent steam cavity shape, e.g., the shape (4) in Fig. 14.

The axial temperature distribution is affected by the expansion and compression waves for the case of under-expanded jet [14,15]. When the nozzle exit pressure is higher than the surrounding water pressure, the expansion wave may occur at a nozzle exit, which leads to supersonic flow and also steam flowing outward. When the supersonic flow is compressed by the ambient water, the compression wave occurs. The expansion and compression waves could reflect periodically for ideal condition. However, the reflection only occurs one or two times due to the condensation and viscosity. When the steam flow is expanded, the axial temperature would decrease, whereas the axial temperature would increase when the steam flow is compressed. Accordingly, the axial temperature distributions reflect the characteristics of steam jet flow. Figure 13 shows the corresponding relation of axial temperature distributions and the steam cavity shapes. The trend of axial temperature is all in accord with the position of expansion (dotted line “A”) and compression (dotted line “B”) of steam cavity, approximately. Although the authors showed no data on the static pressure in the steam cavity, the trends of static pressure might tend to follow that of the temperature profile in the cavity, as confirmed by Del Tin et al. [23].

Following our review on the steam cavity shape, it has been tried to compare the theory of expansion and compression waves with DCC conditions, and Baek [19] showed Pitot impact pressure profile along the centerline of moist air jet as shown in Fig. 15. This figure shows that the lowest pressure occurs near the Mach disk and then pressure gradually and periodically increases like an oscillating pattern. This trend is an ideal pattern of pressure profile for under-expanded jet at the atmospheric condition. In Fig. 14, the lowest pressure was observed at the EE (dotted line “A” in the figure) of the ellipsoidal shape, where the Mach disk exists as mentioned previously.

Here it would be noteworthy to discuss an interesting finding by Baek [19]. The author tested the effect of wall that is located at the downstream of the free jet. In that case, the test result indicated that the wall of the downstream affects the patterns of jet, e.g., the shapes of jet boundary, barrel shock, and the Mach disk location. If the downstream wall comes closer to the nozzle, the overall jet shape tends to shrink axially. Figure 16 shows this kind of trends,

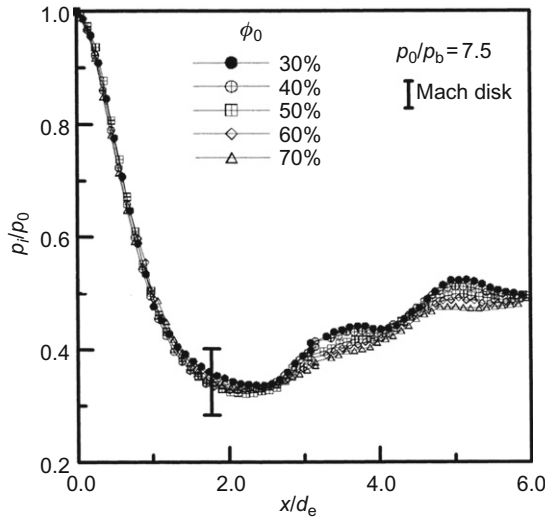


FIG. 15. Pitot impact pressure distributions of moist air jet [19].

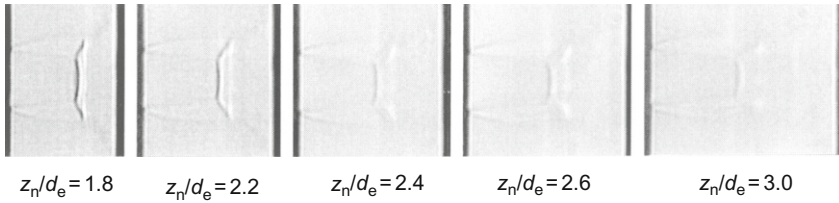


FIG. 16. Visualization pictures of impinging moist air jet ($\phi_0 = 30\%$; $p_0/p_b = 7.5$) [19].

where z_n is the wall distance from the nozzle exit and d_e is the nozzle diameter. The author showed that the dimensionless axial location of the Mach disk is about 1.8 for free jet without downstream wall, which seems to be reasonable when compared with the predictions of Kim et al. [14] as shown in Table III. If there is a wall downstream at about $2d_e$ distance from the nozzle for a free jet, the dimensionless location of the Mach disk became to be about 1.0. For the steam jet injected into water, the water might be a kind of downstream wall even though quite a large condensation occurs between steam jet and water. This trend can be found from the test data measured by Kim et al. [14] as shown in Table III, which shows that the location of EE of the ellipsoidal plume becomes half of the case of no condensation.

E. STEAM JET CONDENSATION LOAD

Any mode of steam jet condensations in a water pool, such as chugging, condensation oscillation, and stable condensation, may make the steam–water interface oscillatory unstably or constantly in a water pool. As for the interfacial oscillation, a portion of water near the phasic interface in the form of a column moves forward and backward across the interface. The movements of the water induce a kind of pressure impulse or load, which is called the *condensation load*. The condensation load can be represented by its magnitude and frequency, which are closely related to each other.

The condensation load depends on the movement of steam–water interface. In the case of a large movement of the interface, like a chugging, a large pressure load is induced. But in a stable condensation, the movement of the interface is small resultantly causing a small pressure load. Since the condensation load is induced by the movement of the water column, its magnitude can be represented by a general equation related to a water hammer load as follows:

$$\Delta F = A\rho a\Delta V \quad (10)$$

Here, A is defined as an equivalent area of the water column, which can be estimated to be proportional to the nozzle diameter, a is the sound speed of the water, and ΔV is the velocity change between consecutive movements, respectively. The velocity change is proportional to the velocity of a water column. If the condensation occurs abruptly, the steam cavity contracts instantly and the water column is accelerated to makeup the contracted space. Here the condensation rate should be considered to be an important parameter for the water column to be accelerated. The condensation rate depends mainly on the HTC and the temperature difference between the phases. When the water column is accelerated backward to make up the contracted space, the injected steam provides a kind of resistance to the water column. This suggests the steam flux is also an important parameter for the movement of the water column.

Chan [27] and Park et al. [28] reported that the condensation pressure pulse is proportional to the nozzle diameter for the same steam flux, and Hong [29] found that the condensation load is proportional to the temperature difference, $T_s - T_f$, and inversely proportional to the steam flux for the same nozzle diameter. For the frequency aspect of the condensation load, the previous work [8,29] can be referred to. Hong [29] conducted an experiment of steam injection into a water pool for a single nozzle of 10 mm diameter and the results of data processing using the fast Fourier transform (FFT) showed that the peak of the dominant frequency occurs at the boundary of condensation oscillation and stable condensation. In Hong's data, the FFT graphs of condensation oscillation and stable condensation showed that one shape is spreading more widely than the other as shown in Fig. 17. The trend of the dominant frequency, in

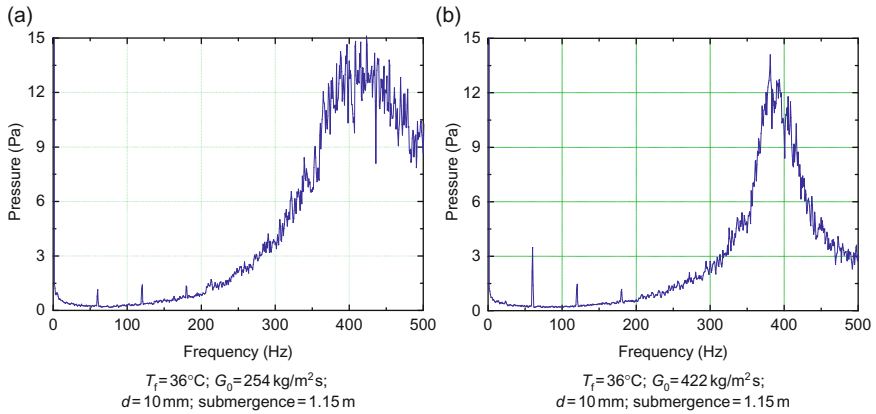


FIG. 17. Comparison of the FFT distributions between the (a) CO and the (b) SC [28].

general, can be obtained from the FFT spectrum. The different patterns of FFT spectrum between the two modes provide a clue to the different condensation patterns between the two types. In the case of condensation oscillation, steam condensation occurs with various types of steam–water interfacial boundaries unlike the case of stable condensation. Fukuda [8] measured the shapes of steam cavity corresponding to the condensation oscillation (C-type condensation defined by the author) and to the stable condensation (E-type condensation also defined by the author). He found that the photos of C-type condensation can be divided into two major types, i.e., C₁-type and C₂-type, but E-type showed just a stable steam jet shape as found by Chun et al. [3]. From Hong's and Fukuda's works, it seems that the condensation pattern gives some insights on the oscillation type of the steam condensation and vice versa.

Fukuda [8] suggested an experimental correlation for the C₁-type condensation oscillation as follows:

$$f = \frac{60\Delta T}{d} \quad (11)$$

From the above equation, the frequency of the condensation oscillation is proportional to the temperature difference between the two phases, $T_s - T_f$, and is inversely proportional to the nozzle size. Arinobu [30] also suggested an experimental correlation for the condensation oscillation as follows:

$$f = 0.8 \frac{\nu}{d} \left(\frac{C_p \Delta T}{h_{fg}} \right)^{1.4} \quad (12)$$

Equation (12) has some physically reasonable sense when compared with the characteristic frequency derived from the Rayleigh equation as follows:

$$f = \frac{2}{d} \sqrt{3k \frac{p_0}{\rho}} \quad (13)$$

Except the constant 3 in Eq. (13), the square root term represents the speed of sound of the steam, so Eq. (13) becomes a simplified form of Eq. (12).

Previous works [31–33] elaborated on the dominant frequency of steam jet condensation by the Strouhal number using the related parameters, such as Jacob number, Reynolds number, Weber number, and so on. Table V shows these correlations with applicable range of experimental conditions.

In spite of their correlations on the condensation frequency, there is no specific relation to the steam condensation regime map such as in Fig. 3. It is noted that the frequency correlation in Table III should be used carefully. For example, Simpson and Chan [31] and Cho et al. [33] just mentioned the range of steam flux used for the correlation, but the interrelation of the steam flux and the condensation regime was not investigated when compared to Damasio et al. [32]. As mentioned before, Hong [29] found that a different trend in the dominant frequency is measured between condensation oscillation and stable condensation, which means that different correlations might exist for respective condensation regimes, which can be found in Damasio et al.'s work.

In general, the dynamic pressure shows a trend that is mainly dependent on the steam mass flux and pool water temperature as observed by Song et al. [26]. The magnitude of the dynamic pressure in pool water showed a peak at a finite subcooling of around 20°C, and becomes smaller as the subcooling decreases as typically shown in Fig. 18. It has been found that the peak value of dynamic pressure varies differently with the steam mass flux and the discharging nozzle size: at a low steam mass flux, the peak magnitude increases with an increasing steam mass flux, whereas at a higher steam mass flux, the trend is reverse. Song et al. [34] have also found that the effect of noncondensable gas on both the DCC and the resultant dynamic pressure is very pronounced.

The variation of dynamic pressure and the shape of a steam jet with the condensation modes are compared in Fig. 19. The pressure load increases gradually with an increase of steam mass flux in the CO regime, but decreases rapidly in the SC regime. The pictures of steam–water interfaces show this trend well. With a higher subcooling (e.g., $T_p = 30^\circ\text{C}$ or 40°C), there are relatively smaller pressure loads indicating that the steam jet is condensed very efficiently and stably, whereas with a very low subcooling (e.g., $T_p = 90^\circ\text{C}$), the steam jet mostly escapes out of the pool without active condensation, and this leads to little variation of pressure loads. These observations can be used

TABLE V
COMPARISON OF St NUMBER FOR SOME PREVIOUS RESEARCHES

Parameters	Simpson and Chan [31]	Damasio et al. [32]	Cho et al. [33]	Remark
d [cm]	0.635–2.22 (single)	0.6–1.2 (single)	0.5 (multiple)	
G [kg/m ² s]	147–333	30–250	70–215	
St correlation	$St = k_0 Ja^{a_0} Re^{b_0}$ $k_0 = 0.011$; $a_0 = 0.72$; $b_0 = 0.25$	$C: St = k_1 Ja^{a_1} Re^{b_1}$ $k_1 = 0.32428 \times 10^{-3}$; $a_1 = 0.55149$; $b_1 = 0.75380$ $k_2 = 0.11904 \times 10^{-2}$; $a_2 = 1.0849$; $b_2 = 0.93892$; $c_2 = -0.76700$	$St = k_3 Ja^{a_3} Re^{b_3} We^{c_3} I\mathcal{Q}^{d_3}$ $k_3 = 0.174 \times 10^{-2}$; $a_3 = 1.093$; $b_3 = 0.891$; $c_3 = -0.827$; $d_3 = 0.298$	Should be used cautiously related to condensation regime map

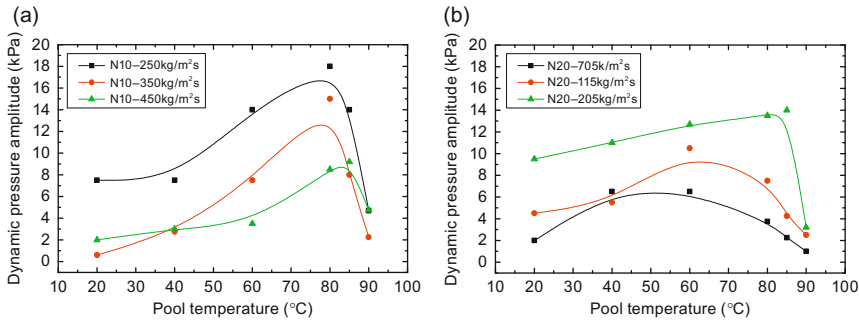


FIG. 18. Variation of the dynamic pressure at the pool wall: (a) $d = 10.15$ mm and (b) $d = 20$ mm [33].

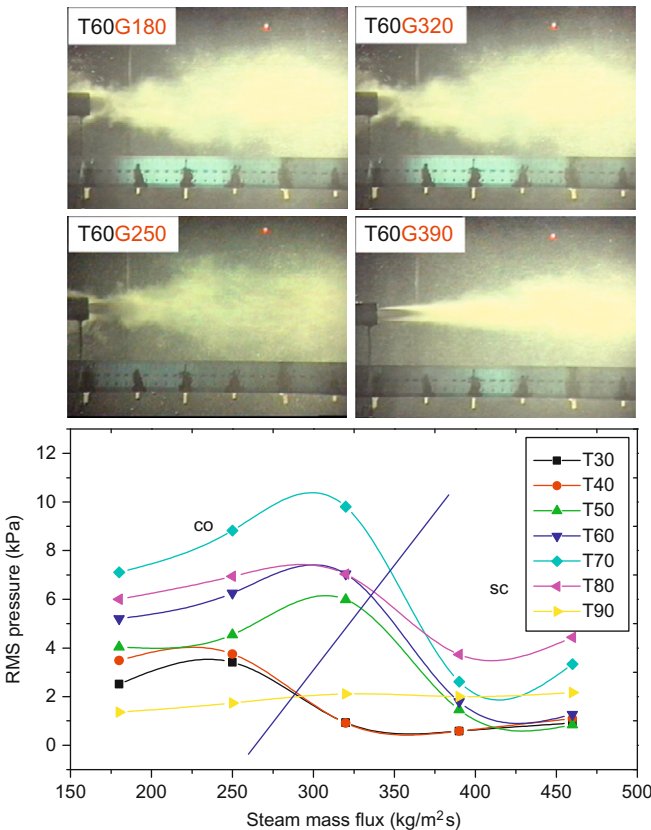


FIG. 19. Variation of pressure load measured at the wall and with the pool temperature and steam mass flux [33].

as technical background information to support certain safety criteria for ensuring a stable and safe operation of the relevant engineering systems.

IV. Interfacial Transport Phenomena

A. INTERFACIAL HEAT TRANSFER COEFFICIENT (HTC)

The outer surface of a steam cavity is the steam–water interface (e.g., the region-2 in Fig. 1). It is the region where steam and water meet each other and along which DCC occurs as a convective heat and mass transfer across the interface. The exact position of the interface depends on interfacial eddies in the surrounding water layer, i.e., hot water layer. The hot water layer (i.e., the region-3 in Fig. 1) is a two-phase layer of conductively heated water toward the saturation temperature at the interface, mixed with small steam bubbles. Both phases in the hot water layer are in turbulent motion with eddies created mainly by the momentum or kinetic energy carried by the condensing steam and the velocity of the water [24]. The eddies have a strong effect on the interface shape and control the interfacial transport. Large eddies have enough inertia to travel away from the interface and dominate the transport process if the turbulent Reynolds number is small ($Re_t < 500$). On the other hand, there are small eddies, which are strongly influenced by the liquid viscosity and are confined near the interface. These eddies typically exist at large turbulent Reynolds numbers ($Re_t > 500$).

Aya and Nariai [10] proposed correlations for the HTC at the steam–water interface assuming a simple interface shape and was found to be in the range of $0.1\text{--}1\text{ MW/m}^2\text{ K}$. Liang and Griffith [35] also investigated the interfacial heat transfer in the regime of oscillatory jets, and a methodology was suggested for calculating the product of interfacial area and the HTC. Chun et al. [3] found that the average HTC increases with an increase in the steam flow rate and the degree of subcooling, and they proposed a semi-empirical correlation for the average HTC, which is in the range of $1.0\text{--}3.5\text{ MW/m}^2\text{ K}$. Kim et al. [14] reported the average HTC to be in the range of $1.24\text{--}2.05\text{ MW/m}^2\text{ K}$ and its dependency on d_0 and G_0 was found to be similar to those reported by Chun et al. [3]. Kim et al. [36] proposed three different models for the interfacial heat transfer, such as interfacial transport model due to the turbulent intensity, the surface renewal model, and the shear stress model, and they reported that the sizes of eddies developed on the liquid side thermal boundary layer are important in determining the HTC by using the turbulent intensity model. For both the surface renewal model and the shear stress model, a measured cavity shape was used in determining the HTC. Further, the model was corrected using the cavity shape factor, which shows good agreement with the test data. Gulawani et al.

[37] proposed a semi-empirical correlation for the HTC based on nozzle diameter. A rational correlation was also developed for the estimation of interfacial area expressed in terms of Nusselt number (Nu), Reynolds number (Re), Prandtl number (Pr), and ratio of viscosity of steam and water. Wu et al. [15] investigated experimentally the condensation characteristics of supersonic steam jet submerged in the quiescent subcooled water. The average HTC of supersonic steam jet condensation using the concept of interfacial transfer model due to the shear stress [36] was found to be in the range of 0.63–3.44 MW/m² K. And Wu et al. [16] suggested the condensation HTCs for different shapes of steam cavity using the surface renewal model [36]. Gulawani et al. [38] used hot film anemometer (HFA) for the evaluation of local HTC and observed the average HTC in a range of 0.1–4 MW/m² K at the vapor–liquid interface, and they evaluated the HTC predictions using four different models, such as the penetration theory, surface renewal model, small eddy model, and large eddy model. Then they found that the small eddies are dominant close to vapor–liquid interface and the small eddy model is relatively closest to experimental HTC. All the semi-empirical correlations proposed in the literature can be summarized in Table VI.

B. INTERFACIAL TRANSPORT MODEL

Kim et al. [36] investigated the steam–water HTC using the three kinds of interfacial transport models. They reviewed previous works on the interfacial transport phenomena related to interfacial mass, momentum, and/or energy transport. They investigated the interfacial transport phenomena according to the two concepts, such as the turbulence generated by submerged vertical jet directed to water–steam interface and the concept of separated concurrent or countercurrent two-phase flow in a channel or a pipe. Most of the works indicate that the turbulent Stanton number (St_t) is in the range of 0.008–0.0131 and about 0.1, respectively.

For the case of steam jet injected into water, Young et al. [5] and Kudo et al. [39] investigated the interfacial transport models. Young et al. [5] derived the interfacial velocity calculated from a Reynolds flux model by taking into account the momentum transfer due to viscous effects and the action of the mass condensing flux. The authors suggested a semi-empirical correlation for the Stanton number as follows:

$$St = 6.5Re^{-0.40} \quad (14)$$

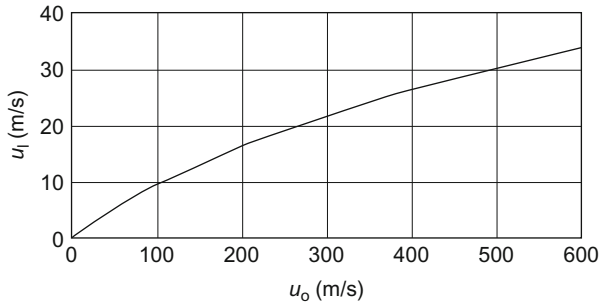
where

$$St = h/\rho C_p v^*; \quad Re = \rho v^* d/\mu; \quad v^* = v_i - v_f$$

TABLE VI
PROPOSED CORRELATIONS FOR INTERFACIAL HEAT TRANSFER COEFFICIENT

Authors	Correlations	HTC (MW/m ² K)
Aya and Nariai [10]	$q = \bar{h}(T_s - T_f)$	0.1–1.0
Liang and Griffith [35]	$\frac{(h_i a_i)_z}{k_f} = \frac{\pi}{4} \frac{d_c}{1} \frac{\rho_f}{\rho_s} Re_f^s Pr Ja^{-1} \frac{dl(z_n)}{dz_n}$	~ 1.0
Chun et al. [3]	$h = 1.3583 C_p G_m B^{0.0405} \left(\frac{G_0}{G_m} \right)^{0.3714}$	1.0–3.5
Kim et al. [14]	$h = 1.4453 C_p G_m B^{0.03587} \left(\frac{G_0}{G_m} \right)^{0.13315}$	1.24–2.05
Kim et al. [36]	Interfacial transport due to turbulent intensity: $h = St_i \left(\frac{1}{2n} \right)^{1/3} \left(\frac{\rho_f}{\rho_s} \right)^{2/3} C_p G_0$ Interfacial transport due to surface renewal: $h = 0.1409 \left(\frac{k_f C_p}{v_f \rho_s} \frac{1}{4 - 2\eta} \right)^{0.5} B^{0.33} G_m^{0.1722} G_0^{0.8278}$ Interfacial transport due to shear stress: $h = 0.1819 \left(\frac{k_f C_p}{v_f \rho_s} \frac{1}{4 - 2\eta} \right)^{0.5} B^{0.33} G_m^{0.1722} G_0^{0.8278}$	0.9–2.0
Gulawani et al. [37]	$\frac{h}{C_p G_0} = 1.12 \left(\frac{G_0}{G_m} \right)^{0.31} B^{0.06} d_c < 2 \text{ mm}$ $\frac{h}{C_p G_0} = 1.12 \left(\frac{G_0}{G_m} \right)^{0.31} B^{0.06} d_c < 6 \text{ mm}$	0.5–3.0
Wu et al. [15]	$h = 0.576 C_p G_e B^{-0.4} \left(\frac{p_a}{p_s} \right)^{0.2}$	0.63–3.44
Wu et al. [16]	Contraction shape: $h = G_e \sqrt{\frac{k_f C_{pf}}{85 v_f \rho_s} (1 + 4L^2)^{1/2}}$ Expansion–contraction shape: $h = G_e \sqrt{\frac{k_f C_{pf}}{85 v_f \rho_s} \left[\frac{(R_{ex}^2 - 1)}{\sin \alpha} + R_{ex} \left(2L - \frac{R_{ex} - 1}{\tan \alpha} \right) \right]^{-1}}$ Double expansion–contraction and divergent shape: $h = G_e \sqrt{\frac{k_f C_{pf}}{85 v_f \rho_s} \left[\frac{3(R_{ex}^2 - 1)}{\sin \alpha} + R_{ex} \left(2L - \frac{3(R_{ex} - 1)}{\tan \alpha} \right) \right]^{-1}}$	0.98–1.45

They showed the interfacial Stanton number is in the range of 0.018–0.035 ($Pr = 1.3$ – 3.0). Kudo et al. [39] proposed a turbulent diffusion model where the length of vapor cone is calculated from the turbulent diffusion of heat in the mixing zone between the vapour cavity and the surround water. They suggested a correlation which can be used to calculate the interfacial velocity if the average steam velocity at the nozzle exit is given. An example of calculated results is shown in Fig. 20.

FIG. 20. Relation between u_i and u_o [39].

V. Steam Jet-induced Turbulent Jet Flow

A. MEASUREMENT OF TURBULENT JET FLOW

The measurements of the turbulent jet flow induced by steam jet were conducted by Van Wiessen et al. [40,41], Kim and Youn [42], Youn et al. [43], and Choo and Song [44]. Van Wiessen et al. [40,41] conducted to measure the turbulent jet flow induced by steam jet using a ring-shaped nozzle at an angle of 30° with the vertical axis, whereas the others conducted using circular nozzle as like a perforation of the sparger used typically in nuclear power plants. Even though their nozzle's shape is different from each other, their findings would be useful for understanding the physical phenomena of the turbulent jet flow induced by steam jet discharged into subcooled water.

Van Wiessen et al. [40] performed an experimental investigation on the turbulence production by steam jet-driven water jet in a water vessel. For the velocity measurement, an optical technique called particle image velocimetry (PIV) was used. The tracer used was polyamide seeding in the bulk liquid. The test section consists of a cylindrical shape Perspex water vessel for minimizing the secondary flow caused by corners, a ring-shaped steam nozzle at the center and bottom of the cylindrical tank, and a square glass tank that is located outside of the inner cylindrical tank, and the space between the two tanks was filled with water to minimize the optical distortion. The gas-liquid interface at the top was set into violent motion by the jet. The waves that occurred would then capture air bubbles into the liquid, which spoils the photos. To reduce this kind of surface motion, a Styrodor grid was used, which floats on the liquid. Due to the strong mixing of the water in the tank by the jet, there were no large temperature gradients in the tank. Therefore, only one thermocouple measurement was used to classify the pool water condition. The schematic of the experimental apparatus is shown in Fig. 21.

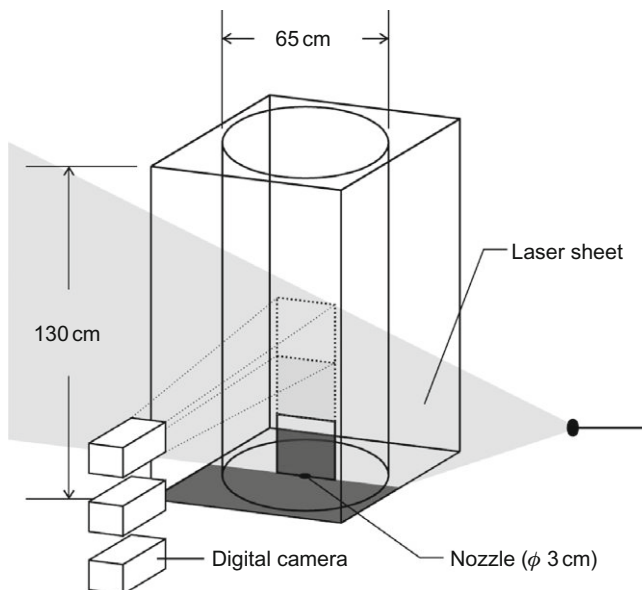


FIG. 21. Schematics of experimental apparatus by Van Wiessen et al. [40].

The authors depicted a schematic of the turbulent jet as shown in Fig. 22. Steam enters the vessel through the ring-shaped nozzle at $z = 0$, after which it almost fully condenses to a length of 10–15 cm. In this region, the jet radius first decreased due to change in density, which was virtually observed as a cone shape of steam above the nozzle. After the condensation region, the jet became a fully developed single-phase water jet. This part of the jet is *self-similar* (discussed in the authors' another work [41]) with a virtual origin (z_0) 10–25 cm upstream of the nozzle.

The authors showed the effects of steam inlet pressure, nozzle opening, and water temperature on the mean strain rate $-\partial u_z / \partial r$. And the results showed clearly the typical trend. A slight increase with increasing pressure and increasing opening was observed, where the effect of temperature was much more pronounced. Although comparison of the mean strain rate with data of other researchers was not possible, the comparison of $\overline{u'_z u'_r}$ data, i.e., turbulent fluctuation in the axial and radial directions, with those of air and helium jets, showed a reasonable agreement to some extent. A strong effect of temperature was observed for the turbulent production of kinetic energy. Both the shear rate and the turbulent production were negligible outside the jet, as expected. The maximum observed value of the production was about $150 \text{ m}^2/\text{s}^3$. The fact

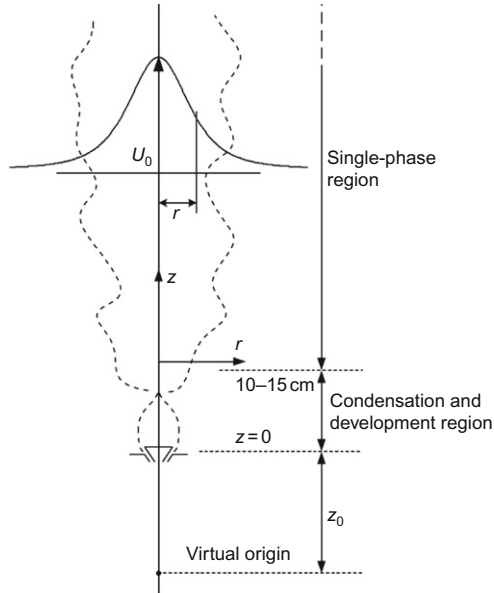


FIG. 22. Schematics of the turbulent jet and virtual origin (z_0) by Van Wiessen et al. [40].

that the turbulent production rate depends primarily on the fluid temperature level can be understood in the following way. The velocity profile in the downstream of the condensing two-phase region depends on the pool water temperature from Weimer et al. [21] who observed that the effective width of a two-phase jet increases with increasing temperature. Since the velocity profile depends on the temperature, the decay parameter and dissipation depend also on the temperature.

Van Wiessen et al. [41] performed another similar test with the same test apparatus as the case of the previous work [40]. In this work, the authors concentrated on the manipulation of steam jet-driven turbulent water jet. They found that the turbulent jet driven by steam jet can be compared with the classical single-phase turbulent jet as shown in Fig. 23. They found that the steam cavity shape looks like onion-shape of the condensation region, which can be understood by the effect of linear momentum. Near the nozzle the momentum of the steam had a component in the radial direction, but the entrainment of liquid from the core in combination with conservation of mass causes a quick redirection of the flow of injected fluid. In the present two-phase case, this redirection is further promoted by the condensation process in the two-phase volume and the action of buoyancy. Downstream of the condensation region, a

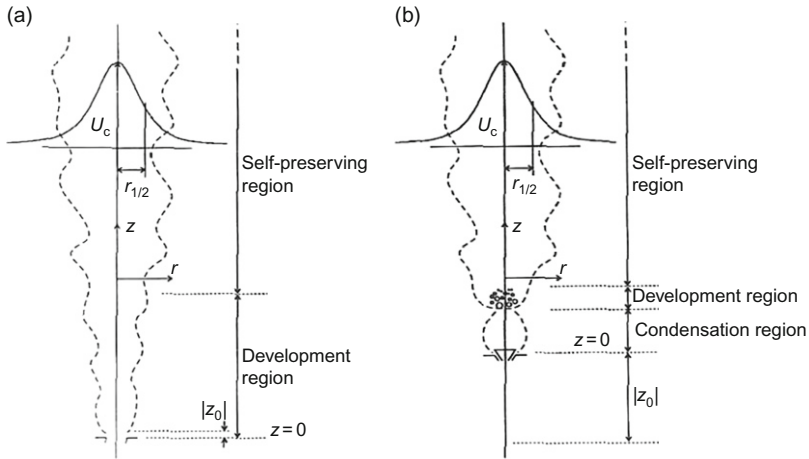


FIG. 23. Schematic representation of (a) single-phase jet and (b) a condensing jet [41].

small development region was distinguished, where a single-phase jet was established. At a temperature-dependent downstream position, a region began where the steam jet becomes single-phase liquid and also self-similar as shown below. This single-phase liquid jet was the target of the PIV measurements.

To prove the self-similarity in the single-phase region, the centerline velocity, U_c , was investigated first. From the data, it was found that U_c complies with the case of single-phase jet, defined as Eq. (15):

$$U_c = \frac{C_0}{z - z_0} \quad (15)$$

Here, C_0 is a coefficient related to the effective radius and centerline decay rate of the jet. The dependency of U_c on C_0 is the characteristic for single-phase jet and is in good agreement with other previous data. The authors found from measured data that five iso-velocity ratio lines were shown to be satisfied with the $u_z/U_c = C$, where C is a constant in the range of 0.4–0.8. The straight lines were linear fits through the measurements. The points where the lines cross the centerline, z_0 , were within ± 1 cm from each other. Independent of what the actual expression of $f(\eta)$ is, this showed that the jet is *self-similar* in this region. In the self-similar region of a turbulent axis-symmetric single-phase jet, the mean axial velocity field, \bar{u}_z , is by definition described by the following equation:

$$\bar{u}_z(z, r, 0) = U_c(z) f(\eta) \quad (16)$$

The function $f(\eta)$ in Eq. (16) is the self-similar velocity profile and U_c is the mean centerline velocity, defined by:

$$U_c(z) \equiv \bar{u}_z(z, 0, 0) \quad (17)$$

Hussein et al. [45] showed that a Gaussian profile for $f(\eta)$ fits most of the data of single-phase unbounded jets with high accuracy:

$$f(\eta) = \exp\left(\ln(2)\left(\frac{\eta}{S}\right)^2\right) \quad (18)$$

Here, S is the spreading rate of the jet, defined by:

$$S \equiv \frac{dr_{1/2}(z)}{dz} \quad (19)$$

where $r_{1/2}$ is the radius at which the mean velocity is half the centreline velocity, at the same height z . A typical result was presented in Fig. 24, which shows more than 1200 time-averaged axial velocities, collected at 42 different heights. From the figure, the self-similarity is obviously evident, and it is clearly shown that the functional relation given in Eq. (18) and presented by Hussein et al. [45] fitted the data in the selected area reasonably well. The authors found that these trends hold for each bulk water temperature.

The authors also investigated the temperature dependence of the turbulent jet profile; the average velocity data obtained at all temperatures had been fitted to Eq. (18). Because of the influence of condensation on z_0 and C_0 , these

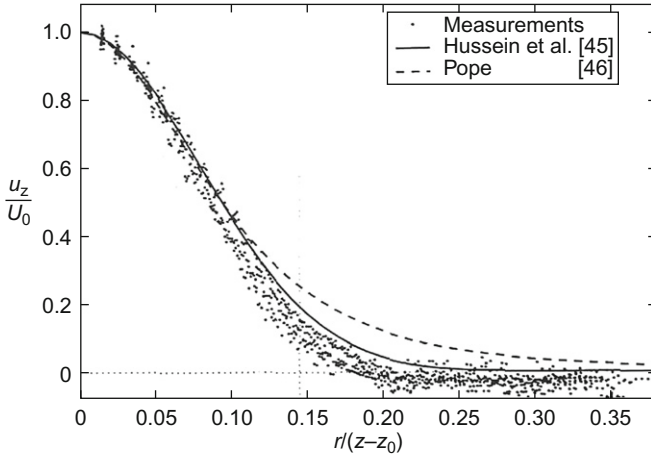


FIG. 24. Self-similar velocity profiles and measured data ($T_{\text{pool}} = 50^\circ\text{C}$; $z = 0.106\text{--}0.205\text{ m}$) [41].

quantities were chosen to be temperature dependent. The fit was done in one run, using 40,000 velocity vectors. When spreading rate (S) was fitted as a function of temperature, only little variation and no systematic dependency on temperature was found. Therefore, S was taken as temperature independent. The value found for S was 0.0937 ± 0.0007 . This value for S is in good agreement with Hussein et al. [45], who found 0.094 ± 0.001 for the hot-wire and LDA measurements of an air jet in and finite environment ($D/d = 31$), with exhaust to the ambient. In contrast to most previous results in the literature for noncondensing jets, however, z_0 for the condensing jet was always negative. This would be caused by the change in mass density during condensation, which squeezes the development region, such that the jet seemingly originated from a source upstream of the nozzle. A strong temperature dependence of z_0 was observed. The authors discussed that the reason of dependency on the temperature of z_0 could be explained with the trend of steam cavity length dependency on the pool temperature variations. If higher the point where most of the steam is condensed, the higher the point from where the liquid of the jet seemingly originates. The virtual origin of the jet was directly linearly related to the height of the condensing steam part above the steam nozzle. And the C_0 value was found to increase with increasing bulk temperature. The authors discussed also that the dependence on temperature of C_0 is a typical aspect of a two-phase condensing jet. The authors showed the turbulence properties, as in their previous work [40], in terms of turbulent intensities and fluctuations in radial and axial directions. The authors mentioned that the turbulent intensity is found to be similar to the intensities usually reported for single-phase jets, even though fully isotropic trend of turbulence was observed only at the distance of 15 nozzle diameters from the nozzle exit.

It would be noteworthy that the authors found a slow *wobbling* motion, which was confirmed by putting a large number of PIV recordings in chronological order and being shown as a video. However, the jet appeared to move from the left to the right, vice versa, at a very low frequency, e.g., 0.04–0.08 Hz. The authors described that this low frequency oscillation might be related to the backflow in the near-wall region, and in particular asymmetry of this backflow with respect to the central axis of the vessel. This means that the low-frequency oscillation would be related to the confinement of the jet. If so, this would be the first instance where the confinement had been shown to have an effect on the core of the jet. The corrected value of S was 0.0921 ± 0.0003 for the rotated fit, which is smaller than the observed 0.0937 ± 0.0007 for the uncorrected fit. This was as expected because a snapshot of a wobbling jet yielded a narrow core than an average value over a long period of time. The authors discussed the reason why the value found for the spreading rate for the uncorrected fit was then in such good correspondence with that for an unconfined jet. This agreement might be coincident and caused

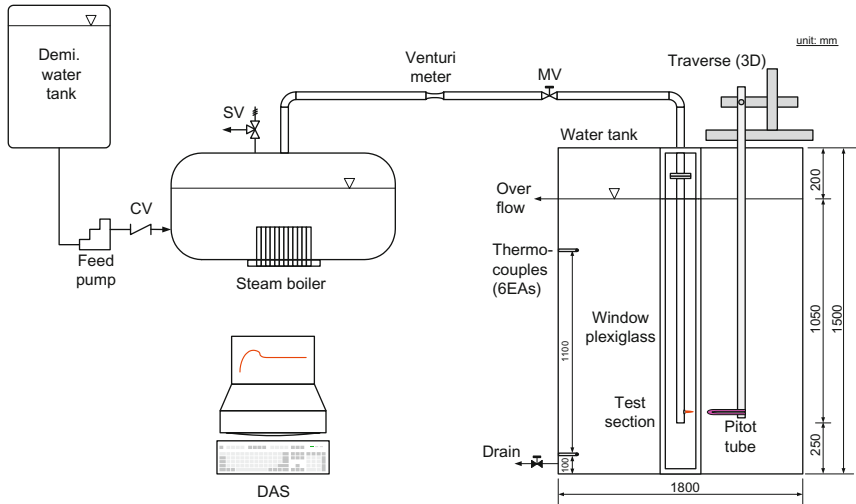


FIG. 25. Schematic diagram of the experimental apparatus [42].

by two compensating effects of the confinement in their measurements. On the one hand, the jet was broadened by the wobbling motion. On the other hand, the backflow caused a slight narrowing of the jet.

Kim and Youn [42] conducted an experimental work to investigate the turbulent jet flow induced by a steam jet using Pitot tube and thermocouples for measuring axial velocity and temperature distribution. Although PIV technique is one of very excellent methods to measure velocity fields, it cannot measure temperature field at the same time. This is the reason why the authors selected the Pitot tube—thermocouple system for the turbulent jet flow. The schematic diagram of the experimental apparatus is shown in Fig. 25, where a traverse system was provided to manipulate the Pitot tube/thermocouples for measuring the velocity and temperature of the region in the downstream region of the steam jet. The steam was injected into water horizontally from a single-hole sparger and the nozzle diameter was 10 mm.

The authors considered that typical turbulent jet flow induced by the condensing steam jet in a water pool could be depicted conceptually as shown in Fig. 26. The steam jet maintains a kind of boundary between injected steam and surrounding water and shows a typically conical shape as shown in the figure. Across the steam—water interface, a kind of equilibrium between the steam jet and the surrounding water sustains thermally and mechanically at the same time in the initial region. At the end of initial region of steam cavity, main region follows where mainly a kind of turbulent jet flow develops. As

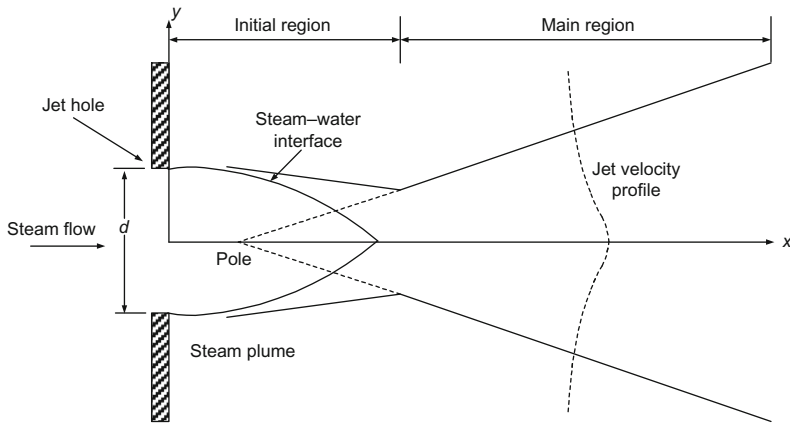


FIG. 26. Condensing steam jet-induced turbulent jet model [42].

shown in the figure, there exists a two-phase flow in the initial part of the turbulent region, and nearly single-phase flow in the main part of the region. The authors focused on the investigation of the turbulent flow in the main region and compared the measured data with a theoretical mode for typical single-phase turbulent jet flow. Their experimental conditions covered five different pool temperatures under a high steam mass flux, e.g., 15–48°C and 1000 kg/m² s, respectively. The virtual origin was located between –0.7 cm and +1.54 cm, where – or + means the negative or positive flow direction from the nozzle exit, respectively. The spreading rate was in the range of 0.10–0.12, which is a little larger than that of single-phase axi-symmetric jet (e.g., 0.097) and those of Van Wiessen et al. [41]. From these findings, the authors suggested that a general theory of free turbulent jets could also be applicable to the case of steam jet-induced turbulent jet flow.

The authors compared their data with the Tollmien's theoretical model for axi-symmetric source jet [46]. The dimensionless velocity and temperature were fitted quite well with the theoretical model as shown in Figs. 27 and 28, respectively. As predicted by the theoretical model, the dimensionless temperature distribution is proportional to the square root of dimensionless velocity distribution. This trend could be found in both Figs. 27 and 28. The authors suggested a semi-empirical correlation for the central velocity of a turbulent jet as follows:

$$u_m = 0.95 \frac{du_0}{y_c} \sqrt{\frac{\rho_v}{\rho_l}} \quad (20)$$

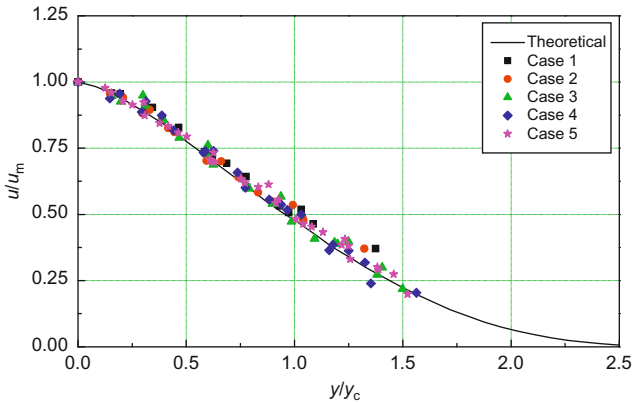


FIG. 27. Comparison of dimensionless velocities with the theoretical model [42].

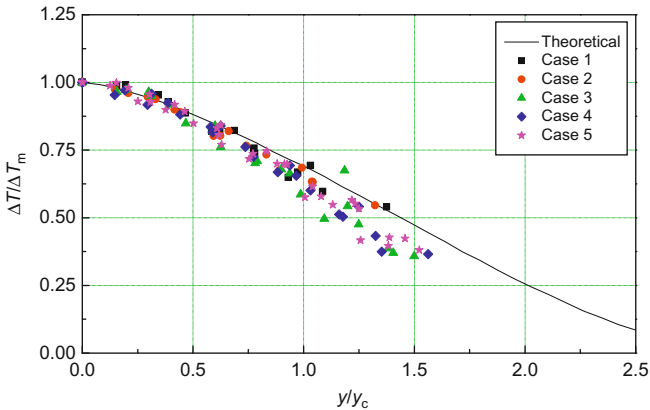


FIG. 28. Comparison of dimensionless temperature with the theoretical model [42].

Similar work has also been conducted by Youn et al. [43]. The same experimental apparatus was used for the turbulent jet experiment, but with vertically upward steam injection nozzle (diameter = 10 mm). The test matrix includes four different mass fluxes in the range of 450–900 kg/m² s and 10 different pool temperatures in the range of 30–85°C. Like Kim and Youn [42], the authors compared their data with the Tollmien’s model for the axially symmetric source jet [46]. The virtual origin was found located between $-2.823d$ and $+0.393d$ (e.g., $d = 10$ mm), where $-$ or $+$ means the negative or positive flow

direction from the nozzle exit, respectively. The spreading rate was in the range of 0.10–0.156, which is a little larger than that of Kim and Youn [42], e.g., 0.10–0.12. The authors suggested another semi-empirical correlation for the central velocity of a turbulent jet, which is best fitted to their measurement data as follows:

$$u_m = 0.968 \frac{du_0}{y_c} \sqrt{\frac{\rho_v}{\rho_l}} \quad (21)$$

Choo and Song [44] conducted an experimental investigation on the two different concerns such as steam jet-induced turbulent jet and the pool mixing. To measure the velocity distribution, the PIV technique was used. The authors assumed that the noncondensable bubbles due to steam condensation are small enough to follow a jet flow having high momentum and could be used as tracers for turbulent jet experiment. In the pool mixing experiment, however, the noncondensable bubble could not be used for local zones with a small momentum, and instead fluorescent solid tracer particles were used. As shown in Fig. 29, the test section consists of two open tanks, an inner cylindrical (an inner diameter of 0.78 m and a height of 2 m) as a mixing pool and an outer square tank (a square cross - section of 1 m \times 1 m and a height of 1.8 m), and a steam nozzle ($d = 5$ mm). Steam is injected into water pool vertically upward

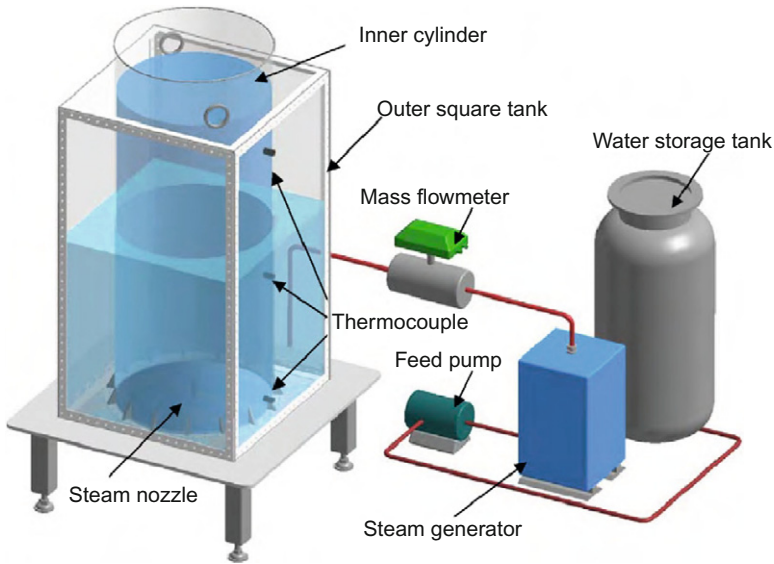


FIG. 29. Schematics of experimental apparatus [44].

for the turbulent jet experiment, while vertically downward for the pool mixing experiment.

The authors explained their measured data of the turbulent jet using the concept of a *self-similarity* or *self-preservation*. The decay coefficient (C), defined as Eq. (15), was observed in the range of 457.1–720.1, and the spreading rate (S), defined as Eq. (19), in the range of 0.0898–0.979. And the virtual origin was in the range of $-3d$ to $-0.5d$ (e.g., $d = 5$ mm) and the velocity profile constant (K), defined as Eq. (22), in the range of 72.4–86.0:

$$\frac{u}{U_c} = e^{-K\eta^2} \quad (22)$$

For the decay coefficient, the test data showed its dependence on the pool temperature. For the virtual origin, however, no dependence of pool water temperature was observed. The spreading rate showed quite a large scattering and most of the test data (e.g., 6 out of 8) showed even smaller values than that of the single-phase jet. It should be careful to compare this work with the test result of Van Wiessen et al.'s [41] because the current result for the steam-driven turbulent jet used the noncondensable bubbles as tracers while Van Wiessen et al. [41] used the combination of small bubbles (10–100 μm) and polyamide seeding as tracers.

In general, the turbulent jet, which is strongly induced by a steam injection, entrains the surrounding water and creates an internal circulation pattern within a pool; it governs the content of a pool mixing. Choo and Song [44] measured the pool mixing behavior and observed that a coherent circulating flow pattern is created by the steam injection. As expected, a stronger internal driving flow can appear with an increasing mass flux as shown in Fig. 30. Key features observed in the internal flow pattern of the pool mixing are the location of the center of the recirculation and the existence of a secondary flow. For all the tests, the eye of a strong recirculation was observed at the bottom right-hand corner as seen in the figure.

Even though they might not concentrate on the wobbling motion, which could be attributed to the instability of the backflow resulting from the confinement, their data would be used as benchmarking data for the validation of a CFD simulation of the relevant phenomena that appears in the nuclear reactor safety problems.

B. ANALYSIS OF STEAM JET

The analytical approaches for the turbulent jet flow induced by steam jet were conducted by Gulawani et al. [37,38] and Kang and Song [47,48]. The previous researches used a commercial computer code for the DCC analysis especially on the steam jet itself or the steam jet-induced turbulent jet flow.

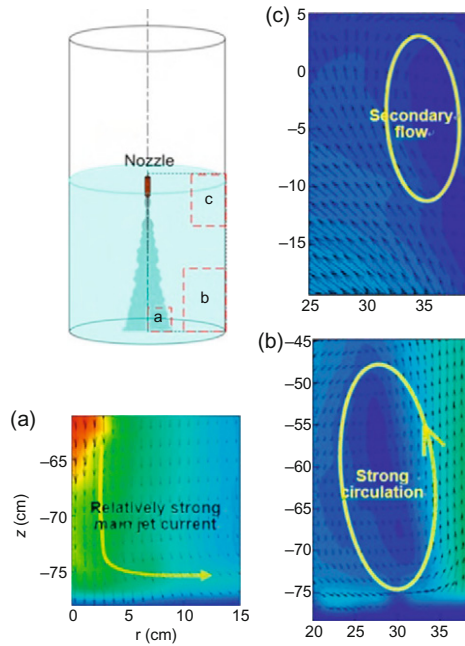


FIG. 30. Local flow patterns for $G = 650 \text{ kg/m}^2 \text{ s}$ [44]. (a) Bottom wall, (b) Bottom corner, (c) Side wall.

Gulawani et al. [37] focused on the analysis of the steam jet itself using a commercial code CFX-5.7. A two-phase model has been formulated in the Euler–Euler framework using the method of interpenetrating continua. Water was considered as the primary phase, whereas the steam as the secondary phase. The interphase mass transfer has been tracked by using the thermal phase-change model. For the turbulence closure, k – ϵ turbulence model was used. The governing equations for the three-dimensional jet flow are mass conservation equation, momentum conservation equation, drag formulation for the jet interface, k – ϵ turbulent equations for liquid phase, phase change modeling, and boundary conditions for the simulation. For the drag coefficient, the authors performed an experiment to achieve mass transfer coefficient across the jet interface using a hot film anemometer. The authors used the Chilton–Colburn analogy of heat and mass transfer to convert the mass transfer coefficient to the drag coefficient at the jet interface. The measured drag coefficient was in the range of 0.41–0.51. The maximum drag has been observed on the top of the jet, while there is observed a small drag in the surrounding of the jet. At the nozzle inlet, total pressure/mass flow rate has been

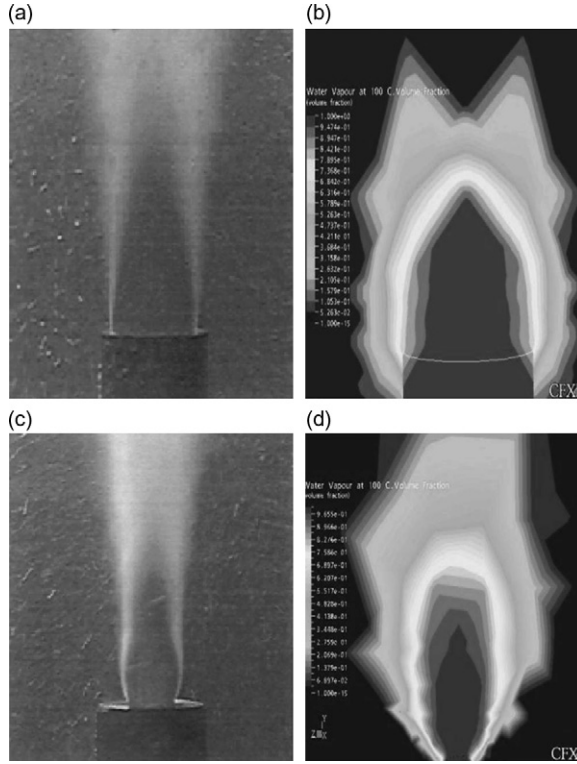


FIG. 31. Comparison of steam cavity shapes: Conical (a: Exp. [14]; b: CFD [37]); elliptical (c: Exp. [14]; d: CFD [37]).

set as the boundary condition. Based on the nozzle inlet velocities, the values for k and ϵ were calculated for initialization as follows:

$$k = 0.03 \left(\frac{\dot{m}_0}{\rho_s} \right)^2 \quad \text{and} \quad \epsilon = \frac{k^{1.5}}{0.3d_0} \quad (23)$$

At the nozzle outlet, ambient conditions have been set for the atmospheric pressure. Thermal phase change model was incorporated in the interface tracking model. The constants used for the k – ϵ turbulent model (C_μ , $C_{\epsilon 1}$, $C_{\epsilon 2}$, σ_k , σ_ϵ) were 0.09, 1.44, 1.92, 1.0, 1.3, respectively.

The authors simulated the variation of axial and radial temperature in the steam cavity, jet cavity shape and size, cavity length, HTC, and interfacial area. Especially, the authors suggested a semi-empirical correlation for HTC, depending on the nozzle size, as shown in Table VI. The comparison of typical conical and elliptical shapes of jets with one of previous work is typically shown in Fig. 31. A good agreement was observed between the experimental data of

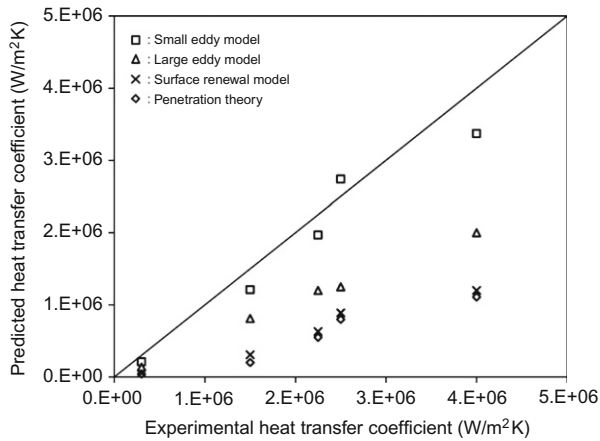


FIG. 32. Comparison of various heat and mass transfer theories with experimental HTC [38].

cavity length, axial and radial temperature, and the suggested model. They also suggested an analytical equation for the estimation of interfacial area, expressed in terms of Nu , Re , Pr , B , and the viscosity ratio of steam and water. Based on the CFD analysis, the interfacial area for condensation has been obtained by the following three methods: (a) directly from simulation, (b) from the cavity shape and size based on a variation in volume fraction, and (c) from the average HTC. In the first method, as simulation proceeded transiently, the interface tracking gave directly the average interfacial area for the heat transfer. In the second method, cavity dimensions (length and width) could be obtained from CFD simulations for different volume fractions. Using these cavity dimensions and identifying the cavity shape from the contours of volume fraction, interfacial area of the cavity could be calculated by using standard mathematical formulas suggested by the authors. In the third method, average HTC in the liquid bath obtained from CFD predictions has been used to estimate the interfacial area.

Gulawani et al. [38] investigated the steam-induced turbulent jet flow distribution analytically. The mathematical models used for the analysis are nearly the same as their previous work [37] and the simulation area corresponds to the pool region including steam nozzle. The authors compared the simulation with experimental data measured by their own experimental apparatus especially on the longitudinal and traverse velocities, pool temperature, and heat transfer. The most interesting parameter would be the interfacial HTC. The comparison of experimental HTC with the theories of heat and mass transfer at the vapor–liquid interface showed that the small eddies close to vapor–liquid interface are dominant. The small eddy model was observed relatively closest to experimental HTC as shown in Fig. 32.

Kang and Song [48] made a numerical analysis of the horizontal turbulent jet flow induced by condensing steam jet using a commercial code CFX-11 [49]. They compared the analytical result with the experimental data by Kim and Youn [42], and suggested the concept of the so-called *steam condensation region model* (SCRM) in which the steam is perfectly condensed to water within the steam penetration length. The basic idea of the SCRM can be depicted as shown in Fig. 33 [50]. The penetration length was determined by the correlation proposed by Kim et al. [14] and was estimated about $5.3d$. The width of the jet at the end of the penetration length was selected from the experimental data. The penetration length and width were used as the constant values in the transient CFD calculation even though those values might be changed due to the variation of surrounding water temperature. For the model, it was assumed that the entrained water located at above and below this condensation region must flow into the condensation region along the direction normal to the surface of this region, and only the condensed water should leave the outlet of the condensation region uniformly with the same velocity and temperature even though the estimated velocity profile showed a variation along the sparger discharging holes. According to the CFD calculation by considering the various velocity profiles, there was no big difference in the analysis results of thermal mixing behaviors for the high steam mass flux discharge conditions. The governing equations in the SCRM region consist of mass, momentum, energy equations, and the pressure relation between nozzle inlet and outlet as follows:

$$\dot{m}_s + \dot{m}_{\text{ent}} = \dot{m}_{\text{con}} \quad (24)$$

$$P_s A_s + P_\infty \left(\frac{\pi}{4} H^2 - A_s \right) + \rho_s V_s^2 A_s = P_\infty A_{\text{con}} + \rho_{\text{con}} V_{\text{con}}^2 A_{\text{con}} \quad (25)$$

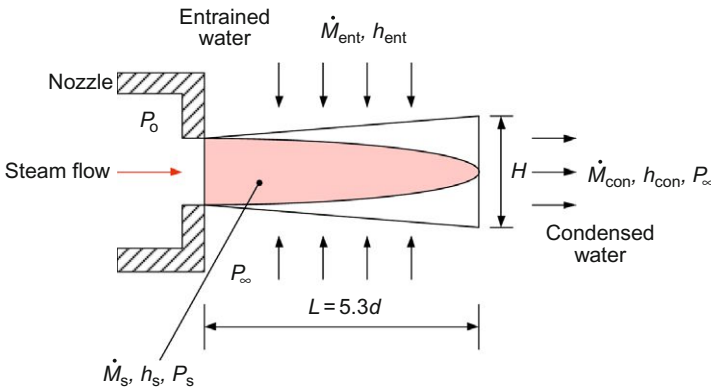


FIG. 33. Steam condensation region model for the DCC [50].

$$\dot{m}_s h_s + \dot{m}_{\text{ent}} h_{\text{ent}} = \dot{m}_{\text{con}} h_{\text{con}} \quad (26)$$

$$\frac{P_s}{P_0} = \left(\frac{2}{k+1} \right)^{k/(k-1)} \quad (27)$$

For the calculation procedure, the velocity of condensed water is obtained by substituting known data into Eq. (25). For this calculation, the static pressure of steam leaving the hole, which can be calculated by the isentropic relation of an ideal gas, is expressed by Eq. (27). The static pressure on the nozzle surface is also assumed to be P_∞ . And then, the mass flow rate of the entrained water is calculated by use of Eq. (24). The obtained mass flow rate (\dot{m}_{ent}) and the assumed enthalpy (h_{ent}) based on the test results are substituted into Eq. (26) to get the enthalpy of the condensed water. The calculated value of the enthalpy of the condensed water is compared with the initial assumed value. If its difference is lower than 5%, the assumed enthalpy value of the condensed water and the entrained water are chosen for the boundary conditions of CFD analysis. With these values, CFX-11 calculated the thermal mixing between condensed water and the subcooled surrounding water by using an appropriate turbulence model and some other physical models. The governing equations used in this work are the Navier–Stokes and energy equations with a homogeneous multi-fluid model under a coupled algorithm. The turbulent flow was simulated by the standard k – ϵ turbulent model or the shear stress transport model, and the buoyancy was modeled by the Boussinesq approximation. As for the numerical model for the convection term, the first-order upwind or the high resolution model was used. In the homogeneous model, the interphase mass and heat transfer were neglected. Each transport quantity in the governing equations except for the volume fraction was summed over all the phases to provide a single transport quantity. The authors performed sensitivity calculations by varying cell dimension, total number of cells, options for convection term discretization, turbulent model, and entrainment model to satisfy the Best Practice Guidelines (BPG) recommended by Mahaffy et al. [51]. Kang and Song [47] found that one of the six cases (e.g., Case-6) predicted the best prediction fitted with the test data as shown in Fig. 34. The best case showed for the case of 2.5 mm of cell dimension, high resolution option for convection term discretization, shear stress transport model for turbulent model, and 40% of entrainment model.

They also found that the value of the turbulent intensity at the inlet region is the most important factor because it determines the jet boundary through a momentum diffusion process in the radial direction. The difference in the CFD analysis results due to a variation of the mesh distribution, the selected convection term methods and the turbulent models was found to be negligible because the flow structure at the region of interest was very simple in this case.

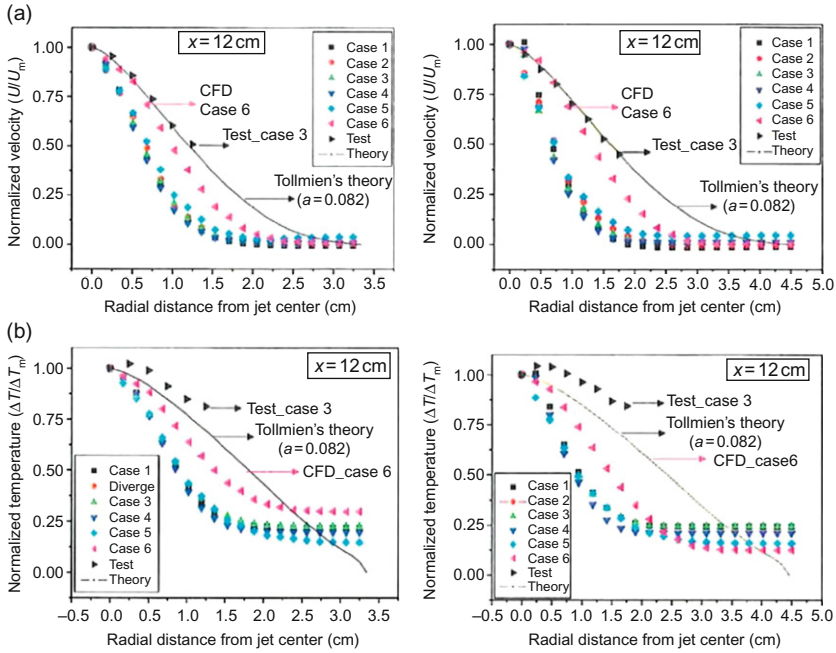


FIG. 34. Comparison of the CFD analysis results with the test data. (a) Velocity comparison of the CFD results with the test results at 12 and 16 cm. (b) Comparison of temperature between CFD and test results at 12 and 16 cm [47].

Kang and Song [48] also performed another analysis of the vertically upward turbulent jet flow induced by condensing steam jet using the CFX-11. The authors compared the analytical result with the experimental data by Youn et al. [43]. The authors used the same governing equations and physical models as their previous work [47]. From the previous sensitivity study, the authors found the best fitted conditions for CFD prediction, e.g., high resolution option for convection term discretization, shear stress transport model for turbulent model, 40% of entrainment model, and so on. In this case, the buoyancy was modeled by the full density model [50].

In Fig. 35, the CFD predictions were compared with test data and the Tollmien's theory with $a = 0.082$ [46], where a represents an expansion coefficient in jet theory. In the figure, most of the data are in quite good agreement with each other except the A-region of the temperature distribution. The authors explained the reason of such discrepancy would be due to the time delay of measurement because of the movable mechanism of instruments. Even with existing discrepancy, the authors concluded that the CFD analysis

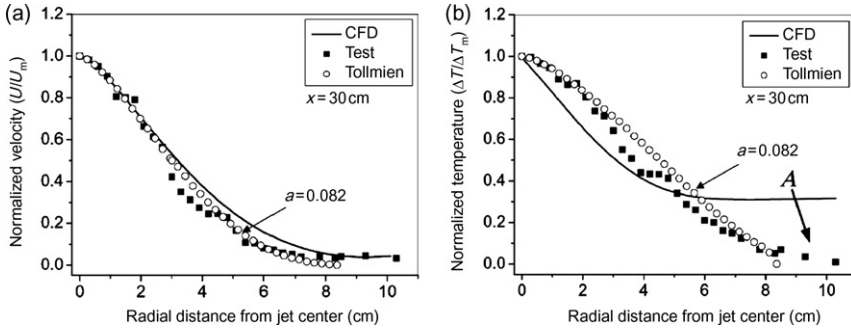


FIG. 35. Comparison of normalized velocity and temperature at the axial location of 30 cm ($G = 900 \text{ kg/m}^2 \text{ s}$; $T_{\text{pool}} = 45^\circ\text{C}$) [50].

can offer a reasonable simulation of the local phenomenon of a turbulent jet downstream of a steam jet only when the CFD analysis reflects the physics of a high intensity of the turbulent jet induced by condensing jets. And it is noteworthy that the authors recommend the high turbulent intensity of 40% and a fine mesh grid model with a cell length of 1–10 mm for a reasonably good CFD analysis.

From the review of steam jet analysis, Gulawani et al. [37,38] might be the first researchers who paved the way for the nearly mechanistic DCC mixing analysis on both the steam jet region itself and the steam jet-induced turbulent jet flow. And Kang and Song [47,48,50] suggested a concept of the *lumped* model for the global analysis of the DCC mixing phenomena, which seems to be useful for the analysis of thermal mixing in a very large pool like the IRWST in APR1400.

VI. Pool Mixing Analysis

A. REVIEW OF RECENT WORKS

There are practically at least two kinds of technical concerns that should be addressed in the DCC process of a steam jet in a pool. The first is a concern about *thermal mixing* in a water pool. At an early stage of a steam discharge process, steam is effectively condensed by mixing with highly subcooled pool water. With an increase of pool water temperature locally or globally above a certain limit, however, the condensation efficiency decreases and resultantly an *unstable* condensation may occur due to smaller degree of subcooling of the pool water. The other concern is about thermo-hydraulically induced *mechanical loads* acting on the structures of relevant systems. These loads can be

induced by the direct influence of the discharging process, or generated by resultant thermo-fluid dynamic phenomena, such as the pressure oscillation due to the unstable condensation of a steam jet discharged in a water pool. Regulatory practice in dealing with such phenomenon in nuclear energy systems is just to restrict the allowable operating temperature so that this instability will not occur [1]. For example, the lower boundary of the BCO and IOC in Fig. 3 would be the restricting limit for local pool temperature.

The thermal mixing phenomena in conjunction with the effect on the hydro-mechanical loads should be investigated in both local and global ways. From the local viewpoint, we can consider a *local hot spot*, which may exist due to an unfavourable thermal mixing in a pool and resultantly affect the stability of condensation phenomena during the long-term operation of a steam discharging system. From the global viewpoint, we can also consider a *thermal stratification*, which usually forms over the whole region of a water pool. Both aspects can be properly described only if the condensing behavior of steam jets and the resultant turbulent jet in the pool are well understood.

Previous works for the pool mixing analysis could be divided by the tools used for analysis, e.g., the system analysis code (e.g., TRAC-G, TRACE, and RELAP), and in-house or commercial CFD (e.g., CFX and Fluent) codes. The analysis using the system codes includes Gamble et al. [52], and Norman and Revankar [53,54], whereas the analysis using CFD code includes Takase et al. [55], Kang and Song [47–49], and Moon et al. [56].

Gamble et al. [52] performed a pool analysis using TRAC-G code and compared with their own test data from the pressure suppression test facility (PSTF), of which the scale is 1/3 of the PSP in a simplified boiling water reactor (SBWR) design. In a LOCA scenario, the steam pushes the water level in the pool to the submerged vent pipe at first and then enters the suppression pool, where vented steam induces transient jet flow due to condensation as shown in Fig. 36.

To model the jet flow in a suppression pool, they assumed that the jet flow due to steam vent condensation consists of developing and fully developed regions as shown in Fig. 37(a). From the figure, the first portion of a jet is a *developing* region where the jet velocity and radius vary only slightly. This region extends to approximately four to five jet diameters downstream. Within this region, the shear layer between the fast moving jet and ambient pool fluid is expanding to reach the centerline of the jet. At a distance of four or five jet diameters the shear layer reaches the centerline and the potential core of the jet disappears. In this developing region, the rate of jet expansion is slower than in the fully developed region. Based on the understanding of forced turbulent jet, the authors suggested a steam jet condensation model as shown in Fig. 37(b). The authors estimated that the entrainment ratio due to steam flow is about 2.3, which is considered as the entrainment flow.

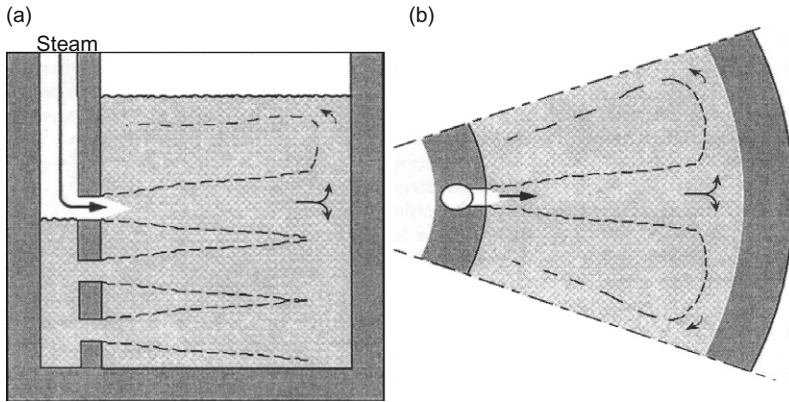


FIG. 36. Steam vent and jet trajectory in suppression pool: (a) Vertical shape; (b) cross-sectional shape [52].

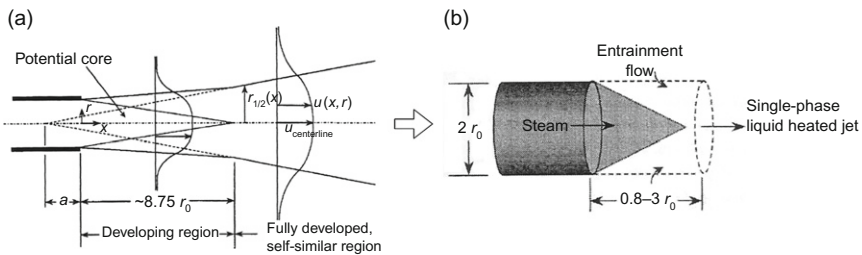


FIG. 37. Forced turbulent jet and steam jet models: (a) Forced turbulent jet; (b) concept of steam jet modeling [52].

The concepts described above were implemented into a large system analysis code, TRAC-G, in an effort to predict the stratification in one of the scaled suppression pool tests. This code does not have the ability to model small jet flow structures, such as jets and plumes, within its large volume cells. Therefore, auxiliary models had to be introduced to provide a mechanism to keep track of the mass and energy transport that occurred within the jet structures in the SP. When the momentum of entering fluid becomes weaker, the fluid tends to be deposited in the cell directly in front of the discharge pipe. For these periods the standard TRAC-G model was used. When a strong discharge occurs, a TRAC-G control system, controlling distributed sources and sinks, is used to model the transport of mass and energy to different parts of the pool by jets. Figure 38 shows the locations of the sources and sinks. The control system was set up to provide a simplified version of the jets described

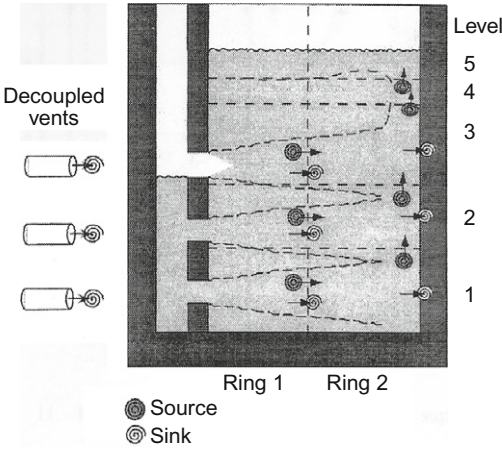


FIG. 38. Forced turbulent jet and steam jet models [52].

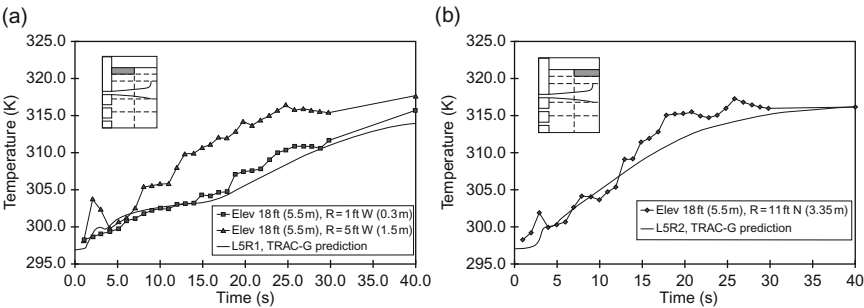


FIG. 39. Comparison between the prediction and measured data: (a) Left top region; (b) right top region [52].

in Fig. 37(b). Basically, the liquid entrained from a cell was modeled as a sink. The mass and energy deposited by the jet in a cell was modeled with a source. In addition, the authors introduced a correlation of distance criteria (from the discharge point) occurring transition from the jet flow to buoyant plume behavior. As the steam flow through the vents diminishes, buoyancy eventually becomes dominant and the warm liquid rises as a buoyant plume. Such transition was checked by a certain criteria and occurred at a velocity of approximately 1.5 m/s.

Figure 39 shows individual thermocouple readings of pool temperature at the top elevation of a pool. The diagram of the suppression pool in the

figure indicates the location of the plotted temperature. Small square and triangle shapes indicate the approximate location of the thermocouples used in the test, and the gray region indicates the node plotted for TRAC-G. From the comparison, overall trends were in quite good agreement between the prediction and the test data even though a significant variation between measured data was found even within the same region. They concluded that a system simulation code, TRAC-G, together with appropriate analytical models can be used to model thermal stratification behavior in a scaled test facility.

Norman and Revankar [53] performed a pool mixing analysis using a system analysis code, TRACE, for the pool mixing in the suppression pool of the SBWR. One important phenomenon is the initial stages of a LOCA event in an SBWR, where the SP serves as the heat sink for immediate removal of heat by DCC, and the case of pool thermal stratification. This arises when the upper water volume above the source becomes thermally active while the lower regions do not participate in heat removal. Thermal stratification acts to reduce the efficiency of the heat removal capacity of the PSP, which functions both as a heat sink and as reactor make-up inventory if the reactor core may be in imminent danger of being uncovered by the coolant. These were the main motivations of the suppression pool analysis to predict the global behavior in a suppression pool due to local thermal-hydraulic phenomena, such as DCC and thermal stratification in a pool.

The analysis code solves the conservation of mass equations for the combined gas and liquid phases with interphase mass transfer and treats the gas mixture as homogeneous, moving with the same gas velocity with the vapor being in thermal and mechanical equilibrium with the noncondensable. A single noncondensable gas field equation of continuity is used, and Dalton's law is applied to give the algebraic sum of the gas partial pressures. The equations of liquid motion and gas motion along with combined internal and combined gas energy equations make a closure for the complete set of equations in the two-fluid model. The phase change rate is evaluated from a thermal energy jump relation. These thermal-hydraulic equations describe the transfer of mass, energy, and momentum between the gas-liquid phases and the interaction of these phases with the heat flow from the system structures. Because these interactions are dependent on the flow topology, a flow regime-dependent constitutive equation package is incorporated into the code. An input deck for TRACE using the three-dimensional vessel component to model the pool was developed, and the results of the code predictions were compared to experimental results. The authors conducted a separate experiment with a suppression pool model by using the height ratio of 1/4.5 and the area ratio of $1/\sqrt{88.9}$ [54].

A quasi-steady-state case (as shown in Fig. 40(a)) of a steam-air mixture shows that the upper region of the pool is thermally active, whereas the lower

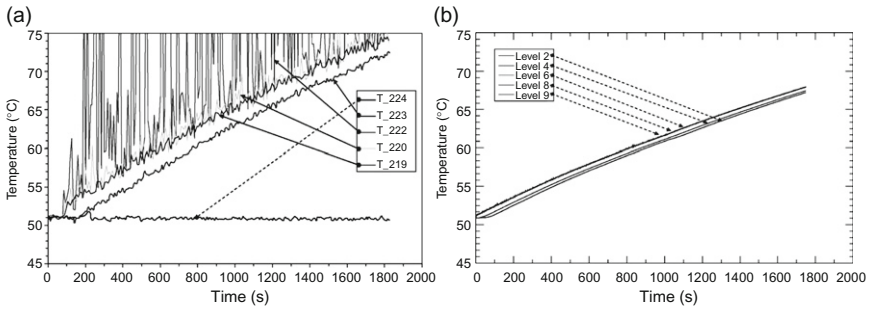


FIG. 40. Thermally stratified case at the near wall for experiment and TRACE prediction: (a) Test results; (b) TRACE prediction [54].

region is thermally inactive. The variation of pool temperature is observed for the near wall of the pool. The experimental results showing thermal stratification were compared with code simulations, shown in Fig. 40(b), which indicates a comparatively well-mixed pool. Within 1800 s, the code showed the underprediction of the pool temperature because the entire pool volume was being utilized as a heat sink, whereas the temperature of the upper pool volume in the experiment attained a temperature higher by more than 5°C due to the thermal stratification phenomenon. The temperature measurement given by the thermocouple T_222 as shown in the figure shows the oscillatory characteristic of condensation oscillations and external chugging.

From the comparison between the test data and TRACE prediction, the authors concluded that the TRACE code has some deficiency in simulating thermal stratification under the same boundary and initial conditions, which can lead to the code to underpredict the pool surface temperature. In this regard, the authors recommended that an effort of model development to improve the code predictive capability is needed.

Takase et al. [55] performed a pool analysis using their in-house analysis code, which had been made for use in BWR, for a simplified suppression tank being operated under vacuum condition in the international thermonuclear experimental reactor (ITER) design. The authors assumed a three-dimensional analytical model for the analysis as shown in Fig. 41(a) and conducted an experiment that simulates the model and boundary condition as shown in Fig. 41(b). For the numerical analysis the multi-interfaces advection and reconstruction solver (MARS) was used, which had been developed by the authors. It can directly analyze the steam–water two-phase flow field without any composition and empirical equations in comparison with typical conventional analytical models as the two-fluid model and drift flux model. Since the treatment of multiphase flows in the MARS method is based on a volume fraction

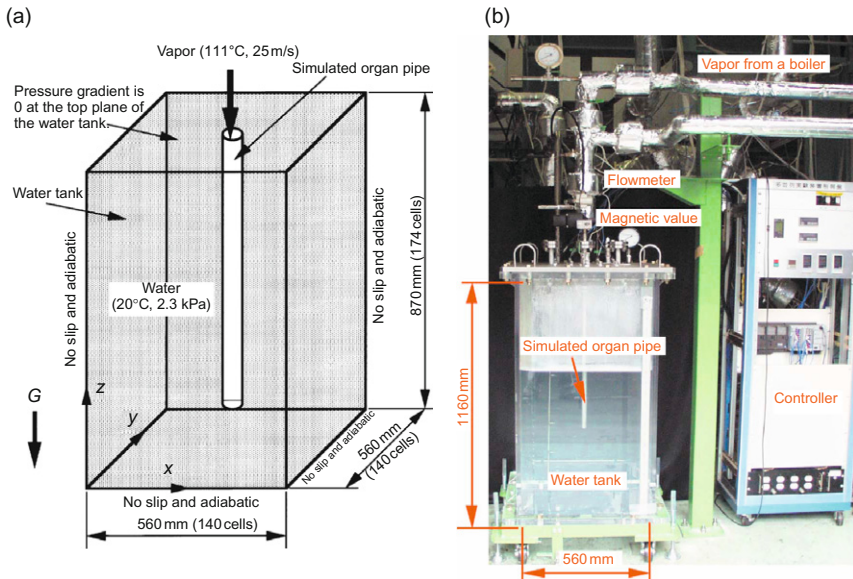


FIG. 41. (a) Three-dimensional analytical model and (b) test apparatus [55].

function, the special distribution of each material was defined. The continuity, momentum, and energy equations were used with the assumption of Newtonian fluid. Figure 42 shows the predicted void fraction, temperature distribution, and flow visualization results at the time of 5 s. From the comparison results, the authors concluded that the predicted flow configurations with the condensation of vapor using the MARS method agree well with the results of the flow visualization experiment and the present numerical approach is very effective to estimate the phase change behavior of vapor under low pressure and cold water.

Kang and Song [50] performed a pool analysis using a commercial CFD code, CFX-4.4. They compared CFX-4.4 prediction with the test data from the B&C test facility, which can simulate the real plant condition. Schematic diagram of the B&C facility is shown in Fig. 43. The authors suggested a model for steam jet condensation called the *steam condensation region model* (SCRM) and applied the model to multi-hole sparger simulation. For the prediction, the authors conducted a sensitivity study especially on the cell number and the convection term discretization to find the optimized methodology for the thermal mixing analysis following the guidelines recommended by Mahaffy et al. [51].

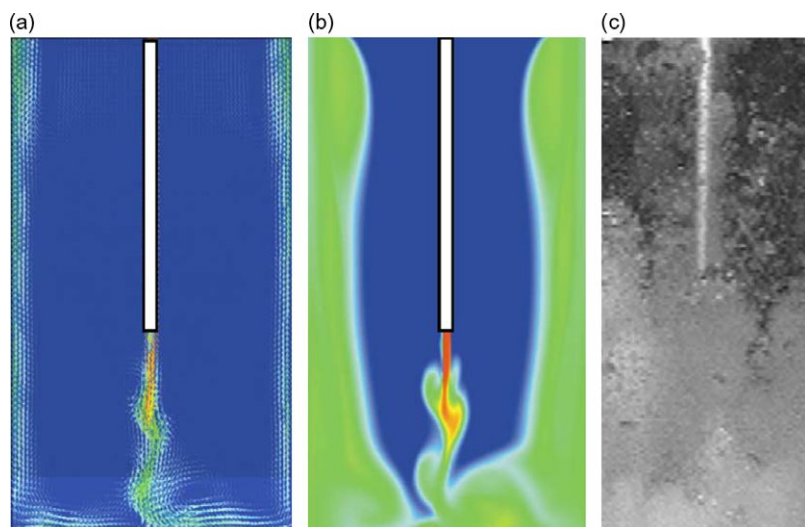


FIG. 42. (a) Predicted void fraction and (b) temperature distribution versus (c) experimental observation [55].

The comparison of CFD results with the test data showed a good agreement within 7–8% of deviation. This difference might arise from that the temperature and the velocity of the calculated condensed water by adopting the SCRM model were higher than the real value. Another reason might be due to an applicable limitation of the SCRM model to adopt the area-average concept. This concept also neglects a three-dimensional flow features in the tank, while the CFX calculation was performed by assuming the axi-symmetry to save a computation time. The sensitivity analysis of CFD calculation for the temperatures at the region between the sparger and the tank wall was very similar to each other regardless of the cases as shown in Fig. 44. In the figure, small circle filled with gray color indicates the approximate location of the thermocouples used in the test. The CFD results, however, showed a small difference in temperature distribution at the upper and lower region where the condensed water jet came back after colliding with the tank wall. Especially for the high upper region, the Case-4 using the QUICK scheme predicted the test data better than the cases using the Upwind scheme. Finally, the authors concluded that the commercial CFD code like CFX-4.4 together with the SCRM proposed in this study can be used to simulate the thermal mixing behavior reasonably well if a sufficient number of mesh distribution and a proper numerical method are adopted.

Moon [56] performed a pool analysis using a commercial code CFX-11. The author conducted local phenomena experiment to confirm the applicability of

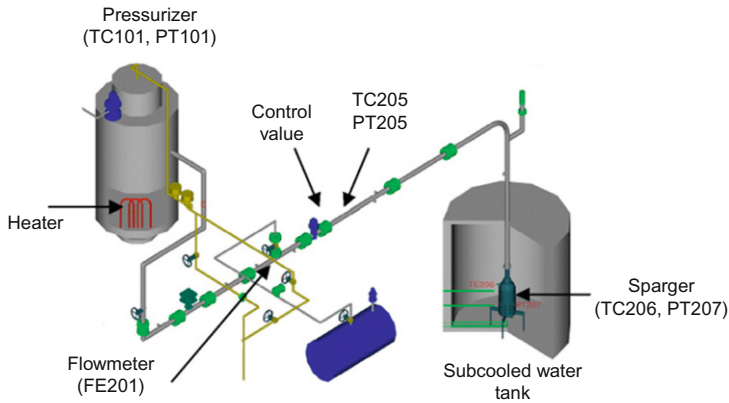


FIG. 43. Schematic diagram of the B&C test facility [50].

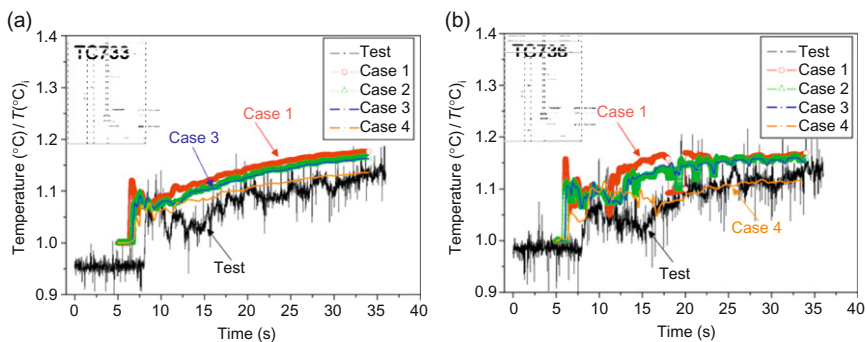


FIG. 44. Comparison of prediction and test data at two different locations: (a) TC733; (b) TC736 [50].

the SCRM to a steam-induced turbulent jet flow, a cylindrical water pool experiment, and an annulus water pool experiment [56,57]. Before applying to a pool mixing analysis, the author evaluated the SCRM concept by applying to local phenomena experiment, which simulates vertically upward steam injection at the center and bottom of a water tank. The author adopted the SCRM concept from Kang and Song [47–49] that additionally considers the entrainment effect to the model. The author discussed the effect of the entrainment to the momentum balance and finally assumed vertically entering entrainment flow to the control surface, which was reasonable as confirmed by the experimental observations (Fig. 45).

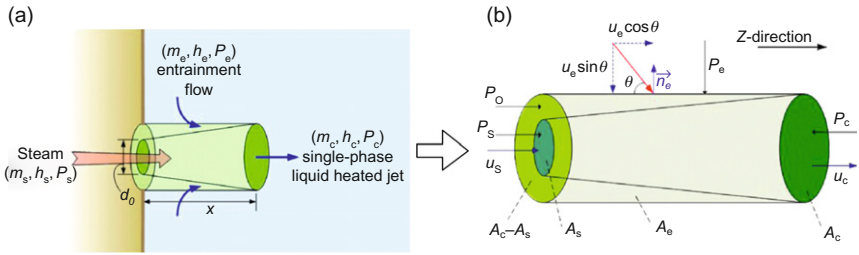


FIG. 45. Schematics of steam condensation region model: (a) SCRM at steam jet hole; (b) control volume of SCRM [56].

The author assumed that the thermal mixing phenomena induced by the steam jet in the subcooled water pool could be treated as incompressible flow with the free surface flow of air. The CFX code based on the finite volume method was used for thermal mixing analysis. The unsteady Navier–Stokes equations in conservation form were used with an inhomogeneous multiphase mode. For the study, this multiphase flow model was used to evaluate the free surface flow, while steam condensation in a subcooled water pool surface was not considered. Those equations were integrated over each control volume, such that the relevant quantities (mass, momentum, energy, etc.) were conserved in a discrete sense for each control volume.

For turbulent flow, the instantaneous equations were time-averaged leading to additional terms. The turbulent model adopted was the shear stress transport (SST) model that accounts for transport of the turbulent shear stress and gives highly accurate predictions of the onset and amount of flow separation under adverse pressure gradients. The buoyancy term was modeled using the Boussinesq approximation, where the density variation is driven only by small temperature variations. The steam condensation region was modeled as a subdomain in CFX. The subdomain was a region of fluid flow and heat transfer in a domain, where the volumetric sources of mass, momentum, energy, turbulence, additional variables, mass fractions, and radiation can be specified. It can also be used to model the flow resistance. The subdomain region is defined in the same way as the domains. The sources on the subdomain were specified as the total source. For local phenomena simulation, the authors performed a sensitivity analysis to examine the effects of the grid system and length of the condensation. They found that all the velocity profiles and thermal mixing patterns were similar regardless of the analysis cases. However, the sensitivity analysis of the turbulence model showed that the $k-\varepsilon$ model has result similar to that of the basis case, but the zero equation model shows a large deviation from others.

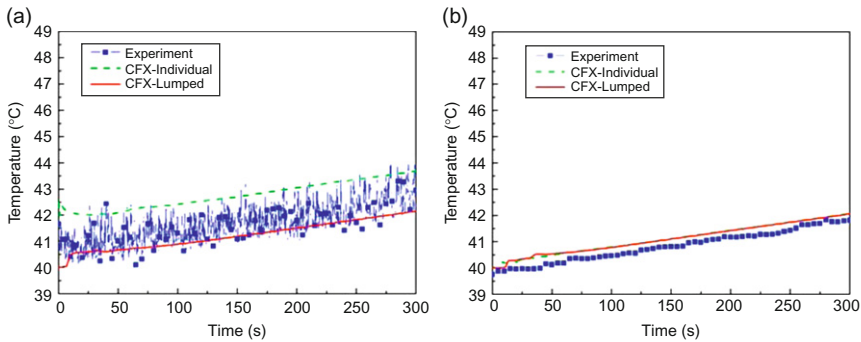


FIG. 46. Temperature profiles in cylindrical water pool simulation at two locations: (a) Near sparger (lower side holes); (b) bottom inner wall [56].

Like the local phenomena analysis, multiple-holes could be simulated for the cylindrical pool mixing analysis using the SCRM concept. A multi-holed sparger was used for the cylindrical pool mixing, which consists of totally 25 holes, e.g., eight holes at LRR, 18 holes at lower side, and one at bottom. The multi-holed sparger was modeled, for two kinds of approach for the steam-induced turbulent jet, in two different ways: the *individual* SCRM for each hole and the *lumped* SCRM for two regions (i.e., load reduction ring (LRR), which is a special device for the APR1400 sparger design, and the lower side holes). Using the lumped SCRM model, the discharge holes could be combined into a single cylindrical type. For the individual SCRM in the cylindrical water pool simulation, much more nodes and elements were needed than the case of lumped concept.

Predictions of the temperature variation at various locations for the cylindrical water pool simulation were compared with the experimental data. The measured temperatures at the elevation of the steam discharge were oscillating severely (see Fig. 46(a)). However, the calculated temperature using both the individual and lumped models could not simulate these temperature fluctuations. At most of other locations, the CFD results for all the cases predicted the observed trends of the temperature variation well, while the CFD results overestimated the temperature at the upper and lower parts of the pool (see Fig. 46(b)). In all cases, the trends of the temperature variation from the individual and lumped condensation region models were similar to each other.

B. POOL MIXING ISSUES AND FUTURE WORKS

The thermal mixing induced by a condensing steam jet in a pool is, in general, affected by the type of steam discharging device, steam discharging

patterns, pool geometry, and the characteristics of pool water cooling. At present, experimental information on the macroscopic flow mixing phenomena in a pool seems to be sufficiently available for validating appropriate analysis tools. The thermal and hydrodynamic information on the local interaction of steam jet with its surrounding pool water, however, is still needed in more detail for a better understanding of the relevant thermal–hydraulic phenomena and also for validating the appropriate CFD tools against those local phenomena, which eventually affect the global mixing behavior.

It is evident that the interfacial transfer of momentum, mass and energy during the DCC of steam in a pool is highly dependent on the condensation regimes, which are usually dependent on many parameters such as steam mass flux and pool temperature. A accurate prediction cannot be made for an associated heat transfer rate unless the relevant condensation regime is correctly identified based on proper understanding the mechanism of condensation.

The physical process that governs the thermal mixing due to condensing steam jets discharged in a large pool, as schematically shown in Fig. 47, is very typical of the *multi-scale* process, and they have three different scales [57–59].

The multi-scale process of condensation-induced thermal mixing in a pool can be summarized as follows: (a) Macro-scale thermal–hydraulic phenomena such as the turbulent jet-induced impinging jet and wall jet, and the interaction

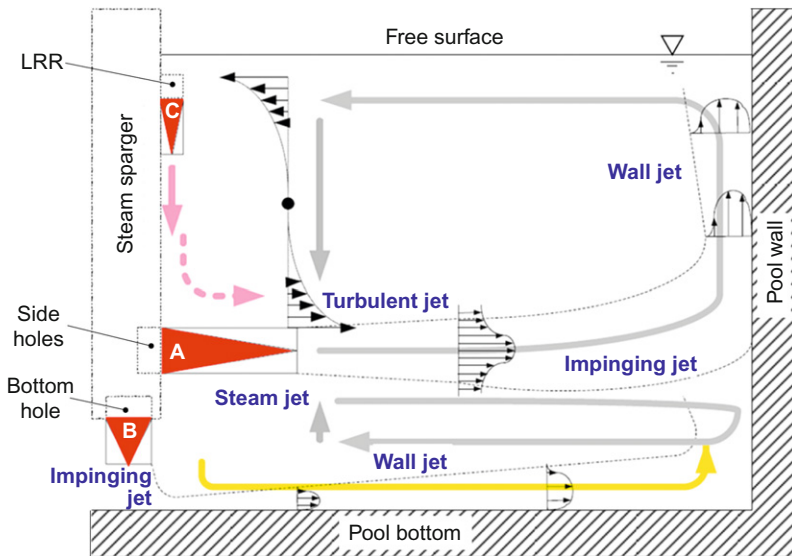


FIG. 47. Flow patterns in a pool due to the I-type sparger of the APR1400 design [57,58].

between these jets and quasi-stagnant surrounding water in a pool. (b) Meso-scale of the phenomena such as the steam jets and their interaction with adjacent ones, and the turbulent jet. Once the information on these meso-scale parameters is known, the macro-scale information can be easily predicted using the state-of-the-art CFD tools. (c) Micro-scale phenomena such as the local characteristics of interfacial transfer of momentum, heat, and mass between steam jets or their induced turbulent jet and the surrounding liquid.

In fact, it is very difficult to properly simulate the two different kinds of steam jet behavior, namely a *forced jet* and a *buoyant plume*, by the analysis using the system analysis codes. Since the phasic interaction between steam cavity and the surrounding liquid at the condensing interfaces is microscopic, the details of a condensing jet and the resultant mixing in a pool, in principle, should be dealt with using a multi-scale analysis approach. In the CFD analysis of macroscopic behavior of the thermal mixing induced by condensing jets in a pool, the most important phenomena are associated with the meso-scale phenomena, as pointed out by Kang and Song [47].

For a better prediction, a numerical simulation of the DCC of a steam jet by the suggested SCRM model [47,48] seems to be mostly desirable at the moment as long as the thermal mixing is concerned. Currently there are still some restrictions in experimentally obtaining detailed information on the characteristics of condensing jet. Advanced techniques on the numerical simulation need to be developed for a better prediction of condensing jet. Even though a number of efforts to develop new numerical methods are underway to analyze the two-phase mixing flow problem, currently there are no effective numerical models, and the use of a state-of-the art CFD method together with more sophisticated models is needed to characterize local behavior around the condensing interfaces.

VII. Conclusion

The direct contact condensation (DCC) of a steam jet discharged into a water pool shows a variety of thermo-fluid dynamic features, such as the condensing steam jets and the resultant turbulent jet, and their understanding is very essential to properly describing the local and global characteristics of thermal mixing in a large pool for engineering application.

In this paper, the DCC-related thermo-fluid dynamic features are discussed focusing on these two concerns. The *local* characteristics of condensing steam jets, such as the fundamental nature of condensing jets and the resultant turbulent jet, are reviewed, both of which importantly affect the macroscopic circulation in a pool. Here the fundamental behavior of condensing jets includes steam cavity shapes, temperature, and pressure profiles in a steam cavity, cavity expansion and penetration length, interfacial mass and heat transfer,

dynamic aspect of steam jet condensation, and condensation regime map. Then a *global* analysis of thermal mixing in a pool is discussed in terms of the local hot spot and the thermal stratification together with some practical applications to engineering design calculation in mind.

In order to analyze the thermal mixing induced by the DCC of steam jet in a pool, three-dimensional analysis capabilities are required together with the physical models on the local behavior of condensing jet and the resultant turbulent jet. Two major technical concerns, such as the local hot spot and thermal stratification, can be well described only if the local behavior of condensing steam jet and the resultant turbulent jet in a pool are well understood. Since these phenomena are closely related to the thermal–hydraulic-induced mechanical loads on the condensing systems, the experimental evidence observed in the DCC process is also expected to provide the technical background information for setting up the safety guidance in the design of steam discharging systems.

Since the phasic interaction at the condensing interfaces is microscopic, details of a condensing jet and the resultant mixing phenomena in a pool should be described based on a multi-scale approach. And for a better prediction of condensing steam jet in a pool based on this multi-scale approach, high precision experimental data that can reveal all the three different scales of thermal–hydraulic phenomena is essential to validating the relevant physical models and analysis results.

ACKNOWLEDGMENTS

The authors are grateful to the colleagues for their research efforts, especially to Drs. C.K. Park, H.S. Kang, S. Cho, H.Y. Kim, and Mr. Y.J. Youn (KAERI), and Drs. Y.T. Moon (KOPEC) and S.J. Hong and Y.J. Choo (FNC). They also would like to acknowledge the financial support by the MEST and MKE of the Korean government as well as Korean nuclear industries such as KHNP and KOPEC.

Nomenclature

ABWR	advanced BWR
AP1000	advanced power reactor 1000 MWe
APR1400	advanced power reactor 1400 MWe
APWR	advanced PWR
BCO	bubbling condensation oscillation
BWR	boiling water reactor
C	chugging
CFD	computational fluid dynamics
CO	condensation oscillation

CMFD	computational multi-field fluid dynamics
DCC	direct contact condensation
EPR	European Power Reactor
ESBWR	essential safety BWR
HTC	heat transfer coefficient
ICO	interfacial oscillation condensation
IRWST	in-containment refuelling water storage tank
ITER	International Thermonuclear Experimental Reactor
ITM	interface tracking methods
LOCA	loss-of-coolant accident
LOCV	loss-of-condenser vacuum
LRR	load reduction ring
MARS	multi-interfaces advection and reconstruction solver
MOC	method of characteristic
PSP	pressure suppression pool
PSTF	pressure suppression test facility
PWR	pressurized water reactor
SBWR	simplified boiling water reactor
SC	stable condensation
SCRM	steam condensation region model
SP	suppression pool
SRV	safety/relief valve
SST	shear stress transport model
TC	transitional region from chugging to condensation oscillation (CO)
TOLFW	total loss of feedwater
A	area (m^2)
a	x coordinate of the center of a sphere or speed of sound (m/s)
a_i	interfacial area per unit length (m^2/m)
B	dimensionless condensation driving potential, $C_p(T_s - T_\infty)/h_{fg}$
C_p	liquid specific heat (J/kg K)
C_0	a coefficient related to the effective radius and centerline decay rate (in Eq. 15)
C_p	specific heat at constant pressure
C_v	specific heat at constant volume
d	diameter of nozzle (mm)
EE	external expansion
f	frequency (Hz)
G	steam mass flux ($\text{kg/m}^2 \text{ s}$)
G_c	critical steam mass flux at atmosphere ($\text{kg/m}^2 \text{ s}$)
h_{fg}	latent heat of vaporization (J/kg)
h_i	heat transfer coefficient ($\text{J/m}^2 \text{ s K}$)

I_Φ	shape factor for sparger, P/d
Ja	Jacob number, $\rho_f C_p \Delta T / \rho_g h_{fg}$
k	ratio of specific heat, C_p / C_v
L	dimensionless penetration length, l/d
l	length of steam plume
Nu	Nusselt number, hd/k
n	ratio of the thermal boundary layer thickness to the eddy size, δ_{tl} / λ_t
P	pitch of sparger holes
Pr	Prandtl number, $\mu C_p / k$ of the liquid
p	pressure (Pa)
R	injector exit radius
Re	steam Reynolds number, $\rho_s v_s d_c / \mu_s$
R_{ex}	expansion ratio
r	radius (mm)
S	dimensionless transport modulus, $h_i / C_p G$
St	Stanton number, $h / \rho C_p u_f$ or Strouhal number, $fd \rho_f / \rho_g v$
St_t	turbulent Stanton number, $h / \rho C_p u_t$
T	temperature ($^{\circ}\text{C}$)
TP	transition point
U_c	center line velocity of jet
u	axial velocity (m/s)
u_l	interracial velocity (m/s)
u_o	average steam velocity at the nozzle exit (m/s)
u_t	turbulent intensity (m/s)
v	velocity (m/s)
We	Weber number, $\rho_f v^2 d / \sigma$
x	axial location (mm)
y_c	half jet width, where $u = 1/2 u_m$ (m)
z	distance from the nozzle or axial coordinate for vertical jet (m)

Greek

α	patulous angle (degree)
δ	expansion angle (degree) or thickness (mm)
η	pressure ratio (exit pressure/inlet pressure)
Φ_0	relative humidity (%)
η	jet cavity shape factor, $1 - x_p/1$
σ	surface tension (N/m)
μ	absolute viscosity (kg/m s)
ν	molecular kinematic viscosity, μ/ρ (m^2/s)
λ	integral eddy size (mm)

Subscripts

a	ambient condition
b	back pressure condition
cr	critical
e	nozzle exit
EE	external expansion
f	water or fluid
i	Pitot impact
l	liquid or water
m	mean value for cavity
n	nozzle
o	stagnation state
pool	water in a tank or pool
p	pool water or axial position, where $dr/dx = 0$
s	steam
sat	saturated condition
t	turbulent
tl	thermal layer
v	vapour or steam
∞	bulk
0	initial value, reference value, virtual origin, or stagnation properties

References

- [1] U.S. NRC, Suppression-pool temperature limits for BWR containments, NUREG-0783, 1981.
- [2] C.K. Chan, C.K.B. Lee, A regime map for direct contact condensation, *Int. J. Multiphase Flow* 8(1) (1982) 11–20.
- [3] M.H. Chun, Y.S. Kim, J.W. Park, An investigation of direct condensation of steam jet in subcooled water, *Int. Comm. Heat Mass Trans.* 23(7) (1996) 947–958.
- [4] S. Cho, C.-H. Song, C.K. Park, S.K. Yang, M.K. Chung, Experimental study on dynamic pressure pulse in direct contact condensation of steam jets discharging into subcooled water, in: *Proc. 1st Korea–Japan Symposium on Nuclear Thermal Hydraulics and Safety (NTHAS98)*, Pusan, Korea, 1998, pp. 291–298.
- [5] R.J. Young, K.T. Yang, J.L. Novotny, Vapor–liquid interaction in a high velocity vapor jet condensing in a coaxial water flow, in: *Proc. 5th Int. Heat Transfer Conf.*, vol. 3, Cs 1.3, Tokyo, 1974, pp. 226–230.
- [6] M. Cumo, G.E. Farello, G.E. Ferrari, Heat transfer in condensing jets of steam in water, in: *Proc. 6th Int. Heat Transfer Conf.*, vol. 5, Toronto, 1978, pp. 101–106.
- [7] G. Del Tin, E. Lavagno, M. Malandrone, Thermal and fluid-dynamic features of vapor condensing jets, *Heat Tech.* 1(1) (1983) 13–35.
- [8] S. Fukuda, Pressure variation due to vapor condensation in liquid (II): phenomena at large vapor mass flow rate, *J. Atom. Energy Soc. Japan* 24 (1982) 466–474.

- [9] H. Narai, I. Aya, Fluid and pressure oscillations occurring at direct contact condensation of steam flow with cold water, *Nucl. Eng. Design* 95 (1986) 35–45.
- [10] I. Aya, H. Narai, Elevation of heat transfer coefficient at direct contact condensation of cold water and steam, *Nucl. Eng. Design* 131(1) (1991) 17–24.
- [11] Y.S. Kim, C.-H. Song, Condensation regime map for a 4-hole sparger, *Trans. Am. Nucl. Soc.* 88 (2003) 278–279.
- [12] A.P. De With, R.K. Calay, G. De With, Three-dimensional condensation regime diagram for direct contact condensation of steam injected into water, *Int. J. Heat Mass Trans.* 50 (2007) 1762–1770.
- [13] X.-Z. Wu, J.-J. Yan, D.-D. Pan, G.-Y. Liu, W.-J. Li, Condensation regime diagram for supersonic/sonic steam jet in subcooled water, *Nucl. Eng. Design* 239 (2009) 3142–3150.
- [14] H.Y. Kim, Y.Y. Bae, C.-H. Song, J.K. Park, S.M. Choi, Experimental study on stable steam condensation in a quenching tank, *Int. J. Energy Res.* 25(3) (2001) 239–252.
- [15] X.-Z. Wu, J.-J. Yan, S.-F. Shao, Y. Cao, J.-P. Liu, Experimental study on the condensation of supersonic steam jet submerged in quiescent subcooled water: steam plume shape and heat transfer, *Int. J. Multiphase Flow* 33(12) (2007) 1296–1307.
- [16] X.-Z. Wu, J.-J. Yan, W.-J. Li, D.-D. Pan, D.-T. Chang, Experimental study on sonic steam jet condensation in quiescent subcooled water, *Chem. Eng. Sci.* 64 (2009) 5002–5012.
- [17] X.-Z. Wu, J.-J. Yan, W.-J. Li, D.-D. Pan, Y. Li, Experimental study on steam plume and temperature distribution for sonic steam jet, *J. Phys.* 147 (2009) 012–079 (conference series).
- [18] X.-Z. Wu, J.-J. Yan, W.-J. Li, D.-D. Pan, G.-Y. Liu, Experimental investigation of over-expanded supersonic steam jet submerged in quiescent water, *Exp. Therm. Fluid Sci.* 34 (2010) 10–19.
- [19] S.C. Baek, A study of the under-expanded moist air jets with non-equilibrium condensation, Ph.D. Dissertation, Department of Mechanical Engineering, Kyungpook National University, Korea (in Korean), 2003.
- [20] P.J. Kerney, G.M. Faeth, D.R. Olson, Penetration characteristics of a submerged steam jet, *AIChE J.* 18 (1972) 548–553.
- [21] J.C. Weimer, G.M. Faeth, D.R. Olson, Penetration of vapor jets submerged in subcooled liquids, *AIChE J.* 19 (1973) 552–558.
- [22] L.D. Chen, G.M. Faeth, Condensation of submerged vapor jets in subcooled liquids, *J. Heat Trans.* 104 (1982) 774–780.
- [23] G. Del Tin, E. Lavagno, M. Malandrone, Experimental study on steam jet condensation in subcooled water pool, in: *Proc. 3rd Multiphase Flow and Heat Transfer Symposium-Workshop Part A*, Miami Beach, FL, USA, 1983, pp. 815–830.
- [24] A. Petrovic, Analytical study of flow regimes for direct contact condensation based on parametrical investigation, *J. Pressure Vessel Tech.* 127 (2005) 20–25.
- [25] A. De With, Steam plume length diagram for direct contact condensation of steam injected into water, *Int. J. Heat Fluid Flow* 30 (2009) 971–982.
- [26] C.-H. Song, S. Cho, H.Y. Kim, Y.Y. Bae, M.K. Chung, Characterization of direct contact condensation of steam jets discharging into a subcooled water, in: *Proc. IAEA Technical Committee Mtg.*, PSI, Villigen, 1998.
- [27] C.K. Chan, Dynamical pressure pulse in steam jet condensation, in: *Proc. 6th Int. Heat Transfer Conference*, CS-3, Toronto, 1978, pp. 395–399.
- [28] C.K. Park, S. Cho, N.H. Choi, S.K. Yang, M.K. Chung, A study on the characteristics of the jet type condensation, in: *Proc. Korean Nuclear Society, Fall Conference 1999* (in Korean), 1999.
- [29] S.J. Hong, Dynamic characteristics of steam jet condensation in sparger, Ph.D. Dissertation, Seoul National University, Korea, 2001.

- [30] M. Arinobu, Studies on the dynamic phenomena caused by steam condensation in water, in: Proc. ANS-ASME-NRC Int. Topical Mtg. Nuclear Reactor Thermal Hydraulics, vol. 1, Saratoga Springs, New York, 1980, pp. 293–302.
- [31] M.E. Simpson, C.K. Chan, Hydrodynamics of a subsonic vapor jet in subcooled liquid, ASME J. Heat Transfer 104 (1982) 271–278.
- [32] C. Damasio, G. Del Tin, G. Fiegna, M. Malandrone, Experimental study on the unstable direct contact condensation regimes, in: Proc. 3rd Int. Topical Mtg. Reactor Thermal Hydraulics, Newport, RI, USA, 1985, pp. 6.C-1–6.C-8.
- [33] S. Cho, C.-H. Song, H.J. Chung, S.Y. Chun, M.K. Chung, Multiple-hole effect on the performance on a sparger during direct contact condensation of steam, KSME Int. J. 15(4) (2001) 482–491.
- [34] C.-H. Song, S. Cho, T.S. Kwon, M.K. Chung, The effect of non-condensable gas on dynamic pressure induced by steam–water direct contact condensation, in: Proc. 5th Int. Symp. Heat Transfer Int., Beijing, China, 2000.
- [35] K.S. Liang, P. Griffith, Experimental and analytical study of direct contact condensation of steam in water, Nucl. Eng. Design 147(3) (1994) 425–435.
- [36] Y.S. Kim, J.W. Park, C.-H. Song, Investigation of the steam–water direct contact condensation heat transfer coefficients using interfacial transport models, Int. Comm. Heat Mass Trans. 31(3) (2004) 397–408.
- [37] S.S. Gulawani, J.B. Joshi, M.S. Shah, C.S. RamaPrasad, D.S. Shukla, CFD analysis of flow pattern and heat transfer in direct contact steam condensation, Chem. Eng. Sci. 61(16) (2006) 5204–5220.
- [38] S.S. Gulawani, S.K. Dahikar, C.S. Mathpati, J.B. Joshi, M.S. Shah, C.S. RamaPrasad, et al., Analysis of flow pattern and heat transfer in direct contact condensation, Chem. Eng. Sci. 64(8) (2009) 1719–1738.
- [39] A. Kudo, T. Egusa, S. Toda, Basic study on vapor suppression, in: Proc. 5th Int. Heat Transfer Conf., vol. 3, Cs1.2, Tokyo, 1974, pp. 221–225.
- [40] R.J.E. Van Wissen, K.R.A.M. Schreel, C.W.M. Van Der Geld, J. Wieringa, Turbulence production by a steam-driven jet in a water vessel, Int. J. Heat and Fluid Flow. 25 (2004) 173–179.
- [41] R.J.E. Van Wissen, K.R.A.M. Schreel, C.W.M.V. Van Der Geld, Particle image velocity measurement of a steam-driven confined turbulent water jet, J. Fluid Mech. 530 (2005) 353–368.
- [42] Y.S. Kim, Y.J. Youn, Experimental study of turbulent jet induced by steam jet condensation through a hole in a water tank, Int. Comm. Heat Mass Trans. 35(1) (2008) 21–29.
- [43] Y.J. Youn, Y.J. Choo, Y.S. Kim, C.-H. Song, Velocity and temperature profiles of a turbulent jet induced by a steam jet discharged into a subcooled water pool, in: Proc. 7th Int. Topical Mtg. Nuclear Reactor Thermal Hydraulics Oper. Saf. (NUTHOS-7), Seoul, Korea, 2008, October 5–9 2008.
- [44] Y.J. Choo, C.-H. Song, PIV measurements of turbulent jet and pool mixing produced by a steam jet in a subcooled water pool, Nucl. Eng. Design 240(9) (2010) 2215–2224.
- [45] H.J. Hussein, S.P. Capp, W.K. George, Velocity measurements in a high-Reynolds-number, momentum-conserving, axisymmetric, turbulent jet, J. Fluid Mech. 258 (1994) 31–75.
- [46] G.N. Abramovich, The Theory of Turbulent Jets, The MIT Press, MA, 1963, pp. 76–85.
- [47] H.S. Kang, C.-H. Song, CFD analysis of a turbulent jet behavior induced by a steam jet discharge through a single hole in a subcooled water tank, Nucl. Eng. Design 240(9) (2010) 2160–2168.
- [48] H.S. Kang, C.-H. Song, CFD Analysis of turbulent jet behavior induced by a steam jet discharged through a vertical upward single hole in a subcooled water pool, Nucl. Eng. Tech. 42 (4) (2010) 382–393.
- [49] ANSYS Inc, CFX-11 Manual, 2008.

- [50] H.S. Kang, C.-H. Song, CFD analysis for thermal mixing in a subcooled water tank under a high steam mass flux discharge condition, *Nucl. Eng. Design* 238(3) (2008) 492–501.
- [51] J. Mahaffy, B.D. Chung, F. Dubois, F. Ducros, E. Graffard, M. Heitsch, et al., Best practice guidelines for the use of CFD in nuclear reactor safety applications, OECD/NEA Report, NEA/CSNI/R(2007)5, 2007.
- [52] R.E. Gamble, T.T. Nguyen, B.S. Shiralkar, P.F. Peterson, R. Greif, Pressure suppression pool mixing in passive advanced BWR plants, *Nucl. Eng. Design* 204 (2001) 321–336.
- [53] T.L. Norman, S.T. Revankar, Jet-plume condensation of steam–air mixtures in subcooled water, Part 1: Experiments, *Nucl. Eng. Design* 240 (2010) 524–532.
- [54] T.L. Norman, S.T. Revankar, Jet-plume condensation of steam–air mixtures in subcooled water, Part 2: Code model, *Nucl. Eng. Design* 240 (2010) 533–537.
- [55] K. Takase, Y. Ose, T. Kunugi, Numerical study on direct-contact condensation of vapor in cold water, *Fusion Eng. Design* 63 (2002) 421–428.
- [56] Y.T. Moon, CFD simulation of steam thermal mixing in subcooled water pool, Ph.D. Thesis, Seoul National University, Korea, 2009.
- [57] C.-H. Song, Steam jet condensation in a pool: from fundamental understanding to engineering scale analysis, Invited Keynote Lecture (IHTC14-23407), in: *Proc. 14th Int. Heat Transfer Conf. (IHTC-14)*, Washington, D.C., USA, 2010.
- [58] C.-H. Song, The steam discharge in a pool, in: D. Bestion, H. Anglart, J. Mahaffy, D. Lucas, C.-H. Song, M. Scheuerer, G. Zigh, M. Andreani, F. Kasahara, M. Heltsch, E. Komen, F. Moretti, T. Morii, P. Mulbauer, B.L. Smith, T. Watanabe (Eds.), *Extension of CFD Codes Application to Two-Phase Flow Safety Problems*, 2010 (Chapter 7, NEA/CSNI/R(2010)2, OECD/NEA Report).
- [59] D. Bestion, Extension of CFD codes application to two-phase flow safety problems, *Nucl. Eng. Tech.* 42(4) (2010) 365–381.

Fluid Flow and Heat Transfer from Circular and Noncircular Cylinders Submerged in Non-Newtonian Liquids

R.P. CHHABRA

Department of Chemical Engineering, Indian Institute of Technology, Kanpur, India

I. Introduction

The external (boundary-layer) flow of fluids over variously shaped bluff bodies represents an important class of problems within the domain of fluid mechanics and transport phenomena, as is evident from the extensive literature for a circular cylinder and a sphere, for instance. Indeed, the earliest references about the investigations concerning the flow characteristics for these two shapes can be easily traced back to the fifteenth century if not earlier! [1,2]. The interest in such model flow configurations stems from both fundamental and pragmatic considerations. From a fundamental standpoint, the flow past a circular cylinder (which is free from geometrical singularities) has served as a useful model to understand the nature of the underlying physical processes such as the nature of flow close to the solid surface, flow separation, wake dynamics (size, volume, shape, etc.), vortex shedding characteristics, and laminar–turbulent transitions, etc. Indeed, even for the simplest case of an unconfined uniform flow over a long circular cylinder oriented transverse to the oncoming free stream, this seemingly simple flow exhibits a rich variety of flow regimes depending upon the value of the sole governing parameter, namely, Reynolds number. For instance, with the increasing value of the Reynolds number, the flow is characterized by multiple length and time scales thereby making it increasingly challenging to tackle even from a computational standpoint. Broadly, cylinders of other shapes like elliptical, square, triangular, and semicircular also display qualitatively similar flow features with added complexities arising from their geometrical singularities and/or orientation with respect to the mean flow direction. Such model flows thus serve as a launching pad to understand more complex flows involving multibody interactions as well as body–wall interactions. From pragmatic considerations, the flow past a circular cylinder denotes an idealization of several industrially

important applications. Typical examples include the flow in tubular, pin-type, and other novel designs of heat exchangers, aerosol filters, rake filters, use of thin wires as measurement probes, support structures, and aerodynamics of tall buildings and structures. Additional examples are found in the continuous thermal treatment of foodstuffs (like carrots, sliced potatoes, and beans), in the filtration of sewage sludge, pulp suspensions, and coating suspensions using screens, and processing of fibrous systems encountered in scores of industrial settings, etc. Notwithstanding the significance of the detailed kinematics in such complex applications, reliable knowledge of the hydrodynamic forces exerted on a single cylinder and the corresponding rate of heat/mass transfer often serve as useful starting points in process design calculations. Of course, this information is obtained using a combination of analytical, numerical, and experimental tools. Such model configurations which are free from sharp edges and corners have also proved to be of considerable value in validating the efficacy of new numerical tools being developed continually. In view of such overwhelming fundamental and practical relevance, a large body of knowledge has accrued on various aspects of the momentum and heat/mass transfer phenomena in different flow regimes from such model shapes as far as the Newtonian fluids are concerned, albeit there are still areas meriting further research [1–4]. A cursory inspection of the aforementioned as well as other authoritative surveys clearly reveal that the bulk of the literature relates to the case of a circular cylinder, followed by that of elliptic cylinders of various aspect ratios. Indeed, the limited body of knowledge relating to the flow of fluids over a square or rectangular or semicircular or triangular cylinder is not only of a relatively recent vintage but is also much less coherent and conclusive than that for a circular cylinder even for Newtonian fluids. This is particularly surprising especially when most compact and novel designs of heat exchangers entail elements of various noncircular shapes [5]. Similarly, during the cooling of electronic components, one also encounters elements of square, rectangular, semicircular, triangular, and other complex shapes.

On the other hand, it is readily acknowledged that many structured fluids of macromolecular nature (polymer melts and their solutions), multiphase systems (foams, emulsions, suspensions, for instance), and solutions containing surface active agents (soap and micellar) encountered in industrial practice exhibit a spectrum of rheological complexities which cannot be described, even qualitatively, using the framework of Newtonian fluid behavior and the well-known Navier–Stokes equations. Accordingly, such fluids are variously known as non-Newtonian or nonlinear or rheologically complex fluids [6–10]. While one may classify the different types of non-Newtonian fluid behavior in several ways, most of these systems exhibit the so-called shear-thinning behavior. This is characterized by an apparent (or effective) viscosity, defined as shear stress divided by the corresponding shear rate, which

decreases with the increasing shear rate. Most emulsions, suspensions, foams, and polymeric systems display shear-thinning behavior under appropriate conditions. Likewise, several particulate slurries, foams, emulsions, and filled polymeric systems resist deformation by offering an enormous resistance when the externally applied stress is below a critical value. The so-called viscoplastic behavior is often rationalized by introducing the notion of a yield stress which demarcates the boundaries of the *solid-like* (unyielded) and *fluid-like* (yielded) regions within a flow field depending upon the local levels of stress prevailing in the flow field, albeit this has been (and continues to be) an area of intense debate! [11,12]. On the other hand, few thick pastes and suspensions exhibit the so-called shear-thickening (or dilatant) fluid behavior which is characterized by an apparent viscosity which gradually increases with the increasing shear rate, for example, see Ref. [13] for an extensive review in this field. Another class of fluids displays evolution or destruction (which may be reversible or irreversible) of structure with time under the application of shear thereby leading to the so-called time-dependent fluid behavior [9,14]. Finally, there is another class of industrially important materials (rubbers, polymers and their derivatives) which show a blend of “viscous” fluid-like and “elastic” solid-like features thereby giving rise to the so-called viscoelastic or elastico-viscous fluid behavior [6,14]. The available voluminous body of knowledge in terms of survey articles, textbooks, and research monographs testifies to the wide occurrence of non-Newtonian flow characteristics in scores of industrial sectors including (but not limited to) food, pharmaceutical, polymer and plastic, mineral suspensions, cosmetics, personal care products, toiletries, construction materials, and biological products [9]. Undoubtedly, over the years, significant advances have been made in the areas of non-Newtonian fluid flow in circular and noncircular ducts [9,15–17], mixing in batch systems [9,15,18–21], and flow in granular and fibrous media [22,23], for instance. A cursory inspection of all the aforementioned as well as the other available resources clearly reveals that even in these settings, flow (momentum transfer) behavior has been investigated much more extensively than the corresponding convective heat and mass transport characteristics [22–27]. In contrast, much less is known about the behavior of such non-Newtonian fluids in the so-called external or boundary-layer flows as that introduced in the beginning of this chapter, albeit over the past 20 years or so, a reasonable body of information has accrued pertaining to the transverse flow of such fluids past long cylinders of circular and noncircular cross sections with the added complexity of confinement and/or combined forced or free convection heat transfer. It is thus deemed timely and appropriate not only to critically review the pertinent literature, but also to identify the existing knowledge gaps and the areas meriting further systematic investigation. This chapter endeavors to accomplish this objective.

II. Scope and Organization

The major thrust of this chapter is on elucidating the role of non-Newtonian flow characteristics of structured fluids (within the framework of continuum mechanics) on the hydrodynamic and convective heat and mass transport processes for bluff bodies of various shapes immersed in streaming (unconfined or confined) or quiescent fluids in different flow regimes. In particular, consideration is given to the steady and laminar vortex shedding regimes of the flow over long cylinders of circular, elliptic, semicircular, square, and triangular cross sections. Within this framework, the flow invariably tends to be two-dimensional and laminar. The assumptions of incompressibility and isotropy of the liquid are also implicit in the ensuing discussion. These are believed to be reasonable simplifications in most cases, the notable exceptions being gas–liquid dispersions and foams which might display deviations from both these assumptions under certain conditions. However, no detailed discussion on the non-Newtonian fluid behavior *per se* is included here, for excellent treatments are available in numerous books, monographs, and review articles, for example, see Refs. [6–10,14,26]. We begin with by presenting the governing equations describing this class of flows under forced, mixed, and free convection regimes together with the appropriate boundary conditions in each case. Scaling considerations are used to extract the pertinent dimensionless parameters which influence the detailed and macroscopic momentum and heat transfer characteristics for each shape of the bluff body considered here. This is followed by a detailed description of the different flow regimes encountered together with the critical values of the Reynolds number denoting the transition from one flow regime to another. As will be seen here, these values are strongly influenced not only by the rheological characteristics, but also by the shape of the bluff body, its orientation with regard to the mean direction of flow, extent and type of confinement, etc. This is followed by a detailed treatment of momentum transport (in terms of streamlines, wake phenomena, hydrodynamic forces exerted on the submerged objects), and finally by the corresponding discussion of heat/mass transport in different flow regimes. The numerical predictions are contrasted with the appropriate experimental data whenever it is possible. Finally, the chapter is concluded by summarizing the current state of the art and by identifying the areas meriting further exploration.

III. Governing Equations, Boundary Conditions, and Dimensionless Parameters

Let us consider the flow of incompressible fluids past a cylinder of arbitrary shape (circular) which is infinitely long in the neutral direction, as shown

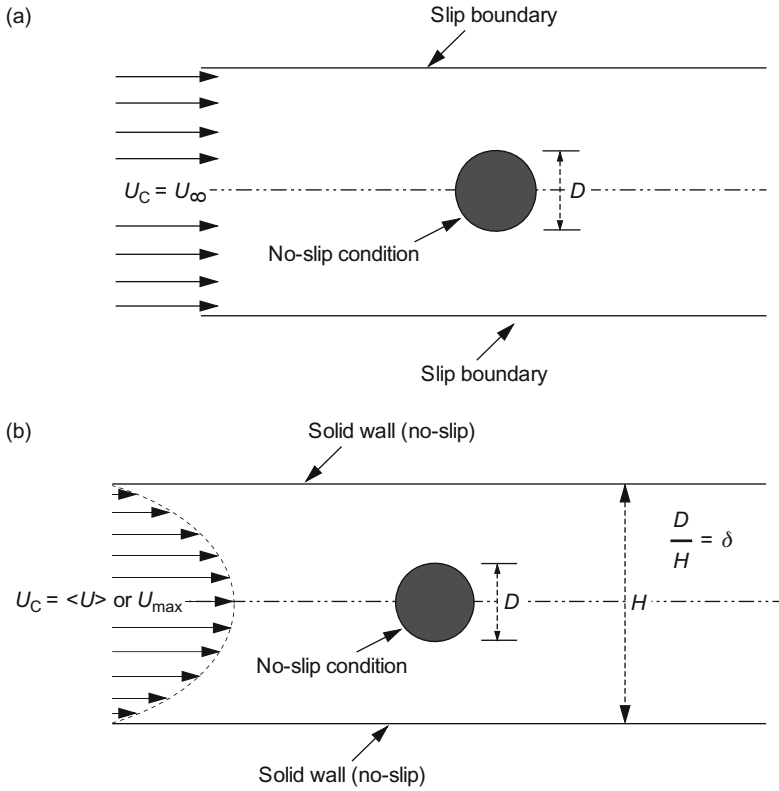


FIG. 1. Schematics of the general unconfined (a) and confined (b) flow past a two-dimensional bluff body.

schematically in Fig. 1. The governing equations are presented in their dimensionless and generalized forms which can be specialized for the shapes of interest like a circular, semicircular, square, rotated square, elliptic, triangular, and cylinder considered in this work. The linear scale is denoted by a characteristic dimension l_c and the characteristic velocity is denoted by U_c . Furthermore, heat transfer may occur in the forced or free or mixed convection regimes. Additional complications arise from the fact that one may prescribe the condition of a constant wall temperature (CWT), T_w , or a constant heat flux (CHF), q_w , on the surface of the bluff body submerged in a fluid. The far-away fluid temperature is denoted by T_∞ . Since the bulk of the discussion in this chapter is limited to the two-dimensional laminar flow regime, the governing equations are written accordingly here. Furthermore, the thermo-physical properties of the fluid (thermal conductivity, k , heat capacity, C , density, ρ ,

viscosity, η) are assumed to be independent of temperature except when heat transfer occurs in the mixed or free convection regime. In the latter case, the assumption of incompressibility is still applicable except for the body force term in the momentum equation which is approximated via the Boussinesq assumption of linear relationship between fluid density and temperature. Finally, the range of conditions considered herein is such that the viscous dissipation effects in the energy equation are assumed to be negligible. Within this framework of simplifying assumptions, the momentum and heat transfer characteristics of fluid flow over a two-dimensional immersed cylinder of an arbitrary cross section are written as follows:

Equation of continuity:

$$\frac{\partial U_x}{\partial x} + \frac{\partial U_y}{\partial y} = 0 \quad (1)$$

x-Component of momentum equation:

$$\frac{DU_x}{Dt} = -\frac{\partial p}{\partial x} + \left(\frac{1}{Re}\right) \left(\frac{\partial \tau_{xx}}{\partial x} + \frac{\partial \tau_{yx}}{\partial y}\right) \quad (2)$$

y-Component of momentum equation:

$$\frac{DU_y}{Dt} = -\frac{\partial p}{\partial y} + \left(\frac{1}{Re}\right) \left(\frac{\partial \tau_{xy}}{\partial x} + \frac{\partial \tau_{yy}}{\partial y}\right) + Ri \cdot T \quad (3)$$

where the Richardson number is defined as $Ri = (Gr/Re^2)$.

Naturally in the absence of the free convection effects, $Ri = 0$ and Eq. (3) reduces to the form of Eq. (2).

Thermal energy equation:

$$\frac{DT}{Dt} = \left(\frac{1}{Re \cdot Pr}\right) \left(\frac{\partial^2 T}{\partial x^2} + \frac{\partial^2 T}{\partial y^2}\right) \quad (4)$$

On the other hand, if heat transfer occurs entirely in the free convection regime ($Re = 0$), while the equation of continuity remains unchanged, the momentum and thermal energy equations are of the following form:

x-Component of momentum equation:

$$\frac{DU_x}{Dt} = -\frac{\partial p}{\partial x} + \frac{1}{\sqrt{Gr}} \left(\frac{\partial \tau_{xx}}{\partial x} + \frac{\partial \tau_{yx}}{\partial y}\right) \quad (5)$$

y-Component of momentum equation:

$$\frac{DU_y}{Dt} = -\frac{\partial p}{\partial y} + \frac{1}{\sqrt{Gr}} \left(\frac{\partial \tau_{xy}}{\partial x} + \frac{\partial \tau_{yy}}{\partial y}\right) \quad (6)$$

For the case of power-law fluids, the thermal energy equation takes the form:

$$\frac{DT}{Dt} = \frac{1}{Pr \cdot Gr^{1/(n+1)}} \left(\frac{\partial^2 T}{\partial x^2} + \frac{\partial^2 T}{\partial y^2} \right) \quad (7)$$

For incompressible fluids, the extra stress tensor, τ_{ij} , is related to the rate of deformation tensor, ε_{ij} , as follows [9,10]:

$$\tau_{ij} = 2\eta\varepsilon_{ij} \quad \text{where } i, j \equiv x, y \quad (8)$$

In turn, the components of the rate of deformation tensor, ε_{ij} , are related to the velocity gradients as [6]:

$$\varepsilon_{ij} = \frac{1}{2} \left(\frac{\partial U_i}{\partial j} + \frac{\partial U_j}{\partial i} \right) \quad (9)$$

Strictly speaking, the scalar viscosity of a non-Newtonian (time-independent) fluid is a function of the three invariants of the rate of deformation tensor, that is, I_1 , I_2 , and I_3 [6,7]. For incompressible fluids, the first invariant is identically zero thereby eliminating it from the viscosity functional. Similarly, the third invariant, I_3 , is also identically zero for viscometric flows (e.g., shearing flow in a tube). But most flows of practical interest like the ones considered in this chapter are far from being truly viscometric flows. However, the available extensive experimental evidence with scores of polymeric systems suggests that the viscosity displays a much stronger dependence on the second invariant of the rate of deformation tensor, I_2 , than that on the third invariant, I_3 [6,7]. It is thus customary to neglect the dependence of the viscosity on the third invariant thereby leading to the following general form:

$$\eta = \eta(I_2) \quad (10)$$

The second invariant I_2 in Cartesian coordinates for a two-dimensional flow is given by:

$$I_2 = \sum_i \sum_j \varepsilon_{ji} \cdot \varepsilon_{ij} \quad \text{where } i = x, y; \quad j = x, y \quad (11)$$

The corresponding expressions for ε_{ij} can be found in standard textbooks [6–8]. Finally, the literature is inundated with functions of varying forms and complexity to approximate the relationship inherent in Eq. (10), and excellent reviews summarizing their relative merits and demerits are available in the literature [6,7,9]. Perhaps the most commonly used model is the so-called power-law model (dimensionless) written as:

$$\eta = \left(\frac{I_2}{2} \right)^{(n-1)/2} \quad (12)$$

In Eq. (12), n is called the flow-behavior index. Evidently, $n = 1$ represents the constant viscosity thereby denoting the Newtonian fluid behavior. On the other hand, $n < 1$ predicts the decreasing value of viscosity with the increasing shear rate thereby predicting the so-called shear-thinning fluid behavior. The lower is the value of n , greater is the degree of shear-thinning. Many polymeric solutions and melts, and suspensions display the value of the flow behavior index (n) as small as 0.1–0.2. Finally, $n > 1$ predicts the so-called shear-thickening behavior, typical of many thick pastes and suspensions used in lubrication, printing, and food process engineering applications [13]. For, instance, corn flour-in-water dispersions can display the value of the flow behavior index, n , as high as 1.6–1.7. This model is used extensively in this chapter and the other viscosity models will be introduced as and when required in this chapter.

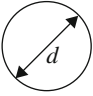
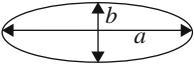

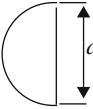
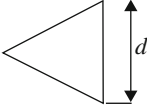
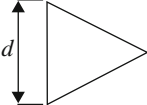
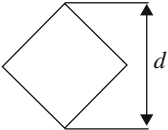
In order to complete the problem statement, one needs to identify appropriate boundary conditions to solve the aforementioned governing equations. Broadly speaking, the standard no-slip condition and either constant wall temperature (CWT) or CHF are prescribed on the surface of the bluff body. For an unconfined flow configuration, the free stream velocity and fluid temperature are prescribed far away from the surface of the obstacles, i.e., at $\mathbf{X} \rightarrow \infty$. When the bluff body is confined in between solid walls, the usual no-slip condition for flow and that of adiabaticity for heat transfer are implemented on the confining walls also.

At this juncture, it is appropriate to discuss the nondimensionalization of the governing differential equations. In Eqs. (1)–(12), the characteristic linear and velocity scales as l_c and U_c , respectively, have been used. The choice of l_c is listed in Table I for two-dimensional cylinders of the shapes of interest in the present context. On the other hand, the choice of U_c varies from one situation to another. Thus, for unconfined uniform flow far away from the bluff body, $U_c = U_\infty$. On the other hand, when the bluff body is confined in between two solid walls, it is possible to approximate U_c either by the center line velocity (U_{\max}) or by the area average velocity $\langle U \rangle$. Finally, for the case of pure free convection, scaling considerations suggest the characteristic velocity scale to be of the order given by $(l_c g \beta \Delta T)^{1/2}$. Therefore, with the appropriate choice of l_c and U_c , one can scale time as (l_c / U_c) , pressure as $\rho_\infty U_c^2$, viscosity of a power-law fluid as $m(U_c / l_c)^{n-1}$, and extra stress components as $m(U_c / l_c)^n$. Similarly, depending upon the type of thermal boundary condition prescribed on the surface of the bluff body, the nondimensional temperature is given as $(T' - T_\infty) / (T_w - T_\infty)$ or $(T' - T_\infty) / (q_w l_c / k)$. This process of rendering the governing equations dimensionless leads to the following inferences for an unconfined flow:

A. FORCED CONVECTION REGIME ($Ri = 0$)

The momentum and heat transfer characteristics are governed by three dimensionless groups, namely, Reynolds number (Re), Prandtl number (Pr),

TABLE I
DEFINITION OF CHARACTERISTIC LINEAR DIMENSION (l_c) AND VELOCITY (U_c) FOR BLUFF BODIES OF DIFFERENT SHAPES

Geometry	Characteristic linear dimension (l_c)
	Diameter of cylinder, d
	Minor axis of ellipse, b
	Side of square, d
	Diameter of semicircular cylinder, d
	Side of equilateral triangle, d
	Side of equilateral triangle, d
	Diagonal of square, d

Note: Characteristic velocity (U_c) is free stream velocity for unconfined flow and is area averaged velocity (or) maximum velocity for a confined flow. Flow is from left to right.

and power-law index (n), appearing in Eqs. (1)–(4). These are defined as follows:

$$Re = \frac{\rho_{\infty} U_c^{2-n} l_c^n}{m} \quad (13)$$

$$Pr = \frac{C_p m}{k} (U_c / l_c)^{n-1} \quad (14)$$

It is, of course, possible to define the so-called Peclet number, Pe , which is simply the product of Re and Pr , i.e., $Pe = Re \cdot Pr$. But only two of these three parameters are independent.

B. MIXED CONVECTION REGIME

In this regime, the buoyancy induced flow may aid or oppose or may be transverse to the imposed flow depending upon the direction of the external flow with respect to that of the gravity vector. The nondimensionalization of the governing equations (Eqs. (1)–(4)) leads to the following dimensionless groups: Reynolds number (Re), Prandtl number (Pr), Grashof number (Gr), or Richardson number $Ri = (Gr/Re^2)$. While the Reynolds and Prandtl numbers are still defined by Eqs. (13) and (14), respectively, the Richardson number, Ri , is defined as:

$$Ri = \frac{g\beta(T_w - T_\infty)l_c}{U_c^2} \quad (15)$$

where U_c denotes the imposed flow and β is the coefficient of volumetric expansion of the fluid given by

$$\beta = -\frac{1}{\rho} \frac{\partial \rho}{\partial T} \bigg|_T \quad (16)$$

Naturally, the Richardson number is a measure of the relative strength of the buoyancy induced current with respect to the imposed flow. Thus, $Ri \rightarrow 0$ denotes the pure forced convection regime whereas $Ri \rightarrow \infty$ represents the pure natural convection regime. At $Ri = 1$, both effects are of comparable magnitude. In the mixed convection regime, the momentum and heat transfer phenomena are influenced by the values of n , Pr , Re , Gr , or Ri .

C. FREE CONVECTION REGIME ($Ri \rightarrow \infty$)

Since there is no external velocity scale in this case, the relevant characteristic velocity is given by $(l_c g \beta \Delta T)^{1/2}$ and the use of this choice leads to the following definitions of the Grashof number (Gr) and Prandtl number (Pr) appearing in Eqs. (1) and (5)–(7):

$$Gr = \frac{\rho_\infty^2 l_c^{n+2} (g \beta \Delta T)^{2-n}}{m^2} \quad (17)$$

$$Pr = \frac{\rho_\infty C}{k} \left(\frac{m}{\rho_\infty} \right)^{2/(1+n)} l_c^{(1-n)/(1+n)} (l_c g \beta \Delta T)^{3(n-1)/2(n+1)} \quad (18)$$

It is also possible to introduce another commonly used dimensionless group in free convection, namely, Rayleigh number, Ra . By analogy with the

definition of the Peclet number, the Rayleigh number is simply the product of the Grashof and Prandtl numbers, i.e., $Ra = Gr \cdot Pr$. However, only two out of these three are independent.

Note that in the limit of the Newtonian fluid behavior, the aforementioned definitions reduce to their expected forms. Thus, for instance, $Re = \rho_{\infty} l_c U_c / \eta$, $Pr = C\eta/k$, and $Gr = \rho_{\infty}^2 l_c^3 (g\beta\Delta T) / \eta^2$.

It is worthwhile to reiterate here that additional dimensionless numbers arise when considering flow and heat transfer from bluff bodies in the other types of non-Newtonian viscosity models or from geometrical considerations like the type and extent of confinement or the orientation of the bluff body with respect to the oncoming flow, etc. These will be introduced as and when needed during the course of our discussion in this chapter.

Irrespective of the prevailing flow regime, it is readily seen that the governing differential equations are nonlinear on two counts: inertial and viscous terms. This complexity alone precludes the possibility of closed form analytical solutions even for Newtonian fluids unless the troubling inertial terms are neglected altogether. On the other hand, for finite values of the influencing parameters like Re and Pr in forced convection regime, Gr and Pr in free convection and Gr , Pr , and Ri in the mixed convection regime, the only way forward is through the numerical solutions of the governing equation. Lastly, it is also useful to recognize here that if the temperature of the fluid varies appreciably in the domain, it may be necessary to account for the temperature dependence of the thermophysical properties of the fluid (ρ , C , k , η) thereby not only adding to the level of complexity due to the coupled nature of the governing differential equations but also due to the additional dimensionless groups arising from such considerations. Hence, it is customary to seek numerical solutions to the field equations. Indeed, a range of numerical techniques including finite difference, finite element, and finite volume methods have been employed in conjunction with the primitive variable or stream function-vorticity formulations of the governing differential equations. Irrespective of the numerical methodology and/or the type of formulation, it is simply not possible to simulate truly unconfined flows in numerical studies. Thus, the far field boundary conditions are satisfied at finite (artificial) boundaries rather than at $\mathbf{X} \rightarrow \infty$. This necessitates special care in terms of treating such artificial boundaries as slip (tractionless) walls. Similarly, under certain conditions, one can invoke symmetry considerations to economize on computational efforts. Notwithstanding such nuances of numerical techniques, the solution to the governing differential equations maps the flow domain in terms of velocities, pressure, and temperature fields. These, in turn, can be processed to infer the microscopic and macroscopic features of the momentum and heat transfer phenomena. It is therefore appropriate to introduce some of these parameters at this juncture.

It is customary to visualize the flow in terms of streamlines and iso-vorticity contours. While the streamlines plots facilitate the identification of the stagnant zones, give a general snapshot of the flow, the vorticity (ω) is a measure of the local rate of rotation, and for a two-dimensional flow it is defined as:

$$\omega = \frac{1}{2} \left(\frac{\partial U_y}{\partial x} - \frac{\partial U_x}{\partial y} \right) \quad (19)$$

At next level, the flow is visualized in terms of the variation of the pressure on the surface of the bluff body, and this is generally achieved by defining a dimensionless coefficient C_p as:

$$C_p = \frac{p - p_\infty}{(1/2)\rho U_c^2} \quad (20)$$

Finally, due to the prevailing tangential and normal stresses present in the fluid, there is a net hydrodynamic force exerted on the immersed body which can be resolved along and normal to the direction of flow. The component along the direction of flow is the usual drag force which is expressed in terms of the dimensionless drag coefficient (C_D) which itself can be split into two components: form (C_{DP}) and friction (C_{DF}). These are defined as follows:

$$C_{DP} = \frac{2F_{DP}}{\rho U_c^2 A_p} = \int_s C_p n_x \, ds \quad (21)$$

However, the definition of the frictional component C_{DF} is different for forced and free convection, and these are given as follows:

For forced convection:

$$C_{DF} = \frac{2F_{DF}}{\rho U_c^2 A_p} = \frac{2^{n+1}}{Re} \int_s (\tau \cdot n_s) ds \quad (22)$$

For free convection:

$$C_{DF} = \frac{2F_{DF}}{\rho U_c^2 A_p} = \frac{2^{1-n}}{\sqrt{Gr}} \int_s (\tau \cdot n_s) ds \quad (23)$$

and the total drag coefficient is simply the sum of these two components, i.e., $C_D = C_{DP} + C_{DF}$.

For unsteady or asymmetrical flows, the component of the hydrodynamic force in the lateral direction acting on the bluff body is called the lift force and it is expressed in a dimensionless form via the so-called lift coefficient (C_L) defined as follows:

$$C_L = \frac{2F_L}{\rho U_c^2 A_p} \quad (24)$$

In the time-periodic flow regime, it is also of interest to describe the time-period of oscillations or the frequency of vortex shedding, f , and this is done via the use of Strouhal number, St , defined as:

$$St = \frac{fl_c}{U_c} \quad (25)$$

where f is the frequency of oscillations in lift coefficient with time.

Naturally, the aforementioned characteristic parameters are expected to be functions of the Reynolds number and power-law index in the forced convection regime, of Re , Pr , Ri , and n in the mixed convection regime and of Gr , Pr , and n in the free convection regime.

Similarly, it is customary to visualize the heat transfer characteristics in terms of isotherm (constant temperature) contours which help in identifying the so-called hot or cold spots in the flow domain, especially during the handling of temperature-sensitive materials. At the next level, the heat transfer characteristics are analyzed in terms of the local Nusselt number Nu which varies from one point to another on the surface of the cylinder, and it is evaluated from the temperature field as:

$$Nu = \frac{hl_c}{k} = -\frac{\partial T}{\partial n} \Big|_{\text{surface}} \quad (\text{for CWT}) \quad (26a)$$

$$= -\frac{1}{T} \Big|_{\text{surface}} \quad (\text{for CHF}) \quad (26b)$$

where T is nondimensional temperature defined as:

$$T = \frac{T' - T_\infty}{T_w - T_\infty} \quad (\text{for CWT}) \quad (27a)$$

$$T = \frac{T' - T_\infty}{(q_w l_c / k)} \quad (\text{for CHF}) \quad (27b)$$

Finally, the global heat transfer characteristics are described in terms of its overall surface averaged value Nu_{avg} as:

$$Nu_{\text{avg}} = \frac{1}{s} \int Nu \, ds \quad (28)$$

Based on the preceding discussion, it is straightforward to postulate the existence of the following functional relationships for fixed shape and orientation of the obstacle:

Forced convection: $Nu_{\text{avg}} = f(Re, Pr, n)$

Free convection: $Nu_{\text{avg}} = f(Gr, Pr, n)$

Mixed convection: $Nu_{\text{avg}} = f(Re, Gr, Pr, n)$

or $Nu_{\text{avg}} = f(Re, Ri, Pr, n)$

In this chapter, these functional relationships are explored and developed for a range of shapes, especially for a circular, semicircular, square and rotated square, equilateral triangular and elliptic cylinders in different flow regimes.

IV. Flow Regimes

As remarked earlier, the unconfined or free flow past a circular cylinder exhibits a rich variety of flow regimes depending upon the intrinsic nature of the flow. It needs to be emphasized here that at finite Reynolds numbers, two flow regimes can be identified in the vicinity of the cylinder, i.e., boundary layer of thickness, δ , which is usually much smaller than the diameter of the cylinder, $(\delta/D) \lll 1$, and the wake region which is of the order of one-to-two times the diameter (D). Indeed, most of the discussions about different flow regimes hinges on the state of the flow in these two regions, for example, see Refs. [1,2,4,28]. Notwithstanding the fundamental significance of delineating the conditions for transition from one flow regime to another, this information is also germane to develop the scaling laws for the gross engineering parameters like drag and lift coefficients, Strouhal number and Nusselt number with the Reynolds number and Prandtl number. Therefore, significant research effort has been expended on exploring this aspect in this field. It is thus instructive to recapitulate the key points pertaining to the onset and distinguishing features of various flow regimes documented for the uniform transverse flow of Newtonian fluids past an unconfined smooth circular cylinder which is long in the transverse direction thereby eliminating the complications arising from the surface roughness and end effects, respectively. This will not only facilitate the subsequent discussion of noncircular cylinders but also that for the type of non-Newtonian fluids considered herein.

For the aforementioned simple flow, the flow is governed by the familiar Reynolds number $Re (=U_\infty D/\gamma)$, where D is the diameter of the cylinder, γ is the kinematic viscosity of the fluid, and U_∞ is the faraway uniform velocity. At vanishingly small values of the Reynolds number ($Re \rightarrow 0$), fluid inertia is negligible and therefore a fluid element is able to follow the surface contour of the cylinder (including sudden changes in the direction like for a square or triangular cylinder) without incurring any loss in its momentum. Under these conditions, the flow remains attached to the surface of the cylinder and it also exhibits the fore and aft as well as the midplane symmetry (Fig. 2). As the value of the Reynolds number is progressively incremented, the viscous effects gradually weaken and fluid inertia increases and naturally, a fluid element is no longer able to negotiate the sudden changes in body shape without incurring losses in its momentum (or kinetic energy). Therefore, a point is reached when due to the diverging area, an adverse pressure gradient is established in the

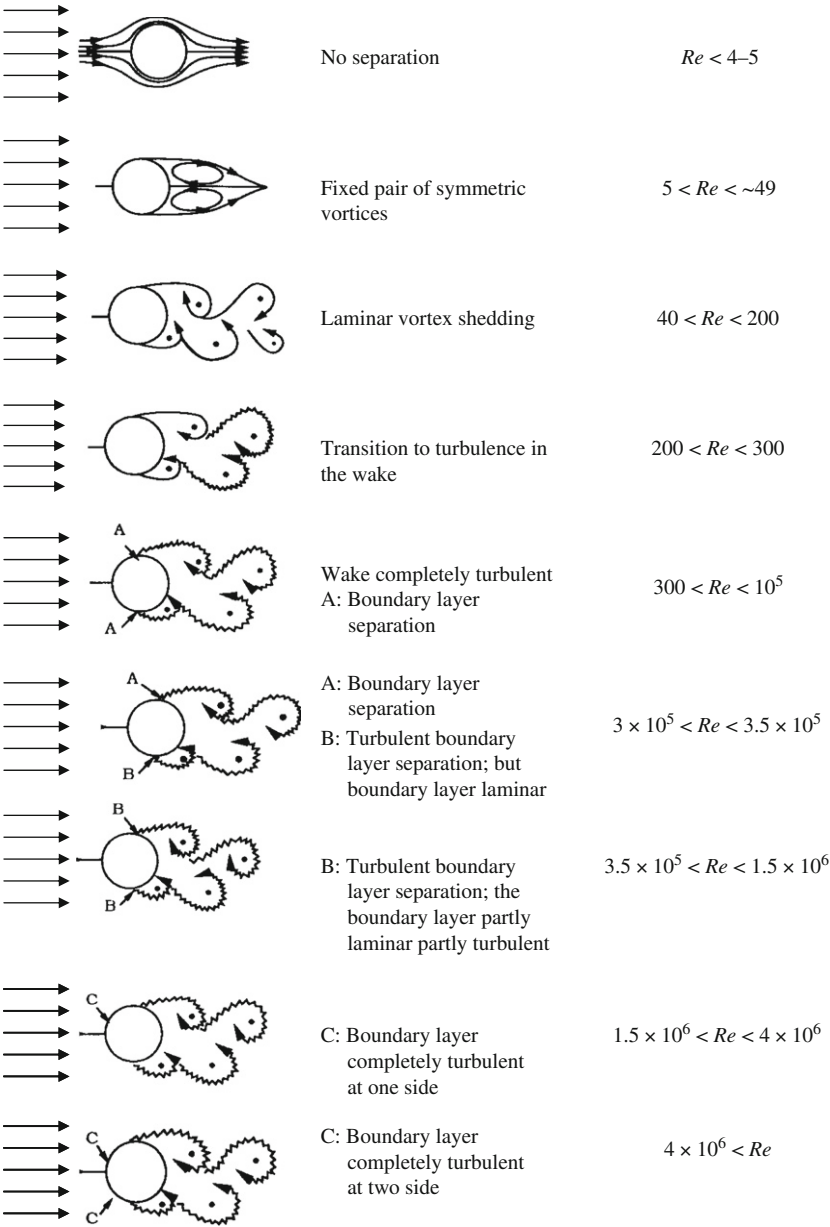


FIG. 2. Schematics of the different flow regimes past an unconfined circular cylinder. Source: Adapted from Ref. [4].

rear of the cylinder thereby leading to the detachment of flow from the surface of the cylinder. The location of the point of separation coincides with that of the change of the sign of the vorticity on the surface of the cylinder. At a slightly higher value of the Reynolds number, visible separated (wake) flow region appears in the rear of the cylinder. Therefore, the flow no longer exhibits the fore and aft symmetry, albeit it is still symmetric about the midplane. This transition is known to occur at about $\sim 4 \leq Re \leq \sim 5$. Thus, the flow remains attached to the surface of the cylinder below $Re < \sim 4$. As the value of the Reynolds number is increased further, the wake region is characterized by a pair of counter-rotating vortices which remain attached (shown schematically in Fig. 2). The wake region is characterized by the so-called recirculation length, L_r which denotes the point downstream of the cylinder at which the near closed streamline reattaches itself and the angle of flow separation (which gives a measure of the wake width). Combined together these two parameters define the size (volume) of the wake region. In this regime, the wake length increases and the point of separation on the surface of the cylinder moves forward (thereby increasing the width of the wake) with the increasing Reynolds number. This inference is based on both experimental observations (e.g., see Refs. [29–32]) and steady numerical computations, for example, see Refs. [33,34], albeit there seem to be some unresolved issues even in this flow regime [28]. This flow regime is known to persist up to about $Re \approx 49$, though these estimates range from ~ 40 to ~ 49 [1]. The flow is two-dimensional and steady up to this value of the Reynolds number.

Next, when the Reynolds number is increased beyond $Re \sim 49$, the wake becomes unstable (initially originating from the downstream end) and the viscous forces are no longer sufficient to quash these disturbances. The instability grows further with the increasing Reynolds number. This transition is also captured rather well in terms of the so-called base pressure coefficient which increases sharply with the Reynolds number [28]. Other signatures of the onset of this instability include the increasing fluctuations in the maximum wake velocity and in Reynolds stresses [28]. Owing to the inherently unstable nature of the pair of vortices, one vortex (the upper one) grows bigger than the other one and a point is reached when it is able to draw the vortex (with opposite sign of vorticity) across the wake. Due to the opposite signs of vorticity, the latter vortex drawn across the wake cuts off the supply of vorticity (from the boundary layer) to the other one. This, in turn, leads to the detachment of the vortex (with no further supply of vorticity) thereby leading to the so-called vortex-shedding regime. Naturally, as soon as a vorticity is shed, a new vortex is formed which is obviously weaker in strength than the one already present on the other side and therefore gets drawn across the wake (but in the opposite direction) and this, in turn, leads to the shedding from this side of the body. Excellent photographs illustrating this phenomenon are available in numerous

books, for example, see Refs. [35,36]. It needs to be emphasized here that the vortex shedding phenomenon is a consequence solely of interaction between these two shear layers (or from communication between two vortices). Therefore, it stands to reason that when such interactions are reduced or eliminated by installing a splitter plate or a confining wall, no vortex shedding would occur under these conditions. This flow regime occurs up to about $Re \sim 200$, and the flow is still laminar and two-dimensional. However, one needs to solve the time-dependent momentum equations to resolve the vortex-shedding characteristics in this flow regime.

Further increase in Reynolds number causes the cessation of the laminar flow with a gradual transition to turbulence. Naturally, initial signatures of turbulence are seen in the (least stable) wake region which gradually propagates toward the cylinder with the increasing Reynolds number (Fig. 2). Such changes in the detailed structure of the flow field also manifest in terms of dramatic changes in the plots of Strouhal number and base pressure coefficient when plotted against the Reynolds number [1,2,4,28]. Some experimental results indicate that the flow is fully turbulent in the wake region at $Re = 400$ while others put this limit at $Re > 300$ [4,37]. This also marks the onset of the three-dimensional flow characteristics.

Further increase in the value of the Reynolds number induces increasing levels of turbulence in the boundary layer and wake region. Thus, as noted above, though the conditions in the wake region might be fully turbulent at Reynolds numbers greater than 300–400, laminar flow occurs in the boundary layer region even up to $Re \sim 3 \times 10^5$ [4]. This flow regime is called the subcritical (shown schematically in Fig. 2). Further increase in the Reynolds number marks the onset of turbulence in the boundary layer also, initially at the point of separation which then extends all the way up to the front stagnation point. Surprisingly, over the rather narrow band of Reynolds numbers ($\sim 3 \times 10^5 \leq Re \leq \sim 3.5 \times 10^5$), the turbulence sets in at the point of separation, but only on one side of the cylinder, i.e., the flow is still laminar on one side and turbulent on the other. This narrow regime is known as the critical regime. Some experiments [38] suggest that the so-called turbulent-side and laminar-side may switch from one side to the other thereby causing the lift also to change its sign. Finally, at $Re > 3.5 \times 10^5$, fully/partially turbulent conditions prevail in the entire flow region in the vicinity of the cylinder and this flow condition is known as the supercritical regime. More detailed discussions and their distinguishing features including several intermediate flow regimes are available in the literature [4,28,32]. It needs to be borne in mind that there is an inherent degree of subjectivity and arbitrariness in describing the different flow regimes as well as in prescribing the critical values of the Reynolds number delineating the transition from one flow regime to another. Furthermore, the critical values of the Reynolds number are also strongly

influenced by the nature of the far field (uniform, parallel or at an angle of incidence, shear flow), confinement and its type (symmetric or asymmetric), length-to-diameter ratio of the cylinder, etc. [4,28].

Currently available scant results with other shapes of cylinders including elliptic [39–44], square [45], equilateral triangular [41,46–52], and semicircular [53,54] indicate qualitatively similar transitions, albeit most of these investigations are limited to only the first two transitions, i.e., the onset of flow separation and of the laminar vortex shedding regimes. Also, in the case of circular and elliptical cylinders, the point of flow separation shifts progressively toward the front stagnation point with the increasing Reynolds number. On the other hand, the flow separation always occurs at fixed points in bluff bodies with sharp corners including square, triangular, semicircular shapes. Finally, with the notable exception of elliptical cylinders, the pertinent literature is indeed very sparse for other shapes even in Newtonian fluids, let alone in non-Newtonian fluids. However, this deficiency in the existing literature is of little concern in the context of this chapter because most non-Newtonian fluids tend to be far more viscous than their Newtonian counterparts like air and water and, therefore, laminar flow conditions prevail more often in such fluids than that in Newtonian fluids like air. However, one exception is the special class of the so-called drag reducing polymer solutions whose shear viscosities are only a few times that of water but produce spectacular effects in such flows due to their inherently different extensional characteristics. We began with a discussion of the flow regimes for a long circular cylinder submerged in streaming power-law fluids.

A. CIRCULAR CYLINDER

In contrast to the voluminous literature regarding the prediction of various flow regimes discussed in the preceding section, there has been only one numerical study on the delineation of critical Reynolds numbers for the flow of power law fluids past a circular cylinder. Sivakumar et al. [55] numerically solved the steady and time-dependent equations to ascertain the critical values of the Reynolds number corresponding to the onset of flow separation (Re^c) and to the onset of the laminar vortex-shedding regimes. Naturally, the values of both Reynolds numbers, Re^c and Re_c are expected to be functions of the power-law index only. The values of field variables like stream function and vorticity were examined at congruent points in the front and rear together with the sign of vorticity on the surface of the cylinder and the velocity vectors, etc. to locate the value of the Reynolds number, Re^c , at which the flow separates. Figure 3 shows the representative streamline patterns in the vicinity of the cylinder for two values of the Reynolds number which supposedly bracket the onset of flow separation for three values of the power-law index. No symptoms of flow separation were detected at the smaller values of the Reynolds number (left column in Fig. 3), whereas there was a visible wake present at the larger

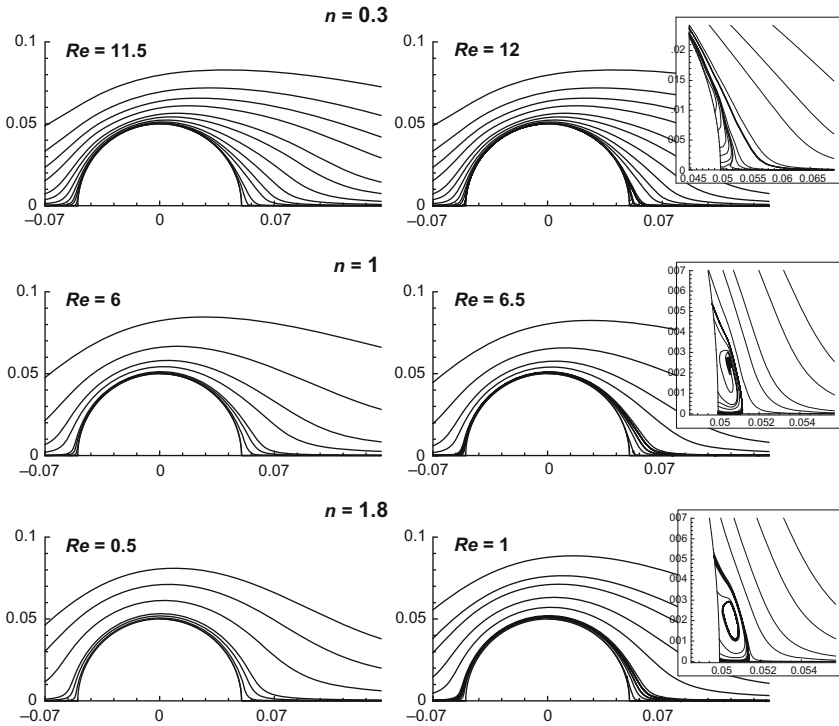


FIG. 3. Representative streamlines patterns close to the onset of flow separation from a circular cylinder in power-law fluids. From Ref. [55].

values of Re (right column in Fig. 3). In the absence of more precise or definite information, they approximated the values of Re^c simply by the mean value of the two Reynolds numbers bracketing the value of the critical Reynolds number. The resulting values of Re^c are plotted against the power-law index, n , in Fig. 4 and are summarized in Table II. It is clearly seen that the flow remains attached to the surface of the cylinder up to much higher values of the Reynolds number in shear-thinning fluids ($n < 1$) than that in Newtonian fluids, e.g., $Re^c \simeq 11.75$ for $n = 0.3$, whereas $Re^c \simeq 6.25$ for $n = 1$. On the other hand, the flow separation occurs at much lower values of the Reynolds number in shear-thickening fluids ($n > 1$) than that in Newtonian fluids. Suffice it to add here that the values presented in Table II are also consistent with the limited results of D'Alessio and Pascal [56] and albeit their drag values are in error due to a missing term [57]. One can explain, at least qualitatively, the dependence of Re^c on the power-law index as follows: for a shear-thinning fluid, the effective viscosity is a minimum near the cylinder due to high levels of shearing, but the viscosity increases rapidly away from the

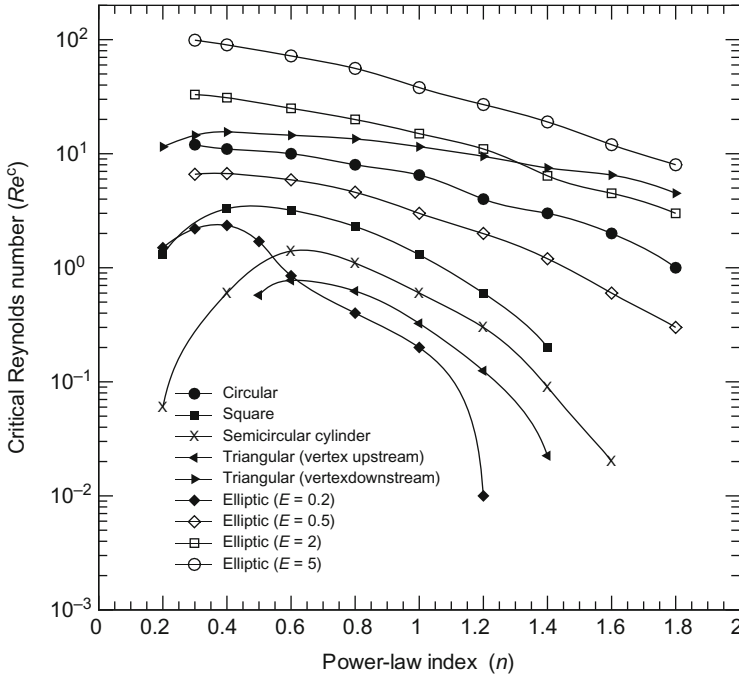


Fig. 4. Dependence of the critical Reynolds number, Re^c , on power-law index.

cylinder. This is tantamount to a small fluid-like zone surrounded by a body of highly viscous fluid which acts as virtual solid boundary. Owing to the extra viscous dissipation, the confining walls tend to defer the flow separation to higher values of the Reynolds number. Conversely, one can argue that the boundary layers tend to be thinner in shear-thinning fluids than that in Newtonian media otherwise under identical conditions, and, therefore, the shearing is confined to a very small region surrounding the immersed cylinder. It is perhaps appropriate to add here that the so-called creeping flow analyses for the cross-flow of power-law fluids over a circular cylinder [58,59] are applicable up to $Re \leq Re^c$. Finally, it is convenient to approximate the functional relationship between Re^c and n by the following expression:

$$Re^c = \sum_{i=0} a_i n^i \quad (29)$$

where the values of the fitted constants, a_i , are summarized in Table III; these values reproduce the results reported in Table II with the mean and maximum deviations of 1% and $\sim 6\%$, respectively.

TABLE II
VALUES OF THE CRITICAL REYNOLDS NUMBER (Re^c) FOR TWO-DIMENSIONAL CYLINDERS OF DIFFERENT SHAPES

n	Square	Circular	Semicircular	Elliptical				Triangular (vertex upstream)	Triangular (vertex downstream)
				$E = 0.2$	$E = 0.5$	$E = 2$	$E = 5$		
0.2	1.3	—	0.06	1.5	—	—	—	—	11.5
0.3	—	12	—	2.2	6.6	33	99	—	14.5
	—	12.5 ^a	—	—	—	—	—	—	—
0.4	3.3	11	0.6	2.35	6.7	31	90	—	15.5
0.5	—	—	—	1.7	—	—	—	0.58	—
0.6	3.2	10	1.4	0.85	5.9	25	72	0.78	14.5
0.8	2.3	8	1.1	0.4	4.6	20	56	0.63	13.5
1.0	1.3	6.5	0.6	0.2	3	15	38	0.33	11.5
1.2	0.6	4	0.3	0.01	2	11	27	0.13	9.5
		5 ^{a,b}	—	—	—	—	—	—	—
1.4	0.2	3	0.09	—	1.2	6.4	19	0.02	7.5
	—	3.5 ^a	—	—	—	—	—	—	—
1.6	—	2	0.02	—	0.6	4.5	12	—	6.5
1.8	—	1	—	—	0.3	3	8	—	4.5
	—	1.5 ^a	—	—	—	—	—	—	—

^aFrom Ref. [60].

^bFrom Ref. [56].

TABLE III
VALUES OF FITTED CONSTANTS, A_i , IN EQ. (29)

Constants	Square	Circular	Semicircular	Elliptical					Triangular (vertex upstream)
				Triangular (vertex downstream)	$E = 0.2$	$E = 0.5$	$E = 2$	$E = 5$	
a_1	-5.4	22.8355	7.0987	11.5189	5.351	10.9443	174.322	-9.9156	-10.2476
a_2	52.2417	-76.0637	-79.3997	-162.198	2.2928	220.322	-506.621	46.9481	193.92
a_3	-117.243	199.474	313.999	951.667	26.009	-763.446	1362.92	-68.2023	-569.265
a_4	135.936	-271.914	-555.088	-2552.77	-91.0695	1158.3	-2173.93	26.6771	839.888
a_5	-99.8264	184.407	492.501	3404.32	97.7151	-921.43	1794.4	21.2963	-673.277
a_1	44.2708	-59.934	-215.75	-2207.45	-44.867	369.005	-727.699	-21.8238	275.463
a_1	-8.6806	7.387	37.2179	555.115	7.6351	-58.3886	115.297	5.3452	-44.8481

With the increasing value of the Reynolds number ($>Re^c$), the wake length grows in the axial direction until it becomes unstable and starts shedding akin to that in Newtonian fluids. The onset of the laminar vortex-shedding was established by running time-dependent simulations and identifying two values of the Reynolds number enclosing this point. At lower value, the solution either converges to a steady solution or to a state in which flapping of the wake is observed but without shedding. On the other hand, at the higher Reynolds number, vortex shedding was observed and the fully time-periodic flow regime was observed. Figure 5 shows representative streamline contours

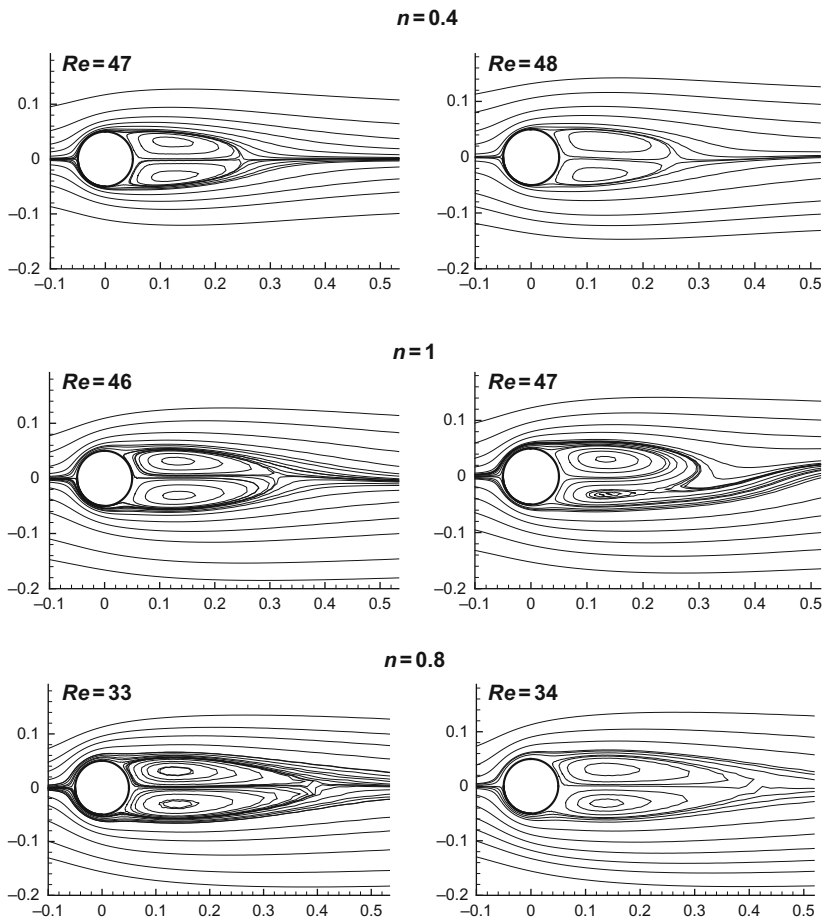


FIG. 5. Representative streamline patterns close to the onset of vortex shedding regime for a circular cylinder. From Ref. [55].

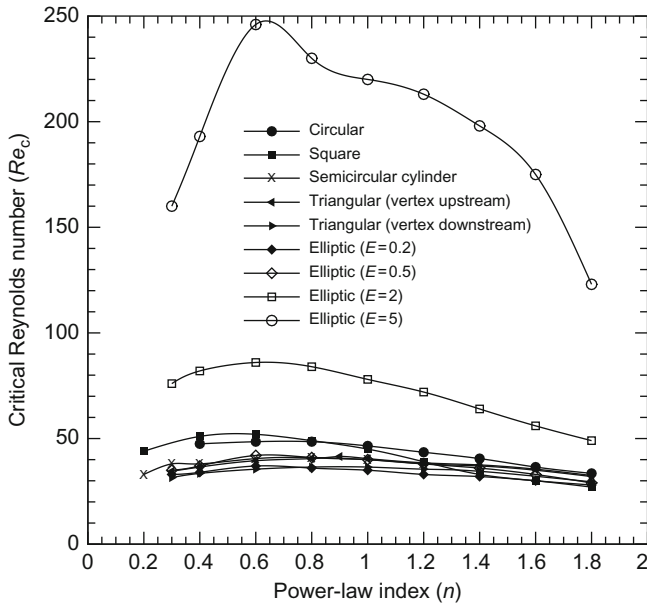


Fig. 6. Dependence of the critical Reynolds number, Re_c , on power-law index.

for three values of power-law index. Once again, Sivakumar et al. [55] approximated the value of Re_c by the arithmetic average of the two bounding Reynolds numbers which is expected to be function of the power-law index alone. This functional relationship is shown in Fig. 6 and the corresponding numerical values are summarized in Table IV. An examination of Table IV reveals that the value of Re_c shows a peak at about $n \simeq 0.6$ or so. Overall, the critical values of the Reynolds number, Re_c , in shear-thinning fluids do not seem to deviate appreciably from the corresponding value of $Re_c \sim 46$ – 47 for Newtonian fluids whereas that in shear-thickening fluids, these decrease continually with the increasing value of the power-law index over the range $1 \leq n \leq 1.8$. This behavior was ascribed to the different scaling of the inertial ($\propto U_c^2$) and viscous ($\propto U_c^n$) forces and to the interaction between these two nonlinear terms in the momentum equations. Thus, for a shear-thinning fluid, viscous forces increase less steeply with velocity than in a Newtonian fluid, whereas it is the other way round in shear-thickening fluids. Finally, the critical values of the Reynolds number, Re_c , can again be approximated by the following expression:

$$Re_c = \sum_{i=0} b_i n^i \quad (30)$$

The resulting values of the constants b_i are summarized in Table V.

TABLE IV
VALUES OF THE CRITICAL REYNOLDS NUMBER (Re_c) FOR TWO-DIMENSIONAL CYLINDERS OF DIFFERENT SHAPES

n	Square	Circular	Semicircular	Elliptical				Triangular (vertex upstream)	Triangular (vertex downstream)
				$E = 0.2$	$E = 0.5$	$E = 2$	$E = 5$		
0.2	44	—	33	—	—	—	—	—	—
0.3	—	—	38	33	35	76	160	34.5	31.5
0.4	51	47.5	38	34	37	82	193	—	33.5
0.5	—	—	—	—	—	—	—	36.5	—
0.6	52	48.5	40.5	37	42	86	246	39.5	35.5
0.8	49	48.5	41	36	41	84	230	40.5	36.5
1.0	45	46.5	40	35	40	78	220	40.5	36.5
1.2	39	43.5	38	33	38	72	213	38.5	35.5
1.4	33	40.5	37	32	36	64	198	37.5	34.5
1.6	30	36.5	35	30	33	56	175	35.5	—
1.8	27	33.5	32	28	29	49	123	32.5	29.5

TABLE V
VALUES OF FITTED CONSTANTS, b_i , IN EQ. (30)

Constant	Square	Circular	Semicircular	Elliptical				Triangular (vertex upstream)	Triangular (vertex downstream)
				$E = 0.2$	$E = 0.5$	$E = 2$	$E = 5$		
b_1	17	107.3	11.92	54.2	55.18	36.04	151.8	85.15	7.10
b_2	221	-448.6	182.4	-215	-234.4	196.2	-926.9	-428.91	175.71
b_3	-586	1290	-508.9	775	910.8	-217.9	5740	1323.79	-492.37
b_4	845	-1816	769.3	-1251	-1513	-9.38	-11238	-1899.91	764.25
b_5	-703	1342	-639.9	1011	1243	149.5	10064	1402.51	-653.17
b_6	301	-504.3	270.5	-402.7	-500.9	-95.04	-4262.5	-518.50	283.84
b_7	-50.7	75.95	-45.26	62.98	78.9	19.03	690.1	76.00	-48.88

Aside from the aforementioned detailed study [55] for power-law fluids, there has been a recent study on flow regimes for a circular cylinder submerged in viscoplastic fluids [60]. Mossaz et al. [60] extended the study of Sivakumar et al. [55] to Herschel–Bulkley model fluids [9]. This extension is far from being straightforward due to the presence of *unyielded* and *yielded* zones near the cylinder, and therefore the physical interpretation of Re^c and Re_c is slightly different in this case than that for power-law fluids [55]. For instance, the vortices are formed in the rear of the cylinder in Newtonian fluids or in fluids without a yield stress. In viscoplastic fluids, on the other hand, recirculation region develops in between the unyielded regions behind the cylinder. In this case, the both critical Reynolds numbers are functions of the flow-behavior index (n) and the so-called Oldroyd (Od) or Herschel–Bulkley (Bi_{HB}) parameter defined as follows:

$$Od = Bi_{HB} = \frac{\tau_0^{HB}}{m(U_c/D)^n} \quad (31)$$

where τ_0^{HB} is the yield stress in the Herschel–Bulkley fluid model. Thus, at $Bi_{HB} \sim 1$, the yield stress of the fluid and the viscous stress induced by the fluid flow over a cylinder are of comparable magnitudes. Broadly speaking, for a fixed value of the flow behavior index (n), the critical Reynolds number, Re_c , increases with the increasing value of Bi_{HB} . For the limiting case of $n = 1$, i.e., the Bingham fluid, this dependence is seen to be linear over the range $Bi_{HB} < 10$, i.e.,

$$Re^c = 45.8Bi_{HB} + 47 \quad (32)$$

This is not surprising as an increasing amount of energy (faster flow) is needed to counter the increasing level of yield stress. On the other hand, as far as the instability of the wake is concerned, shear-thinning viscous effects ($n < 1$) seem to destabilize the flow at lower Reynolds numbers, whereas shear-thickening ($n > 1$) seems to stabilize it at a fixed value of Bi_{HB} . For instance, at $n = 0.6$, the values of Re_c are 56 and 46, respectively, for $Bi_{HB} = 0.2$ and $Bi_{HB} = 0$ (power-law fluid). Similarly, the corresponding Strouhal number also increases with the Herschel–Bulkley parameter (Bi_{HB}) irrespective of the value of power-law index. Lastly, there have been a few studies dealing with the stability of viscoelastic fluid flow over a circular cylinder. However, it needs to be emphasized here that the aforementioned discussion relates to instabilities, arising from the relative magnitudes of the inertial and viscous forces (value of the Reynolds number), whereas in the case of viscoelastic liquids, altogether different kinds of instabilities have been observed even in the limit of vanishingly small values of the Reynolds number, i.e., in the absence of any inertial effects [61,62]. These are triggered by the so-called elastic turbulence [63]. There have been a few studies dealing with the

instabilities at finite Reynolds numbers for viscoelastic flow past a cylinder [64–66]. Thus, for instance, Sahin and Owens [64] carried out a linear stability analysis in inertial flows (finite Reynolds numbers) using FENE-p model. This analysis demonstrated that for the constant viscosity Boger fluids, polymeric additives tend to stabilize the flow as is borne out by some of the available experimental studies, for example, see Refs. [67,68]. The increased stability is attributed to the extensional effects in the wake region and this, in turn, postpones the onset of vortex shedding to higher Reynolds numbers. These findings are further sharpened by the recent three-dimensional treatment [66] accompanied by the Floquet stability analysis [65] of the FENE-p fluid flow over a circular cylinder. The three-dimensional numerical study [66] revealed that for a suitable choice (high value) of the polymer extensibility parameter, the flow was two-dimensional even at $Re = 300$. It is useful to recall here that, at this value of the Reynolds number, the flow would exhibit mode B instability in Newtonian fluids [1,2]. However, at low to medium values of the extensibility parameter, the state of the flow was seen to be quite different from both mode-A and mode-B type instabilities. Needless to add here that the increasing value of the extensibility parameter implies increasing extensional viscosity of the fluid. Subsequent stability analysis [65], using the base solution corresponding to $Re = 300$ and Weissenberg number, $Wi = 10$, clearly establishes that viscoelasticity of the fluid stabilizes the flow by modifying the base flow itself, through lowering the vorticity and strain rates in the primary vortex. Furthermore, viscoelasticity also leads to lower levels of disturbance energy thereby minimizing the possibility of mode-A and mode-B type instabilities. In summary, this flow is stabilized through the presence of extensional effects present in the wake region. Notwithstanding the valuable insights provided by such studies which elucidate the role of viscoelasticity in the absence of shear-dependent viscosity, most practical fluids, however, exhibit both these characteristics simultaneously. There is a reasonably sized-body of experimental observations available on the non-Newtonian flow past a circular cylinder, as reviewed elsewhere [22,25,27]. It is convenient to classify the available studies broadly into two categories. The early studies have almost exclusively focused on the flow characteristics of the so-called drag reducing polymer solutions in boundary layer flows. Such solutions are characterized by their constant shear viscosities, albeit generally assumed to be viscoelastic particularly in extension. For example, James and Acosta [69] reported drag measurements on thin wires in dilute aqueous solution of polyethylene oxide (PEO WSR205, PEO WSR301) up to $Re \leq 50$. The drag was enhanced above its value in water at a fixed value of the Reynolds number. More importantly, they reported the drag coefficient to be independent of velocity, i.e., the Reynolds number beyond a critical value. This was ascribed to the strong elongational component present in the wake region. Qualitatively similar behavior

was observed by Koniuta et al. [70] and Manero and Mena [71] who described the formation of a wide stagnant zone encapsulating the cylinder, as has also been observed experimentally in surfactant solutions [72]. In other words, there was only a weak flow due to the significantly higher extensional viscosities of the dilute polymer solution, as has also been borne out by numerical studies [65,66] as well as other experimental studies. Similarly, the studies of Gadd [73], Kalashnikov and Kudin [74], James and Gupta [75], and Usui et al. [76] spanning Reynolds numbers ranging from 50 to 400 reported vortex-shedding to be suppressed in such polymer solutions due to the significant extensional effects in the wake region. In fact, Usui et al. [76] were able to correlate the reduction in Strouhal number to a suitably defined Weissenberg number. On the other hand, Turgut et al. [77] and Kim and Telionis [78] reported no such effect over the range $100 \leq Re \leq 10^4$. However, reduction in drag [77], mass transfer [79], and heat transfer [80] was observed over this range which was postulated to be caused by the shortening of the wake. The literature also abounds with other findings regarding the role of viscoelasticity in this flow configuration. For instance, the role of cylinder (or wire) diameter seems to go way beyond its occurrence in the dimensionless groups like Reynolds number, drag coefficient, and Weissenberg number [22,79,80]. Similarly whether the drag on a cylinder is increased or decreased with reference to its Newtonian value is also strongly dependent upon the type of polymer, its concentration, and the Reynolds number range. For instance, while using surfactant solutions as model fluids, Ogata et al. [81] reported that the drag on a 20 mm diameter cylinder was higher than that in water in the range $1000 \leq Re \leq 3000$, while drag was reduced below the water curve for $Re > 3000$. Indeed they reported the maximum drag reduction of 55% observed at $Re = 7000$ in a 200 ppm surfactant solution. On the other hand, the drag on a 2 mm diameter cylinder could be as high as 1000 times the corresponding value in water. They ascribed this to the formation of the so-called stagnant zone on all sides of the cylinder and the size of this zone gradually diminished with the increasing Reynolds number thereby paving the way for drag reduction observed at high Reynolds numbers and at still higher values of the Reynolds number, this zone disappeared completely. They also documented significant changes in the surface pressure profiles, particularly in terms of pressure recovery which directly influences the form (main component) drag. Qualitatively similar findings have been reported by many others [81–84]. However, none of these studies have attempted to develop criterion for the transition of flow from one regime to another for a well-defined test fluid.

Some qualitative ideas in this regard were also developed by others [85,86] who studied forced convection heat transfer in shear-thinning elastic fluids up to $Re = 12,000$, and they identified three main flow regimes, namely, the laminar vortex shedding regime, mode-A and mode-B, and the shear-layer

transition. Similarly, Sarpkaya et al. [86] explored the effect of polymer degradation on the drag, surface pressure distribution, angle of separation, and vortex-shedding phenomenon over a rather narrow range of condition as $5 \times 10^4 \leq Re \leq 3 \times 10^5$. However, the most definitive contribution in this regard lies in the recent extensive experimental studies of Coelho and coworkers [87–89] and of Pipe and Monkewitz [90].

In particular, Coelho and Pinho [87,88] have reported different flow regimes in polymer solutions exhibiting shear-thinning behavior together with weak to moderate viscoelastic effects. The complex interplay between the influence of two nonlinear fluid characteristics, i.e., shear-dependent viscosity and elasticity, are further compounded by the end effects stemming from the relatively small values of the length-to-diameter ratios of 6 and 12 for the cylinders used in this series of investigations. One of the objectives was to identify an appropriate representative shear rate (and hence the fluid viscosity) so that the transition from one flow regime to another will occur at the same Reynolds number as in Newtonian fluids. Based on the choice of a mean shear rate of $(U_\infty/2d)$, their study spanned the range of Reynolds number $50 \leq Re \leq 9000$. The viscoelasticity was found not only to advance the transition to lower Reynolds number, but also to shorten the window over which transition occurred. This finding is consistent with some of the early studies also [86]. On the other hand, shear-thinning viscosity not only increased the value of the Strouhal number but also increased the size of vortex filaments. They proposed three transitional Reynolds numbers corresponding to the onset of laminar vortex-shedding, onset, and end of the transition regimes. Over the range $40 \leq Re \leq 700$, the Strouhal number showed positive dependence on polymer concentration (increasing degree of shear-thinning and elasticity) and the values were seen to be 20–30% above the corresponding Newtonian curve thereby suggesting that shear-thinning promotes vortex shedding. In the transition region ($120 \leq Re \leq 2000$), the Strouhal number data showed significant scatter around the Newtonian curve [91] and the Strouhal number really peaked in the shear-layer transition regime. The role of shear-thinning was explained via the thinning of the boundary layer thereby shortening the diffusion path which in turn facilitates vortex shedding. As seen by many earlier investigators, elasticity was shown to reduce vortex shedding and also to advance the transitions. For instance, for a cylinder of $(L/d) = 12$, the critical Reynolds number for the onset of the laminar vortex shedding regime in Newtonian fluids is known to be somewhere in the vicinity of $Re = 63$ – 68 , but it was observed to occur at as low values as $Re = 43$ in some of the polymer solution [87–89]. It is expected that the critical Reynolds number would decrease with the increasing value of (L/d) due to the diminishing end effects, but no definitive information is available about these asymptotic values. Similarly, Pipe and Monkewitz [90] studied vortex shedding from cylinders

($L/d = 20$) in PEO solutions (50–150 ppm, $Wi \sim 0.1$) and found that the critical Reynolds number, Re_c , showed positive dependence on polymer concentration. Furthermore, both Coelho and Pinho [87–89] and Pipe and Monkewitz [90] have argued that the use of the elasticity number correlates experimental results better than that of the usual Weissenberg number.

In summary, it is appropriate to say here that the transition from one flow regime to another is determined by a complex interplay between shear-thinning and viscoelasticity which, in turn, are strongly influenced by the micro-structural aspects of the non-Newtonian fluids. It is therefore neither possible nor justifiable to provide generalizations but suffice it to say here that viscoelasticity advances the effects associated with high Reynolds numbers (in Newtonian media) to lower values. The role of shear-thinning and viscoelasticity are really modulated by the kinematic (value of Re) and geometric (L/d value) conditions. Finally, the available scant numerical results show that confinement tends to stabilize the flow by postponing the onset of the laminar vortex shedding regime to higher Reynolds number, at least in power-law fluids [92].

B. ELLIPTIC CYLINDERS

An elliptic cylinder denotes the simplest departure from a circular cylinder and yet retains some geometrical features of the circular cylinder. For instance, it is also free sharp corners and edges, but two geometric parameters (minor and major axis or aspect ratio, E) are needed to describe their shape. Naturally, $E = 1$ represents the circular shape, and $E \rightarrow 0$ or ∞ denote a plate oriented along and transverse to the direction of flow. Therefore, both transition Reynolds numbers, Re^c and Re_c , are now functions of the aspect ratio for Newtonian fluids which show additional dependence on non-Newtonian model parameters (for instance, power-law index, n). The mechanics of fluid flow around elliptic cylinders has been explored much less extensively than that for circular cylinder (e.g., see Refs. [1,2,4]), especially as far as the delineation of flow regimes is concerned even in Newtonian fluids [39–44]. Since the bulk of the literature on this aspect has been reviewed elsewhere [44], suffice it to say here that slender configuration ($E > 1$) aligned with the flow will behave more like a streamlined object, whereas the blunt configuration ($E < 1$) will behave like a bluff body. There has been only one numerical study dealing with the predictions of Re^c and Re_c in power-law fluids for elliptical cylinders ($0.2 \leq E \leq 5$). Figures 7 and 8 show representative streamlines in the vicinity of elliptical cylinders for three values of power-law index at two nearby Reynolds numbers supposedly enclosing the onset of flow separation for $E = 0.2$ and 5, respectively. Evidently, as surmised above, irrespective of the value of the power-law index, the flow remains attached to the surface of the cylinder up to higher values of the Reynolds number with the increasing value

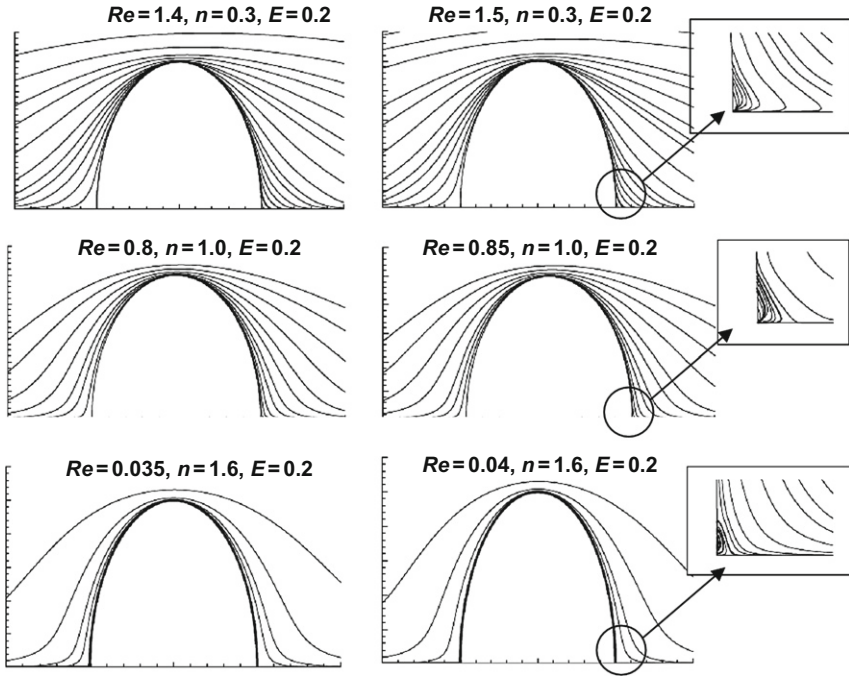


FIG. 7. Representative streamlines patterns close to the onset of flow separation for an elliptical cylinder of $E = 0.2$. Replotted from Ref. [44].

of E . For instance, for a fluid with $n = 0.2$, the flow detaches at about $Re \sim 99$ for an elliptical cylinder with aspect ratio of $E = 5$. Conversely, the shape exerts much more influence on this transition than the value of the power-law index. The resulting values of Re^c are also included in Fig. 4 where it is clearly seen that these show the expected dependence on the shape of the cylinder. These values are again correlated using the generic form of Eq. (29) and the constants are presented in Table III. Figures 9 and 10 show the representative (instantaneous) streamline contours corresponding to the onset of the laminar vortex shedding flow regime for a few combinations of the values of E and power-law index, n . Qualitatively similar trends are also seen here as that seen previously for a circular cylinder. With respect to the circular cylinder, this regime commences at higher values of the Reynolds number for $E > 1$ and at lower values for $E < 1$. The resulting values of the critical Reynolds number, Re_c , denoting the onset of the laminar vortex shedding regime are included in Fig. 6. The numerical values are approximated by Eq. (30) and the resulting values of the fitted constants (b_i) are presented in Table V.

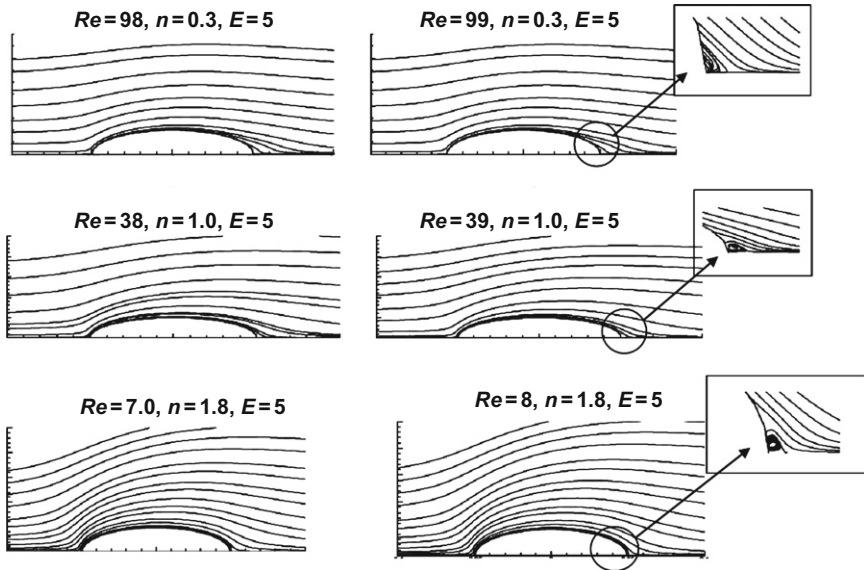


FIG. 8. Representative streamlines patterns close to the onset of flow separation for an elliptical cylinder of $E = 5$. Replotted from Ref. [44].

C. SEMICIRCULAR CYLINDER

While a few investigators have studied the two-dimensional flow over solid and hollow semicircular cylinders in different configurations [93–99] which have been reviewed recently [53,100], the issue of the transitions from one flow regime to another has been tackled only recently [54]. In an extensive study, on the two-dimensional unconfined flow of power-law fluids over a semicircular cylinder with its curved surface oriented toward the oncoming flow, Chandra and Chhabra [54] established the conditions for the onset of flow separation and of the laminar vortex shedding regime. Figure 11 shows the representative streamline and velocity vectors plots in the immediate proximity of the bluff body for a range of values of power-law index and at two closeby values of the Reynolds number bracketing the onset of flow separation. The mean of these two values is designated as Re^c , the critical Reynolds number corresponding to this transition. Hence, the flow remains attached to the surface of the cylinder for $Re < Re^c$. These values are also included in Fig. 4 and Table V, whereas that of the fitted constants, a_i , in Eq. (29) are presented in Table III which facilitate the interpolation of the present results for intermediate values of the power-law index. As detailed elsewhere [54], the

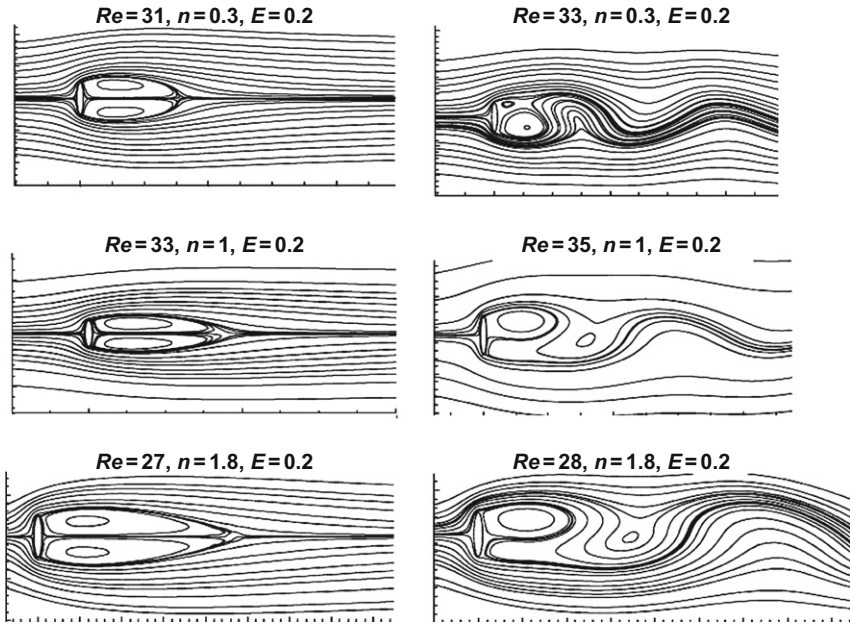


FIG. 9. Typical instantaneous streamlines contours showing the onset of vortex shedding for an elliptical cylinder of $E = 0.2$. Replotted from Ref. [44].

presence of the two corners together with the sudden termination of the rear surface results in early separation in this case, the values of Re^c being almost an order of magnitude lower than that for circular and elliptic cylinders (Fig. 4 and Table V).

As the Reynolds number is progressively increased beyond Re^c , the prevailing viscous stresses are no longer adequate to suppress the minor disturbances initiated in the wake region. Thus a point is reached when the wake becomes asymmetric about the midplane, undergoes flapping (without shedding), and ultimately resulting in the usual vortex shedding phenomena. The vortices in the upper part carry negative vorticity, whereas those in the lower region carry positive vorticity. Figure 12 shows the representative streamline (instantaneous) contours clearly showing this sequence of loss of symmetry/flapping and vortex shedding for a range of values of power-law index at two values of the Reynolds number bracketing the value of Re_c ; once again the latter in approximated by the arithmetic mean of the two values. The resulting values of Re_c for a semicircular cylinder are again included in Fig. 6 and in Table V, whereas the values of the constants in Eq. (30) are listed in Table III. This transitional Reynolds number is seen to be comparable to that for circular and

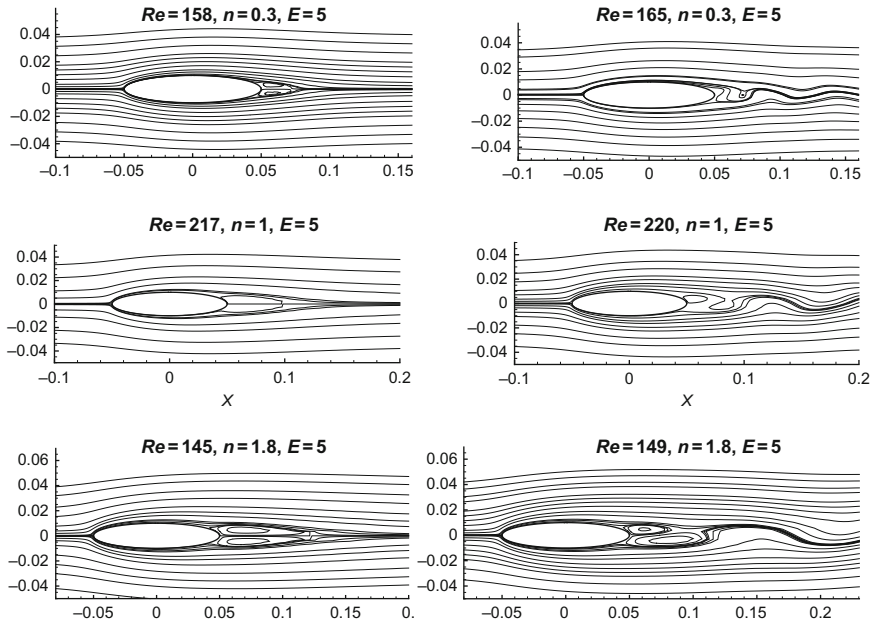


FIG. 10. Typical instantaneous streamlines contours showing the onset of vortex shedding for an elliptical cylinder of $E = 5$. Replotted from Ref. [44].

elliptic cylinders thereby emphasizing the underlying inherent similarity in the phenomenon of vortex shedding in variously shaped bluff bodies.

D. EQUILATERAL TRIANGULAR CYLINDERS

There have been a few studies on the two-dimensional flow past cylinders of triangular cross section [46–51,101,102], but their major thrust has been on elucidating the momentum and heat transfer characteristics under various conditions of orientation, confined or unconfined, forced and mixed convection regimes, etc. The bulk of the literature has been reviewed recently [52]. Even for Newtonian fluids, only a few studies have addressed the cessation of the steady flow regime, i.e., the prediction of Re_c . For instance, Jackson [41], De and Dalal [46,102], Zielinska and Wesfreid [47], and Wesfreid et al. [48] all report a value of Re_c in the range ~ 36.4 to ~ 40 when one of the apex of the equilateral triangular prism is aligned with the direction of the oncoming flow. On the other hand, Faruquee and Olatunji [50] reported the value of Re_c in the range 40–42 for the aforementioned orientation as well as when one of the

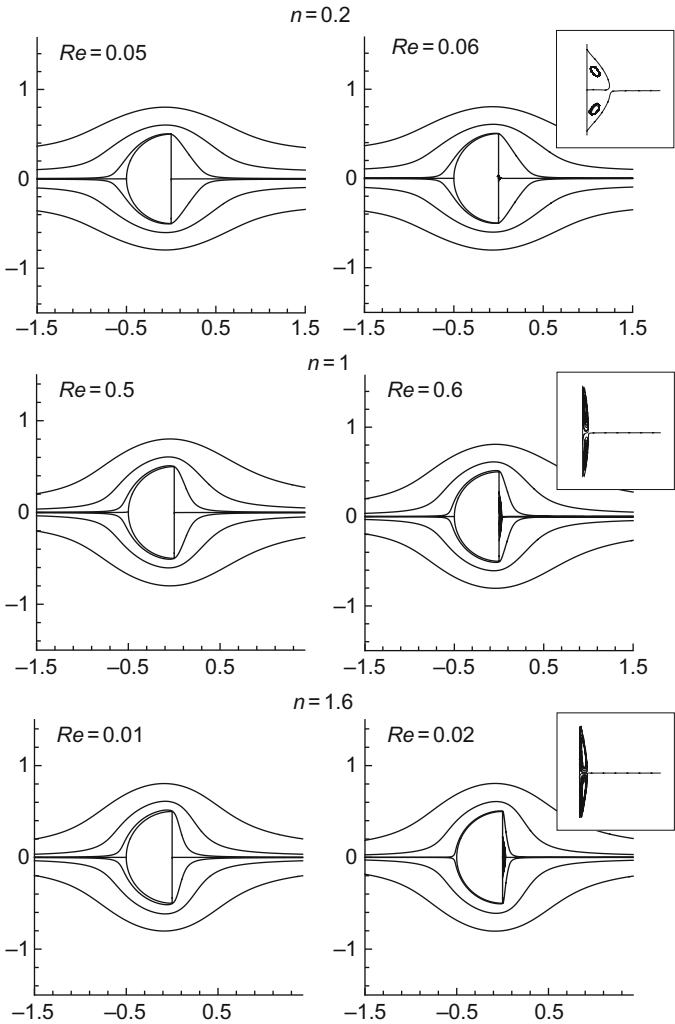


FIG. 11. Typical streamline patterns and velocity vectors closed to the surface of the semicircular cylinder displaying the onset of flow separation. Replotted from Ref. [54].

sides is oriented perpendicular to the oncoming flow. Scant numerical results seem to suggest that the flow could be stabilized even up to $Re = 58-59$ in a confined configuration [51]. This is attributed to the extra dissipation at the confining walls. In a recent study, Prhashanna et al. [52] have elucidated the influence of power-law index on the two transitional Reynolds numbers, Re^c

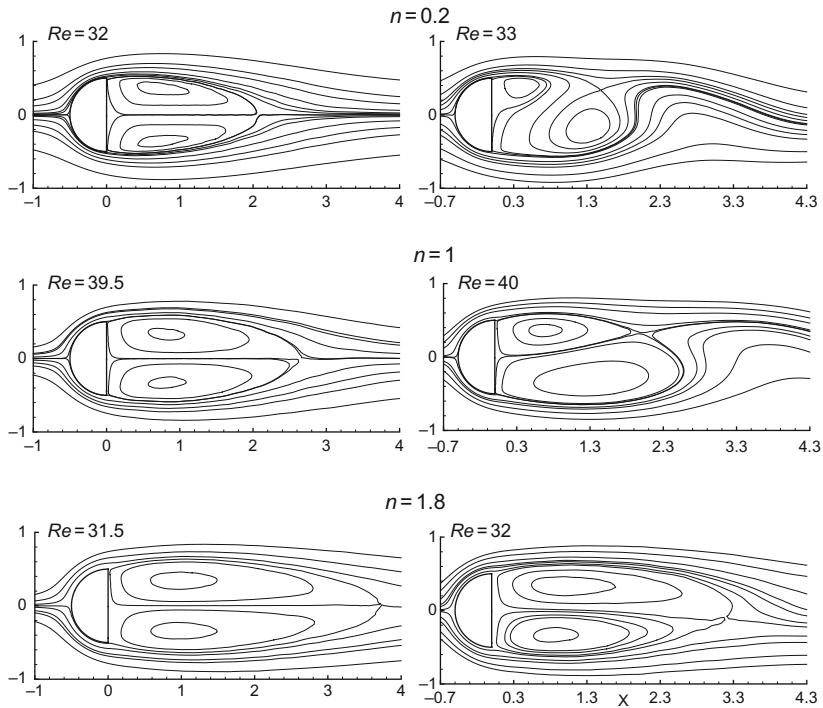


FIG. 12. Representative instantaneous streamline patterns in the vicinity of a semicircular cylinder showing the initiation of vortex shedding. Replotted from Ref. [54].

and Re_c , for an equilateral triangular cylinder in both orientations, i.e., one of its vertex oriented upstream or downstream.

Figures 13 and 14 show typical streamline patterns in the vicinity of the cylinder in two orientations. Once again, the flow is seen to be attached to the surface of the cylinder at lower Reynolds number (left column), whereas it is clearly seen to have detached itself in the right column thereby suggesting the value of Re_c to lie in between this interval. The resulting values of Re^c for both configurations are included in Fig. 3 and in Table V, where as the values of a_i (constants in Eq. (29)) are included in Table III. Evidently, the differences in the values of Re^c for the two configurations arise from the reduced degree of streamlining in the case of vertex oriented in the upstream direction. Conversely, due to the sudden termination of the rear surface (similar to the case of a semicircular cylinder), the fluid element is not able to negotiate such an abrupt change in direction which causes the flow to detach. Furthermore, for the vertex orientated downstream, the center of the vortex gradually shifts

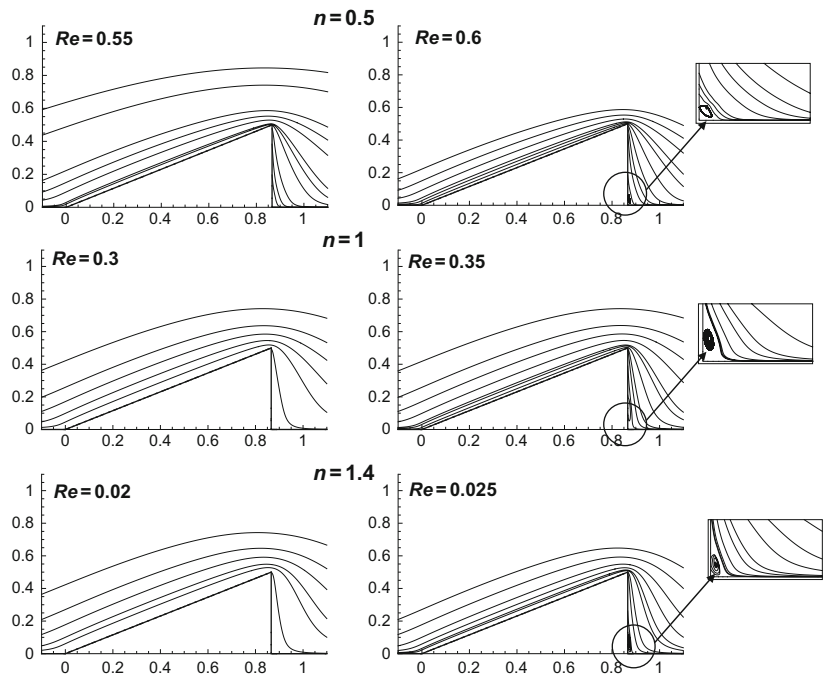


FIG. 13. Representative streamline pattern adjacent to an equilateral triangular cylinder (with its apex oriented in upstream direction) showing the onset of flow separation. Replotted from Ref. [52].

upstream toward the corner as the fluid behavior changes from shear-thickening ($n > 1$) to shear-thinning ($n < 1$) via the Newtonian fluid behavior.

Typical instantaneous streamline contours are shown in Figs. 15 and 16 for the two configurations to delineate the limits of the steady flow regime in which the vortices remain attached to the surface, albeit these might flap in highly shear-thinning fluids. The resulting values of Re_c are again included in Fig. 6 and Table V together with the values of b_i in Table III. These values are again seemed to be qualitatively similar to that seen for the other shapes included in Fig. 6.

E. SQUARE CYLINDER

Undoubtedly, this geometry occupies its position, following the circular and elliptical cylinders, which has received considerable attention in the literature, at least in the laminar vortex shedding regime which seems to persist up to

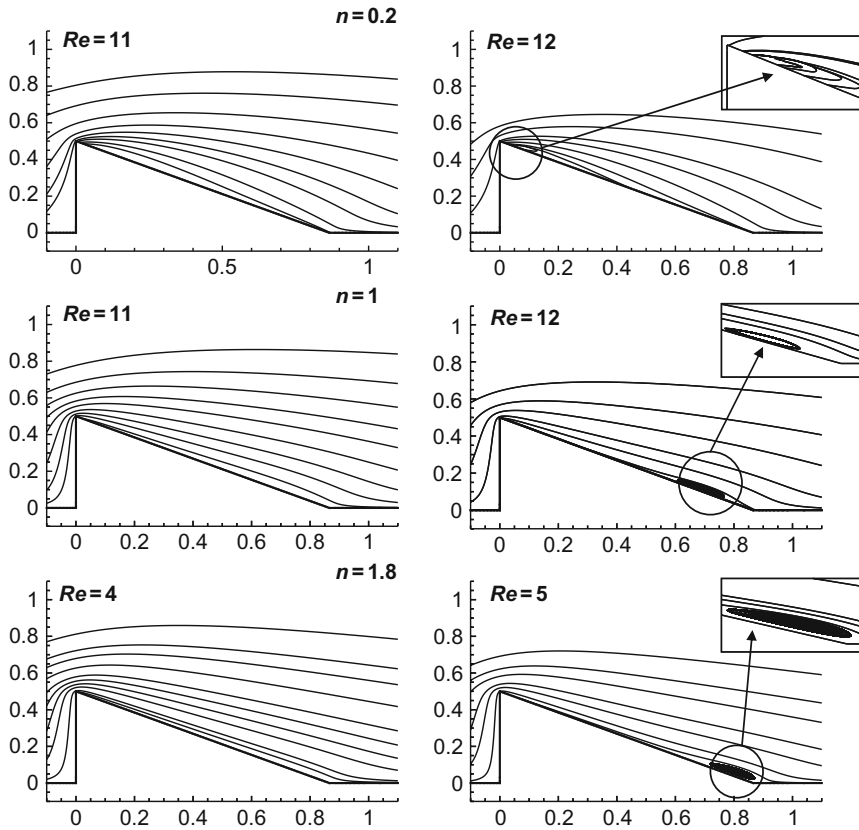


FIG. 14. Representative streamline pattern adjacent to an equilateral triangular cylinder (with its apex oriented in downstream direction) showing the onset of flow separation. Replotted from Ref. [52].

about $Re = 160$ in the unconfined flow of Newtonian fluids. The bulk of the literature in this field has been reviewed in a series of doctoral dissertations [103–105] as well as in numerous other papers [106–114]. For an unconfined Newtonian fluid, the flow is known to remain attached up to about $Re \sim 1$ –2, whereas the limit of the steady flow regime is predicted to be somewhere in the range 45–53. In spite of the significant differences in terms of the reduced streamlining of a square cylinder, these values are remarkably similar to that reported for a circular cylinder. Much less is known about the other transitions in this case.

On the other hand, analogous results for power-law fluids are not only scarce but are also of a very recent vintage [45]. While depending upon the

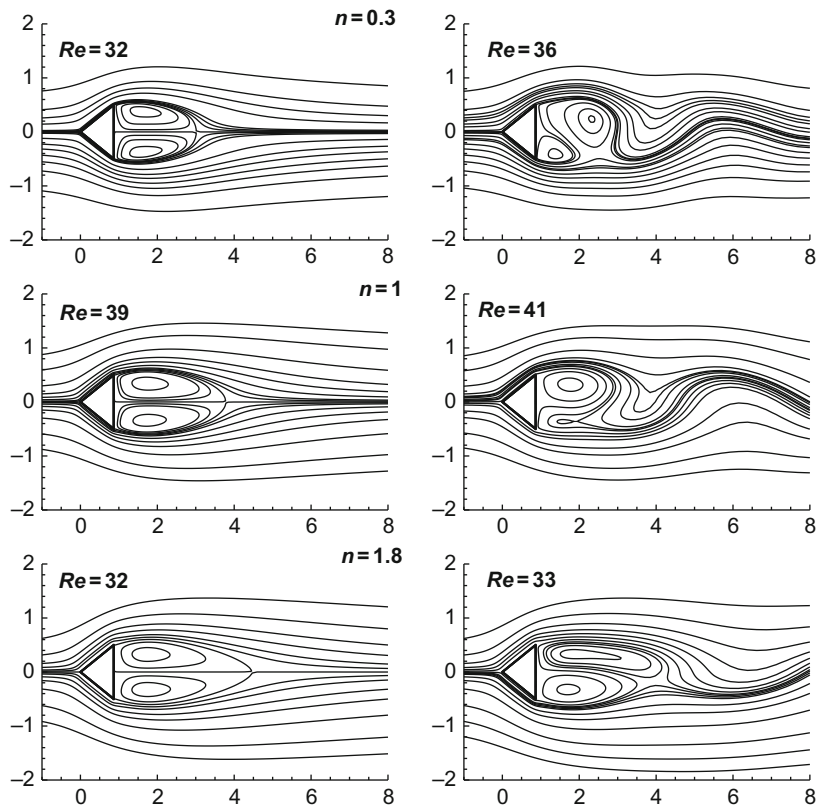


FIG. 15. Representative instantaneous streamline contours showing the initiation of vortex shedding regime for an equilateral triangular cylinder with apex facing upstream. Replotted from Ref. [52].

values of the Reynolds number and power-law index, the flow may or may not separate at the top/bottom surfaces (which may reattach itself), the wake region is primarily defined by the separated flow region in the rear of a square cross-section cylinder. Following the same strategies as that used in the preceding sections, representative streamline and velocity vector plots are shown in Fig. 17 for two adjacent values of the Reynolds number. The value of Re^c was simply approximated by the mean of these two and its variation with power-law index is depicted in Fig. 4 and Table V together with the values of a_i corresponding to Eq. (29) in Table III. These values are seen to be lower by from that for a circular cylinder a factor ranging from about ~ 3 to ~ 10 depending upon the values of power-law index. Such early separation can safely be

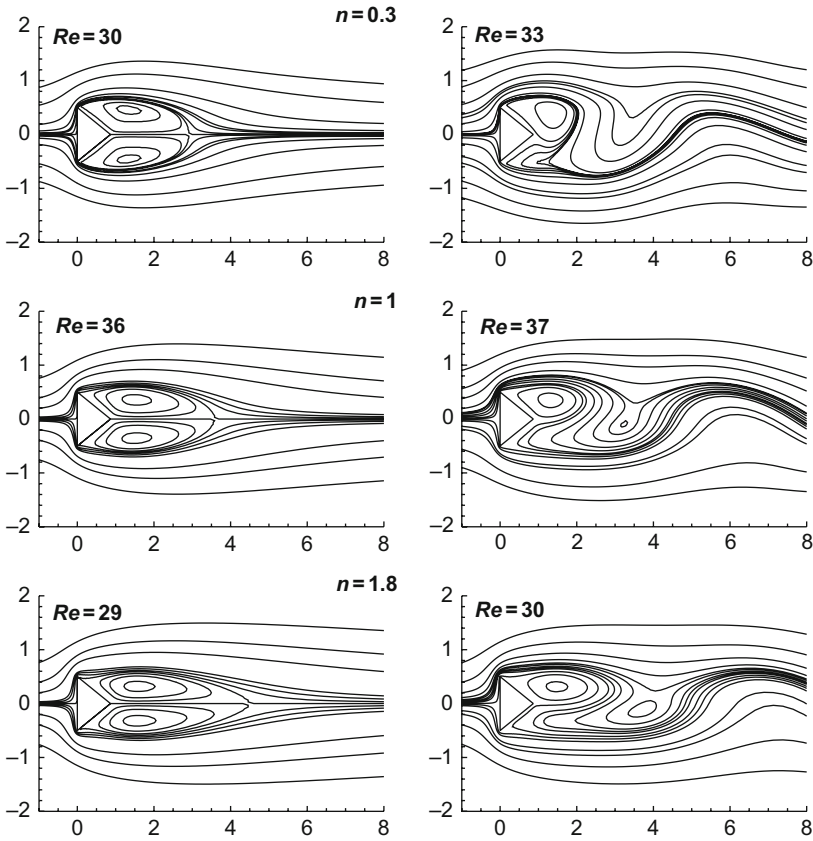


FIG. 16. Representative instantaneous streamline contours showing the initiation of vortex shedding regime for an equilateral triangular cylinder with apex facing downstream. Replotted from Ref. [52].

attributed to the presence of the sharp corners which enhance the propensity for early separation due to sudden changes in the contour of the body [45].

Figure 18 shows the corresponding streamline contours [45] delineating the conditions for the onset of the laminar vortex shedding regime in different types of fluids, namely, shear-thickening ($n = 1.8$), Newtonian ($n = 1$), and shear-thinning ($n = 0.2$) fluids. The shear filaments are seen to be somewhat smaller in shear-thinning fluids than that in a shear-thickening fluid which is consistent with the observations of Coelho and coworkers [87–89] for a circular cylinder. The resulting values of the critical Reynolds number, Re_c , are also included in Table V and Fig. 6, whereas the values of constants b_i are

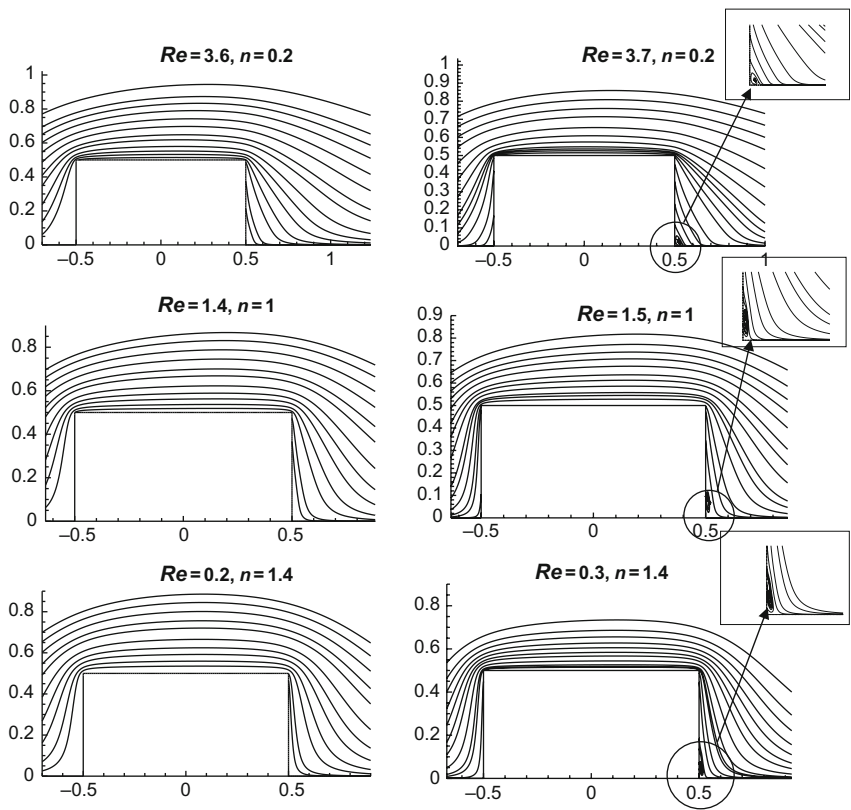


FIG. 17. Streamline contours showing the onset of flow separation from a square cylinder in power-law liquids. Replotted from Ref. [45].

provided in Table III. These values of Re_c are also seen to be comparable to that for a circular cylinder.

Finally, before concluding this section, it needs to be emphasized here that as of now, no results are available on the values of the transitional Reynolds numbers for bluff bodies of other shapes, or for other fluid models, or elucidating the effect of confinement or about the other transitions at still higher Reynolds numbers. Similarly, both Re^c and Re_c seem to exhibit maximum values in shear-thinning fluids, somewhere in the range $\sim 0.4 \leq n \leq \sim 0.6$ and these are due to the different scaling of the inertial and viscous forces with velocity and their rate of change with varying power-law index, as detailed above in the context of the circular cylinder and elsewhere for the other shapes [44,45,52,54]. Lastly, the currently available numerical simulations are

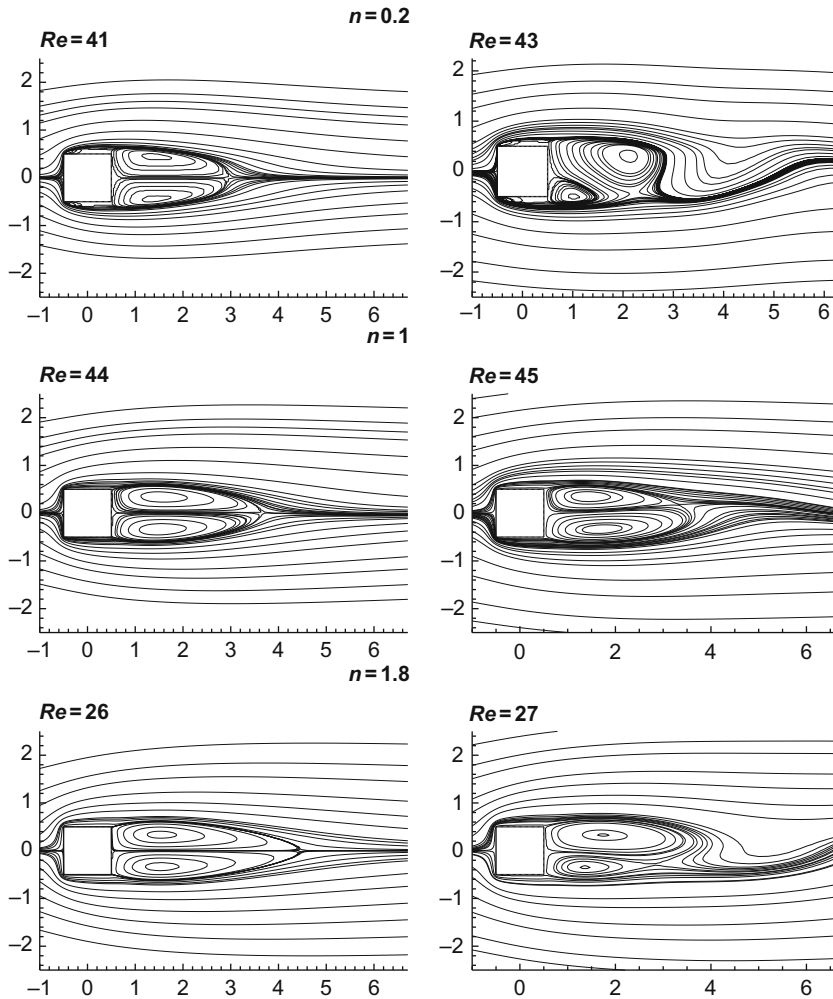


FIG. 18. Instantaneous streamline contours showing the onset of vortex shedding from a square cylinder in power-law fluids. Replotted from Ref. [45].

available for either purely viscous models (power-law, for instance) or viscoelastic fluids in the absence of shear-thinning behavior whereas the available experimental results entail the use of test fluids which exhibit both shear-thinning and viscoelastic characteristics and this indeed precludes the possibility of detailed quantitative comparisons between the predictions and observations. On the other hand, detailed comparisons between the predictions and observations

for circular, square, and triangular cylinders in Newtonian fluids tend to be affirmative and encouraging.

V. Fluid Mechanical Aspects

Notwithstanding the intimate connection between the fluid mechanics and heat transfer characteristics, it is customary to begin with the fluid flow phenomena associated with the flow of non-Newtonian fluids past cylinders of circular and noncircular cross sections. Following the pattern adopted in Section IV, this section is also organized into several subsections depending upon the shape of the cylinder. Furthermore, the fluid mechanical aspects are typically analyzed using a range of tools including streamline and vorticity contours near the surface of the submerged bluff body, surface pressure distribution, wake characteristics (size and angle of separation), drag and lift coefficients, and Strouhal number depending upon the objective and/or the flow regime. As seen in the preceding section, the bulk of the available information pertains to the so-called steady ($Re \leq Re_c$) and the laminar vortex shedding regimes ($Re > Re_c$). Furthermore, as will be seen later, the flow characteristics have been investigated much more extensively than the corresponding heat/mass transfer characteristics (see [Table VI](#)). We begin with the case of a circular cylinder.

A. CIRCULAR CYLINDER

Despite the fact that the flow of non-Newtonian fluids across a long circular cylinder has attracted considerable attention thus far, the corresponding body of knowledge is nowhere near as extensive or cohesive as that for Newtonian fluids. On the contrary, the field is still in its infancy. A cursory examination of the pertinent literature shows a preponderance of studies based on the use of the simple power-law model. From a theoretical standpoint, owing to the nonlinear form of the extra stress tensor in the momentum equations, analytical solutions are not possible even when the nonlinear inertial terms are neglected. Therefore, early analyses in this field are based on the application of the boundary layer flow approximation, for example, see Refs. [\[85,115–118\]](#). Naturally, this approach implicitly assumes thin boundary layers (large values of Reynolds number or Prandtl number or both) so that the curvature effects can be neglected thereby simplifying the analysis. Nor does this approach take into account the presence of the wake region seen at finite Reynolds numbers. This body of information together with its relative merits and demerits has been reviewed thoroughly elsewhere [\[22,25,27,118\]](#). Instead, consideration is given here to the recent developments based on the numerical solution of the

TABLE VI

SUMMARY OF STUDIES AVAILABLE ON THE CROSS-FLOW OF GENERALIZED NEWTONIAN FLUIDS OVER CIRCULAR AND NONCIRCULAR CYLINDERS

Investigator	Fluid model	Nature of study	Remarks
<i>1. Circular cylinder</i>			
Tanner [58]	Power-law ($n < 1$)	Numerical	The first set of approximate results in the creeping flow region up to $n \geq 0.5$; the drag increases and then it falls below its value for Newtonian fluids.
D'Alessio and Pascal [56]	Power-law $0.65 \leq n \leq 1.2$ $Re = 5, 20, 40$	Finite difference	Detailed information on surface pressure, streamlines, and vorticity. However, their drag results are in error.
Whitney and Rodin [59]	Power-law $n \leq 1$ $Re \rightarrow 0$	Numerical	The predictions of drag for a sphere and a cylinder are in good agreement with prior results.
Marusic–Paloka [123]	Power-law $n \leq 1$ $Re \rightarrow 0$	Analytical/numerical	Established that the Stokes paradox is irrelevant for power-law shear-thinning fluids.
Chhabra et al. [127]	Power-law $0.2 \leq n \leq 1.4$ $Re = 1, 10, 40$	Finite difference	Replicated the study of D'Alessio and Pascal [56] and presented the corrected values of drag.
D'Alessio and Finlay [57]	Power-law	Analytical/asymptotic	Presented approximate stream functions for faraway field for $Re = 5$ and $Re = 20$ for mildly non-Newtonian fluids.
Soares et al. [128]	Power-law $Re = 5, 20, 40$ $0.2 \leq n \leq 1.4$ $1 \leq Pr \leq 100$	Finite difference	Detailed results on forced convection heat transfer.
Bharti et al. [126,130,207,208]	Power-law $1 \leq Re \leq 40$ $0.2 \leq n \leq 1.9$ $0.7 \leq Pr \leq 1000$ $\beta = 1.1, 1.6, 2, 4, \infty$	Finite volume	Extensive results on flow and forced convection heat transfer characteristics from a confined and unconfined circular cylinder for the steady flow regime.

(Continued)

TABLE VI
(CONTINUED)

Investigator	Fluid model	Nature of study	Remarks
Patnana et al. [129,209]	Power-law $40 \leq Re \leq 140$ $1 \leq Pr \leq 100$ $0.4 \leq n \leq 1.8$	Finite volume	Extensive results on flow and heat transfer parameters in the laminar vortex shredding regime.
Srinivas et al. [268]	Power-law $1 \leq Re \leq 40$ $0 \leq Ri \leq 2$ $0.2 \leq n \leq 1.8$ $1 \leq Pr \leq 100$	Finite volume	Mixed convection in the aiding-buoyancy configuration.
Soares et al. [267]	Power-law $1 \leq Re \leq 30$ $0 \leq Ri \leq 3$ $0.6 \leq n \leq 1.6$ $1 \leq Pr \leq 100$	Finite difference	Mixed convection heat transfer where buoyancy is transverse to the imposed flow.
Soares et al. [210]	Power-law $1 \leq Re \leq 30$ $1 \leq Pr \leq 100$ $0.6 \leq n \leq 1.6$ $0 \leq b \leq 0.5$	Finite difference	Effect of temperature-dependent viscosity on flow and heat transfer characteristics.
Rao et al. [92]	Power-law $40 \leq Re \leq 140$ $0.4 \leq n \leq 1.8$ $2 \leq \beta \leq 6$	Finite volume	Effect of planar confinement on the flow parameters in the laminar vortex shedding regime.
Prhashanna and Chhabra [238]	Power-law $0.72 \leq Pr \leq 100$ $10 \leq Gr \leq 10^5$ $0.3 \leq n \leq 1.8$	Finite volume	Extensive results on free convection heat transfer.

Nejat et al. [131]	Power-law $Re \leq 40$	LBM	Flow over a confined circular cylinder.
Mossaz et al. [60]	Bingham plastic	Finite volume	Critical Reynolds number.
Coelho and Pinho [87–89]	—	—	Experimental results on different flow regimes.
Pipe and Monkewitz [90]	Dilute polymer solutions	Experimental studies	Elucidated effect of viscoelasticity on vortex shedding
Panda and Chhabra [311,312]	Power-law $0.1 \leq Re \leq 40$ $1 \leq Pr \leq 100$ $0.2 \leq n \leq 1$ $0 \leq \alpha \leq 6$	Finite volume	Effect of rotation of cylinder on flow and heat transfer characteristics.
Patil et al. [313,314]	Power-law $1 \leq Re \leq 40$ $1 \leq Pr \leq 100$ $0.2 \leq n \leq 1.8$ $2 \leq G \leq 10$	Finite volume	Momentum and heat transfer characteristics of two cylinders in tandem configuration.
2. Elliptical cylinder			
Sivakumar et al. [167]	Power-law	Finite volume	Extensive results on critical Reynolds number, drag, and heat transfer.
Bharti et al. [168]	$Re \leq 40$		
Rao et al. [44]	$0.3 \leq n \leq 1.8$ $Pr \leq 100$		
3. Semicircular cylinder			
Chandra and Chhabra [54,100]	Power-law $Pr \leq 100$ $n \leq 1.8$	Finite volume	Extensive results on critical Reynolds number, drag, and heat transfer.
4. Triangular cylinder			
Prhashanna et al. [52]	Power-law $Pr \leq 100$ $Re \leq 30$ $n \leq 1$	Finite volume	Extensive results on critical Reynolds number, drag, and heat transfer.

(Continued)

TABLE VI
(CONTINUED)

Investigator	Fluid model	Nature of study	Remarks
<i>5. Square cylinder</i>			
Dhiman et al. [107,171,174,294,297,298]	Power-law $Pr \leq 100$ $Re \leq 40$ $n \leq 1.5$	Finite volume	Momentum, forced and mixed convection heat transfer in the steady flow regime.
Sahu et al. [172,175,293,295,296]	Power-law $Pr \leq 100$ $40 \leq Re \leq 160$ $n \leq 1.5$	Finite volume	Extended the work to the laminar vortex shedding regime.
Bouaziz et al. [173]	Power-law $n = 0.5, 1, 1.5$	Finite volume	Limited results on effect of blockage, mixed convection.
Rao et al. [45]	Power-law	Finite volume	Critical Reynolds number, drag, and heat transfer in highly shear-thinning fluids.
Sasmal and Chhabra [309]	Power-law $Gr \leq 10^5$ $0.3 \leq n \leq 1.8$ $Pr \leq 100$	Finite volume	Free convection heat transfer.

complete governing equations for finite values of the Reynolds and Prandtl numbers. Any discussion on the flow past a circular cylinder must inevitably begin with the so-called Stokes paradox, for example, see Refs. [119,120]. Thus, unlike in the case of a sphere, the Navier–Stokes equations do not admit a solution for the steady, unconfined flow across a circular cylinder in the limit of zero Reynolds number. In physical terms, this difficulty stems from the fact that the inertial effects are not negligible even far away from the cylinder, i.e., at $r \rightarrow \infty$. This can also be explained by considering the plausible form of the corresponding stream function given as follows:

$$\psi = \left(A_0 r^3 + A_1 r \ln r + A_2 r + \frac{A_3}{r} \right) \sin \theta \quad (33)$$

The four constants, A_0, A_1, A_2, A_3 , are to be evaluated using the condition of no-slip on the surface of the cylinder ($r = 1$) and of uniform flow far away ($r \rightarrow \infty$) from the cylinder. It is readily seen that $V_r = (1/r)(\partial\psi/\partial\theta)$ will behave like $A_0 r^2$ which diverges as $r \rightarrow \infty$ and hence, it is not possible to satisfy the requirement of uniform flow far away from the cylinder. This difficulty can be, at least partially, circumvented by setting $A_0 = 0$, as suggested by Van Dyke [121]. Utilizing the no-slip condition at $r = 1$ leads to the following form of the stream function:

$$\psi = 2A_2[-r \ln r + (r/2) - (1/2r)] \sin \theta \quad (34)$$

The remaining unknown constant A_2 thus must be evaluated using the condition of uniform flow, i.e., $\psi \rightarrow r \sin \theta$ as $r \rightarrow \infty$. Unfortunately no value of A_2 can satisfy this condition and hence the Stokes paradox. Some approximate treatments have been obtained by dividing the flow domain into two parts, the so-called inner and outer regions [121,122]. On the other hand, this difficulty is of no consequence in numerical studies where the faraway boundary conditions are applied at finite boundaries. In a significant paper [58], Tanner argued that for a shear-thinning power-law fluid, the Stokes paradox is irrelevant. His argument hinges on the fact that as the uniform flow condition is approached far away from the cylinder, the velocity gradient (hence shear rate) approaches zero and therefore, a shear-thinning power-law fluid would exhibit infinite viscosity and therefore, unlike in the case of a Newtonian fluid, viscous forces would far outweigh the inertial forces at $r \rightarrow \infty$ thereby rendering the Stokes paradox to be irrelevant in this case for $n < 1$. A slightly more formal proof is also available in the literature [123], though it is still not possible to obtain a solution of the form, $\psi \rightarrow f(r) \sin \theta$ [124]. Therefore, one must resort to numerical solutions of the governing differential equations which by necessity impose the uniform flow condition at a finite distance, and thus, the Stokes paradox also becomes inconsequential for power-law fluids with flow behavior index greater than unity, albeit the values of the Reynolds number

required to approach the truly creeping flow limit appear to be extremely small and depend strongly on the values of power-law index and the location of the far-field boundary [125]. With this brief preamble, we begin with the surface pressure distribution over the surface of a circular cylinder.

1. Surface Pressure Distribution

Due to the prevailing velocity gradients in the fluid, pressure varies from one point to another on the surface of the cylinder. This is usually expressed in terms of a nondimensional coefficient C_p , defined in Eq. (20). A fluid element traveling at the centerline comes to a complete halt at the front stagnation point thereby converting its kinetic energy into pressure and therefore one would expect the pressure or the value of C_p to be a maximum at this point. As the fluid element negotiates the shape of the cylinder and it accelerates gradually and therefore the pressure coefficient gradually reduces. In the case of inviscid fluid (no friction), the velocity is maximum and hence the value of C_p is minimum at $\theta = \pi/2$ and beyond this position, the velocity decreases, becoming zero at the rear stagnation point at $\theta = \pi$ where again the pressure coefficient, C_p , exhibits its maximum value. Thus, under these conditions, the pressure distribution will exhibit fore and aft symmetry.

Figure 19 shows representative results on the surface pressure distribution for a circular cylinder as a function of power-law index and the Reynolds number. At low Reynolds numbers, when the flow remains attached, the pressure continually decreases from its maximum value at $\theta = 0$ to a minimum value at $\theta = \pi$. On the other hand, once the flow has detached itself from the surface of the cylinder and the separated flow region is established in the rear of the cylinder, surface pressure decreases up to the point of separation and, thereafter, it shows some recovery due to the enhanced circulation of fluid in this region. At the point of flow separation, the vorticity also changes its sign. Furthermore, at low Reynolds numbers (e.g., $Re = 0.01$), the power-law index is seen to exert much more influence on the surface pressure than that at high Reynolds numbers. This is so presumably due to the fact that the role of viscous forces diminishes with the increasing Reynolds number and hence the viscous characteristics are of little relevance under these conditions. Broadly, the local surface pressure increases with the increasing degree of shear-thinning behavior, i.e., with the decreasing value of power-law index in the front half of the cylinder and the pressure is seen to be minimum for the lowest value of power-law index in the rear. As expected, the reverse trend is seen in shear-thickening fluids. With the increasing Reynolds number, very little influence of power-law index is seen in the front half of the cylinder. Over the range of conditions spanned in Fig. 19, the flow is known to be steady [55]. Qualitatively similar results have been reported in the other pertinent

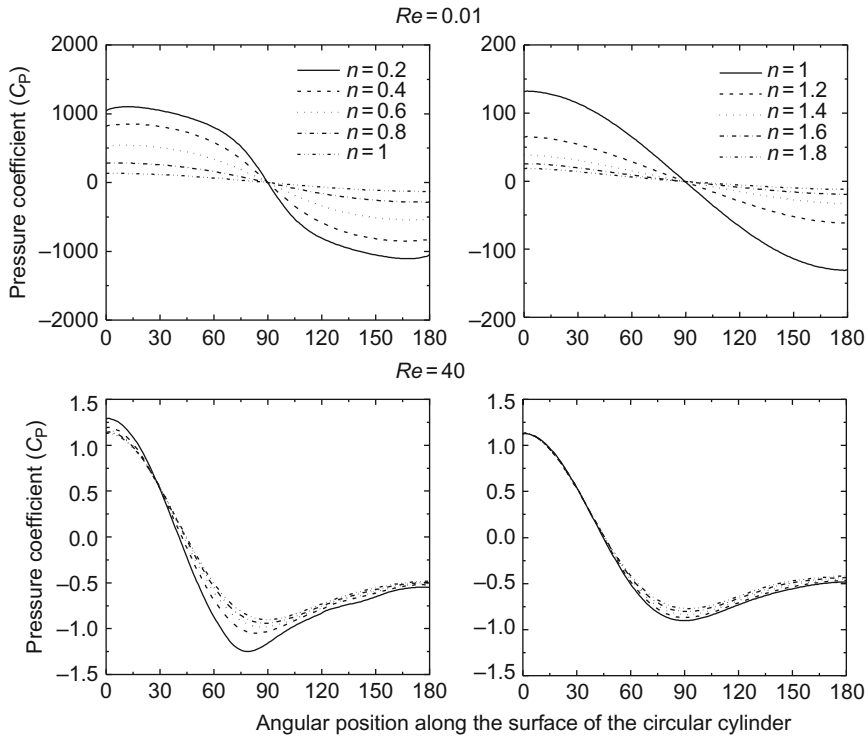


FIG. 19. Typical pressure distribution on the surface of a circular cylinder in the steady flow regime. Replotted from Ref. [126].

studies also [56,126–128]. On the other hand, once the value of the Reynolds number exceeds the corresponding critical Reynolds number (Re_c), the flow transits to the so-called laminar vortex shedding regime and time-periodic regime is established. Under these conditions, the surface pressure exhibits temporal variation also in addition to its spatial distribution [129]. It is customary to capture the temporal variation by dividing a periodic cycle into four equal parts corresponding to $t = 0, T/4, T/2, 3T/4$, and T (where T is the time period). Figure 20 shows representative results elucidating the combined effects of the Reynolds number and the power-law index in this flow regime. At any instant during the cycle, irrespective of the value of power-law index, the pressure variation is qualitatively similar to that seen in the steady flow regime (Fig. 19) but at a fixed point, it varies with time showing periodic behavior. The temporal dependence becomes stronger with the increasing value of the Reynolds number and/or with the decreasing value of the

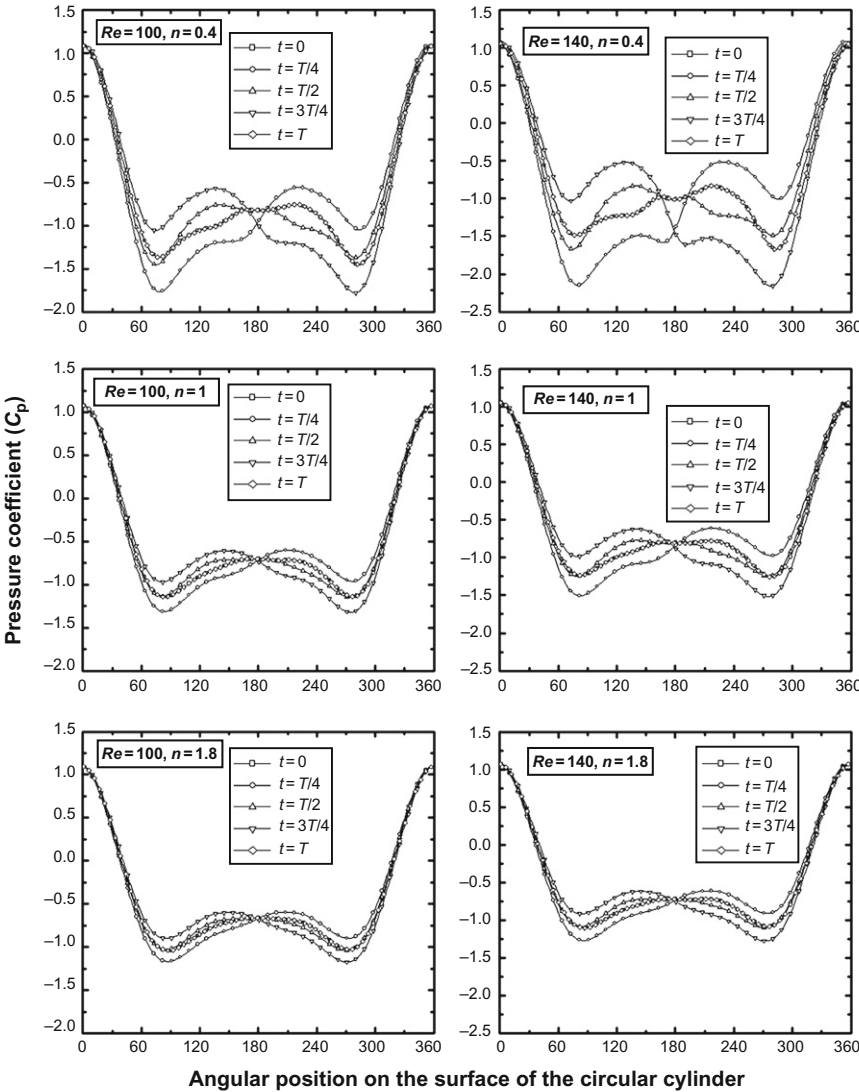


FIG. 20. Typical pressure distribution on the surface of a circular cylinder in the laminar vortex shedding regime. Replotted from Ref. [129].

power-law index. In fact, the instantaneous values of the pressure coefficient at the rear stagnation point are very sensitive and change rapidly and this is why many authors prefer to use the value of C_p ($\theta = \pi$) to gage the state of flow [4,28].

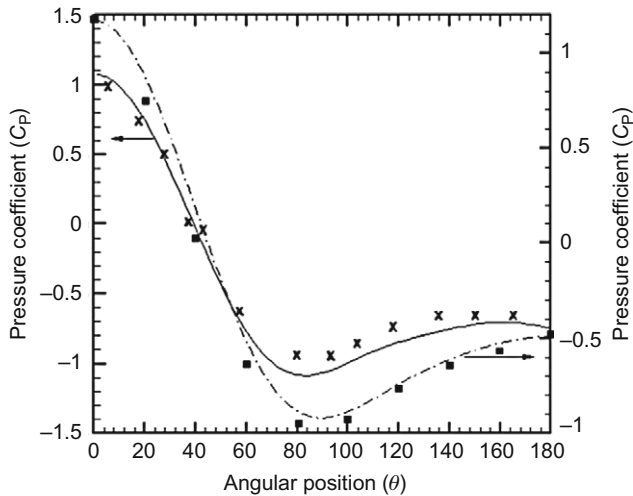


FIG. 21. Comparison between the predicted [129] and experimental [132,133] surface pressure profiles for a circular cylinder in Newtonian fluids. Lines are predictions and symbols are experimental: ■, $Re = 40$; X, $Re = 107$. Replotted from Ref. [92].

Limited results are also available on the role of planar confinement on the surface pressure distribution in the steady [130] and time-periodic [92,131] flow regimes. In the steady flow regime, the effect of blockage was seen to be somewhat suppressed in shear-thinning fluids and it was amplified in shear-thickening fluids [130]. On the other hand, the temporal variation of the surface pressure gets accentuated in shear-thinning fluids due to blockage in the laminar vortex shedding regime [92].

Finally, we close this section by showing a typical comparison between predictions and observations of the surface pressure (Fig. 21) in the steady [132] and laminar vortex shedding [133] regimes in Newtonian fluids, for no analogous data are available in power-law fluids. The agreement is seen to be rather good in both flow regimes.

2. Drag Phenomena

In the so-called creeping flow regime ($Re \rightarrow 0$), there are essentially four independent studies available employing a range of numerics, perturbation method [58], boundary element [58], finite element method [59], finite volume method [55], and finite difference method [125]. On the other hand, Ferreira and Chhabra [134] studied the transverse flow over a bank of cylinders and recovered the limiting case of a single cylinder by letting the solid volume

fraction approach zero. Furthermore, owing to the nature of approximations inherent in their analysis, these results are reliable only for mildly shear-thinning fluids, i.e., $\sim 0.6 \leq n \leq 1$. It appears that broadly most predictions are consistent with each other except for the perturbation analysis of Tanner [58]. On the other hand, perhaps the most reliable predictions are that of Despeyroux et al. [125]. They expressed their results on drag in the form of a correction to the corresponding Newtonian value [120]. Their results can be recast in the present format as follows:

$$C_D \cdot Re = 8\pi X(n) \quad (35)$$

where the correction factor $X(n)$ is given by the following fitted expression:

$$X(n) = 0.978 + 1.202n - 4.047n^2 + 1.382n^3 + 1.925n^4 - 2.758n^5 + 1.328n^6 \quad (36)$$

Qualitatively, the drag is reduced in shear-thinning fluids. However, it is not evident as to what value of the Reynolds number constitutes the limit of the Stokes regime. Based on an extensive numerical exploration, Despeyroux et al. [125] have demonstrated that smaller is the confinement and/or the value of power-law index, lower is the value of the limiting Reynolds number. For instance, for $n = 0.6$ and extent of confinement $< 0.1\%$, the limiting Reynolds number is of the order of $O(10^{-1})$. On the other hand, the corresponding values are $O(10^{-2})$ and $O(10^{-5})$ for $n = 0.9$ and $n = 1.4$, respectively. They attributed this behavior to the rapid spatial decay of the velocity field in highly shear-thinning fluids.

Analogous results at finite Reynolds numbers are also rather scant. D'Alessio and Pascal [56] were seemingly the first to report a numerical study for three values of the Reynolds number as $Re = 1, 20$, and 40 , and they noted acute convergence difficulties with the decreasing value of power-law index. This has been shown subsequently to be due to their poor numerics and, furthermore, owing to the inadvertent omission of a factor, their drag values are also known to be in error [57,127]. In the steady flow regime ($Re \leq Re_c$), there are only three independent investigations available [126–128,131] for the unconfined flow of power-law fluids past a circular cylinder. The key results in terms of the individual drag values, angle of separation, and wake length are summarized in Tables VII–IX, respectively. A detailed examination of this table reveals the following overall trends: Irrespective of the value of the flow behavior index, both components of drag (hence total drag) show the classical inverse dependence on the Reynolds number, as can be seen in Fig. 22. In shear-thinning fluids ($n < 1$), the relative contribution of the frictional drag diminishes rapidly with the increasing value of the Reynolds number (Fig. 22). This is not at all surprising because the inertial forces become increasingly

TABLE VII
SUMMARY OF NUMERICAL RESULTS ON DRAG COEFFICIENT FOR A CIRCULAR CYLINDER IN THE STEADY
FLOW REGIME

n		$Re = 5$	10	15	20	25	30	35	40
0.6	C_{DP}	3.365	1.957	1.490	1.249	1.113	1.021	0.955	0.909
	C_{DF}	6.028	3.256	2.303	1.863	1.516	1.279	1.106	0.968
0.65	C_{DP}	3.095	1.903	1.491	1.277	1.142	1.056	0.990	0.939
	C_{DF}	5.614	3.084	2.24	1.751	1.444	1.235	1.079	0.961
0.7	C_{DP}	2.904	1.832	1.473	1.270	1.149	1.067	1.005	0.957
	C_{DF}	5.298	2.971	2.18	1.722	1.433	1.234	1.086	0.974
0.8	C_{DP}	2.594	1.732	1.419	1.256	1.152	1.078	1.023	0.979
	C_{DF}	4.749	2.813	2.084	1.687	1.430	1.248	1.113	1.007
0.9	C_{DP}	2.316	1.643	1.381	1.241	1.149	1.081	1.033	0.993
	C_{DF}	4.234	2.647	2.014	1.663	1.432	1.263	1.139	1.039
1.0	C_{DP}	2.135	1.572	1.35	1.224	1.141	1.081	1.034	0.998
	C_{DF}	3.839	2.508	1.959	1.642	1.430	1.275	1.157	1.063
1.2	C_{DP}	1.877	1.461	1.29	1.189	1.120	1.069	1.030	0.998
	C_{DF}	3.273	2.289	1.859	1.599	1.420	1.287	1.184	1.1
1.4	C_{DP}	1.710	1.384	1.241	1.156	1.097	1.054	1.019	0.986
	C_{DF}	2.894	2.131	1.776	1.557	1.404	1.288	1.196	1.115
1.5	C_{DP}	1.646	1.352	1.216	1.141	1.087	1.0456	1.014	0.984
	C_{DF}	2.745	2.063	1.734	1.537	1.394	1.284	1.199	1.126
1.6	C_{DP}	1.591	1.321	1.200	1.127	1.076	1.037	1.006	0.979
	C_{DF}	2.614	1.998	1.703	1.516	1.383	1.281	1.199	1.13
1.8	C_{DP}	1.501	1.271	1.161	1.096	1.055	1.02	0.991	0.969
	C_{DF}	2.398	1.888	1.630	1.468	1.358	1.267	1.194	1.134
2.0	C_{DP}	1.432	1.231	1.136	1.073	1.034	1.003	0.976	0.956
	C_{DF}	2.225	1.775	1.578	1.43	1.329	1.250	1.183	1.129

From Ref. [126].

important at high Reynolds numbers and, therefore, the viscous characteristics are of little relevance under these conditions. Note that at $Re = 5$ and $n = 0.6$, the ratio (C_{DP}/C_{DF}) is little less than 0.5, but it is close to ~ 1 at $Re = 40$. One can also argue that since the viscous component of stress scales as U_c^n which increases less rapidly than the corresponding inertial force (as U_c^2) and therefore, the ratio (C_{DP}/C_{DF}) increases with the increasing velocity or Reynolds number. Likewise in shear-thickening fluids ($n > 1$), this ratio starts off at slightly larger values than ~ 0.5 at $Re = 5$ and rises to about ~ 0.9 at $Re = 40$. Figure 23 elucidates this complex functional dependence.

Similarly, Fig. 24 shows the influence of power-law index and Reynolds number on the nondimensional pressure coefficient at the front and rear stagnation points of the cylinder. Notwithstanding the fact that the value of $C_p(\pi)$ is negative, absolute values of both $C_p(0)$ and $C_p(\pi)$ are seen to decrease with the

TABLE VIII
EFFECT OF POWER-LAW INDEX AND REYNOLDS NUMBER ON RECIRCULATION LENGTH (L_R) FOR A CIRCULAR CYLINDER IN THE STEADY FLOW REGIME

n	$Re = 5$	$Re = 10$	$Re = 15$	$Re = 20$	$Re = 25$	$Re = 30$	$Re = 35$	$Re = 40$
0.6	—	0.351	0.685	1.044	1.458	1.871	2.269	2.663
0.65	—	0.268	0.633	1.024	1.457	1.906	2.360	2.799
0.7	—	0.219	0.577	0.949	1.352	1.763	2.182	2.588
0.8	—	0.195	0.537	0.888	1.248	1.615	1.983	2.347
0.9	—	0.212	0.546	0.885	1.227	1.570	1.908	2.244
1.0	—	0.249	0.582	0.916	1.249	1.580	1.908	2.225
1.2	0.029	0.358	0.700	1.036	1.365	1.690	2.010	2.324
1.4	0.132	0.499	0.859	1.210	1.554	1.893	2.227	2.567
1.5	0.192	0.579	0.955	1.315	1.671	2.026	2.368	2.715
1.6	0.257	0.666	1.055	1.434	1.807	2.175	2.540	2.888
1.8	0.401	0.860	1.301	1.734	2.141	2.556	2.974	3.346
2.0	0.562	1.086	1.587	2.099	2.578	3.047	3.514	3.941

Based on Ref. [126].

TABLE IX
EFFECT OF POWER-LAW INDEX AND REYNOLDS NUMBER ON ANGLE OF SEPARATION FOR A CIRCULAR CYLINDER IN THE STEADY FLOW REGIME

n	$Re = 5$	$Re = 10$	$Re = 15$	$Re = 20$	$Re = 25$	$Re = 30$	$Re = 35$	$Re = 40$
0.6	—	38.75	47.17	51.09	54.42	57.11	59.22	61.65
0.65	—	34.25	45.74	50.78	54.31	57.21	59.83	61.97
0.7	—	30.89	43.00	48.35	52.06	55.06	57.48	59.61
0.8	—	28.70	40.12	45.63	49.35	52.16	54.58	56.64
0.9	—	28.56	38.96	44.26	47.85	50.59	52.87	54.82
1.0	—	29.53	38.73	43.69	47.11	49.74	51.88	53.71
1.2	9.78	32.27	39.55	43.83	46.87	49.21	51.15	52.80
1.4	21.70	35.21	41.17	44.87	47.50	49.61	51.34	52.87
1.5	25.11	36.65	42.07	45.50	48.03	50.05	51.66	53.11
1.6	27.85	38.09	43.06	46.25	48.64	50.51	52.09	53.40
1.8	32.46	40.70	45.04	47.79	49.90	51.57	52.96	54.23
2.0	36.16	43.18	46.90	49.35	51.22	52.77	54.12	55.16

From Ref. [126].

increasing value of the Reynolds number and/or of the flow behavior index, though in shear-thinning fluids both tend to be higher than that in Newtonian media otherwise under identical conditions.

Tables VIII and IX show the currently available data on the angle of separation (θ_s) and wake length (l_w). Similar to the behavior seen in Newtonian

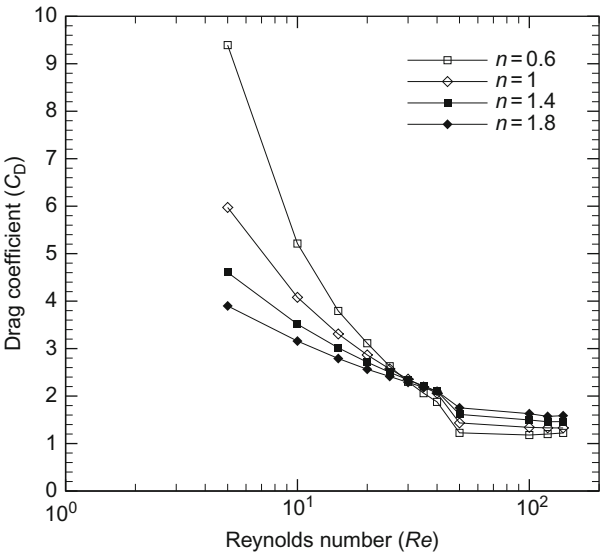


FIG. 22. Drag coefficient–Reynolds number relationship for a circular cylinder in power-law fluids. The time-averaged values are shown in the vortex shedding regime.

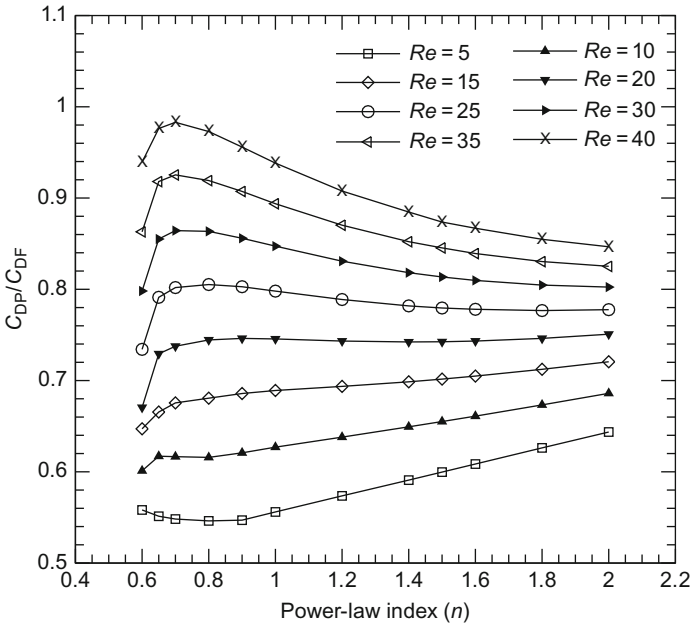


FIG. 23. Dependence of the ratio (C_{DP}/C_{DF}) for a circular cylinder in power-law fluids.

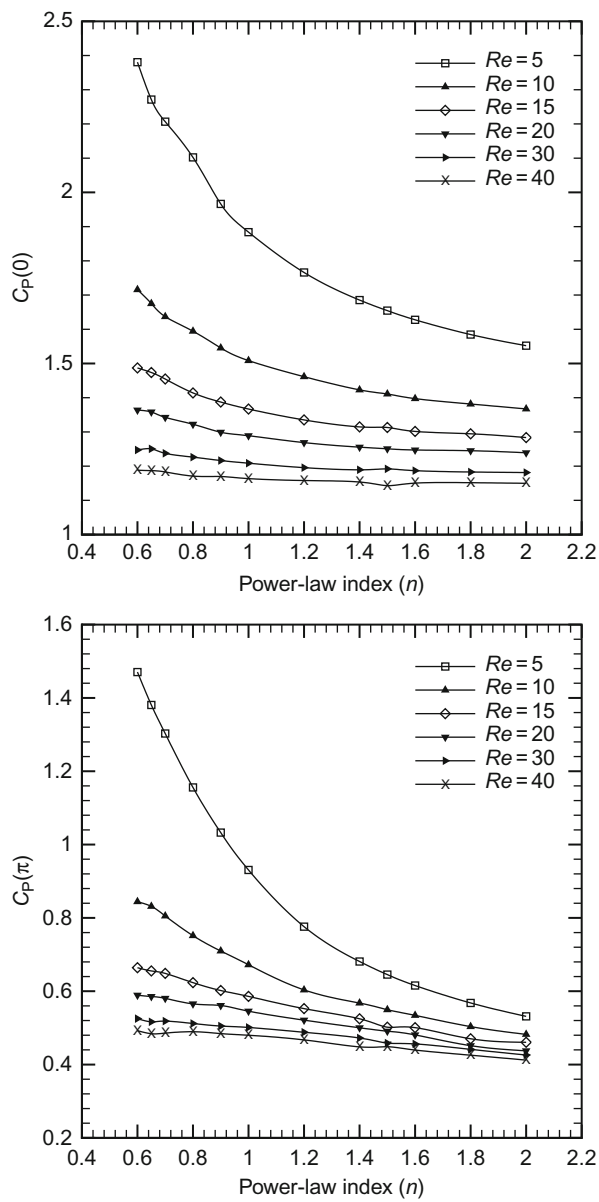


FIG. 24. Effect of power-law index and Reynolds number on the surface pressure at the front and rear stagnation points for a circular cylinder. Modified from Ref. [126].

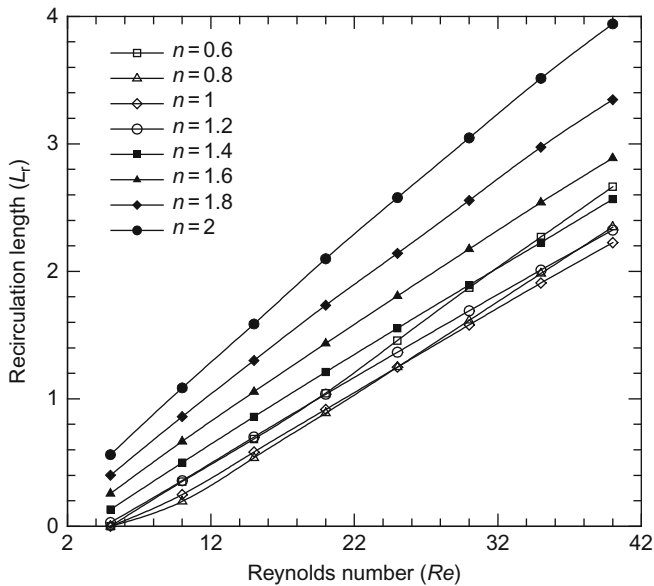


FIG. 25. Variation of recirculation length with Reynolds number for a circular cylinder in power-law fluids.

fluids, wake length increases with the increasing Reynolds number regardless of the value of power-law index, as can be seen in Fig. 25. Broadly, all else being equal, the wakes tend to be longer in shear-thickening fluids ($n > 1$) and may be longer or shorter in shear-thinning fluids depending upon the values of power-law index and of the Reynolds number. Intuitively, it appears that the effective viscosity of a shear-thickening fluid will gradually decrease from its maximum value at the cylinder to a lower value far away from it. This is tantamount to a highly viscous body of fluid surrounded by a less viscous fluid. This can be approximated as a virtual cylinder of larger diameter than its actual diameter and thus would imply a larger effective Reynolds number and hence the wake is longer. On the other hand, in a shear-thinning fluid, the region of high viscosity acts as a virtual wall and confinement is known to stabilize the flow by resulting in shorter wakes. This simple reasoning does seem to explain the trends seen in Tables VIII and IX, at least qualitatively. Further examinations of the values of θ_s suggest slight widening of wakes in shear-thinning and corresponding slight narrowing of wakes in shear-thickening ($n > 1$) fluids, while the dependence of θ_s on Reynolds number is qualitatively similar in Newtonian and power-law fluids.

TABLE X
DEPENDENCE OF STROUHAL NUMBER, St , ON REYNOLDS NUMBER, Re , AND POWER-LAW INDEX, n

Re	$n = 0.4$	$n = 0.6$	$n = 1$	$n = 1.4$	$n = 1.8$
40	—	—	—	—	0.1048
50	0.1612	0.1348	0.1232	0.1172	0.1130
100	0.2067	0.1801	0.1657	0.1497	0.1392
120	0.2155	0.1996	0.1747	0.1551	0.1417
140	0.2231	0.2066	0.1800	0.1637	0.1511

Once the value of the Reynolds number exceeds the critical value corresponding to the limit of the steady flow regime ($Re > Re_c$), the flow over a cylinder exhibits both spatial and temporal variation. Even at the macroscopic level, drag coefficient displays time-dependent characteristics which are examined in terms of its mean value and the amplitude of oscillation, i.e., $\overline{C_D}$ and its root mean square (rms) value. This also gives rise to a net force acting on the cylinder in the transverse direction the so-called lift-force, which also shows time-periodic behavior. Obviously the time-averaged value of lift will be zero in this case. Finally, the frequency of vortex shedding is expressed in a dimensionless form using the familiar Strouhal number, St . Table X shows the influence of power-law index and Reynolds number on drag and lift coefficient and on Strouhal number [129]. Intuitively, it appears that vortex-shedding is facilitated in shear-thinning fluids ($n < 1$) simply because of the lower effective viscosity in the vicinity of the cylinder. Likewise, one would expect to see some reduction in the frequency of vortex-shedding in shear-thickening fluids ($n > 1$). This conjecture is well supported by the numerical results shown in Table X and is also borne out by the scant experimental results [87–89]. Note that this is in stark contrast to the influence of viscoelasticity which makes the process of vortex shedding somewhat sluggish due to the enormous extensional resistance in the wake region [76]. Increasing Reynolds number also leads to an increase in the rms values of both drag and lift coefficients. Broadly, the rms values of lift coefficients are seen to be higher in shear-thickening fluids than that in Newtonian fluids and vice versa in shear-thinning media. Since no experimental results are available in power-law fluids, it is useful to make such comparisons in Newtonian fluids. The predicted values of $St = 0.1355$ and 0.18 are in excellent agreement with the corresponding experimental values $St = 0.1361$ and 0.1664 at $Re = 60$ and 100, respectively [135,136]. This together with the close match seen in Fig. 21 inspires confidence in the veracity of numerical predictions.

3. *Effect of Confinement*

Many investigations have elucidated the influence of blockage on the fluid flow characteristics of Newtonian fluids for a cylinder confined symmetrically or asymmetrically in between two plane walls. The presence of walls can influence the flow phenomena, at least, in three ways. First, the approaching fluid stream exhibits a fully developed parabolic profile in the case of a confined flow and it is no longer shear-free as in the case of an unconfined flow. Therefore, the vorticity of the incoming fluid interacts with the vortex shedding from the cylinder. Second, due to the solid walls, the fluid accelerates appreciably in the annular region formed by the cylinder and the wall. Depending upon the extent of blockage, this can shift the separation point in the downstream direction. Finally, due to the imposition of the no-slip condition on the confining walls, vortices can form on these walls also which interact with those in the wake region. Naturally, the relative importance of each of these potential effects arising from blockage is strongly dependent upon the severity of the confinement and the Reynolds number (i.e., on the prevailing flow regime). In Newtonian fluids, it is generally agreed [1,2,4] that wall effects are negligible up to about 10% blockage. Over the range 10–60% blockage, the confining walls modify the flow and it is thus necessary to use appropriate correction factors. Conversely, it is still possible to link the values of the engineering parameters like drag coefficient and Nusselt number in the confined and unconfined configurations via a function of blockage ratio, δ , for example, see Refs. [137–148]. For still higher confinements ($\delta > 65\%$), the confinement alters the flow field to such an extent that it is no longer possible to correct the results for an unconfined cylinder via a function of the blockage ratio alone. The literature is indeed limited on this aspect even in Newtonian liquids. The scant experimental studies [139,140,149–151] endeavored to measure the hydrodynamic drag on a cylinder confined symmetrically and asymmetrically between two parallel walls under conditions which may correspond to the free fall or Poiseuille flow. Notwithstanding the additional complications arising from the end effects (finite length-to-diameter ratio of test cylinders) in such experiments, the correspondence between predictions and experiments is generally very good [139,140,149–151]. Some predictions are also available on the influence of the blockage on the stability of flow. For instance, low to moderate values of blockage tend to extend the steady flow regime, for example, see Ref. [141] whereas severe blockage can advance this transition to lower values of the Reynolds number. While the additional dissipation of energy at walls probably acts to stabilize the flow, the local acceleration in the annular region tends to destabilize it; intuitively, the latter effect is likely to be more pertinent in conditions of acute blockage only. While many authors have provided

the correction factors in terms of the blockage ratio to connect the values of the momentum and heat transfer parameters (drag coefficient and Nusselt number) in confined and unconfined cases [146,147,152,153], preliminary results [153] also suggest the onset of flow separation to be delayed due to such confinement.

In contrast, little is known about the analogous flow of power-law and other generalized Newtonian fluids over a circular cylinder in a planar confinement. In the creeping flow limit, Despeyroux et al. [125] have extensively studied the influence of planar blockage on the drag characteristics of a long cylinder confined in between two plane walls. Indeed, not only this study spans almost the entire range of blockage, but it also encompasses both configurations of the symmetric as well as asymmetric confinements. This study clearly shows that higher the blockage, larger is the value of the Reynolds number required to eliminate the Stokes paradox. They invoked the lubrication flow approximation when the blockage was $>95\%$ or so. This creeping flow steady is supplemented by that of Bharti et al. [130] who elucidated the role of power-law rheology and planar confinement on the hydrodynamics of a cylinder in the steady Poiseuille flow regime. The flow separation was reported to be delayed in shear-thickening fluids. The drag was reported to be augmented above its value in an unconfined medium. However, for fixed values of blockage and Reynolds number, shear-thinning lowers drag below its value in Newtonian media and shear-thickening enhances it, though this effect is more dramatic at low Reynolds numbers than that at high Reynolds numbers. This work has recently been extended to the laminar vortex shedding regime [92]. It appears that confinement stabilizes the flow in the laminar vortex shedding regime also. For instance, for $n > 1$ and 50% blockage, the flow was found to be steady even up to $Re = 140$. On the other hand, in a shear-thinning fluid ($n = 0.4$), the flow was found to be unsteady even at $Re = 40$ with 50% blockage. Rao et al. [92] explained the influence of blockage as follows. For a shear-thinning fluid, the effective fluid viscosity is minimum near the both solid boundaries, i.e., cylinder and the confining walls. These two regions of low viscosity are separated by a high viscosity region where the velocity goes through a maximum and the velocity gradient changes its sign. Strictly speaking, the power-law model will predict an infinite viscosity and hence this acts as a virtual wall. This suggests significant fluid acceleration in this region thereby making the local Reynolds number to be much larger than its global value. Naturally, this will tend to destabilize the flow at lower values of the nominal Reynolds numbers than that for an unconfined cylinder. One can similarly postulate that shear-thickening fluid behavior will tend to stabilize the wake and defer the cessation of the steady flow regime to higher Reynolds numbers than that expected for an unconfined flow. A summary of their results is presented in Table XI where an intricate role of blockage and power-law index is seen on

TABLE XI
EFFECT OF POWER-LAW INDEX AND BLOCKAGE ON THE NATURE OF FLOW REGIME

n	$Re = 40$	$Re = 50$	$Re = 100$	$Re = 120$	$Re = 140$
$\beta = 2$					
0.4	U	U	U	U	U
0.6	S	S	U	U	U
1	S	S	U	U	U
1.4	S	S	S	S	S
1.8	S	S	S	S	S
$\beta = 4$					
0.4	S	U	U	U	U
0.6	S	U	U	U	U
1	S	S	U	U	U
1.4	S	S	U	U	U
1.8	S	S	S	S	U
$\beta = 6$					
0.4		U	U	U	U
0.6		U	U	U	U
1		U	U	U	U
1.4		S	U	U	U
1.8		S	U	U	U

U denotes unsteady flow regime and S denotes the steady flow regime.
From Ref. [92].

the type of the flow regime expected for given values of β , Re and n . However, no experimental observations are currently available to substantiate or refute these predictions in power-law fluids.

Before concluding this section, it is thus fair to say that currently available various predictions of drag and wake characteristics are consistent with each other. Suffice it to say here that the extensive literature available on the creeping flow of viscoelastic fluids past a cylinder (50% blockage) in between two plane walls has been reviewed elsewhere [22].

B. ELLIPTICAL CYLINDERS

A cylinder of elliptical cross section is perhaps the simplest deviation from the perfectly symmetric circular cylinder yet retaining the axisymmetry attributes and still free from geometric singularities. Furthermore, it affords the possibility of elucidating the influence of the degree of streamlining on the hydrodynamics by simply varying the value of its aspect ratio, E . While the flow of Newtonian fluids over an elliptical cylinder has received some attention over the past 60 years or so, the resulting literature is nowhere near

as extensive as that for a circular cylinder [1,2,4,39] and that for non-Newtonian fluids, it is really scant. In this field, the early studies [154,155] simply paralleled the Oseen's linearization analysis to obtain the expressions for hydrodynamic drag applicable at low Reynolds numbers. Some of the initial studies seeking numerical solutions of the governing differential equations for elliptical cylinders are possibly due to Lugt and Haussling [156] and of Meller [157]. Subsequently, many others, for example, see Refs. [40–44,158–160], have presented numerical solutions at relatively low Reynolds numbers ranging from $\sim 1 \leq Re \leq \sim 200$. On the other hand, the currently available experimental studies, for example, see Refs. [161–165], relate to the conditions which are way beyond the range of numerical predictions available thus far. The use of von Karman–Pohlhausen integral method has also been extended to two-dimensional elliptical cylinders [166]. Broadly, it is perhaps fair to say that the detailed as well as the macroscopic flow behavior like drag, wake size, etc. is much more influenced by the shape of the elliptic cross section than that by the values of the Reynolds number or confinement. For instance, the so-called slender shapes are more streamlined and therefore the flow remains attached as well as is steady up to higher values of the Reynolds number (as seen in the preceding section). Similarly, slender shapes lead to the reduced drag also.

On the other hand, there have been only three studies of the power-law fluid flow over an unconfined elliptical cylinders [44,167,168]. The study of Rao et al. [44] dealt with the delineation of the critical Reynolds numbers, Re^c and Re_c , as was outlined in the preceding section. Sivakumar et al. [167] presented steady-state solutions of the momentum equations over the ranges of conditions as $0.2 \leq E \leq 5$, $0.01 \leq Re \leq 40$, and $0.2 \leq n \leq 1.8$. Table XII shows representative values of the pressure and total drag coefficients highlighting the role of power-law index, Reynolds number, and aspect ratio on these parameters. More detailed listing can be found in Ref. [167]. Figure 26 shows that, irrespective of the value of E , drag is enhanced in shear-thinning fluids and reduced in shear-thickening fluids. The effect, however, progressively diminishes with the increasing Reynolds number and indeed the effect of n is reversed beyond $Re \sim 20$ or so. This behavior is also consistent with that seen for a sphere in power-law fluids. Figure 27 shows the representative trends in terms of the relative contributions of the two drag components (C_{DP}/C_{DF}) for scores of values of the Reynolds number and power-law index spanning the range $0.2 \leq n \leq 1.8$. As asserted above, the shape is seen to exert much more influence than the power-law index or even the Reynolds number on the value of this ratio (C_{DP}/C_{DF}). However, it is possible to achieve a degree of reconciliation by employing the drag coefficient normalized using the corresponding value in Newtonian fluids at the same values of the Reynolds number and aspect ratio. Figure 28 shows the results replotted in this format. This clearly

TABLE XII

NUMERICAL VALUES OF PRESSURE AND TOTAL DRAG COEFFICIENTS FOR AN ELLIPTICAL CYLINDER AS A FUNCTION OF ASPECT RATIO (E), POWER-LAW INDEX (n), AND REYNOLDS NUMBER (Re)

Pressure drag coefficient, C_{DP}								
n	$E = 0.2$							
	$Re = 0.01$	$Re = 0.1$	$Re = 1$	$Re = 5$	$Re = 10$	$Re = 20$	$Re = 30$	$Re = 40$
0.2	2376	237.6	23.96	5.388	3.143	2.069	1.726	1.545
0.4	1984	198.3	20.01	4.582	2.787	1.922	1.630	1.471
0.6	1346	134.9	14.37	3.949	2.592	1.874	1.612	1.465
0.8	726.2	76.96	10.51	3.516	2.452	1.844	1.605	1.466
1	333.6	44.74	8.103	3.178	2.327	1.808	1.592	1.462
1.2	157.7	28.71	6.572	2.930	2.231	1.777	1.579	1.457
1.4	86.85	19.97	5.522	2.732	2.145	1.745	1.563	1.448
1.6	54.01	14.79	4.774	2.570	2.069	1.711	1.543	1.434
1.8	36.41	11.51	4.222	2.436	1.999	1.676	1.520	1.417
n	$E = 0.5$							
	$Re = 0.01$	$Re = 0.1$	$Re = 1$	$Re = 5$	$Re = 10$	$Re = 20$	$Re = 30$	$Re = 40$
0.2	2186	218.7	22.04	4.899	2.819	1.768	1.439	1.287
0.4	1756	175.6	17.71	4.058	2.461	1.653	1.383	1.241
0.6	1145	114.6	12.25	3.395	2.231	1.597	1.368	1.241
0.8	598.1	63.45	8.721	2.952	2.065	1.553	1.354	1.240
1	266.2	36.09	6.598	2.617	1.925	1.504	1.331	1.229
1.2	124.7	22.92	5.292	2.380	1.822	1.464	1.310	1.217
1.4	68.39	15.84	4.411	2.198	1.736	1.426	1.287	1.202
1.6	42.43	11.68	3.791	2.055	1.664	1.389	1.263	1.184
1.8	28.57	9.073	3.341	1.940	1.601	1.354	1.238	1.164
n	$E = 2$							
	$Re = 0.01$	$Re = 0.1$	$Re = 1$	$Re = 5$	$Re = 10$	$Re = 20$	$Re = 30$	$Re = 40$
0.2	1646	164.6	16.58	3.626	2.013	1.184	0.8965	0.7461
0.4	1159	115.9	11.72	2.734	1.646	1.065	0.8498	0.7319
0.6	674.1	67.53	7.36	2.146	1.415	0.9900	0.8220	0.7271
0.8	326.4	34.88	5.015	1.794	1.262	0.9340	0.7989	0.7210
1	141.4	19.54	3.760	1.560	1.160	0.8893	0.7781	0.7126
1.2	65.86	12.41	2.997	1.394	1.069	0.8533	0.7590	0.7023
1.4	36.47	8.639	2.496	1.273	1.007	0.8235	0.7414	0.6912
1.6	22.92	6.441	2.152	1.183	0.9583	0.7983	0.7251	0.6800
1.8	15.66	5.064	1.906	1.114	0.9195	0.7767	0.7102	0.6689
n	$E = 5$							
	$Re = 0.01$	$Re = 0.1$	$Re = 1$	$Re = 5$	$Re = 10$	$Re = 20$	$Re = 30$	$Re = 40$
0.2	1296	129.63	13.08	2.854	1.573	0.9017	0.6653	0.5417
0.4	777.4	77.76	7.908	1.921	1.168	0.7481	0.5866	0.4970
0.6	402.9	40.40	4.580	1.437	0.9571	0.6645	0.5436	0.4737
0.8	183.3	19.86	3.087	1.175	0.8308	0.6089	0.5129	0.4560
1	77.64	11.08	2.310	1.009	0.7456	0.5668	0.4879	0.4403
1.2	36.76	7.202	1.863	0.8985	0.6862	0.5368	0.4693	0.4281
1.4	20.96	5.149	1.573	0.8210	0.6430	0.5142	0.4549	0.4183
1.6	13.57	3.941	1.376	0.7647	0.6111	0.4971	0.4436	0.4103
1.8	9.533	3.177	1.236	0.7228	0.5871	0.4839	0.4347	0.4038

(Continued)

TABLE XII
(CONTINUED)

Pressure drag coefficient, C_{DP}								
n	$E = 0.2$							
	$Re = 0.01$	$Re = 0.1$	$Re = 1$	$Re = 5$	$Re = 10$	$Re = 20$	$Re = 30$	$Re = 40$
Total drag coefficient, C_D								
$E = 0.2$								
0.2	2511	251.0	25.31	5.648	3.250	2.109	1.752	1.565
0.4	2158	215.7	21.75	4.953	2.975	2.011	1.689	1.517
0.6	1517	151.9	16.19	4.410	2.854	2.018	1.713	1.543
0.8	847.3	89.79	12.26	4.052	2.781	2.042	1.750	1.582
1	404.5	54.25	9.806	3.790	2.728	2.065	1.787	1.621
1.2	197.0	35.86	8.185	3.589	2.684	2.083	1.819	1.656
1.4	111.5	25.63	7.061	3.429	2.644	2.095	1.843	1.685
1.6	71.11	19.47	6.253	3.298	2.607	2.101	1.861	1.707
1.8	49.08	15.52	5.652	3.189	2.571	2.102	1.873	1.723
$E = 0.5$								
0.2	2554	255.4	25.72	5.628	3.161	1.905	1.520	1.343
0.4	2202	220.2	22.19	5.006	2.957	1.899	1.544	1.361
0.6	1544	154.5	16.49	4.467	2.845	1.942	1.611	1.431
0.8	858.1	91.03	12.48	4.101	2.775	1.986	1.675	1.498
1	404.2	54.81	9.968	3.828	2.720	2.020	1.728	1.557
1.2	196.9	36.20	8.309	3.615	2.674	2.046	1.771	1.605
1.4	111.7	25.86	7.156	3.447	2.632	2.063	1.804	1.644
1.6	71.28	19.64	6.327	3.309	2.594	2.072	1.828	1.673
1.8	49.24	15.65	5.710	3.195	2.557	2.076	1.844	1.695
$E = 2$								
0.2	3015	301.6	30.28	6.390	3.409	1.886	1.362	1.092
0.4	2580	258.0	25.99	5.776	3.276	1.951	1.469	1.211
0.6	1749	175.3	18.95	5.117	3.142	2.004	1.564	1.321
0.8	935.9	100.0	14.14	4.628	3.026	2.040	1.641	1.414
1	429.2	59.26	11.17	4.247	2.923	2.063	1.700	1.489
1.2	206.4	38.85	9.204	3.948	2.834	2.076	1.745	1.547
1.4	116.5	27.63	7.848	3.709	2.756	2.082	1.777	1.593
1.6	74.18	20.92	6.874	3.517	2.689	2.082	1.800	1.627
1.8	51.18	16.64	6.151	3.359	2.628	2.077	1.816	1.652
$E = 5$								
0.2	4197	419.7	42.11	8.736	4.572	2.449	1.720	1.347
0.4	3395	339.5	34.25	7.619	4.256	2.461	1.808	1.461
0.6	2139	214.5	23.78	6.502	3.927	2.438	1.861	1.542
0.8	1072	116.0	17.25	5.675	3.649	2.399	1.889	1.599
1	471.8	67.11	13.31	5.072	3.433	2.358	1.905	1.641
1.2	222.4	43.51	10.76	4.596	3.243	2.314	1.908	1.668
1.4	124.8	30.74	9.027	4.226	3.084	2.271	1.906	1.686
1.6	79.25	23.16	7.796	3.932	2.951	2.231	1.899	1.697
1.8	54.63	18.34	6.887	3.693	2.838	2.193	1.890	1.703

Based on Refs. [44] and [167].

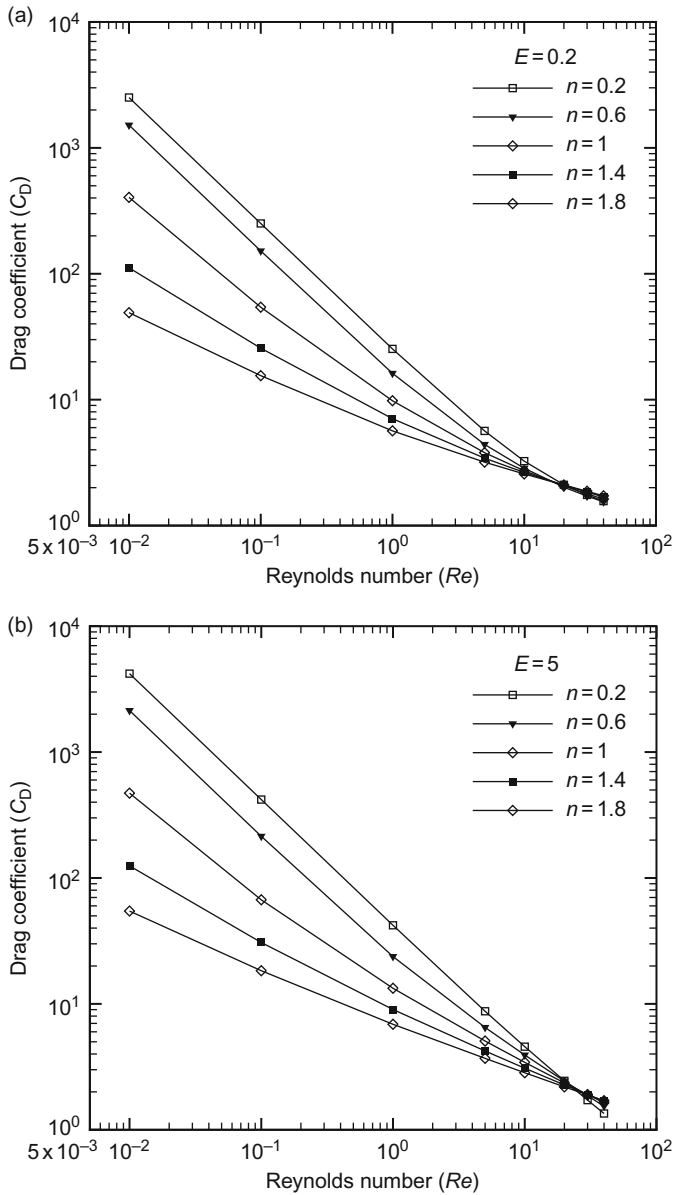


FIG. 26. Drag coefficient–Reynolds number relationship for elliptical cylinders in power-law media (a) $E = 0.2$ and (b) $E = 5$.

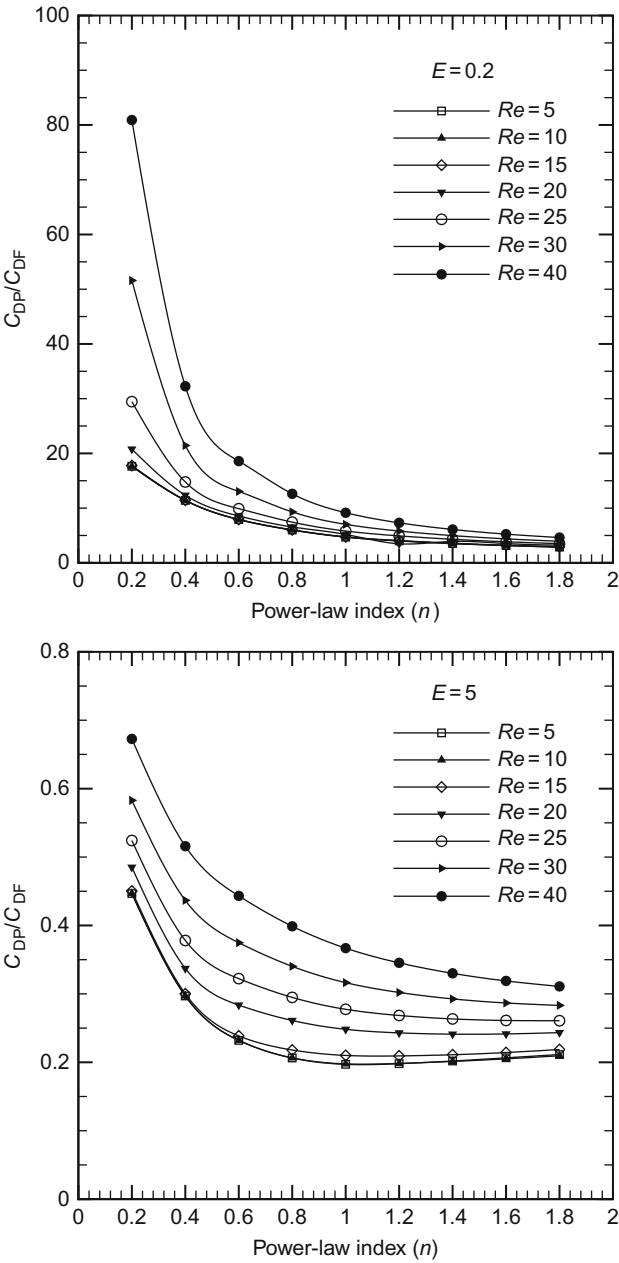


FIG. 27. Influence of n , Re , and E on the ratio (C_{DP}/C_{DF}) for an elliptic cylinder. Modified after Sivakumar et al. [167].

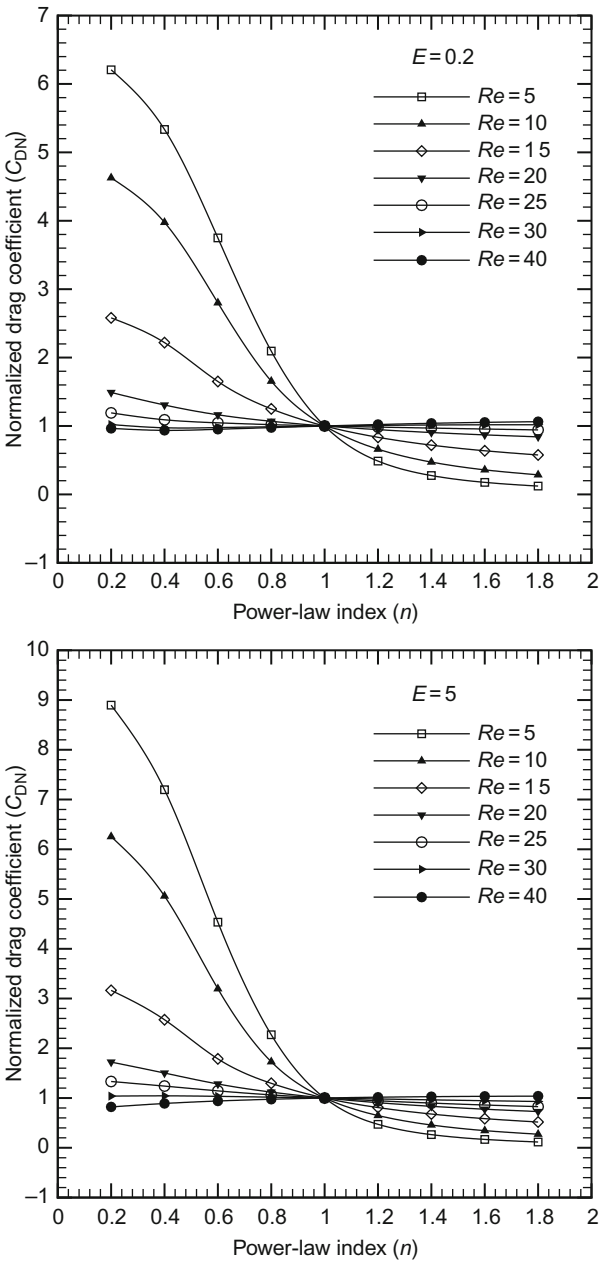


FIG. 28. Normalized drag coefficient for an elliptical cylinder. From Ref. [167].

suggests that the role of shape is qualitatively similar in both Newtonian and power-law fluids. Broadly, the drag is increased in shear-thinning fluids above its value in Newtonian media otherwise under identical conditions. As expected, shear-thickening ($n > 1$) fluids exhibit the opposite trend. However, the influence of power-law behavior index gradually diminishes with the increasing value of the Reynolds number. This can be rationalized by postulating that the viscous forces weaken as compared to the inertial forces with the increasing Reynolds number and, therefore, the power-law index is of little relevance under these conditions.

In the steady flow regime, the twin standing vortices remain attached to the surface of the cylinder and therefore, it is customary to characterize the separated flow region in terms of the wake length l_w . Figure 29 shows typical dependence of the nondimensional wake length L_r for the same range of conditions as that used in Figs. 27 and 28. It is clearly seen here that more streamlined (large value of E) the shape, higher is the Reynolds number at which the flow detaches itself from the surface of the cylinder. Indeed, no flow separation was observed in shear-thinning fluids for $E = 5$ over the range of $Re \leq 40$.

As of now, no results are available beyond the steady flow regime or about the influence of confinement on the flow characteristics of elliptical cylinders in power-law or any other type of non-Newtonian fluids. Nor are there any experimental results available on elliptic cylinders in power-law or any other type of non-Newtonian fluid systems to validate the aforementioned numerical predictions.

C. SEMICIRCULAR CYLINDER

A semicircular cylinder is much more complex to study than a circular or elliptical cylinder. This difficulty stems from the sudden termination of a part of the surface and thus the two corners denote singularities. Besides, further complications arise from the orientation of a semicircular cylinder with respect to the direction of the oncoming flow, e.g., curved or flat surface oriented transverse or parallel to incoming fluid, or whether it is a hollow cylinder. To date, very scant results are available on a semicircular cylinder immersed in Newtonian [53] and in power-law fluids [54,100]. These relate to the configuration when the curved surface is oriented toward the free stream. While along the front surface, a fluid element is able to negotiate the shape without any difficulty, but the abrupt termination of the rear surface promotes early onset of the flow separation, as discussed in the previous section.

In this case, it is instructive to study the variation of the surface pressure, for the form drag dominates the total drag. Since the flow is steady, one would expect it to be symmetric about the horizontal midplane. Figure 30 shows the interplay between the power-law index, Reynolds number, and surface pressure

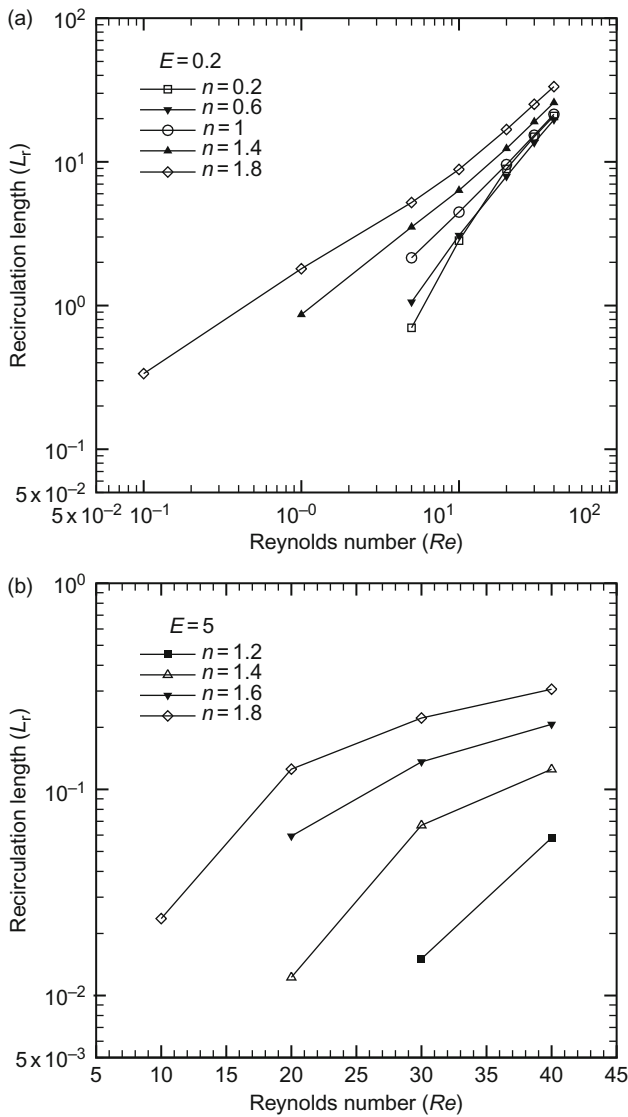


FIG. 29. Effect of n , Re , and E on wake length for an elliptical cylinder (based on the results reported in Ref. [167]). (a) $E = 0.2$ and (b) $E = 5$.

along the surface of the semicircular cylinder. The pressure is seen to be maximum in almost all cases at the front stagnation point (A) and it gradually decreases along the surface (AB) due to the gradual fluid acceleration and it suddenly drops to negative values at point B. This is clearly due to the abrupt

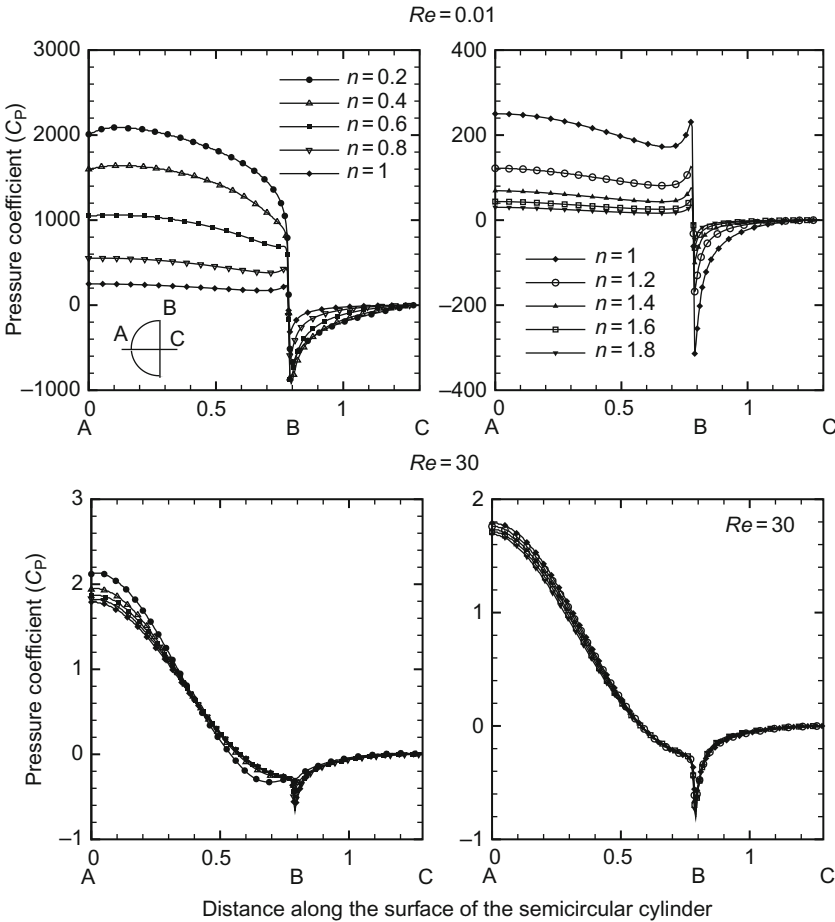


FIG. 30. Effect of power-law index and Reynolds number on surface pressure distribution for a semicircular cylinder. Replotted from Ref. [100].

loss of rear surface. However, some recovery is seen along the flat surface (BC). As always, the effect of power-law index progressively diminishes with the increasing values of the Reynolds number. The pressure at the front stagnation point (A) can be approximated by the following expression:

$$C_p = 1.6 - \frac{(2.8 - 8\sqrt{n})}{n^2 Re} \tag{37}$$

Figure 31 shows the corresponding streamline patterns where one can see the fully developed separated flow region and the so-called wake length

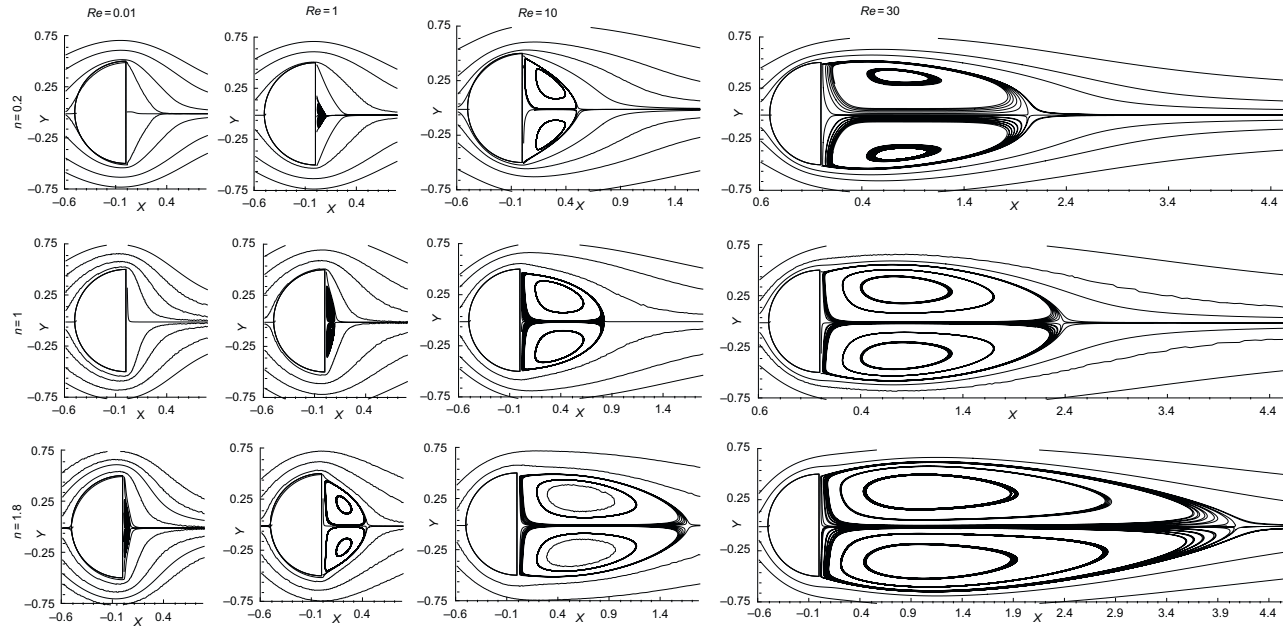


FIG. 31. Typical streamline patterns as a function of the Reynolds number for a semicircular cylinder in the steady flow regime. Adapted from Ref. [100].

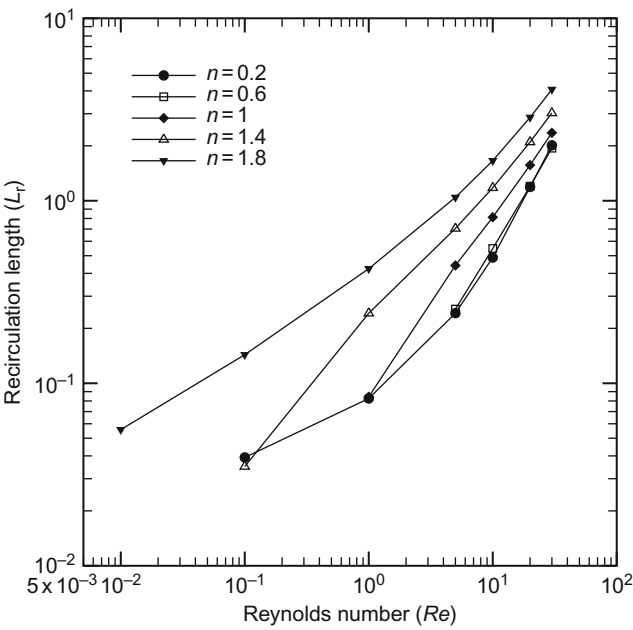


FIG. 32. Effect of Reynolds number and power-law index on wake length for a semicircular cylinder. Replotted from Ref. [100].

(nondimensional) shows almost a linear dependence on the Reynolds number (Fig. 32). Broadly, wakes tend to be longer in shear-thickening fluids than that in Newtonian media at the same value of the Reynolds number and somewhat shorter in shear-thinning fluids, as noted earlier for a circular cylinder also.

Finally, Fig. 33 plots the normalized drag coefficient which shows qualitatively similar features as that seen in Fig. 28 for elliptical cylinders.

D. EQUILATERAL TRIANGULAR CYLINDER

A two-dimensional triangular prism is an exceedingly complex shape to entertain an appropriate analysis even in Newtonian media, and therefore the currently available body of knowledge hinges on a few numerical solutions and experimental results [46,49,51,52,101,102]. Apart from the presence of three corners, additional complications arise from the nature of the triangular cross section (isosceles, equilateral, right-angled, etc.) and, of course, its orientation with respect to the oncoming fluid stream. For power-law fluids, there has been only one numerical study [52] which, in addition to delineating the values of Re^c and Re_c , also reported the values of drag coefficient for equilateral triangular prisms with its apex facing forward or backward to the

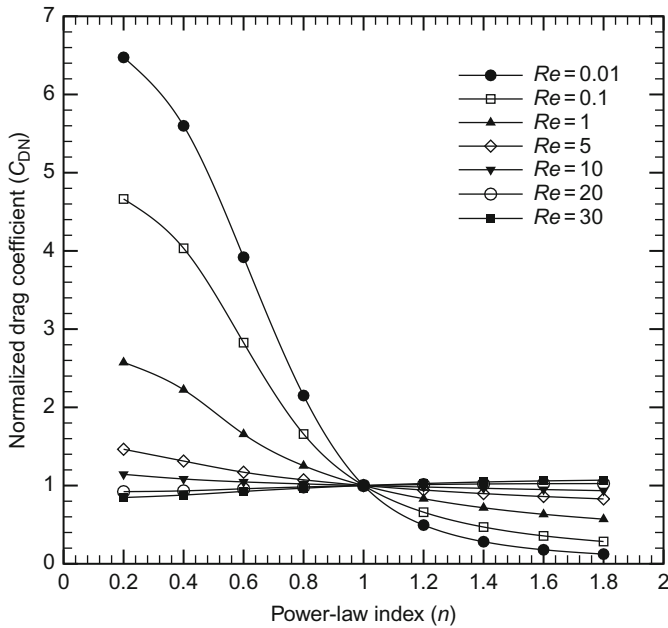


FIG. 33. Normalized drag coefficient for a semicircular cylinder.

oncoming free stream of power-law fluids (Table XIII). Apart from the fact that the total drag is dominated by the form drag under most conditions of flow, the orientation seems to have little influence on the pressure or total drag coefficient. No other study is available in the open literature about the other aspects like wake size, or the effect of confinement, or about the time-dependent behavior at still higher Reynolds numbers.

E. SQUARE CYLINDER

In spite of its reduced degree of streamlining, the flow over a two-dimensional square cross section bar has been accorded the importance which is second only to the circular cylinder, as can be seen from the numerous references cited here and that indicated in the two monumental volumes [1,2]. Correspondingly, the flow of power-law fluids past a square cylinder has also been studied more extensively than that for, say, elliptical or triangular cylinders. Early studies [169,170] were based on relatively coarse numerical meshes, but subsequently these computations have been refined significantly. Overall, currently available results span the unconfined flow in the steady and time-periodic flow regimes [45,171–173], and confined configurations [174,175]. Figure 34 shows the variation of the drag coefficient with Reynolds number and power-law index. In the periodic-flow regime, time-averaged values of the

TABLE XIII
NUMERICAL VALUES OF PRESSURE AND TOTAL DRAG COEFFICIENTS FOR AN EQUILATERAL TRIANGULAR
CYLINDER IN THE STEADY FLOW REGIME

Re	Pressure drag coefficient, C_{DP}						
	$n = 0.3$	$n = 0.4$	$n = 0.6$	$n = 0.8$	$n = 1$	$n = 1.5$	$n = 1.8$
<i>Vertex upstream</i>							
1	18.36	16.05	11.10	7.781	5.777	4.885	2.588
5	3.866	3.418	2.742	2.292	1.972	2.039	1.310
10	2.188	2.002	1.738	1.553	1.413	1.548	1.082
20	1.403	1.322	1.210	1.133	1.071	1.177	0.899
30	1.159	1.107	1.036	0.9867	0.9433	1.033	0.822
<i>Vertex downstream</i>							
1	18.87	16.62	12.07	9.145	7.395	5.177	4.489
5	4.512	4.138	3.682	3.398	3.196	3.196	3.196
10	2.873	2.776	2.650	2.578	2.525	2.423	2.525
20	2.173	2.110	2.062	2.049	2.046	2.038	2.126
30	1.908	1.868	1.836	1.834	1.841	1.856	1.855
Re	Total drag coefficient, C_D						
	$n = 0.3$	$n = 0.4$	$n = 0.6$	$n = 0.8$	$n = 1$	$n = 1.5$	$n = 1.8$
<i>Vertex upstream</i>							
1	24.33	22.10	16.55	12.60	10.08	9.582	9.582
5	5.297	4.949	4.419	4.056	3.781	4.438	4.438
10	3.002	2.936	2.863	2.818	2.782	3.597	3.597
20	1.853	1.861	1.909	1.963	2.010	2.703	2.704
30	1.479	1.497	1.560	1.630	1.693	2.316	2.316
<i>Vertex downstream</i>							
1	24.29	22.03	16.72	12.84	10.31	5.765	5.901
5	5.359	4.997	4.490	4.134	3.862	3.126	3.862
10	3.141	3.062	2.944	2.871	2.818	2.664	2.818
20	2.082	2.055	2.057	2.085	2.116	2.112	2.021
30	1.788	1.757	1.760	1.797	3.860	1.854	1.967

From Ref. [52].

drag coefficient are included here. The drag is seen to be increased in shear-thinning fluids in the steady flow regime, but its dependence on power-law index switches over in the time-periodic regime. This is so presumably due to the fact that the wakes are shorter in shear-thinning fluids which tend to oscillate/shed with a higher frequency than that in Newtonian fluids. Overall, the functional relationship seen in Fig. 34 is found to be qualitatively similar to that reported for a sphere [22,176–178] or a circular cylinder, as seen in the preceding section. Table XIV presents a compilation of numerical drag values from various studies showing their internal consistency. For the steady flow regime, one can unambiguously define the wake length. On the other hand, in the time-dependent flow regime, one needs to introduce the notion of the time-averaged wake

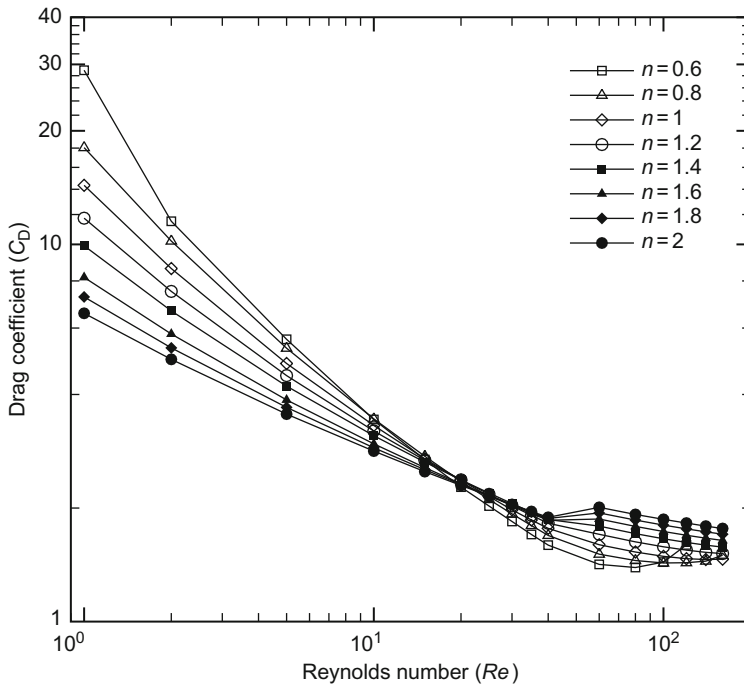


FIG. 34. Dependence of drag coefficient (for a square cylinder) on power-law index and Reynolds number.

length over a finite number of cycles. Following this strategy, Fig. 35 shows the variation of the recirculation length spanning both the steady and the fully periodic flow regimes. While in the steady flow regime, the recirculation length shows the expected positive dependence on the Reynolds number (being shorter in shear-thinning fluids than that in Newtonian media), but it is seen to drop with Reynolds number in the time-periodic regime. The exact reasons for this behavior are not fully known [172,173], but a possible reason for this behavior is that under certain conditions (low values of n and/or high Re), the flow does not reattach itself at the top corner and therefore the two separated regions coalesce into one thereby increasing the width of the “modified” wake in the lateral direction and shortening it in the axial direction. This behavior is observed only for unconfined flow conditions.

The imposition of moderate confinement (up to 50%) does not seem to change the fundamental nature of the flow except for the fact that the solid walls seem to have a stabilizing influence on the flow and, of course, the drag is somewhat augmented due to the additional viscous dissipation at the solid boundaries.

TABLE XIV
NUMERICAL VALUES OF PRESSURE AND TOTAL DRAG COEFFICIENTS FOR A SQUARE CYLINDER
IN POWER-LAW FLUIDS

Re	Pressure drag coefficient, C_{DP}								
	$n = 0.5$	$n = 0.6$	$n = 0.8$	$n = 1$	$n = 1.2$	$n = 1.4$	$n = 1.6$	$n = 1.8$	$n = 2$
1	26.62	30.16	34.24	37.54	40.72	43.91	47.31	50.80	54.55
2	13.66	15.25	17.34	18.99	20.56	22.15	23.84	25.58	27.46
5	7.074	7.404	7.435	7.973	8.577	9.210	9.914	10.63	11.34
10	3.835	3.976	4.222	4.508	4.803	5.103	5.460	5.818	6.166
15	3.032	3.082	3.222	3.414	3.609	3.812	4.037	4.271	4.520
20	2.623	2.628	2.735	2.883	3.035	3.191	3.363	3.546	3.729
25	2.332	2.333	2.438	2.568	2.698	2.828	2.969	3.112	3.267
30	2.157	2.153	2.239	2.358	2.477	2.589	2.712	2.833	2.967
35	1.757	2.017	2.097	2.207	2.315	2.420	2.529	2.636	2.754
40	1.909	1.918	1.988	2.093	2.195	2.292	2.393	2.491	2.596
45	1.846	1.843	1.908	2.004	2.102	2.194	2.287	2.378	2.475
60	1.413	1.407	1.429	1.453	1.504	1.538	1.568	1.594	1.622
80	1.462	1.438	1.430	1.442	1.488	1.520	1.548	1.573	1.597
100	1.689	1.515	1.447	1.441	1.482	1.510	1.537	1.561	1.584
120	—	1.669	1.476	1.452	1.481	1.506	1.530	1.553	1.576
140	—	—	1.503	1.467	1.484	1.504	1.527	1.548	1.568
160	—	—	1.562	1.483	1.491	1.505	1.525	1.545	1.564
Total drag coefficient, C_D									
1	26.62	30.16	34.24	37.54	40.72	43.91	47.31	50.80	54.55
2	13.66	15.25	17.34	18.99	20.56	22.15	23.84	25.58	27.46
5	7.074	7.404	7.435	7.973	8.577	9.210	9.914	10.63	11.34
10	3.835	3.976	4.222	4.508	4.803	5.103	5.460	5.818	6.166
15	3.032	3.082	3.222	3.414	3.609	3.812	4.037	4.271	4.520
20	2.623	2.628	2.735	2.883	3.035	3.191	3.363	3.546	3.729
25	2.332	2.333	2.438	2.568	2.698	2.828	2.969	3.112	3.267
30	2.157	2.153	2.239	2.358	2.477	2.589	2.712	2.833	2.967
35	1.757	2.017	2.097	2.207	2.315	2.420	2.529	2.636	2.754
40	1.909	1.918	1.988	2.093	2.195	2.292	2.393	2.491	2.596
45	1.846	1.843	1.908	2.004	2.102	2.194	2.287	2.378	2.475
60	1.413	1.407	1.429	1.453	1.504	1.538	1.568	1.594	1.622
80	1.462	1.438	1.430	1.442	1.488	1.520	1.548	1.573	1.597
100	1.689	1.515	1.447	1.441	1.482	1.510	1.537	1.561	1.584
120	—	1.669	1.476	1.452	1.481	1.506	1.530	1.553	1.576
140	—	—	1.503	1.467	1.484	1.504	1.527	1.548	1.568
160	—	—	1.562	1.483	1.491	1.505	1.525	1.545	1.564

In a very recent study, Rao et al. [179] have studied the momentum and heat transfer characteristics of a slanted (45°) square cylinder. This configuration seemingly offers some enhancement in convective heat transfer over that for its straight configuration, as well be seen in the ensuing section on heat transfer. In the steady flow regime, Fig. 36 shows the well-formed separated flow

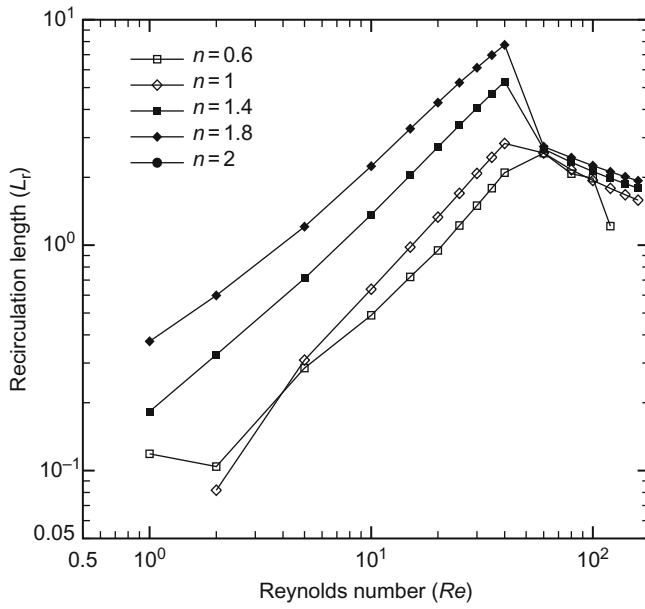


FIG. 35. Variation of wake length with power-law index and Reynolds number for a square cylinder.

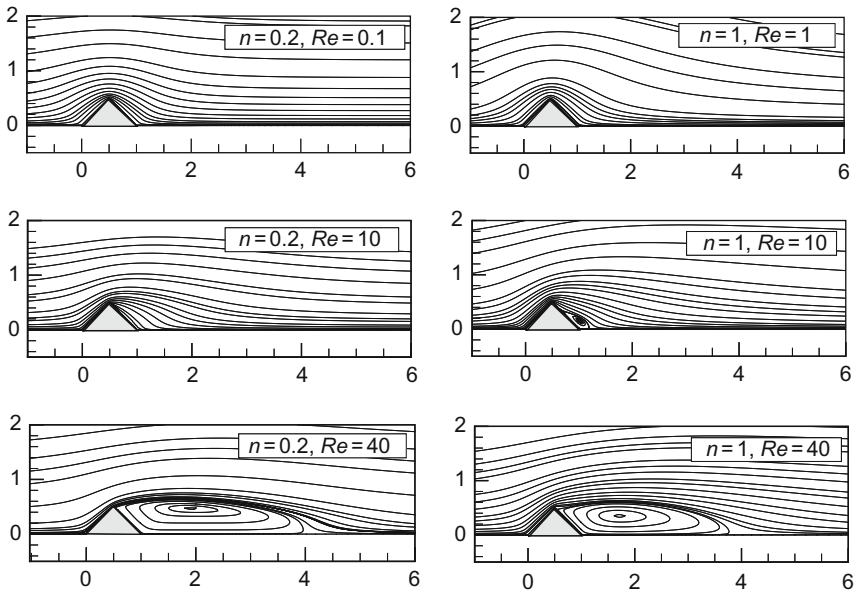


FIG. 36. Streamline patterns and wake region for a tilted square cylinder in power-law fluids [179].

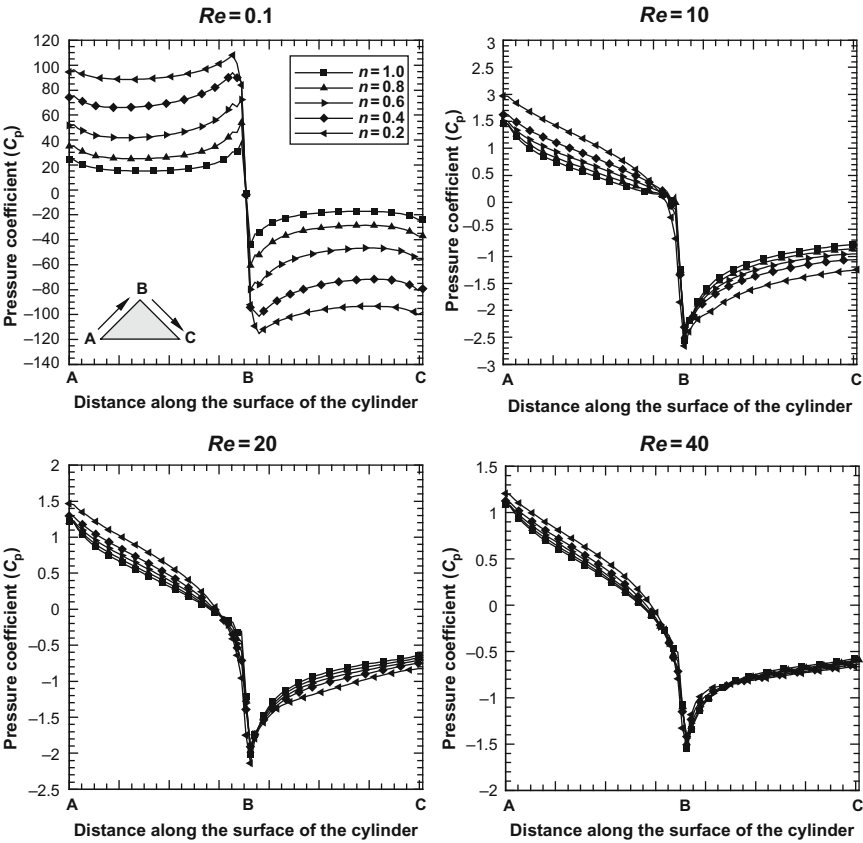


Fig. 37. Typical pressure distribution over the surface of a tilted square cylinder [179].

region which tends to be slightly larger than that for a normal square cylinder under otherwise identical conditions. Owing to the shape effects, surface pressure distribution in this case is significantly different here (Fig. 37), though the drag coefficient exhibits the classical inverse dependence on the Reynolds number (Fig. 38). Once again, the drag is seen to be increased in shear-thinning fluids by up to 100%, but the role of power-law index progressively vanishes with the increasing Reynolds number. Similarly, there has been a preliminary study [180] which examined the momentum and heat transfer characteristics from a two-dimensional prism of rectangular cross section in the power-law fluids in the steady flow regime. The side of the rectangular prism in the direction of flow was twice as long as the one in the transverse direction. The role of power-law index on drag and Nusselt number was found to be qualitatively similar to that reported for a square cylinder [169–171].

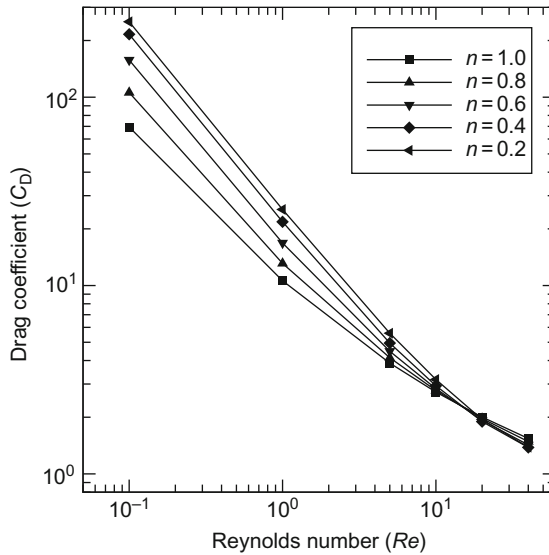


FIG. 38. Drag coefficient—Reynolds number relationship in power-law fluids for a tilted square cylinder [179].

This section is concluded by noting that this branch of power-law fluid dynamics is still in its infancy, as can be gaged from the foregoing scant literature, even for the circular cylinder; the other shapes have received even less attention. Furthermore, there has been a very little experimental activity also in this domain. It is hoped that the numerical results summarized here will not only be extended to the other flow regimes and/or configurations, but will also act as a stimulant to trigger experimental activity in this field.

VI. Heat Transfer

Depending upon the prevailing flow conditions (e.g., value of Reynolds number, value of ΔT , and density—temperature relationship for liquid), heat transfer can occur in pure free (natural), forced or mixed convection regimes. Owing to the inherent differences in the underlying physical mechanisms, the governing differential equations and the corresponding pertinent dimensionless groups vary from one regime to another. For instance, as seen in Section III, the Reynolds and Prandtl numbers are the main parameters influencing the rate of heat transfer in the forced convection regime, whereas the Grashof number plays the same role in free convection as the Reynolds number in forced

convection. As expected, an additional parameter (Richardson number, Ri , for instance) is required to quantify the relative importance of the free and forced convection in the mixed regime. Thus, free convection is characterized by large values of Ri whereas $Ri = 0$ denotes the forced convection regime. Additional complications arise from the type of the boundary condition (for heat transfer) prescribed on the surface of the immersed body. In fluid mechanics, it is customary to employ the usual no-slip boundary condition on solid surfaces. However, from a heat transfer view, the boundary conditions on solid surfaces can be quite complex including that of a CWT, CHF, variable temperature, or heat flux or combinations thereof, albeit the use of CWT or CHF is most common in the numerical modeling of heat transfer in such situations. Finally, it is readily acknowledged that the thermophysical properties of the liquid medium (density ρ , thermal conductivity k , heat capacity C , viscosity, m and n) all exhibit varying levels of dependence on temperature. Indeed, temperature-dependent density plays a central role in the free and mixed convection heat transfer. While the thermal conductivity and heat capacity of most liquids are relatively insensitive to moderate temperature variations, the temperature dependence of the viscosity cannot be generally overlooked even for Newtonian fluids, for example, see Refs. [181–183]. Similarly, the flow properties of non-Newtonian substances also exhibit varying levels of dependence on temperature. For instance, for power-law fluids, the available scant experimental evidence suggests that power-law index, n , is fairly robust against 20–30 K temperature variation, but the power-law consistency index, m , exhibits classical exponential dependence on temperature ([9,18,21,27], for instance). Incorporation of such effects into analysis or interpretation of exponential data warrants the introduction of additional dimensionless groups thereby adding to the degree of complexity. From a theoretical standpoint, when the maximum temperature difference present in the system ($T_w - T_\infty$) is such that it is justified to ignore the variation in the values of the aforementioned properties including density, it is possible to solve the flow and energy equations in an independent manner. On the other hand, if it is not possible to ignore the temperature dependence, the flow and energy equations become coupled whence must be solved simultaneously. With this short discussion, it is convenient to return to the classification scheme used in previous sections based on the shape of the submerged obstacle with further subclassification based on the regime and/or boundary conditions imposed on the surface of the cylinder.

A. CIRCULAR CYLINDER

Over the years, significant advances have been made as far as heat transfer from a circular cylinder in Newtonian fluids is concerned. Indeed based on a

combination of analytical, numerical, and experimental results, it is now possible to estimate the value of the convective heat transfer coefficient over most conditions of practical interest. Excellent survey articles together with a critical assessment of the various predictive formulae are available in the literature [1–3,184–195]. Suffice it to add here that, even in Newtonian fluids, forced convection regime has been investigated most extensively, whereas the free and mixed-convection regimes have received relatively less attention. Despite this deficiency, adequate information is now available enabling the estimation of the convective heat transfer coefficient over the entire range of conditions of practical interest. In contrast, as will be seen below, the analogous information for non-Newtonian fluids is indeed very limited. We begin with the discussion of heat transfer in the forced convection regime [24,25].

1. Forced Convection Regime

Most of the available approximate analytical, numerical, and experimental studies are based on the use of the simple power-law model [115,117,118,128,168,196–210]. Early studies are based on the applicability of the thin boundary layer approximation which implicitly assume large values of Reynolds number and/or of Prandtl number. Under these conditions, one can possibly ignore the curvature effects to simplify the analyses of the governing boundary layer equations. Acrivos and coworkers [115,117] and subsequently others [196–206] have made pioneering contributions based on this approach. Obviously, this approach cannot describe the wake region nor it is possible to delineate the limiting values of the Reynolds number and Prandtl number above which these results can be used. Despite these deficiencies, this approach has yielded reasonable scalings of the Nusselt number with the Reynolds and Prandtl numbers. In order to predict the rate of heat transfer at finite values of the Reynolds and Prandtl numbers, one must seek numerical solutions to the momentum and energy equations. It is rather surprising that the first complete numerical study was reported only in 2005 [128]. Soares et al. [128] reported scant heat transfer results in the steady flow regime ($5 \leq Re \leq 40$) encompassing a 100-fold variation in the value of Prandtl number over the power-law index range as $0.5 \leq n \leq 1.4$. They employed both types of thermal boundary conditions on the surface of the cylinder, i.e., CWT and CHF. Their key finding is that it is possible to enhance the rate of heat transfer in shear-thinning fluids ($n < 1$) by up to about 25% over that observed in Newtonian fluids otherwise under identical conditions. This was attributed to the lower effective viscosity of the fluid in the immediate vicinity of the heated cylinder. Conversely, shear-thickening fluid behavior was shown to adversely influence heat transfer. Following this preliminary study, Bharti et al. [207,208] reported a much more detailed and systematic study of forced

convection heat transfer from a cylinder in power-law fluids spanning the ranges of conditions as: $0.6 \leq n \leq 2$, $1 \leq Pr \leq 1000$, and $5 \leq Re \leq 40$. However, the maximum value of the Peclet number, $Pe = Re \cdot Pr$, was restricted to 5000 and the maximum value of the Reynolds number is such that the flow is likely to be steady under these conditions. Figures 39 and 40 show representative results highlighting the combined influence of the Reynolds number, Prandtl number, power-law index, and the type of boundary condition on the local Nusselt number variation on the surface of the cylinder. While the value of the Nusselt number for the CHF condition tends to be a little higher than that for the CWT condition at fixed values of n , Re , Pr , the dependence of the Nusselt number is seen to be qualitatively similar for the two boundary conditions. At low values of Re or Pr or both, irrespective of the type of thermal boundary condition and the value of n , the Nusselt number varies very little over the surface of the cylinder. This is simply so due to the fact that at such small values of the Peclet number, advection is weak and heat transfer occurs mainly by conduction. However, as the value of the Reynolds number or Prandtl number or both is progressively increased, advection becomes stronger and the Nusselt number can vary by a factor of 5–8 from its value at the front and rear stagnation points. Undoubtedly, the temperature gradient is maximum at the front stagnation point irrespective of the type of fluid behavior. While for a Newtonian fluid the viscosity is constant, the local Nusselt number decreases from its maximum value at the front stagnation point ($\theta = 0$) all the way to the rear stagnation point ($\theta = \pi$) provided the flow does not separate from the surface of the cylinder. This behavior is clearly seen in Fig. 39. On the other hand, once the flow detaches itself, the Nusselt number decreases continually from $\theta = 0$ to θ_s (point of flow separation) and Nusselt number increases over the surface $\theta_s \leq \theta \leq \pi$ due to the enhanced fluid circulation in this region. This behavior is clearly seen in Fig. 40 for Newtonian fluids. However, for power-law fluids, not only the temperature gradient but also the velocity gradient (and hence local viscosity) varies along the surface. While the rate of heat transfer is directly proportional to the temperature gradient, increasing viscosity will impede convection and decreasing viscosity will promote heat transfer. For a power-law fluid, the rate of change of viscosity with shear rate is given by $(d\eta/d\dot{\gamma}) \propto (n-1)(\dot{\gamma})^{n-2}$. For shear-thinning fluids ($n < 1$), the rate of decrease of viscosity with shear rate, i.e., $(d\eta/d\dot{\gamma}) < 0$ and it would be given by $(d\eta/d\dot{\gamma}) > 0$ for shear-thickening fluids. Thus, the local Nusselt number at a point on the surface of the cylinder is determined by the complex interplay between these competing mechanisms. For shear-thickening fluids, both mechanisms seem to go hand in hand, thereby resulting in the faster spatial decay with θ on the surface of the cylinder than that in Newtonian fluids. This behavior is clearly seen at $n = 2$ in Figs. 39 and 40. On the other hand, in shear-thinning fluids, the initial increase in the local Nusselt number is due to the decreasing viscosity and the subsequent downward curve is

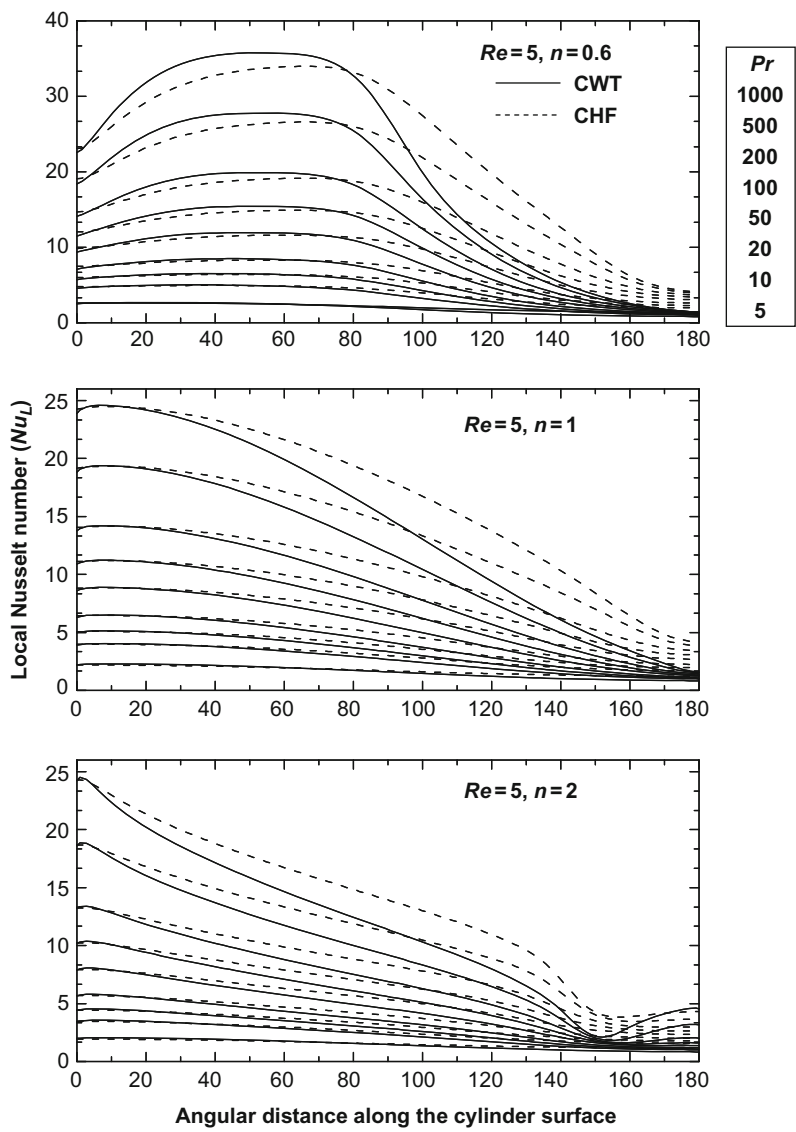


FIG. 39. Local Nusselt number distribution over the surface of a circular cylinder as a function of n and Pr for the CHF and CWT boundary conditions at $Re = 5$. Adapted from Ref. [207].

probably influenced much more by the temperature gradient than the change in local viscosity. The two effects nullify each other somewhere in between thereby leading to the maximum value of Nusselt number at locations other than $\theta = 0$. Indeed, qualitatively similar trends have been reported for a sphere

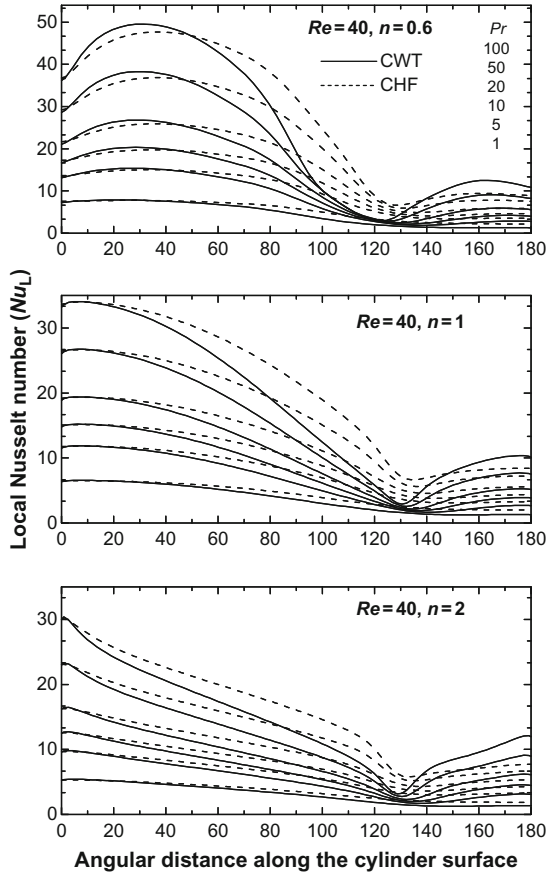


FIG. 40. Local Nusselt number distribution over the surface of a circular cylinder as a function of n , Re , and Pr for the CHF and CWT boundary conditions at $Re = 40$. Adapted from Ref. [207].

also [211, 211a]. Bharti et al. [207] were able to correlate the Nusselt number at the front stagnation point as:

$$Nu(\theta = 0) = \phi(n)Re^a Pr^b \Delta^c \quad (38)$$

where $\Delta = ((3n + 1)/4n)$

Note that $\Delta > 1$ for shear-thinning fluids and $\Delta < 1$ for shear-thickening fluids. For the CWT condition, the values of the constants are as follows: $a = 0.532$, $b = 0.348$, $c = 0.229$, and $\phi(n) = 0.932^n$. The corresponding values for the CHF case are $a = 0.533$, $b = 0.347$, $c = 0.4$, and $\phi(n) = 0.947^n$, respectively. Note that the values of a are nearly in line with the expected \sqrt{Re}

dependence as predicted by the laminar boundary layer analysis and the values of b also conform to the customary $Nu \sim Pr^{1/3}$ dependence.

While the local Nusselt number distribution on the surface of the cylinder provides insights regarding the relative contribution of different parts of the surface to the overall heat transfer, it is often required in process engineering calculations to estimate the rate of heat transfer when both temperatures are known, or to estimate one of the temperatures if the heat flux is known. This calculation necessitates the value of the surface averaged heat transfer coefficient or Nusselt number. The available boundary layer analyses suggest that the thermal boundary layers tend to be thinner in shear-thinning fluids than that in Newtonian fluids at fixed values of Re and Pr . Therefore, it is reasonable to expect a positive correlation between the mean Nusselt number and both the Reynolds and Prandtl numbers. At fixed values of Re and Pr , one can anticipate some enhancement in Nusselt number in shear-thinning fluids, and some deterioration in shear-thickening fluids. Indeed all these conjectures are borne out by the results of Soares et al. [128] and Bharti et al. [207,208], as can be seen in Fig. 41. In order to reconcile the results for wide-ranging values of the Prandtl number, it is customary to employ the so-called Colburn j -factor defined as follows:

$$j = \frac{Nu}{RePr^{1/3}} \quad (39)$$

Bharti et al. [207] correlated their numerical results using the following generic form of the functional relationship:

$$j = \frac{a_0}{n^{a_1} Re^{a_2}} \quad (40)$$

The best values of a_0 , a_1 , and a_2 are 0.761, 0.413, and 0.561, respectively, for the CWT condition. The corresponding values are 0.861, 0.43, and 0.556, respectively, for the CHF case.

Beyond the steady flow regime, there has been only one study [209] which reported the forced convection heat transfer characteristics of a circular cylinder in the laminar vortex shedding regime of power-law fluids. Patnana et al. [209] reported the time-averaged values of the Nusselt number for the CWT condition at $Re = 40, 50, 100, 120$, and 140 spanning the ranges of the other parameters as $0.4 \leq n \leq 1.8$ and $1 \leq Pr \leq 100$. The range of the Reynolds number is such that the flow is expected to be two-dimensional and laminar. While the detailed listing of numerical results can be found in their original paper [209], the key findings can be summarized as follows: shear-thinning can augment the value of the Nusselt number by up to ~ 50 – 60% under appropriate conditions, whereas shear-thickening can impede it up to ~ 10 – 15% with reference to the corresponding value in Newtonian media otherwise under

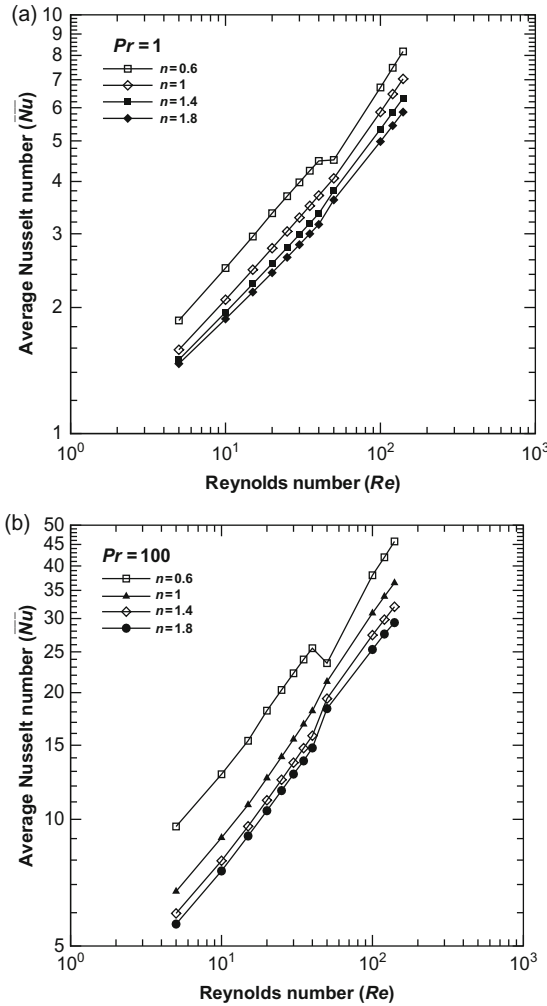


FIG. 41. Dependence of Nusselt number on Reynolds number and power-law index. (a) $Pr = 1$ and (b) $Pr = 100$.

identical conditions. Their numerical results are well approximated by the following analytical expression:

$$Nu_{\text{avg}} = 0.36 Re^{0.6} Pr^{0.36} \Delta \quad (41)$$

Equation (41) correlates their [209] numerical results with an average error of $\sim 5\%$.

The effect of planar confinement on Nusselt number for the circular cylinder in the steady flow regime has been studied by Bharti et al. [208] for the CWT condition. This study spans the ranges of conditions as follows: $1 \leq Re \leq 40$, $0.2 \leq n \leq 1.8$, $1 \leq Pr \leq 100$, and $\delta = 0.25$ and 0.67 . As expected, for fixed values of n and δ , the average Nusselt number exhibits positive dependence on both Reynolds and Prandtl numbers. The presence of the confining walls sharpens the temperature and velocity gradients close to the cylinder, and therefore it is fair to postulate that, all else being equal, confinement can enhance the rate of heat transfer between the fluid and the cylinder. Indeed, this conjecture is also well supported by the results of Bharti et al. [208].

It is worthwhile to add here that the aforementioned numerical studies are based on the assumption of the constant thermophysical properties thereby allowing the momentum and thermal energy equations to be solved independently of each other. Soares et al. [210] have examined the influence of the temperature-dependent power-law viscosity on convective heat transfer from a cylinder in the steady flow regime ($Re \leq 30$). They assumed the flow behavior index to be temperature-independent and the power-law consistency index to vary exponentially with temperature (similar to the Arrhenius form). One would expect this dependence to promote the rate of heat transfer from a heated cylinder. However, for the reverse case of a cold cylinder submerged in a heated power-law fluid, it is not expected to be so. Obviously, it is not possible to provide valid generalizations because the severity of temperature-dependence varies from one substance to another. Qualitatively, this finding is also in line with that reported by others for a cylinder [183] and for a sphere [212] as well as with the experimental results which entail an empirical correction factor of the form $(\eta_b/\eta_w)^{0.14}$.

The aforementioned scant numerical studies have also been supplemented by a few experimental studies dealing with heat and mass transfer from cylinders in flowing power-law fluids [213–222]. Unfortunately, most of these either relate to viscoelastic fluids [221,222] or to the values of the Prandtl and/or Reynolds numbers which are at least an order of magnitude higher than that spanned by the currently available numerical predictions [217,220]. On the other hand, Ghosh et al. [25] have compiled limited mass transfer data for a cylinder in cross-flow of power-law fluids, and by invoking the usual heat and mass transfer analogy, it is possible to make a comparison with the numerical predictions presented in the preceding section. Ghosh et al. [25,219] reported the following correlation over the range of conditions ($0.72 \leq n \leq 1$, $Re \leq \sim 513$):

$$Nu = A_1 Re^{A_2} Pr^{1/3} \quad (42)$$

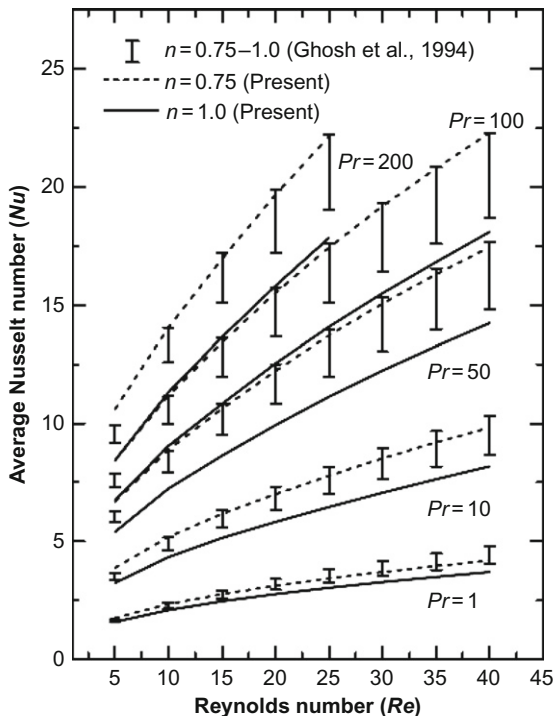


FIG. 42. Typical comparison between the experimental [25] and predicted [208,209] values of average Nusselt number for a circular cylinder (replotted from ref. [207]).

For $Re \leq 10$:

$$A_1 = 2.26; \quad A_2 = (1/3) + \frac{n-1}{3(n+1)} \quad (43a)$$

For $Re \geq 10$:

$$A_1 = 0.785; \quad A_2 = 0.5 + \frac{n-1}{3(n+1)} \quad (43b)$$

Figure 42 shows a representative comparison between the experimental values estimated using Eq. (42) and the numerical predictions [207,208]. The correspondence is seen to be less satisfactory and this is so partly due to the finite wall effects and end effects present in the experiments which are obviously not incorporated in these simulations. Finally, Fig. 43 shows a typical

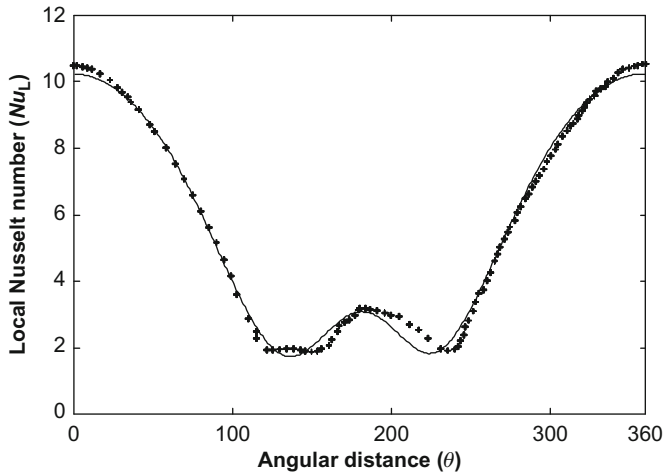


FIG. 43. Typical comparison between experimental (+) [223] and predicted (line) [208,209] local Nusselt number distribution on the surface of the cylinder in air at $Re = 120$.

comparison between the experimental [223] and predictions of the local Nusselt number in air at $Re = 120$. Such a close correspondence inspires confidence in the reliability of numerical simulations reported for heat transfer in power-law fluids also, albeit no such detailed experimental results are available in polymer solutions.

2. Free Convection Regime

Unlike in forced convection, since heat is transported entirely by the buoyancy induced flow currents in the natural or free convection regime, the orientation of the cylinder has a profound effect on the resulting rate of heat transfer. Indeed all else being equal, the value of the Nusselt number can vary appreciably from a horizontal to a vertical cylinder and from the intermediate inclined configurations [192]. This section is thus concerned with the free convection heat transfer from a horizontal heated cylinder. As noted earlier, from a theoretical standpoint, the governing equations are coupled via the body force term in the momentum equation. Early studies in this field even for Newtonian fluids exploited the boundary layer approach, for example, see Refs. [224–227]. The assumption of high Rayleigh numbers is implicit in all such analyses to justify the thin boundary layer approximation with negligible curvature effects. Similarly, the other limit of low values of the Rayleigh number can be approached via the well-known matched asymptotic analysis [192].

Obviously, neither of these approaches is applicable for finite values of the Grashof number or Prandtl number or Rayleigh number. Furthermore, the aforementioned studies also relate to the case of CWT condition. Wilks [228] extended the boundary layer analysis to the CHF condition. Indeed, the first steady and transient numerical simulations of free convection from a horizontal circular cylinder even in Newtonian fluids like air and water were reported only about 30 years ago [229–237] and are still restricted to the laminar flow regime. However, such numerical results together with the available experimental results have led to the development of reliable archival correlations which allow the prediction of the convection heat transfer coefficient for a horizontal circular cylinder (CWT) in the free convection regime over wide ranges of conditions. One such correlation due to Fand et al. [190] is given here:

$$Nu_{\text{avg}} = 0.474 Ra_D^{0.25} Pr^{0.047} \quad (44)$$

Equation (44) embraces the ranges of the Prandtl number and Rayleigh number as $0.7 \leq Pr \leq \sim 3100$ and $250 \leq Ra_D \leq 1.8 \times 10^7$. The correspondence between the numerical values and these predicted using Eqs. (41a) and (41b) has been found to be excellent [238].

For power-law fluids, Acrivos [239] was seemingly the first to develop an approximate boundary layer treatment for free convection from axisymmetric shapes (including a cylinder) in non-Newtonian fluids. By an appropriate choice of a shape factor, his results can be specialized for a sphere, or a cylinder or a plane surface. Subsequent similar analyses [201,240] confirm that the results of Acrivos [239] are reliable at large values of the Grashof and Prandtl numbers. Indeed, only recently an extensive study [238] has been reported on laminar free convection from a horizontal heated (CWT) circular cylinder in power-law fluids which encompasses the ranges of conditions as $0.72 \leq Pr \leq 100$, $10 \leq Gr \leq 10^5$, and $0.3 \leq n \leq 1.8$. Figure 44 shows representative results elucidating the influence of Grashof number, Prandtl number, and power-law index on the distribution of the local Nusselt number on the surface of the cylinder. The range of the Grashof number is such that the flow remains attached to the surface of the cylinder, and therefore the Nusselt number decreases continually along the surface of the cylinder in Newtonian and shear-thickening fluids, whereas it exhibits its maximum value slightly away from the front stagnation point in shear-thinning fluids; the latter behavior was explained via the inherently different scaling of the viscous forces on velocity in shear-thinning and shear-thickening fluids as postulated in the preceding section in the context of the forced convection regime. In view of the trends present in Fig. 44, one would intuitively expect to see a positive correlation between the Nusselt number on one hand and the Grashof and Prandtl numbers on the other. Similarly, all else being equal, boundary layers tend to be thinner

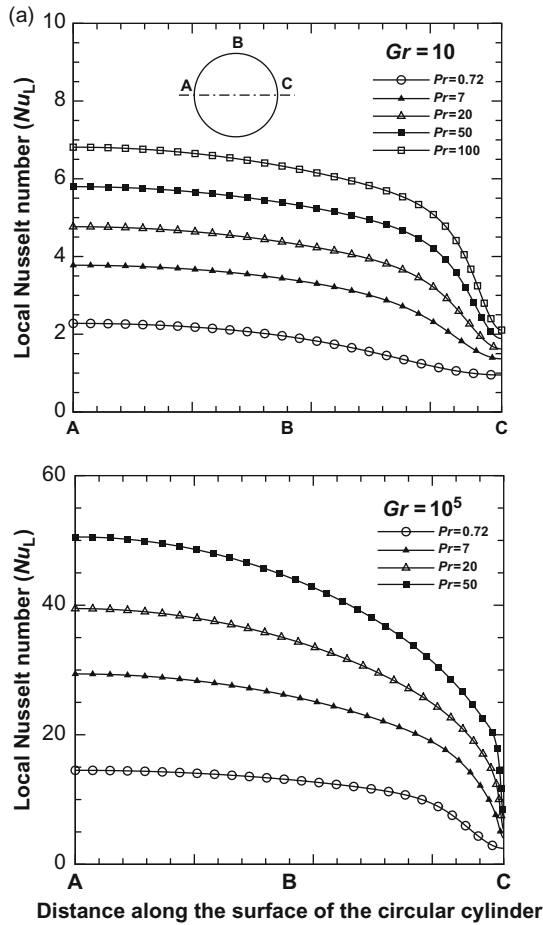


FIG. 44. Effect of Grashof number, Prandtl number, and power-law index on the variation of local Nusselt number on the surface of an isothermal circular cylinder. (a) $n = 1$, (b) $n = 0.3$, and (c) $n = 1.8$. From Ref. [238].

in shear-thinning ($n < 1$) fluids than that in Newtonian media and this implies that shear-thinning behavior facilitates heat transfer. Conversely, shear-thickening behavior ($n > 1$) impedes it. Indeed all these conjectures are well borne out by the results of Prhashanna and Chhabra [238] who correlated the surface averaged values of the Nusselt number as follows:

$$Nu_{avg} = 1.19\Omega^{0.59} \quad (45)$$

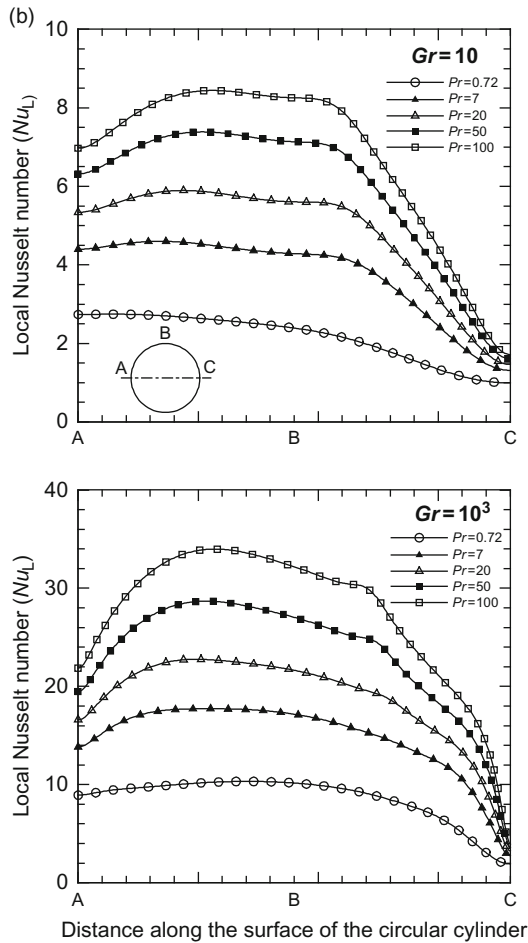


FIG. 44. (Continued).

where

$$\Omega = Gr^{1/2(n+1)} Pr^{n/(3n+1)} \tag{46}$$

Equation (46) was stated to reproduce their numerical data with an average error of about 7%. Furthermore, Eq. (46) also indicates the increasing influence of Grashof number with the decreasing value of the power-law index which is also consistent with the findings of Acrivos [239]. Indeed, the

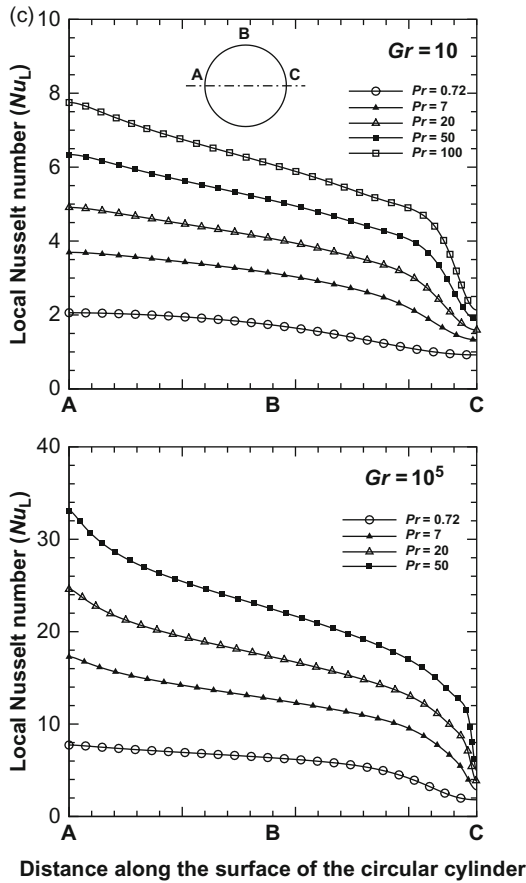


FIG. 44. (Continued).

predictions of Eq. (45) are fairly close to that of Acrivos [239] for $\Omega > 10$, and therefore this might be interpreted as the limiting value below which the boundary layer approach is likely to be inapplicable. Also, attention is drawn to the fact that in the limiting case of Newtonian fluid behavior ($n = 1$), Eq. (45) reduces correctly to the expected forms.

Limited experimental results on free convection heat transfer from horizontal cylinders in polymer solutions are available [241–246]; however, some of these relate to the dilute drag reducing polyox solution [241] or viscoelastic fluids [246] thereby rendering them unsuitable for comparison with Eq. (45) which accounts for neither of these fluid characteristics. On the other hand,

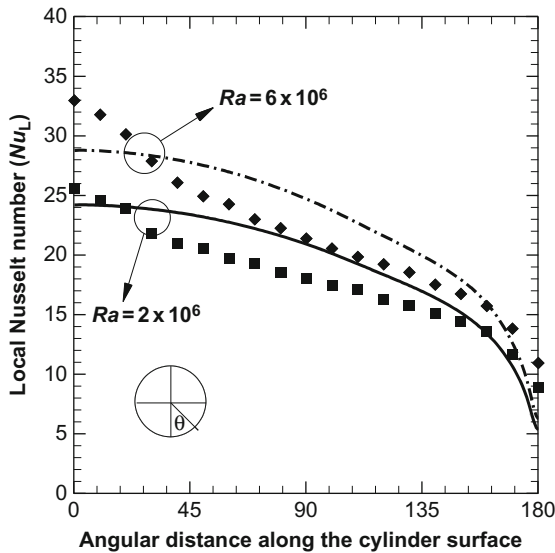


FIG. 45. Typical comparison between the predictions (lines) [238] and experimental (symbols) [286] results on free convection from a horizontal cylinder in water.

Gentry and Wollersheim [242] and others [243,244] have not presented sufficient experimental details for their results to be recalculated in the format consistent with Eq. (45). Scant experimental results on free convective heat and mass transfer from vertical cylinders are also available in the literature [247,248]. Figure 45, however, shows a representative comparison between observations and predictions of free convection from a heated horizontal cylinder in water.

3. Mixed Convection Regime

This mode of heat transfer exhibits yet another complexity which stems from the fact that the direction of the imposed flow vis-à-vis that of the buoyancy induced flow exert an appreciable influence. For instance, when the cylinder is at a higher temperature than the ambient fluid, buoyancy-induced flow in the proximity of the heated cylinder will be in upward direction. An imposed flow in upward direction will facilitate heat transfer due to the so-called aiding buoyancy configuration. Likewise, a downward imposed flow will have an adverse influence on the overall rate of heat transfer due to the so-called opposing buoyancy effect. Yet another possibility exists when the

imposed flow is transverse to the direction of gravity vector, the so-called cross-buoyancy effect. From another vantage point, this flow is more complex to analyze theoretically also due to the fact, for instance, that the cross-flow can induce asymmetry in the flow field thereby inducing a lift force exerted on the cylinder. Similarly, depending upon the value of the Reynolds number and configuration, the presence of buoyancy-induced flow can act to stabilize or destabilize the flow thereby leading to transition from one flow regime to another at values of the parameters which can differ significantly from the corresponding values in isothermal conditions. Therefore, experimental [249,250] and numerical [251–254] results are very limited in this regime even in Newtonian fluids. Similarly, for the case of aiding-buoyancy, Collis and Williams [255] argued that the effect of aiding buoyancy can be neglected below the value of $Re = 1.85Gr^{0.35}$ whereas Fand and Keswani [256] reported four subregimes for this configuration. Using their experimental results in water, heat transfer occurs predominantly by forced convection for $Ri \leq \sim 0.5$. In the second regime $\sim 0.5 \leq Ri \leq \sim 2$, free convection contributes up to 10% to the overall heat transfer. In the range $2 \leq Ri \leq 40$, both natural and forced convections contribute, approximately equally but the value of the heat transfer oscillates with a random period of oscillations. Finally, heat transfer is dominated by natural convection for $Ri > 40$. Other experimental studies in the aiding/opposing-buoyancy cases are due to Villimpoc et al. [257], Sarma and Sukhatme [258], etc. While the early boundary layer solutions for aiding/opposing configurations are due to Sparrow and Lee [259], the results based on the complete Navier–Stokes equations have been initiated by Badr and coworkers [251,260–264]. The effect of heating/cooling of a cylinder on the vortex shedding characteristics has been studied by Chang and Sa [265] and Patnaik et al. [266]. Detailed accounts of the studies dealing with the aiding—and cross-buoyancy cases of mixed convection from a horizontal circular cylinder in Newtonian fluids are available elsewhere [267,268].

For power-law fluids, there have been only two preliminary studies on mixed convection from a circular cylinder [267,268]. Soares et al. [267] investigated the effect of cross-buoyancy on the structure of the flow field and Nusselt number in the so-called steady flow regime for limited values of the influencing parameters as $Pr = 1$ and 100 , $n = 0.6, 0.8, 1$, and 1.6 , $Re \leq 30$, and $Ri \leq 3$. However, they assumed *a priori* the flow to be steady and thus sought only the steady state solution. Figure 46 shows the combined effects of Re , Pr , n , and Ri on the streamline patterns where increasing asymmetry is seen to be present with the increasing value of the Richardson number. Broadly, all else being equal, the average Nusselt number was seen to be augmented by up to 10–15% under appropriate values of the Re , Pr , n , and Ri . This study is supplemented by that of Srinivas et al. [268] who studied the analogous configuration of aiding-buoyancy. They also assumed the flow to be

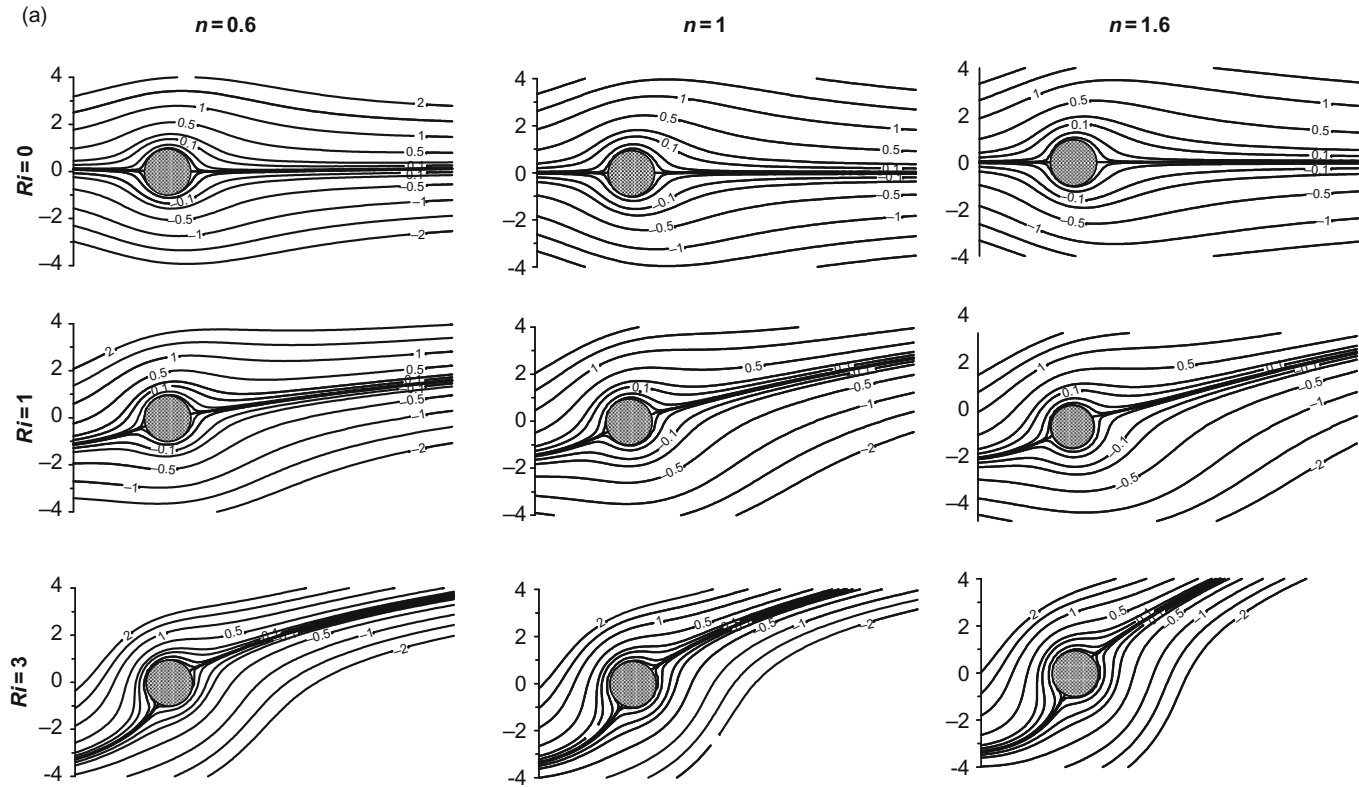


FIG. 46. Asymmetric streamline patterns in mixed convection heat transfer from a heated cylinder in power-law fluids. (a) $Re = 1$, $Pr = 1$; (b) $Re = 1$, $Pr = 100$; (c) $Re = 30$, $Pr = 1$; and (d) $Re = 30$, $Pr = 100$. From Ref. [267].

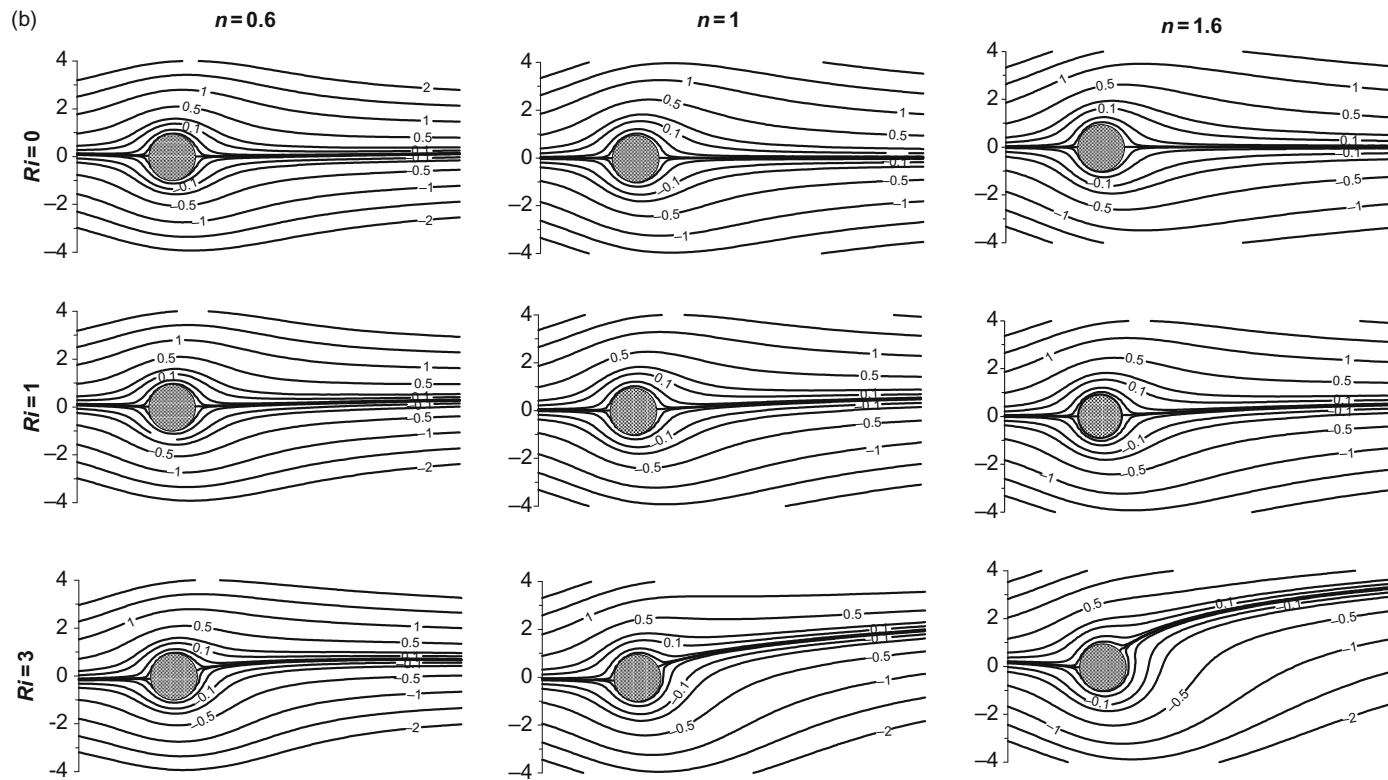


FIG. 46. (Continued).

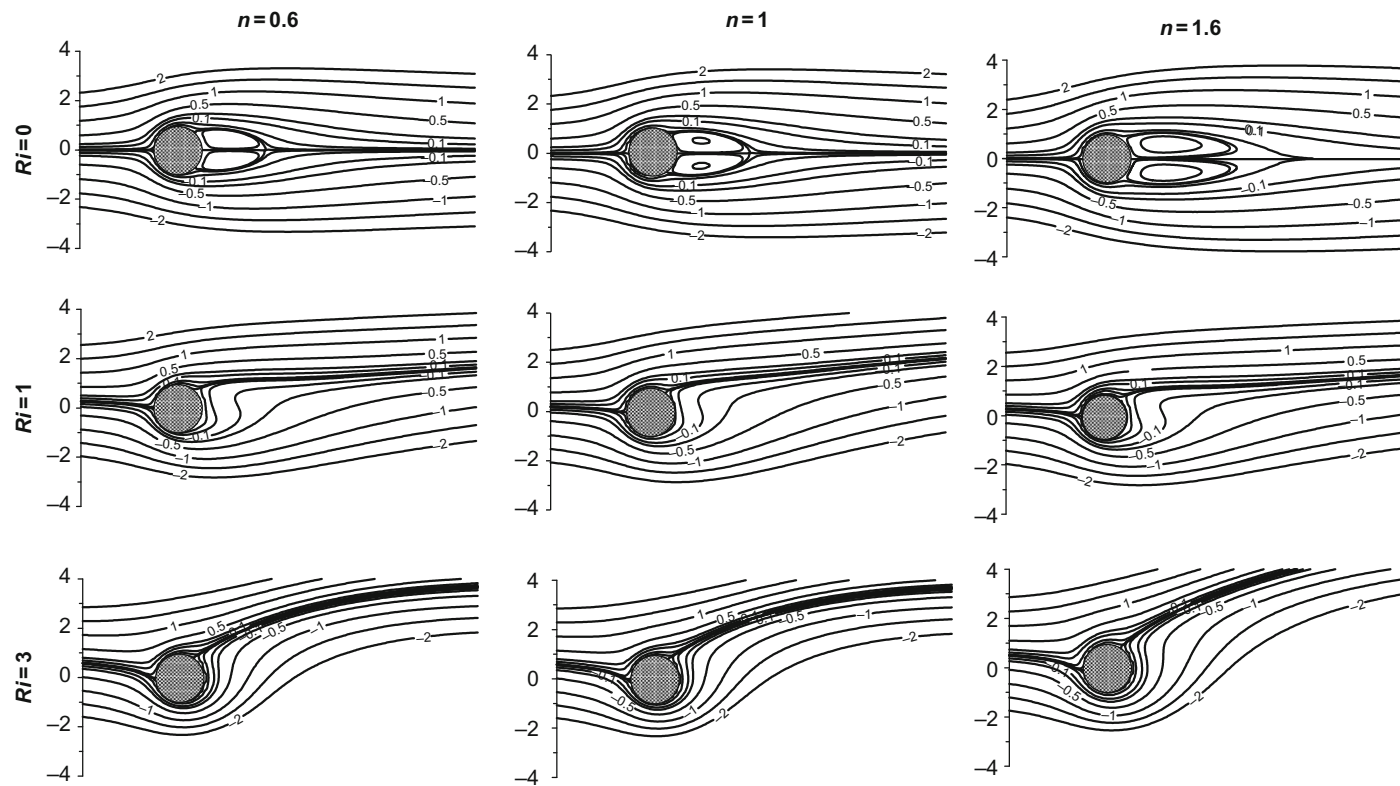


FIG. 46. (Continued).

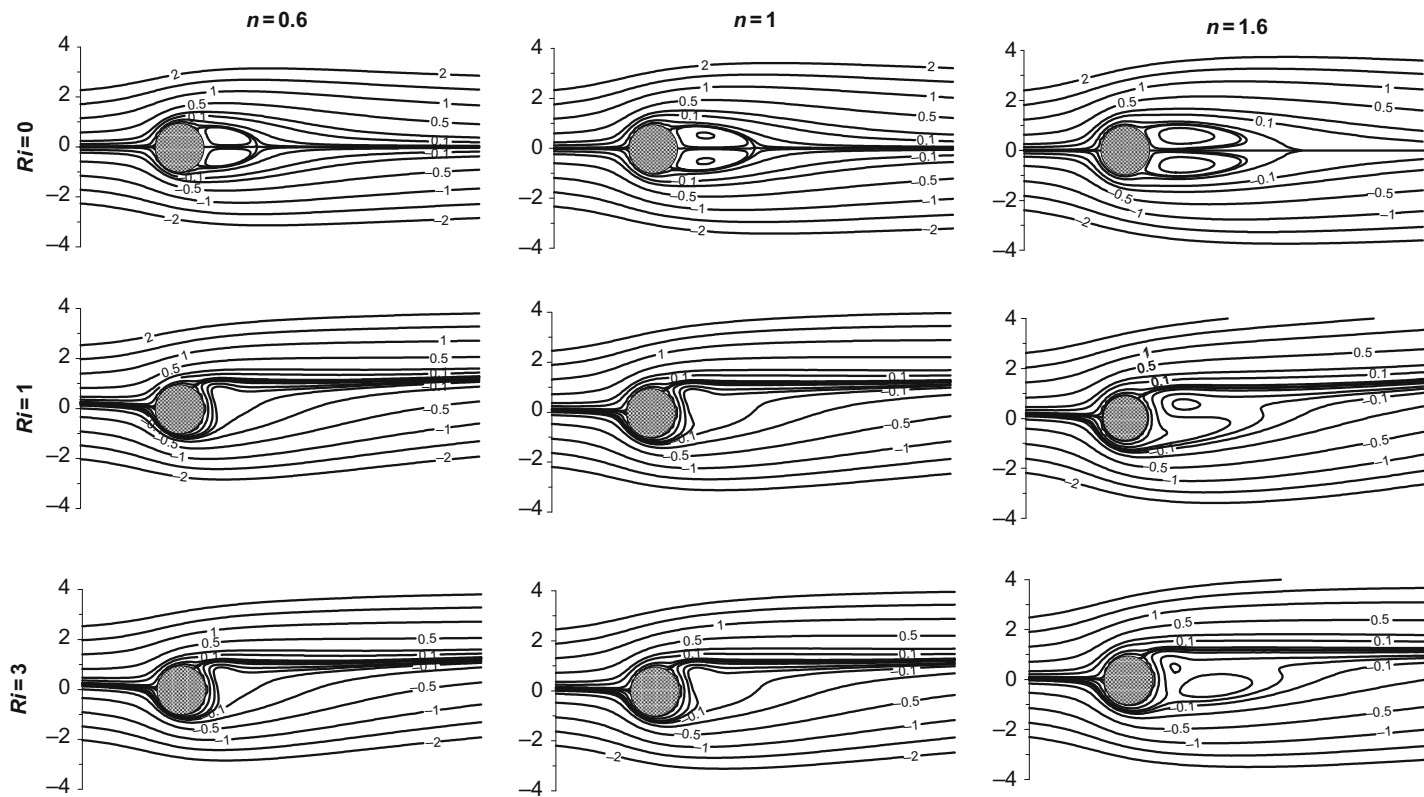


FIG. 46. (Continued).

steady over the range of conditions as: $0.2 \leq n \leq 1.8$, $1 \leq Re \leq 40$, $Ri \leq 2$, and $1 \leq Pr \leq 100$. They reported the wakes to be smaller in mixed convection than that in forced flow under otherwise identical conditions. The heat transfer was reported to increase by up to 40–45% due to the imposed buoyancy but only at the expense of the increased drag.

B. ELLIPTICAL CYLINDERS

While heat transfer from two-dimensional cylinders of elliptic cross section in Newtonian fluids like air and water has received some attention, the analogous body of information is indeed very meager in power-law fluids, or in general in non-Newtonian media. As usual, early attempts at such analysis for forced convection are based on the boundary layer flow approximation [166,269]. Numerical simulations of heat transfer in forced and mixed convection regimes for an elliptical cylinder have been pioneered by D'Alessio and Dennis [270] and Badr and coworkers [271–273]. Most of the numerical results are limited to relatively low values of the Reynolds number, and these have been supplemented at high Reynolds number by scant experimental results [161,163]. Similarly, natural convection in Newtonian fluids from heated elliptical cylinders has been investigated numerically amongst others by Badr and coworkers [274,275], Chen and Wang [276], Mahfouz and Kocabiyik [277], and others [278–281]. The numerical activity in this field has also been matched by the increasing number of experimental investigations on various aspects of free convection heat transfer from elliptic cylinders in Newtonian media, for example, see Refs. [282–286]. All in all, the currently available experimental results extend up to about $Ra \sim 10^8$. These as well as the other pertinent studies in this field have been reviewed recently [287].

In contrast, only Bharti et al. [168] have numerically investigated forced convection heat transfer from elliptical cylinders in power-law fluids. Their study embraces a 100-fold variation in the value of Prandtl number ($1 \leq Pr \leq 100$) and the ranges of the other parameters are as follows: $0.2 \leq n \leq 1.8$, $0.01 \leq Re \leq 40$, and $0.2 \leq E \leq 5$. However, they assumed the flow to be steady *a priori* which has been shown to be a reasonable assumption by a subsequent study [44]. All else being equal, their results clearly suggest that it is possible to enhance the value of the Nusselt number by up to ~50–60% in highly shear-thinning fluids under appropriate conditions, i.e., the values of E , Re , and Pr , as shown in Fig. 47. On the other hand, slight (~15–20%) deterioration is observed in shear-thickening fluids with reference to that in Newtonian fluids. This lone study has been recently complemented by an analogous investigation of laminar natural convection from elliptic cylinders in power-law fluids [287]. Sasmal and Chhabra [287] numerically solved

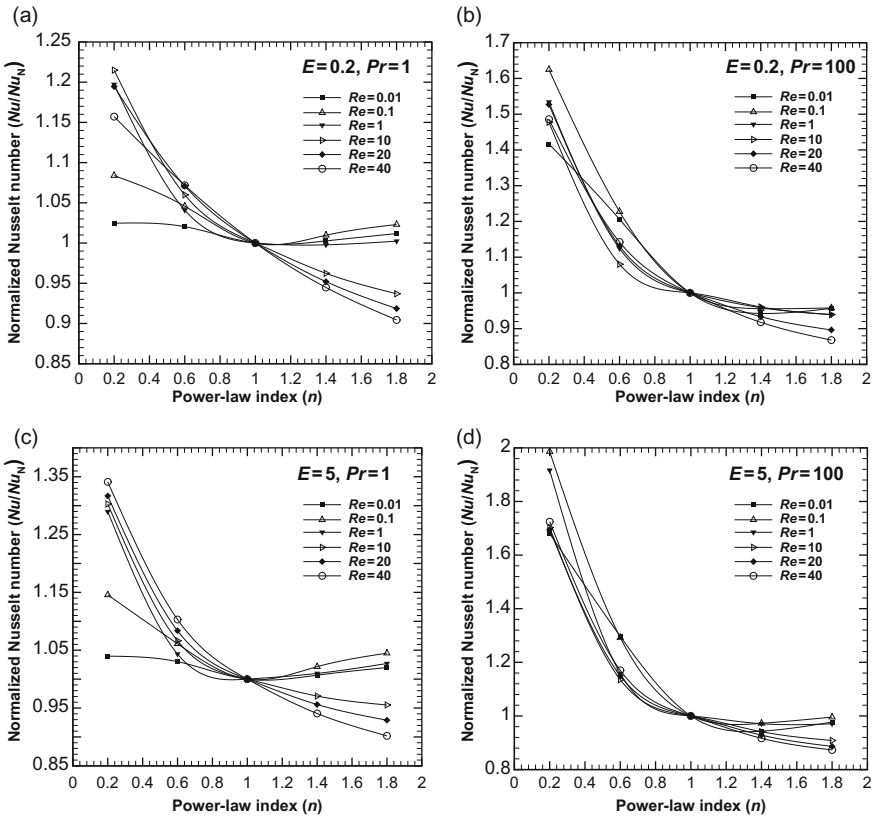


FIG. 47. Normalized Nusselt number as a function of E , Re , Pr , and n for elliptical cylinders. (a) $E = 0.2$, $Pr = 1$; (b) $E = 0.2$, $Pr = 100$; (c) $E = 5$, $Pr = 1$; and (d) $E = 5$, $Pr = 100$.

the coupled momentum and energy equations to elucidate the functional dependence of the surface mean Nusselt number on aspect ratio of the isothermal cylinder ($0.2 \leq E \leq 5$), Prandtl number ($0.72 \leq Pr \leq 100$), Grashof number ($10 \leq Gr \leq 10^5$), and power-law index ($0.3 \leq n \leq 1.5$). Obviously, not only the mean Nusselt number shows a positive dependence on the Grashof number and Prandtl number, but the effect of Grashof number gets accentuated with the decreasing value of power-law index whereas that of Prandtl number somewhat diminishes. Furthermore, they reported the value of the Nusselt number to progressively increase as the shape of the cylinder gradually passes from being blunt to slender with respect to the direction of gravity vector. They were able to fit their numerical data to the following analytical forms thereby

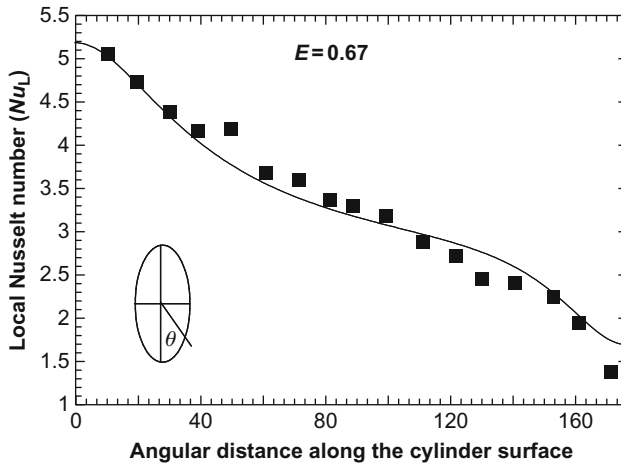


FIG. 48. Comparison between predictions [287] and observations (symbols) [284] on free convection from a heated elliptical cylinder in air at $Ra = 10^3$.

enabling the interpolation of results for the intermediate values of the influencing parameters:

For $0.2 \leq E \leq 1$:

$$Nu_{\text{avg}} = 0.833\Omega^{0.89}\{E^{-0.464/(2(n+1))}\} \quad (47a)$$

For $1 \leq E \leq 5$:

$$Nu_{\text{avg}} = 0.833\Omega^{0.89}E^{-1.285/(2(n+1))} \quad (47b)$$

In Eq. (47), the form of the shape function is such that it is greater than unity for $E < 1$ thereby capturing the increase in Nusselt number. While no suitable experimental results are available in power-law fluids, Fig. 48 shows typical comparisons between the numerical [287] and experimental values [284] of the local Nusselt number on the surface of the cylinder in air. Such close correspondence lends credibility to the reliability of numerical simulations.

C. SEMICIRCULAR CYLINDER

This configuration has received very little attention even in Newtonian fluids [53], let alone in power-law fluids [54,100]. Nada and Mowad [98], for instance, reported an experimental study delineating the effect of orientation on free convection heat transfer from a semicircular cylinder in air. Subsequently, they [288] reported an experimental and numerical study on forced convection

for the angle of incidence ranging from 30° to 90° . However, the range of Reynolds number ($2200 \leq Re \leq 45,000$) in their experimental study was way beyond their and other numerical predictions available presently thereby ruling out the possibility of detailed comparisons between experiments and simulations. At low Reynolds numbers, forced convection from a two-dimensional semicircular cylinder (with curved surface orientated toward the free stream) in Newtonian [53] and power-law [100] has been numerically investigated very recently. Broadly, all else being equal, shear-thinning facilitates the rate of heat transfer (Fig. 49). In Newtonian fluids, Chandra and Chhabra [53] found that their results on average Nusselt number conformed to the expected scaling of $Nu \sim Pr^{1/3}$ over the whole range whereas it scaled as $\sim Re^{1/4}$ and \sqrt{Re} for $Re < \sim 1$ and $Re > \sim 1$, respectively. This dependence was explained by postulating that at low Peclet numbers, heat transfer is dominated by conduction, and therefore the dependence on Reynolds number gradually increases with the increasing Reynolds number. Subsequently, this work has been extended to the power-law fluids [100]. Over the range of Peclet number ($50 \leq Pe \leq 3000$) and power-law index ($0.2 \leq n \leq 1.8$), they reported the following equation based on their numerical data:

$$Nu_{\text{avg}} = 0.64Re^{0.49}Pr^{0.36}\Delta^{0.76} \quad (48)$$

Admittedly, numerical results for lower values of Peclet number (< 50) are available in their original paper, but these could not be included in Eq. (48) due to weak advection under these conditions.

D. EQUILATERAL TRIANGULAR CYLINDER

While some numerical and experimental studies on forced [49,51,101,102,289], free, and mixed-convection heat transfer from a two-dimensional cylinder of triangular cross section in Newtonian media (mostly air) are available, only Prashanna et al. [52] have systematically investigated the effect of power-law index on heat transfer from an isothermal equilateral triangular cylinder with its apex facing upstream or downstream. While this study is restricted to the so-called steady flow regime ($Re \leq 30$), it does embrace wide ranging values of the power-law index ($0.2 \leq n \leq 1$) and Prandtl number ($1 \leq Pr \leq 100$). Within this range, the average Nusselt number is best approximated by the following expressions:

For apex facing downstream:

$$Nu_{\text{avg}} = 0.66Re^{0.41}Pr^{0.33}\Delta^{0.51} \quad (49a)$$

For apex facing upstream:

$$Nu_{\text{avg}} = 0.894Re^{0.41}Pr^{0.33}\Delta^{0.51} \quad (49b)$$

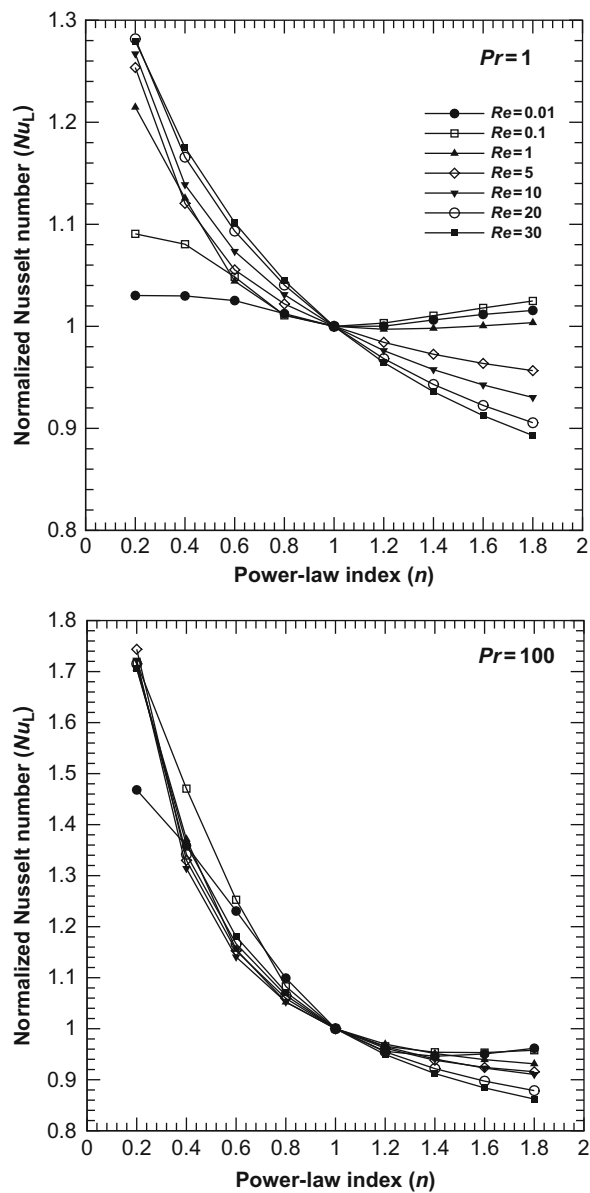


FIG. 49. Normalized Nusselt number for a semicircular cylinder.

Equations (47a) and (47b) reproduce their numerical data with an average error of $\sim 12\%$ which reaches the maximum value of $\sim 25\%$.

E. SQUARE CYLINDER

This is the most studied configuration following that of the circular cylinder. Extensive studies on forced and mixed convection in the laminar flow regime, particularly, for air ($Pr = 0.71$) have been reported by Sharma and Eswaran [108,109] and a detailed review of the laminar vortex shedding regime is provided in Ref. [290]. The effect of a 100-fold variation in the value of Prandtl number on forced convection in Newtonian fluids from a confined and unconfined square cylinder has also been investigated recently [291–293]. Broadly, these predictions are not only in line with the available scant experimental results, but also confirm the scaling of the average Nusselt number with Reynolds number as $\sim \sqrt{Re}$ and Prandtl number as $\sim Pr^{1/3}$ over the entire range except for the conditions when advection is weak, i.e., $Pe \leq \sim 50$ – 100 . At present, reliable predictions of forced convection from a heated square cylinder in power-law fluids are documented in the literature which extends up to the laminar vortex shedding regime. Preliminary results using relatively coarse computational meshes were reported by Gupta et al. [169] and Paliwal et al. [170]. Over the relatively narrow range of Peclet number ($5 \leq Pe \leq 400$), both studies confirmed the general observation that shear-thinning behavior fosters heat transfer, whereas shear-thickening has a deleterious influence on the value of the Nusselt number with reference to the corresponding value in Newtonian fluids (Fig. 50). Subsequently, more extensive and accurate results employing much finer grids than those used earlier [169,170] have been reported by Dhiman and coworkers [294–296] and others [45,107]. Combined together these studies encompass the following ranges of conditions: $0.2 \leq n \leq 2$, $0.1 \leq Re \leq 160$, and $0.7 \leq Pr \leq 100$ for the CWT boundary condition and for two values of blockage, namely, 25% and 50%. Owing to the strong diffusional effects at low Peclet numbers, it is always not possible to correlate the results under such conditions. On the other hand, Sahu et al. [295] were able to correlate their numerical data over the range of conditions as $60 \leq Re \leq 160$ and $0.5 \leq n \leq 2$ for an unconfined cylinder as follows:

$$Nu_{\text{avg}} = 0.55 Re^{0.46} Pr^{0.35} \Delta^{0.5} \quad (50)$$

Limited available results also indicate that the average Nusselt number is slightly higher for a confined cylinder than that for an unconfined square cylinder [296]. Further enhancements of varying levels in heat transfer have been reported when the buoyancy effects are incorporated into such analysis [173,297,298]. Mixed convection from a square cylinder in power-law fluids has received very little attention thus far.

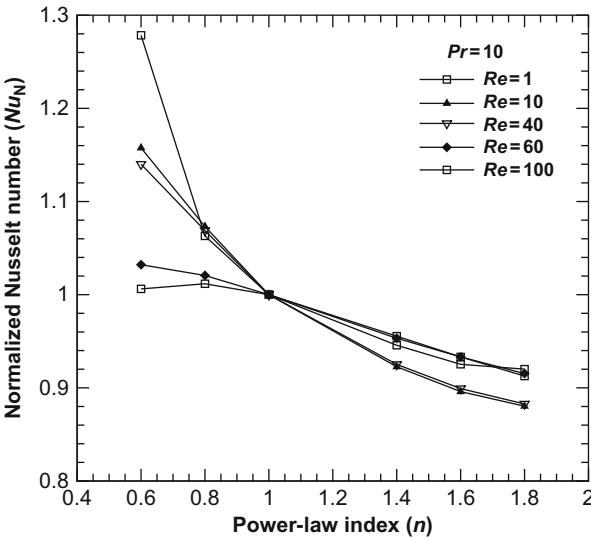


FIG. 50. Representative results on normalized Nusselt number for a square cylinder in power-law fluids.

On the other hand, free convection heat transfer from a two-dimensional square cylinder has not been investigated as systematically as for a circular cylinder even in Newtonian fluids. For instance, early studies [299–301] are of very approximate nature based on the boundary layer equations often aided by dimensional considerations. Chang and Choi [302] appeared to be the first to have solved the complete Navier–Stokes equations for natural convection heat transfer from a square cylinder in quiescent air. They reported the flow to remain attached to the surface of the cylinder up to about $Ra \simeq 1000$; this finding is in line with the available experimental results [303]. Subsequently, Chang et al. [304] have revisited this configuration over somewhat wider ranges of conditions of the Rayleigh number as $10^3 \leq Ra \leq 10^5$ for a fixed value of $Pr = 0.7$ and these results have been corroborated by an independent numerical study [305]. The limited numerical activity in this field is also matched only by equally meager experimental studies on free convection from a square cylinder in air [306–308]. These as well as the other pertinent studies have been reviewed recently elsewhere [309]. Sasmal and Chhabra [309] have recently reported the first numerical study of laminar natural convection from a two-dimensional square cylinder (CWT) in unconfined power-law fluids. This study spans the ranges of conditions as: $0.3 \leq n \leq 1.8$, $0.72 \leq Pr \leq 100$, and $10 \leq Gr \leq 10^5$. The flow was observed to remain attached to the surface of

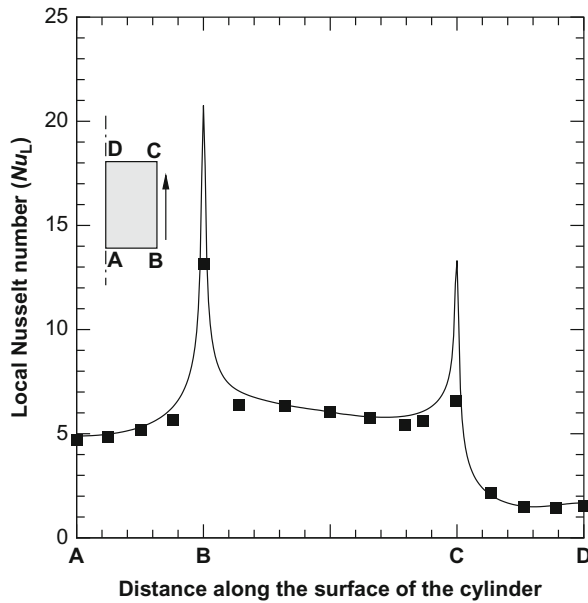


FIG. 51. Comparison between predictions [309] and observations (symbols) [310] on free convection from a square cylinder in air at $Ra = 4 \times 10^4$.

the square cylinder over these ranges of conditions. Qualitatively their results are similar to that discussed previously for a circular cylinder as far as the role of power-law index is concerned. That is, all else being equal, shear-thinning fluid behavior enhances heat transfer over and above that observed in Newtonian fluids. As expected, shear-thickening behavior has an adverse effect. Based on their numerical results, they put forward the following expressions for the average Nusselt number:

$$Nu_{\text{avg}} = 0.605\Omega^{0.924} \quad (51)$$

The average error was reported to be about 11%. In the absence of experiments in power-law fluids, Fig. 51 shows a comparison between the predicted and experimental values of the local Nusselt number in air at $Ra = 4 \times 10^4$ [310]. Once again, such a close match inspires confidence in the use of the numerical results.

In addition to the aforementioned studies, limited results are available on forced convection heat transfer from a tilted square cylinder in power-law fluids [179]. While this work embraces wide ranges of Prandtl number ($0.7 \leq Pr \leq 100$) and power-law index ($0.2 \leq n \leq 1$), it is restricted to the

steady flow regime ($0.1 \leq Re \leq 40$). Over this range of conditions, they put forward the following equations for the average Nusselt number:

For CWT condition:

$$Nu_{\text{avg}} = 0.44Re^{0.55}Pr^{0.39}\Delta^{0.62} \quad (52a)$$

For CHF condition:

$$Nu_{\text{avg}} = 0.60Re^{0.52}Pr^{0.38}\Delta^{0.58} \quad (52b)$$

The mean deviations associated with Eqs. (52a) and (52b) are 8.3% and 5.2% which rise to the maximum values of $\sim 33\%$ and $\sim 20\%$, respectively.

The foregoing discussion clearly demonstrates that the currently available body of knowledge concerning the momentum and heat transfer characteristics of variously shaped two-dimensional bluff bodies in power-law fluids in particular and in non-Newtonian fluids in general is less extensive and coherent than that in Newtonian fluids. In summary, reliable results for a square and circular cylinder submerged in power-law fluids are available up to the laminar vortex shedding regime, though the limits of the cessation of this flow regime itself are not yet known. The corresponding literature is even more limited for elliptical, triangular, semicircular cylinders, and other novel shapes. Before leaving this section, it is appropriate to add here that limited results for a circular cylinder rotating in streaming power-law fluids are also available [311,312]. Similarly, some results are also available on the transverse flow of power-law fluids past two circular cylinders in tandem configuration [313,314]. Both these studies are limited to the steady flow regime. The related studies on the flow of power-law and Bingham plastic fluids past arrays of circular and elliptical cylinders are summarized in some recent studies [315–324]. In some of these studies, an attempt has been made to recover the limiting case of a single cylinder by progressively reducing the solid volume fraction of the array to vanishingly small values. Of course, there is an extensive body of literature on the flow of viscoelastic fluids past a single and arrays of circular cylinders and this has been thoroughly reviewed elsewhere [22].

VII. Concluding Remarks

The currently available literature on the momentum and heat transfer characteristics associated with the transverse flow of generalized Newtonian fluids, especially power-law fluids, over two-dimensional bluff bodies of different cross sections has been reviewed critically and thoroughly. Undoubtedly, the flow past a circular cylinder has been studied most extensively. In spite of this, the current state of the art is only limited to the steady and laminar vortex

shedding regimes. Furthermore, the momentum transfer characteristics have been explored more extensively than the corresponding heat transfer characteristics. Hence reliable values of drag coefficient, wake characteristics, Strouhal number, etc. are available for design purpose. On the other hand, heat transfer characteristics are known reasonably well in the forced convection regime and there is a real paucity of the analogous information on heat transfer in the free- and mixed-convection regimes. Following the case of circular cylinder, square cross section cylinders have been studied systematically over the steady and laminar vortex shedding regimes. Generally, only a small fraction of the currently available literature concerns heat transfer, particularly in the mixed and free convection regimes. Though the components of elliptical, rectangular, triangular, and semicircular shapes are often encountered in compact heat exchangers and in microelectronics process engineering applications, these have been studied even less extensively.

Broadly speaking, the flow remains attached to the surface of the bluff body in shear-thinning fluids up to higher Reynolds numbers than that in Newtonian fluids. Of course, flow separation is advanced to lower Reynolds numbers in shear-thickening fluids with reference to that in Newtonian media. This inference is valid for all shapes considered herein. Therefore, it is possible to stabilize or destabilize the flow by modifying the non-Newtonian characteristics of the liquid via the use of appropriate additives. Similarly, irrespective of the shape of the bluff body and the heat transfer regime (forced, free, or mixed), shear-thinning fluid behavior ($n < 1$) promotes heat transfer and indeed it is possible to augment the value of heat transfer coefficient by up to 70–80% under appropriate conditions, i.e., values of Reynolds number and Prandtl number in forced convection, or Grashof number and Prandtl number in free convection, or of Reynolds number, Richardson number, and Prandtl number in mixed convection. This can lead to significant energy savings in process engineering applications. However, the aforementioned enhancement in heat transfer is realized only at the expense of increased drag (or pressure drop), and therefore much work is required to arrive at optimal operating conditions which would maximize the heat transfer enhancement without excessive pressure drop penalty. Also, most of the available studies have ignored the variation of thermo-physical properties of the fluid (heat capacity, density, thermal conductivity, viscosity) with temperature. Depending upon the type of the fluid (shear-thinning or shear-thickening) and direction of heat transfer (heated bluff body in cold fluid or vice versa), consideration of temperature-dependent viscosity not only adds to the level of mathematical complexity, but it may also influence the rate of heat transfer favorably or adversely. Also, the bulk of the literature pertains to the case of single unconfined bluff bodies, whereas in most practical situations (like in tubular heat exchangers), the flow occurs either in a confined medium or over multiple bluff bodies arranged in various

geometrical configurations. Unfortunately little is known about the wall-bluff body or inter-bluff body interactions. It also needs to be emphasized here that most of the currently available information is based on numerical solutions of the governing differential equations and the experimental results are indeed scarce in this field. It is hoped that the numerical results summarized in this chapter will act to stimulate experimental activity in the area which is needed not only to substantiate and/or refute the numerical predictions, but also to span the range of conditions (like high values of Reynolds number, and Prandtl number) which are currently beyond the reach of numerical simulations or vice versa. Lastly, undoubtedly this branch of non-Newtonian fluid mechanics certainly merits much more attention than it has received thus far.

Acknowledgments

I am grateful to my past and present graduate students who have carried out the research work which has formed the basis of this chapter. A. Chandra, M. Sairamu, S. Sivakumar and C. Sasmal have prepared most of the figures included here and their assistance is greatly appreciated.

Nomenclature

A_1, A_2, A_3, A_4	Dimensionless constants Eqs. (33), (34), (42), and (43a) and (43b)
A_p	Projected area of cylinder transverse to flow (m^2)
a_i	Dimensionless constant, Eq. (29)
b_i	Dimensionless constant, Eq. (30)
Bi_{HB}	Dimensionless parameter, Eq. (31)
C	Heat capacity of fluid (J/kg K)
C_D	Drag coefficient
C_{DF}	Friction component of drag coefficient
C_{DP}	Pressure component of drag coefficient
C_L	Lift coefficient
C_P	Pressure coefficient, Eq. (20)
D	Diameter (or side) of cylinder (m)
E	Aspect ratio of an elliptic cylinder
F_{DF}	Friction component of drag force (N)
F_{DP}	Pressure component of drag force (N)
F_L	Lift force exerted on cylinder (N)
f	Frequency of vortex shedding (s^{-1})
Gr	Grashof number, Eq. (17)

g	Acceleration due to gravity (m/s^2)
h	Convective heat transfer coefficient ($\text{W/m}^2 \text{ K}$)
I_1, I_2, I_3	Invariants of the rate of deformation tensor
j	Colburn heat transfer factor, Eq. (39)
k	Thermal conductivity of fluid (W/m K)
L	Length of the cylinder in the neutral direction (m)
l_c	Characteristic linear dimension, Table I (m)
m	Power-law consistency index ($\text{Pa} \cdot \text{s}^n$)
Nu	Nusselt number
n	Power-law index
n_s	Unit vector normal to surface (m)
n_x	Component of unit vector in x -direction
Od	Oldroyd number, Eq. (31)
Pe	Peclet number $= Re \cdot Pr$
Pr	Prandtl number, Eq. (14)
Pr_N	Prandtl number in free convection, Eq. (18)
p	Pressure in fluid (Pa)
p_∞	Free stream pressure faraway from fluid (Pa)
q_w	Constant heat flux on the surface (W/m^2)
Ra	Rayleigh number
Re	Reynolds number
Re_c	Critical Reynolds number corresponding to the limit of the steady flow regime
Re^c	Critical Reynolds number denoting the onset of the flow separation
Ri	Richardson number $= Gr/Re^2$
r	Radial coordinate (m)
S	Surface area of immersed bluff body (m^2)
St	Strouhal number
T'	Fluid temperature (K)
T	Dimensionless temperature
T_w	Temperature on the surface of cylinder (K)
T_∞	Temperature far away from the cylinder (K)
ΔT	Temperature difference $= T_w - T_\infty $ (K)
t	Time (s)
U_c	Characteristic velocity scale, Table I (m/s)
U_x, U_y	x - and y -components of velocity
U_∞	Far away fluid velocity (m/s)
$\langle U \rangle$	Area-average velocity (m/s)
Wi	Weissenberg number
x, y	Cartesian coordinates (m)
$X(n)$	Correction factor, Eqs. (35) and (36)

Greek letters

β	Volumetric coefficient of expansion (K^{-1}) or blockage ratio (channel height/ diameter) (-)
γ	Kinematic viscosity (m^2/s)
δ	Confinement (diameter/channel height), or boundary layer thickness (m)
ε_{ij}	Component of the rate of deformation tensor (s^{-1})
η	Viscosity (Pa s)
θ_s	Angle of separation ($^\circ$)
ρ	Fluid density (kg/m^3)
τ_{ij}	Component of extra stress tensor (Pa)
τ_0^{HB}	Herschel–Bulkley yield stress (Pa)
ψ	Stream function
Ω	Dimensionless parameter, Eq. (46)
ω	Vorticity, Eq. (19)

Subscripts

avg	Averaged over surface
b	Bulk
D	Based on diameter
w	Wall
∞	Corresponds to free stream condition

Abbreviations

CHF	Constant heat flux
CWT	Constant wall temperature

References

- [1] M.M. Zdravkovich, Flow Around Circular Cylinders, Volume 1: Fundamentals, Oxford University Press, New York, NY, 1997.
- [2] M.M. Zdravkovich, Flow Around Circular Cylinders, Volume 2: Applications, Oxford University Press, New York, NY, 2003.
- [3] V.T. Morgan, The overall convective heat transfer from smooth circular cylinders, Adv. Heat Transfer 11 (1975) 199–264.
- [4] B.M. Sumer, J. Fredsoe, Hydrodynamics Around Cylindrical Structures, World Scientific, Singapore, 2006.

- [5] J.E. Hesselgreaves, *Compact Heat Exchangers: Selection, Design and Operation*, Pergamon, Oxford, 2001.
- [6] R.B. Bird, R.C. Armstrong, O. Hassager, *Dynamics of Polymeric Liquids*, vol. 1, second ed. Wiley, New York, NY, 1987.
- [7] R.I. Tanner, *Engineering Rheology*, second ed., Oxford University Press, New York, NY, 2000.
- [8] R.G. Larson, *The Structure and Rheology of Complex Fluids*, Oxford University Press, New York, NY, 1998.
- [9] R.P. Chhabra, J.F. Richardson, *Non-Newtonian Flow and Applied Rheology*, second ed., Butterworth-Heinemann, Oxford, UK, 2008.
- [10] C.D. Han, *Rheology and Processing of Polymeric Materials*, Oxford University Press, New York, NY, 2007.
- [11] H.A. Barnes, The yield stress—a review, *J. Non-Newtonian Fluid Mech.* 81 (1989) 133–178.
- [12] R.B. Bird, G.C. Dai, B.J. Yarrusso, The rheology and flow of viscoplastic materials, *Rev. Chem. Eng.* 1 (1983) 1–70.
- [13] H.A. Barnes, Shear-thickening (dilatancy) in suspensions of nonaggregating solid particles in Newtonian liquids, *J. Rheol.* 33 (1989) 329–366.
- [14] R.P. Chhabra, Non-Newtonian fluids: an introduction, in: *Rheology of Complex Fluids* A.P. Deshpande, J. Murali Krishnan, P.B. Sunil Kumar (Eds.), Springer, New York, NY, 2010 (Chapter 1).
- [15] A.B. Metzner, Non-Newtonian technology: fluid mechanics, mixing and heat transfer, *Adv. Chem. Eng.* 1 (1956) 77–153.
- [16] Y.I. Cho, J.P. Hartnett, Non-Newtonian fluids in circular pipe flow, *Adv. Heat Transfer* 15 (1982) 59–141.
- [17] A.S. Mujumdar, A. Lawal, Laminar duct flow and heat transfer in purely viscous non-Newtonian fluids, *Adv. Transport Process.* 7 (1989) 353–442.
- [18] R.P. Chhabra, Fluid flow, heat and mass transfer in non-Newtonian fluids: multiphase systems, *Adv. Heat Transfer* 23 (1993) 187–278.
- [19] E.L. Paul, S.M. Kresta, V. Atiemo-Obeng, *Handbook of Industrial Mixing: Science and Practice*, Wiley, New York, NY, 2004.
- [20] N. Harnby, M.F. Edwards, A.W. Nienow, *Mixing in the Process Industries*, second ed., Butterworth-Heinemann, Oxford, 1997.
- [21] R.P. Chhabra, Fluid mechanics and heat transfer with non-Newtonian liquids in mechanically agitated vessels, *Adv. Heat Transfer* 37 (2003) 77–178.
- [22] R.P. Chhabra, *Bubbles, Drops and Particles in Non-Newtonian Fluids*, second ed., CRC Press, Boca Raton, FL, 2006.
- [23] R.P. Chhabra, J. Comiti, I. Machac, Non-Newtonian fluid flow in packed and fluidised beds, *Chem. Eng. Sci.* 56 (2001) 1–27.
- [24] G. Astarita, R.A. Mashelkar, Heat and mass transfer in non-Newtonian fluids, *Chem. Eng.* 317 (1977) 100–105.
- [25] U.K. Ghosh, S.N. Upadhyay, R.P. Chhabra, Heat and mass transfer from immersed bodies to non-Newtonian fluids, *Adv. Heat Transfer* 25 (1994) 251–319.
- [26] P.J. Carreau, D. DeKee, R.P. Chhabra, *Rheology of Polymeric Systems: Principles and Applications*, Hanser, Munich, 1997.
- [27] R.P. Chhabra, Heat and mass transfer in rheologically complex systems, in: D.A. Siginer, D. Dekee, R.P. Chhabra (Eds.), Elsevier, Amsterdam, 1999 (Chapter 39).
- [28] C.H.K. Williamson, Vortex dynamics in the cylinder wake, *Annu. Rev. Fluid Mech.* 28 (1996) 477–539.
- [29] A. Thom, The flow past circular cylinders at low speeds, *Proc. R. Soc. Lond. A* 141 (1933) 651–669.

- [30] R.D. Henderson, Details of the drag curve near the onset of vortex shedding, *Phys. Fluids* 7 (1995) 2102–2104.
- [31] S. Taneda, Experimental investigation of the wakes behind cylinders and plates at low Reynolds numbers, *J. Phys. Soc. Jpn.* 11 (1956) 302–307.
- [32] M. Coutanceau, J.R. Defaye, Circular cylinder wake configurations: a flow visualization survey, *Appl. Mech. Rev.* 44 (1991) 255–305.
- [33] S.C.R. Dennis, G.-Z. Chang, Numerical solutions for steady flow past a circular cylinder at Reynolds numbers up to 100, *J. Fluid Mech.* 42 (1970) 471–489.
- [34] B. Fornberg, Steady viscous flow past a circular cylinder up to Reynolds number 600, *J. Comput. Phys.* 61 (1985) 297–320.
- [35] M. Van Dyke, *An Album of Fluid Motion*, Parabolic Press, Stanford, CA, 1982.
- [36] Y. Nakayama, Y. Tanida, *Atlas of Visualization*, CRC Press, Boca Raton, FL, 1996.
- [37] M.S. Bloor, The transition to turbulence in the wake of a cylinder, *J. Fluid Mech.* 19 (1964) 290–304.
- [38] G. Schewe, On the force fluctuations acting on a circular cylinder in cross-flow from subcritical up to transcritical Reynolds numbers, *J. Fluid Mech.* 133 (1983) 265–285.
- [39] V.J. Modi, E. Wiland, A.K. Dikshit, T. Yokomizo, On the fluid mechanics of elliptic cylinders, *Proceedings of 2nd International Offshore and Polar Engineering Conference*, vol. III, San Francisco, CA, 1992, pp. 595–614.
- [40] S.A. Johnson, M.C. Thompson, K. Hourigan, Flow past elliptical cylinders at low Reynolds numbers, *Proceedings of 14th Australasian Fluid Mechanics Conference*, Adelaide, December 10–14, 2001, pp. 343–346.
- [41] C.P. Jackson, A finite-element study of the onset of vortex shedding in flow past variously shaped bodies, *J. Fluid Mech.* 182 (1987) 23–45.
- [42] Z. Faruquee, D.S.-K. Ting, A. Fartaja, R.M. Barron, R. Carreveau, The effects of axis ratio on laminar fluid flow around an elliptical cylinder, *Int. J. Heat Fluid Flow* 28 (2007) 1178–1189.
- [43] D. Stack, H.R. Bravo, Flow separation behind ellipses at Reynolds number less than 10, *Appl. Math. Modell.* 33 (2009) 1633–1643.
- [44] P.K. Rao, A.K. Sahu, R.P. Chhabra, Flow of Newtonian and power-law fluids past an elliptical cylinder: a numerical study, *Ind. Eng. Chem. Res.* 49 (2010) 6649–6661.
- [45] P.K. Rao, A.K. Sahu, R.P. Chhabra, Momentum and heat transfer from a square cylinder in power-law fluids, *Int. J. Heat Mass Transfer* 54 (2010) 390–403.
- [46] A.K. De, A. Dalal, Numerical simulation of unconfined flow past a triangular cylinder, *Int. J. Numer. Methods Fluids* 52 (2006) 801–821.
- [47] B.J. Zielinska, J.E. Wesfreid, On the spatial structure of global modes in wake flow, *Phys. Fluids* 7 (1995) 1418–1424.
- [48] J.E. Wesfreid, S. Goujon-Durand, B.J. Zielinska, Global mode behaviour of the streamwise velocity in wakes, *J. Phys. II* 6 (1996) 1343–1357.
- [49] H. Abbassi, S. Turki, S.N. Nasrallah, Numerical investigation of forced convection in a plane channel with a built-in triangular prism, *Int. J. Thermal Sci.* 40 (2001) 649–658.
- [50] Z. Faruquee, T.V. Olatunji, Natural and mixed convection heat transfer around a horizontal cylinder within confining walls, *Proceedings of 5th Joint ASME/JSME Fluids Engineering Conference*, San Diego, 2006, pp. 1445–1450.
- [51] S. Srikanth, A.K. Dhiman, S. Bijjam, Confined flow and heat transfer across a triangular cylinder in a channel, *Int. J. Thermal Sci.* 49 (2010) 2191–2200.
- [52] A. Prhashanna, A.K. Sahu, R.P. Chhabra, Flow of power-law fluids past an equilateral triangular cylinder: momentum and heat transfer characteristics, *Int. J. Thermal Sci.* 50 (2011) 2027–2041.

- [53] A. Chandra, R.P. Chhabra, Flow over and forced convection heat transfer in Newtonian fluids from a semi-circular cylinder, *Int. J. Heat Mass Transfer* 54 (2011) 225–241.
- [54] A. Chandra, R.P. Chhabra, Influence of power-law index on transitional Reynolds numbers for flow over a semi-circular cylinder, *Appl. Math. Modell.* 35 (2011) 5766–5785.
- [55] P. Sivakumar, R.P. Bharti, R.P. Chhabra, Effect of power-law index on critical parameters for power-law flow across an unconfined circular cylinder, *Chem. Eng. Sci.* 61 (2006) 6035–6046.
- [56] S.J.D. D'Alessio, J.P. Pascal, Steady flow of power-law fluids past a cylinder, *Acta Mech.* 117 (1996) 87–100.
- [57] S.J.D. D'Alessio, L.A. Finlay, Power-law flow past a cylinder at large distances, *Ind. Eng. Chem. Res.* 43 (2004) 8407–8410.
- [58] R.I. Tanner, Stokes paradox for power-law fluids around a cylinder, *J. Non-Newtonian Fluid Mech.* 50 (1993) 217–224.
- [59] M.J. Whitney, G.J. Rodin, Force–velocity relationships for rigid bodies translating through unbounded shear-thinning power-law fluids, *Int. J. Non-Linear Mech.* 36 (2001) 947–953.
- [60] S. Mossaz, P. Jay, A. Magnin, Criteria for the appearance of recirculating and non-stationary regimes behind a cylinder in a visco-plastic fluid, *J. Non-Newtonian Fluid Mech.* 165 (2010) 1525–1535.
- [61] G.H. McKinley, R.C. Armstrong, R.A. Brown, The wake instability in viscoelastic flow past confined circular cylinder, *Philos. Trans. Phys. Sci. Eng.* 344 (1993) 265–304.
- [62] G.H. McKinley, Steady and transient motion of spherical particles in viscoelastic liquids, in: R. Chhabra, D. De Kee (Eds.), second ed., Taylor & Francis, New York, NY, 2002, p. 338.
- [63] A. Groisman, V. Steinberg, Elastic turbulence in a polymer solution flow, *Nature* 405 (2000) 53–55.
- [64] M. Sahin, R.G. Owens, On the effects of viscoelasticity on two-dimensional vortex dynamics in the cylinder wake, *J. Non-Newtonian Fluid Mech.* 123 (2004) 121–139.
- [65] D. Richter, E.S.G. Shaqfeh, G. Iaccarino, Floquet stability analysis of viscoelastic flow over a cylinder, *J. Non-Newtonian Fluid Mech.* 166 (2011) 554–565.
- [66] D. Richter, G. Iaccarino, E.S.G. Shaqfeh, Simulation of three-dimensional viscoelastic flows past a circular cylinder at moderate Reynolds numbers, *J. Fluid Mech.* 651 (2010) 415–442.
- [67] J.R. Cressman, Q. Bailey, W.I. Goldburg, Modification of a vortex street by a polymer additive, *Phys. Fluids* 13 (2001) 867–871.
- [68] O. Cadot, S. Kumar, Experimental characterization of viscoelastic effects on two- and three-dimensional shear instabilities, *J. Fluid Mech.* 416 (2000) 151–172.
- [69] D.F. James, A.J. Acosta, The laminar flow of dilute polymer solutions around circular cylinders, *J. Fluid Mech.* 42 (1970) 269–288.
- [70] A. Koniuta, P.M. Adler, J.M. Piau, Flow of dilute polymer solutions around circular cylinders, *J. Non-Newtonian Fluid Mech.* 7 (1980) 101–106.
- [71] O. Manero, B. Mena, On the slow flow of viscoelastic liquids past a circular cylinder, *J. Non-Newtonian Fluid Mech.* 9 (1981) 379–387.
- [72] T. Nishimura, K. Kunitsugu, Y. Ochi, K. Konishi, K. Tanoue, The fluid dynamical properties of a dilute surfactant solution around a circular cylinder, *J. Environ. Eng.* 3 (2008) 83–91.
- [73] G.E. Gadd, Effects of long chain molecule additives in water on vortex streets, *Nature* 211 (1966) 169–170.
- [74] V.N. Kalashnikov, A.M. Kudin, Karman vortices in the flow of drag-reducing polymer solutions, *Nature* 225 (1970) 445–446.
- [75] D.F. James, O.P. Gupta, Drag on circular cylinders in dilute polymer solutions, *Chem. Eng. Prog. Symp. Ser.* 67 (1971) 62–73.

- [76] H. Usui, T. Shibata, Y. Sano, Karman vortex behind a circular cylinder in dilute polymer solutions, *J. Chem. Eng. Jpn.* 13 (1980) 77–79.
- [77] S. Turgut, P.G. Rainey, R.E. Kell, Flow of dilute polymer solutions about circular cylinders, *J. Fluid Mech.* 57 (1973) 177–208.
- [78] B.K. Kim, D.P. Telionis, The effect of polymer addition on laminar separation, *Phys. Fluids* 1 (1989) 267–273.
- [79] A.V. Luikov, Z.P. Shulman, B.I. Puris, Mass transfer of a cylinder in forced flow of non-Newtonian viscoelastic fluid, *Heat Transfer Sov. Res.* 1 (1961) 121–132.
- [80] J.W. Hoyt, R.H.J. Sellin, Cylinder cross-flow heat transfer in drag reducing fluid, *Exp. Heat Transfer* 2 (1989) 113–127.
- [81] S. Ogata, Y. Osano, K. Watanabe, Effect of surfactant solutions on the drag and flow pattern of a circular cylinder, *AIChE J.* 52 (2006) 49–57.
- [82] H. Kato, Y. Mizuno, An experimental investigation of viscoelastic flow past a circular cylinder, *Bull. JSME* 26 (1983) 529–536.
- [83] C. Bergin, M. Nowak, M. Urban, The flow of a dilute cationic surfactant solution past a circular cylinder, *Exp. Fluids* 30 (2001) 410–417.
- [84] T. McClanahan, P.J. Ridgley, Drag of Circular Cylinders in Dilute Aqueous Poly (ethylene oxide) Solutions for Flows Characterised by Laminar Boundary Layer Separation, M.S. Dissertation, Naval Postgraduate School, Monterey, CA, 1968.
- [85] M.J. Shah, E.E. Petersen, A. Acrivos, Heat transfer from a cylinder to a power-law non-Newtonian fluid, *AIChE J.* 8 (1962) 542–549.
- [86] T. Sarpkaya, P.G. Rainey, R.E. Kell, Flow of dilute polymer solutions about circular cylinders, *J. Fluid Mech.* 57 (1973) 177–208.
- [87] P.M. Coelho, F.T. Pinho, Vortex shedding in cylinder flow of shear-thinning fluids. I. Identification and demarcation of flow regime, *J. Non-Newtonian Fluid Mech.* 110 (2003) 143–176.
- [88] P.M. Coelho, F.T. Pinho, Vortex shedding in cylinder flow of shear-thinning fluids. II. Flow characteristics, *J. Non-Newtonian Fluid Mech.* 110 (2003) 177–193.
- [89] P.M. Coelho, F.T. Pinho, Vortex shedding in cylinder flow of shear-thinning fluids. III. Pressure measurements, *J. Non-Newtonian Fluid Mech.* 121 (2004) 55–68.
- [90] C.J. Pipe, P.A. Monkewitz, Vortex shedding in flow of dilute polymer solutions, *J. Non-Newtonian Fluid Mech.* 139 (2006) 54–67.
- [91] M.F. Unal, D. Rockwell, On vortex formation from a cylinder, Part 1: The initial instability, *J. Fluid Mech.* 190 (1988) 491–512.
- [92] M.K. Rao, A.K. Sahu, R.P. Chhabra, Effect of confinement on power-law fluid flow past a circular cylinder, *Polym. Eng. Sci.* 51 (2011) 2044–2065.
- [93] N. Boisaubert, M. Coutanceau, P. Ehrmann, Comparative early development of wake vortices behind a short semicircular-section cylinder in two opposite arrangements, *J. Fluid Mech.* 327 (1996) 73–99.
- [94] N. Boisaubert, A. Texier, Effect of splitter plate on the near-wake development of a semi-circular cylinder, *Exp. Thermal Fluid Sci.* 16 (1998) 100–111.
- [95] N. Boisaubert, M. Coutanceau, A. Texier, Manipulation of the starting semicircular cylinder near-wake by means of a splitter plate, *J. Flow Visualization Image Process.* 4 (1997) 211–221.
- [96] M. Kiya, M. Arie, Viscous shear flow past small bluff bodies attached to a plane wall, *J. Fluid Mech.* 69 (1975) 803–823.
- [97] M. Kotake, S. Suwa, Flow visualization around a semi-circular cylinder in a uniform shear flow, *J. Visualization Soc. Jpn.* 21 (2001) 95–98.
- [98] S.A. Nada, M. Mowad, Free convection from a vertical and inclined semicircular cylinder at different orientations, *Alexandria Eng. J.* 42 (2003) 273–283.

- [99] T. Sophy, H. Sada, D. Bouard, Calcul de l'écoulement autour d'un cylindre semi-circulaire par une method de collocation, *C R Mecanique* 330 (2002) 193–198.
- [100] A. Chandra, R.P. Chhabra, Momentum and heat transfer characteristics of a semi-circular cylinder immersed in power-law fluids in the steady flow regime, *Int. J. Heat Mass Transfer* 54 (2011) 2734–2750.
- [101] O. Zeitoun, M. Ali, A. Nuhait, Convective heat transfer around a triangular cylinder in cross-flow, *Int. J. Thermal Sci.* 50 (2011) 1685–1697.
- [102] A.K. De, A. Dalal, Numerical study of laminar forced convection fluid flow and heat transfer from a triangular cylinder placed in a channel, *J. Heat Transfer* 129 (2007) 646–656.
- [103] A. Sharma, Numerical investigation of unconfined and channel confined flow across a square cylinder with forced and mixed convection heat transfer, Ph.D. Thesis, Indian Institute of Technology, Kanpur, India, 2003.
- [104] A.K. Dhiman, Flow over and heat transfer to power-law fluids across a square cylinder in steady regime: A numerical study, Ph.D. Thesis, Indian Institute of Technology, Kanpur, India, 2006.
- [105] A.K. Sahu, Momentum and heat transfer characteristics of a square cylinder in power-law fluids in laminar vortex shedding regime, Ph.D. Thesis, Indian Institute of Technology, Kanpur, India, 2010.
- [106] M. Breuer, J. Bernsdorf, T. Zeiser, F. Durst, Accurate computations of the laminar flow past a square cylinder based on two different methods: lattice-Boltzmann and finite-volume, *Int. J. Heat Fluid Flow* 21 (2000) 186–196.
- [107] A.K. Dhiman, Heat transfer to power-law dilatant fluids in a channel with a built-in square cylinder, *Int. J. Thermal Sci.* 48 (2009) 1552–1563.
- [108] A. Sharma, V. Eswaran, Heat and fluid flow across a square cylinder in the two dimensional laminar flow regime, *Numer. Heat Transfer A* 45 (2004) 247–269.
- [109] A. Sharma, V. Eswaran, Effect of channel confinement on the two-dimensional laminar flow and heat transfer across a square cylinder, *Numer. Heat Transfer A* 47 (2005) 79–107.
- [110] A. Sohankar, C. Norberg, L. Davidson, Numerical simulation of unsteady low-Reynolds number flow around rectangular cylinders at incidence, *J. Wind Eng. Ind. Aerodyn.* 69–71 (1997) 189–201.
- [111] A. Sohankar, C. Norberg, L. Davidson, Low-Reynolds number flow around a cylinder at incidence: study of blockage, onset of vortex shedding and outlet boundary condition, *Int. J. Numer. Methods Fluids* 26 (1998) 39–56.
- [112] A. Okajima, Strouhal numbers of rectangular cylinders, *J. Fluid Mech.* 123 (1982) 379–398.
- [113] R.W. Davis, E.F. Moore, A numerical study of vortex shedding from rectangles, *J. Fluid Mech.* 116 (1982) 475–506.
- [114] A. Okajima, Numerical simulation of flow around rectangular cylinders, *J. Wind Eng. Ind. Aerodyn.* 33 (1990) 171–180.
- [115] A. Acrivos, M.J. Shah, E.E. Petersen, Momentum and heat transfer in laminar boundary-layer flows of non-Newtonian fluids past external surfaces, *AIChE J.* 6 (1960) 312–317.
- [116] W.R. Schowalter, The application of boundary-layer theory to power-law pseudoplastic fluids: similar solutions, *AIChE J.* 6 (1960) 24–28.
- [117] A. Acrivos, M.J. Shah, E.E. Petersen, On the solution of the two-dimensional boundary-layer flow equations for non-Newtonian power-law fluids, *Chem. Eng. Sci.* 20 (1965) 101–105.
- [118] W.A. Khan, J.R. Culham, M.M. Yovanovich, Fluid flow and heat transfer in power-law fluids across circular cylinders: analytical study, *J. Heat Transfer* 128 (2006) 870–878.
- [119] L.D. Landau, E.M. Lifshitz, *Fluid Mechanics*, second ed., Butterworth-Heinemann, Oxford, 1987.

- [120] H. Lamb, *Hydrodynamics*, sixth ed., Dover, New York, NY, 1945.
- [121] M. Van Dyke, *Perturbation Methods in Fluid Mechanics*, Academic Press, New York, NY, 1964.
- [122] I. Proudman, J.R.A. Pearson, Expansions at small Reynolds numbers for the flow past a sphere and a circular cylinder, *J. Fluid Mech.* 2 (1957) 237–262.
- [123] E. Marusic-Paloka, On the Stokes paradox for power-law fluids, *Z. Angew. Math. Mech.* 81 (2001) 31–36.
- [124] P.N. Kaloni, R.P. Chhabra, Creeping flow of a power-law fluid past a cylinder, *Proceedings of 21st Canadian Congress of Applied Mechanics*, Paper #PNK142, June 3–7, Ryerson University, Toronto, Canada, 2007.
- [125] A. Despeyroux, A. Ambari, A. Ben Richou, Wall effects on the transportation of a cylindrical particle in power-law fluids, *J. Non-Newtonian Fluid Mech.* 166 (2011) 1173–1182.
- [126] R.P. Bharti, R.P. Chhabra, V. Eswaran, Steady flow of power-law fluids across a circular cylinder, *Can. J. Chem. Eng.* 84 (2006) 406–421.
- [127] R.P. Chhabra, A.A. Soares, J.M. Ferreira, Steady non-Newtonian flow past a circular cylinder, *Acta Mech.* 172 (2004) 1–16.
- [128] A.A. Soares, J.M. Ferreira, R.P. Chhabra, Flow and forced convection heat transfer in cross-flow of non-Newtonian fluids over a circular cylinder, *Ind. Eng. Chem. Res.* 44 (2005) 5815–5827.
- [129] V.K. Patnana, R.P. Bharti, R.P. Chhabra, Two-dimensional unsteady flow of power-law fluids over a cylinder, *Chem. Eng. Sci.* 64 (2009) 2978–2999.
- [130] R.P. Bharti, R.P. Chhabra, V. Eswaran, Two-dimensional steady Poiseuille flow of power-law fluids across a circular cylinder in a plane confined channel: wall effect and drag coefficient, *Ind. Eng. Chem. Res.* 46 (2007) 3820–3840.
- [131] A. Nejat, V. Abdollahi, K. Vahidkhan, Lattice Boltzmann simulation of non-Newtonian flows past confined cylinders, *J. Non-Newtonian Fluid Mech.* 166 (2011) 689–697.
- [132] A.S. Grove, F.H. Shair, E.E. Petersen, An experimental investigation of the steady separated flow past a circular cylinder, *J. Fluid Mech.* 19 (1964) 60–80.
- [133] F. Homann, Influence of higher viscosity on flow around cylinder, *Forsch. Gebiete Ingenieur* 17 (1936) 1–10.
- [134] J.M. Ferreira, R.P. Chhabra, Analytical study of drag and mass transfer in creeping power-law flow across tube banks, *Ind. Eng. Chem. Res.* 43 (2004) 3439–3450.
- [135] F.H. Barnes, Vortex shedding in the wake of a rotating cylinder at low Reynolds numbers, *J. Phys. D* 33 (2000) L141–L144.
- [136] C.-Y. Wen, C.-Y. Lin, Two-dimensional vortex shedding of a circular cylinder, *Phys. Fluids* 13 (2001) 557–560.
- [137] O.H. Faxen, Forces exerted on a rigid cylinder in a viscous fluid between two parallel fixed planes, *Proc. R. Swed. Acad. Eng. Sci.* 187 (1946) 1–13.
- [138] P.Y. Huang, J. Feng, Wall effects on the flow of viscoelastic fluids around a circular cylinder, *J. Non-Newtonian Fluid Mech.* 60 (1990) 179–198.
- [139] A. Ben Richou, A. Ambari, J.K. Naciri, Drag force on a circular cylinder midway between two parallel plates at very low Reynolds numbers, Part 1: Poiseuille flow (numerical), *Chem. Eng. Sci.* 59 (2004) 3215–3222.
- [140] A. Ben Richou, A. Ambari, M. Lebey, J.K. Naciri, Drag force on a circular cylinder midway between two parallel plates at $Re \ll 1$, Part 2: Moving uniformly (numerical and experimental), *Chem. Eng. Sci.* 60 (2005) 2535–2543.
- [141] B. Kumar, S. Mittal, Effect of blockage on critical parameters for flow past a circular cylinder at low Reynolds numbers, *Int. J. Numer. Methods Fluids* 50 (2006) 987–1001.
- [142] P. Anagnostopoulos, G. Illiadis, S. Richardson, Numerical study of the blockage effect on viscous flow past a circular cylinder, *Int. J. Numer. Method Fluids* 22 (1996) 1061–1074.

- [143] L. Zovatto, G. Pedrizetti, Flow about a circular cylinder between parallel walls, *J. Fluid Mech.* 440 (2002) 1–25.
- [144] J.H. Chen, W.G. Pritchard, S.J. Tavener, Bifurcation for flow past a circular cylinder between parallel walls, *J. Fluid Mech.* 284 (1995) 23–41.
- [145] M. Sahin, R.G. Owens, Numerical investigations of wall effects up to high blockage ratios on two-dimensional flow past a confined circular cylinder, *Phys. Fluids* 16 (2004) 1305–1320.
- [146] J. Chakraborty, N. Verma, R.P. Chhabra, Wall effects in the flow past a circular cylinder in a plane channel: a numerical study, *Chem. Eng. Process.* 43 (2004) 1529–1537.
- [147] S. Mettu, N. Verma, R.P. Chhabra, Momentum and heat transfer from an asymmetrically confined circular cylinder in a plane channel, *Heat Mass Transfer* 42 (2006) 1037–1048.
- [148] H.H. Hu, Motion of a circular cylinder in a viscous liquid between parallel plates, *Theor. Comput. Fluid Dyn.* 7 (1995) 441–455.
- [149] N.J. de Mestre, Low-Reynolds number fall of slender cylinders near boundaries, *J. Fluid Mech.* 58 (1973) 641–656.
- [150] A.S. Dvinsky, A.S. Popel, Motion of a rigid cylinder between parallel plates in Stokes flow, *Comput. Fluids* 15 (1987) 391–404.
- [151] B. Semin, J.P. Hulin, H. Auradou, Influence of flow confinement on the drag force on a static cylinder, *Phys. Fluids* 21 (2009) 1036041–1036049.
- [152] N. Jalaiah, V.R. Raghavan, Effects of blockage on flow and heat transfer over a tube in cross flow, *Proceedings of the 12th International Heat Transfer Conference, Grenoble, France, 2002*, pp. 711–716.
- [153] T.C. Hsieh, J.H. Chen, Emergence of attached recirculating eddy for flow around a circular cylinder asymmetrically placed in a channel, *J. Mar. Sci. Technol.* 14 (2006) 147–154.
- [154] I. Imai, A new method of solving Oseen's equations and its applications to the flow past an inclined elliptic cylinder, *Proc. R. Soc. Lond. A* 224 (1954) 141–160.
- [155] H. Hasimoto, On the flow of a viscous fluid past an inclined elliptic cylinder at small Reynolds numbers, *J. Phys. Soc. Jpn.* 8 (1958) 653–661.
- [156] H.J. Lugt, H.J. Haussling, Laminar flow past an abruptly accelerated elliptic cylinder at 45° incidence, *J. Fluid Mech.* 65 (1974) 711–734.
- [157] N.A. Meller, Viscous flow past an elliptic cylinder, *Comput. Methods Math. Phys.* 18 (1978) 138–149.
- [158] V.A. Patel, Flow around the impulsively started elliptic cylinder at various angles of attack, *Comput. Fluids* 9 (1981) 435–462.
- [159] S.J.D. D'Alessio, S.C.R. Dennis, A vorticity model for viscous flow past a cylinder, *Comput. Fluids* 23 (1994) 279–293.
- [160] S.C.R. Dennis, P.J.S. Young, Steady flow past an elliptic cylinder inclined to the stream, *J. Eng. Math.* 47 (2003) 101–120.
- [161] U.R. Ilgarbuis, A. Butkus, Hydraulic drag and average heat transfer coefficients for compact bundles of elliptical finned tubes, *Heat Transfer Sov. Res.* 20 (1988) 12–21.
- [162] H. Nishiyama, T. Ota, T. Matsuno, Forced convection heat transfer from two elliptic cylinders in a tandem arrangement, *Trans. JSME, B* 52 (1986) 2677–2681.
- [163] H. Nishiyama, T. Ota, T. Matsuno, Heat transfer and flow around elliptical cylinders in a tandem arrangement, *JSME Int. Ser. II* 31 (1988) 410–419.
- [164] T. Ota, H. Nishiyama, Y. Taoka, Flow around an elliptic cylinder in the critical Reynolds number regime, *J. Fluids Eng.* 109 (1987) 149–155.
- [165] M. Sugihara-Seki, The motion of an elliptical cylinder in channel flow at low Reynolds numbers, *J. Fluid Mech.* 257 (1993) 575–596.
- [166] W.A. Khan, J.R. Culham, M.M. Yovanovich, Fluid flow around and heat transfer from elliptical cylinders: analytical approach, *J. Thermophys. Heat Transfer* 19 (2005) 178–185.

- [167] P. Sivakumar, R.P. Bharti, R.P. Chhabra, Steady flow of power-law fluids across an unconfined elliptical cylinder, *Chem. Eng. Sci.* 62 (2007) 1682–1702.
- [168] R.P. Bharti, P. Sivakumar, R.P. Chhabra, Forced convection heat transfer from an elliptical cylinder to power-law fluids, *Int. J. Heat Mass Transfer* 51 (2008) 1838–1853.
- [169] A.K. Gupta, A. Sharma, R.P. Chhabra, V. Eswaran, Two-dimensional steady flow of a power-law fluid past a square cylinder in a plane channel: momentum and heat transfer characteristics, *Ind. Eng. Chem. Res.* 42 (2003) 5674–5686.
- [170] B. Paliwal, A. Sharma, R.P. Chhabra, V. Eswaran, Power law fluid flow past a square cylinder: momentum and heat transfer characteristics, *Chem. Eng. Sci.* 58 (2003) 5315–5329.
- [171] A.K. Dhiman, R.P. Chhabra, V. Eswaran, Steady flow of power-law fluids across a square cylinder, *Chem. Eng. Res. Des.* 84 (2006) 300–310.
- [172] A.K. Sahu, R.P. Chhabra, V. Eswaran, Two dimensional unsteady laminar flow of a power-law fluid across a square cylinder, *J. Non-Newtonian Fluid Mech.* 160 (2009) 157–167.
- [173] M. Bouaziz, S. Kessentini, S. Turki, Numerical prediction of flow and heat transfer of power-law fluids in a plane channel with a built-in heated square cylinder, *Int. J. Heat Mass Transfer* 53 (2010) 5420–5429.
- [174] A.K. Dhiman, R.P. Chhabra, V. Eswaran, Steady flow across a confined square cylinder: effects of power-law index and of blockage, *J. Non-Newtonian Fluid Mech.* 148 (2008) 141–150.
- [175] A.K. Sahu, R.P. Chhabra, V. Eswaran, Two-dimensional laminar flow of a power-law fluid across a confined square cylinder, *J. Non-Newtonian Fluid Mech.* 165 (2010) 752–763.
- [176] S.D. Dhole, R.P. Chhabra, V. Eswaran, Flow of power-law fluids past a sphere at intermediate Reynolds numbers, *Ind. Eng. Chem. Res.* 45 (2006) 4773–4781.
- [177] D. Song, R.K. Gupta, R.P. Chhabra, Wall effects on a sphere falling in quiescent power-law fluids in cylindrical tubes, *Ind. Eng. Chem. Res.* 48 (2009) 5845–5856.
- [178] D. Song, R.K. Gupta, R.P. Chhabra, Drag on a sphere in Poiseuille flow of shear-thinning power-law fluids, *Ind. Eng. Chem. Res.* 51 (2011) doi:10.1021/ie102120p.
- [179] P.K. Rao, C. Sasmal, A.K. Sahu, R.P. Chhabra, V. Eswaran, Effect of power-law fluid behaviour on momentum and heat transfer characteristics of an inclined square cylinder in steady flow regime, *Int. J. Heat Mass Transfer* 54 (2011), 2854–2867.
- [180] S. Nitin, R.P. Chhabra, Non-isothermal flow of a power-law fluid past a rectangular obstacle (of aspect ratio 1×2) in a channel: drag and heat transfer, *Int. J. Eng. Sci.* 43 (2005) 707–720.
- [181] R.C. Reid, J.M. Prausnitz, B. Poling, *The Properties of Gases and Liquids*, fifth ed., McGraw Hill, New York, NY, 1988.
- [182] M.W. Chang, B.A. Finlayson, Heat transfer in flow past cylinders at $Re \leq 150$, Part I: Calculations for constant fluid properties, *Numer. Heat Transfer* 12 (1987) 179–195.
- [183] M.W. Chang, B.A. Finlayson, C.A. Sleicher, Heat transfer in flow past cylinder at $Re < 150$, Part II: Experiments and theory for variable fluid properties, *Numer. Heat Transfer* 12 (1987) 197–210.
- [184] R.A. Ahmad, Steady-state numerical solution of the Navier–Stokes and energy equations around a horizontal cylinder at moderate Reynolds numbers from 100 to 500, *Heat Transfer Eng.* 17 (1996) 31–81.
- [185] C.F. Lange, F. Durst, M. Breuer, Momentum and heat transfer from cylinders in laminar crossflow at $10^{-4} \leq Re \leq 200$, *Int. J. Heat Mass Transfer* 41 (1998) 3409–3430.
- [186] A. Zukauskas, Convective heat transfer in cross-flow, in: *Handbook of single-phase convective heat transfer*, A. Zukauskas, S. Kakac, R.K. Shah, W. Aung (Eds.), Wiley, New York, NY, 1987, pp. 6.1–6.45.

- [187] R.P. Bharti, R.P. Chhabra, V. Eswaran, A numerical study of the steady forced convection heat transfer from an unconfined circular cylinder, *Heat Mass Transfer* 43 (2007) 639–648.
- [188] S.W. Churchill, H.H.S. Chu, Correlating equations for laminar and turbulent free convection from a horizontal cylinder, *Int. J. Heat Mass Transfer* 18 (1975) 1049–1053.
- [189] R.M. Fand, J.A. Brucker, A correlation for heat transfer by natural convection from horizontal cylinders that accounts for viscous dissipation, *Int. J. Heat Mass Transfer* 26 (1983) 709–726.
- [190] R.M. Fand, E.W. Morris, M. Lum, Natural convection from horizontal cylinders to air, water and silicone oils for Rayleigh numbers between 300 and 2×10^7 , *Int. J. Heat Mass Transfer* 20 (1977) 1173–1184.
- [191] F. Kreith, *The CRC Handbook of Thermal Engineering*, CRC Press, Boca Raton, FL, 2000.
- [192] O.G. Martynenko, P.P. Khramstov, *Free Convective Heat Transfer*, Springer, New York, NY, 2005.
- [193] A. Zukauskas, A. Zingza, *Heat Transfer of Cylinder in Cross Flow*, Hemisphere, Washington, DC, 1985.
- [194] E.M. Sparrow, J.P. Abraham, J.C.K. Tong, Archival correlations for average heat transfer coefficients for non-circular and circular cylinders and for spheres in crossflow, *Int. J. Heat Mass Transfer* 47 (2004) 5285–5296.
- [195] S. Sanitjai, R.J. Goldstein, Heat transfer from a circular cylinder in mixtures of water and ethylene glycol, *Int. J. Heat Mass Transfer* 47 (2004) 4785–4805.
- [196] R.W. Serth, K.M. Kiser, A solution of the two-dimensional boundary-layer equations for an Ostwald-de Waele fluid, *Chem. Eng. Sci.* 22 (1967) 945–956.
- [197] T. Mizushima, H. Usui, Approximate solution of the boundary layer equations for the flow of a non-Newtonian fluid around a circular cylinder, *Heat Transfer Jpn. Res.* 7 (1978) 83–92.
- [198] G.D. Bizzell, J.C. Slattery, Non-Newtonian boundary-layer flow, *Chem. Eng. Sci.* 17 (1962) 777–782.
- [199] C.J. Wolf, A.A. Szweczyk, Laminar heat transfer to non-Newtonian fluids from arbitrary cylinders, *Proceedings of Third International Heat Transfer Conference*, Chicago, vol. 1, 1966, pp. 388–397.
- [200] F.N. Lin, S.Y. Chern, Laminar boundary-layer flow of non-Newtonian fluid, *Int. J. Heat Mass Transfer* 22 (1979) 1323–1329.
- [201] H.W. Kim, D.R. Jeng, K.J. De Witt, Momentum and heat transfer in power-law fluid flow over two-dimensional or axisymmetric bodies, *Int. J. Heat Mass Transfer* 26 (1983) 245–259.
- [202] A. Nakayama, A.V. Shenoy, H. Koyama, An analysis for forced convection heat transfer from external surfaces to non-Newtonian fluids, *Warme-und Stoffubertragung* 20 (1986) 219–227.
- [203] A.V. Shenoy, A. Nakayama, Forced convection heat transfer for axisymmetric bodies to non-Newtonian fluids, *Can. J. Chem. Eng.* 64 (1986) 680–686.
- [204] H.I. Andersson, The Nakayama–Koyama approach to laminar forced convection heat transfer to power-law fluids, *Int. J. Heat Fluid Flow* 9 (1988) 343–346.
- [205] T.Y. Wang, C. Kleinstreuer, Local skin friction and heat transfer in combined free-forced convection from a cylinder or sphere to a power-law fluid, *Int. J. Heat Fluid Flow* 9 (1988) 182–187.
- [206] W.A. Khan, J.R. Culham, M.M. Yovanovich, Fluid flow and heat transfer in power-law fluids across circular cylinders—analytical study, *Proceedings of International Mechanical Engineering Congress and Exposition, IMECE 2005-79941*, Orlando, FL, 2005, pp. 1–13.
- [207] R.P. Bharti, R.P. Chhabra, V. Eswaran, Steady forced convection heat transfer from a heated circular cylinder to power-law fluids, *Int. J. Heat Mass Transfer* 50 (2007) 977–990.

- [208] R.P. Bharti, R.P. Chhabra, V. Eswaran, Effect of blockage on heat transfer from a cylinder to power-law fluids, *Chem. Eng. Sci.* 62 (2007) 4729–4741.
- [209] V.K. Patnana, R.P. Bharti, R.P. Chhabra, Two dimensional unsteady forced convection heat transfer in power-law fluids from a cylinder, *Int. J. Heat Mass Transfer* 53 (2010) 4152–4167.
- [210] A.A. Soares, J.M. Ferreira, L. Caramelo, J. Anacleto, R.P. Chhabra, Effect of temperature-dependent viscosity on forced convection heat transfer from a cylinder in cross flow of power-law fluids, *Int. J. Heat Mass Transfer* 53 (2010) 4152–4167.
- [211] S.D. Dhole, R.P. Chhabra, V. Eswaran, Forced convection heat transfer from a sphere to non-Newtonian power-law fluids, *AIChE J.* 52 (2006) 3658–3667.
- [211a] D. Song, R.K. Gupta, R.P. Chhabra, Effect of blockage on heat transfer from a sphere in power-law fluids, *Ind. Eng. Chem. Res.* 49 (2010) 3849–3861.
- [212] K.W. Westerberg, B.A. Finlayson, Heat transfer to spheres from a polymer melt, *Numer. Heat Transfer A* 17 (1990) 329–348.
- [213] A.V. Luikov, Z.P. Shulman, B.M. Berkovsky, Heat and mass transfer in a boundary layer of non-Newtonian fluids, *Proceedings of Third International Heat Transfer Conference, Chicago, vol. 1, 1966.*
- [214] A.V. Luikov, Z.P. Shulman, B.I. Puris, Mass transfer of cylinder in forced flow of non-Newtonian viscoelastic fluid, *Heat Transfer Sov. Res.* 1 (1969) 121–132.
- [215] A.V. Luikov, Z.P. Shulman, B.I. Puris, External convection mass transfer of cylinder in non-Newtonian fluids, *Int. J. Heat Mass Transfer* 12 (1969) 377–391.
- [216] K. Takashi, M. Maeda, S. Ikai, Experimental study of heat transfer from a cylinder submerged in a non-Newtonian fluid, *Die dem Nahenungsansatz von K. Pohlhausen Genugen, Lilenthal Bericht* 510 (1977) 335–339.
- [217] T. Mizushima, H. Usui, K. Veno, T. Kato, Experiments of pseudo-plastic fluid cross flow around a circular cylinder, *Heat Transfer Jpn. Res.* 7 (1978) 92–101.
- [218] S. Kumar, B.K. Mall, S.N. Upadhyay, On the mass transfer in non-Newtonian fluids. II. Transfer from cylinders to power-law fluids, *Lett. Heat Mass Transfer* 7 (1980) 55–64.
- [219] U.K. Ghosh, S.N. Gupta, S. Kumar, S.N. Upadhyay, Mass transfer in cross-flow of non-Newtonian fluid around a circular cylinder, *Int. J. Heat Mass Transfer* 29 (1986) 955–960.
- [220] B.K. Rao, Heat transfer to non-Newtonian flows over a cylinder in cross flow, *Int. J. Heat Fluid Flow* 21 (2000) 693–700.
- [221] K. Ogawa, C. Kuroda, I. Inoue, Forced convection mass transfer in viscoelastic fluid around a sphere and a cylinder, *J. Chem. Eng. Jpn.* 17 (1984) 654–656.
- [222] B.K. Rao, B.J. Phillips, J. Andrews, Heat transfer to viscoelastic polymer solutions flowing over a smooth cylinder, *Appl. Thermal Eng.* 1 (1996) 355–365.
- [223] E.R.G. Eckert, E. Soehngen, Distribution of heat transfer coefficients around circular cylinders in cross flow at Reynolds numbers from 20 to 500, *Trans. ASME* 74 (1952) 343–347.
- [224] J.P. Narain, Free and forced convective heat transfer from slender cylinders, *Lett. Heat Mass Transfer* 3 (1976) 21–30.
- [225] L.S. Yao, I. Catton, J.M. McDonough, Free-forced convection from a heated longitudinal horizontal cylinder, *Numer. Heat Transfer* 1 (1978) 255–266.
- [226] B. Farouk, S.I. Guceri, Natural and mixed convection heat transfer around a horizontal cylinder within confining walls, *Numer. Heat Transfer* 5 (1982) 329–341.
- [227] H.J. Merk, J.A. Prins, Thermal convection in laminar boundary layers, Parts I, II and III, *Appl. Sci. Res.* 4 (1953–54) 11–24, 195–206, 207–224.
- [228] G. Wilks, External natural convection about two-dimensional bodies with constant heat flux, *Int. J. Heat Mass Transfer* 15 (1972) 351–354.
- [229] J.A. Peterka, P.D. Richardson, Natural convection from a horizontal cylinder at moderate Grashof numbers, *Int. J. Heat Mass Transfer* 12 (1969) 749–752.

- [230] T.N. Kuehn, R.J. Goldstein, Numerical solution to the Navier–Stokes equations for laminar natural convection about a horizontal isothermal circular cylinder, *Int. J. Heat Mass Transfer* 23 (1980) 971–979.
- [231] K. Kitamura, F. Kami-iwa, T. Misumi, Heat transfer and fluid flow of natural convection around large horizontal cylinders, *Int. J. Heat Mass Transfer* 42 (1999) 4093–4106.
- [232] S.O. Atayilmaz, I. Teke, Experimental and numerical study of the natural convection from a heated horizontal cylinder, *Int. Commun. Heat Mass Transfer* 36 (2009) 731–738.
- [233] S.H. Moon, A.T. Johnson, T.M. Shih, Numerical analysis of mixed convection from horizontal cylinders, *J. Agric. Eng. Res.* 38 (1987) 289–300.
- [234] T. Saitoh, T. Sajik, K. Maruhara, Benchmark solutions to natural convection heat transfer problem around a horizontal circular cylinder, *Int. J. Heat Mass Transfer* 36 (1993) 1251–1259.
- [235] O. Zeitoun, M. Ali, Numerical investigation of natural convection around isothermal horizontal rectangular ducts, *Numer. Heat Transfer* 50A (2006) 189–204.
- [236] P. Wang, R. Kahawita, T.H. Nguyen, Numerical computation of the natural convection flow about a horizontal cylinder using splines, *Numer. Heat Transfer A* 17 (1990) 191–215.
- [237] P. Wang, R. Kahawita, D.L. Nguyen, Transient laminar natural convection from horizontal cylinders, *Int. J. Heat Mass Transfer* 34 (1991) 1429–1442.
- [238] A. Prhashanna, R.P. Chhabra, Laminar natural convection from a horizontal cylinder in power-law fluids, *Ind. Eng. Chem. Res.* 50 (2011) 2424–2440.
- [239] A. Acrivos, Heat transfer from a cylinder to a power-law non-Newtonian fluid, *AIChE J.* 6 (1960) 584–590.
- [240] T.C.A. Chang, D.R. Jeng, K.J. DeWitt, Natural convection to power-law fluids from two-dimensional or axisymmetric bodies of arbitrary contour, *Int. J. Heat Mass Transfer* 31 (1988) 615–624.
- [241] D.W. Lyons, J.W. White, J.D. Hatcher, Laminar natural convection heat transfer in dilute polymer solutions, *Ind. Eng. Chem. Fundam.* 11 (1972) 586–588.
- [242] C.C. Gentry, D.E. Wollersheim, Local free convection to non-Newtonian fluids from a horizontal isothermal cylinder, *J. Heat Transfer* 96 (1974) 3–8.
- [243] M.L. Ng, J.P. Hartnett, Natural convection in power-law fluids, *Int. Commun. Heat Mass Transfer* 13 (1986) 115–120.
- [244] M.L. Ng, J.P. Hartnett, Free convection heat transfer from horizontal wires to pseudoplastic fluids, *Int. J. Heat Mass Transfer* 31 (1988) 441–447.
- [245] M.L. Ng, J.P. Hartnett, R.Y.Z. Hu, Natural convection to horizontal wires—the conduction limit, *Int. Commun. Heat Mass Transfer* 15 (1988) 293–302.
- [246] M.L. Ng, J.P. Hartnett, E.Y. Kwack, Natural convection from horizontal wires to viscoelastic fluids, *J. Heat Transfer* 108 (1986) 790–795.
- [247] T. Fujii, M. Takeuchi, M. Fujii, K. Suzuki, H. Uehara, Experiments on natural convection heat transfer from the outer surface of a vertical cylinder to liquids, *Int. J. Heat Mass Transfer* 13 (1970) 753–787.
- [248] R.P. Chhabra, Free convective mass transfer from vertical short cylinders to non-Newtonian fluids, *Proceedings of Third ISHMT-ASME Heat and Mass Transfer Conference*, 1997, pp. 507–512.
- [249] A.P. Hatton, D.D. James, H.V. Swire, Combined forced and natural convection with low-speed air flow over horizontal cylinders, *J. Fluid Mech.* 42 (1970) 17–31.
- [250] R.N. Kieft, C.C.M. Rindt, A.A.V. Steenhoven, The wake behaviour behind a heated horizontal cylinder, *Exp. Thermal Fluid Sci.* 19 (1999) 183–193.
- [251] H.M. Badr, A theoretical study of laminar mixed convection from a horizontal cylinder in a cross stream, *Int. J. Heat Mass Transfer* 26 (1983) 639–653.

- [252] H. Hu, M. Kochesfahani, The wake behind a heated cylinder in forced and mixed convection regimes, ASME Summer Heat Transfer Conference, ASME, San Francisco, CA, 2005.
- [253] B.V. Khyati, H. Hui, Z.J. Wang, Numerical investigation of effect of buoyancy on the wake instability of a heated cylinder in contra flow, AIAA 0801 (2007) 1–19.
- [254] C-K. Chen, Y-T. Yang, S-R. Wu, Laminar mixed convection from a circular cylinder using a body-fitted coordinate system, *J. Thermophys. Heat Transfer* 8 (1994) 695–701.
- [255] D.C. Collis, M.J. Williams, Two-dimensional convection from heated wires at low Reynolds number, *J. Fluid Mech.* 9 (1959) 357–384.
- [256] R.M. Fand, K.K. Keswani, Combined natural and forced convection heat transfer from horizontal cylinders to water, *Int. J. Heat Mass Transfer* 16 (1973) 1175–1191.
- [257] V. Villimpoc, R. Cole, P.C. Sukanek, Heat transfer in Newtonian liquids around a circular cylinder, *Int. J. Heat Mass Transfer* 33 (1990) 447–456.
- [258] G.K. Sarma, S.P. Sukhatme, Combined free and forced convection heat transfer from a heated tube to a transverse air stream, *J. Heat Transfer* 91 (1969) 457–459.
- [259] E.M. Sparrow, L. Lee, Analysis of mixed convection about a horizontal cylinder, *Int. J. Heat Mass Transfer* 19 (1976) 229–232.
- [260] H.M. Badr, Laminar combined convection from a horizontal cylinder—parallel and contra flow regimes, *Int. J. Heat Mass Transfer* 27 (1984) 15–27.
- [261] H.M. Badr, On the effect of flow direction on mixed convection from a horizontal cylinder, *Int. J. Numer. Methods Fluids* 5 (1985) 1–12.
- [262] R.A. Ahmad, Z.H. Qureshi, Laminar mixed convection from a uniform heat flux horizontal cylinder in a crossflow, *J. Thermophys. Heat Transfer* 6 (1992) 277–287.
- [263] R.A. Ahmad, Z.H. Qureshi, Buoyancy effects on forced convection from a horizontal cylinder in a cross flow, *J. Thermophys. Heat Transfer* 7 (1993) 574–581.
- [264] K.-L. Wong, C.-K. Chen, The finite element solution of laminar combined convection from a horizontal cylinder, *Comput. Methods Appl. Mech. Eng.* 50 (1985) 147–161.
- [265] K.-S. Chang, J.-Y. Sa, The effect of buoyancy on vortex shedding in the near wake of a circular cylinder, *J. Fluid Mech.* 220 (1990) 253–266.
- [266] B.S.V. Patnaik, P.S.A. Narayana, K.N. Seetharamu, Numerical simulation of vortex shedding past a circular cylinder under the influence of buoyancy, *Int. J. Heat Mass Transfer* 42 (1999) 3495–3507.
- [267] A.A. Soares, J. Anacleto, L. Caramelo, J.M. Ferreira, R.P. Chhabra, Mixed convection from a circular cylinder to power-law fluids, *Ind. Eng. Chem. Res.* 48 (2009) 8219–8231.
- [268] A.T. Srinivas, R.P. Bharti, R.P. Chhabra, Mixed convection heat transfer from a cylinder in power-law fluids: effect of aiding buoyancy, *Ind. Eng. Chem. Res.* 48 (2009) 9735–9754.
- [269] B. Chao, R. Fagbenle, On Merk's methods of calculating boundary layer transfer, *Int. J. Heat Mass Transfer* 17 (1974) 223–240.
- [270] S.J.D. D'Alessio, S.C.R. Dennis, Steady laminar forced convection from an elliptic cylinder, *J. Eng. Math.* 29 (1995) 181–193.
- [271] H.M. Badr, Mixed convection from a straight isothermal tube of elliptic cross-section, *Int. J. Heat Mass Transfer* 37 (1994) 2343–2365.
- [272] H.M. Badr, Forced convection from a straight elliptical tube, *Heat Mass Transfer* 34 (1998) 229–236.
- [273] E.H. Ahmad, H.M. Badr, Mixed convection from an elliptic tube placed in a fluctuating free stream, *Int. J. Eng. Sci.* 39 (2001) 669–693.
- [274] H.M. Badr, K. Shamsheer, Free convection from an elliptic cylinder with major axis vertical, *Int. J. Heat Mass Transfer* 36 (1993) 3593–3602.
- [275] H.M. Badr, Laminar natural convection from an elliptic tube with different orientations, *J. Heat Transfer* 119 (1997) 709–718.

- [276] Y.-M. Chen, K.-C. Wang, Numerical and experimental studies on natural convection from a horizontal elliptic cylinder, *J. Chin. Inst. Chem. Eng.* 27 (1996) 353–362.
- [277] F.M. Mahfouz, S. Kocabiyik, Transient numerical simulation of buoyancy driven flow adjacent to an elliptic tube, *Int. J. Heat Fluid Flow* 24 (2003) 864–873.
- [278] S. Ahmad, N.M. Arifin, R. Nazar, I. Pop, Free convection boundary layer flow over cylinders of elliptic cross section with constant surface heat flux, *Eur. J. Sci. Res.* 23 (2008) 613–625.
- [279] S.J.D. D'Alessio, L.A. Finlay, J.P. Pascal, Free convection from elliptic cylinders at small Grashof numbers, *Int. J. Heat Mass Transfer* 51 (2008) 1379–1392.
- [280] S.J.D. D'Alessio, R.N. Perera, Unsteady free convection from elliptic cylinders at large Grashof numbers, *Int. J. Heat Mass Transfer* 52 (2009) 5940–5953.
- [281] M. Corcione, E. Habib, Multi-Prandtl correlating equations for free convection heat transfer from a horizontal tube of elliptic cross-section, *Int. J. Heat Mass Transfer* 52 (2009) 1353–1364.
- [282] S.Y. Huang, F. Mayinger, Heat transfer with natural convection around elliptic tubes, *Warne-und Stoffübertragung* 18 (1984) 175–183.
- [283] A.O. Elsayed, E.Z. Ibrahim, S.A. Elsayed, Free convection from a constant heat flux elliptic tube, *Energy Convers. Manage.* 44 (2003) 2445–2453.
- [284] T. Yousefi, M. Ashjaee, Experimental study of natural convection heat transfer from vertical array of isothermal horizontal elliptic cylinders, *Exp. Thermal Fluid Sci.* 32 (2007) 240–248.
- [285] M. Ashjaee, T. Yousefi, M. Amiri, Free convection heat transfer from a confined horizontal elliptic cylinder, *Heat Transfer Eng.* 27 (2006) 116–124.
- [286] O. Reymond, D.B. Murray, T.S. O'Donovan, Natural convection heat transfer from two horizontal cylinders, *Exp. Fluid Thermal Sci.* 32 (2008) 1702–1709.
- [287] C. Sasmal, R.P. Chhabra, Heat transfer by natural convection from a heated horizontal elliptic cylinder submerged in stagnant power-law liquids, Submitted for publication, 2011.
- [288] S.A. Nada, H. El-Batsh, M. Moawed, Heat transfer and fluid flow around semi-circular tube in cross flow at different orientations, *Heat Mass Transfer* 43 (2007) 1157–1169.
- [289] M. Farhadi, K. Sedighi, A.M. Korayem, Effect of wall proximity on forced convection in a plane channel with a built-in triangular cylinder, *Int. J. Thermal Sci.* 49 (2010) 1–9.
- [290] C.W. Knisely, Strouhal numbers of rectangular cylinders at incidence: a review and new data, *J. Fluids Struct.* 4 (1990) 371–393.
- [291] A.K. Dhiman, R.P. Chhabra, V. Eswaran, Flow and heat transfer across a confined square cylinder in the steady flow regime: effect of Peclet number, *Int. J. Heat Mass Transfer* 48 (2005) 4598–4614.
- [292] A.K. Dhiman, R.P. Chhabra, A. Sharma, V. Eswaran, Effects of Reynolds and Prandtl numbers on heat transfer across a square cylinder in the steady flow regime, *Numer. Heat Transfer A* 49 (2006) 717–731.
- [293] A.K. Sahu, R.P. Chhabra, V. Eswaran, Effects of Reynolds and Prandtl numbers on heat transfer from a square cylinder in the unsteady flow regime, *Int. J. Heat Mass Transfer* 52 (2009) 839–850.
- [294] A.K. Dhiman, R.P. Chhabra, V. Eswaran, Heat transfer to power-law fluids from a heated square cylinder, *Numer. Heat Transfer* 52 (2007) 185–201.
- [295] A.K. Sahu, R.P. Chhabra, V. Eswaran, Forced convection heat transfer from a heated square cylinder to power law fluids in the unsteady flow regime, *Numer. Heat Transfer A* 56 (2009) 109–131.
- [296] A.K. Sahu, R.P. Chhabra, V. Eswaran, Effect of blockage on forced convection heat transfer from a heated square cylinder to power-law fluids, *Numer. Heat Transfer A* 58 (2010) 641–659.

- [297] A.K. Dhiman, N. Anjaiah, R.P. Chhabra, V. Eswaran, Mixed convection from a heated square cylinder to Newtonian and power-law fluids, *J. Fluids Eng.* 129 (2007) 506–513.
- [298] A.K. Dhiman, R.P. Chhabra, V. Eswaran, Steady mixed convection from a confined square cylinder, *Int. Commun. Heat Mass Transfer* 35 (2008) 47–55.
- [299] G.D. Raithby, K.G.T. Hollands, A general method of obtaining approximate solutions to laminar and turbulent free convection problems, *Adv. Heat Transfer* 11 (1975) 265–315.
- [300] A.V. Hassani, Natural convection heat transfer from cylinders of arbitrary cross-section, *J. Heat Transfer* 114 (1992) 768–773.
- [301] A.V. Hassani, K.G.T. Hollands, On natural convection heat transfer from three-dimensional bodies of arbitrary shape, *J. Heat Transfer* 111 (1989) 363–372.
- [302] K.S. Chang, C.J. Choi, Separated laminar natural convection above a horizontal isothermal square cylinder, *Int. Commun. Heat Mass Transfer* 13 (1986) 201–208.
- [303] C.H. Cho, K.S. Chang, Experimental observations of temperature inversions over the horizontal square cylinder in natural convection, *Int. Commun. Heat Mass Transfer* 11 (1984) 275–281.
- [304] K.S. Chang, C.J. Choi, C.H. Cho, Laminar natural convection heat transfer from sharp-edged horizontal bars with flow separation, *Int. J. Heat Mass Transfer* 31 (1988) 1177–1187.
- [305] O. Zeitoun, M. Ali, Numerical investigation of natural convection around isothermal horizontal rectangular ducts, *Numer. Heat Transfer A* 50 (2006) 189–204.
- [306] M. Al-Arabi, A. Sarhan, Natural convection heat transfer from square cylinders, *Appl. Sci. Res.* 41 (1984) 93–104.
- [307] C.O. Popiel, J. Wojtkowiak, Experiments on free convective heat transfer from side walls of a vertical square cylinder in air, *Exp. Thermal Fluid Sci.* 29 (2004) 1–8.
- [308] M.E. Ali, Natural convection heat transfer from horizontal rectangular ducts, *J. Heat Transfer* 129 (2007) 1195–1202.
- [309] C. Sasmal, R.P. Chhabra, Laminar natural convection from a heated square cylinder immersed in power-law liquids, *J. Non-Newtonian Fluid Mech.* 166 (2011) 811–830.
- [310] E.R.G. Eckert, E.E. Soehngen, Studies on heat transfer with laminar free convection with the Zehnder–Mach interferometer, *Tech. Rep.* (1948) 5747, USAF Air Material Command.
- [311] S.K. Panda, R.P. Chhabra, Laminar flow of power-law fluids past a rotating cylinder, *J. Non-Newtonian Fluid Mech.* 165 (2010) 1442–1461.
- [312] S.K. Panda, R.P. Chhabra, Laminar forced convection heat transfer from a rotating cylinder to power-law fluids, *Numer. Heat Transfer* 59A (2011) 297–319.
- [313] R.C. Patil, R.P. Bharti, R.P. Chhabra, Steady flow of power-law fluids over a pair of cylinders in tandem arrangement, *Ind. Eng. Chem. Res.* 47 (2008) 1660–1683.
- [314] R.C. Patil, R.P. Bharti, R.P. Chhabra, Forced convection heat transfer in power-law liquids from a pair of cylinders in tandem arrangement, *Ind. Eng. Chem. Res.* 47 (2008) 9141–9164.
- [315] A. Tripathi, R.P. Chhabra, Slow power-law fluid flow relative to an array of cylinders, *Ind. Eng. Chem. Res.* 31 (1992) 2754–2759.
- [316] A. Tripathi, R.P. Chhabra, Transverse laminar flow of non-Newtonian fluids over a bank of cylinders, *Chem. Eng. Commun.* 147 (1996) 197–212.
- [317] M. Vijaysri, R.P. Chhabra, V. Eswaran, Power-law fluid flow across an array of infinite circular cylinders: a numerical study, *J. Non-Newtonian Fluid Mech.* 87 (1999) 263–282.
- [318] S. Shibu, R.P. Chhabra, V. Eswaran, Power-law fluid flow over a bundle of cylinders at intermediate Reynolds numbers, *Chem. Eng. Sci.* 56 (2001) 5545–5554.
- [319] B.N. Dhotkar, R.P. Chhabra, V. Eswaran, Flow of non-Newtonian polymeric solutions in fibrous media, *J. Appl. Polym. Sci.* 76 (2000) 1171–1185.

- [320] R.P. Chhabra, B.N. Dhotkar, V. Eswaran, V.K. Satheesh, M. Vijaysri, Steady flow of Newtonian and dilatant fluids over an array of long circular cylinders, *J. Chem. Eng. Jpn.* 33 (2000) 832–841.
- [321] N. Mangadoddy, R. Prakash, R.P. Chhabra, V. Eswaran, Forced convection in cross flow of power-law fluids over a tube bank, *Chem. Eng. Sci.* 59 (2004) 2213–2222.
- [322] P.D.M. Spelt, T. Selerland, C.J. Lawrence, P.D. Lee, Flow of inelastic non-Newtonian fluids through arrays of aligned cylinders, Part 1: Creeping flow, *J. Eng. Math.* 51 (2004) 57–80, Also see p. 81.
- [323] P.D.M. Spelt, A.Y. Yeow, C.J. Lawrence, T. Selerland, Creeping flows of Bingham fluids through arrays of aligned cylinders, *J. Non-Newtonian Fluid Mech.* 129 (2005) 66–74.
- [324] J.K. Woods, P.D.M. Spelt, P.D. Lee, T. Selerland, C.J. Lawrence, Creeping flows of power-law fluids through periodic arrays of elliptical cylinders, *J. Non-Newtonian Fluid Mech.* 111 (2003) 211–228.

AUTHOR INDEX

A

Abbassi, H., 306, 323, 362, 393
 Abdel Khalik, S., 105, 125, 138
 Abdel-Khalik, S.I., 87, 152, 195
 Abdollahi, V., 335, 341, 342
 Abdullah, Z., 89
 Abraham, J.P., 371
 Abraham, M.A., 190
 Abramovich, G.N., 259, 260
 Acosta, A.J., 316
 Acrivos, A., 317, 332, 371, 380, 382, 383
 Adler, P.M., 317
 Agostini, B., 82, 82, 96, 97, 105, 125, 195
 Agrawal, A., 183
 Ahmad, E.H., 390
 Ahmad, R.A., 371, 385
 Ahmad, S., 390
 Ahmed, S., 47
 Ahn, H.S., 30, 31, 34, 59, 63, 64
 Akbar, M.K., 96
 Akiyama, M., 16
 Al-Arabi, M., 396
 Al-Hayes, R.A.M., 89
 Ali, M., 323, 362, 380, 393, 396
 Ali, M.E., 396
 Allen, M.P., 86
 Ambari, A., 338, 341, 342, 349, 350
 Ameal, T., 130
 Amitestov, Y.V., 17, 23
 Ammerman, C.N., 49
 Anacleto, J., 334, 371, 377, 385, 386
 Anagnostopoulos, P., 349
 Anderson, G.H., 89, 162, 163, 164
 Anderson, T.M., 7, 14, 25, 44
 Andersson, H.I., 371
 Andrews, J., 377
 Anjaiah, N., 336, 395
 ANSYS Inc, 266, 270, 277
 Arbalaez, F., 36
 Arcanjo, A.A., 95, 96, 97, 98
 Arie, M., 321
 Arifin, N.M., 390

Arik, M., 4, 8, 9, 10, 12, 13, 14, 16, 20, 21,
 22, 38, 40, 43, 46, 48
 Arinobu, M., 245
 Armand, A.A., 177
 Armstrong, R.C., 290, 291, 292, 295, 315
 Ashjaee, M., 390, 392
 Astarita, G., 291, 371
 Atayilmaz, S.O., 380
 Atiemo-Obeng, V., 291
 Auradou, H., 349
 Aussillous, P., 188
 Avedisian, C.T., 46
 Aya, I., 231, 249, 251

B

Bachelder, D.M., 137
 Badr, H.M., 385, 390
 Bae, Y.Y., 233, 235, 237, 238, 240, 242, 243,
 246, 249, 251, 264, 266
 Baek, S.C., 235, 236, 242, 243
 Bailey, Q., 316
 Balasubramanian, P., 101, 102, 103, 105, 119
 Balch, S.E., 32
 Banerjee, D., 30, 31, 34
 Bang, I.C., 51, 54, 55
 Bao, Z.Y., 101, 105, 138
 Bar-Cohen, A., 4, 5, 6, 7, 13, 17, 18, 19,
 20, 21, 22, 24, 33, 38, 43, 46, 47, 48,
 49, 65
 Baranenko, V.I., 48
 Barnea, D., 95, 96
 Barnes, F.H., 348
 Barnes, H.A., 291, 296
 Barron, R.F., 137
 Barron, R.M., 306, 319, 323, 352
 Bau, H., 137
 Beardmore, R.H., 82, 83
 Behar, M., 48
 Belov, L.A., 48
 Ben Richou, A., 338, 341, 342, 349, 350
 Berenssen, P.J., 25
 Bergin, C., 317

Bergles, A.E., 7, 17, 20, 23, 25, 48, 65, 82, 99,
100, 101, 105, 138, 152, 162, 163, 164,
191, 192, 195, 196
Berkovsky, B.M., 377
Bernath, L., 16
Bernsdorf, J., 327
Bertsch, S.S., 82, 82, 130
Bestion, D., 280
Bharti, R.P., 306, 307, 311, 312, 315,
323, 333, 334, 335, 338, 339, 340,
341, 342, 343, 344, 346, 348, 350,
352, 354, 356, 357, 359, 371, 373,
374, 375, 376, 377, 378, 379, 385,
390, 398
Bhavnani, S.H., 32, 33
Bi, Q.C., 105
Bier, K., 47
Bijjam, S., 306, 323, 324, 362, 393
Bird, R.B., 290, 291, 292, 295
Bizzell, G.D., 371
Black, S.H., 103, 104, 105, 118, 123, 124,
134
Bloor, M.S., 305
Bogojevic, D., 82, 82
Boisaubert, N., 321
Bon, B., 82
Bonekamp, S., 47
Bonilla, C.F., 191
Bontemps, A., 105
Borishanskii, V.M., 191
Borrelli, J., 162, 163, 168, 169, 192
Bosnick, M.G., 138
Bostanci, H., 13, 41, 42, 46
Bouard, D., 321
Bouaziz, M., 336, 363, 365, 395
Boure, J.A., 82
Bowen, V., 137
Bowers, M.B., 80, 82, 90, 91, 137, 138
Boye, H., 114, 138, 139
Brauner, N., 80, 96
Bravo, H.R., 306, 319, 352
Breuer, M., 327, 371
Brown, R.A., 315
Brucker, J.A., 371
Brusstar, M.J., 7, 8, 21
Brutin, B., 105
Buongiorno, J., 51, 54, 55, 63, 64, 65
Busse, C.A., 112
Butkus, A., 352, 390

C

Cadot, O., 316
Calay, R.K., 230, 231
Calmi, D., 195
Cao, Y., 233, 235, 238, 242, 250, 251
Capp, S.P., 256, 257
Caramelo, L., 334, 371, 377, 385, 386
Carey, V.P., 47
Carne, M., 16
Carrano, A.L., 165
Carreau, P.J., 291, 292
Carreveau, R., 306, 319, 323, 352
Cartwright, M.D., 163, 164
Carvalho, R.D.M., 7, 17, 25, 65
Catton, I., 379
Celata, G.P., 105, 136, 156, 191
Cerro, R.L., 189, 190
Chakraborty, J., 349, 350
Chan, C.K., 229, 232, 244, 246, 247
Chandra, A., 306, 321, 323, 324, 325, 330,
335, 358, 360, 361, 362, 392, 393
Chandra, R., 56, 63
Chandratilleke, G.R., 169
Chang, D.-T., 233, 235, 237, 250, 251
Chang, G.-Z., 304
Chang, J.Y., 18, 33, 46
Chang, K.S., 385, 396
Chang, M.W., 370, 377
Chang, S.H., 51, 54
Chang, T.C.A., 380
Chang, Y., 95
Chang, Y.P., 192
Chantry, R.A.R., 86
Chao, B., 390
Charlesworth, D.H., 16
Chen, C.-K., 385
Chen, G., 189
Chen, H., 82
Chen, J., 137
Chen, J.C., 114, 116, 118
Chen, J.H., 349, 350
Chen, L., 132
Chen, L.D., 238
Chen, T., 100
Chen, X.J., 152
Chen, Y.-M., 390
Cheng, P., 82, 99, 100, 101, 103, 105, 156,
157, 168, 171, 172, 192

Cheng, X., 195
 Cheol, H., 105
 Chern, S.Y., 371
 Cherniakov, P.S., 192
 Cheung, L.S.L., 165
 Chhabra, R.P., 290, 291, 292, 295, 306, 307, 311, 312, 315, 316, 317, 319, 320, 321, 322, 323, 324, 325, 327, 328, 329, 330, 331, 332, 333, 334, 335, 336, 337, 338, 339, 340, 341, 342, 343, 344, 346, 348, 349, 350, 351, 352, 354, 356, 357, 358, 359, 360, 361, 362, 363, 364, 365, 366, 367, 368, 369, 370, 371, 373, 374, 375, 376, 377, 378, 379, 380, 381, 384, 385, 386, 390, 392, 393, 395, 396, 397, 398
 Chih-Ming, H., 105
 Chisholm, D., 134, 135, 138
 Chiyu, M.C., 105, 140
 Cho, C.H., 396
 Cho, S., 230, 235, 240, 244, 245, 246, 247, 248
 Cho, Y.I., 291
 Choi, C.J., 396
 Choi, C.W., 182
 Choi, K., 118
 Choi, K.I., 130, 132, 134
 Choi, N.H., 244, 245
 Choi, S.B., 137
 Choi, S.M., 233, 235, 237, 238, 240, 242, 243, 249, 251, 264, 266
 Choo, Y.J., 252, 260, 261, 262, 263, 268
 Chow, L.C., 41, 42
 Christopher, D.M., 172
 Chu, H.H.S., 371
 Chu, R.C., 25
 Chun, M.H., 230, 232, 233, 235, 236, 238, 245, 249, 251
 Chun, S.Y., 246, 247, 248
 Chung, B.D., 266, 267, 275
 Chung, H.J., 246, 247, 248
 Chung, M.K., 230, 235, 240, 244, 245, 246, 247, 248
 Chung, P.M., 80
 Chung, P.M.-Y., 105, 138, 178, 179, 180, 181, 182, 187
 Churchill, S.W., 371
 Cleveland, R.G., 140, 144
 Coelho, P.M., 318, 319, 329, 335, 348
 Cole, G.S., 195

Cole, R., 16, 385
 Colin, S., 162, 192
 Collier, J.H., 89
 Collis, D.C., 385
 Comiti, J., 291
 Consolini, L., 82, 82, 103, 152
 Cooper, M.G., 118
 Corcione, M., 390
 Cornwell, K., 80, 101, 105, 117, 118
 Courtaud, M., 48
 Coutanceau, M., 304, 305, 321
 Cressman, J.R., 316
 Cubaud, T., 105
 Culham, J.R., 332, 352, 371, 390
 Cullion, R., 182
 Cummins, G., 82, 82
 Cumo, M., 136, 231, 235
 Czyzewska, E., 137

D

Dahikar, S.K., 250, 262, 265, 269
 Dai, G.C., 291
 Daiguji, H., 116, 124, 125, 126, 134
 Dalal, A., 306, 323, 362, 393
 Dale, J.D., 122, 123
 D'Alessio, S.J.D., 307, 309, 333, 339, 342, 352, 390
 Damasio, C., 246, 247
 D'Amico, S., 50, 51
 Danielsen, R.D., 5
 Dao, R., 137
 David, M., 183, 188
 Davidson, L., 327
 Davis, E.J., 89, 162, 163, 164
 Davis, R.W., 327
 Daw, V., 192
 de Mestre, N.J., 349
 De With, A.P., 230, 231
 De With, G., 230, 231
 De Witt, K.J., 371, 380
 De, A., 239
 De, A.K., 306, 323, 362, 393
 Defaye, J.R., 304, 305
 DeKee, D., 291, 292
 Del Tin, G., 231, 238, 240, 241, 242, 246, 247
 Dennis, S.C.R., 304, 352, 390
 Despeyroux, A., 338, 341, 342, 350
 Dessiatoun, S.V., 138

Dew, E., 48
 DeWitt, K.J., 380
 Dharaiya, V.V., 166, 168
 Dhiman, A.K., 306, 323, 324, 327, 336, 362, 363, 368, 393, 395
 Dhir, V.K., 22, 67, 117, 192
 Dhole, S.D., 364, 374
 Dhotkar, B.N., 398
 D'Humieres, D., 82
 Diaz, A.C., 103
 Dietz, C., 40
 Dikshit, A.K., 306, 319, 352
 Ding, L.S., 91
 Ding, Y., 152
 Dinh, T.N., 82
 Dowling, M.F., 87, 152, 195
 Droll, M., 138
 Du, D.X., 135, 136
 Dubois, F., 266, 267, 275
 Ducros, F., 266, 267, 275
 Dukler, A.E., 96, 140, 144
 Dunskus, T., 46
 Dupont, V., 103, 105, 113, 125, 127, 133, 134
 Durst, F., 327, 371
 Duttagupta, S.P., 183
 Dvinsky, A.S., 349

E

Eckert, E.R.G., 379, 397
 Edwards, M.F., 291
 Egusa, T., 250, 251, 252
 Ehrmann, P., 321
 El-Batsh, H., 392
 El-Genk, M.S., 12, 13, 37, 38, 39, 46
 Elkassabgi, Y., 6
 Elsayed, A.O., 390
 Elsayed, S.A., 390
 Englert, S.B., 202, 208
 Epstein, N., 123
 Erbacher, F.J., 195
 Eswaran, V., 327, 333, 336, 339, 341, 342, 343, 344, 346, 350, 363, 364, 365, 366, 367, 368, 369, 371, 373, 374, 375, 377, 378, 379, 395, 397, 398

F

Fabbri, M., 195
 Faeth, G.M., 238, 254

Fagbenle, R., 390
 Fand, R.M., 371, 380, 385
 Fang, C., 188
 Fareello, G.E., 231, 235
 Farhadi, M., 393
 Farouk, B., 379
 Fartaja, A., 306, 319, 323, 352
 Faruquee, Z., 306, 319, 323, 352
 Faxen, O.H., 349
 Felcar, H.O.M., 95
 Feng, J., 349
 Feng, Z., 80, 105, 176, 177, 178, 186, 187
 Fernando, P., 130
 Ferrari, G.E., 231, 235
 Ferreira, J.M., 333, 334, 339, 341, 342, 371, 375, 377, 385, 386
 Fiegna, G., 246, 247
 Findlay, J.A., 97, 135
 Finlay, L.A., 307, 333, 342, 390
 Finlayson, B.A., 370, 377
 Fisenko, V.V., 48
 Fisher, T., 30, 31
 Fisher, T.S., 169
 Fletcher, D.F., 101, 105
 Fogg, D., 183
 Fornberg, B., 304
 France, D.M., 101, 105, 117, 140
 Francesco, D., 173
 Fredsoe, J., 290, 302, 305, 306, 319, 340, 349, 352
 Freitas, J.O., 95, 96, 97, 98
 Friedel, L., 138
 Fries, D.M., 189
 Fritz, W., 80
 Fu, L.Q., 152
 Fujii, M., 384
 Fujii, T., 384
 Fujishior, T., 48
 Fujita, Y., 47
 Fukamachi, N., 138, 187
 Fukano, T., 138
 Fukuda, S., 231, 244, 245

G

Gadd, G.E., 317
 Galloway, J.E., 4
 Gamble, R.E., 270, 271, 272
 Gan, Y., 103

Gan, Y.H., 103, 105
 Garimella, S., 100, 162, 166, 192
 Garimella, S.V., 81, 82, 81, 82, 98, 99,
 103, 130, 168
 Gau, C., 169
 Gentry, C.C., 383, 384
 George, W.K., 256, 257
 Gerner, F.M., 79
 Gersey, C., 24
 Ghiaasiaan, S., 105, 125, 138
 Ghiaasiaan, S.M., 87, 96, 152, 195
 Ghosh, U.K., 291, 316, 332, 371,
 377, 378
 Giavedoni, A.D., 85
 Goldberg, W.I., 316
 Goldstein, R.J., 371, 380
 Golobic, I., 20
 Gonthier, Y., 189
 Goodson, K., 183
 Goodson, K.E., 82, 82, 109, 165,
 168, 188
 Goujon-Durand, S., 306, 323
 Graffard, E., 266, 267, 275
 Grande, W.J., 80
 Granryd, E., 130
 Greif, R., 270, 271, 272
 Griffith, P., 1, 80, 191, 249
 Grigoriev, V.A., 17, 23
 Groisman, A.
 Groll, E.A., 82, 82, 130
 Groll, M., 82
 Grotberg, J.B., 188
 Grove, A.S., 341
 Gubbins, K.E., 86
 Gucer, S.I., 379
 Guglielmini, G., 17
 Gui, F., 79, 82
 Guilpart, J., 82, 82
 Gulawani, S.S., 249, 250, 251, 262, 263,
 264, 265, 269
 Gulielmi, M., 136
 Gulliksen, M., 36
 Gungor, K.E., 118, 126
 Guo, L.J., 27
 Guo, Z.Y., 135, 136, 137
 Gupta, A., 56, 63
 Gupta, A.K., 363, 368, 395
 Gupta, O.P., 317
 Gupta, R.K., 364, 374
 Gupta, S.N., 377

H

Habib, E., 390
 Haile, J.M., 86
 Hall, D.D., 80
 Han, C.D., 290, 292, 295
 Han, Y., 187, 188, 189
 Hapke, I., 138, 139
 Haramura, Y., 3, 66, 192
 Harirchian, T., 81, 82, 81, 98, 99, 103
 Harley, J., 137
 Harms, T.M., 79
 Harnby, N., 291
 Hartnett, J.P., 291, 383, 384
 Hashiguchi, H., 182
 Hasimoto, H., 352
 Hassager, O., 290, 291, 292, 295
 Hassan, I.G., 96
 Hassani, A.V., 396
 Hatcher, J.D., 383
 Hatton, A.P., 385
 Haugerud, H., 36
 Haussling, H.J., 352
 Haynes, B.S., 101, 105, 138
 Hazuku, T., 138, 187
 Heck, K., 105
 Heitsch, M., 266, 267, 275
 Henderson, R.D., 304
 Heo, J.H., 128
 Hesselgreaves, J.E., 290
 Hetsroni, G., 82, 82, 91, 93, 94, 95, 100, 101,
 102, 103, 113, 114, 115, 152, 153, 154,
 155, 156
 Heyes, D.M., 87
 Hibiki, T., 99, 105, 116, 137, 138, 140, 142,
 143, 144, 145, 147, 187, 202
 Hidehiko, K., 128
 Hidrovo, C.H., 187
 Hihara, E., 116, 124, 125, 126, 134, 172
 Hollands, K.G.T., 396
 Homann, F., 341
 Honda, H., 26, 27, 28
 Hong, C.P., 172
 Hong, F.J., 82
 Hong, S.J., 244, 246
 Hong, Y., 41, 42
 Hong, Y.S., 49
 Hourigan, K., 306, 319, 323, 352
 Howard, A.H., 24
 Hoyt, J.W., 317

Hsieh, T.C., 350
 Hsu, Y.Y., 91, 161, 162, 164
 Hu, H., 385
 Hu, H.H., 349
 Hu, H.Y., 87, 89, 90, 91, 92
 Hu, L., 63, 64, 65
 Hu, L.W., 51, 54, 55
 Hu, R.Y.Z., 383
 Huai, X., 128
 Huang, P.Y., 349
 Huang, S.Y., 390
 Huh, D., 188
 Hui, H., 385
 Hulin, J.P., 349
 Hull, J.R., 101, 117
 Huo, X., 130, 132, 134
 Hussein, H.J., 256, 257
 Hwan, Y.W., 138
 Hwang, U.P., 6

I

Iaccarino, G., 316, 317
 Ibrahim, E.Z., 390
 Ide, H., 182
 Ikai, S., 377
 Ikawa, H., 201, 208
 Ikenze, E., 163, 164
 Ilgarbuis, U.R., 352, 390
 Illiadis, G., 349
 Im, Y., 40
 Imai, I., 352
 Inada, S., 169
 Inasaka, F., 195
 Innoue, A., 103, 104
 Inoue, A., 138
 Inoue, I., 377
 Ishibashi, E., 82, 82, 109
 Ishii, M., 138, 187, 201, 206
 Ishimaru, J., 170
 Ishizuka, M., 79, 170
 Israelachvili, J., 86
 Ivey, H.J., 6, 8, 44
 Iwasaki, H., 79, 170

J

Jackson, C.P., 306, 319, 323, 352
 Jacobi, A.M., 80, 103, 105, 113, 125, 127,
 133, 134

Jaeger, R.C., 32, 33
 Jain, A., 183
 Jalaiah, N., 350
 James, D.D., 385
 James, D.F., 316, 317
 Jay, P., 309, 315, 335
 Jendrzeczyk, J.A., 101
 Jeng, D.R., 371, 380
 Jensen, M.K., 138, 195
 Jeter, S.M., 87, 152, 195
 Jiang, L., 87
 Jiang, M.J., 91
 Johnson, A.T., 380
 Johnson, S.A., 306, 319, 323, 352
 Jones, B.J., 166
 Jones, J., 137
 Joshi, J.B., 250, 251, 262, 263, 264, 265, 269
 Joshi, Y., 40
 Júlio do Nascimento, F., 186

K

Kaew-On, J., 82, 83, 128, 130, 131, 132, 133,
 134
 Kagawa, M., 138
 Kahawita, R., 380
 Kakac, S., 82, 152
 Kalashnikov, V.N., 317
 Kaloni, P.N., 337
 Kami-iwa, F., 380
 Kaminaga, M., 201, 208
 Kandlikar, S.G., 8, 21, 80, 82, 82, 100, 101,
 102, 103, 105, 109, 117, 119, 121, 126,
 139, 140, 152, 162, 163, 164, 165, 166,
 167, 168, 169, 190, 191, 192, 193, 194,
 195, 196, 197, 198, 202, 207, 336
 Kang, H.S., 266, 267, 268, 269, 270, 275, 277,
 281
 Karayiannis, T.G., 130, 132, 134
 Kariyasaki, A., 138
 Kasagi, N., 187, 189
 Kashiwabara, Y., 190
 Kathiravan, R., 56, 63
 Kato, H., 317
 Kato, T., 377
 Katto, Y., 3, 191, 192, 201, 206, 207
 Kawahara, A., 138, 178, 179, 180, 181, 182,
 187
 Kawaji, M., 80, 105, 138, 178, 179, 180, 181,
 182, 187

- Kawamura, H., 16, 170, 171
 Kawano, K., 79, 170
 Kawara, Z., 105, 176, 177, 178, 186, 187
 Kazmierczak, M.J., 79
 Kell, R.E., 317, 318
 Keller, R.B., 7, 21
 Kennedy, J.E., 87, 152
 Kennel, W.E., 48
 Kenning, D.B.R., 105, 118, 130, 134
 Kenny, T.W., 82, 82, 109, 165, 168
 Kerney, P.J., 238
 Kessentini, S., 336, 363, 365, 395
 Keswani, K.K., 385
 Kew, P.A., 80, 101, 105, 117, 118
 Khan, W.A., 332, 352, 371, 390
 Khanikar, V., 169
 Khramstov, P.P., 371, 379
 Khyati, B.V., 385
 Kieft, R.N., 385
 Kim, B.K., 317
 Kim, H., 52, 56, 57, 58, 59, 63, 64
 Kim, H.W., 371, 380
 Kim, H.Y., 233, 235, 237, 238, 240, 242, 243, 246, 249, 251, 264, 266
 Kim, J., 52, 56, 57, 58, 59
 Kim, J.H., 49, 50, 51, 52
 Kim, K.H., 49, 50, 51, 52
 Kim, K.J., 37
 Kim, M., 52, 56, 57, 58, 59
 Kim, M.H., 59, 63, 64, 182
 Kim, M.S., 128, 138
 Kim, S.J., 51, 54, 55
 Kim, Y., 128
 Kim, Y.S., 230, 231, 232, 233, 235, 236, 238, 245, 249, 250, 251, 252, 258, 259, 260, 261, 266, 268
 Kimura, R., 182
 King, M., 162, 192
 Kinjo, T., 87
 Kirby, B., 7, 21
 Kirby, D.B., 3
 Kirishenko, Y.A., 192
 Kiser, K.M., 371
 Kitamura, K., 380
 Kiya, M., 321
 Kizito, J.P., 41, 42
 Kleinstreuer, C., 371
 Klimentko, V.V., 17, 23
 Knisely, C.W., 395
 Kocabiyik, S., 390
 Kochofahani, M., 385
 Kokubu, T., 171
 Kolb, W.B., 189
 Konishi, K., 317
 Koniuta, A., 317
 Korayem, A.M., 393
 Korenevskiy, V.A., 48
 Kosar, A., 195
 Kotake, M., 321
 Koyama, H., 371
 Koyama, S., 128
 Kramer, T.A., 187
 Kreith, F., 371
 Kresta, S.M., 291
 Kries, H.H., 137
 Kristiansen, H., 36
 Kuan, W.K., 192, 195
 Kudin, A.M., 317
 Kudo, A., 250, 251, 252
 Kuehn, T.N., 380
 Kulenovic, R., 138
 Kumar, B., 349
 Kumar, R., 50, 51, 52, 53, 56, 63, 65, 66, 67
 Kumar, S., 377
 Kumar, S., 316
 Kunitsugu, K., 317
 Kunugi, T., 270, 274, 275, 276
 Kuo, C.-H., 188
 Kuo, C.-J., 195
 Kuo, C.J., 166, 168, 169, 192
 Kuroda, C., 377
 Kutateladze, S.S., 6, 33, 44, 191
 Kuzma-Kichta, Y., 172
 Kwack, E.Y., 383
 Kwark, S.M., 65, 66, 67
 Kwon, T.S., 246
- L**
- Lai, R.I., 128
 Lallemand, P., 82
 Lamb, H., 337, 342
 Landau, L.D., 337
 Lange, C.F., 371
 Larson, R.G., 290, 292, 295
 Lau, S.C., 31, 34
 Lavagno, E., 231, 238, 240, 241, 242
 Lawal, A., 291
 Lawrence, C.J., 398

- Lazarek, G.M., 103, 104, 105, 118, 123, 124, 134
 Lebey, M., 349
 Lee, C.K.B., 229, 232
 Lee, D.J., 170
 Lee, E.S., 187
 Lee, H.J., 105, 118, 137, 140
 Lee, J.D., 82, 82
 Lee, L., 385
 Lee, M., 165
 Lee, P.-S., 168
 Lee, P.C., 95, 105, 169
 Lee, P.D., 398
 Lee, S., 10, 11, 14, 15, 43, 44, 49
 Lee, S.S., 40
 Lee, S.Y., 105
 Lee, T.Y., 46
 Lee, T.Y.T., 6, 7, 46
 Lee, Y.K., 165
 LeMouel, A., 138
 Lepere, V.J., 25
 Leung, A.M., 137
 Levine, S., 123
 Levy, S., 89
 Li, D., 122, 123, 137, 162, 192
 Li, J., 105, 168
 Li, P.L., 169
 Li, W., 81, 105, 109, 119, 120, 144, 148, 149, 150, 151, 202
 Li, W.-J., 231, 232, 233, 234, 235, 237, 240, 241, 250, 251
 Li, X.H., 103, 105
 Li, Y., 103, 233, 235, 240, 241
 Li, Z.X., 135, 136, 137
 Liang, K.S., 249
 Liao, L., 54, 60
 Liaw, S.P., 67
 Liburdy, J., 182
 Lie, Y.M., 128
 Lienhard, J.H., 6, 14, 19, 22, 23, 192
 Lifshitz, E.M., 337
 Lin, C.-Y., 348
 Lin, F.N., 371
 Lin, H., 82, 82
 Lin, L., 90, 91
 Lin, S., 101, 105
 Lin, T., 101, 105, 128
 Lin, T.F., 128
 Lin, Z., 91, 93, 94, 113, 114
 Little, W.A., 137
 Liu, C.W., 169
 Liu, D., 168
 Liu, G.-Y., 231, 232, 233, 234, 235
 Liu, J.-P., 233, 235, 238, 242, 250, 251
 Liu, M.N., 13, 47
 Liu, T.Y., 169
 Liu, Z., 54, 60, 105
 Lockhart, R.W., 134, 135
 Lorenzini, E., 82
 Lugt, H.J., 352
 Luikov, A.V., 317, 377
 Lum, M., 371, 380
 Lundquist, P., 130
 Luninski, Y., 95, 96
 Luo, L., 189
 Luo, X.B., 137
 Lyons, D.W., 383
- ## M
- Ma, H.B., 90
 Maa, J.R., 13, 47, 95
 Machac, I., 291
 Machi, H., 82, 82
 Maeda, M., 377
 Magnin, A., 309, 315, 335
 Magrini, U., 17
 Mahaffy, J., 266, 267, 275
 Mahajan, R.L., 36
 Mahalingam, M., 6, 7, 46
 Mahfouz, F.M., 390
 Makuta, T., 172
 Mala, G.M., 122, 123, 137
 Malandrone, M., 231, 238, 240, 241, 242, 246, 247
 Mall, B.K., 377
 Manero, O., 317
 Mangadoddy, N., 398
 Maracy, M., 67
 Mariani, A., 191
 Marriott, J.R., 123
 Martin-Callizo, C., 105, 128
 Martinelli, R.C., 134, 135
 Marto, P.J., 25
 Martynenko, O.G., 371, 379
 Martys, N.S., 82
 Maruhara, K., 380
 Marusic-Paloka, E., 333, 337

- Maruyama, S., 86
 Masaki, M., 128
 Mashelkar, R.A., 291, 371
 Mathpati, C.S., 250, 262, 265, 269
 Matsumoto, M., 87
 Matsumoto, Y., 172
 Matsumura, H., 89, 162, 163, 164
 Matsuno, T., 352, 390
 Matsuo, H., 182
 Mavko, B., 103
 Mayinger, F., 390
 McAdams, W.H., 48
 McClanahan, T., 317
 McCord, B., 138
 McDonough, J.M., 379
 McGillis, W.R., 47
 McKinley, G.H., 315
 McKrell, T., 63, 64, 65
 Mcleod, D., 89
 McNeil, A., 6, 18, 20
 McNeil, A.C., 7, 8, 17, 18, 24
 Mehendale, S.S., 80
 Meller, N.A., 352
 Mena, B., 317
 Merk, H.J., 379
 Merte, H., 7, 8, 21
 Mertz, R., 82
 Mesler, R.B., 3, 21
 Mettu, S., 349, 350
 Metzner, A.B., 291
 Mi, Y., 138, 202
 Michel, B., 195
 Milanova, D., 50, 51, 52, 53
 Milanovic, V., 137
 Minakami, K., 79
 Minden, C.S., 48
 Mishima, K., 99, 105, 114, 116, 118, 137, 138,
 140, 142, 143, 144, 145, 147, 201, 202, 206
 Misumi, T., 380
 Mittal, S., 349
 Miyasaka, Y., 169
 Miyata, K., 201, 208
 Mizo, V.R., 163, 164
 Mizuno, Y., 317
 Mizushina, T., 371, 377
 Moalem-Maron, D., 80
 Moawed, M., 392
 Modi, V.J., 306, 319, 352
 Molki, M., 138
 Monkewitz, P.A., 318, 335
 Moo, H.K., 105
 Moon, H., 66, 67
 Moon, S.H., 380
 Moon, Y.T., 270, 276, 277, 278, 279
 Moore, E.F., 327
 Moran, K.P., 6, 25
 Moreno, G., 65, 66, 67
 Morgan, D.E., 137
 Morgan, V.T., 290, 371
 Mori, S., 137
 Moriyama, K., 103, 104, 138
 Morozov, V.G., 14
 Morris, D.J., 6, 8, 44
 Morris, E.W., 371, 380
 Mossaz, S., 309, 315, 335
 Mosyak, A., 82, 82, 91, 93, 94, 95, 100, 101,
 102, 103, 113, 114, 115, 152, 153, 154,
 155, 156
 Mowad, M., 321, 392
 Mudawar, I., 4, 7, 14, 24, 25, 26, 30, 31, 44,
 79, 80, 82, 89, 90, 91, 100, 101, 105,
 113, 118, 125, 137, 139, 140, 169, 195,
 202
 Mudawar, I., 137, 138
 Mujumdar, A.S., 291
 Muller, U., 195
 Muller-Steinhagen, R., 105
 Murphy, R.W., 48
 Murray, D.B., 384
- N**
- Naciri, J.K., 349
 Nada, S.A., 321, 392
 Nakano, M., 171
 Nakayama, A., 371
 Nakayama, Y., 305
 Nannei, E., 17
 Narai, H., 231
 Narain, J.P., 379
 Narayan, V., 182
 Narayana, P.S.A., 385
 Nariai, H., 195, 231, 249, 251
 Nasrallah, S.N., 306, 323, 362, 393
 Nazar, R., 390
 Neale, G., 123
 Nei, K., 182
 Nejat, A., 335, 341, 342

Nelson, D.B., 134, 135
 Nelson, R.A., 192
 Ng, M.L., 383, 384
 Nguyen, D.L., 380
 Nguyen, T.H., 380
 Nguyen, T.T., 270, 271, 272
 Nienow, A.W., 291
 Nimkar, N.D., 32, 33
 Nishihara, H., 138
 Nishikawa, K., 82, 82, 109
 Nishimura, T., 317
 Nishiyama, H., 352, 390
 Nitin, S., 368
 Nomura, T., 172
 Norberg, C., 327
 Norman, T.L., 270, 273, 274
 Normington, P.J., 46
 Normington, P.J.C., 6, 7, 46
 Norris, P.M., 90
 Nourgaliev, R.R., 82
 Novotny, J.L., 231, 250
 Nowak, M., 317
 Nuhait, A., 323, 362, 393

O

O'Connor, J.P., 33, 34, 35, 36
 O'Donovan, T.S., 384
 Ochi, Y., 317
 Ogata, S., 317
 Ogawa, K., 377
 Oh, C.H., 202, 208
 Oh, C.Y., 130, 132, 134
 Oh, H.K., 118
 Oh, J.T., 118, 130, 132, 134
 Ohadi, M.M., 138
 Ohguchi, K., 87
 Ohira, H., 138
 Ohkawara, M., 201, 208
 Okajima, A., 327
 Oktay, S., 25
 Olatunji, T.V., 306, 323
 Olson, D.R., 238, 254
 Ong, C.I., 130, 133
 Osano, Y., 317
 Ose, Y., 270, 274, 275, 276
 Ota, T., 352, 390
 Ousaka, A., 138
 Owens, R.G., 316, 349
 Owhaib, W., 105, 128

P

Padki, M.M., 152
 Pais, C., 26
 Paliwal, B., 363, 368, 395
 Palm, B., 82, 84, 85, 86, 87, 105, 128, 130
 Pamitran, A.S., 118, 130, 132, 134
 Pan, C., 82, 82, 95, 105, 169
 Pan, D.-D., 231, 232, 233, 234, 235, 237, 240, 241, 250, 251
 Pan, T., 117
 Pancallo, E.A., 91, 93, 94, 113, 114
 Panda, S.K., 335, 398
 Pang, F.G., 195
 Park, C.K., 230, 235, 244, 245
 Park, J.K., 233, 235, 237, 238, 240, 242, 243, 249, 251, 264, 266
 Park, J.W., 230, 232, 233, 235, 236, 238, 245, 249, 250, 251
 Park, K.A., 23, 25
 Park, S.H., 86, 87, 88, 89
 Parker, J.S., 12, 37, 38, 39
 Parker, M.E., 86
 Pasamehmetoglu, K.O., 19
 Pascal, J.P., 307, 309, 333, 339, 342, 390
 Pascal, M., 137
 Patel, V.A., 352
 Patil, R.C., 335, 398
 Patnaik, B.S.V., 385
 Patnana, V.K., 334, 339, 340, 341, 348, 371, 375, 376, 378, 379
 Paul, E.L., 291
 Pavlov, Y.M., 17, 23
 Pearson, J.R.A., 337
 Pease, R.F., 79, 82
 Pedrizetti, G., 349
 Pehlivan, K.K., 96
 Peles, Y., 166, 168, 169, 192, 195
 Pence, D., 182
 Peng, X.F., 87, 89, 90, 91, 92, 105, 121, 122, 170, 172
 Perera, R.N., 390
 Perry, C.W., 191
 Peterka, J.A., 380
 Petersen, E.E., 317, 332, 341, 371
 Peterson, G.P., 90, 105, 121, 122
 Peterson, P.F., 270, 271, 272
 Petrovic, A., 238, 239, 249
 Pettersen, J., 105, 128
 Pfahler, J., 137

Phillips, B.J., 377
 Phillips, R.J., 79
 Piau, J.M., 317
 Picornell, P.M., 48
 Pinho, F.T., 318, 319, 329, 335, 348
 Pipe, C.J., 318, 335
 Pisano, A.P., 90, 91
 Plummer, D.A., 96
 Pogrebnyak, E., 95, 100, 101, 102, 103, 114,
 115, 152, 153, 154, 155, 156
 Poirier, D., 89
 Poling, B., 370
 Pop, I., 390
 Popel, A.S., 349
 Popiel, C.O., 396
 Prakash, R., 398
 Prausnitz, J.M., 370
 Premoli, A., 173
 Prhashanna, A., 306, 323, 324, 327, 328, 329,
 330, 334, 335, 362, 364, 380, 381, 384,
 393
 Price, D.C., 33, 34, 35, 36
 Prina, A., 173
 Prins, J.A., 379
 Pritchard, W.G., 349
 Proudman, I., 337
 Purdy, D.J., 46
 Puris, B.I., 317, 377

Q

Qi, S., 202, 206
 Qian, Y.H., 82
 Qiu, T.Q., 90
 Qu, W., 79, 89, 90, 100, 101, 105, 113, 125,
 137, 139, 195, 202
 Quan, X.J., 82
 Quere, D., 188
 Quiben, J.M., 140
 Qureshi, Z.H., 385

R

Raghavan, V.R., 350
 Rahman, M.M., 79, 82
 Rainey, K.N., 10, 11, 14, 15, 43, 44, 49
 Rainey, P.G., 317, 318
 Raithby, G.D., 396
 RamaPrasad, C.S., 250, 251, 262, 263, 264,
 265, 269

Ramilson, J.M., 19
 Rao, B.K., 377
 Rao, M.K., 319, 334, 341, 350, 351
 Rao, P.K., 306, 319, 320, 321, 322, 323, 327,
 329, 330, 331, 335, 336, 352, 354, 363,
 366, 367, 368, 369, 390, 395, 397
 Rath, C.D., 190
 Ravigururajan, T.S., 103, 113
 Reid, R.C., 370
 Ren, L., 137
 Revankar, S.T., 270, 273, 274
 Revellin, R., 83, 96, 97, 105, 125, 133, 195,
 202
 Reymond, O., 384
 Ribatski, G., 82, 95, 96, 97, 98, 105, 114, 125,
 127, 128, 129, 131, 186
 Rice, C.L., 123
 Richardson, J.F., 290, 291, 292, 295, 315, 370
 Richardson, P.D., 380
 Richardson, S., 349
 Richter, D., 316, 317
 Ricque, R., 48
 Ridgley, P.J., 317
 Rindt, C.C.M., 385
 Roach Jr.
 G.M., 87, 152
 Roach, G.M., 195
 Rockwell, D., 318
 Roday, A.P., 195
 Rodin, G.J., 308, 333, 341
 Rogers, J.T., 89
 Rohsenow, W.M., 1, 2, 162, 163, 164, 191
 Rowlinson, J.S., 86
 Rozenblit, R., 91, 93, 94, 113, 114
 Rudolf Carl, P.M., 48

S

Sa, J.-Y., 385
 Sada, H., 321
 Sadatomi, M., 182
 Sadowski, D.L., 105, 125
 Saha, S.K., 156
 Sahin, M., 316, 349
 Sahu, A.K., 306, 319, 320, 321, 322, 323, 324,
 327, 328, 329, 330, 331, 334, 335, 336,
 341, 350, 351, 352, 354, 362, 363, 364,
 365, 366, 367, 368, 369, 390, 393, 395,
 397
 Saisorn, S., 83, 133, 134, 144

- Saita, F.A., 85
 Saitoh, S., 116, 124, 125, 126, 134
 Saitoh, T., 380
 Saiz-Jabardo, J.M., 95
 Sajik, T., 380
 Sakakibara, M., 137
 Sakamatapan, K., 82, 83, 128, 130, 131, 132
 Sakamoto, S., 169
 Salcudean, M., 89
 Sanitjai, S., 371
 Sano, Y., 317, 348
 Sarhan, A., 396
 Sarma, G.K., 385
 Sarpkaya, T., 317, 318
 Sasmal, C., 336, 366, 367, 368, 369, 390, 392, 396, 397
 Satheesh, V.K., 398
 Sathyamurthi, V., 30, 31, 34
 Sato, T., 89, 162, 163, 164
 Satoh, H., 170
 Saylor, J.R., 17, 18, 23, 24
 Schewe, G., 305
 Schmeckenbecher, A.F., 25
 Schmidt, J., 103, 114, 138, 139
 Schmitt, D., 165
 Schneiderman, L.L., 6
 Schowalter, W.R., 332
 Schreel, K.R.A.M., 252, 253, 254, 255, 257, 259, 262
 Schrock, V.E., 14
 Sedighi, K., 393
 Seetharamu, K.N., 385
 Sefiane, K., 55, 82, 82
 Segal, Z., 95, 100, 101, 102, 103, 114, 115, 152, 153, 154, 155, 156
 Sehgal, B.R., 82, 84, 85, 86, 87
 Selerland, T., 398
 Sellin, R.H.J., 317
 Semeria, R., 48
 Semin, B., 349
 Serizawa, A., 80, 105, 176, 177, 178, 186, 187
 Serth, R.W., 371
 Sett, S., 36
 Shah, M.J., 317, 332, 371
 Shah, M.M., 201, 206, 207
 Shah, M.S., 250, 251, 262, 263, 264, 265, 269
 Shah, R.K., 80
 Shailesh, J., 80, 139, 140
 Shair, F.H., 341
 Shamsher, K., 390
 Shan, X., 82
 Shao, S.-F., 233, 235, 238, 242, 250, 251
 Shaqfeh, E.S.G., 316, 317
 Sharma, A., 327, 363, 368, 395
 Shen, S., 103
 Shenoy, A.V., 371
 Shibata, T., 317, 348
 Shibata, Y., 180, 181, 182
 Shibu, S., 398
 Shida, H., 171
 Shiferaw, D., 130, 134
 Shih, T.M., 380
 Shikazono, N., 187, 188, 189
 Shimamune, H., 48
 Shinimura, E., 128
 Shiralkar, B.S., 270, 271, 272
 Shoji, M., 169, 170, 172
 Shuai, J., 138
 Shukla, D.S., 250, 251, 262, 263, 264, 269
 Shulman, H.L., 16
 Shulman, Z.P., 317, 377
 Simon, T.W., 33
 Simpson, M.E., 246, 247
 Singh, S.G., 183
 Sivakumar, P., 306, 307, 311, 312, 315, 323, 335, 338, 341, 352, 354, 356, 357, 359, 371, 390
 Slattery, J.C., 371
 Sleicher, C.A., 370, 377
 Soares, A.A., 333, 334, 339, 342, 371, 375, 377, 385, 386
 Sobhan, C.B., 82
 Soehngen, E., 379
 Soehngen, E.E., 397
 Sohankar, A., 327
 Song, C.-H., 230, 231, 233, 235, 236, 237, 238, 240, 242, 243, 246, 247, 248, 249, 250, 251, 252, 260, 261, 262, 263, 264, 266, 267, 268, 269, 270, 275, 277, 280, 281
 Song, D., 364, 374
 Sophy, T., 321
 Sparrow, E.M., 371, 385
 Spelt, P.D.M., 398
 Spiesman, P.H., 165, 166, 167
 Sridharan, A., 183
 Srikanth, S., 306, 323, 324, 362, 393
 Srinivas, A.T., 334, 385
 Staate, Y., 114
 Stack, D., 306, 319, 352
 Staub, F.W., 89

Steenhoven, A.A.V., 385
 Steinberg, V., 315
 Steimbrenner, J.E., 187
 Steinke, M.E., 100, 102, 103, 105, 119, 336
 Stephan, P.C., 112
 Su, F.Q., 128
 Su, M., 41, 42
 Su, Q., 103
 Sudo, Y., 201, 208
 Sugihara-Seki, M., 352
 Sukanek, P.C., 385
 Sukhatme, S.P., 385
 Sumer, B.M., 290, 302, 305, 306, 319, 340, 349, 352
 Sun, H., 91
 Sun, K.H., 22
 Sun, L., 114, 118
 Suo, M., 80
 Sutherland, L.A., 134, 135
 Suwa, S., 321
 Suzuki, K., 384
 Suzuki, K., 170, 171, 172
 Swire, H.V., 385
 Szewczyk, A.A., 371

T

Tachibana, F., 16
 Tadrist, L., 82, 105
 Taitel, Y., 95, 96
 Takagi, S., 170, 172
 Takamasa, T., 138, 187
 Takamastu, H., 26, 27, 28
 Takase, K., 270, 274, 275, 276
 Takashi, K., 377
 Takayama, S., 188
 Takemura, F., 172
 Takeuchi, M., 384
 Tamura, N., 138
 Tanaka, Y., 170
 Taneda, S., 304
 Tang, Y.S., 191
 Tange, M., 170, 172
 Tanida, Y., 305
 Tanimoto, A., 137
 Tanner, R.I., 290, 292, 295, 308, 333, 337, 341, 342
 Tanoue, K., 317
 Taoka, Y., 352
 Tavener, S.J., 349

Taylor, J.B., 165
 Teke, I., 380
 Telionis, D.P., 317
 Texier, A., 321
 Thom, A., 304
 Thome, J.R., 26, 82, 82, 83, 89, 96, 97, 103, 105, 113, 114, 125, 127, 130, 133, 134, 140, 195, 202
 Thompson, M.C., 306, 319, 323, 352
 Thompson, S.M., 86
 Thonon, B., 105
 Thulasidas, T.C., 190
 Tian, S., 80, 139, 140
 Tian, Y.S., 132
 Tibirica, C.B., 95, 96, 97, 98, 125, 127, 128, 129, 131, 186
 Tien, C.L., 86, 87, 88, 89, 90
 Tildsley, D.J., 86
 Ting, D.S.-K., 306, 319, 323, 352
 Tiselj, I., 103
 Toda, S., 250, 251, 252
 Tolman, R.C., 87
 Tong, J.C.K., 371
 Tong, L.S., 82, 191
 Tong, W., 138
 Torakai, K., 48
 Torikai, K., 170
 Tousignat, L., 5
 Tran, T.N., 101, 105, 117, 140
 Traschsel, F., 189
 Tripathi, A., 398
 Triplett, K., 105, 125, 138
 Truong, B., 63, 64, 65
 Tseng, F.C., 105
 Tseng, F.G., 95
 Tsutsui, K.T., 86
 Tsutsui, M., 47
 Tuckerman, D.B., 79, 82
 Turgut, S., 317
 Turki, S., 306, 323, 336, 362, 363, 365, 393, 395

U

U.S. NRC, 227, 270
 Udell, K.S., 90, 91
 Uehara, H., 384
 Ueno, I., 171
 Ujereh, S., 30, 31
 Ullmann, A., 96

Unal, C., 19, 192
 Unal, M.F., 318
 Upadhyay, S.N., 291, 316, 332, 371, 377, 378
 Urban, M., 317
 Ursenbacher, T., 96
 Usui, H., 317, 348, 371, 377
 Utaka, Y., 190

V

Vahidkhah, K., 335, 341, 342
 Vaillancourt, M., 96
 Van Der Geld, C.W.M., 252, 253, 254, 257
 Van Der Geld, C.W.M.V., 252, 253, 254, 255, 259, 262
 Van Dyke, M., 305, 337
 Van Wissen, R.J.E., 252, 253, 254, 255, 257, 259, 262
 Vassallo, P., 50, 51
 Vemuri, S., 37
 Veno, K., 377
 Verma, N., 349, 350
 Veziroglu, T.N., 152
 Vigneron, S., 187
 Vijaysri, M., 398
 Villimpoc, V., 385
 Vlasie, C., 82, 82
 von Rohr, P.R., 189

W

Walton, A.J., 82, 82
 Walton, J.P.R.B., 86
 Wambsganss, M.W., 101, 105, 117, 140
 Wang, B.X., 87, 89, 90, 91, 92, 105, 121, 122, 170, 172
 Wang, E., 165, 168
 Wang, E.N., 82, 82, 109
 Wang, F.-M., 187, 188
 Wang, G., 156, 157, 171, 172
 Wang, G.D., 82, 99, 100, 101, 103, 105, 192
 Wang, H., 170, 172
 Wang, K.-C., 390
 Wang, P., 380
 Wang, Q., 152
 Wang, R., 202, 206
 Wang, T.Y., 371
 Wang, Z.J., 385
 Warrior, G.R., 117

Warrington, R.Q., 137
 Watanabe, K., 14, 22, 23, 317
 Watel, B., 105
 Watwe, A.A., 7, 8, 11, 14, 17, 18, 19, 20, 21, 24, 47, 49, 65
 Webb, R.L., 26, 105, 138
 Wei, J.J., 26, 27, 28
 Weimer, J.C., 238, 254
 Wen, C.-Y., 348
 Wen, D., 55, 61, 62
 Wen, D.S., 105
 Weng, J.G., 86, 87, 88, 89
 Werner, C., 137
 Wesfreid, J.E., 306, 323
 Westerberg, K.W., 377
 Westwater, J.W., 3, 46
 White, E., 82, 83
 White, J.W., 383
 Whitehead, R., 123
 Whitney, M.J., 308, 333, 341
 Wicks III, M., 140, 144
 Widom, B., 86
 Wieringa, J., 252, 253, 254, 257
 Wiland, E., 306, 319, 352
 Wilks, G., 380
 Williams, M.J., 385
 Williamson, 302, 304, 305, 306, 340, C.H.K.
 Willistein, D.A., 162, 163, 168, 169, 192
 Winterton, R.H.S., 67, 89, 105, 118, 126
 Wojtan, L., 82, 105, 114, 125, 202
 Wojtkowiak, J., 396
 Wolf, C.J., 371
 Wollersheim, D.E., 383, 384
 Wong, K.-L., 385
 Wong, M., 87
 Wongwises, S., 82, 83, 128, 130, 131, 132, 133, 134, 144
 Woods, J.K., 398
 Wu, H., 156, 157
 Wu, H.Y., 82, 192
 Wu, P.Y., 137
 Wu, S.-R., 385
 Wu, W., 41, 42
 Wu, W.T., 95
 Wu, X.-Z., 231, 232, 233, 234, 235, 237, 238, 240, 241, 242, 250, 251
 Wu, X.B., 137
 Wu, Z., 81, 105, 109, 119, 120, 144, 148, 149, 150, 151, 202

X

Xia, Z.Z., 135
 Xu, J.L., 103, 105
 Xu, L., 202, 206

Y

Yan, J.-J., 231, 232, 233, 234, 235, 237, 238,
 240, 241, 242, 250, 251
 Yan, Y., 101, 105, 128
 Yang, C., 137
 Yang, K.T., 231, 250
 Yang, S.K., 230, 235, 244, 245
 Yang, W.J., 86, 90
 Yang, Y-T., 385
 Yang, Y.J., 137
 Yang, Y.M., 13, 47, 95
 Yang, Z.L., 82, 84, 85, 86, 87
 Yao, L.S., 379
 Yao, S.C., 95
 Yarin, L.P., 82, 82, 114
 Yarrusso, B.J., 291
 Yasuoka, K., 87
 Ye, S., 202
 Yeow, A.Y., 398
 Yokomizo, T., 306, 319, 352
 Yokoya, S., 192
 Yoo, J., 65, 66
 Yoshihara, M., 169
 You, S.M., 7, 10, 11, 12, 14, 15, 18, 33, 34,
 35, 36, 38, 43, 44, 46, 48, 49, 50, 51, 52,
 65, 66, 67
 Youn, Y.J., 252, 258, 259, 260, 261,
 266, 268
 Young, P.J.S., 352
 Young, R.J., 231, 250
 Yousefi, T., 390, 392

Yovanovich, M.M., 332, 352, 371, 390
 Yu, C.L., 3, 21
 Yu, D.I., 182
 Yu, W., 101, 117
 Yuan, Q., 189
 Yuasa, M., 170, 172
 Yue, J., 189
 Yuki, K., 172
 Yun, R., 128

Z

Zaghloul, M.E., 137
 Zakin, J.L., 91, 93, 94, 113, 114
 Zdravkovich, M.M., 289, 290, 302, 304, 305,
 316, 319, 349, 352, 363, 371
 Zeiser, T., 327
 Zeitoun, O., 323, 362, 380, 393, 396
 Zhang, D.C., 103, 105
 Zhang, L., 82, 82, 109, 165, 168
 Zhang, M., 105, 138
 Zhang, N.L., 90
 Zhang, P., 202, 206
 Zhang, W., 103, 105, 116, 137, 138, 140, 142,
 143, 144, 145, 147, 202
 Zhang, Y., 190
 Zhang, Z., 137
 Zhao, T.S., 105, 128
 Zhao, Y., 138
 Zhou, J.J., 105
 Zielinska, B.J., 306, 323
 Zingza, A., 371
 Zohar, Y., 87, 165
 Zovatto, L., 349
 Zuber, N., 2, 4, 17, 32, 44, 97, 135, 191
 Zukauskas, A., 371
 Zummo, G., 136, 156
 Zun, I., 105

SUBJECT INDEX

Page numbers followed by *f* and *t* indicate figures and tables, respectively.

A

- Active cavity radii
 - for bubble nucleation, 162–163, 163*f*
- Adiabatic two-phase flow
 - influence on void fraction, 175
- Aiding buoyancy configuration, 384
- Air clearing phase, of discharge process, 228
- Air-water two-phase flow
 - void fraction in microchannels and, 177–178, 177*f*
- Annular flow
 - influence on void fraction, 175
 - in microchannels, 83, 96, 97, 97*f*
- Axial temperature distributions
 - steam jet cavity, 240–242, 241*f*

B

- Base pressure coefficient, 304
- BCO. *See* Bubbling condensation oscillation (BCO)
- Bernath, L., 16
- Boiling, nucleate. *See* Nucleate boiling
- Boiling heat transfer, with porous coatings, 34–36
- Boiling water reactor (BWR) plants, 227
 - design of, 227
- Boundary conditions
 - non-Newtonian liquids, cylinder in, 292–302
- Boundary layer of thickness (δ)
 - flow regimes, 302
- Bubble collapse model, of MEB, 171–172, 171*f*
- Bubble growth. *See also* Bubble nucleation
 - flow patterns and, 204
 - stages of, 161–162, 161*f*
- Bubble growth, in microchannels, 82–99

- bubble length on bubble velocity, 98*f*
 - dynamics, on heated flat plate, 94*f*
 - flow regime transition, 85–92, 86*f*, 87*f*, 88*f*, 92*f*
 - evaporating space in, 91
 - fictitious boiling in, 91
 - at incipient boiling, 89, 90*f*
 - liquid phase change transition in, 89–91
 - nucleate boiling and, 87
 - nucleation in. *See* Nucleation
 - surface tension on, 85–87, 89*f*
 - in narrow channel
 - behavior, 84–85, 84*f*, 85*f*
 - movement, 86*f*, 87*f*
 - stages, 93*f*
 - visualization, 93–99, 93*f*, 94*f*
- Bubble nucleation. *See also* Onset of nucleate boiling (ONB)
 - on heated surface, 160–164, 161*f*
 - active cavity radii for, 162–163, 163*f*
 - bubble growth, stages of, 161–162, 161*f*
 - condition for, 161
 - in microchannels, 164–172
 - in microchannels
 - criteria for, 165
 - effect of nanostructures, and flow boiling in microchannels, 169
 - and instability, 169
 - location of sites, 166, 168, 168*f*
 - microbubble emission boiling (MEB), 169–172, 170*f*, 171*f*
 - roughness, effect of, 165–166, 166*t*, 167*f*
 - overview, 159
- Bubble packing model, CHF on, 1–2
- Bubbling condensation oscillation (BCO), 230
- Bubbling mode, of DCC, 229, 230
- Bubbly flow
 - influence on void fraction, 174

Buoyancy effect
 aiding buoyancy configuration, 384
 cross-buoyancy effect, 384–385
 opposing buoyancy effect, 384
 BWR plants. *See* Boiling water reactor (BWR)
 plants

C

Carbon nanotube (CNT)
 arrays on FC-72 pool boiling, 30, 31*f*
 coated silicon surfaces, boiling curves for,
 30, 31*f*
 Cavities, surface enhancements, 31–32, 32*f*,
 33*f*, 34*f*
 Cavity size distributions
 variation in, sandpaper roughened surface,
 167*f*
 CFX-4.4 code
 in pool mixing analysis, 275, 276
 CFX-11 code
 in pool mixing analysis, 276–277
 CHF. *See* Constant heat flux (CHF); Critical
 heat flux (CHF)
 Chugging mode, of DCC, 229, 230
 Churn flow, in microchannels, 83
 Circular cylinders
 flow regimes, 306–319, 307*f*, 308*f*, 309*t*,
 310*t*–312*f*, 313*t*, 314*t*
 heat transfer, 370–390
 heat transfer, in non-Newtonian liquids,
 370–390
 forced convection regime, 371–379,
 373*f*–374*f*, 376*f*, 378*f*–379*f*
 free convection regime, 379–384,
 381*f*–384*f*
 mixed convection regime, 384–390,
 386*f*–389*f*
 mechanical aspects, in non-Newtonian
 liquids, 332–351
 drag phenomena, 341–348, 343*t*–344*t*,
 345*f*–347*f*, 348*t*
 effect of confinement, 349–351, 351*t*
 surface pressure distribution, 338–341,
 339*f*–341*f*
 non-Newtonian liquids, heat transfer,
 370–390
 CNT. *See* Carbon nanotube (CNT)
 Coalescing bubble (CB) regime, 82, 84
 Colburn j-factor, 375

Compressibility effect
 on friction factor. *See* Friction factor,
 compressibility effect on
 Compressible volume instabilities, 152, 153
 Condensation load, steam jet, 244–249, 245*f*,
 247*t*, 248*f*
 Condensation modes, in DCC, 229, 230
 Condensation oscillation (CO), 230
 FFT distributions, 244–245, 245*f*
 Confinement, effect of
 circular cylinder in non-Newtonian liquids,
 349–351, 351*t*
 Confinement number (*Co*), in microchannels,
 79
 Confinement transition criterion
 flow regime map, comparison of, 81*t*
 vs. unconfinement, 80*f*
 Constant heat flux (CHF), 293
 Constant wall temperature (CWT), 293
 Contact angle, on CHF, 66–67, 67*f*
 Convective confinement number, defined, 79
 Correlations, CHF, 200, 201*t*–202*t*
 Creeping flow regime, 341
 Critical cavity radius
 defined, 163
 and wall superheat at ONB, 163–164
 Critical heat flux (CHF)
 correlations, 200, 201*t*–202*t*
 defined, 191
 mechanisms during flow boiling in
 microchannels, 191–192
 data comparison, 194–195, 196*f*
 factors influencing, 192
 L/D ratio, effect of, 195–196
 liquid-vapor interface near heater surface,
 193–194, 193*f*
 pool boiling application, 192–194
 surface tension, and viscous and inertia
 forces, relative influence of, 196–200,
 197*f*–199*f*
 theoretical model, 192–195
 overview, 190–191
 research directions, 205
 Critical heat flux (CHF), pool boiling
 on bubble packing model, 1–2
 in dielectric liquids and nanofluids, 1–77
 Haramura–Katto models of. *See*
 Macrolayer model
 Kutateladze–Zuber model of, 2–3, 2*f*
 macrolayer model of, 3–5, 4*f*

- overview, 1–5
- parametric effects. *See* Parametric effects, on CHF
- Critical regime, 305
- Cross-buoyancy effect, 384–385
- CWT. *See* Constant wall temperature (CWT)
- Cylinders, in non-Newtonian liquids. *See* Non-Newtonian liquids, cylinder in

D

- Dalton's law, 273
- DCC. *See* Direct contact condensation (DCC)
- Decay coefficient, 262
- Density wave oscillation (DWO), 152
- Dielectric liquid mixtures, on CHF, 46–48
 - FC-72, 47–48. *See also* FC-72, perfluorinated liquid
 - heater size, 23
 - heater thickness, 17
 - isopropanol on, 46
 - subcooling effects, 6–7
 - surface enhancement method in, 25
- Dilatant fluid behavior, 291
- Dimensionless parameters
 - non-Newtonian liquids, cylinder in, 292–302, 297*t*
- DIP. *See* Dual inline package (DIP)
- Direct contact condensation (DCC), of steam
 - jet in pool
 - condensation load, 244–249, 245*f*, 247*t*, 248*f*
 - condensation modes, 229, 230
 - condensation regime map for, 229–231, 229*f*–230*f*, 231*t*
 - interfacial HTC, 249–250, 251*t*
 - interfacial transport model, 250–251, 252*f*
 - overview, 227–229
 - pool mixing analysis, 269–281
 - regions in, 227–228, 228*f*
 - steam jet cavity. *See* Steam jet cavity
 - turbulent jet flow
 - analytical approaches for, 262–269
 - measurement of, 252–262
- Discharge processes, phases of, 227–228. *See also* Direct contact condensation (DCC)
- Dissolved gas effects, on CHF, 48–49
- Drag coefficient (C_D), 300
- Drag coefficient (C_{DP}), 300

- friction (C_{DF}), 300
- total, 300
- Drag phenomena
 - non-Newtonian liquids, circular cylinder in, 341–348, 343*t*–344*t*, 345*f*–347*f*
- Drag reducing polymer solutions, 306, 316
- Dual inline package (DIP)
 - subcooling enhancement for, 8, 10
- DWO. *See* Density wave oscillation (DWO)
- Dynamic instabilities, in microchannels, 150–152
 - density wave type oscillations, 152
 - pressure drop type oscillations, 151
 - thermal oscillations, 152

E

- EBO. *See* Explosive boiling oscillations (EBO)
- EDL. *See* Electric double layer (EDL)
- EDM. *See* Electrical discharge machining (EDM) process
- EE. *See* External expansion (EE)
- Elastico-viscous fluid behavior, 291
- Elastic turbulence, 315
- Electrical discharge machining (EDM)
 - process, 166
- Electric double layer (EDL), 122–123, 123*f*
- Ellipsoidal steam jet
 - expansion ratio and location for, 237, 237*f*
 - external expansion of, 235–236, 236*f*
- Elliptical cylinders
 - flow regimes, 319–321, 320*f*–323*f*
 - heat transfer, 390–392, 391*f*–392*f*
 - in non-Newtonian liquids, mechanical
 - aspects, 351–358, 353*t*–354*t*, 355*f*–357*f*, 359*f*
- Equilateral triangular cylinders
 - flow regimes, 323–326, 325*f*–329*f*
 - heat transfer, 393–395
 - in non-Newtonian liquids, mechanical
 - aspects, 362–363, 364*t*
- Evaporating space, defined, 91
- Expansion ratio
 - of steam jet cavity, 237, 237*t*
- Explosive boiling oscillations (EBO), 152
- External expansion (EE)
 - of ellipsoidal steam jet cavity, 235–236, 236*f*

F

Fast Fourier transform (FFT), 244
 distributions (CO vs. SC), 244–245, 245*f*
 FC-72, perfluorinated liquid
 CHF for, 5
 pool boiling, CNT arrays on, 30, 31*f*
 pressure effects on CHF for, 14–15, 16*f*
 subcooling effect on CHF for, 7–13
 as working fluid, 8, 9*f*
 FENE-p model, 316
 FFT. *See* Fast Fourier transform (FFT)
 Fictitious boiling, defined, 91
 Flow-behavior index, 295–296
 Flow boiling, 163
 data, correlation of frictional pressure drop
 on homogeneous model, 143*t*
 on separated flow model, 145*t*
 data, Dukler correlation and, 144*f*
 Hsu's model for, 165
 in microchannels, 164, 169. *See also*
 Microchannels
 CHF mechanisms during. *See* Critical
 heat flux (CHF)
 factors influencing, 192
 research directions, 206
 saturated, in microchannels, 106*t*–109*t*
 for saturated and subcooled, 105, 110–111
 void fraction measurement under, 183
 Flow instability
 effects on CHF in microchannels, 192
 research directions, 205
 Flow patterns
 and bubble growth, 204
 changes in, liquid film thickness
 measurement and, 186
 influence on void fraction, 174–176
 adiabatic two-phase flow, 175
 annular flow, 175
 bubbly flow, 174
 effect of channel aspect ratio, 182–183
 mist flow, 175
 slug flow, 174–175
 Flow patterns, in microchannels, 82–99, 83*f*
 alternate annular-rivulet flow, 83
 annular flow, 83, 96, 97, 97*f*
 bubble growth for. *See* Bubble growth, in
 microchannels
 churn flow, 83, 97

comprehensive flow map regime, 99*f*
 dispersed flow, 96, 97*f*
 downstream of ONB, 95*f*
 intermittent flow, 96, 97*f*
 on pressure drop, 139
 slug flow, 83, 97
 stratified flow, 96, 97*f*
 throat-annular flow, 83
 transition, 96–97, 97*f*
 upstream of ONB, 153*f*
 Flow regimes, 302–332, 303*f*
 circular cylinder, 306–319, 307*f*, 308*f*,
 309*t*, 310*t*–312*f*, 313*t*, 314*t*
 elliptic cylinder, 319–321, 320*f*–323*f*
 equilateral triangular cylinders, 323–326,
 325*f*–329*f*
 semicircular cylinders, 321–323, 324*f*–325*f*
 square cylinder, 326–332, 330*f*–331*f*
 Fluid-like (yielded) regions, 291
 Forced convection regime
 heat transfer in, 371–379, 373*f*–374*f*, 376*f*,
 378*f*–379*f*
 non-Newtonian liquids, governing
 equations, 296–298
 Free convection regime
 heat transfer in, 379–384, 381*f*–384*f*
 non-Newtonian liquids, governing
 equations, 298–302
 Frictional component of drag coefficient
 (C_{DF}), 300
 for forced convection, 300
 for free convection, 300
 Friction factor, compressibility effect on,
 135–136, 137
 Eckert number, variation of, 135*f*
 for laminar and turbulent flow of gases, 137
 Nusselt number, variation of, 135*f*

G

Grashof number (Gr), 298

H

Haramura–Katto models, of CHF. *See*
 Macrolayer model
 Heated surface
 bubble nucleation on, 160–164, 161*f*
 active cavity radii for, 162–163, 163*f*

- bubble growth, stages of, 161–162, 161*f*
 - condition for, 161
 - in microchannels, 164–172
 - Heater, on CHF
 - size, 22–24, 23*f*
 - surface effect, 24–44
 - surface enhancements. *See* Surface enhancements, heater
 - thermal conductivity, 15, 16, 17, 18
 - thermal properties, 15–22, 21*f*, 22*f*
 - thickness, 15–20
 - Heater surface orientation
 - and subcooling, on CHF, 7–8
 - Heat flux
 - on boiling curve, 113
 - heat transfer coefficient and, 127, 128
 - in microregion, 112, 112*f*
 - Heat transfer
 - research directions, 204–205
 - Heat transfer, in microchannels, 99–134
 - boiling curves, 113–122, 113*f*, 123–125, 124*f*
 - of R-134a in multiport minichannel, 131*f*
 - coefficient, 113–122, 113*f*
 - along tube perimeter, 125, 126, 127*f*
 - boiling, 114*f*
 - on boiling number, 115*f*
 - comparison of experimental average, 132*f*–133*f*
 - as function of local vapor quality, 103, 104*f*
 - heat flux and, 127, 128
 - parametric analyses of experimental results, 127–134
 - saturated boiling correlation, 105, 110–111
 - saturation temperature on, 128, 129*f*, 133
 - on thermodynamic equilibrium vapor quality, 101, 102*f*
 - vs. exit quality, 99, 100*f*
 - vs. Kandlikar correlation, 100, 101*f*
 - vs. vapor quality, 103, 104*f*
 - correlations, 114, 115*f*, 116–121, 119*t*, 120*f*
 - EDL in, 122–123, 123*f*
 - local heat transfer coefficient, 123–125, 126*f*, 127*f*
 - in parallel microchannels with working fluid
 - methanol, 121, 122*f*
 - saturated flow boiling, summary of, 106*t*–109*t*
 - size effect mechanism, 112–113, 112*f*
 - time interval between cycles on heat flux, 101, 102*f*
- Heat transfer, non-Newtonian liquids, 369–398
 - circular cylinder, 370–390
 - elliptical cylinder, 390–392, 391*f*–392*f*
 - equilateral triangular cylinder, 393–395
 - semicircular cylinder, 392–393, 394*f*
 - square cylinder, 395–398, 396*f*, 397*f*
- Heat transfer coefficient (HTC)
 - of DCC, 239
 - interfacial, 249–250
 - interfacial transport model, 250–251, 252*f*
 - proposed correlations for, 251*f*
 - nucleation sites in microchannels and, 166, 168, 168*f*
 - shear stress model, 249
 - surface renewal model, 249
- Herschel-Bulkley (Bi_{HB}) parameter, 315
- HFE-7100, Novec fluid
 - liquid subcooling on CHF of, 12*f*
 - pressure effects on CHF for, 14
- Homogeneous void fraction, 173, 182
- Hovering period, defined, 3
- Hsu's model for flow boiling, 165
- HTC. *See* Heat transfer coefficient (HTC)
- Hydraulic diameter
 - in microchannels, 78, 79
- ## I
- ICO. *See* Interfacial oscillation condensation (ICO)
 - In-containment refuelling water storage tank (IRWST), 227
 - Inertia force
 - effect on CHF modeling in microchannels, 196–200, 197*f*–199*f*
 - Instabilities, in microchannels, 150–156
 - compressible volume, 152, 153
 - dynamic. *See* Dynamic instabilities, in microchannels
 - flow pattern upstream ONB, 153*f*
 - parallel channel, 152, 153
 - stable and unstable flow boiling regimes, 157*f*
 - static, 151
 - time variation

Instabilities, in microchannels (*Continued*)
 of average and maximum heater temperature, 156*f*
 of fluid temperature, 155*f*
 of pressure drop, 154*f*

Instability
 nucleation and, 169

Interface instability model, of MEB, 171, 171*f*, 172

Interfacial HTC, 249–250
 interfacial transport model, 250–251, 252*f*
 proposed correlations for, 251*t*
 shear stress model, 249
 surface renewal model, 249

Interfacial oscillation condensation (ICO), 230

Interferometer technique
 for liquid film thickness measurement, 187

International thermonuclear experimental reactor (ITER) design, 274

IRWST. *See* In-containment refuelling water storage tank (IRWST)

Isolated bubble (IB) regime, 84

ITER. *See* International thermonuclear experimental reactor (ITER) design

J

Jetting mode, of DCC, 229, 230

K

Kandlikar, S.G.
 correlation, boiling heat transfer coefficient vs., 101*f*

Kutateladze–Zuber model, of CHF, 2–3, 2*f*

L

Laminar vortex shedding regime, 339

Laser confocal scanning microscopy (LSM)
 for liquid film thickness measurement, 189

Laser focus displacement meter
 for liquid film thickness measurement, 187

Laser induced fluorescence (LIF)
 for liquid film thickness measurement, 189

L/D ratio. *See* Length to diameter ratio (L/D ratio)

Length to diameter ratio (L/D ratio)

effect on CHF modeling in microchannels, 195–196

LIF. *See* Laser induced fluorescence (LIF)

Lift coefficient (C_L), 300

Lift force, 300, 348

Liquid droplet flow, 177

Liquid film thickness
 distribution, channel geometry and, 189–190, 189*f*
 factors, 184
 measurement
 with CCD camera, 187
 challenges in, 184–185
 flow pattern changes and, 186
 interferometer technique, 187
 laser confocal scanning microscopy (LSM), 189
 laser focus displacement meter technique, 187
 laser induced fluorescence (LIF), 189
 microscope used in, 186
 optical fluorescence imaging technique, 187–188
 optical interferometry, 188
 research directions, 203–204
 and results, 185–190
 visible light used in, 185
 overview, 184
 research directions, 203–206

Local heat transfer coefficient, in microchannels, 123–125, 126*f*, 127*f*

LOCV. *See* Loss of condenser vacuum (LOCV)

Loss of condenser vacuum (LOCV), 227

LSM. *See* Laser confocal scanning microscopy (LSM)

M

Macrolayer model, of CHF, 3–5, 4*f*
 hovering period in, 3

MARS method. *See* Multi-interfaces advection and reconstruction solver (MARS) method

MEB. *See* Microbubble emission boiling (MEB)

Mechanical loads
 and pool mixing analysis, 269–270

Method of characteristic (MOC)
 wave propagation by, 233

Microbubble emission boiling (MEB),
 169–172, 170*f*
 bubble collapse model of, 171–172, 171*f*
 interface instability model of, 171, 171*f*,
 172

Microchannels
 bubble growth in. *See* Bubble growth, in
 microchannels
 bubble nucleation in
 criteria for, 165
 effect of nanostructures, and flow boiling
 in microchannels, 169
 and instability, 169
 location of sites, 166, 168, 168*f*
 microbubble emission boiling (MEB),
 169–172, 170*f*, 171*f*
 roughness, effect of, 165–166, 166*t*, 167*f*
 CHF mechanism in. *See* Critical heat flux
 (CHF)
 defined, 78
 flow boiling in, 164, 169
 flow pattern in. *See* Flow patterns, in
 microchannels
 geometry, effects on liquid film distribution,
 189–190, 189*f*
 heat transfer with models. *See* Heat transfer,
 in microchannels
 hydraulic diameter in, 78, 79
 instabilities in. *See* Instabilities, in
 microchannels
 liquid film thickness measurements in. *See*
 Liquid film thickness
 oscillatory instabilities in, 80, 82
 overview, 77–82
 pressure drop in. *See* Pressure drop, in
 micro/minichannels
 thermofluid dynamics of boiling in, 77–158
 threshold, defined, 78–79
 two-phase flow in, liquid film thickness
 measurement during
 challenges, 184–185
 results, 185–190
 void fraction in, 176–183
 air-water two-phase flow, 177–178, 177*f*
 effect of channel aspect ratio on flow
 patterns and, 182–183
 entrance mixing zones, 176–177, 176*f*
 inlet mixing section, 178, 179*f*
 nitrogen-water flow, 180, 181*f*
 tube lengths and, 181–182

variation in, 179, 180*f*

Microporous enhancement coatings, 33–38,
 35*f*, 36*f*, 37*f*, 39*f*, 40*t*

Mist flow
 influence on void fraction, 175

Mixed convection regime
 heat transfer in, 384–390, 386*f*–389*f*
 non-Newtonian liquids, governing
 equations, 298

MOC. *See* Method of characteristic (MOC)

Multi-interfaces advection and reconstruction
 solver (MARS) method, 274–275

N

Nanofluids, 49–67

CHF enhancement
 Al_2O_3 , CuO, and diamond nanoparticles
 in, 64–65, 65*f*, 66*f*
 Al_2O_3 -ethanol nanofluids, 65–66, 67*f*
 contact angle on, 66–67, 67*f*
 copper nanoparticles in water, 56, 62*f*
 liquid pH on, 50, 52*f*
 nanoparticle size on, 50, 52*f*
 porosity on surface in, 50, 53*f*
 with pure water and alumina, zirconia,
 and silica nanofluids, 51–52, 54*f*, 55*f*
 roughness of heater, 56, 63*t*
 sandblasted plate heaters and, 61, 63, 64*f*,
 65*t*
 with silica–water nanofluids, 49–50,
 51*f*
 TiO_2 and Al_2O_3 nanoparticles in, 52–53,
 56*f*, 57*f*, 58*f*, 59*f*
 with water– Al_2O_3 nanofluids, 49,
 50–51, 50*f*, 54*t*
 with water- and alcohol-based nanofluids
 with CuO and SiO_2 nanoparticles,
 53–55, 60*f*
 water-based nanofluids, with alumina
 and titania particles, 58–59, 61, 63*f*,
 64*t*
 water-based nanofluids, with diamond,
 zinc oxide, and alumina nanoparticle,
 61, 63, 64*f*, 65*t*

Nanoscale surface modifications, 38–43,
 40*f*, 41*f*, 42*f*

Nanostructures
 effect on nucleation, 169

Nitrogen-water flow

microchannels in void fraction and, 180,
181*f*

Non-Newtonian liquids, cylinder in

boundary conditions, 292–302

dimensionless parameters, 292–302, 297*t*

flow regimes, 302–332, 303*f*

circular cylinder, 306–319, 307*f*, 308*f*,

309*t*, 310*t*–312*f*, 313*t*, 314*t*

elliptic cylinder, 319–321, 320*f*–323*f*

equilateral triangular cylinders, 323–326,

325*f*–329*f*

semicircular cylinders, 321–323,

324*f*–325*f*

square cylinder, 326–332, 330*f*–331*f*

governing equations, 292–302, 293*f*

forced convection regime, 296–298

free convection regime, 298–302

mixed convection regime, 298

heat transfer, 369–398

circular cylinder, 370–390

elliptical cylinder, 390–392,

391*f*–392*f*

equilateral triangular cylinder, 393–395

semicircular cylinder, 392–393, 394*f*

square cylinder, 395–398, 396*f*, 397*f*

mechanical aspects, 332–369, 333*t*–336*t*

circular cylinder, 332–351. *See also*

Circular cylinders

elliptical cylinder, 351–358, 353*t*–354*t*,

355*f*–357*f*, 359*f*. *See also* Elliptical

cylinders

equilateral triangular cylinder, 362–363,

364*t*. *See also* Equilateral triangular

cylinders

semicircular cylinders, 358–362,

360*f*–363*f*. *See also* Semicircular

cylinders

square cylinder, 363–369, 365*f*, 366*t*,

367*f*–369*f*. *See also* Square cylinders

overview, 289–291

Nucleate boiling, 1, 87, 89, 93

onset of. *See* Onset of nucleate boiling
(ONB)

Nucleation. *See also* Bubble nucleation

in microchannels, 89–91

minimum heat flux for, 91, 92*f*

and small bubble growth, 87

wall superheat for, 92*f*

Nusselt number (Nu), 301

O

Oldroyd (Od) parameter, 315

ONB. *See* Onset of nucleate boiling (ONB)

Onset of nucleate boiling (ONB)

bubble nucleation in microchannels,

164–172

criteria for, 165

effect of nanostructures, and flow boiling
in microchannels, 169

and instability, 169

location of sites, 166, 168, 168*f*

microbubble emission boiling (MEB),

169–172, 170*f*, 171*f*

roughness, effect of, 165–166, 166*t*,

167*f*

bubble nucleation on heated surface,

160–164, 161*f*

active cavity radii for, 162–163, 163*f*

bubble growth, stages of, 161–162, 161*f*

bubbles growth and, 89, 93

critical cavity radius and wall superheat at,
163–164

defined, 163

flow pattern downstream of, 95*f*

overview, 159

pressure-temperature relationship in vapor

bubble, 159–160, 160*f*

upstream of, flow pattern and, 153*f*

Opposing buoyancy effect, 384

Optical fluorescence imaging technique

for liquid film thickness measurement,

187–188

Optical interferometry

for liquid film thickness measurement, 188

Oscillatory instabilities

in microchannels, 80, 82

Over-expanded jet, 232–233, 234*f*. *See also*

Steam jet cavity

P

Painting technique, for microporous structures,
34, 35*f*, 36*f*

Parallel channel instability, 152, 153

Parametric effects, on CHF, 5–67

dielectric liquid mixtures, 46–48

dissolved gas effects, 48–49

heater length, 22–24, 23*f*

heater surface effect, 24–44

- heater thermal properties, 5–6, 15–22, 21*f*, 22*f*
- nanofluids, effects of. *See* Nanofluids, CHF enhancement
- pressure. *See* Pressure effects, on CHF
- subcooling. *See* Subcooling effects, on CHF
- surface orientation effect, 44–46, 45*f*
- working liquid, 5
- Particle image velocimetry (PIV), 252, 258
- Peclet number (Pe), 298, 299
- Penetration length, of steam jet cavity, 237–239, 239*f*
 - correlations for, 238, 238*t*
 - defined, 237
 - measurement, methods of, 238
- PIV. *See* Particle image velocimetry (PIV)
- Pool boiling
 - CHF. *See also* Critical heat flux (CHF), pool boiling
 - nucleate, 1
 - defined, 1
- Pool mixing analysis, 269–281
 - B&C test facility, 275, 277*f*
 - forced turbulent jet and steam jet models, 270, 271*f*, 272*f*
 - mechanical loads and, 269–270
 - multi-scale process of condensation-induced thermal mixing, 280–281
 - prediction vs. measured data, 272–273, 272*f*
 - quasi-steady-state case, 273–274, 274*f*
 - related issues and future perspectives, 279–281
 - SCRM model, 275–277, 278*f*
 - steam vent and jet trajectory in suppression pool, 270, 271*f*
 - temperature profiles in cylindrical water pool simulation, 279, 279*f*
 - thermal mixing and, 269, 270
 - thermal stratification and, 270
 - using CFX-4.4 code, 275, 276
 - using CFX-11 code, 276–277
 - using system analysis code, 270
 - TRACE, 273, 274
 - TRAC-G, 270, 271, 273
 - void fraction, predicted, 275, 276*f*
- Porous coatings, surface enhancements, 32–38, 35*f*, 39*f*, 40*t*
 - boiling heat transfer and, 34–36
 - microporous coating, 33, 35*f*
 - SEM images of porous graphite surface, 37–38, 37*f*
 - spraying and painting techniques, 34, 35*f*, 36*f*
- Power-law index (n), 297
 - Reynolds number and, 312, 312*f*
- Power-law model, 295–296
- Prandtl number (Pr), 296–297, 298
- Pressure drop, in micro/minichannels, 134–150
 - adiabatic two-phase, 148*t*
 - Chisholm parameter *C*, averages of, 146*t*–147*t*
 - distribution of database against different parameters, 150*f*
 - existing predicting methods, 149*t*
 - flow boiling, data for. *See* Flow boiling
 - flow compressibility effect, 135–136, 135*f*, 136*f*, 137
 - flow patterns on, 139
 - Li – Wu correlation, assessment of, 151*t*
 - predominant factors, variation of, 137–150
 - predominant forces, variation of, 137
 - Reynolds number on, 138
 - of single- and two-phase flow in tubes and channels, 138*f*
 - surface roughness, effect of, 136
 - time variation of, 154*f*
 - two-phase frictional, 141*t*–142*t*
 - vs. boiling number for n-heptane and water, 138, 139*f*
 - vs. Reynolds number for microchannel, 139, 140*f*
- Pressure drop type oscillations, dynamic instabilities, 151
- Pressure effects, on CHF, 13–15, 13*f*
 - for FC-72, 14
 - in FC-72 for various liquid temperatures, 14–15, 16*f*
 - on saturated CHF, 14, 15*f*
- Pressure suppression pool (PSP), 227
- Pressure suppression test facility (PSTF), 270
- Pressure-temperature relationship
 - in vapor bubble, 159–160, 160*f*
- Protrusions, surface enhancements, 26–31, 27*f*, 28*f*, 29*f*, 30*f*, 31*f*
- PSP. *See* Pressure suppression pool (PSP)
- PSTF. *See* Pressure suppression test facility (PSTF)

R

- Rayleigh number (Ra), 298–299
 Recirculation length (L_r), 304
 Reynolds number (Re), 296–297, 302, 304
 defined, 174
 flow regime and, 302–306
 circular cylinder, 306–308, 307*f*–308*f*, 309*t*, 311–312, 312*f*, 313*t*
 elliptic cylinder, 309*t*, 313*t*, 319–320, 320*f*–323*f*
 equilateral triangular cylinder, 309*t*, 313*t*, 323–326, 326*f*–327*f*
 semicircular cylinders, 309*t*, 313*t*, 321–323, 324*f*–325*f*
 square cylinders, 309*t*, 310*t*, 313*t*, 328–330, 330*f*–331*f*
 fluid inertia and, 302
 for microchannel, pressure drop vs., 139, 140*f*
 power-law index and, 312, 312*f*
 on pressure drop, 138
 Richardson number, 294, 298
 Roughness
 effect on nucleation in microchannels, 165–166, 166*t*, 167*f*
 surface. *See* Surface roughness

S

- Safety/relief valves (SRVs), 227
 Sandpaper polishing, 165–166
 Saturated boiling, correlation for, 105, 110–111
 SBWR. *See* Simplified boiling water reactor (SBWR) design
 SC. *See* Stable condensation (SC)
 Scanning electron microscope (SEM) images
 of porous graphite surface, 37–38, 37*f*
 SCRM. *See* Steam condensation region model (SCRM)
 SEM. *See* Scanning electron microscope (SEM) images
 Semicircular cylinders
 flow regimes, 321–323, 324*f*–325*f*
 heat transfer, 392–393, 394*f*
 in non-Newtonian liquids, mechanical aspects, 358–362, 360*f*–363*f*
 Shape, of steam jet cavity, 232–236
 analysis model for, 233, 234*f*
 conical, 232
 divergent, 232
 ellipsoidal, 232
 high steam mass flux, 232, 233*f*
 over-expanded, 232–233, 234*f*
 sonic vs. highly under-expanded supersonic conditions, 235*f*
 under-expanded, 232, 233–235, 234*f*, 236*f*
 wave propagation by MOC and, 233
 Shear rate, 290–291
 Shear stress, 290
 Shear stress model, 249
 Shear stress transport (SST) model, 278
 Shear-thickening fluid behavior, 291
 Shear-thinning behavior
 non-Newtonian fluid and, 290–291, 296, 318
 Shear-thinning power-law fluid
 Stokes paradox and, 337
 Simplified boiling water reactor (SBWR)
 design, 271
 Single-phase heat transfer, 203
 Slug flow
 influence on void fraction, 174–175
 in microchannels, 83
 Solid-like (unyielded) regions, 291
 Spraying technique, for microporous structures, 34, 35*f*, 36*f*
 Square cylinders
 flow regimes, 326–332, 330*f*–331*f*
 heat transfer, 395–398, 396*f*, 397*f*
 in non-Newtonian liquids, mechanical aspects, 363–369, 365*f*, 366*t*, 367*f*–369*f*
 SRVs. *See* Safety/relief valves (SRVs)
 SST. *See* Shear stress transport (SST) model
 Stable condensation (SC), 230
 FFT distributions, 244–245, 245*f*
 Stagnant zone, 317
 Static instabilities, in microchannels, 151
 Steady flow regime, 385, 393
 Steam cavity, in DCC, 228–229, 228*f*
 Steam condensation regime map, 229–231, 229*f*–230*f*, 231*t*
 three-dimensional, 230–231, 231*f*–232*f*
 Steam condensation region model (SCRM), 236, 266, 266*f*, 275–277, 278*f*
 Steam discharge phase, of discharge process, 228
 Steam jet cavity, 228–229, 228*f*
 expansion ratio, 237, 237*t*

- penetration length, 237–239, 239*f*
 - correlations for, 238, 238*t*
 - defined, 237
 - measurement, methods of, 238
 - shape of, 232–236
 - analysis model for, 233, 234*f*
 - conical, 232
 - divergent, 232
 - ellipsoidal, 232
 - high steam mass flux, 232, 233*f*
 - over-expanded, 232–233, 234*f*
 - sonic vs. highly under-expanded
 - supersonic conditions, 235*f*
 - under-expanded, 232, 233–235, 234*f*, 236*f*
 - wave propagation by MOC and, 233
 - thermal-hydraulic condition of, 240–243
 - axial temperature distributions, 240–242, 241*f*
 - axial temperature profiles at center line, 240*f*
 - pitot impact pressure distributions of
 - moist air jet, 242, 243*f*
 - Steam jet condensation load, 244–249, 245*f*, 247*t*, 248*f*
 - Steam jet-induced turbulent jet flow
 - analytical approaches for, 262–269, 264*f*, 268*f*, 269*f*
 - measurement of, 252–262
 - comparison with Tollmien's theoretical model, 259–260, 260*f*
 - condensing steam jet model, 258, 259*f*
 - experimental set-up/apparatus, 252–253, 253*f*, 258*f*, 261, 261*f*
 - schematics of, 253, 254*f*
 - self-similar velocity profiles, 255–256, 256*f*, 262
 - temperature effect on, 253–254
 - vs. classical single-phase turbulent jet, 254, 255*f*
 - Stokes paradox, 337
 - shear-thinning power-law fluid, 337
 - Strouhal number (St), 301, 318
 - Structural disjoining pressure
 - defined, 55
 - with DLVO forces, 56, 61*f*
 - four-zoned microlayer model of thermal nanofluids and, 55–56, 61*f*
 - interfacial shapes with and without nanoparticles, 56, 62*f*
 - Subcooling effects, on CHF, 6–13
 - for DIP, 8, 10
 - at elevated pressure, 9*f*, 10*f*
 - for FC-72, 7–13
 - heater orientation and, 7–8
 - saturated conditions, 10, 11*f*
 - subcooled conditions, 12–13, 12*f*
 - test heater design for, 10, 11*f*
 - Subcritical regime, 305
 - Supercritical regime, 305
 - Surface enhancements, heater, 24–44
 - cavities, 31–32, 32*f*, 33*f*, 34*f*
 - correlations, 43–44, 43*f*
 - nanoscale surface modifications, 38–43, 40*f*, 41*f*, 42*f*
 - porous coatings, 32–38, 35*f*, 36*f*, 37*f*, 39*f*, 40*t*
 - protrusions, 26–31, 27*f*, 28*f*, 29*f*, 30*f*, 31*f*
 - Surface orientation effect, on CHF, 44–46, 45*f*
 - Surface pressure distribution
 - circular cylinder in non-Newtonian liquids, 338–341, 339*f*–341*f*
 - Surface renewal model, 249
 - Surface roughness
 - flow in microchannels, 136
 - Surface tension
 - effect on CHF modeling in microchannels, 196–200, 197*f*–199*f*
 - Surface tension (γ), of bubbles
 - on flow regime transition, 85–87, 89*f*
 - System analysis code, in pool mixing analysis, 270
 - TRACE, 273, 274
 - TRAC-G, 270, 271, 273
- ## T
- TC. *See* Transitional region from chugging to CO (TC)
 - Temperature-pressure relationship
 - in vapor bubble, 159–160, 160*f*
 - Thermal-hydraulic condition
 - of steam jet cavity, 240–243, 240*f*, 241*f*, 243*f*
 - Thermal mixing, 269, 270. *See also* Pool mixing analysis
 - Thermal oscillations, dynamic instabilities, 152

Thermal stratification, 270. *See also* Pool mixing analysis

Three-dimensional condensation regime map, 230–231, 231*f*–232*f*

Throat-annular flow, in microchannels, 83

Time-dependent fluid behavior, 291

Time-periodic regime, 339

TOLFW. *See* Total loss of feedwater (TOLFW)

Tollmien's theoretical model
vs. steam jet-induced turbulent flow model, 259–260, 260*f*

Tolman's length (δ)
for bubbles, 89*f*

Total loss of feedwater (TOLFW), 227

Transitional region from chugging to CO (TC), 230

Transition boiling, 169

Tube perimeter, heat transfer coefficient along, 125, 126, 127*f*

Two-phase flow
in microchannels, liquid film thickness measurement during challenges, 184–185 results, 185–190

U

Ultrasound
on pool boiling heat transfer, 47

Under-expanded jet, 232, 233–235, 234*f*, 236*f*. *See also* Steam jet cavity analysis model of steam cavity for, 233, 234*f*

V

Vapor bubble
pressure-temperature relationship in, 159–160, 160*f*

Viscoelastic fluid behavior, 291

Viscoplastic behavior, 291

Viscosity, of non-Newtonian fluid
rate of deformation tensor and, invariants of, 295

Viscous force
effect on CHF modeling in microchannels, 196–200, 197*f*–199*f*

Void fraction
defined, 172–173
flow pattern influence on, 174–176
adiabatic two-phase flow, 175
annular flow, 175
bubbly flow, 174
mist flow, 175
slug flow, 174–175
homogeneous, 173, 182
measurement under flow boiling, 183
in microchannels, 176–183
air-water two-phase flow, 177–178, 177*f*
effect of channel aspect ratio on flow patterns and, 182–183
entrance mixing zones, 176–177, 176*f*
inlet mixing section, 178, 179*f*
nitrogen-water flow, 180, 181*f*
tube lengths and, 181–182
variation in, 179, 180*f*
overview, 172–174
research directions, 203–204

Volume flow fraction
defined, 173

Vortex-shedding regime, 304–305

Vorticity (ω), 300

W

Wake region
flow regimes, 302, 304

Wall superheat
and critical cavity radius at ONB, 163–164

Water clearing phase, of discharge process, 228

Wave propagation
by MOC, 233

Weber number
defined, 174

Weissenberg number, 317

Working fluid
on CHF, 5
FC-72 as, 8, 9*f*